GHENT UNIVERSITY

FACULTY OF SCIENCES

GHENT UNIVERSITY

DOCTORAL THESIS

Muon Detector Development for the CMS Phase-2 Upgrade and Muon Radiography Applications

Author:
Amrutha Samalan

Supervisors:
Prof. Dr. Michael Tytgat
Prof. Dr. Didar Dobur

CERN-THESIS-2024-025
26/03/2024

A thesis submitted in fulfillment of the requirements for the degree of Doctor of Science: Physics

Faculty of Sciences
Department of Physics and Astronomy

March 19, 2024

Supervisors:	Prof. Dr. Michael Tytgat (UGent and VUB)
	Prof. Dr. Didar Dobur (UGent)
Chairman of the Examination Board:	Prof. Dr. Toon Verstraelen (UGent)
Members of the Examination Board:	Prof. Dr. Gabriella Pugliese (POLIBA)
	Prof. Dr. Eduardo Cortina (UCLouvain)
	Dr. Luigi Cimmino (UNINA)
	Prof. Dr. Matthieu Boone (UGent)
	Prof. Dr. Christophe Detavernier (UGent)

"Fall in love with some activity, and do it! Nobody ever figures out what life is all about, and it doesn't matter. Explore the world. Nearly everything is really interesting if you go into it deeply enough. Work as hard and as much as you want to on the things you like to do the best. Don't think about what you want to be, but what you want to do. Keep up some kind of a minimum with other things so that society doesn't stop you from doing anything at all."

— Richard P. Feynman

Abstract

This work contributed to the advancement of muon detector technology for the CERN Compact Muon Solenoid (CMS) experiment and explored broader applications of muon detectors in interdisciplinary research. The CMS experiment at the Large Hadron Collider (LHC) is undergoing crucial upgrades in preparation for the upcoming high-luminosity phase of the accelerator. The research presented in this thesis includes the design and construction of new Resistive Plate Chambers (RPCs) to enhance the CMS muon system. To address the concerns related to the high global warming potential of the gas mixtures that are currently used in RPCs, alternative, eco-friendly mixtures were explored. Additionally, investigations were undertaken to study muon detectors for interdisciplinary applications, particularly for muon radiography—a technique utilising cosmic-ray muons to study the internal structures of large-scale objects. As part of a project to develop a light-weight, portable muon radiography telescope, small-size glass-RPCs were designed. Further insights into this imaging technique were gained through participation in the MURAVES project, where scintillator-based muon telescopes are used to study the internal structure of the active Mt. Vesuvius volcano near Naples, Italy.

Contents

Abstract **vii**

Introduction **1**

I The CMS RPC System Upgrades for HL-LHC **5**

1 The CMS Experiment and the Muon System Upgrade **7**
1.1 Introduction . . . 7
1.2 The Large Hadron Collider . . . 7
1.2.1 The LHC Machine . . . 8
1.2.2 LHC Beam Injection . . . 10
1.3 The CMS Experiment . . . 11
1.3.1 Detector Layout . . . 12
1.3.2 Tracking System . . . 13
1.3.3 Calorimeters . . . 14
1.3.4 Solenoid Magnet . . . 15
1.3.5 Muon System . . . 16
1.3.6 Trigger and Data Acquisition . . . 20
1.3.7 The CMS Phase-2 Upgrade for HL-LHC . . . 20
1.4 The Phase-2 Upgrade of the CMS Muon System . . . 21
1.4.1 Upgrade of the Existing Muon Detectors . . . 22
1.4.2 New Detectors in the Forward Region . . . 24
1.4.3 Studies for Long-Term Operation of Detectors . . . 26
1.4.4 The Gamma Irradiation Facility at CERN . . . 27

2 Resistive Plate Chambers **31**
2.1 Introduction . . . 31
2.2 Ionisation Detectors and their Working Principle . . . 31
2.2.1 Earliest Ionisation Detectors . . . 32
2.2.2 Ionisation and Gas Transport . . . 33
2.2.3 Avalanche Formation . . . 36
2.3 Evolution of RPCs . . . 37
2.3.1 Importance of Parallel Plate Geometry . . . 37
2.3.2 Parallel-Plate Counters . . . 38
2.3.3 Birth of RPCs . . . 38
2.4 RPC: Principles and Operation . . . 39
2.4.1 Working Principle . . . 39
2.4.2 Modern RPC layout . . . 41
2.4.3 Operation Modes . . . 43
2.4.4 Signal Formation and Charge Distribution . . . 47
2.4.5 Important Parameters . . . 49
2.4.6 Gas Mixture . . . 52

2.4.7 Effect of Temperature and Pressure . . . 53
2.4.8 Ageing Phenomena . . . 54
2.5 Double-gap and Multi-gap RPCs . . . 55
2.5.1 Double-gap RPC . . . 56
2.5.2 Multi-gap RPC . . . 57

3 The iRPCs for the CMS Phase-2 Upgrade 61
3.1 Introduction . . . 61
3.2 Motivation . . . 63
3.3 The iRPC Technology and Design . . . 64
3.3.1 Improved Technical Layout of iRPCs . . . 66
3.3.2 Front-end Electronics for iRPCs . . . 70
3.4 The iRPC Demonstrator Project . . . 73
3.4.1 QC1 for Detector Components . . . 75
3.4.2 Gap Production and QC2 . . . 76
3.4.3 CMS RPC Laboratory at Ghent University . . . 82
3.4.4 QC2 at Assembly Sites . . . 89
3.4.5 Detector Assembly . . . 97
3.4.6 QC3 at Assembly Sites . . . 102
3.4.7 QC4 at 904-CERN . . . 108
3.4.8 Installation and Integration at CMS . . . 110
3.5 iRPC Performance Studies at GIF++ . . . 111
3.5.1 Experimental Setup at GIF++ . . . 111
3.5.2 Results . . . 113
3.6 iRPC Mass Production . . . 117
3.6.1 Assembly Sites . . . 118
3.6.2 Activities at UGent . . . 118
3.7 Summary and Conclusions . . . 122

4 Exploring Eco-Friendly Gas Mixtures for RPCs 125
4.1 Introduction . . . 125
4.2 Motivation . . . 127
4.2.1 GHG Emission: LHC Experiments . . . 127
4.2.2 GHG Emission: Current Measures . . . 127
4.3 Search for Alternatives . . . 130
4.4 The ECOgas@GIF++ Collaboration: Experimental Setups . . . 131
4.4.1 Gas System . . . 132
4.4.2 Detectors . . . 133
4.4.3 Trigger and DAQ . . . 135
4.4.4 Online Monitoring and Controlling . . . 136
4.5 Performance Tests Under Irradiation . . . 136
4.5.1 Detector Parameters: CMS RPC RE1/1 . . . 138
4.5.2 Data Taking Strategy . . . 138
4.5.3 Data Analysis . . . 140
4.5.4 Test Beam Results . . . 142
4.6 Ageing Studies with ECO2 . . . 150
4.6.1 Experimental Setup . . . 152
4.6.2 Data Collection and Analysis . . . 153
4.6.3 Results . . . 154
4.6.4 Current/Current Density . . . 155
4.6.5 Charge Integrated Over Time . . . 160

4.7 Summary and Conclusions 170

II Cosmic Rays for Imaging: Muography **173**

5 Fundamentals of Muography **175**
5.1 Introduction 175
5.2 Cosmic Rays and Muons 176
5.2.1 Cosmic Rays 176
5.2.2 Extensive Air Shower 177
5.2.3 Cosmic Muons 178
5.2.4 Muon Interaction with Matter 181
5.3 Radiographic Imaging with Muons 183
5.3.1 Two-dimensional Imaging 183
5.3.2 Three-dimensional Imaging 185
5.3.3 Major Challenges 187
5.4 Detector Technologies 189
5.4.1 Scintillator Detectors 190
5.4.2 Nuclear Emulsion Detectors 191
5.4.3 Gaseous Detectors 192
5.4.4 Other Technologies 195
5.5 Applications 195
5.5.1 Geophysics 195
5.5.2 Archaeology and Civil Engineering 199

6 Development of Small-Scale RPCs for Muography **203**
6.1 Introduction and Motivation 203
6.2 Development of Resistive Plates 204
6.2.1 Coating Procedure 205
6.2.2 Measurements and Results 208
6.3 Single-gap gRPC 213
6.3.1 Detector Construction 214
6.3.2 Leak Test and Dark Current Test 217
6.3.3 Performance Studies and Results 219
6.4 Double-gap gRPC 225
6.4.1 Detector Components 225
6.4.2 Detector Construction 229
6.4.3 Qualification Tests 232
6.4.4 Performance Studies and Results 234
6.5 Advanced Gaseous Detector Muon Telescope 236
6.5.1 mRPC Prototype Development 238
6.5.2 Preliminary Tests 242
6.5.3 Geant4 simulation studies 245
6.6 Summary and Conclusions 246

7 The MURAVES Experiment **249**
7.1 Introduction and Motivation 249
7.2 The MURAVES Experiment 254
7.2.1 Experiment Site Selection 255
7.2.2 Laboratory Setups 255
7.3 The MURAVES Detector and Electronics 259

7.3.1 Design and Components . . . 259
7.3.2 Photo Sensor and Front-End Electronics . . . 260
7.3.3 Temperature Stabilisation System . . . 262
7.4 Data Collection . . . 263
7.4.1 Trigger Logic . . . 263
7.4.2 SiPM Working Points . . . 264
7.4.3 Data Taking Period . . . 265
7.5 Data Analysis . . . 267
7.5.1 SiPM Response and Photoelectron Counting . . . 267
7.5.2 Clustering and Tracking . . . 269
7.6 Simulation Studies . . . 274
7.6.1 Particle Generation . . . 275
7.6.2 Muon Transport Through Vesuvius . . . 278
7.6.3 Detector Response . . . 279
7.6.4 Digitisation, Clustering and Tracking . . . 281
7.6.5 Comparison Studies: Monte Carlo vs Real Data . . . 284
7.6.6 Tracing Back to the Parent Particles . . . 289
7.6.7 Noise Implementation . . . 293
7.6.8 Introducing 3D Tracking . . . 297
7.7 Density Evaluation Study . . . 301
7.7.1 Density Evaluation: Procedure . . . 302
7.7.2 Density Evaluation: Results . . . 306
7.8 Summary and Conclusions . . . 308

Summary and Outlook **311**

Nederlandstalige samenvatting **317**

Acknowledgments **323**

Bibliography **327**

List of Figures

1.1 LHC/HL-LHC operation schedule. 8
1.2 Schematic representation of the LHC layout. 9
1.3 Schematic layout of the particle acceleration chain of LHC. 10
1.4 Coordinate system used by the CMS experiment. 11
1.5 Schematic layout of the CMS detector explaining the different layers of subdetector systems. 12
1.6 Graphical illustration of CMS tracker. 13
1.7 Geometrical view of one quarter of CMS-ECAL. 14
1.8 Geometrical view of one quarter of CMS-HCAL. 15
1.9 A quadrant of CMS experiment illustrating the DT, CSC and RPC stations. 16
1.10 Schematic representation of a single DT cell and the installation of DTs at CMS. 17
1.11 Geometrical layout of a CSCs and their installation at CMS. 17
1.12 A CMS RPC endcap disk with the installed chambers. 18
1.13 Graphical layout of the positions of DT and RPC detectors in CMS barrel wheels. 19
1.14 Block diagram of the Phase-2 L1 muon trigger data flow. 21
1.15 Image of a CMS GEM foil and the amplification process in GEM. . . . 25
1.16 Layout of the GIF++ facility. 27
1.17 Schematic drawing of the GIF++ irradiator and nominal attenuation factors. 28

2.1 Basic configuration of ionisation chambers. 32
2.2 Number of ions collected as a function of applied voltage in a basic wire gas chamber. 33
2.3 Avalanche formation in gaseous detectors. 37
2.4 Schematic of the first planar detector with resistive electrodes. 39
2.5 Simplified circuit diagram of an RPC. 40
2.6 Schematic of the initial prototype developed by Santonico and Cardarelli. 42
2.7 Signal waveforms recorded with an RPC. 44
2.8 The prompt signal charge from an RPC operated in streamer mode. . . 45
2.9 Charge measurements conducted with an RPC with varying concentrations of CF_3Br (Freon 13B1). 46
2.10 The efficiency measured as a function of incident particle rate. 46
2.11 Charge distributions for single-gap RPCs with different gap width. . . 49
2.12 Efficiencies measured for a single-gap RPC at different temperatures as a function of applied voltage and effective voltage. 54
2.13 Schematic representation of the double-gap RPC layout. 56
2.14 Schematic layout of mRPC. 57
2.15 Schematic diagrams of a single-gap RPC and an mRPC. 59

3.1 A quadrant of the CMS experiment . . . 62
3.2 The effect of Including RPC Hits on the local trigger primitive efficiency 64
3.3 Single muon trigger efficiencies with and without the iRPC timing information . . . 64
3.4 MC estimation of the sensitivity of the iRPC detector to different background particles . . . 65
3.5 MC estimation of the background hit rate expected at RE3/1 station . . 65
3.6 The RE3/1 chambers mounted on the endcap disk . . . 66
3.7 The layout of the current RPC system used in the endcap stations . . . 66
3.8 Average charge per avalanche measured on different sizes of double-gap RPCs vs electric field strength . . . 68
3.9 Schematic view of the strip panel of RPCs RE2/1 that are currently installed at CMS. . . . 68
3.10 Schematic view of the iRPC strip PCB and its components. . . . 69
3.11 Schematic view of the gas pipe layout in the LR and HR sides of the iRPC chamber . . . 70
3.12 View of the iRPC chamber chamber and the layers inside the chamber 71
3.13 Schematic of iRPC FEB v2.2 with its major components . . . 71
3.14 The distribution of the time differences between the two ends of an iRPC strip . . . 72
3.15 The distribution of time differences between two iRPC channels without a delay line and the time difference for different values of the delay line . . . 72
3.16 The iRPC RE3/1 prototype chamber developed at UGent . . . 73
3.17 Various views of the RE3/1 iRPC demonstrator chamber produced at UGent . . . 74
3.18 Tests being conducted on the iRPC FEBv2.2. and the strip PCB . . . 75
3.19 The washing procedure of the HPL plates . . . 76
3.20 The silk screen-based coating procedure for HPL plates used in the iRPC production . . . 77
3.21 PET film coating for the HPL electrodes . . . 79
3.22 Corner view of an iRPC electrode with PET film coating . . . 79
3.23 The circular spacer used in making the gas gap and the gas inlet/outlet profile. . . . 79
3.24 Spacer jig made of 3-mm-thick Plexiglas . . . 80
3.25 The gluing process of gaps and the glued gaps placed on metric tables in glue-curing slots . . . 81
3.26 The rectangular polycarbonate insulator block for the insulation of the high-voltage connections . . . 82
3.27 The CMS RPC lab infrastructure at UGent . . . 83
3.28 The CMS RPC lab at UGent . . . 84
3.29 The five rack stand and cosmic test bench inside the AirCo room at CMS RPC lab at UGent . . . 85
3.30 Gas system setups at RPC lab, UGent . . . 86
3.31 Schematic diagram of the leak test setup at CMS RPC lab at UGent . . 87
3.32 The picture of the leak test setup at CMS RPC lab at UGent . . . 87
3.33 The CAEN SY 1527LC multi-channel power supply system at the CMS RPC lab at UGent . . . 88
3.34 The mechanical workshop at the CMS RPC laboratory site . . . 89
3.35 QC2 Results: Leak rate measured for the RE3/1 gaps used in iRPC demonstrator chamber assembly . . . 91

3.36 QC2 Results: Leak rate measured for the RE4/1 gaps used in iRPC demonstrator chamber assembly . . . 92
3.37 QC2 Results: Spacer test measurements of the RE3/1 gaps used in iRPC demonstrator chamber assembly . . . 93
3.38 QC2 Results: Spacer test measurements of the RE4/1 gaps used in iRPC demonstrator chamber assembly . . . 94
3.39 QC2 Results: Dark current measurements performed for six iRPC RE3/1 gaps used in the demonstrator chamber assembly . . . 95
3.40 QC2 Results: Dark current measurements performed for two iRPC RE3/1 and four iRPC RE4/1 gas gaps used in the demonstrator chamber assembly . . . 96
3.41 Pictures of the iRPC assembly procedure . . . 98
3.42 Tools for bending gas pipes and cooling a bent gas pipe in water . . . 99
3.43 PCB layer prepared for assembly and placing the top gas gap into the chamber. . . . 99
3.44 Gas connection layout for the iRPC chamber assembly . . . 100
3.45 Placing the top copper plate over the Mylar foil to construct the Faraday cage . . . 100
3.46 All the cables, pipes, FEBs and cooling plates . . . 101
3.47 Installation of the iRPC cover plate on the chamber . . . 101
3.48 QC3 Results: Leak rate measured for the RE3/1 gaps installed in the iRPC chambers . . . 103
3.49 QC3 Results: Leak rate measured for the RE4/1 gaps installed in the iRPC chambers . . . 104
3.50 QC3 Results: Dark current measurements performed for six iRPC RE3/1 gaps installed in the iRPC RE3/1 demonstrator chambers . . . 105
3.51 QC4 Results: Dark current measurements performed for two iRPC RE3/1 and four iRPC RE4/1 gaps installed in the iRPC RE4/1 demonstrator chambers . . . 106
3.52 The CMS RPC lab at 904-CERN and the cosmic test bench in the lab used for QC4 cosmic muon tests . . . 108
3.53 Installation of iRPC demonstrator chambers at CMS . . . 110
3.54 Noise rate measurements of the iRPC DEMO-RE3-1-Ghent-186 chamber installed at CMS . . . 111
3.55 An interior view of the GIF++ facility, featuring the installation of the iRPC demonstrator chamber. . . . 112
3.56 Variation of the detector's working point (WP) with respect to the gamma cluster rate . . . 113
3.57 Gamma cluster size as a function of the gamma cluster rate measured at the WP and the average avalanche charge per gamma cluster relative to the gamma cluster rate measured at WP . . . 114
3.58 Cluster position resolution as a function of gamma background rates . 115
3.59 Muon efficiencies as a function of HV_{eff} at various background rates and muon efficiency at WP as a function of gamma cluster rate . . . 116
3.60 Muon efficiencies as a function of HV_{eff} for regions located at specific y positions . . . 116
3.61 Comparison of muon efficiency in single-gap and double-gap modes . 117
3.62 Efficiency measurements at the WP for the HR and LR regions of the chamber . . . 118
3.63 The iRPC assembly labs at Building 904, CERN, and UIA, Mexico . . . 119

3.64 Honeycomb panels and gas gaps received at CMS RPC lab at UGent for the iRPC mass production . . . 119
3.65 Bending observed in one of the iRPC RE3/1 gas gap . . . 120
3.66 QC2 results for the first batch of iRPC RE3/1 gas gaps . . . 121
3.67 The first iRPC chamber produced at CMS RPC lab at UGent as part of the mass production and the assembly team . . . 122

4.1 The progress of the EU-wide phase-down for HFCs implemented according to the EU Regulation on F-gases (No 517/2014) . . . 126
4.2 GHG Emissions from LHC Experiments . . . 127
4.3 Distribution of the leaking chambers and the repaired chambers in each of the CMS barrel wheel as of June 2022 . . . 128
4.4 The gas supply strategy at CMS . . . 129
4.5 The schematic diagram of the operation of the first R134a recuperation prototype system . . . 129
4.6 The chemical composition of R134a and HFO-1234ze . . . 131
4.7 Efficiency, streamer probability and time resolution as a function of effective HV for various HFO + CO_2-based gas mixtures . . . 132
4.8 The gas system for studies of the ECOgas@GIF++, installed in the GIF++ service zone . . . 133
4.9 The layout of the GIF++ facility . . . 134
4.10 The trolleys T1 and T3 housing the detectors of the ECOgas@GIF++ Collaboration . . . 135
4.11 A part of the Grafana dashboard . . . 137
4.12 The 3D models showing the interior of the CMS RE1/1 chamber, the arrangement of FEBs and schematic representation of the strip layout . 139
4.13 The CMS RE1/1 chamber installed in T3 within the GIF++ bunker . . . 140
4.14 The WPs of the three gas mixtures (STDmix, ECO2, and ECO3) as a function of gamma rate . . . 142
4.15 Current density trends for STDmix, ECO2, and ECO3 under various irradiation conditions . . . 144
4.16 Comparison of the current densities of the three gas mixtures as a function of gamma rate. . . . 145
4.17 Cluster size as a function of HV_{eff} for the detector tested with three different gas mixtures under varying irradiation rates . . . 146
4.18 Cluster size at the WP for the three gas mixtures with respect to the measured gamma rate . . . 147
4.19 Muon efficiencies as a function of HV_{eff} for the three gas mixtures tested at different absorption factors. . . . 148
4.20 Muon Efficiencies as function of HV_{gas} ($HV_{eff} - I_{tot} \cdot R_{eqv}$) for the three gas mixtures tested at different absorption factors . . . 149
4.21 Muon efficiencies as a function of HV_{eff} for the three gas mixtures under source-off conditions . . . 150
4.22 Efficiency measurements for the three gas mixtures under four different irradiation conditions . . . 151
4.23 The efficiencies at the WPs for three STDmix, ECO2, and ECO3 as a function of gamma rates . . . 152
4.24 Dose measurements at two trolley locations at the GIF++ bunker as functions of ABS values . . . 153
4.25 Current and current density as a function of time for the RPCs of the ECOgas@GIF++ Collaboration . . . 157

4.26 I-V curves for all tested detectors obtained using the data of the source-off scans . . . 160
4.27 Estimation of the ohmic component for all five detectors based on a selected source-off scan . . . 162
4.28 Current density, with and without the ohmic component as a function of the charge integrated for all the detector systems. . . . 164
4.29 Current density with and without ohmic components as a function of integrated charge for all the detectors under test . . . 165
4.30 The results of 3-day irradiation run . . . 166
4.31 The operational status of the ^{137}Cs source at GIF++ during the three stability runs . . . 167
4.32 Integrated charge over time for all detectors during the one-year irradiation period with ECO2 . . . 168

5.1 Cosmic ray energy spectrum. . . . 177
5.2 Vertical fluxes of particles as a function of atmospheric depth . . . 180
5.3 Configurations of installation of muon telescopes for obtaining 2D and 3D images. . . . 186
5.4 Three different configurations of detector plane construction using scintillator bars. . . . 190
5.5 Track of a cosmic ray muon on an emulsion film. . . . 192
5.6 Schematic diagrams of an MWPC. . . . 193
5.7 Major results of the muography conducted to study the interior structure of Mt. Asama. . . . 196
5.8 Muographic image of Satsuma-Iwojima volcano. . . . 197
5.9 Results of the muography conducted for the Puy de Dome volcano. . . . 198
5.10 Results of the muography studies of Khufu's Pyramid. . . . 200
5.11 Muography of Mt. Echia: 3D CAD model and detector installation locations. . . . 200
5.12 Relative transmissions observed from three detector locations. . . . 201
5.13 Two perspectives of the 3D reconstruction of the hidden cavity inside Mt. Echia. . . . 201

6.1 Glass plate preparation steps . . . 205
6.2 Wooden light box used for the coating procedure, and baking the plate in the oven at $100^{\circ}C$ . . . 206
6.3 The front and back views of the resistive plates produced using the in-house spray gun-based coating technique . . . 207
6.4 Glass plate with extensive cracking and application of silver conductive paint on the edges of the copper tape . . . 207
6.5 Surface resistivity as a function of the computed mass ratio r_c and resistivity measurements based on the varying quantities of resistive paint . . . 209
6.6 The concentric ring probe used for resistance measurementand schematic representation of the four distinct measurement locations on the $15 \times 15\ cm$ sample resistive plates . . . 209
6.7 Surface resistivity variation over time for four sample glass plates . . . 210
6.8 Result of long-term resistivity monitoring of a $30 \times 30\ cm$ resistive electrode used in detector construction . . . 211

6.9 Thickness measurement procedure of the coating on the glass plates and resistive layer coated silicon wafer samples prepared for SEM-based thickness measurements 212
6.10 SEM images of the resistive layer coating for the thickness measurement 213
6.11 The PVC box with a rectangular base plate, sidebars, and corner seals and 200 μm copper foil covers the bottom and sides for the construction of Faraday cage 215
6.12 Strip PCB placed within the detector box and placement of the first resistive plate in the chamber between cylindrical spacers 215
6.13 Arrangement of fish wire to create the 1 mm gas gap and the procedure for fixing the fish wire to cylindrical spacers 216
6.14 The second electrode positioned on top of the fish wire and the procedure of implementing the HV connection 216
6.15 Image of grounding the signal cables to a copper foil atop the upper Mylar foil and the inside view of the chamber after closing the Faraday cage 217
6.16 An exploded view of the single-gap gRPC chamber 218
6.17 The procedure for identifying leaks in the single-gap RPC 219
6.18 HV test results for the single-gap RPC 220
6.19 Experimental setup featuring the single-gap gRPC chamber with two trigger scintillators and the top view of the setup displaying the scintillator's coverage 220
6.20 Block diagram of the trigger generation process for data collection . . . 221
6.21 Connection diagram of the signal flat cable from the detector to the CAEN QDC module (v792) 221
6.22 Result of the cosmic muon efficiency scan of the single-gap gRPC. . . . 222
6.23 Inside view of the gRPC detector B1 and the image of the portable DAQ for gRPCs. 224
6.24 Placement of gRPC-B1 between trigger scintillators and schematic view of the alignment. 224
6.25 Comparison of strip occupancy and cluster size of gRPC-A1 and gRPC-B1. 225
6.26 PCB technical drawings with details on connection slots and resistors . 227
6.27 CAD models of the 3D printed detector frame 228
6.28 CAD model of the 3D printed spacer 228
6.29 Strip PCB of the double-gap gRPC chamber. 229
6.30 Inside view of the double-gap gRPC chamber-1 230
6.31 Inside view of the double-gap gRPC chamber-2 and the closed view of the detector 231
6.32 Schematic of the technical layout of the double-gap gRPC. 231
6.33 X-ray scanning for the 3D printed detector frame 232
6.34 Results of the X-ray scanning tests of the 3D printed detector frame. . . 233
6.35 Leak test result of the double-gap gRPC. 233
6.36 Dark current test result of the double-gap gRPC. 234
6.37 Experimental setup for data collection with the double-gap gRPC. . . . 235
6.38 Double-gap RPC occupancy plot. 235
6.39 Cluster size distributions of the double-gap gRPC. 236
6.40 Results of charge measurements conducted with the double-gap gRPC 237
6.41 Result of the cosmic muon efficiency scan of the double-gap gRPC. . . 237
6.42 Cross-sectional view of the mRPC prototype detector 239
6.43 mRPC prototype detector: detector frame drawing and construction. . 239

6.44 Mylar circular spacers for the gas gap construction of mRPC prototype detector. . . . 240
6.45 Major steps involved in the construction of the mRPC prototype detector. . . . 241
6.46 Pictures of the mRPC prototype detector construction along with the team members participated in the assembly. . . . 242
6.47 Result of the dark current scan conducted with the mRPC prototype detector. . . . 243
6.48 mRPC detector setup with the trigger scintillators and the results of the first performance study. . . . 243
6.49 Images of securely sealing the signal connection slots on the mRPC PCB. . . . 244
6.50 Methods used for securing the HV connection of the mRPC detector. . 245
6.51 Interaction of ten 800 MeV muons with the mRPC muon telescope in the Geant4 simulation. . . . 245

7.1 Map indicating the location of Mt. Vesuvius on the west coast of Italy . 250
7.2 The schematic of the evolution of the Mt. Vesuvius crater between 1906 and 1944 . . . 251
7.3 The crater's appearance before the 1944 eruption and its transformation after the eruption . . . 251
7.4 the steep, hazardous slopes and the gas emissions through a fumarole vent in the Vesuvius crater . . . 252
7.5 Monitoring Room of the INGV Vesuvius Observatory in Naples 253
7.6 The stamen terrain map of the Vesuvius region . . . 254
7.7 Vesuvius red, yellow, and blue risk zones delimited by the Italian 'Protezione Civile' . . . 254
7.8 The MURAVES observatory location and View of the Vesuvius crater seen from the laboratory on Google Earth . . . 256
7.9 The container housing the MURAVES hodoscopes situated inside the Vesuvius national park . . . 256
7.10 Schematic representation of the slots of the MURAVES detectors inside the laboratory . . . 257
7.11 MURAVES hodoscopes: NERO and ROSSO . . . 257
7.12 The solar panels installed on the container's roof and the array of batteries connected to the solar panel system . . . 258
7.13 One-month summary of the remote power supply monitoring system at the MURAVES laboratory . . . 258
7.14 The schematic diagram of MURAVES hodoscope . . . 259
7.15 The three MURAVES hodoscopes fully operational installed at the laboratory . . . 260
7.16 The side-by-side alignment of the triangular bars within the detector plane and a half-tracking plane with 32 scintillator bars . . . 261
7.17 PCB used in MURAVES hodoscopes . . . 261
7.18 The SLAVE and MASTER board of the MURAVES hodoscopes' front-end electronics . . . 262
7.19 The components of temperature stabilisation system . . . 263
7.20 Trigger rates measured for the MURAVES detectors . . . 264
7.21 Digital terrain model of Vesuvius crater . . . 265
7.22 The rock thickness map of Vesuvius . . . 266

7.23 Minimum data-taking period required to attain the targeted density resolution . . . 267
7.24 ADC spectrum obtained from a specific channel in a control run dataset 268
7.25 ADC distributions of two distinct channels for various runs . . . 269
7.26 The ADC responses of 16 randomly selected channels . . . 270
7.27 Schematic of muon tracks in the scintillator bars . . . 271
7.28 Cluster size distribution of events in the ROSSO detector's y-planes . . 272
7.29 The energy distributions of the strips, clusters, as well as the distribution of cluster multiplicity . . . 273
7.30 A schematic representation of the MURAVES simulation chain . . . 275
7.31 Energy distribution of muons generated from 100 showers for each high-energy model in CORSIKA . . . 276
7.32 The muon charge ratio for various energy ranges and models . . . 277
7.33 Muon fluxes generated using CRY and three different high-energy hadronic interaction models in CORSIKA . . . 277
7.34 Expected muon flux per year considering the geometrical acceptance of the detector simulated using PUMAS . . . 279
7.35 Muon energy loss and scattering angle distributions simulated using PUMAS and Geant4 in standard rock . . . 280
7.36 Simulation illustrating the interaction of a 1 GeV muon with the MURAVES hodoscope . . . 281
7.37 Survival probability of muons reaching the 4^{th} station of the detector . 282
7.38 Event display of three example events generated in the simulation . . 283
7.39 Distributions of energy deposited per bar and energy of clusters for all y and z planes . . . 284
7.40 Cluster energies between real and simulated data for all Y and Z planes in the hodoscope . . . 286
7.41 Cluster sizes for clusters belonging to the best track in all Y and Z planes 287
7.42 Cluster multiplicity between real and simulated data or all Y and Z planes . . . 288
7.43 Chi-square values for 4-plane tracks reconstructed in real data and simulated data . . . 289
7.44 Chi-square values for 3-plane tracks between simulated and real data . 290
7.45 Summary of the particle tracking study using CRY-generated particles 291
7.46 Cluster energies within the hodoscope for different event types . . . 292
7.47 Cluster multiplicities in muon and non-muon events across the Y and Z planes of the hodoscope . . . 294
7.48 Chi-square values for muon and non-muon tracks in the Y and Z planes of the hodoscope . . . 295
7.49 Event displays of proton and electron tracks within the hodoscope . . 295
7.50 Gaussian-based position and Landau-based frequency distributions used for assigning positions and frequencies to noise clusters . . . 296
7.51 Distribution of non-track cluster energy in all Y and Z planes of the NERO detector . . . 298
7.52 Track chi-square values between different datasets . . . 299
7.53 Illustration of the 3D tracking process . . . 302
7.54 Residue values for both 3-plane and 4-plane tracking scenarios . . . 303
7.55 Chi-square values for track selection between 3-plane and 4-plane tracking scenarios . . . 303
7.56 Track energies between the best tracks and rejected tracks in the 3-plane and 4-plane tracking cases . . . 304

7.57 Angular regions defined for the evaluation of the average density . . . 305
7.58 Densities measured in the six chosen angular regions 307
7.59 Right/left asymmetries 308

List of Tables

1.1 Details of the GEM detector systems. 25

2.1 Excitation and ionisation characteristics of various gases. 34

3.1 Comparison of the major parameters of existing RPCs and iRPCs . . . 67
3.2 Summary of the details of the five iRPC RE3/1 and three RE4/1 iRPC demonstrator chambers 107
3.3 Summary of the QC procedures that were validated during the iRPC demonstrator project 109

4.1 The summary of chamber specifications of different RPC chambers of the ECOgas@GIF++ Collaboration 134
4.2 The summary of characteristics of the electronics of each detector of ECOgas@GIF++ Collaboration 136
4.3 The gas mixtures used in the tests conducted by the ECOgas@GIF++ Collaboration 137
4.4 Absorption factors corresponding to the data selected for the July and August 2023 test beam data analysis 142
4.5 The resistance values for the CMS RE1/1 chamber's gaps 147
4.6 The estimated ohmic components for all the detectors 163
4.7 Total charge integrated for all detectors during the one year irradiation period with ECO2 169

5.1 Parameters used in Eqn. 5.9 181

6.1 Details of the amount of the 2-butoxy ethyl acetate used in case of each glass plate and the corresponding mean surface resistivity achieved . . 211
6.2 Overview of the geometric characteristics of the two single-gap gRPCs, A1 and B1 223

7.1 Particle generation with CRY and their traversal through the first three and all four tracking stations 290
7.2 An overview of the key outcomes from the 3D tracking analysis 301
7.3 The acquisition times for datasets corresponding to the ROSSO and NERO detectors at different operating temperatures 303
7.4 The event counts recorded in different angular regions 306

This thesis is dedicated to my family, friends, and all those who taught me to dream high and supported me in turning those dreams into reality…

Introduction

The evolution of particle physics over the past century has been a testament to human curiosity and technological advancement. From the early days of identifying fundamental particles like electrons and protons to the development of the Standard Model (SM), our understanding of the microscopic building blocks of the universe has grown exponentially. Particle detectors have been indispensable tools in unravelling the mysteries of particle physics. As experimental capabilities expanded, detectors evolved from early stage cloud chambers and spark counters to present day sophisticated instruments like the Compact Muon Solenoid (CMS) and A Toroidal LHC ApparatuS (ATLAS) detectors at the Large Hadron Collider (LHC). These modern detectors are engineering marvels that precisely measure particles' properties, including their energy, momentum, and charge. Their intricate designs reflect the collaboration between physicists, engineers and IT specialists, pushing the boundaries of technology to facilitate groundbreaking discoveries.

The applications of particle physics and its associated detectors extend far beyond the quest for fundamental knowledge. In medical imaging, technologies inspired by particle detectors, including PET scanners and the recently developed Medipix detectors, have revolutionized diagnostics. Moreover, particle accelerators find applications in cancer treatment through techniques like proton therapy. Additionally, pioneering methods like muon radiography (muography), which utilises naturally occurring cosmic muons for imaging purposes, represent another innovative technique at the crossroads of particle physics and interdisciplinary applications. The interplay between fundamental research and real-world applications highlights the societal significance of particle physics, reinforcing its relevance beyond the realm of pure science—an essential message conveyed throughout this thesis.

This thesis primarily focuses on the study of muon detectors for high-energy physics and interdisciplinary applications. The research journey began with the development and study of Resistive Plate Chambers (RPCs) for the CMS experiment. Recognising the significance of eco-friendly gas mixtures for RPCs, the scope expanded to include studies on eco-friendly gas alternatives. Drawing from expertise in CMS RPCs, an exploration of the same technology for interdisciplinary applications was initiated. This was particularly focused on the growing field of muography, where RPCs are not yet widely employed. The R&D activities involved the fabrication of small-scale RPCs for muography and efforts to construct an advanced gaseous detector telescope designed for this purpose. As this marked the first involvement of the Ghent University (UGent) muography group in R&D for this technique, it was crucial to understand its principles, requirements, and potential challenges thoroughly. This understanding was gained through participation in an ongoing project, the MUon RAdiography of VESuvius (MURAVES) experiment. Engaging in the experiment's activities provided a comprehensive insight, covering aspects from detector assembly to muon tracking and data analysis in muography.

The thesis is structured into two parts. The first part (Part I) is dedicated to the upgrade of the RPC system of the CMS experiment for the upcoming High-Luminosity Phase of the LHC (HL-LHC). The second part (Part II) discusses the research and development (R&D) efforts conducted for the fabrication of small-scale portable glass RPC detectors (gRPC) for muography, along with the exploration of an advanced gaseous detector muon telescope designed for muography. Additionally, it covers studies conducted for a muography experiment, namely, the MURAVES experiment.

Part I

The SM outlines our current understanding of matter constituents and the forces between them. In 1964, Robert Brout, François Englert, Peter W. Higgs, Thomas W. B. Kibble, Carl R. Hagen, and Gerald Guralnik proposed a mechanism that explains the origin of masses of force-carrying particles. This theory suggested the existence of a new elementary particle, and in 2012, this particle, the Higgs boson, was discovered by the ATLAS and CMS experiments at the LHC.

The LHC, renowned as today's largest and most powerful particle accelerator, has been instrumental in validating and refining the SM. To amplify its discovery potential, it is transitioning into the next operation phase, the HL-LHC, during which the instantaneous luminosity, indicating the rate of particle interactions, will be augmented. In 2015–2017, the maximum luminosity exceeded the design value by more than 1.7, bringing the CMS subsystems close to their rate capability limits. During High Luminosity HL-LHC operation, the instantaneous luminosity will be increased to $5\times10^{34}\text{cm}^{-2}\text{s}^{-1}$, five times the machine's original design value. This increase in luminosity at the HL-LHC has many implications for the CMS sub-detector systems. It will increase the average pileup, resulting in worse background conditions, higher trigger rates, more difficult event reconstruction, and accelerated ageing of components. To guarantee that the performance of the sub-detectors will be maintained during the HL-LHC running, CMS is undergoing different upgrades (CMS Phase-2 upgrade) of the present systems, e.g., silicon tracker, endcap calorimeter and muon system.

As part of the muon system upgrade, enhancements will be made to the readout electronics of the current RPCs, and the third and fourth endcap disks of the CMS detector will be instrumented with an improved version of existing RPCs, referred to as iRPCs. Given that RPCs operate using a gas mixture primarily composed of fluorine, a potent Greenhouse Gas (GHG), and are significant contributors to GHG emissions at CERN, the upgrade activities include the investigation of alternative eco-friendly gas mixtures for RPC detectors. The CMS collaboration has also undertaken measures to reduce GHG gas consumption and emissions, including minimising gas leaks and introducing gas recirculating systems. Recognising the widespread use of RPCs at LHC experiments, a collaborative effort named ECOgas@GIF++ was established in 2019. This collaboration involves RPC groups from all LHC experiments and CERN EP-DT groups, aiming to explore new eco-friendly gas mixtures for RPCs operating at CERN.

Chapter 1 provides a comprehensive overview of the CMS experiment and the upgrade plans for the CMS Muon System in the context of the HL-LHC. It discusses the details and operation of both LHC and CMS. Furthermore, detailed information

about each subdetector system of the CMS detector is presented. It also discusses the CMS Phase-2 upgrade for HL-LHC, focusing on upgrading existing muon detectors, the incorporation of new detectors in the experiment, and studies for long-term detector operation.

Chapter 2 Chapter 1 focuses on the physics and operation of RPCs. In the first part of the chapter, details on the ionisation detectors and their operation principle are provided. In the subsequent sections, information on the evolution of RPCs from the earliest ionisation detectors, the working principles and the details of the detector operation is provided. The final section of the chapter presents the details of the different types of RPCs, which are relevant to the thesis.

Chapter 3 centres on the CMS iRPC upgrade, presenting motivations for the upgrade and detailed information on iRPC technology and electronics. The chapter also describes the major iRPC activities conducted in the past few years and the significant results achieved. These activities include the iRPC demonstrator project, beam test studies at the Gamma Irradiation Facility (GIF++) at CERN, and iRPC mass production activities.

Chapter 4 discusses the studies conducted by the ECOgas@GIF++ collaboration to find new eco-friendly gas mixtures for RPCs at LHC. The chapter describes the project's motivation, outlines the gas mixtures scrutinised, details the experimental setups employed, and presents the significant findings derived from the beam test and ageing studies conducted at GIF++.

Part II

Muography, an imaging technique based on the absorption of cosmic-ray muons in matter, finds applications in archaeology, volcanology, geosciences, nuclear waste characterization, border controls, and more. **Chapter 5** introduces muography, covering cosmic ray muons, the physics behind muography, various technologies employed in muography, and its diverse applications.

While most muography projects use large-area detectors for surrounding large volumes or studying extensive targets, certain applications, such as archaeology or geophysical exploration in confined spaces, necessitate small and portable detector setups. **Chapter 6** describes the motivation behind conducting R&D for the development of small-scale portable gRPCs for muography. It details the construction of detector components and the detectors themselves and highlights major results achieved with the developed detectors. Additionally, the chapter discusses activities related to developing an advanced gaseous detector-based muon telescope for muography, offering insights into the current status of the projects and the achieved results.

The MURAVES project focuses on studying the summital cone of Mt. Vesuvius, an active volcano near Naples (Italy), utilising muon flux attenuation to measure its density profile. **Chapter 7** presents a comprehensive overview of the experiment, including details about the scintillator-based MURAVES detectors, their operation, and data collection. In addition, the chapter provides insights into the data analysis process, MC simulation studies conducted for comparison with real data, and the

enhancement of existing tracking methods by understanding the characteristics of background particles along with the achieved results. Additionally, the last section of the chapter summarises the key findings of the experiment related to the density evaluation of Mt. Vesuvius.

In summary, the initial two chapters (Chapters 1 and 2) in Part I and in Part II, along with the first chapter in Part II (Chapter 5), presents the theoretical foundations and relevant details for the thesis. The remaining chapters, 3, 4, 6 and 7, focus on the four projects I participated as part of my PhD research and begins with a dedicated section outlining my contributions to the respective project, and concludes with a comprehensive summary and conclusions section, providing an overview of the major results. Most of the research findings discussed in this thesis are published in peer-reviewed journals and presented at various conferences and workshops. The details of the selected publications (**first author and corresponding author**) follow.

Selected Publications:

[1] Samalan, A., et al. "Improved resistive plate chambers for HL-LHC upgrade of CMS." Nuclear Instruments and Methods in Physics Research Section A: Accelerators, Spectrometers, Detectors and Associated Equipment (2024): 169075.

[2] Samalan, A., et al. "Small-area Portable Resistive Plate Chambers for Muography (submitted)." Journal of Advanced Instrumentation in Science (2023). arXiv: 2311.11451.

[3] Samalan, A., et al. "Exploring Advanced Detector Technologies for Muon Radiography Applications." 2022 IEEE Nuclear Science Symposium and Medical Imaging Conference (NSS/MIC). IEEE, 2022. IEEE, 2022.

[4] Samalan, A., et al. "End-to-end simulations of the MUon RAdiography of VESuvius experiment." Journal of Instrumentation 17.01 (2022): C01015.

[5] Samalan, A., et al. "Upgrade of the CMS resistive plate chambers for the high luminosity LHC." Journal of Instrumentation 17.01 (2022): C01011.

[6] Samalan, A., and CMS Collaboration. "Improved Resistive Plate Chambers for the upgrade of the CMS muon detector." Journal of Physics: Conference Series. Vol. 2374. No. 1. IOP Publishing, 2022.

Part I

The CMS RPC System Upgrades for HL-LHC

Chapter 1

The CMS Experiment and the Muon System Upgrade

1.1 Introduction

The CMS experiment serves as a general-purpose experiment for the exploration of physics phenomena at the highest luminosity within the LHC at CERN. In the forthcoming phase of the LHC physics program, scheduled to commence in 2029, the CMS experiment anticipates an additional integrated luminosity of approximately 2500 fb^{-1} over the course of 10 years. This extended data collection period aims to significantly enlarge the mass reach in the search for new particles and will also greatly extend the potential to study the properties of the Higgs boson discovered at the LHC in 2012 [7, 8]. To effectively address the experimental challenges associated with unprecedented proton-proton (p-p) luminosity, the CMS collaboration is conducting several upgrades for the present systems known as the CMS Phase-2 upgrade. This involves the upgrade of the CMS muon system equipped with different gaseous detectors.

The work presented in Chapter 2 and Chapter 3 significantly contributes to the ongoing activities related to the CMS muon system upgrade, specifically for the upgrade of the RPC system. Considering this, this chapter is dedicated to provide an overview of the CMS experiment, with a primary focus on its Phase-2 upgrade program, particularly emphasising the upgrades to the muon system. The initial section, Sec. 1.2, discusses the intricate details of the LHC and its operation. Section 1.3 expands upon the specifics of the CMS experiment, including its subsystems, and provides insights into the Phase-2 upgrade program. In the last section, Sec. 1.4, a detailed understanding of the CMS muon system upgrades is provided.

1.2 The Large Hadron Collider

The LHC at CERN [9] stands as the world's largest and most powerful circular hadron accelerator, situated in the tunnel formerly occupied by the Large Electron-Positron (LEP) collider [10]. Spanning 27 km beneath the Geneva lake, the Jura Mountains and Cessy, France, the LHC is designed for proton-proton collisions with a center of mass energy of $\sqrt{s} = 14\ TeV$ and a maximum luminosity of $10^{34}\ cm^{-2}\ s^{-1}$. Additionally, it facilitates heavy-ion collisions, including lead-lead ($Pb - Pb$) [11], proton-lead ($p - Pb$) [12], and Xenon-Xenon ($Xe - Xe$) [13] interactions at various energies.

The commissioning of LHC started in 2008, but initially faced setbacks due to faulty electrical connections among the superconducting magnets, leading to a temporary halt. After a year, on 20 November 2009, the first proton-proton collisions at LHC were successfully conducted at a center-of-mass energy of 900 GeV. Subsequent upgrades increased the proton beam energy to 3.5 TeV, achieving a center-of-mass energy of $\sqrt{s}$ = 7 TeV on March 30, 2010. The first data collection phase, known as "Run I", spanned from 2010 to 2013. After a two-year shutdown (LS1) for upgrades, "Run II" commenced in 2015 with proton beams at 6.5 TeV, resulting in a center of mass energy of $\sqrt{s}$ = 13 TeV. "Run II" ended on 3 December 2018, leading to the second extended shutdown (LS2). "Run III" commenced in July 2022, with $\sqrt{s}$ = 13.6 TeV and targeting an integrated luminosity of 450 fb^{-1} with an anticipated conclusion by the end of 2025. Following this phase, a three-year-long shutdown (LS3) is planned (2026-2029), during which significant enhancements are planned to achieve an unprecedented instantaneous luminosity ranging from 5.0 to 7.5 $\times$ 10^{34} cm^{-2} s^{-1}, contributing to a total data accumulation of 3000 to 4000 fb^{-1} throughout the accelerator's lifetime. This upcoming operational phase of the LHC after LS3 is known as the HL-LHC. Figure 1.1 shows the details of the LHC/HL-LHC operation schedule.

FIGURE 1.1: LHC/HL-LHC operation schedule.

1.2.1 The LHC Machine

The LHC features two rings with counter-rotating beams. Originally designed for the LEP, the tunnel geometry includes eight crossing points with long straight sections that accommodate radio frequency (RF) cavities to compensate for synchrotron radiation losses. Although a proton machine like the LHC doesn't encounter the same synchrotron radiation issues, the decision was made to utilise the existing tunnel, resulting in a cost-effective solution. However, to minimise beam disruption, only four of the eight potential interaction regions were equipped, with beam crossings suppressed in the remaining four.

The tunnels in the arc have an internal diameter of 3.7 m, posing a significant challenge for the installation of two entirely separate proton rings. This space constraint prompted the adoption of the twin-bore magnet design, initially proposed by

John Blewett at the Brookhaven laboratory in 1971 [14]. Originally termed the "two-in-one" superconducting magnet design, it was suggested as a cost-saving measure [15].

In order to to manipulate particle trajectories and bunch sizes at the LHC, superconducting magnets (1232 main dipoles and 392 quadrupoles), covering about 19 km of the total circumference, are incorporated. Dipole magnets are responsible for bending particle trajectories, while quadrupole magnets focus the particle beam. The superconductivity within these magnets is maintained through a closed circuit of superfluid helium, keeping the temperature at $1.9°K$ [16].

Figure 1.2 shows the layout of LHC comprising eight insertion regions (IR) connected by arc sections. These beams collide at four experimental caverns located at

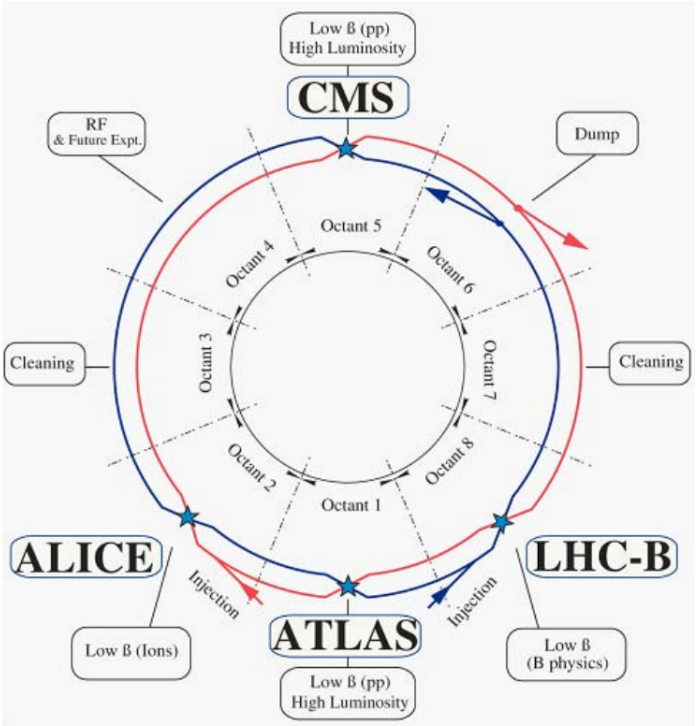

FIGURE 1.2: Schematic representation of the LHC layout, featuring the eight insertion regions connected by arc sections and the four beam collision points housing LHC experiments: ATLAS, CMS, ALICE, and LHCb [9].

Points 1, 2, 5, and 8, each equipped with corresponding detectors. The two high luminosity experimental points are at opposite straight sections: ATLAS (A Toroidal LHC Apparatus) [17] at point 1 and CMS [18] at point 5. Additional experimental insertions, including injection systems for Beam 1 and Beam 2, are at Points 2 (ALICE) [19] and 8 (LHCb) [20]. Point 3 houses beam monitoring systems, while point 7 hosts one of the LHC cooling plants responsible for maintaining the superconductive magnets at the appropriate temperatures. Point 4 has two independent RF systems [21] for each LHC beam. The straight section of point 6 facilitates beam extraction using fast-pulsed magnets for beam dump [9]. The figure also illustrates two beam lines at LHC, represented by red and blue lines in opposite directions. The smaller lines labeled "injection" with arrows indicate the beam injection lines

through which particles are introduced into the LHC beam lines. Further details about the beam injection mechanism are discussed in the following section.

1.2.2 LHC Beam Injection

Before entering the LHC ring, particles undergo acceleration in a series of smaller accelerators, each designed to boost the beam to the required injection energy for the subsequent stage. This stepwise acceleration is essential for maintaining beam stability within the LHC. The graphical representation of the acceleration chain is shown in Fig. 1.3.

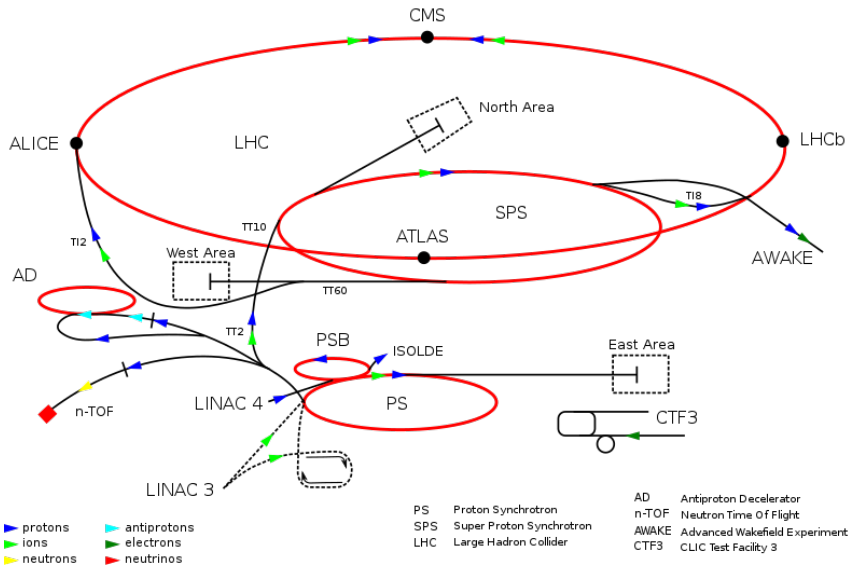

FIGURE 1.3: The schematic layout of the particle acceleration chain of LHC [22].

Protons are extracted from a small canister of ionised hydrogen gas by applying a large electric field and the initial stage begins with the Linear Accelerator 4 (Linac 4), which accelerates protons to energies up to 160 MeV. Subsequently, the Proton Synchrotron Booster (PSB) takes over, further boosting the proton energy to 2 GeV. The next accelerator in the sequence is the Proton Synchrotron (PS), which accelerates protons to an energy of 25 GeV. The final acceleration before injection into the LHC is performed in the superproton synchroniser (SPS), increasing the proton energy to 450 GeV. As explained in the previous section (Sec. 1.2.1), the beam is injected into LHC through the injection points close to points 2 and 8.

The injection chain for heavy ions typically begins with the production of heavy ion beams, such as lead ions from a heated Pb filament: a few electrons are stripped and the resulting ions pre-acceleration in linear accelerator LINAC 3, reaching energies on the order of a few MeV per nucleon. Subsequently, the ions enter the Low Energy Ion Ring (LEIR), where they receive further acceleration, reaching energies of around 72 MeV per nucleon. Similar to that of protons, the next stage in the injection chain is the PS, where the heavy ions undergo additional acceleration, reaching energies of approximately 5.9 GeV per nucleon and then at the SPS, the ions reach energies of about 177 GeV per nucleon. After that, similar to the process explained for proton beams, the heavy ion beams are injected into the LHC through their respective injection lines.

1.3 The CMS Experiment

As detailed in Sec. 1.2.1, the CMS detector is located at Point 5 (P5), 100 m below the ground level, diametrically opposite to the ATLAS experiment within the LHC. While both the CMS and ATLAS detectors share common physics objectives, they employ distinct detection techniques. Designed to measure all stable particles produced in collision events, except for weakly interacting neutrinos, the CMS detector offers accuracy in energy and momentum measurements, along with spatial resolution, facilitating the precise reconstruction of intermediate, unstable particles and enabling the analysis of a diverse range of physics processes.

For the description of the positions and directions of measured objects, the CMS experiment employs a coordinate system detailed in Fig. 1.4. centred at the point of

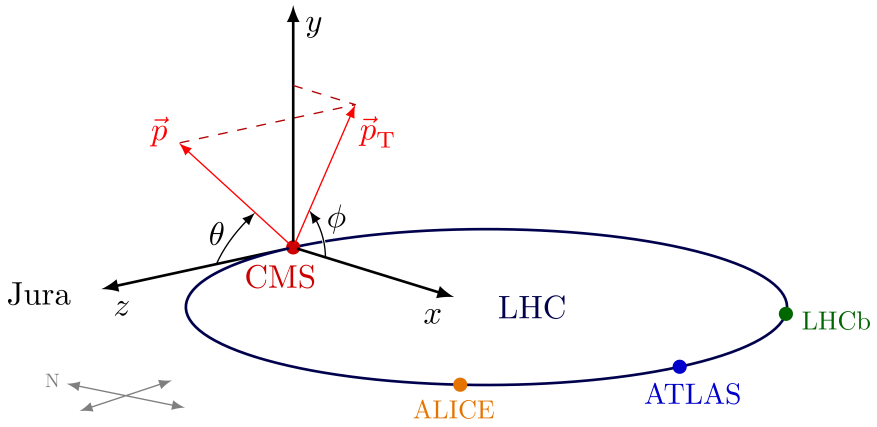

FIGURE 1.4: The coordinate system used by the CMS experiment. The x-axis extends toward the center of the LHC, the y-axis is directed upwards, and the z-axis aligns parallel to the beam line in a counter-clockwise orientation [23].

collision for the two proton beams within the detector, the x-axis extends towards the center of the LHC, with the y-axis oriented upwards, spanning the transverse plane. The azimuthal angle ϕ is defined as zero in the direction of the x-axis, and the z-axis, perpendicular to the transverse plane and parallel to the beam axis, possesses a positive counterclockwise direction. The directions in expressed using the pseudorapidity (η) relative to the z-axis, , providing a Lorentz-invariant measure independent of longitudinal boosts for particles with varying momenta.

$$\eta = -ln\ tan(\frac{\theta}{2}) = -\frac{1}{2} ln\ \frac{p + p_z}{p - p_z} = arctanh\ \frac{p_z}{p} \tag{1.1}$$

Here, θ is the polar angle, p is the absolute momentum of a particle, p_z is its z-component and p_T is the transverse component.

The physics program of the CMS experiment is primarily directed towards the Higgs boson, a fundamental particle whose discovery in 2012 by the CMS and ATLAS collaborations represented a landmark achievement in the field of particle physics [8, 24]. The CMS initiative significantly contributes to the precise measurement of the Higgs boson's properties, encompassing parameters such as its mass, spin, and decay modes. Furthermore, the program includes searches for New Physics and rigorous tests of the SM. This includes investigations into quantum chromodynamics (QCD), electroweak measurements, top-quark physics, b-physics, and also

there are studies being conducted to look for signs of physics beyond the standard model (BSM) [7].

This section provides an overview of the CMS experiment, detailing its layout, various subsystems, operational aspects, and the Phase-2 upgrade program.

1.3.1 Detector Layout

The CMS detector, with a length of 21.6 *m*, a diameter of 14.6 *m*, and a mass of approximately 14,000 *tonnes* [18], follows a cylindrical structure, incorporating multiple subdetectors in layers aligned around the beam axis symmetrically to the primary interaction point. The name CMS conveys essential design characteristics of the detector, rooted in three primary features. The tracking and calorimetry subdetectors are positioned predominantly within the solenoidal magnet, resulting in a significantly smaller size compared to the ATLAS detector. This substantiates the descriptors "Compact" and "Solenoid" within the name. The emphasis on muon identification and reconstruction within the experiment explains the term "Muon" in its name.

Figure 1.5 presents the schematic cutaway view detailing the layout of the CMS detector. The design resembles a colossal cylindrical onion, with each layer comprising distinct subdetectors (indicated in the image) dedicated to tracking, identifying, and filtering various particles emerging from proton-proton or heavy-ion collisions. The subdetector systems aligned parallel to the beam pipe are referred as the barrel regions, while those closing the detector are referred to as the endcap regions. The

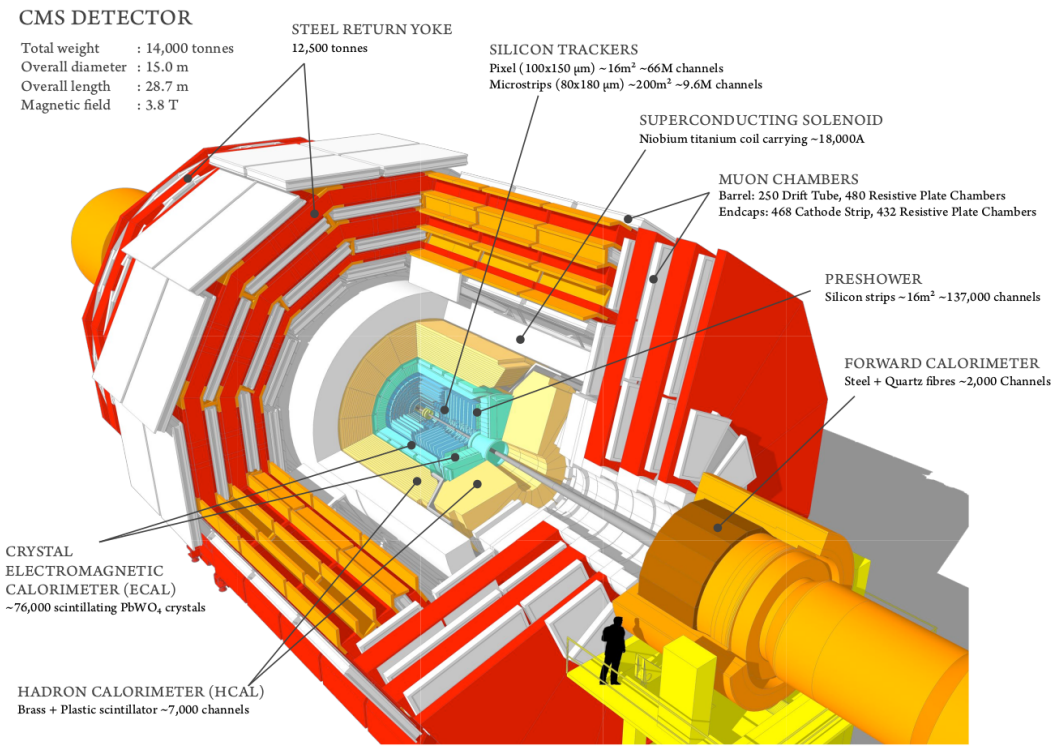

FIGURE 1.5: The schematic layout of the CMS detector explaining the different layers of subdetector systems [25].

following subsections of this section provides the brief details of the CMS subdetector systems.

1.3.2 Tracking System

The silicon tracking detectors at CMS [26] constitute a critical element in the particle detection framework, playing an important role in disentangling particle tracks from the large number of PU events. Positioned in close proximity to the beamline, the tracking system utilises a combination of silicon pixel and strip layouts to achieve high-resolution tracking, covering a total active area of approximately 200 m^2. The pixel detector, located closest to the collision point, employs a small-scale pixel geometry for complete track reconstruction and precise vertex determination. Comprising 1440 pixel modules, it spans the pseudorapidity range of $|\eta| < 2.5$ with three Barrel Pixel (BPix) layers and two Forward Pixel (FPix) disks. The strip tracker, featuring silicon microstrips, is subdivided into an inner region having 4 barrel layers (Tracker Inner Barrel, TIB) and 3 endcap layers (Tracker Inner Disks, TID), and an outer region having 6 barrel layers (Tracker Outer Barrel, TOB) and 9 endcap disks (Tracker Endcaps, TEC) respectively. Figure 1.6 shows the schematic of the CMS tracker system.

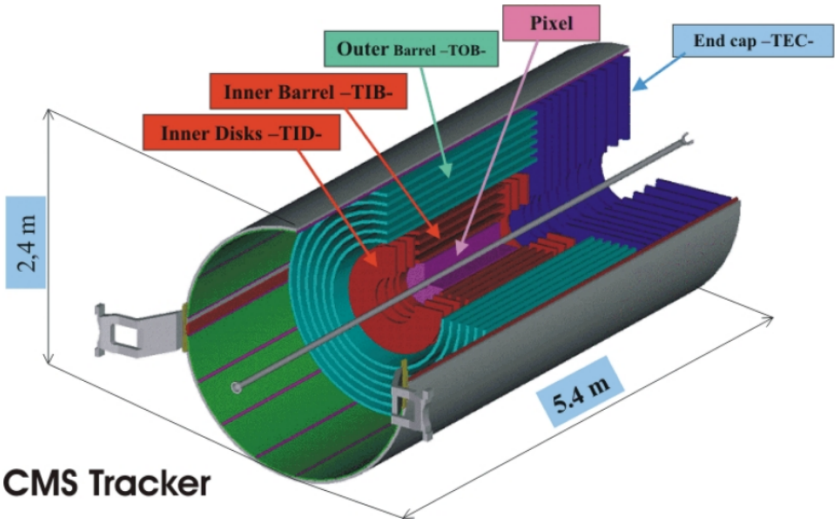

FIGURE 1.6:
The graphical illustration of CMS tracker [27].

Due to their proximity to the interaction point, both the silicon pixel and strip trackers endure elevated levels of radiation damage. To guarantee durability throughout years of operation in this demanding environment, a dedicated cooling system maintains their operational temperature at -10°C. The tracker's transverse momentum resolution varies from 0.7% at 1 GeV to 1.5% at 100 GeV, facilitating precise measurements crucial for vertex reconstruction, particle identification, charge determination, and assessment of charged particle momenta. This tracker system, with 75 million individual readout channels, ranks as the world's largest silicon detector, ensuring precise measurements of particle tracks with a remarkable precision of about 10 μm.

1.3.3 Calorimeters

Calorimeters are used to quantify the energy of diverse particles by decelerating and ultimately stopping their movement; nonetheless, they are incapable of stopping muons and neutrinos. The incoming particles engage with the calorimeter material, generating showers of lower-energy secondary particles until the energy of the initial particle descends below a critical threshold, preventing further ionisation or excitation of the material.

The Electromagnetic Calorimeter (ECAL) of CMS [28], housed within the 3.8 T solenoid and Hadron Calorimeter (HCAL) [29], is designed for high-resolution detection of electrons/positrons and photons. The ECAL, with 61,200 lead tungstate (PbWO4) crystals in the barrel regions (EB) and 14,648 in the endcaps (EE), covers a pseudorapidity range up to $|\eta| = 3$. The choice of PbWO4 material is motivated by its high density, small Moli´ere length of 0.89 cm, and short radiation length of 2.2 cm, ensuring high granularity and energy resolution. The ECAL's total thickness exceeds 25 radiation lengths (X_0), enhancing its performance.

To detect the released energy, silicon Avalanche PhotoDiodes (APD) and Vacuum PhotoTriodes (VPT) are employed in the EB and EE regions, respectively, due to varying radiation exposures and orientations in the magnetic field. The inclusion of a pre-shower detector (ES) in front of the EE sections improves resolution, especially for closely spaced photons. The pre-shower consists of two lead plates and silicon strips, aiding in distinguishing photon pairs induced into showering. The signal is read out in groups of 5×5 crystals called supermodules, where zero suppression is applied to reduce signal noise. The energy resolution for photons varies with pseudorapidity and time of conversion, achieving values around 1% for unconverted or late-converted photons and up to 2.5% in the EE. Photons converting early exhibit a less favorable energy resolution, ranging from 1.3% to 2.5% in the EB region and up to 4% in the EE.

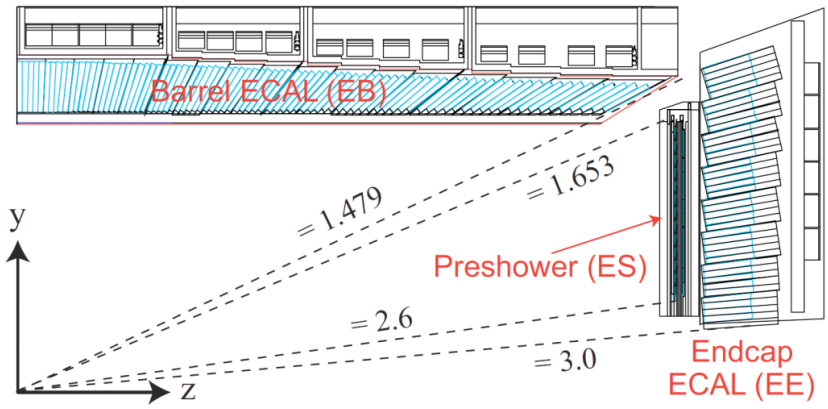

FIGURE 1.7: The geometrical view of one quarter of ECAL. The pseudorapidity coverage of the barrel, endcap and preshower systems are marked [30].

The HCAL together with the ECAL is designed to identify and measure the energies of hadrons and jets. Positioned around the ECAL, the HCAL serves as the last

primary layer of the detector housed within the solenoid magnet volume. Comprising the barrel (HB), endcap (HE), outer (HO), and forward (HF) sections, the HCAL extends the pseudorapidity range up to $|\eta| = 5$, crucial for calculating the total missing transverse energy. The HB and HE, located between the ECAL and the magnet, are sampling calorimeters constructed with alternating layers of brass and plastic scintillator plates. While the HB covers $|\eta| < 1.4$, and the HE extends to $1.5 < |\eta| < 3.0$, both utilise wavelength-shifting fibers embedded in the scintillator plates for readout by Hybrid Photo Diodes (HPD) detectors. The HO in the forward section (HCAL layer just outside the magnet to fully stop all hadrons) is a scintillator detector, intercepts the tails of hadronic showers, covering the region $|\eta| < 1.26$. The HF is situated at $3.0 < |\eta| < 5.0$, beyond the magnetic coil, uses steel as an absorber and quartz fibers as an active medium. With the use of short and long fibers, HF calorimeters are specifically designed to identify high-energy jets with a precision ranging from 20% to 30% at 1 TeV. The geometrical view of one quater of the HCAL is shown in Fig. 1.8

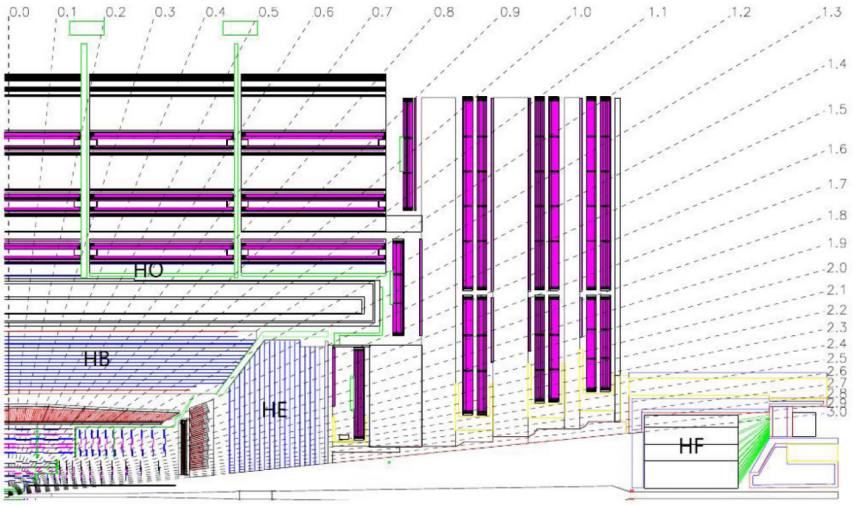

FIGURE 1.8: The geometrical view of one quarter of HCAL. Different subdetectors of HCAL are marked [31].

1.3.4 Solenoid Magnet

The CMS experiment incorporates a robust superconducting solenoid magnet of an internal diameter of 6 m and a length of 12.5 m. While designed to reach a magnetic field flux density of 4 T, the operational magnetic field is set at 3.8 T to optimise the solenoid's lifespan. The magnetic field is achieved by running a 20 kA current through layers of wound niobium-titanium wires cooled to 4.6 K. The solenoidal structure ensures near-homogeneous magnetic field distribution within its volume. This magnetic field, which approximately 100,000 times stronger than the Earth's magnetic field, induces highly curved trajectories for charged particles, facilitating accurate momentum measurements up to $|\eta| < 2.4$ and preventing low p_T particles ($p_T \leq 0.75$ GeV) from reaching the ECAL surface, thereby mitigating PU effects. To contain the magnetic field, a massive 10,000 *tonnes* iron yoke with a diameter of 14.6 m and a length of 21.6 m encloses all subdetectors. This robust structure functions as a partial barrier, impeding the penetration of hadrons into the muon systems within the detector.

1.3.5 Muon System

The muon system, positioned as the outermost layer of the CMS detector and intertwined with the iron return yoke of the magnet system, serves as a crucial element for the identification and measurement of muons. It contributes to the reconstruction of muon tracks, particularly at extended distances from the interaction point, where muons exhibit minimal energy loss to bremsstrahlung and extend beyond the solenoid volume. Due to the considerable distance from the interaction point, the muon system necessitates extensive coverage, leading to the deployment of cost-effective detectors. These detectors play a crucial role in identifying, measuring the momentum, and determining the charge of muons. The specific detector systems employed in the current muon system include Drift Tube chambers (DTs), Cathode Strip Chambers (CSCs), and RPCs. These three systems employed are gaseous detectors, with the DT and CSC systems used to obtain highly accurate and precise position measurements, while RPCs contribute to precise time measurements. A quadrant of CMS (Run II layout) explaining the DT, CSC and RPC stations are shown in Fig. 1.9.

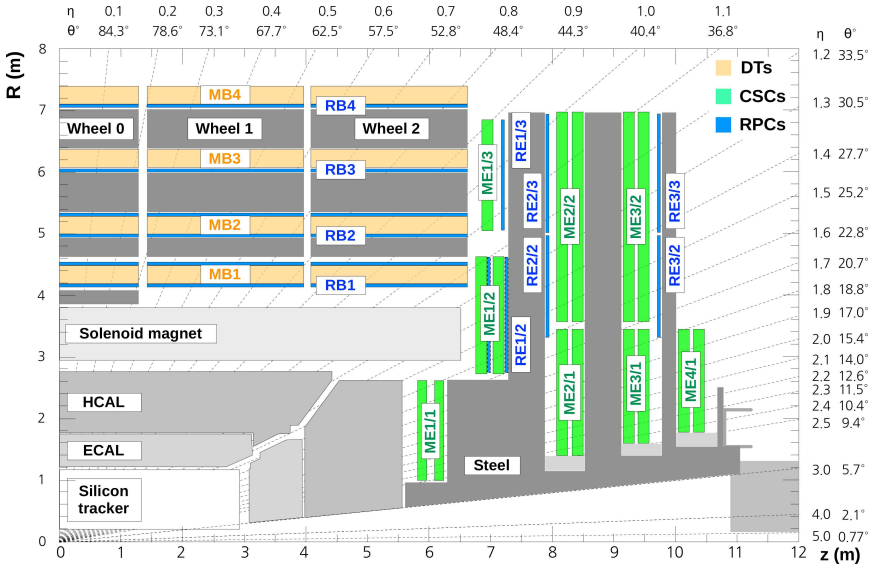

FIGURE 1.9: A quadrant of CMS experiment (Run II layout). The four DT stations in the barrel (MB1–MB4, yellow), the four CSC stations in the endcap (ME1–ME4, green), and the RPC stations (RB1–RB4 and RE1–RE3) are shown [32].

DTs

In the barrel region ($|\eta| < 1.2$), there are four layers (MB1, MB2, MB3 and MB4) consisting of a total of 250 Drift Tube (DT) chambers, accompanied by five layers of RPCs. The first three DT chambers incorporate twelve planes of aluminum drift tubes, with eight dedicated to measuring coordinates in the transverse $r - \phi$ (r and ϕ are radial and azimuthal coordinates, respectively) plane and the remaining four in the longitudinal $r - z$ plane. The outermost chambers exclusively measure in the $r - \phi$ direction, featuring eight planes of drift tubes each.

Each layer of DTs in the muon system, referred as superlayers, comprises four layers of 60 to 70 DT cells arranged in grid pattern to precisely reconstruct the muon path through the layers. Each DT cell is a rectangular (42×13 mm^2) aluminum

gas volume with a central anode wire, surrounded by cathode strips on the narrow surface and electrode strips on the wide surface. The working principle relies on the ionisation of charged particles, where the electrons drift to the central wire, inducing a fast signal. The gas mixture used, Ar/CO_2 (85/15), is effective for quenching and provides a saturated drift velocity of about 5.6 $cm/\mu s$, with a single cell exhibiting an efficiency of approximately 99.8% and a resolution of 180 μm. In Fig. 1.10, the image on the left illustrates the schematic diagram of a single DT cell, while the image on the right depicts the DTs (aluminum) installed at CMS, situated between the steel plates of the yoke (red).

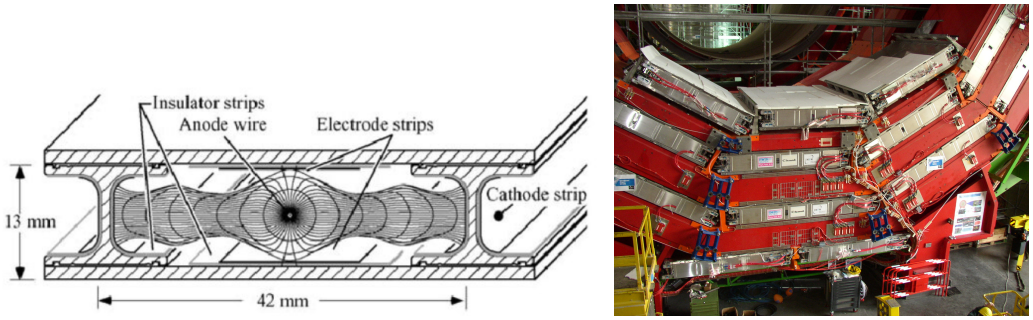

FIGURE 1.10: Schematic representation of a single DT cell (left) and the installation of DTs (aluminum) at CMS, sandwiched between the steel plates of the yoke (in red).

CSCs

The 250 CSCs installed in the endcap region of CMS covers the pseudorapidity region $0.9 < |\eta| < 2.4$ where the muon rate is high and the magnetic field is non-uniform. The are four CSC stations at CMS namely ME1, ME2, ME3, and ME4. The CSCs are multi-wire proportional counters in trapezoidal shape that offers fast response times and enhanced radiation resistance compared to DTs. Each module of CSC at CMS consists of six CSC panels, featuring a wide gas volume containing anode wires and cathode surfaces. The anode wires, spaced at 0.50 μm (or 0.30 μm for specific cases), measure r, while cathode strips, divided trapezoidally and arranged radially, measures ϕ. In Fig. 1.11, the left image shows the geometric layout of a CSC, while the right image depicts the installation of CSCs (ME4/2) within the CMS detector. The gas used in the case of CSCs is a mixture of 40% Ar, 50%

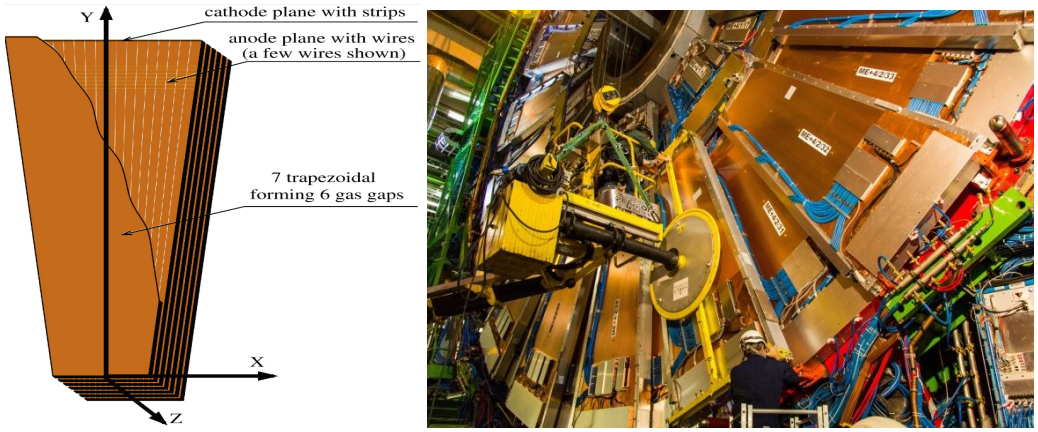

FIGURE 1.11: Left: Geometrical layout of a CSC used at CMS. Right: Installation of CSCs (ME4/2) within the CMS detector.

CO_2, and 10% CF_4. The multiple CSC panels collectively provide a highly precise measurement of muon tracks. To achieve this, cathode strip signals are read out by Cathode Front-End Boards (CFEBs), which digitise the charge and transfer it to off-chamber Data Acquisition Mother Boards (DMBs). Additionally, the combined information from CFEBs and anode wires is processed by on-chamber Anode Local Charged Track Boards (ALCTs) to generate fast trigger information, transmitted to off-chamber Trigger Mother Boards (TMBs).

RPCs

RPCs serve as a redundant system in the CMS muon system, contributing significantly to muon triggering in both barrel (with DTs) and endcap (with CSCs) regions. A total of 1056 RPCs detectors covers $|\eta|$ region up to 1.9 and are distributed in five barrels and eight disks. Figure. 1.12 shows a CMS RPC endcap disk with the installed chambers.

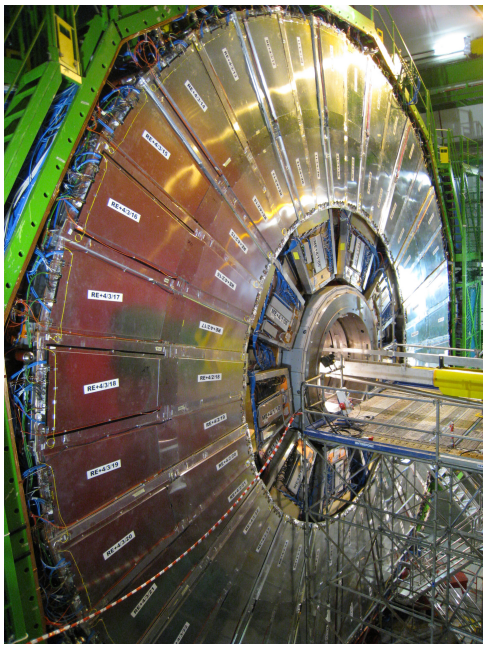

FIGURE 1.12: A CMS RPC endcap disk with the installed chambers [33].

In the barrel region, every RPC layer comprises twelve sectors, providing complete 2π coverage. A wheel consists of four detector stations aligned at the same radius (R) around the beam line, as depicted in Fig. 1.13 (top). The first two stations feature two RPC layers on either side of a DT module, while the subsequent stations, positioned farther from the beam line, have a single layer of two RPCs installed alongside each DT chamber, except for the fourth station. The barrel RPCs are denoted as "RB$n \pm w$", where n represents the station number increasing with R, and $\pm w$ indicates the wheel number (w = 0 corresponds to the central wheel). Within each layer, RPCs are distinguished using additional descriptors such as "in" and "out" for stations 1 and 2, or "-" and "+" for stations 3 and 4.

In the endcap, detectors are mounted on disks arranged in three rings, two of which are equipped with RPCs, serving as stations. Figure 1.13 (bottom) provides a view of an RPC endcap disk (+2). Unlike the barrel stations, the endcap stations

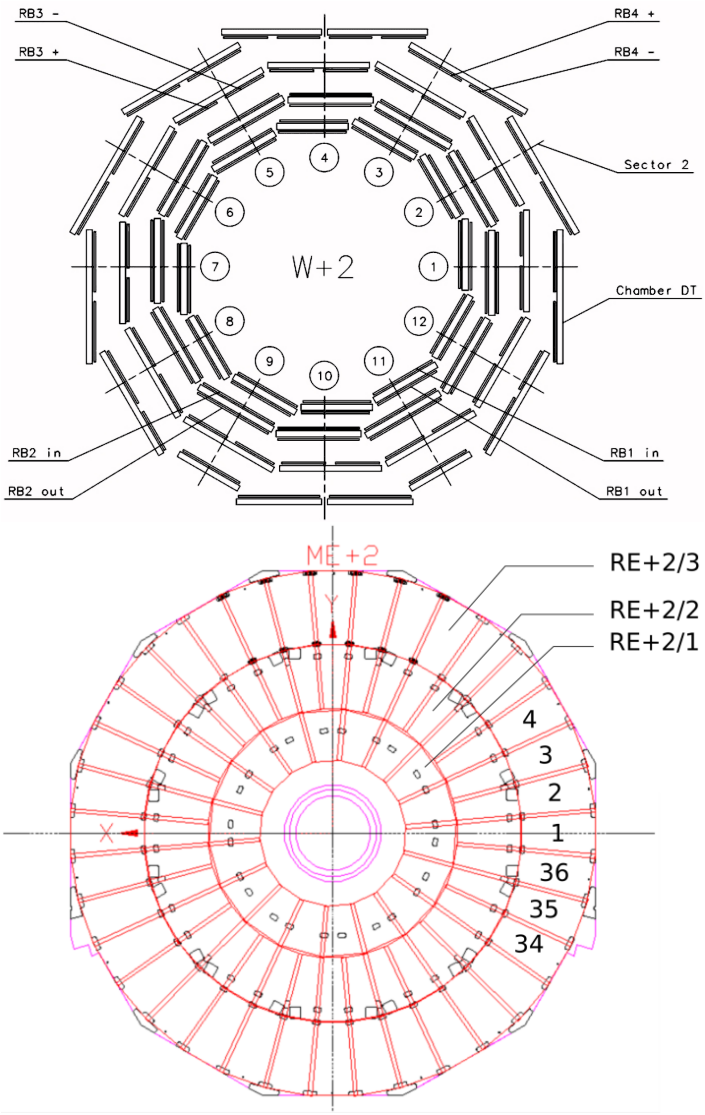

FIGURE 1.13: Top: Graphical layout of the positions of DT and RPC detectors in barrel wheel W+2. Bottom: Graphical layout of the positions of RPC detectors in endcap disk ME+2 [34].

correspond to detectors positioned at similar z values, perpendicular to the beam line. Each ring covers a distinct R range and consists of 36 trapezoidal detectors. The endcap RPCs are labeled as "RE$\pm n/r$", where n represents the station number (i.e., the endcap disk), and r indicates the ring number increasing with R.

The CMS RPCs are gaseous detectors with a rectangular shape in the barrel region and trapezoidal shape in the endcap region, characterised by two gas gaps and a strip readout plane sandwiched in between them. Utilising a gas mixture of 95.2% $C_2H_2F_4$, 4.5% i-C_4H_{10}, and 0.3% SF_6, RPCs are integral in addressing the limitations of wire chambers like DTs and CSCs[1], offering a superior time precision of approximately 1 ns, making them well-suited for efficient muon triggering.

[1]While wire chambers such as DTs and CSCs offer impressive spatial resolution, their time resolution is constrained by the requirement for the charge to drift towards the anode wire and be collected before particle detection confirmation.

The working principle of RPCs and details of double-gap RPCs are provided in Sec. 2.4.1 and Sec. 2.5.1, respectively. The geometry and layout of CMS endcap RPCs and the details of the chamber components are explained in Sec. 3.3.1. For more detailed information of the complete muon system, the reader is referred to [23]

1.3.6 Trigger and Data Acquisition

The operation of the CMS experiment at the LHC involves a complex synergy between the data acquisition system (DAQ) [35] and the trigger system [36], crucial for managing the vast amount of data generated. With the LHC producing approximately 10^9 proton-proton collisions per second, each event could result in a staggering 950 TB per second of data. However, the DAQ system, capable of processing around 100 MB per second, necessitates the implementation of a sophisticated trigger system to filter and select events of interest. The trigger system comprises detector electronics, a readout system, Level 1 (L1) trigger processors [37] for quick decisions, and software-based High-Level Triggers (HLT) [38] running on a computing cluster. The L1 trigger operates with a maximum output rate of $\sim$100 kHz, using reduced granularity information to construct "trigger primitive" objects. Events passing the L1 trigger are further processed by the HLT, which employs more sophisticated criteria and information from the inner tracking system, achieving an output frequency of 100 Hz. In case of overwhelming data rates, certain trigger paths may be "pre-scaled" to manage the load effectively.The selected events are permanently recorded by the DAQ system and transferred to the CERN Tier0 storage system. Data quality monitoring (DQM) ensures the quality of recorded data, certifying datasets for subsequent physics analysis.

1.3.7 The CMS Phase-2 Upgrade for HL-LHC

The LHC was originally designed for an instantaneous luminosity of $10^{34}\ cm^{-2}\ s^{-1}$ and an integrated luminosity target around 300 fb^{-1}. The substantial increase in luminosity during the HL-LHC, as detailed in Sec. 1.2, to five times the machine's original design, poses several challenges for the CMS subdetectors. This includes the increased pileup (PU), leading to more challenging background conditions, higher trigger rates, increased complexity in event reconstruction, and accelerated ageing of detector components. To address the challenges posed by these conditions, CMS is undergoing a series of upgrades, with a focus on the tracker and endcap calorimeters due to radiation damage. The increased tracker granularity aids particle-flow event reconstruction, crucial for PU effects mitigation.

To maintain efficient event selection, low transverse momentum triggers are essential, necessitating upgrades to the trigger electronics, specifically the L1 trigger. The introduction of tracking information at L1 enhances the trigger performance, demanding a new hardware architecture for the Phase-2 Tracker. In Run 2, the Phase-1 upgrade of the CMS muon trigger involved the integration of RPC hits with DT and CSC trigger primitives (TPs) in both the barrel and endcap regions before the track-finding stage. The previously independent RPC track finding was discontinued, resulting in enhanced TP efficiency. The RPC information in the barrel also contributed to improved timing. In the overlap region ($0.9 < |\eta| < 1.2$), TP from all three subsystems are utilised in the L1 track finding. During Phase-2, there will be an increase in the maximum L1 rate from 100 kHz to 750 kHz, and adjustments in the front-end data buffers to accommodate a higher L1 trigger latency, extended from

the current 3.6 μs to 12.5 μs. The Phase-2 L1 muon trigger architecture, illustrated in Fig. 1.14, integrates TPs from various muon subdetectors, similar to Phase-1. En-

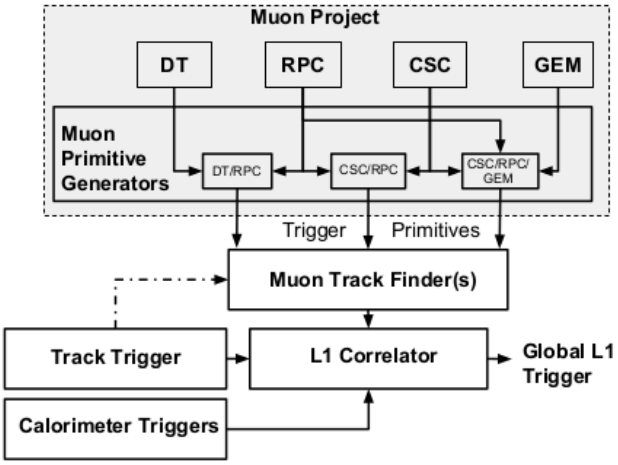

FIGURE 1.14: Block diagram of the Phase-2 L1 muon trigger data flow [39].

hanced capabilities are introduced with the incorporation of GEM and RPC forward chambers, along with improved timing for DT and RPC. The early combination of hits from new GEM chambers and trigger primitives from nearby CSC chambers improves efficiency and provides local muon direction and position measurements. Standalone muon candidates are still generated by Track Finders [40]. The L1 muon trigger's momentum resolution for muons originating from the primary vertex sees significant improvement with the addition of information from the "Track Trigger," a feature inherent in the design of the new silicon outer tracker [41]. The spatial coincidence with L1 standalone muon candidates facilitates the identification of well-measured muons with enhanced momentum resolution. The combination of the L1 Global Muon Trigger candidate with L1 Tracker Track candidates is managed by a correlator in development [39].

Upgrades also extend to the muon system, endcap calorimeter, and readout electronics, ensuring efficient data-taking under high PU conditions. The sustainability of high luminosity will be influenced by sub-detectors not replaced for Phase-2, and simulation studies will explore alternatives to luminosity leveling schemes and PU beyond 140, with a focus on improving PU mitigation strategies.

A detailed overview of the CMS Phase-2 upgrade program can be found in [42]. Additionally, dedicated documentation is available for each specific upgrade program, covering the tracker [43], calorimeters [44, 45], muon system [39], L1 trigger [46], and DAQ [47]. As this thesis focuses on the activities related to the CMS muon system upgrade, with a specific emphasis on the upgrade of the endcap RPC system, the subsequent section provides details regarding the muon system upgrade.

1.4 The Phase-2 Upgrade of the CMS Muon System

To ensure the CMS muon system maintains its exceptional performance during the HL-LHC phase, several crucial measures are required. The details of upgrade

program of CMS for the current muon detectors, the installation of new muon detectors in the forward region and ongoing studies aimed at ensuring the long-term operation of the existing muon detectors are discussed in this section.

1.4.1 Upgrade of the Existing Muon Detectors

The sustained operation of the existing muon detectors is important for the precise identification and measurement of muons, meeting the rigorous requirements of the CMS physics program during HL-LHC. This requires multiple upgrades to the electronics of the current systems, as detailed in the following subsections.

DT Upgrades

The hit rates in DT chambers at the HL-LHC are projected to reach up to 50 kHz per drift cell, with MB1 chambers in large-z wheels and MB4 chambers facing elevated neutron induced background experiencing the highest rates. Longevity tests demonstrate that most chambers maintain performance, except for MB1 stations in outer wheels and MB4 detectors, where a notable drop in hit efficiency is predicted due to gas gain reduction caused by deposits on anode wires. The MB1 chambers in outer wheels are anticipated to have hit efficiency drop below 50% during HL-LHC, but considering the large number of hits per muon track, the overall track reconstruction efficiency remains above 90% in the barrel and 95% in the barrel-endcap overlap pseudorapidity range. Mitigation measures, including increased high voltage and improved neutron shielding for MB4 chambers, are under active consideration. Despite challenges, the current DT chamber system is expected to operate efficiently throughout Phase-2, eliminating the need for replacement.

The existing Minicrate electronics (MiC1), linked to individual DT chambers, necessitate an upgrade to enhanced Minicrates (MiC2) for HL-LHC. This transition is required due to MiC1's inadequacies in handling the required L1 trigger rate (limited to 300 kHz), falling short of the Phase-2 specifications. In addition, longevity concerns and potential failures of MiC1 components underscore the need for MiC2. The MiC2 design involves relocating complex trigger logic to the CMS underground control room, reducing Minicrate interventions, lowering power consumption, and improving cooling efficiency. The MiC2, with On-Board electronics for DT boards (OBDT), facilitates data transfer via high bandwidth optical links to the back-end located outside the experimental cavern. This new architecture enhances trigger algorithm capabilities, removes constraints on CMS DAQ conditions, and improves overall system accessibility. The installation of MiC2 is planned for LS3, ensuring a smooth transition from MiC1. For the details and current status of the DT upgrades, the reader is referred to [48, 49].

CSC Upgrades

The CSC upgrades aim to address trigger latency, data loss, and power consumption concerns. The replacement of some read-out electronic boards is essential to address increased L1 trigger rates and chamber occupancies. The new boards will utilise high-speed output optical links and faster processors, allowing them to cope with higher trigger rates and latency. Current cathode front-end boards (CFEBs) using analog charge storage will be replaced with digital cathode front-end boards (DCFEBs) to enhance rate capability and radiation resistance. The DCFEBs send the

trigger data via 3.2 Gb/s optical links, therefore the trigger mother boards (TMBs) servicing the inner rings will be upgraded to optical TMBs (OTMBs). The ME1/1 ring, equipped with DCFEBs, will undergo upgrades, while CFEBs in other rings, close to the beam, face potential memory overflows and inefficiencies at HL-LHC due to high trigger rates. Similar to TMBs, the data acquisition mother boards (DMBs) in the inner rings will be upgraded with new optical DMBs (ODMBs) to handle the HL-LHC data rates. These boards will have output bandwidths of up to 25.6 Gb/s, achieved with multiple 6.4 Gb/s links. The back-end electronics collecting all the CSC data will be upgraded accordingly.

Anode local charged track boards (ALCTs) detecting charge deposits on CSC anode wires will be also upgraded. ALCT mezzanine boards in rings closest to the beam will be replaced, except for upgraded ME1/1 and ME4/2 chambers. This upgraded ALCTs in inner and outer CSC rings will incorporate more powerful FPGAs and optical links, with output bandwidths up to 6.4 Gb/s (ten times higher than before).

Additionally, Low Voltage Distribution boards (LVDB) and High Voltage (HV) systems will be upgraded to ensure reliable CSC operation during HL-LHC. The new electronics, consuming more power, require LV system redesign with higher currents and appropriate voltage levels. Altogether, the upgrade involves replacing a total of 1044 on-chamber electronics boards and 302 trigger and DAQ modules in the CSC system. A series of upgrade activities of CSCs were already conducted during LS2 and the remaining will be performed during LS3 (for details, the reader is referred to [50, 51]).

RPC Upgrades

The RPC system anticipates two upgrade measures. While the existing RPC chambers remain operational through Phase-2, there is a need to replace the link system that connects the front-end board to the trigger processors. Moreover, the introduction of new version of RPC detectors, RE3/1 and RE4/1, is proposed for the CMS forward region (explained in Sec. 1.4.2).

During HL-LHC a maximum rate of 600 Hz/cm^2 is expected for existing RPC chambers. All other RPC electronics boards, including front-end electronics, are certified radiation-hard for Phase-2. However, the current link system, comprises electronic boards utilising outdated IC components, most of which are no longer available in the market. Additionally, the supply of spare boards for the existing system is limited, and these boards contain fragile electronic components susceptible to electromagnetic interference, lacking certification for the full HL-LHC life cycle. To address these challenges, an upgrade to the current link system is necessary.

The upgraded link system comprises 1376 Link Boards, with additional construction of new Control Boards and optical links. The previous Link Boards, which utilised ASICs, will be replaced with faster FPGAs. These new FPGAs can concurrently process signals from multiple RPC detectors, ensuring the required speed is easily achieved. The fresh Control Boards will transmit data in parallel to the main computer via Ethernet, replacing the current token ring logic. The Link Boxes, housing both Link and Control Boards, will be retained. Long-term radiation resistance is

assured, as the expected total ionisation dose in the link boards at HL-LHC is below 100 *Rad*, well within the tolerated dose limit of a few *kRad*. Despite efforts to minimise single event upsets (SEU) in FPGAs through error correction code and regular configuration data reloading, complete avoidance remains challenging. Presently, the link system records hit times in 25 *ns* increments, synchronised with LHC bunch crossings and the upgraded system will eliminate this limitation, fully exploiting the intrinsic time resolution of RPC chambers, which is approximately 1.5 *ns* [52, 53].

1.4.2 New Detectors in the Forward Region

Throughout the HL-LHC, the two endcap regions of CMS will face elevated muon and background rates and the magnetic field in this region will be weaker. To guarantee effective muon triggering and accurate offline muon identification and reconstruction, it is important to measure a substantial number of detector hits for each muon track. As a result, to enhance the redundancy of the muon system and achieve robust track reconstruction, new detectors (GE1/1, GE2/1, RE3/1, and RE4/1) will be introduced in the forward region as part of the Phase-2 upgrades. The details of these new detector stations are described in this section.

Improved RPCs: RE3/1 and RE4/1

An improved version of the existing RPCs, referred as iRPCs, will be installed in the CMS forward region in the third (RE3/1) and fourth endcap disks (4/1). This will extend the geometrical acceptance of the RPCs from $|\eta|$ = 1.9 to 2.4. Although the potential installation of RPCs in this region was explored in the original CMS muon Technical Design Report (TDR)[54], it was not implemented due to the limitations of the existing RPC detector generation in handling high hit rates. The iRPCs have been specifically designed to address these challenges. The work described in Chapter 3 centers on the iRPC upgrade activities for the CMS experiment and the complete details of the project, emphasising the my contributions, are presented in the chapter.

Gas Electron Multipliers

The GEM (Gas Electron Multiplier) technology, successfully utilised in various particle physics experiments such as COMPASS [55] and LHCb, has demonstrated reliable operation at hit rates around a few MHz/cm^2, meeting the requirements for CMS at the HL-LHC. No ageing issues have been reported so far.

GEMs are gaseous detectors [56] designed with a gas volume confined between two planar electrodes, where the anode serves as the read out panel. The gas volume is partitioned into multiple regions by one or more thin GEM foils, typically a few tens of micrometers thick. These foils are perforated with holes, as depicted in Fig. 1.15 (Left), and both surfaces are coated with copper to create a strong electric field across the holes. The region between the cathode and the GEM foil, known as the drift region, experiences a moderate electric field, insufficient to initiate avalanches and amplification (details of operation of gaseous detectors is explained in Sec. 2.2). Primary electrons drift toward the foil, where they are accelerated and amplified within the holes, as illustrated in Fig. 1.15 (Right). Subsequently, the electrons enter the second drift region, inducing a signal on the read-out located on the anode. By limiting the amplification process to the holes, the electrons remain confined in a

GEM Detector	$\|\eta\|$ region	Expected rate (kHz/cm^2)	Aging threshold (mC/cm^2)
GE1/1	1.55-2.2	10	200
GE2/1	1.62-2.43	2.1	9
ME0	>2.4	150	840

TABLE 1.1: $|\eta|$ regions, expected hit rates and the charge that need to be integrated during the aging campaign for the qualification of the detectors (aging threshold) of the GEM detector systems.

small space, producing highly localised currents. This characteristic imparts exceptional spatial resolution to GEMs. The process can be iterated for stronger amplification.

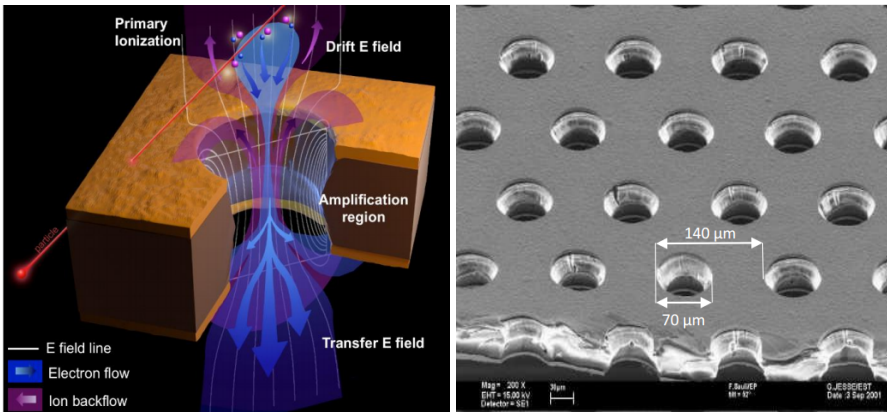

FIGURE 1.15: Left: Image of a CMS GEM foil obtained with a scanning electron microscope. Right: Graphical representation of the amplification process in the hole of a GEM foil [57].

The GEMs chosen for CMS [57, 58] are triple-GEM detectors using a 70/30 gas mixture of Ar/CO_2. They consist of three GEM foils, each clad with 5 μm of copper on each side, and pierced with double-canonical holes (inner and outer diameters of 50 and 70 μm) spaced 140 μm apart in a hexagonal pattern, as shown in Fig. 1.15 (Right). These detectors exhibit a time resolution better than 10 ns and achieve excellent spatial resolution of less than 200 μrad. Notably, the position of the hits is determined not along the strips but following the azimuthal angle granularity of the radially organised trapezoidal strips.

Three sets of GEM detectors are to be used in CMS: GE1/1, GE2/1 and ME0. The details of each systems which includes the $|\eta|$ regions, expected hit rates and the maximum charge (aging threshold) that need to be integrated during the aging campaign for the qualification of the detectors are given in Tab. 1.1. All three detectors require time resolution <10 ns and angular resolution <500 μrad. Incorporating GEMs in the muon system's forward region significantly improves L1 trigger performance. The triggering efficiency in the region $1.6 < |\eta| < 2.4$ rises consistently from 80-90% to 92-94%. In addition, beyond $|\eta| = 2.4$, the ME0 detector extends muon acceptance which is beyond the reach of any other CMS muon detector due to mechanical constraints [58].The addition of GEMs enhances precision in muon measurements by an order of magnitude, enhancing overall system performance.

1.4.3 Studies for Long-Term Operation of Detectors

Longevity Studies

Prolonged radiation exposure can induce ageing effects in gaseous detectors, leading to a loss of gas gain, increased spurious signal rates ("dark rate"), elevated leakage currents ("dark current"), and the development of self-sustained discharges (Malter effect [59]). Causes include chemical processes in electron multiplication avalanches, forming polymers on anode wires, cathode surfaces, and anode-cathode insulating elements. CSCs and DTs could experience wire thickening and oxidation, impacting gas gain. Deposits on CSC cathodes can affect spatial resolution, while in DTs, conductive deposits distort electric fields, affecting signal efficiency. RPCs and GEMs are susceptible to polymerisation on surfaces, impacting gas gain and operational stability. The details of ageing effects in RPC detectors can be found in Sec. 2.4.8.

In addition to possible ageing effects in the gaseous detectors themselves, their electronics, particularly semiconductor chips, are vulnerable to radiation damage. Two main mechanisms contribute to this damage: ionisation from charged particles and photons, and displacement of atoms' nuclei caused by neutrons. These mechanisms can lead to ageing effects in electronics, resulting in permanent degradation of performance, increased noise, altered response characteristics, and functional failures.

Therefore, in order to ensure stable and efficient operation during HL-LHC, all muon subsystems and their electronics undergo a series of ageing tests. Test chambers are installed at the GIF++ facility at CERN [60], where detectors are continuously irradiated at levels significantly higher than expected during HL-LHC. So far, there are no signs of ageing observed in the DT [61], CSC [62], RPC [63] test chambers. Despite the absence of ageing effects, minor drops in parameters like detection efficiency and spatial resolution are anticipated. Overall, the current systems demonstrate capability under HL-LHC conditions.

Measures for Restricting Greenhouse Gas Consumption

In 2014, the European Commission implemented the "F-gas regulation" to control the use of fluorinated Greenhouse Gases (GHGs) in the EU. CERN is actively responding to these regulations. Within the CMS experiment, CSCs and RPCs operate using fluorinated gas mixtures, while DTs and GEMs utilise Ar/CO_2-based mixtures. The use of fluorinated gases is crucial for CSCs and RPCs, with CF_4 enhancing CSC longevity, ensuring fast electron drift velocity, and serving as a non-flammable photon quencher. In RPCs, $C_2H_2F_4$ acts as the main ionising gas, while SF_6, a strongly electronegative gas, is essential for maintaining stable RPC operation. Details of European Union (EU) regulations aimed at reducing GHG emissions, the GHG emission situation at LHC, and strategies implemented by the CMS collaboration to minimise the use of fluorinated gases are provided in Sec. 4.1 and Sec. 4.2.

The RPC systems significantly contribute to GHG emissions at CERN. In 2019, a new collaboration named ECOgas@GIF++ was established to explore eco-friendly gas mixtures as alternatives for RPCs at LHC [64]. Participation includes all LHC experiments and the EP-DT group at CERN. RPC test detectors from all these groups

are undergoing irradiation studies at GIF++ with different eco-friendly alternative gas mixtures. The Chapter 4 provides detailed insights into the collaboration's activities, the current gas mixtures under study focusing on my contributions to the project.

Since the GIF++ facility plays a crucial role in the longevity and alternative gas search studies of CMS RPC group and ECOgas@GIF++ collaboration, and the beam tests and the ageing studies described in Chapter 3 and Chapter 4 were conducted at GIF++, an overview of the facility and its operation is provided in the following section.

1.4.4 The Gamma Irradiation Facility at CERN

The GIF++, operational since spring 2015, is an experimental facility at CERN developed to focus on the characterisation and understanding of the long-term behavior of large gas-based particle detectors. GIF++ utilises a 12.5 TBq ^{137}Cs[2] source of 662 keV gamma photons with adjustable filters to modulate intensity and a high-energy muon beam (100 GeV/c) from the secondary SPS beamline H4 in EHN1 [65]. The layout of GIF++ and the coordinate system is depicted in Fig. 1.16. The GIF++ bunker, encompassing 100 m^2 and standing approximately 5 m tall, features two independent irradiation zones named upstream and downstream. This design facilitates simultaneous testing of full-size detectors, measuring up to several square meters, and a diverse range of smaller prototype detectors and electronic components

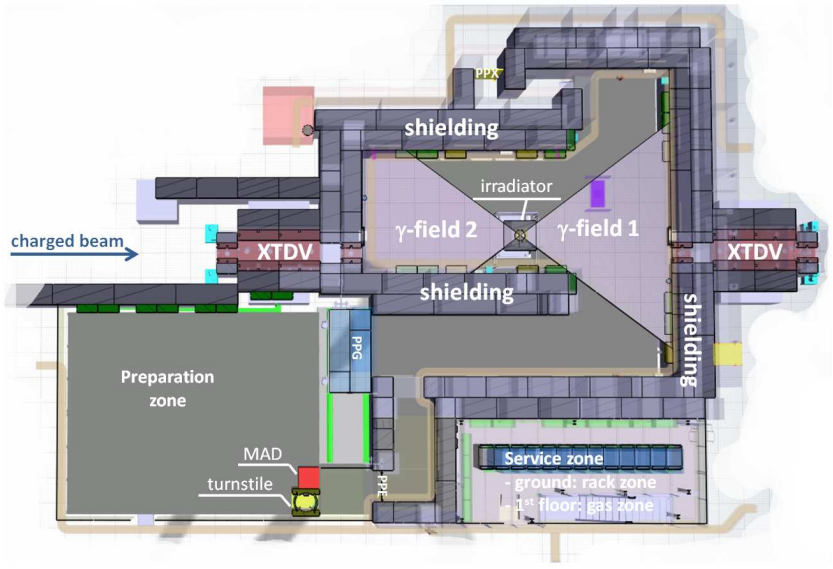

FIGURE 1.16: Layout of the GIF++ facility, showcasing entry points including MAD (material access door), PPG (personal protection gate), PPE (personal protection entrance), and PPX (personal protection exit). In cases where the facility downstream of GIF++ employs an electron beam, a beam pipe is installed along the z-axis between the vertical mobile beam dump (XTDV) [66].

[2]The choice of ^{137}Cs over ^{60}Co is driven by its longer half-life, minimising the photon rate decrease over the facility's expected lifetime.

GIF++ is a primary user of the H4 beam line [67] for six to eight weeks annually, receiving parasitic muon beam halo during 30–50% of SPS operation time. The muon beam, generated as a secondary beam from the primary SPS proton beam, spans an energy range of 57–100% of the nominal beam energy. The spill structure aligns with the primary proton beam, arriving approximately every 30 s. With full acceptance, the muon beam intensity can reach up to 10^4 muons per spill, constrained by radiation protection considerations. The secondary beam can be adjusted for hadrons and/or electrons. The muon beam distribution depends on factors such as final focusing and settings chosen by the primary beam line user. Generally, the muon beam core covers a 10 $cm\times$ 10 cm surface, with the remaining beam halo spread over an approximately 1 m^2 footprint. Gamma irradiation is consistently available throughout the entire year, excluding brief maintenance intervals.

Figure 1.17 (Left) illustrates the GIF++ irradiator and its filter systems. The cesium source in the irradiator is movable, allowing transition from the garage position at the bottom to the irradiation position at the top of the support tube. Equipped with two panoramic collimators with a $\pm 37^\circ$ range, the irradiation zone spans a significant part of the bunker area in both downstream and upstream regions. Both outlets of the irradiator, as depicted in Fig. 1.17 (Left), feature a lens-shaped angular correction filter to ensure a uniform photon distribution over a plane, ideal for flat large area detectors. There are two complete and independent attenuation systems are available where each system consists of a 3 $\times$ 3 array of convex lead attenuation filters, enabling precise adjustment of the photon flux for each irradiation field.

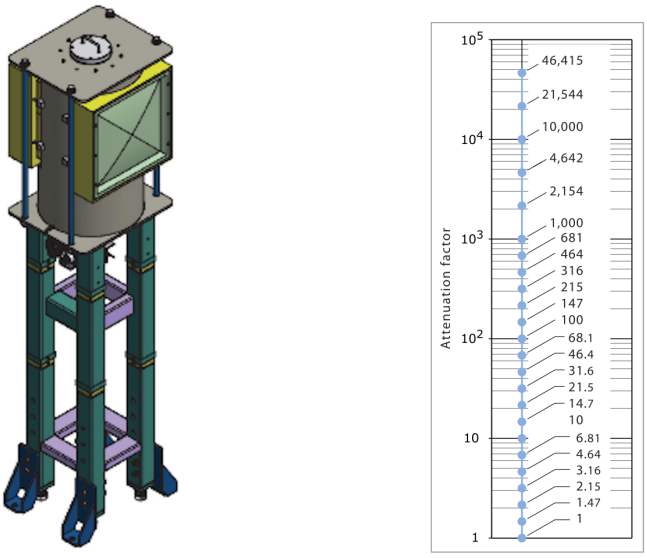

FIGURE 1.17: Left: (a) Schematic drawing of the GIF++ irradiator with angular correction filters and independent filter systems at both sides. Right: Each set of 3 $\times$ 3 movable attenuation filters, with 27 combinations of filters, leads to 24 different attenuation factors between 1 and 46415. [66].

Three planes of filters (A, B, C), with three filters per plane, are installed. These filters have nominal attenuation factors ranging from 1 (A1, B1, C1), 1.5 (B2), 2.2 (C2), 4.6 (C3), 10 (A2), to 100 (A3, B3). The total attenuation factor, determined by the three filter layers, can be adjusted using a dedicated control panel and the GIF++ control system. In total, 24 different attenuation factors between 1 and 46415 are achievable,

offering 27 possible combinations. The selection of factors is nearly equidistant on a logarithmic scale across the first three orders of magnitude, as illustrated in Fig. 1.17 (Right). The irradiator and the two filter systems are mounted on rails, allowing the entire assembly to be transversely moved in the direction perpendicular to the muon beam. An angular correction filter is also incorporated into the irradiator, converting the irradiation field from a point-like source dependency ($\propto 1/r^2$) to a uniform distribution in a vertical plane perpendicular to the bunker walls.

The CMS RPC group and the ECOgas@GIF++ collaboration have positioned their individual test chambers within the GIF++ bunker using specialised mechanical trolleys. The details of the experimental setups are explained in Sec. 3.5.1 and Sec. 4.4.

Chapter 2

Resistive Plate Chambers

2.1 Introduction

RPCs serve as spark-protected, position-sensitive detectors designed for charged particles, gamma photons and neutrons. These detectors demonstrate remarkable precision, achieving position resolutions below 100 μm and time resolutions better than 50 ps. Their notable features include robustness, simplicity of construction and cost-effectiveness.

RPCs are extensively employed in various experiments, such as those conducted at the LHC, CERN, including the CMS experiment mentioned in the preceding chapter (Chapter 1), where the total RPC coverage exceeds 10,000 m^2. Other experiments utilising RPCs include the Belle detector at the High Energy Accelerator Research Organisation (KEK) [68], the Beijing Spectrometer III (BESIII) experiment at the Beijing Electron-Positron Collider II (BEPCII) [69], the ARGO-YBJ experiment at the YangBaJing Cosmic Ray Laboratory [70] and the nuclear physics experiment HADES (High Acceptance Di-Electron Spectrometer) at GSI [71]. As discussed in the previous chapter, new versions of RPCs are also being designed and implemented as part of the upgrade programs for LHC experiments.

More recently, RPCs are being explored and adapted for interdisciplinary applications, including their use in time-of-flight positron emission tomography (TOF-PET) [72] and imaging applications utilising cosmic muons [73].

The majority of the research activities discussed in this thesis, primarily focuses on the development and study of RPC detectors for different applications. This chapter is dedicated to providing insights into the physics of RPCs. A concise overview of ionisation detectors and their working principles is presented in Sec. 2.2. Section 2.3 provides the details of the evolution of RPCs, offering details on the early-stage parallel plate detectors and their progression into modern RPCs. In Sec. 2.4.1, the specifics of modern RPCs are discussed, encompassing their layout, working principles, operational details, gas mixtures, etc. The final section, Sec. 2.5, elucidates the details of two RPC types relevant to this thesis.

2.2 Ionisation Detectors and their Working Principle

This section provides insights into the earliest advancements in radiation detection technology, specifically ionisation detectors. Brief details of the ionisation mechanisms, early ionisation detectors: ionisation chamber, proportional counter and

Geiger-Muller counter, and the operational principle of ionisation detectors are provided.

2.2.1 Earliest Ionisation Detectors

Ionisation detectors represent the initial advancements in radiation detection technology, relying on the direct collection of ionisation electrons and ions generated in a gas by incident radiation. Throughout the first half of the twentieth century, three primary types of detectors emerged: the ionisation chamber, the proportional counter and the Geiger-Muller counter. While these devices are not extensively utilised in modern nuclear and particle physics experiments, they persist as valuable tools in laboratories for radiation monitoring. Their continued relevance is attributed to their cost-effectiveness, straightforward operation and ease of maintenance.

The fundamental structure of the ionisation chamber, the proportional counter and the Geiger-Muller counter is essentially the same, differing primarily in their operational parameters. Figure 2.1 shows the basic configuration of the detectors with conductive walls and a thin end window. The cylinder is filled with a suitable

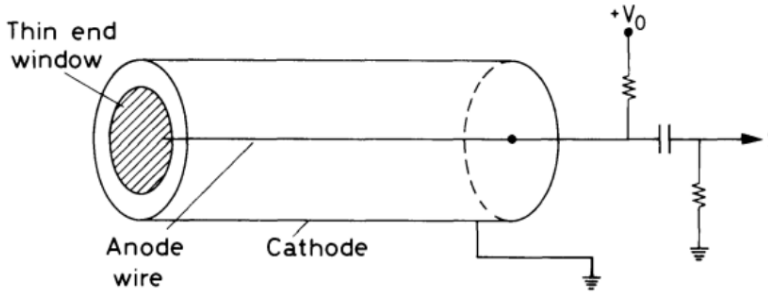

FIGURE 2.1: Basic configuration of ionisation chambers [74].

gas, typically a noble gas like argon. A conducting wire, suspended along its axis, is subjected to a positive voltage (V_0) relative to the walls, creating a radial electric field (E_{rad}) with parameters r (radial distance from the axis), b (inside radius of the cylinder) and a (radius of the central wire), described by the formula:

$$E_{rad} = \frac{1}{r} \frac{V_0}{ln(b/a)} \tag{2.1}$$

Upon the penetration of radiation into the cylinder, a specific number of electron-ion pairs are generated, either directly for charged particles or indirectly through secondary reactions for neutral radiation. The average number of pairs formed is directly proportional to the energy deposited in the counter. Guided by the electric field, electrons move toward the anode, whereas ions move toward the cathode, where they are collected.

The number of electron-ion pairs generated depends on the applied electric field and this relation is explained by Fig. 2.2. Initially, at zero voltage, no charge is collected due to ion-electron pair recombination. As voltage rises, the recombination forces are overcome, leading to increased current until all created pairs are collected, marking the first flat region (Region II) in Fig. 2.2. Detectors operating in this region

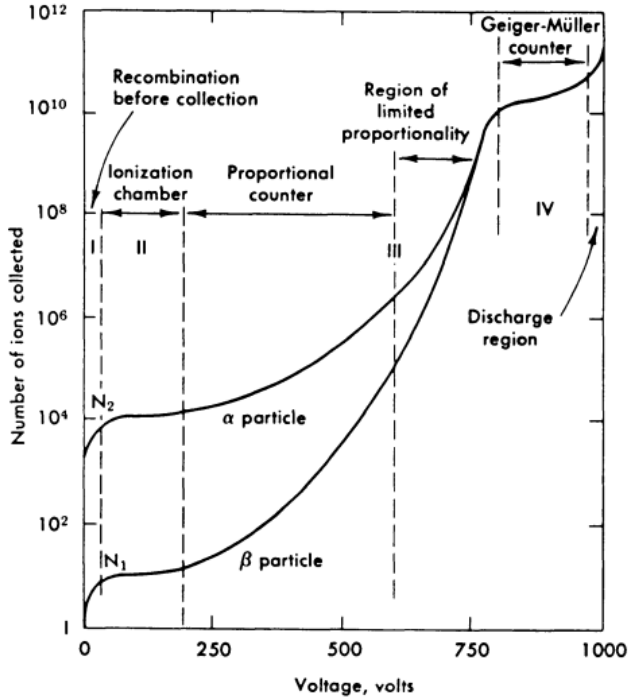

FIGURE 2.2: Number of ions collected as a function of applied voltage in a basic wire gas chamber [74].

are termed ionisation chambers, suitable for measuring gamma ray exposure and monitoring large radiation fluxes. Beyond Region II, further voltage increases result in an ionisation avalanche, causing a proportional amplification of the current, characterising the proportional chamber (Region III). If voltage surpasses Region III, the total amount of ionisation created through multiplication becomes sufficiently large and the space charge created distorts the applied electric field, leading to limited proportionality. Further increasing voltage triggers discharge, marking the Geiger-Muller or breakdown counters region, characterised by a plateau in count rate. Continuous breakdown, with or without radiation, occurs at higher voltages, posing a risk of counter damage and should be avoided for radiation detection applications. This illustration demonstrates how gas multiplication, discharge and gas ionisation contribute to radiation detection phenomena.

2.2.2 Ionisation and Gas Transport

Ionisation Mechanisms:

The primary ionisation is defined as the process where electrons and ions are produced by incident radiation, as outlined in the equation 2.2.

$$X + p \rightarrow X^{+} + p + e^{-} \tag{2.2}$$

Here, X is the excitation of an atom, and p and e^{-} are proton and electron respectively. However, in certain instances, an electron may receive sufficient energy during primary ionisation to initiate the creation of additional ion-electron pairs, constituting secondary ionisation. If the energy of these secondary ionisation electrons is sufficiently high, they can, in turn, induce further ionisations, creating a cascading effect until the ionisation reaction threshold is reached.

A second gas ionisation mechanism is the "Penning Effect", occurring in specific atoms where metastable states, due to significant spin-parity differences, cannot promptly deexcite to the ground state by emitting a photon. In such atoms, deexcitation may transpire through collisions with other atoms, resulting in the ionisation of the latter. This effect is notable in the interaction between molecular gases and noble gases, including the interactions among noble gases themselves, exemplified by equations such as:

$$Ne^* + Ar \rightarrow Ne + Ar^+ + e^- \tag{2.3}$$

A third noteworthy mechanism observed in noble gases involves the creation of molecular ions. In this process, a positive gas ion interacts with a neutral atom of the same type, forming a molecular ion, represented by the equation:

$$He^+ + He \rightarrow He_2^+ \tag{2.4}$$

Due to the statistical nature of ionising reactions, it is observed that identical particles generally do not produce the same number of ion-electron pairs. The exploration of the average number of ion-electron pairs created for a specific energy loss is significant. It is important to note that this average is not equivalent to the energy loss divided by the ionisation potential, as some energy is also lost to excitation. In gases, this average is approximately one ion-electron pair per 30 eV of energy lost. Notably, this average value exhibits relatively weak dependence on particle type and gas composition. Table. 2.1 provides a comparison of measured average values for various gases utilised in ionisation detectors. The significance of the average energy, lies in its role in determining both the efficiency and energy resolution of the detector [74].

Gas	Excitation potential [ev]	ionisation potential [ev]	Mean energy for ion-electron pair creation [ev]
H_2	10.8	15.4	37
He	19.8	24.6	41
N_2	8.1	15.5	35
O_2	7.9	12.2	31
Ne	16.6	21.6	36
Ar	11.6	15.8	26
Kr	10.0	14.0	24
Xe	8.4	12.1	22
CO_2	10.0	13.7	33
CH_4		13.1	28
C_4H_{10}		10.8	23

TABLE 2.1: Excitation and ionisation characteristics of various gases [74]

In the context of ionisation detectors, an understanding of the trajectories of electrons and ions within gases holds great significance, as these dynamics significantly impact various operational characteristics of the detector. Predominantly, these trajectories are elucidated through the framework of classical kinetic theory applied to

gases. Of particular relevance are two key phenomena: diffusion and drift within an electric field.

Diffusion:

In the absence of an electric field, electrons and ions produced by incident radiation diffuse uniformly outward from their origin, undergoing numerous collisions with gas molecules, resulting in energy loss. Consequently, they rapidly reach thermal equilibrium with the gas and eventually recombine. At thermal energies, the velocities of the charges conform to the Maxwell distribution, yielding a mean speed given by:

$$v = \sqrt{\frac{8kT}{\pi m}} \tag{2.5}$$

where k represents Boltzmann's constant, T denotes the temperature and m signifies the particle's mass. Clearly, the average speed of electrons significantly exceeds that of ions due to their smaller mass. At room temperature, electrons can reach speeds on the order of a few times 10^6 cm/s, while positive ions typically attain speeds around 10^4 cm/s.

According to kinetic theory, the dispersion of charges over a distance after a time interval t can be demonstrated to follow a Gaussian distribution:

$$\frac{dN}{dx} = \frac{N_0}{\sqrt{4\pi Dt}} exp\left(-\frac{x^2}{4Dt}\right) \tag{2.6}$$

Here, N_0 is the total number of charges, x is the distance from the point of creation and D is the diffusion coefficient. The root mean square (rms) spread in x is given by:

$$\sigma(x) = \sqrt{2Dt} \tag{2.7}$$

In three dimensions, considering radial distance r, the spherical spread is:

$$\sigma(r) = \sqrt{6Dt} \tag{2.8}$$

The radial spread of ions in air under normal conditions is approximately 1 mm after 1 s [75]. The diffusion coefficient is a parameter derivable from kinetic theory:

$$D = \frac{1}{3} v\lambda \tag{2.9}$$

Here, λ represents the mean free path of the electron or ion within the gas. For a classical ideal gas, the mean free path is related to the temperature T and the pressure p as explained by Eqn. 2.10.

$$\lambda = \frac{1}{\sqrt{2}} \frac{kT}{\sigma_0 p} \tag{2.10}$$

Here, σ_0 denotes the total cross-section for a collision with a gas molecule. Substituting Eqn. 2.5 and Eqn. 2.10 into Eqn. 2.9 gives:

$$D = \frac{2}{3\sqrt{\pi}} \frac{1}{p\sigma_0} \sqrt{\frac{(kT)^3}{m}} \tag{2.11}$$

This equations explains the dependence of diffusion coefficient D on different parameters of the gas.

Drift and Mobility:

In the presence of an electric field, freed electrons and ions from radiation experience acceleration towards the anode and cathode along the field lines. Collisions with gas molecules limit their maximum average velocity, resulting in a drift velocity. While the ions exhibit a relatively slow drift speed compared to their thermal velocities, electrons, being significantly lighter, can achieve much higher drift speeds. The mobility of a charge, defined as $\mu = u/E$, where u is the drift velocity and E is the electric field strength. For positive ions, the drift velocity depends linearly on the ratio E/p, up to relatively high electric fields. Therefore, for a given E, μ varies inversely with respect to the pressure p.

For ideal gases, the moving charges remain in thermal equilibrium and the mobility is related to the diffusion constant by:

$$\frac{D}{\mu} = \frac{kT}{e}, \tag{2.12}$$

known as the Einstein relation.

In contrast to positive ions, electrons exhibit significantly higher mobility, which is dependent on the electric field strength E. Velocities reaching up to several times $10^6\ cm/s$ can typically be achieved before reaching saturation. The associated electric fields at this point generally range around $1\ kV/cm$.

The change in velocity of electrons can impact the diffusion rate if their mean energy surpasses thermal energies. In such cases, the factor kT in Eqn. 2.12 is substituted with this mean energy. Consequently, the diffusion constant D increases, leading to a broader spread of the electron cloud, as given by Eqn. 2.7 and Eqn. 2.8. This has significant implications for detectors like drift chambers, which aim to determine track positions by measuring the drift time of ionisation electrons.

2.2.3 Avalanche Formation

In gas detectors, multiplication occurs when the primary ionisation electrons acquire enough energy from the electric field to ionise gas molecules. The subsequent secondary electrons initiate tertiary ionisation, creating a cascade effect and forming an avalanche. Due to the higher mobility of electrons, the avalanche resembles a liquid-drop, with electrons concentrated near the head and slower ions trailing behind, as depicted in Fig. 2.3.

If λ represents the mean free path of the electron for a secondary ionising collision, then $\alpha = 1/\lambda$ is the probability of ionisation per unit path length, commonly known as the first Townsend coefficient. If there are n electrons, then in a path dx, there will be dn (Eqn. 2.13) new electrons created.

$$dn = n\alpha dx \tag{2.13}$$

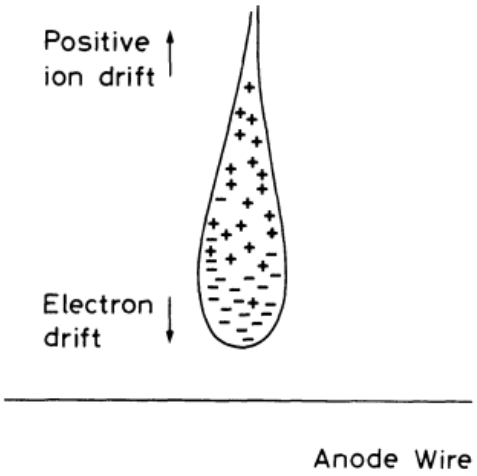

FIGURE 2.3: Illustration depicting the formation of an avalanche resembling a liquid drop, due to the higher mobility of electrons relative to ions [74].

By integrating, The total number of electrons, denoted as n (Eqn. 2.14), generated along a path x can be estimated.

$$n = n_0 e^{(\alpha x)} \tag{2.14}$$

Here, n_0 is the original number of electrons. The multiplication factor M can be defined as:

$$M = n/n_0 = e^{(\alpha x)} \tag{2.15}$$

In the case of non uniform electric fields like Eqn. 2.1, α is a function of x and M becomes:

$$M = e^{\left[\int_{r_1}^{r_2} \alpha(x) dx\right]} \tag{2.16}$$

The multiplication factor is limited to about M<10^8 or αx<20 and after that, breakdown occurs. This is known as Raether limit [74].

2.3 Evolution of RPCs

The initial gaseous detectors, as discussed in the preceding section, were characterised by a cylindrical geometry, where primary electrons from ionising particles were collected at a central wire and avalanche processes occurred in the surrounding region (see Fig. 2.1). Despite their origin in the early 1900s, detectors of this family remain highly successful and are still used in current experiments. Notably, detectors with a planar geometry were developed later than cylindrical ones, driven by the need to achieve superior time resolution compared to devices like the Geiger–Muller detector.

2.3.1 Importance of Parallel Plate Geometry

To explore the potential to achieve superior time resolution with parallel plate detectors compared to cylindrical devices, we consider the distinct electric field characteristics between a central wire detector and a planar geometry detector. In the former, the electric field diminishes inversely with distance from the central wire, while in the latter, it remains uniform. Since electron avalanche processes require

an intense electric field, typically exceeding a few kV/cm, central wire detectors experience multiplication phenomena only in close proximity to the wire, where the electric field surpasses the multiplication threshold. In contrast, in a parallel-plate detector, the entire volume is theoretically available for multiplication, without favoring or disadvantaging any region. Nonetheless, in both cases, primary ionisation can occur at any point in the gas volume, leading to variable drift times for primary electrons in a cylindrical detector. This variability, depending on the generation position, inherently introduces fluctuations in the time between the creation of the primary electron and the initiation of the output signal.

The electron drift velocity in gases is highly dependent on the gas mixture and, to some extent, the applied electric field (explained in Sec. 2.2.2). Given that the transversal dimensions of central wire detectors are typically a few centimeters and because of the time fluctuations related to the primary ionisation location, the time resolution usually observed is on the order of hundreds of nanoseconds, which is a quite challenging issue to resolve.

In contrast, planar geometry eliminates the need for primary electrons to drift toward the amplification region before initiating an avalanche. In parallel-plate detectors, the entire gas volume is available for amplification without a distinct separation between drift and multiplication regions, significantly reducing timing fluctuations. The resultant signal is a cumulative sum of signals from multiple avalanches, further minimising timing fluctuations. Consequently, planar detectors within the gaseous detector family have achieved time resolutions for charged particles that significantly exceed 1 ns. The multi-gap resistive plate chamber (mRPC), detailed in Sec. 2.5.2, holds the record in this domain, boasting a time resolution that can reach 35 ps.

2.3.2 Parallel-Plate Counters

In 1948, J. W. Keuffel introduced the first parallel-plate counters (PPCs) [76], consisting initially of two molybdenum disks separated by a 3.0 mm gap. Subsequent designs involved copper plates or steel coated with copper at a 2.5-mm distance. These counters used xylene vapors and Argon in a spark mode, exhibiting a wide counting plateau with output pulses around 100 V. The efficiency, measured with cosmic rays, was approximately 90% and time resolution varied from 18 ns to 5 ns. Keuffel PPCs, despite their simple structure, were delicate devices requiring precise electrode surface preparation and complex assembly procedures. Their working time was limited, often disrupted by spark origins on the electrodes. The need for an external switching-off circuit, a downtime of 0.01–0.05 s after detecting an ionising particle and limitations in particle flux detection marked them as rate-limited devices.

2.3.3 Birth of RPCs

The roots of planar spark counters (PSCs) with resistive electrodes can be attributed to the pioneering efforts of Babykin et al., (1956) [77]. Initially experimenting with segmented metallic pads connected to a resistive load in parallel-plate counters (PPCs), the aim was to electronically record the spark's position using quenching mechanisms. The Novosibirsk group [78] is credited with developing the first planar detectors with resistive electrodes (in 1971), schematically shown in

Fig. 2.4 [79]. These detectors utilised glass coated with a conductive layer, featur-

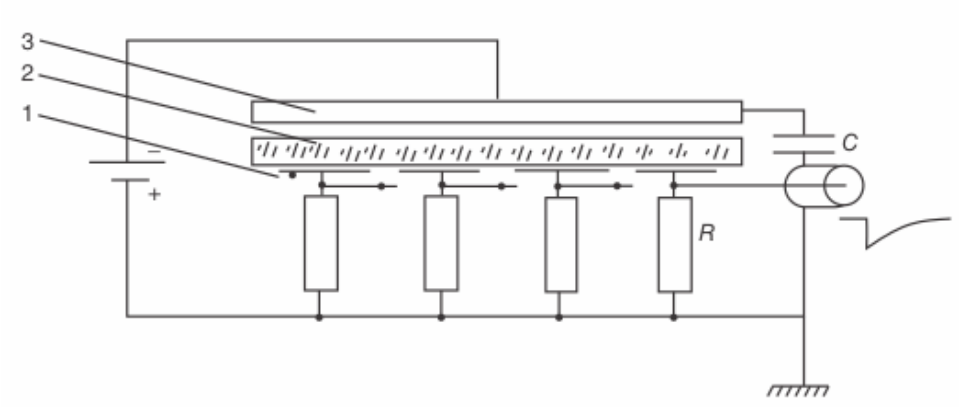

FIGURE 2.4: Schematics of the first planar detector with resistive electrodes constructed and tested by Parkhomchuk et al [78]; the various materials indicated in the figure are 1 – conductive layer, 2 – semi-conductive glass, 3 – copper cathode [79].

ing a 1 *mm* electrode gap and a gas mixture of 55% Ar, 30% ether vapor, 10% air and 5% divinyl vapor. Triggered sparks had limited energy due to glass resistivity, with signal extraction from the conductive layer. Despite smaller signals compared to traditional spark counters, the time resolution exceeded 1 *ns*. The resistive anode's internal quenching (see Sec. 2.4.1 for details) mechanism eliminated the need for pulsed high voltage, enabling the construction of large-area, cost-effective detectors. Importantly, these detectors, unlike Keuffel chambers, exhibited localised discharges (see Sec. 2.4.1 for details) and dead zones, maintaining full sensitivity in the rest of the counter after the passage of an ionising particle. Therefore, during that time, these detectors were referred as continuous operation spark counters.

Another significant milestone was the introduction of the multiwire proportional chamber (MWPC) by G. Charpak in 1968 [80]. Unlike spark counters, MWPCs operated continuously, offering self-triggering capability and fast electronic readout (for more detector specific details, the reader is referred to Sec. 5.4.3). MWPCs quickly became the preferred choice in high-energy physics experiments, surpassing spark counters and other traditional detectors. Despite their success, MWPCs had limitations in time resolution due to the variable drift time of primary electrons.

As advancements in particle physics detector technology continued, the evolving needs of high energy physics experiments extended beyond spatial resolution and rapid electronic readout to include improved timing characteristics. Expanding upon the principles of parallel plate detectors, known for their minimal jitters and outstanding timing and drawing inspiration from the continuous operation spark counters, these collective insights culminated in the development of RPCs in the 1980s by Santonico and Cardarelli [81].

2.4 RPC: Principles and Operation

2.4.1 Working Principle

The basic structure of an RPC is very similar to that of a spark counter with a major difference lying in the materials used for RPC electrodes. Unlike spark counters,

RPC electrodes are made from materials that possess a relatively high electrical resistivity, typically in the range of 10^{10} to 10^{12} Ω cm, using 1–2 mm Bakelite or glass plates. The external surfaces of these electrodes are coated with a conductive or semiconductive layer to facilitate a dependable connection with an externally applied constant high voltage.

Upon application of the required electric field for the detector's operation, the primary ionisation and avalanche formation in the case of an RPC occur similarly to basic gaseous detectors as explained in Sec. 2.2.2 and Sec.2.2.3. When the total charge in the avalanche approaches or exceeds the Raether limit (for details, the reader is referred to Sec. 2.2.3), the avalanche transitions into a streamer. Unlike metal electrodes, the resistive cathode plate is incapable of supplying the streamer with high current density, as high resistivity materials generally lack efficient electron-emitting properties. Additionally, the anode plate is not an ideal dielectric but rather a high resistivity layer, which, under the applied high voltage, becomes positively charged. Consequently, when an avalanche or streamer reaches the anode surface, it undergoes local discharge, leading to a reduction in electric field intensity and a significant decrease in charge-supporting processes. Both phenomena contribute to restricting the discharge current, with the local partial discharging effect likely being dominant.

The simplified circuit diagram of the RPC detector is depicted in Fig. 2.5. The RPC exhibits a structure similar to a capacitor from a semi-quantitative viewpoint, integrating two layers of dielectric material within. Furthermore, the electrodes are made from resistive material and this attribute is denoted by the inclusion of their resistance R_b in the diagram.

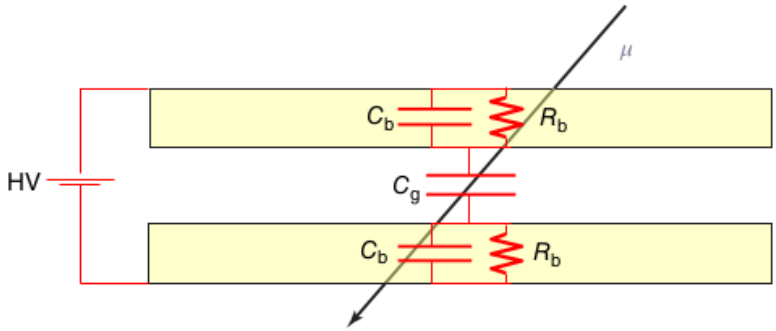

FIGURE 2.5: Simplified circuit diagram of an RPC, with the black arrow denoting the passage of an ionising particle through the detector. C_b and C_g represent the capacitance of individual electrode plates and the gas gap, respectively, while R_b signifies the resistance of the electrodes [79].

There are two possible scenarios: 1) In the absence of particles traversing the gaseous volume, resulting in no ionisation, the applied voltage is supplied to the gas and no current flows. 2) When an ionising particle traverses the detector, the corresponding discharge can be conceptualised as a current generator. This generator discharges the capacitor C_g (associated with the gas gap) in a manner such that the initially applied voltage to the gas transfers to the resistive electrodes, characterised by the capacitance C_b and, as previously mentioned, the resistance R_b. The system returns to its initial configuration following an exponential pattern, governed by a

characteristic time constant τ. Equation 2.17 explains the time constant.

$$\tau = 2R_{\mathrm{b}}\left(\frac{C_{\mathrm{b}}}{2} + C_{\mathrm{g}}\right) = 2\rho_{\mathrm{b}}\frac{d}{S}\left(\frac{1}{2}\varepsilon_0\varepsilon_{\mathrm{r}}\frac{S}{d} + \varepsilon_0\frac{S}{g}\right) = \rho_{\mathrm{b}}\varepsilon_0\left(\varepsilon_{\mathrm{r}} + 2\frac{d}{g}\right) \tag{2.17}$$

Here,

ρ_b=electrode resistivity

d=electrode thickness

S=surface area of the electrode affected by the discharge

g=gas gap thickness

ϵ_0=dielectric constant of vacuum

ϵ_r=relative dielectric constant

The Eqn. 2.17 reveals that τ is independent of S. The effectiveness of spark quenching is enhanced with a smaller C_b, making the thickness and dielectric constant of the anode plate crucial factors in this process.

For RPCs with High-Pressure Laminate (HPL, commonly known as Bakelite) electrodes [82], τ is approximately 10 ms, significantly exceeding the avalanche collection time ($\sim$10 ns). During this time frame, the electrodes function as ideal dielectric materials, acting as flawless insulators. Consequently, the voltage across the gas gap remains minimal, preventing the sustainability of discharge within the gas. This auto-quenching mechanism forms the foundation of the detector's operation.

Unlike traditional spark counters, where the voltage decreases throughout the gap after discharge, RPCs maintain sensitivity throughout the unaffected area following a local partial discharge event (with sensitivity only decreasing in the avalanche / streamer region). Within a few times τ the voltage on this limited area is restored and the detector regains efficiency. However, the presence of resistive materials introduces counting rate limitations due to voltage drops (V_{drop}) across them.

The readout process of RPCs relies on the induction of signals on the readout electrodes due to the movement of electric charges in the gas gap. This induction is facilitated by the high resistivity of the resistive electrodes and graphite paint, rendering them transparent to rapid signals. If a metallic electrode were used instead of graphite paint, signals would be shielded, preventing position measurements with external readout strips.

2.4.2 Modern RPC layout

The initial prototypes of modern RPCs developed by Rinaldo Santonico and Roberto Cardarelli in the 1980s [79], used Bakelite resin, a phenolic sheet material produced by applying heat and pressure to layers of paper or glass cloth impregnated with the resin. Bakelite phenolic sheets, formed through polymerisation, were crafted into HPLs with additives to meet specific mechanical and electrical needs for the RPCs.

Figure 2.6 shows the schematic diagram of the RPC prototype which consists of two 2 mm thick parallel Bakelite electrode plates with resistivity in the range 10^{10}-10^{12} Ω cm. A voltage of 7-10 kV was applied depending on the gas mixture used.

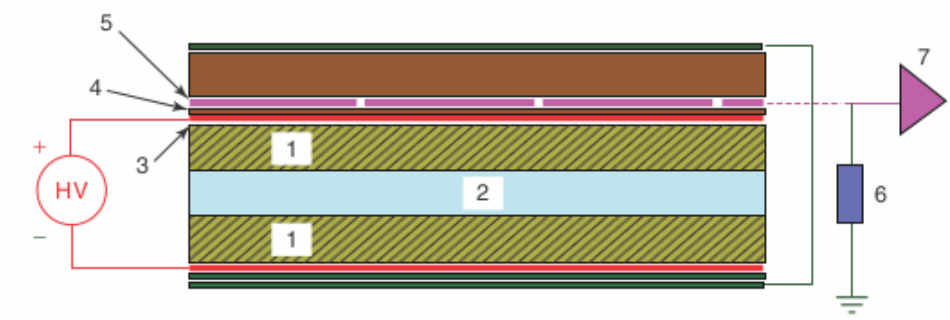

FIGURE 2.6: Schematic of the initial prototype developed by Santonico and Cardarelli. (1) Bakelite electrodes (2 mm), (2) gas gap (2 mm), (3) Resistive coating (200 μm of graphite), (4) Mylar insulator (50 μm), (5) readout strips, (6) resistor and (7) readout electronics [79].

Bakelite electrodes were sealed with a Polyvinyl Chloride (PVC) frame and constant separation throughout the gas gap was achieved using a network of button-like spacers ($100/m^2$), built with an accuracy within 0.01 mm and glued to the electrodes. This construction resulted in a robust framework allowing the flow of the gas mixture, serving as the detector's active medium, through four holes placed on opposite sides of the PVC frame.

To mitigate local nonuniformities on the gas-facing planes of Bakelite, efforts were made to improve surface smoothness at the microscopic level. The application of a coating, composed of linseed oil diluted in pentane, effectively achieved this by filling the assembled detectors with the oil mixture and subsequently emptying them in a vertical position. This procedure substantially lowered the "dark" counting rate, representing the detector's counting rate in the absence of external radiation [83].

Signal readout in the detector can occur on either one or both sides. Readout electrodes can be of diverse shapes and dimensions. A common approach implemented for prototypes was aluminium or copper strips, typically a few centimeters wide, on one side and aluminum foil on the other. Alternatively, employing two sets of perpendicular strips on opposite sides enabled achieving two dimensional position information of the particle hits. Another prevalent configuration tested was a network of rectangular readout electrodes, often referred to as "pads," typically a few centimeters in size.

The initial RPC prototypes exhibited highly promising performance, with efficiency approaching nearly 100% and a time resolution of approximately 1 ns. For the details of the results of the performance studies conducted with the initial prototypes, see [81].

Glass RPCs

A notable breakthrough was the adoption of common glass for electrodes, offering enhanced mechanical rigidity and eliminating the need for linseed oil coating due to its naturally smoother surface. Glass RPCs, popular in high-energy physics

experiments, remain in use today. An exemplary glass RPC, part of the MONOLITH project [84], utilised commercially available materials (float glass electrodes), featuring high-quality surfaces, streamlined assembly procedures and cost-effective large sensitive planes. With a uniform time resolution of approximately 1 ns, this glass RPC showcased design features optimising gas flow and ensuring operational efficiency.

Contrasted with Bakelite RPCs, glass RPCs are considered more suitable for large-scale production, simplifying construction procedures and minimising manpower requirements. The absence of linseed oil treatment for glass electrodes, replacement of graphite coating with adhesive foil, glue-free assembly of spacers and solder-free HV contacts contribute to the streamlined production of glass RPCs (examples of all these procedures can be found in Sec. 6.3, Sec. 6.4 and Sec. 6.5). An additional benefit lies in employing an envelope to contain the gas (example explained in Sec. 6.4.2), rather than relying on a glued frame between the electrodes. This approach has the potential to decrease the likelihood of gas leakages.

While glass RPCs come with numerous benefits, their rate capability is limited due to their relative high resistivity compared to Bakelite RPCs. Consequently, they are majorly employed in cosmic ray experiments, such as the OPERA [85] experiment and accelerator experiments like BELLE [86], where rate requirements are not as stringent. Furthermore, due to the same reason, glass RPCs prove to be promising candidates for imaging techniques utilising cosmic muons, such as muography and tomography (Chapter 6).

2.4.3 Operation Modes

This section provides a brief explanation of the two operational modes of RPCs: streamer mode and avalanche mode.

Streamer Mode

In RPCs, streamers are produced when the total charge in the avalanche approaches or exceeds the Raether limit. When the applied electric field is significantly high, the secondary avalanches initiated in proximity to the primary avalanche drift toward it and experience significant amplification. This rapid growth of the ionic column toward the cathode results in the formation of a slender plasma channel known as a streamer. Upon reaching both electrodes, the transition to a spark is observed.

RPCs were originally designed to operate in streamer mode. The avalanche to streamer transition was studied by many physicists and the result taken from [87] is shown in Fig. 2.7. The cases a-d corresponds to four different voltages applied: (a) 9.4 kV, (b) 9.6 kV, (c) 10.2 kV, and (d) 14.0 kV. From (b), two distinct signals can be identified. The initial signal generated by a primary avalanche and a subsequent signal emerging after a certain delay (which diminishes with increasing applied voltage), corresponding to the discharge triggered by the streamer. In particular, at higher applied voltage values, the avalanche nearly converges with the subsequent streamer, making them indistinguishable from each other.

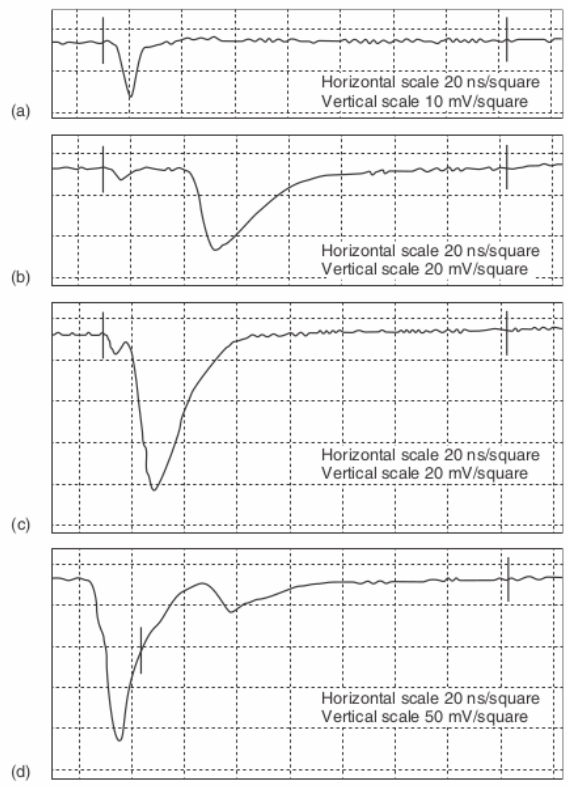

FIGURE 2.7: Signal waveforms recorded with an RPC operating in $Ar/n - C_4H_{10}/C_2H_2F_4$ (10/7/83 in volume) at gradually increasing operating voltages: (a) 9.4 kV, (b) 9.6 kV, (c) 10.2 kV, and (d) 14.0 kV [87].

The charge induced on the readout was valuated by integrating the amplitude profile of the current measured on the same electrode with respect to time. Figure. 2.8 shows the charge measured as a function of the applied voltage. The trend marked with triangular indicators illustrates the precursor signal's charge, while the circular indicators depict the total charge (precursor plus streamer). Up to approximately 9.2 kV, corresponding to an induced avalanche charge of about 1 pC, the precursor charge exhibits exponential growth. Beyond this point, a knee emerges, signifying a change in slope and suggesting a saturation effect, likely attributed to space charge effects. Nearly at the same point where the slope change occurs, the appearance of streamers initiates (upper curve), accompanied by similar saturation effects. It is noteworthy that the transition from avalanche to streamer is influenced by factors such as the width of the avalanche gap and the gas composition.

The integrated fast signal observed from an RPC comprises two components: a rapid component (3–20 ns duration for gas gaps ranging from 0.3 to 2 mm), associated with the gathering of avalanche electrons and a slower one persisting for several microseconds, resulting from the motion of positive ions in the avalanche toward the cathode. Usually, an appropriate current amplifier to record the fast signal is used to exploit RPCs excellent timing characteristics.

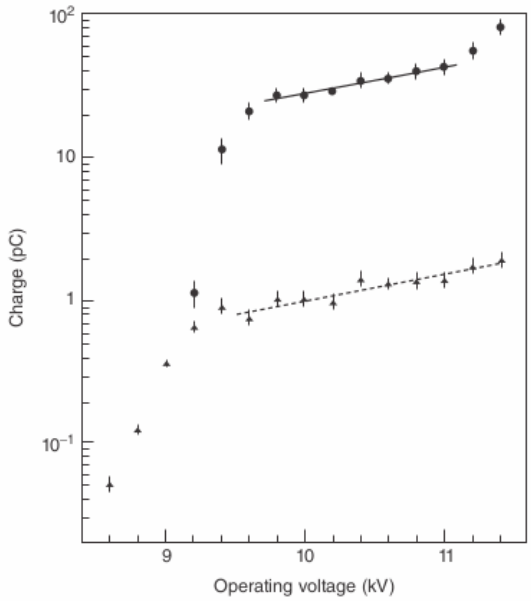

FIGURE 2.8: The prompt signal charge measured for an RPC operated in streamer mode as function of the applied voltage. The lower curve corresponds to the precursor charge and the upper curve corresponds to the total charge (precursor plus streamer)[87].

Avalanche Mode

The concept of operating RPCs in avalanche mode primarily emerged to enhance the rate capability of the detector, particularly for its application in LHC experiments. This increased rate capability in avalanche mode results from the reduced charge generated within the gas gap. However, a trade-off arises because although the signals produced are smaller in amplitude, sufficient amplification is required before further processing.

In the study conducted by Cardarelli et al. [88], it was noted that the addition of electronegative components, specifically certain types of Freon, in substantial proportions to the RPC gas mixture led to a reduction in the induced signal size on the readout strips. The results of the charge measurements while operating an RPC with different concentrations ((a) 0%, (b) 4% and (c) 8%) of CF_3Br (Freon 13B1) mixed in an Ar/isobutane gas mixture (60/40 in volume) are illustrated in Fig. 2.9. This observation is expected, considering that Freon is an electronegative gas, implying that some avalanche electrons may be captured by Freon components, resulting in the formation of slow-drifting electronegative ions . This phenomenon decreases the number of free electrons in the gas [89].

Figure 2.10 illustrates the rate capability of RPCs operated in the streamer / spark mode and the avalanche mode, depicting the detection efficiency as a function of the particle rate. The findings showed a more pronounced decrease in efficiency as particle rates rise when operating in streamer mode, emphasising the importance of employing RPCs in avalanche mode for high-rate scenarios.

As mentioned earlier, the reduced charge produced in avalanche mode leads to a smaller voltage drop and, consequently, faster recovery times, enhancing rate capability. Furthermore, the resistivity of the electrode, influenced by environmental

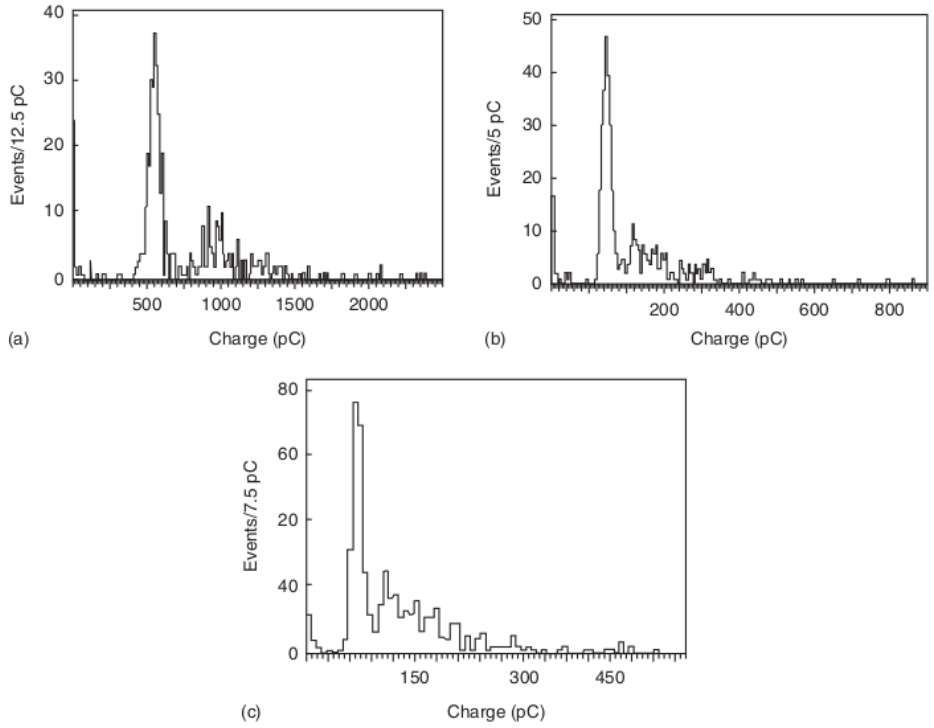

FIGURE 2.9: Charge measurements conducted with an RPC with varying concentrations of CF_3Br (Freon 13B1) in an Ar/isobutane gas mixture (60/40 in volume). Panels (a), (b) and (c) correspond to concentrations of 0%, 4% and 8%, respectively. The detector was operated at 7.2 kV in the first two scenarios and at 7.8 kV in the last case [88].

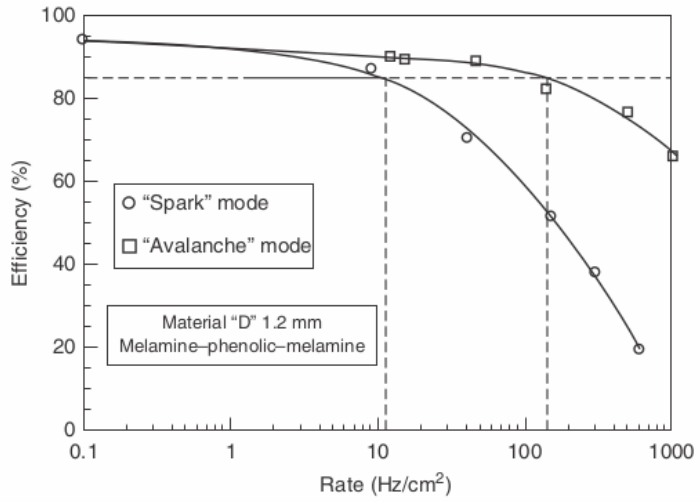

FIGURE 2.10: The efficiency measured as a function of incident particle rate for an RPC operated in avalanche mode (square data points) and streamer mode (circle data points) with a gas mixture of 81% Ar, 13% isobutane, 6% Freon-12 [79].

exposure, can impact recovery time. In the case of Bakelite RPCs, the RPC gas mixture is humidified by introducing water vapor (40-50%) [79, 90]. If the Bakelite gas gaps are supplied with a dry gas mixture for an extended period of time, the gas will continuously remove moisture content from the Bakelite RPCs, causing deformation of the Bakelite panels and a subsequent increase in resistivity by approximately an order of magnitude (10 times). This leads to a reduced rate capability (refer Sec. 2.4.5 to see the relation between rate capability and resistivity), and the original resistivity

values can never be fully restored.

2.4.4 Signal Formation and Charge Distribution

When an ionising particle traverses an RPC, as detailed in Sec. 2.2.2, primary ionisation occurs, generating electron-ion pairs if the primary electron's kinetic energy is sufficiently high. A "cluster" refers to a primary ion-electron pair and additional pairs generated by the primary electron. The actual number of clusters, denoted as n_{cl}, varies stochastically from event to event and it depends linearly on the gas thickness g crossed by the particle. Experimental measurements provide average values for the number of clusters per unit length (λ) for various gases and for gas mixtures, λ is the weighted average of components based on their gas fractions.

The parameter λ is generally influenced by the energy of the incoming particle. Assuming that the energy lost by the particle within the gas gap is negligible compared to its kinetic energy, a common scenario in cosmic ray and LHC muon experiments, the kinetic and total energy and consequently, the primary ion/electron pair density (λ) can be considered to be constant along the particle's path in the gas gap. If the particle traverses the RPC gas gap at a non-perpendicular angle, $\lambda_{eff} = \lambda / cos\phi$ is introduced, where ϕ represents the azimuthal angle of the track. The probability of detecting n_{cl} ion-electron clusters when a particle traverses a gas thickness g follows a Poisson distribution with an average value of $g\lambda_{eff}$ and the probability of having zero clusters is determined by:

$$P_{cl}(n_{cl} = 0) = e^{-g\lambda_{eff}} \tag{2.18}$$

Equation 2.18 is crucial as it reveals the inherent inefficiency of a gaseous detector, placing constraints on the thickness of gas layers for maintaining reasonable efficiency. For example, withλ = 5.5 $clusters/mm$ and a gas gap of g = 0.2 mm, Eqn. 2.18 suggests an intrinsic inefficiency of approximately 11%. These simple considerations offer insights into the design of particle detectors, explaining typical dimension choices, such as gap thickness in the range of 1–2 mm.

Now if the effect of a uniform electric field in the gas gap, due to an applied external voltage is considered free electrons drift toward the anode, while ions move toward the cathode. With ion mobility much lower (about 3 orders of magnitude) than electron mobility, the focus is on the induced signal by electrons. If the electric field is sufficiently intense, the electrons in the cluster gain kinetic energy, initiating an avalanche and the charge contained in the avalanche at a certain position x can be expressed as:

$$q(x) = \sum_{j=1}^{n_{\mathrm{cl}}} q_{\mathrm{e}} n_0^j M_j e^{\alpha^* \left(x - x_0^j\right)} \quad x_0^{n_{\mathrm{cl}}} < x \leq g \tag{2.19}$$

Here, n_0 represents the number of primary electrons in the jth cluster, α^* is the effective first Townsend coefficient (α minus the attachment coefficient η[1]), q_e denotes the elementary electron charge and M_j is a quantity used to take into account stochastic fluctuations in the avalanche process. It's essential to note that this equation strictly

[1] η gives the probability (per unit length) for an electron to undergo attachment- the process when an electron, drifting in gas under the influence of a strong applied electric field, interacts with the atoms and molecules of the gas, forming negative ions with some of them. This interaction results in a reduction of the number of free electrons in the gas.

applies between the last cluster (farthest from the cathode) and the anode. It is commonly utilised to calculate the avalanche charge when reaching the anode ($x = g$).

The stochastic nature of the charge multiplication process is described by the Polya distribution [91](Eqn. 2.20), enabling the calculation of the probability of having n_e electrons in the avalanche after covering a distance $l = g - x_0$ (where g is the thickness of the gas gap and x_0 is the initial position of the cluster).

$$P_{\mathrm{P}}(n_e) = \left[\frac{n_e}{N}(1+\theta)\right]^{\theta} \exp\left[-\frac{n_e}{N}(1+\theta)\right] \tag{2.20}$$

Here, $N = e^{\alpha(g-x_0)}$. The θ is a parameter challenging to theoretically estimate, typically assumed to be around 0.5 for the mixtures employed in gaseous detectors.

When dealing with detectors, what is more intriguing than the size of the avalanche is the signal induced by the avalanche on the readout strips. The charge q_{ind} induced on the external pickup electrodes of an RPC is given by (Shockley-Ramo theorem):

$$q_{\mathrm{ind}} = \frac{\varepsilon_{\mathrm{r}} g}{\varepsilon_{\mathrm{r}} g + 2d} \frac{q_{\mathrm{e}}}{\alpha^* g} \sum_{j=1}^{n_{\mathrm{cl}}} n_0^j M_j \left[e^{\alpha^*\left(g - x_0^j\right)} - 1\right] \tag{2.21}$$

Here,ϵ_r is the electrode relative dielectric constant, d is its thickness, g is the gas thickness and α^* is the effective first Townsend coefficient. For full derivation, the reader is referred to [79].

The charge distribution resulting from an ionising particle traversing the gas gap of an RPC and affecting an external readout electrode can be computationally determined. Sophisticated calculations, often utilising Monte Carlo (MC) methods due to the presence of multiple stochastic variables in Eqn. 2.21, predict the shape of this distribution. Figure 2.11 displays the charge distributions for single-gap RPCs with gap widths of 2 *mm* ("narrow gap") and 9 *mm* ("wide gap", respectively, computed through MC techniques applied to Eqn. 2.21.

The distributions from the two gap widths exhibit notable differences. In the narrow-gap scenario, the curves show divergence as q_{ind} approaches zero, indicating a higher occurrence of small charge events. Conversely, in the wide-gap case, the curves tend to vanish for charges close to zero, suggesting fewer events with minimal charge. Additionally, there is an excess of events in the right tail of the distribution for narrow gaps, offset by fewer events in the central part compared to the 9 *mm* gap scenario. The events with charges below specific electronic thresholds are prone to go undetected, often mistaken for "electronic" noise—referring to fluctuations around the baseline amplifier output voltage caused by various factors. Thus, the characterisation of the charge distribution near zero holds crucial significance in anticipation.

Taking into account the assumptions presented in [79], it becomes evident that the charge distribution depends only on λ/α^*. Three possible scenarios can arise:

- (λ/α^*)<1: Charge distribution strictly decreases (as in the case of the narrow gap RPC shown in Fig. 2.11)

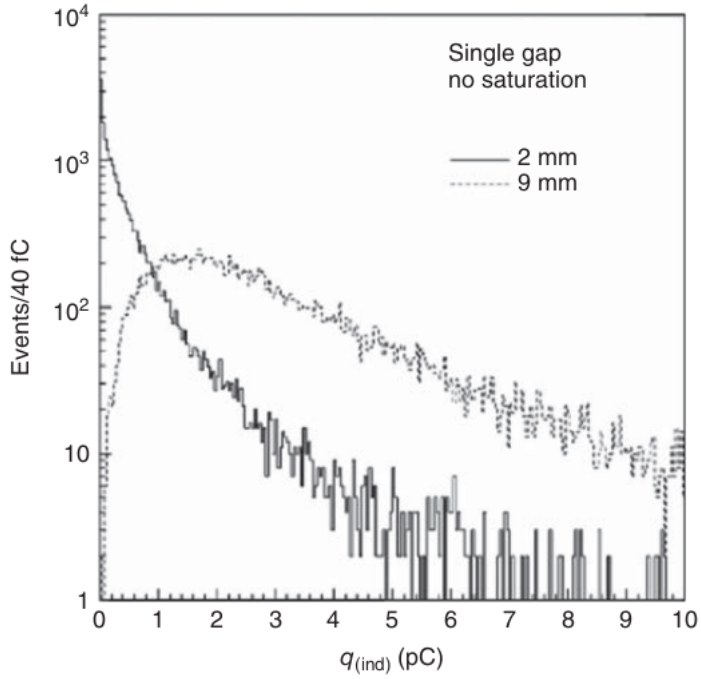

FIGURE 2.11: Results of MC simulations conducted to study the charge distributions for single-gap RPCs with gap widths of 2 *mm* and 9 *mm* [79].

- $(\lambda/\alpha^*) \approx 1$: Charge distribution is constant around $q_{ind} = 0$
- $(\lambda/\alpha^*) > 1$: Charge distribution strictly increases and starts at 0 for $q_{ind} = 0$ (as in the case of the the wide gap RPC shown in Fig. 2.11)

2.4.5 Important Parameters

Efficiency

RPC efficiency can be determined by analysing the charge distribution near zero, specifically counting the events falling below a certain electronic threshold. For simplicity, Eqn. 2.21 is considered, with focus on the contribution from only one cluster, particularly the closest to the cathode. For an event to be distinguishable from the system's intrinsic electronic noise, its induced charge q_{ind} must surpass a certain electronic threshold q_{thr}, characteristic of the readout electronics. Only these events contribute to the detector's efficiency. When Eqn. 2.21 is truncated at cluster (j = 1) and inverted, it reveals that the considered cluster must originate at a distance from the cathode less than:

$$x_0^1 < g - \frac{\ln\left(\frac{q_{\text{thr}}}{A_1} + 1\right)}{\alpha^*} \tag{2.22}$$

Here, $A1$ represents a parameter that incorporates certain constants from Eqn. 2.21. The chamber's efficiency (ε_c) is expressed as:

$$\varepsilon_c = 1 - e^{-\lambda\left[g - \frac{1}{\alpha^*}\ln\left(\frac{q_{\text{thr}}}{A_1}+1\right)\right]} \tag{2.23}$$

Possible refinements can be considered as reported in [92], such as the average distance of cluster creation and the factor contributing to the efficiency. A 2-*mm* single-gap RPC, typically operated at $\alpha^* \approx 9\,\text{mm}^{-1}$, exhibits ratios $q_{\text{ind}}^{2nd}/q_{\text{ind}}^{1st} = 0.2$,

$q_{\text{ind}}^{3rd}/q_{\text{ind}}^{1st} = 0.04$ and so forth. To account for multiple clusters contributing to the efficiency, a simple approximation multiplies the total induced charge by a factor of roughly 1.25.

Time Resolution

Time resolution calculations can be approached using simplified formulas, as discussed in [93]. The concept involves examining the induced current signal of a single primary electron within the RPC gas gap:

$$i_{\text{ind}}(t) = I_s e^{\alpha^* v_d t} \tag{2.24}$$

Here, I_s represents the signal current amplitude, which varies between events and follows an exponential distribution around a mean amplitude. The time t at which the signal crosses a certain threshold I_{thr} is given by:

$$t = \frac{1}{\alpha^* v_d} \ln\left(\frac{I_{\text{thr}}}{I_s}\right) \tag{2.25}$$

Inverting this expression yields the fluctuations in the crossing time t, denoted as the RPC time resolution (σ_t), given by the formula:

$$\sigma_t = \frac{1.28}{\alpha^* v_d} \tag{2.26}$$

This suggests that the intrinsic time resolution primarily depends on the drift velocity (v_d) and the effective Townsend coefficient (α^*), independent of the threshold. MC simulations support this, with the formula providing $\sigma_t \approx 1\ ns$ for a standard RPC and $\sigma_t \approx 50\ ps$ for a small-gap timing RPC, aligning well with experimental data [93].

Refined approaches by various authors, including a comprehensive treatment by Riegler (2009) [94], further explored theoretical timing distributions under simplified conditions. While the basic scaling remains valid, the timing variance is shown to decrease with the variable $n_{\text{av}} = \frac{\alpha^*}{\alpha}\lambda g$, representing the average number of initiated avalanches. The asymptotic behavior of the timing standard deviation is approximately $\frac{1}{\sqrt{n_{\text{av}}}}$. In the context of multi-gap RPCs discussed in Sec. 2.5.2, each of the N_g gaps is expected to have, on average, λ_g sub-avalanches. As the signals from each gap combine on the readout electrodes, this is essentially equivalent to scaling λ in proportion to the number of gaps.

These formulas, applied to efficiency and time resolution, are widely used to predict RPC performance based on construction parameters, providing valuable information on the physics of the RPC detector.

Position Resolution

In many RPC implementations, centimeter-wide strips are commonly used for modest avalanche localisation (referred to as position resolution). However, certain applications, such as muon tomography and biomedicine, require significantly improved position measurement at both coordinates. To achieve this, millimeter-scale

strips are employed, allowing for better resolution. Placing these strips in perpendicular directions on each side of the chamber enables identical resolution on both coordinates in the chamber plane, a unique capability of RPCs/PPCs unmatched by other gaseous detectors. Although the distribution of induced charges on electrode shapes can be calculated, dedicated measurements, such as those in [95, 96], focus on the distribution of the charge in strips and its impact on the resolution of the position. Applying charge interpolation to RPCs with millimeter-scale strip pitch has demonstrated position resolutions nearing 100 μm in one dimension under beam conditions [97]. Another method, involving digital readout of finely spaced strips, achieved a resolution of 50 μm in a small prototype illuminated by collimated X-rays [98].

Rate Capability

The distribution of current density across electrodes exhibits variability on the millimeter scale, depending on the spatial pattern of the gas ionisation points. On average, under uniform irradiation density, a working current (I) flowing through electrodes with total resistance (R_b) induces a voltage drop:

$$V_{drop} = V_{app} - V_{gas} = IR_b \tag{2.27}$$

Where, V_{app} and V_{gas} are the voltages applied to the electrodes and across the gas gap, respectively.

Maintaining a high rate capability requires keeping V_{drop} at a negligible value compared to V_{gas} even under intense irradiation. The voltage drop across the electrodes can be expressed as a function of the fundamental detector parameters through the following relationship.

$$V_{drop} = \rho t < Q > r_\mu \tag{2.28}$$

Here, ρ is the bulk resistivity of the electrode, t is the thickness of both electrodes, $< Q >$ is the average charge delivered in the gas for each count and r_μ is the counting rate per unit surface. The rate capability can be defined as the achieved rate per unit voltage drop across the electrodes:

$$Rate\ Capability = \frac{r_\mu}{V_{drop}} = \frac{1}{\rho t < Q >} \tag{2.29}$$

From the Eqn. 2.29, it is clear that the rate capability can be increased by decreasing the parameters ρ, t and $< Q >$. Lowering the resistivity of electrode materials is a common strategy used to enhance rate capability, but it comes with increased operating current and potential pollutant generation inside the gas gap and leading to ageing issues. Another way is the reduction of electrode thickness, which not only impacts the total electrode resistance but also amplifies the signal induced on readout electrodes, leading to an enhanced signal-to-noise ratio. Therefore, it is important to reduce electrode thickness according to the gap size. The strategy of reducing the average charge $< Q >$ offers the advantage of enhancing the attainable rate with minimal or no penalty on other parameters, such as detector ageing. This approach involves: i) fine tuning the gas gap size to strike an optimal balance between detection efficiency and the delivered charge; ii) shifting a substantial portion of the required amplification from the gas to the front-end electronics. The circuit dedicated to this purpose must exhibit high sensitivity and an excellent signal-to-noise ratio.

Moreover, careful optimisation of the chamber structure as a Faraday cage becomes important to suppress noise originating from both the detector and external sources. Notably, this low charge approach proves particularly suitable for RPCs featuring electrodes made of HPL. The resistivity of HPL electrodes is inherently low (10^9-10^{11} Ω cm), making them well-suited for large RPC detectors in experiments such as LHC experiments CMS and ATLAS [99].

2.4.6 Gas Mixture

The optimal operation of RPCs depends on the critical selection of gas mixtures. To achieve this, various factors must be carefully optimised when choosing the gas mixture. First, achieving a high density of primary ion-electron clusters is essential to achieve high detection efficiency and this is influenced by factors such as particle energy deposition, which can be computed using the Bethe–Bloch formula. Additionally, the average atomic number, density and specific ionisation potential of the used gas mixture play crucial roles. Second, the gas mixture should exhibit relevant quenching properties, characterised by low photon emission and/or transmission, to minimise photon feedback phenomena. Third, the gas should be electronegative to reduce the transversal side of discharges and enhance their localisation. Finally, it is preferable for the chosen gas mixture not to pose risks to human health. Consideration of these factors is vital for optimising the operational efficiency of RPCs. Moreover, it is essential to control the chemical processes during electron multiplication to limit the production of aggressive substances like hydrofluoric acid and to prevent the formation of polymerisation materials that could lead to unwanted depositions. Additionally, environmental considerations play a crucial role, requiring the chosen gas mixture to have a minimal ozone depletion power (ODP) and a low global warming potential (GWP) when released into the atmosphere. Compliance with international regulations, such as those outlined in the Kyoto Protocol and enforced by entities such as the European Community, is vital to minimise damage to the ozone layer and mitigate the greenhouse effect.

In the initial stages, gas mixtures for RPCs operating in streamer mode often consisted of a mixture of noble gases, such as argon (Ar) or xenon (Xe) and quenching agents such as isobutane (C_4H_{10}) or tetrafluoromethane (CF_4). A typical example included Ar/isobutane with varying volume ratios, utilising Ar for charge multiplication as the active component and isobutane for quenching to absorb photons. The introduction of CF_4 into the mixture was aimed at using its electronegative property to capture free electrons.

To fulfill conditions for RPCs operating in avalanche mode, the common approach involves utilising mixtures of tetrafluoroethane ($C_2H_2F_4$), commonly known as R134a (widely used in refrigeration). This is a dense gas that provides a high density of primary ion-electron pairs. Additionally, an electronegative gas sulfur hexafluoride (SF_6) (used for industrial electrical insulation), to absorb free electrons, thereby limiting the spread of the avalanche. Isobutane (i-C_4H_{10}) is also included for quenching purposes. The predominant component is typically tetrafluoroethane, constituting over 90% of the mixture, with small volume percentages of other components. As previously discussed in Sec. 2.4.3, Bakelite RPCs requires an amount of water vapor in the gas mixture (typically ranging from 30% to 50% relative humidity). This addition is essential to maintain stable electrode resistivity over time.

The drawback associated with current gas mixture lies in the elevated GWP of R134a (GWP=1430) and SF_6 (GWP=22800). GWP is a metric used to gauge the environmental impact of gas emissions compared to the equivalent mass of CO_2 (assigned a GWP of 1). Specifically, R134a exhibits a GWP of approximately 1488 (as per the 4th Intergovernmental Panel on Climate Change [100]), signifying that the emission of one ton of R134a absorbs heat 1488 times more than an equivalent mass of CO_2. This raises significant environmental concerns, particularly in light of the 2014 regulations imposed by the European Union [101], mandating a gradual reduction in the production and use of fluorinated greenhouse gases. This regulatory framework, aimed at mitigating global warming, has resulted in limited availability and increased procurement costs for such gases.

Various efforts are being made within the RPC community to address the environmental concerns associated with the current gas mixture and explore alternative eco-friendly options. CERN, in particular, has taken specific measures to limit the use of greenhouse gases and explore new environmentally friendly gas mixtures for RPCs at the LHC. Chapter 4 of this thesis discusses the details of the restrictions mandated by European regulations to diminish greenhouse gas consumption, outlines the initiatives undertaken by CERN, explores the alternative gases under consideration and highlights the results achieved thus far.

2.4.7 Effect of Temperature and Pressure

The resistivity of electrode materials, such as Bakelite and glass, is directly affected by temperature variations. For Bakelite, studies showed that an increase in temperature results in a notable decrease in resistivity (eg. [90]). The resistivity of Bakelite can decrease by an order of magnitude with just a $20^{\circ}C$ temperature increase. This temperature-induced variation in electrode resistivity has a direct impact on the ohmic component of the current drawn by these devices. In the case of float glass, a measured exponential effect indicates a tenfold decrease in resistivity for a $25^{\circ}C$ temperature increase, as confirmed by the studies discussed in [84].

In addition, Temperature (T) and pressure (p) exert a direct influence on the density of the gas mixture (ρ_g), impacting gas parameters, including drift and multiplication parameters, through the E/ρ_g ratio. Keeping a constant E/ρ_g ratio is crucial to maintain stable RPC performance under fluctuating environmental conditions. Operating RPCs at different temperatures leads to variations in current, noise rate, efficiency and time resolution. These changes leads to alterations in both electrode resistivity and gas density.

Temperature-induced resistivity reduction contributes to an increased ohmic current. Additionally, a temperature rise, assuming stable pressure, leads to decreased gas density, elevating the E/ρ_g ratio. Consequently, RPCs operate with an increased effective first Townsend coefficient, resulting in a shifted operating point, just as if the applied voltage was increased by the same relative amount. Contrastingly, pressure increase shifts the RPC operating point in the opposite direction of a temperature increase. This interplay of factors necessitates a deep understanding to interpret observed effects accurately.

When examining data obtained from the same RPC but under different T and p conditions, the concept "effective voltage" V_{eff} is typically introduced and defined as:

$$\Delta V_{eff} = \Delta V_{app} \frac{T}{T_0} \frac{p_0}{p} \tag{2.30}$$

where p and T represent the actual temperature and pressure values (which vary over time), while p_0 and T_0 serve as reference values for temperature and pressure, often chosen as $p_0 = 1013\ mbar$ and $T_0 = 273\ K$. The term ΔV_{app} represents the applied high voltage across the RPC [102]. Using this formula corrects the $p - T$ dependence of RPC performance. During the operation of the detector, to maintain uniform performance unaffected by temperature or pressure variations, V_{eff} is kept constant, while V_{app} is varied according to the $p - T$ values.

Figure 2.12 (a) and (b) shows the efficiency plotted against ΔV_{app} and ΔV_{eff}, respectively at various temperatures. In the initial plot, the efficiency fluctuation resulting from temperature changes is evident, while the second plot superimposes efficiency curves, demonstrating temperature-independent results. This correction factor applied to ΔV_{app} is commonly referred to as the "PT correction".

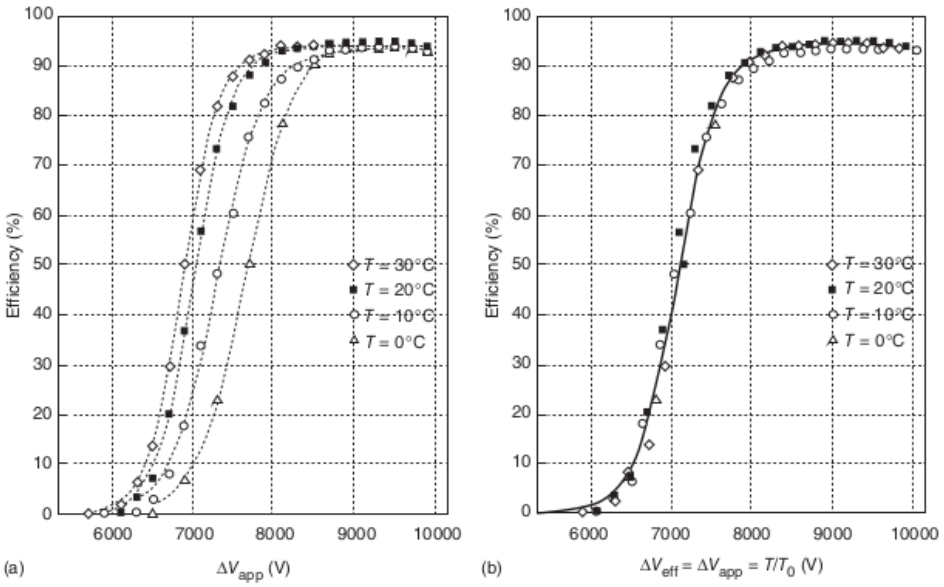

FIGURE 2.12: Efficiency measurements for a single-gap RPC at different temperatures as a function of applied voltage (ΔV_{app}) in (a) and effective voltage (ΔV_{eff}) after PT correction in (b). The plots show the importance of applying PT correction for RPC operation [102].

2.4.8 Ageing Phenomena

The ageing process in gaseous detectors refers to the degradation of performance over prolonged exposure to ionising radiation, involving complex factors such as electrode materials, gas composition, radiation exposure details and other parameters. In RPCs, ageing is often characterised by an increase in dark current and noise pulses, potentially leading to operational issues. Detection efficiency may progressively decrease and visual or microscopic inspection upon disassembly may reveal electrode erosion or polymer deposits. While the basic phenomenology of ageing is widely studied, obtaining a comprehensive understanding at a fundamental level

remains challenging due to the simultaneous occurrence of various chemical processes and limited quantitative descriptions of ageing effects.

RPCs used in early high-energy physics experiments, such as those at L3 in the Large Electron Positron (LEP) collider, initially showed minimal performance degradation attributed to ageing [103]. In subsequent experiments in B-factories, such as Belle and BaBar, the RPCs operating in the streamer mode exhibited signs of ageing, especially in the presence of tetrafluoroethane ($C_2H_2F_4$), a key component in RPC gas mixtures [86, 104]. This led to rapid deterioration, higher dark currents and decreased efficiency. Investigations revealed that fluorine ions etched the glass and avalanche products deposited on electrodes, causing damage. Measures were implemented, such as reducing water concentration and using ammonia flushing, to mitigate ageing effects. Speculations also surfaced on long-term instabilities in glass RPCs due to the migration of alkali ions under intense electric fields [105].

The experience with RPCs in the BaBar experiment highlighted the impact of linseed-oiled Bakelite electrodes [106]. Initial success was followed by deteriorating efficiency and increased dark currents, attributed to excessive linseed oil, elevated temperatures softening the oil film and the intense electric field pulling the softened oil layer away. The modification of electrode spacers in BaBar, designed to minimise leak currents, inadvertently created hidden cavities that trapped unpolymerised linseed oil, exacerbating the issues. Subsequent efforts focused on developing oilless Bakelite RPCs [107], integrating a thin film of plastic during fabrication and addressing the ageing effects observed in accelerated tests.

The challenges posed by the LHC required RPCs with a total area of approximately 10,000 m^2 to work reliably for many years at a high count rate. Intensive R&D efforts were initiated to address these challenges, with the decision to run ATLAS and CMS RPCs in avalanche mode and with electrodes of reduced resistivity (1-6$\times$ 10^{10} Ω cm) to improve their rate capability and reduce ageing effects [108, 109]. Ageing studies investigated graphite coating degradation, temperature effects, the impact of HF and other fragments on oil coating and other changes in Bakelite electrodes.

When implementing new gas mixtures for RPC operation, it becomes essential to explore potential ageing effects associated with these mixtures. This is particularly critical when considering the replacement of gas mixtures for RPCs at LHC, where the higher particle rate during HL-LHC could accelerate the ageing effects. The details of the ageing studies conducted with new eco-friendly gas mixtures for LHC's RPCs is provided in Sec. 4.6.

2.5 Double-gap and Multi-gap RPCs

As detailed in preceding sections, the initial iteration of RPCs was characterised by single-gap configurations. Studies conducted with these single-gap RPCs paved the way for a multitude of subsequent advancements in the field, utilising the single-gap design as a foundational framework and progressively modifying and enhancing its geometric layout. Given that the research activities outlined in this thesis include the development and study of single-gap (Sec. 6.3), double-gap (Sec. 3.3.1, Sec. 6.4 and

Sec. 4.5.1) and multi-gap RPCs (Sec. 6.5.1), some important details of the double-gap and multi-gap configurations are provided in this section.

2.5.1 Double-gap RPC

The "double-gap" layout is achieved by employing two single-gap RPC modules in a configuration where their signals influence the same set of readout electrodes (for the layout see Fig. 2.13). Typically, in this arrangement, the readout strips are sandwiched between two gaps, as illustrated in Fig. 2.13. When an ionising particle

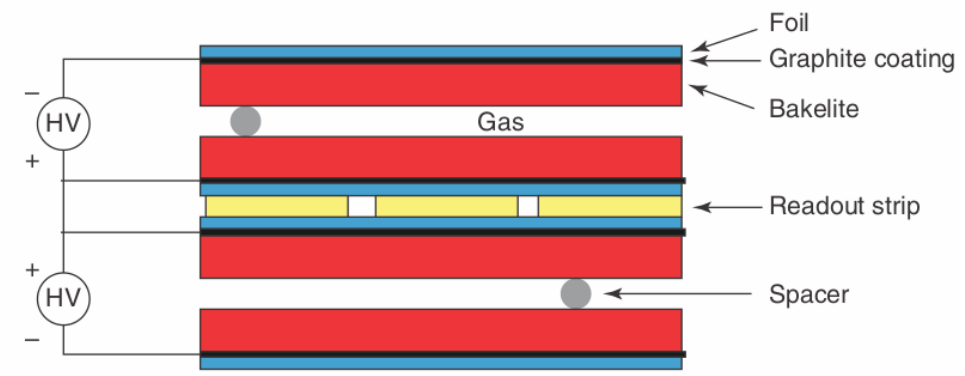

FIGURE 2.13: Schematic representation of the double-gap RPC layout, featuring two gas gaps and the readout strips arranged in between [79].

traverses this device, it generates ion-electron pairs in both gaps. With optimised electric field configurations, the signals induced by the avalanches in the two gaps become nearly simultaneous, contributing to the central readout electrodes. This design significantly increases the efficiency of the detector [79]. Even when considering the two single gaps in a logical OR, where a signal is detected if avalanches in either gap induce a signal, the efficiency becomes:

$$\epsilon_{tot} = \epsilon_1 + \epsilon_2 - \epsilon_1\epsilon_2 \tag{2.31}$$

It's important to note that Eqn. 2.31 is a simplistic approximation and the actual overall efficiency tends to surpass this value. This is attributed to the fact that the signal on the central readout electrodes is not a digital sum but an analog sum, where the instantaneous values of the two signals combine. Consequently, the total amplitude can surpass the threshold for signal detection, even if both gap signals are individually below the threshold.

The benefits of a double-gap layout include an expected improvement of at least $1/\sqrt{2}$ in time resolution compared to a single-gap RPC under identical conditions of geometry, gas composition and applied electric field. This improvement arises from the presence of two independent signals corresponding to the same incident particles, where the faster signal dictates the threshold crossing time measured by the detector. Notably, the total signal, constituting an analog sum rather than a simple OR of the two signals, usually results in a slightly superior overall time resolution. Demonstrating enhanced performance even at high rates under equivalent conditions of the basic modules, double-gap RPCs were selected for various high-energy physics experiments in the mid-1990s. This includes the RPCs used in CMS experiment at CERN and the double-gap layout of the CMS RPCs are discussed in Sec. 3.3.1 and Sec. 4.5.1.

2.5.2 Multi-gap RPC

Multi-gap RPCs (mRPCs), proposed in 1996 by M.C.S. Williams' group [110], evolved from the double-gap concept. They also combine advantages of wide-gap RPCs with enhanced rate capability and reduced charge dynamic range [111, 112]. The approach involves dividing the gas gap into smaller slices using a stack of resistive electrodes, where only the outermost ones are connected to high voltage and the internal ones remain electrically floating as shown in Fig. 2.14.

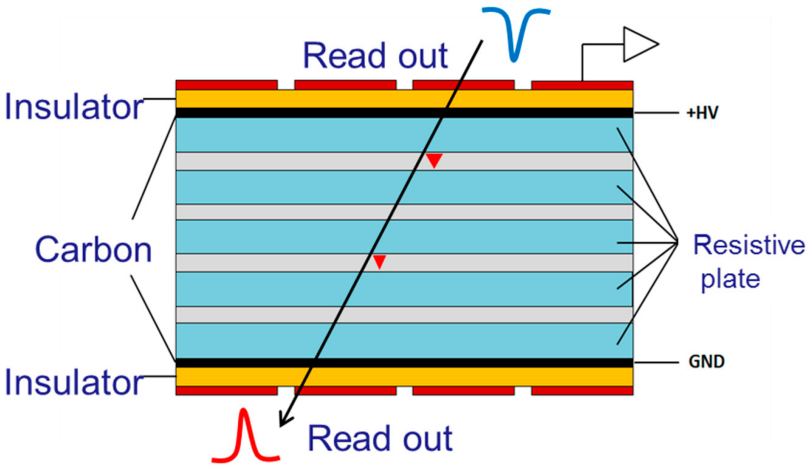

FIGURE 2.14: Schematic layout of mRPC showing the multiple gas gaps and the generation of both negative (blue pulse) and positive signals (red pulse) induced by the avalanches (red triangles in the gaps) produced by the ionising particle traversing the detector [113].

The internal plates, despite being left electrically floating, automatically attain the correct voltage. No additional connections within the frame are necessary to apply voltage to these inner resistive plates due to the principles of electrostatics and the system's symmetry under static conditions. Furthermore, dynamic conditions introduce a feedback mechanism that maintains the electrodes at the correct potential, ensuring equal current across all gaps. In this mechanism, any deviation in voltage on one resistive plate triggers adjustments in the electric field among sub-gaps. Larger avalanches in the sub-gap with the higher field lead to increased current, bringing more charge to the neighboring gap's resistive electrodes. This process ultimately restores the correct field and gain in both gaps [114].

mRPCs feature significantly smaller gap spacings compared to standard RPCs, typically in the range of a few hundred micrometers per gap (eg. Sec. 6.5.1). This design commonly incorporates five or more gaps, ensuring the generation of a sufficient number of primary ion-electron pairs each time an ionising particle traverses the device.

The majority of mRPCs have been manufactured with electrodes composed of float glass, a readily available material commonly used for windows, exhibiting a typical resistivity in the order of several times 10^{12} Ωcm, which is significantly higher than the characteristic resistivity of Bakelite RPCs (resistivity around 10^{10} – 10^{11} Ωcm). The outermost plates are resistive paint coated electrodes (For details on the construction of resistive glass electrodes, see Sec. 6.2), connected—one to the HV

and the other to the ground. Insulating rods of appropriate diameter, often fishing lines, are used for uniform gas gap construction. For details of RPC gas gap construction using fish wires, the reader is referred to Sec. 6.3.1. It is worth noting that, more recently, mRPCs with electrodes made from Bakelite have also been developed, yielding promising results [115].

The fundamental operating principle of an mRPC and the readout strategy closely resembles that of standard RPCs (discussed in Sec. 2.4.1). In the case of mRPC, since the avalanches in multiple gas gaps are generated almost simultaneously, their signals are aggregated on the readout electrodes. Therefore, even if the signal from a single avalanche is small and falls below the electronic threshold, their sum may surpass the threshold. The signal induced on readout electrodes by a moving charge generally depends on the distance covered by the charge's movement (discussed in Sec. 2.4.4). Consequently, one would anticipate a lower signal induced per gap in narrow-gap RPCs compared to wide-gap RPCs, assuming the same avalanche size.

In a multi-gap configuration, the readout electrodes are positioned on one side of the gap stack, contrasting with the double gap where they are positioned in the middle, impacting the induced charge amount. If a charge of 1 pC is considered to drift in each gap for the three cases, with the assumption of infinitely thin resistive electrodes, the induced charge (q_{ind}) would be 1 pC in the single-gap scenario, 2 pC in the double-gap setup and 1 pC again for the multi-gap case (independent of number of gas gaps, N_g, in this approximation). This is commonly expressed by stating that in mRPCs, the charge drifting in each gap contributes a factor of $1/N_g$ to the induced charge. Moreover, in practical terms, the induced charge is further reduced due to the finite thickness of the resistive electrodes compared to the gap width.

Typically, a region of about 1–1.5 mm from the cathode(s) is necessary, with the exact value dependent on the gas mixture, for an avalanche to grow. In the case of mRPC, since this region is distributed among the various gaps, the distance available for the avalanches to develop and to induce a signal on the readout electrodes is smaller with respect to an RPC with a single gap with the same total gap thickness (comparison shown in Fig. 2.15). Therefore, in order for the avalanches produced in one gap of an mRPC to give rise to a signal above the threshold, an increased value of the effective first Townsend coefficient (α^*) must be used [114] which will require an increased operating voltage.

The reduced gas gap width in mRPCs contributes to an enhanced time resolution, a crucial factor in particle detectors. As defined in Eqn. 2.26, the time resolution (σ_t) is inversely proportional to α^* and the electron drift velocity (v_d). Due to the reduced gas gap width in mRPCs, as explained in the preceding paragraph, the electric field is substantially increased to ensure sufficient avalanche production. This results in a much higher α^* and an elevated electron drift velocity, consequently yielding superior time resolution compared to single-gap RPCs.

The enhanced time resolution of mRPCs makes them widely employed in Time-of-Flight (ToF) measurements for particle identification (PID) in experiments such as the STAR-ToF System [116] and CBM-ToF System [117]. PID can be used for effective background rejection, particularly valuable in imaging techniques like muography.

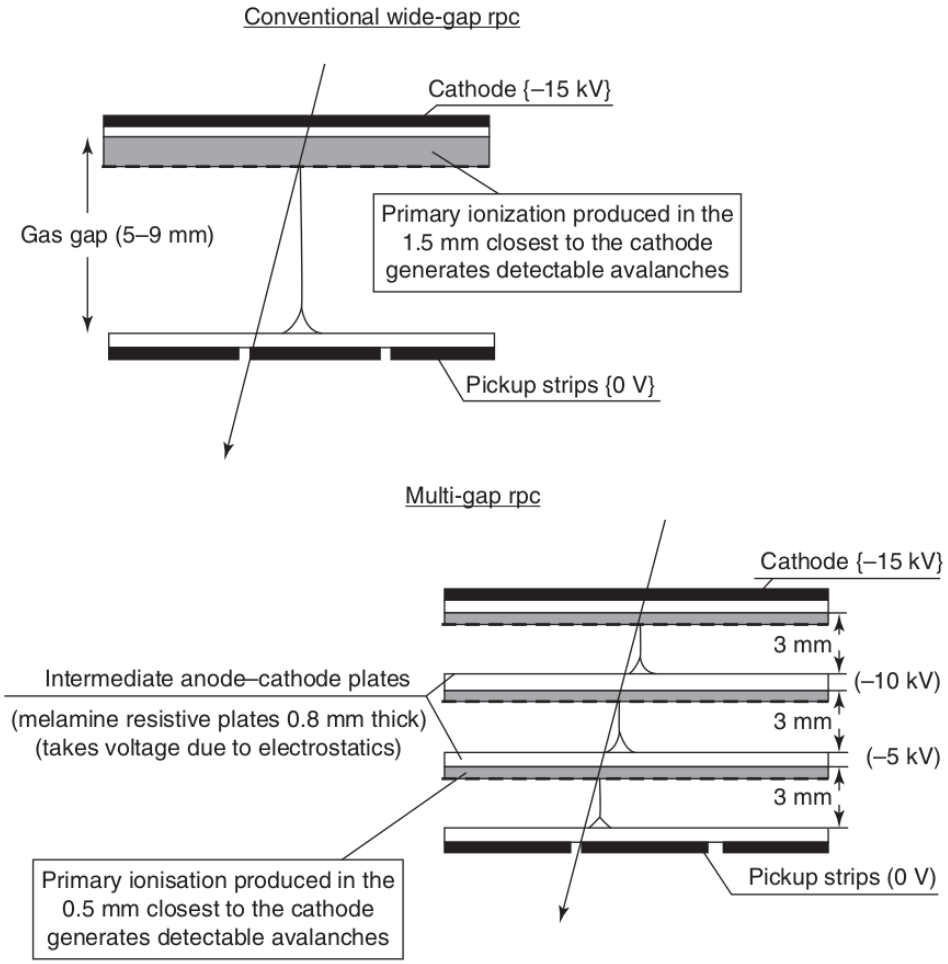

FIGURE 2.15: Schematic diagrams of a single-gap RPC (9 *mm* wide gap) and an mRPC (three 3 *mm* gaps), providing a comparison of the operational principles of both detectors [110].

The mRPC detector constructed in view of developing an advanced gaseous detector telescope for muography (detailed in Sec. 6.5) aim to exploit the timing properties of mRPCs for background rejection.

Chapter 3

The iRPCs for the CMS Phase-2 Upgrade

This chapter provides a detailed overview of the CMS iRPC upgrade for the HL-LHC phase, with a particular focus on the activities in which I participated. During the first year of my PhD (2019-2020), I took part in the construction of two iRPC prototype detectors and conducted studies aimed at optimising the detector's technical layout. In the subsequent year, the iRPC demonstrator project was initiated, and I played a key role in the construction and evaluation of eight iRPC demonstrator chambers. Additionally, I validated and documented all quality control (QC) procedures for both detector components and the assembled detectors that need to be performed at assembly sites. Detailed insights into the finalised technical layout of the iRPC chambers, the construction of prototype and demonstrator chambers, and the finalised QC protocols are provided in the chapter. I also participated in several test beam campaigns conducted at GIF++, CERN to assess the performance of the detectors I constructed and to validate the iRPC front-end electronics. My involvement included hardware setup, data collection, and subsequent data analysis for the test beam campaigns. The major results obtained from data collected during the July 2022 test beam is discussed in the chapter. Currently, four of the iRPC demonstrator chambers produced are successfully installed and operational at CMS.

Considering my significant contributions to the project, I was nominated as the iRPC mass production coordinator of the CMS RPC lab at UGent. My major responsibilities were to prepare the laboratory and necessary setups for the iRPC mass production and training new team members and students for the construction of detectors as well as conducting QC tests. Additionally, I performed the QC tests for the initial batch of iRPC gas gaps upon their arrival for mass production. Furthermore, I actively participated in the construction of the initial iRPC chambers produced as part of the mass production at the RPC lab, UGent. My involvement in mass production activities, along with highlighting the significant results achieved during this phase of the project are also described in the chapter.

3.1 Introduction

In preparation for the HL-LHC phase, where the instantaneous luminosity will be increased to $5\times10^{34}\ cm^{-2}s^{-1}$, surpassing the LHC's original design value by a factor of five, and the integrated luminosity is set to rise from 300 fb^{-1} in Phase-1 to a remarkable 3000 fb^{-1} in Phase-2, significant enhancements are underway within the CMS experiment at the LHC. These adaptations are crucial to enhance the experiment's sensitivity for physics searches and to address the forthcoming challenges

in terms of increased background rates, event PU, and potential ageing of current detectors.

One pressing concern is the lack of redundancy in the high $|\eta|$ region of CMS, where background noise is most pronounced, and the magnetic field is weaker. This poses considerable difficulties in muon triggering, identification, and measurements. Currently, CMS employs 480 RPC chambers in the barrel and 576 chambers in the endcap disks, but these arrangements fall short in the high η region ($1.8< |\eta| <2.4$). To address this issue, CMS is introducing an improved iteration of existing RPCs, named iRPCs: RE3/1 and RE4/1 (as discussed in Sec. 1.4.2). These advanced chambers will be installed in the third and fourth endcap disks, thereby extending the RPC coverage to the high η regions. Figure 3.1 shows the region where these new RPCs will be placed (marked by the red box) [39]. As seen in the picture,

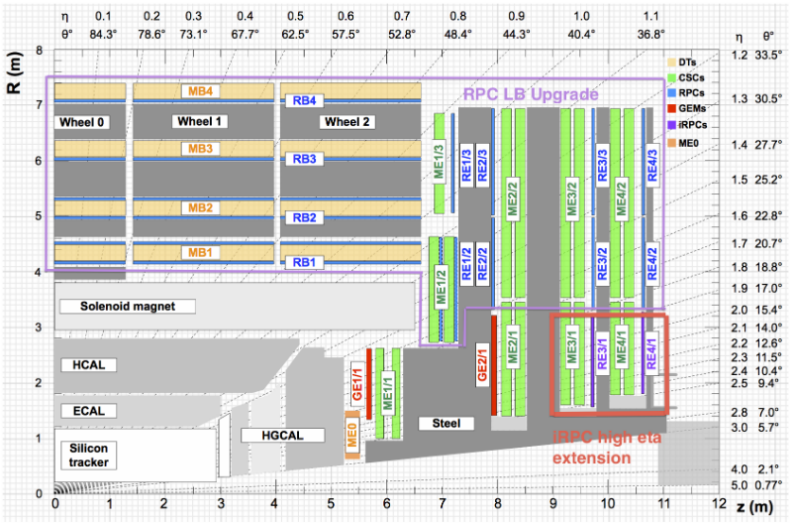

FIGURE 3.1: A quadrant of the CMS experiment. The iRPCs will be installed in the region enclosed by the red box [39].

these new chambers will complement the already existing CSC chambers ME3/1 and ME4/1. The space required for installing these detectors already exists in CMS, as it was previously not utilised by the existing RPCs due to their inability to withstand the high particle rate.

Since the CMS iRPCs feature a new and improved technical layout compared to the existing RPCs, the development of prototype detectors becomes essential to thoroughly assess and confirm their performance, ensuring they meet the expected performance and the standards for installation in CMS. As part of the CMS iRPC project, two prototypes and several demonstrator chambers were built and tested. These chambers played an important role in validating the detector's technical layout, finalising construction protocols and QC procedures, and certifying both construction and test sites. Furthermore, they serve as crucial tools for testing the new front-end electronics designed for the iRPCs. Additionally, they facilitate the integration of CMS detector control software and DAQ systems, all while enabling a study of detector performance under real CMS operating conditions. All the chambers constructed underwent successful validation, with several of them currently operational at CMS. In 2023, the first phase of mass-producing iRPC chambers commenced and is currently in progress.

This chapter predominantly focuses on detailing the design, construction, and qualification of CMS iRPC detectors, with special emphasis on my contributions. Section 3.2 outlines the key motivations behind the iRPC upgrade. In Sect. 3.3, details on iRPC technology and new front-end electronics are presented. Section 3.4 offers an overview of the iRPC demonstrator project, where I played an important role in chamber production and qualification. To validate the performance of the iRPC detector, test beam campaigns were conducted at GIF++ and CERN, and the specifics of the experimental setup and major results are discussed in Sec. 3.5. Lastly, this chapter provides insights into the ongoing iRPC mass production, with a particular focus on activities at the CMS RPC laboratory at UGent.

3.2 Motivation

The major motivations behind upgrading the RPC forward system with iRPC chambers, RE3/1 and RE4/1 are:

- The RE3/1 and RE4/1 chambers complement the existing CSC stations, ME3/1 and ME4/1, enhancing local muon measurements by providing additional track hits and increasing the lever arm. These RPC chambers were always part of the CMS detector plans but are yet to be installed. The older RPC detectors cannot handle the HL-LHC rates, aligning with the original CMS design, whereas the new iRPCs can.

- Combining measurements from RE3/1 and RE4/1 with existing CSC chambers improves intrinsic time resolution by over two times, aiding in background hit rejection and the identification and reconstruction of slowly moving Heavy Stable Charged Particles (HSCP).

- The new iRPCs offer superior spatial resolution, measuring time differences between signals at both ends of the readout strips. This helps resolve ambiguities in the endcap trigger for multiple tracks.

- The Level-1 muon trigger needs to suppress tracks with low transverse momentum (p_T) which can saturate the trigger rate if mis-measured as having high transverse momentum. The additional iRPCs play a crucial role by improving time and spatial resolution, enhancing p_T assignment when combined with RPC and CSC data. This is especially valuable in border regions of adjacent CSC chambers where the number of crossed layers by a muon is lower, preventing low p_T tracks from being misidentified as having high transverse momentum.

- RE3/1 and RE4/1 RPC detectors increase redundancy in the challenging endcap region. If there are issues with associated CSC chambers ME3/1 and ME4/1, muons can still be identified and reconstructed.

The impact of adding the RPC and iRPC hit information to the single muon trigger is shown in Fig. 3.2. This figure illustrates the efficiency of identifying trigger primitive stubs at the station 3 (left) and station 4 (right) levels, both with and without the inclusion of information from the existing RPC and new iRPC detectors in the Endcap Muon Trigger Finder (EMTF). The cumulative effect of introducing RPC hits into the single muon trigger is further elucidated in Fig. 3.3, which compares single muon trigger efficiencies with and without RPC information. Notably, a noticeable

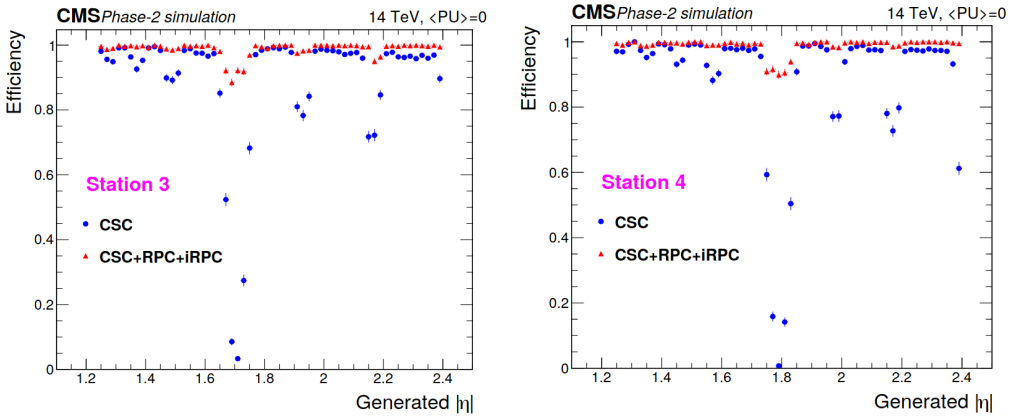

FIGURE 3.2: The effect of Including RPC Hits on the local trigger primitive efficiency in Station 3 (left) and Station 4 (right). The contribution of iRPC becomes significant above $|\eta|$ = 1.8 [39].

enhancement of approximately 15% is observed within the $|\eta|$ range of 2.1 to 2.2. In the event of any CSC trigger issues in ME3/1 and ME4/1, additional improvements can be anticipated.

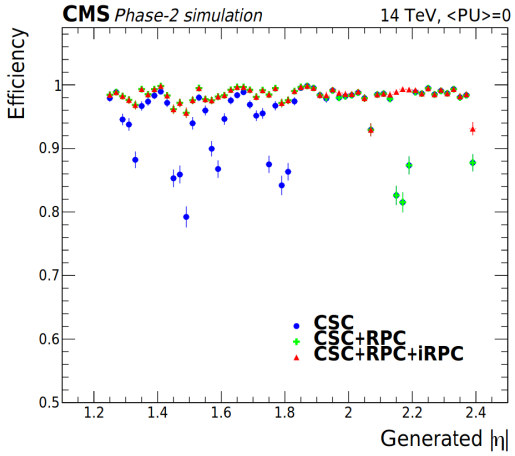

FIGURE 3.3: Simulated comparison between the single muon trigger efficiencies with and without the iRPC timing information, as a function of $|\eta|$ [39].

3.3 The iRPC Technology and Design

According to simulation studies conducted using Fluka [118] and Geant4 [119], it is anticipated that the hottest points in the new RPC stations will experience an average hit rate of approximately 600 Hz/cm^2 (without the safety factor) during the HL-LHC period. The background hit rate at the iRPC stations is primarily caused by neutrons, photons, electrons, and positrons. The sensitivity of the iRPC detector to these background particles is depicted in Fig.3.4, illustrating the likelihood of a particle with a specific energy reaching the detector and generating a signal. The blue, red, green and black colour data points in the plot corresponds to the particles neutrons, photons, electrons and positrons respectively. The anticipated background

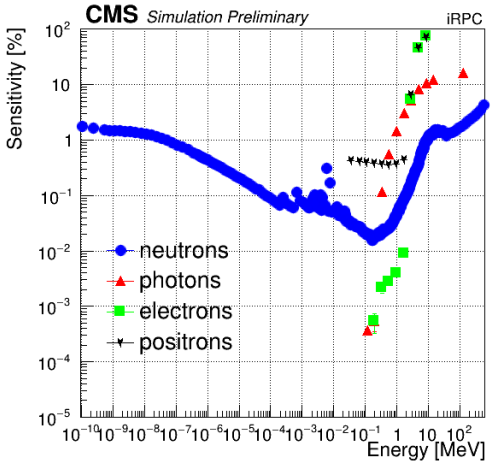

FIGURE 3.4: MC estimation of the sensitivity of the iRPC detector to different background particles as a function of their energy. In the plot, different colors represent different particle types: blue for neutrons, red for photons, green for electrons, and black for positrons [120].

hit rate of incident particles as a function of their energy at the RE3/1 station is estimated using sensitivity and particle flux data, as shown in Fig. 3.5 (left). Additionally, Fig. 3.5 (right) presents the expected background hit rates of various particles at the RE3/1 station concerning their distance (R) from the center of the CMS beam pipe [121]. It's worth noting that the background hit rates at the RE4/1 station are slightly lower due to a minor reduction in the particle flux [122].

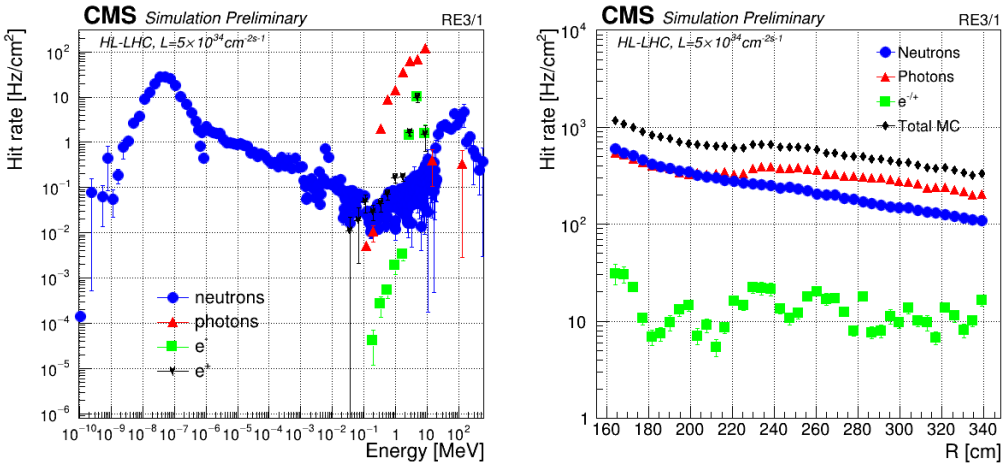

FIGURE 3.5: MC estimation of the background hit rate expected at RE3/1 station at an instantaneous luminosity of $5 \times 10^{-34} cm^{-2} s^{-1}$ with respect to the energy of the incident particles (left) and the distance (R) from the center of CMS beam pipe (right). In both plots, blue, red, green and black colour correspond to the particles neutrons, photons, electrons and positrons respectively [121].

The installation of iRPCs substantially increases the number of chambers per muon disk by 18, resulting in a combined total of 72 chambers spanning both endcaps to serve the RE3/1 and RE4/1 stations. Each of these stations will provide a single-hit for muon reconstruction, delivering precise time information of approximately 1.5 ns and a spatial resolution of around 0.3 cm (perpendicular to the strips) and 2 cm

(along the strips). For a visual representation, see Fig. 3.6, which offers a schematic overview of two RE3/1 chambers mounted on the CMS endcap disk (left), accompanied by a more detailed perspective shown on the right [6].

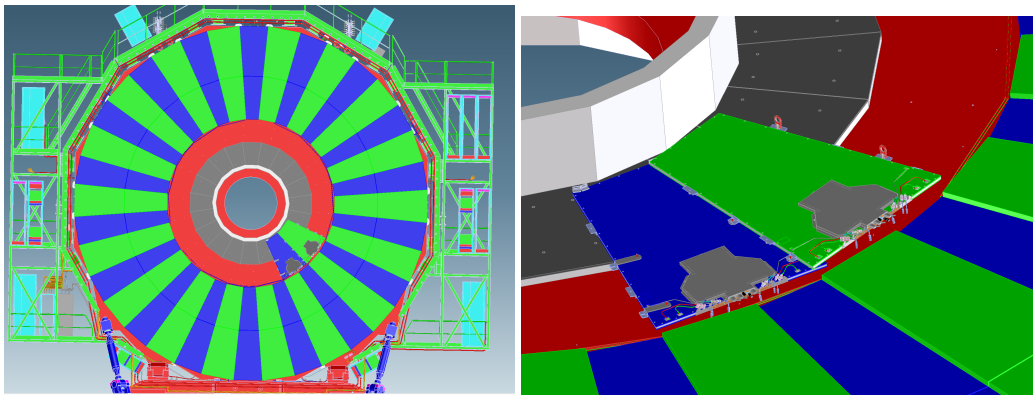

FIGURE 3.6: Schematic view of the RE3/1 chambers mounted on the endcap disk (left) [6]. Detailed view of the mounting of the RE3/1 chambers (right).

In order to ensure a hit efficiency exceeding 95% throughout the HL-LHC operation and to withstand the aforementioned conditions, several enhancements have been made in the case of the iRPC chambers. These include an improved technical layout compared to the existing RPCs at CMS, as well as the introduction of new low-noise front-end electronics. The technical design of the iRPCs is elaborated in Sec. 3.3.1, while Sec. 3.3.2 provides details regarding the newly introduced front-end electronics.

3.3.1 Improved Technical Layout of iRPCs

The current RPCs installed at the endcap stations (RE1, RE2, RE3, and RE4) consist of double-gap wedge-shaped RPCs with two layers of gas gaps. The bottom layer is a single unit, while the top layer is divided into two parts to facilitate signal extraction from the strips located between these two gas gap layers. The layout of the gas gaps and strips are shown in Fig. 3.7 (left), while the cross-sectional diagram of the gas gap is presented in Fig. 3.7 (right). The complete information of the geometry and layout of the current endcap RPCs can be found in [123]. In resemblance

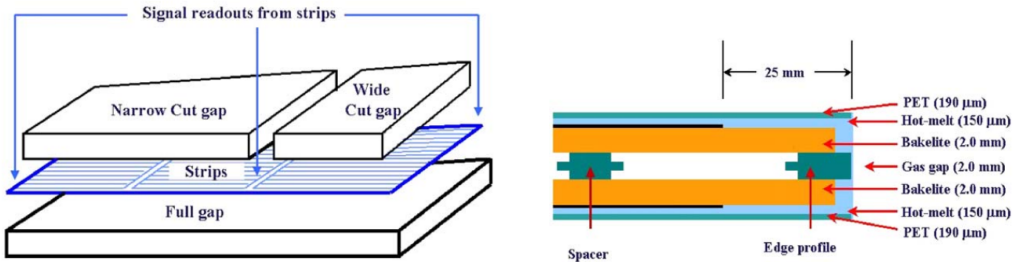

FIGURE 3.7: Figure illustrates the layout of the current RPC system used in the endcap stations (RE1, RE2, RE3, and RE4). On the left, the arrangement of gas gaps and strips is depicted, while the right side offers a cross-sectional diagram of the gas gap structure [124].

to these RPCs, iRPCs also are of a wedge-shaped design, featuring radially oriented readout strips positioned between the gaps and operating in avalanche mode. To

highlight the key distinctions between RPCs and iRPCs, a comparative summary is presented in Tab. 3.1. The technical layout of the RE3/1 and RE4/1 chambers are exactly same except their size. The following subsections provide detailed descriptions of the technology and components of iRPCs, highlighting the key distinctions from the design of the existing RPCs.

Parameters	RPC	iRPC
High Pressure Laminate (HPL) thickness (mm)	2	1.4
No of gas gaps	2	2
Gas gap width (mm)	2	1.4
Resistivity (Ωcm)	1-6$\times 10^{10}$	0.9-3$\times 10^{10}$
Charge threshold (fC)	150	50
Strip pitch (cm)	2.0-4.0	0.6-1.2
$\lvert\eta\rvert$ segmentation	3$\lvert\eta\rvert$ partitions	2D readout

TABLE 3.1: Comparison of the major parameters of existing RPCs and iRPCs.

Gas gaps and Electrodes

An iRPC chamber comprises two gaps, namely the top and bottom gaps. Each gap consists of two HPL electrodes coated with a thin graphite resistive layer, and the gas gap is constructed by placing circular spacers between the HPL plates. Fine-tuning various detector parameters is crucial for mitigating ageing effects and enhancing rate capability. The primary limiting factor for the rate capability is the voltage drop (V_{drop}) induced by the current of irradiation passing through the electrodes. This V_{drop} depends on the resistivity and thickness of the electrodes and the average charge produced in the gas gap (see Sec. 2.4.1 for detailed explanation). To minimise V_{drop}, the electrode resistivity of iRPCs is reduced from the $1 - 6 \times 10^{10}$ Ωcm range of RPCs to $0.9 - 3 \times 10^{10}$ Ωcm. However, the resistivity remains in the mega ohm range because excessively reducing it would increase the operating current, accelerating ageing effects and detector noise. The thickness of the HPL electrodes as well as the gas gap is reduced from 2 to 1.4 mm in iRPCs to lower the average charge produced. Figure 3.8 illustrates the induced charge as a function of the electric field strength for double-gap RPCs with six different gas gap thicknesses. Thinner gas gaps also lead to a reduction in the high-voltage working point, from 9.5 kV to 7.1 kV, enhancing system robustness. A 1.4 mm thickness is chosen for iRPCs as thinner gas gaps are more sensitive to electrode distance non-uniformities, and 1.4 mm represents a safe compromise between sensitivity and uniformity. The effects of reducing the avalanche charge are compensated by amplifying the signal and increasing the

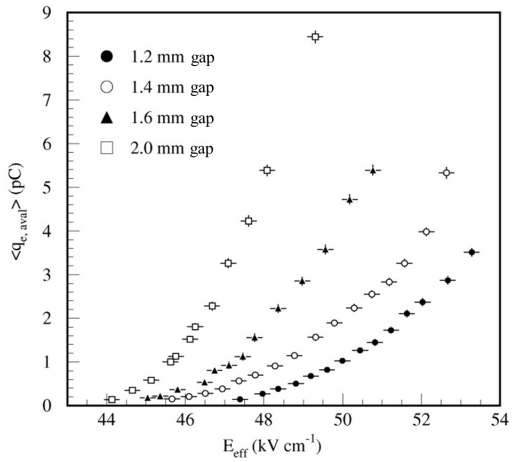

FIGURE 3.8: Average charge per avalanche measured on different sizes of double-gap RPCs: 1.20 *mm*, 1.40 *mm*, 1.60 *mm*, and 2.0 *mm*, as function of the electric field strength [125].

sensitivity of the front-end electronics system five times compared to the existing system.

Strip PCB

In the case of the existing RPCs, the strip plane has a trapezoidal shape and consists of four separate segments, with each segment containing trapezoidal-shaped strips. The schematic of the strip panel of one of the endcap RPC RE2/1 is shown in Fig. 3.9. These strip planes are constructed using either etched strip panels or copper foil strips attached to mylar sheets. Signal cables are soldered to the edges of the strips within each segment and connected to the associated Front-End Board (FEB) mounted on the chamber. Detailed information on the geometry of the strip panels in each type of the end-cap RPC, including the number of strips, strip dimensions, signal extraction layout, and more, can be found in the document [123], which provides an explanation of the technical layout and geometry of all end-cap RPCs.

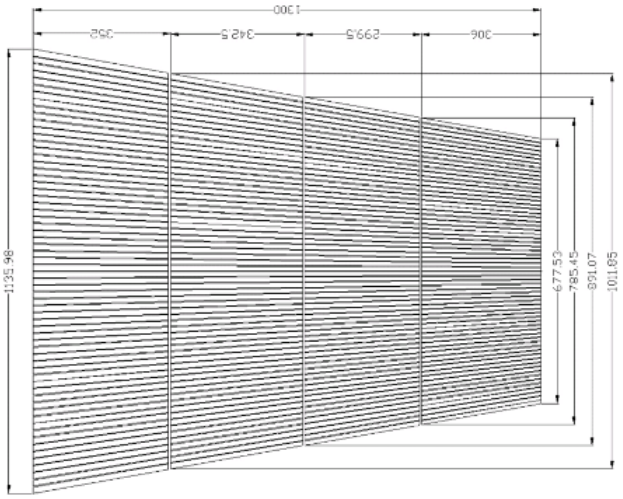

FIGURE 3.9: Schematic view of the strip panel of RPCs RE2/1 that are currently installed at CMS.

Unlike the present RPC design, in case of iRPCs, the strips are integrated into a large trapezoidal printed circuit board (PCB) made of two parts (PCB left and PCB right). The shape is optimised to fully cover the active area. Each PCB comprises 96 readout strips in total (48 strips in the PCB left and 48 strips in the PCB right), with a pitch of approximately 12.3 *mm* in the high-radius (HR) section and about 6 *mm* in the low-radius (LR) section. Compared to the existing RPC system, the new readout scheme offers a better spatial resolution and reduces the number of electronic channels by 60% [126]. Furthermore, the new layout scheme offers the additional advantage of simplifying the cabling layout and chamber construction. This is because the strip signals need to be extracted from only two sides of the chamber, as opposed to the multiple partitions required in the existing RPCs. Additionally, the PCB of the iRPC incorporates three ERNI connectors (female) per side, which are connected to the traces originating from the strips. The FEBs are directly plugged into these connectors, eliminating the need for separate signal cables. The external edges of both part of the PCB are covered with a copper band for grounding. Figure. 3.10 shows the schematic view of the strip PCB.

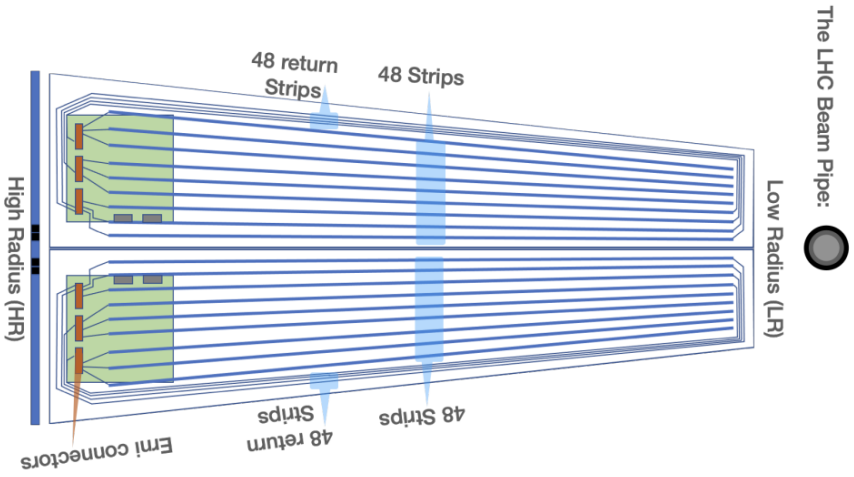

FIGURE 3.10: Schematic view of the iRPC strip PCB and its components.

Gas Layout

Present endcap RPCs in the are operated using the single inlet-outlet method which leads to the diagonal flushing. To improve the uniformity of the gas flow and the readiness, a double inlet-outlet method (gas layout of the existing barrel RPCs) is introduced for iRPCs. Apart from this, the gas loop of the gaps are not interconnected which provides the possibility of single gap flushing if necessary. To implement the double inlet-outlet method, the usage of three gas pipe connectors: L, Y, and T are proposed [127, 128]. Gas is supplied to the gaps through the T connectors. The two T connectors are connected to the two gas inlets in the HR side of the gaps and the connectors equally distributes the gas flow to the inlets. The gas exits through the outlets in the LR side of the gaps and the outlet gas pipes of each gap is connected to the Y connector. The Y connectors are then connected to the L connectors through which the gas is extracted out from the chamber. The schematic of the gas connection layout in the HR and LR regions and positions of the gas connectors inside the chamber is shown in Fig. 3.11. All iRPC internal gas pipes are of

radiation-tolerant polyethylene (PE LD tube FT 12 1001 0604) and all external gas pipes mounted on the chamber are of copper.

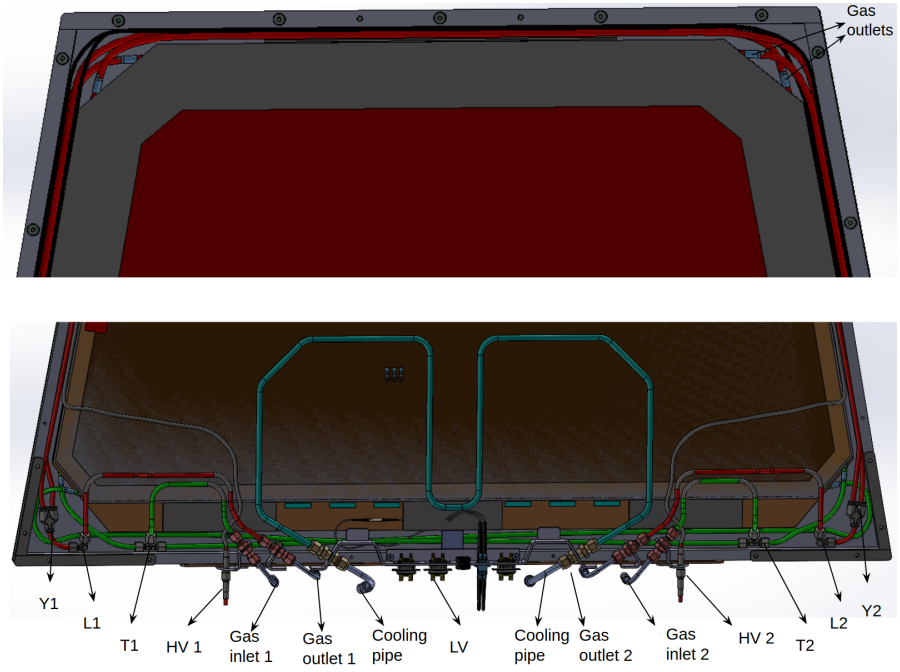

FIGURE 3.11: Schematic view of the gas pipe layout in the LR side (top) and HR side (bottom) of the iRPC chamber. The bottom picture also shows all the connectors and cables present in the LR side of the chamber.

Other components: All layers including two insulation layers (Mylar foils), two copper plates (for Faraday cage), and the gas connection circuits are stacked inside a honeycomb panel based box. To hold all the layers in position, five aluminum brackets are mounted in four sides of the layer, inside the box. The chamber also includes a fiber optic sensor (FOS) to monitor environmental parameters (temperature, pressure, and humidity). A patch panel is mounted on the HR to hold all the mechanics and cables in position. Two FEBs hosting the front-end electronics are plugged directly to the PCBs and two copper cooling pads are fixed on top of the FEBs for temperature controlled operation. A cover plate is installed on the top side of the chamber to protect the FEB connections and cooling circuit. An exploded view of an iRPC chamber is shown in Fig. 3.12 [1]. All technical drawings and details of the iRPC components are documented in the CERN Information and Document Management Software (EDMS) and can be accessed using the link in [129].

3.3.2 Front-end Electronics for iRPCs

The new front-end electronics FEB version 2.2[1] (FEB v2.2) for iRPC has been designed to maintain high efficiency even with the lower charge signal of the detector. The FEB is equipped with low-noise front-end electronics and is capable of detecting signals with a charge as low as 30 fC [130]. The FEB v2.2 is composed of three ERNI connectors (female) of 32 channels each, six Petiroc 2C ASICs controlled by three Cyclone-V (non-radiation hard) Field-Programmable Gate Arrays (FPGAs), and the

[1]FEB v2.2 is not the final version. The development studies of FEBs for iRPCs are still ongoing.

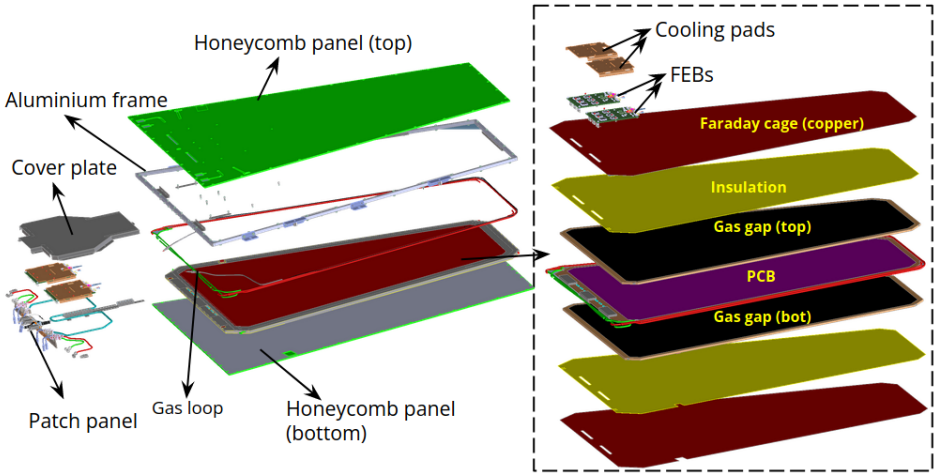

FIGURE 3.12: Exploded view of the iRPC chamber chamber and the layers inside the chamber (inside black dashed line box).

chips GBTx, GBT-SCA, and VTRx for the data transfer and slow control. The picture of FEB v2.2 is shown in Fig. 3.13.

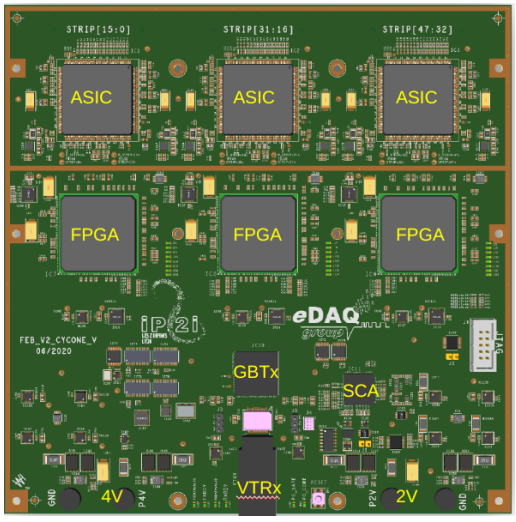

FIGURE 3.13: Schematic of iRPC FEB v2.2 with it's major components labeled in the picture: 6 Petiroc 2C ASICs (3 in the back side), 3 Cyclone-V FPGAs, GBTx, GBT-SCA and VTRx.

In the existing RPC system, signals are read from one side of the copper strips, while in the case of iRPCs, the PCB strips are read from both sides. Each end of a strip is connected to different Petirocs, a configuration designed to mitigate interference and electronic cross-talk originating from the Petiroc processors. When the detected signal exceeds the applied threshold, the Petiroc generates an output signal directed to the corresponding Time-to-Digital Converter (TDC) channel on the FPGAs. The two-dimensional position information is determined by measuring the time difference between the arrival of signals at the two ends of the electrodes. Figure 3.14 illustrates the distribution of signal arrival time differences (ΔT) between both ends

of a strip in a RE3/1 prototype chamber. After noise rejection, the standard devia-

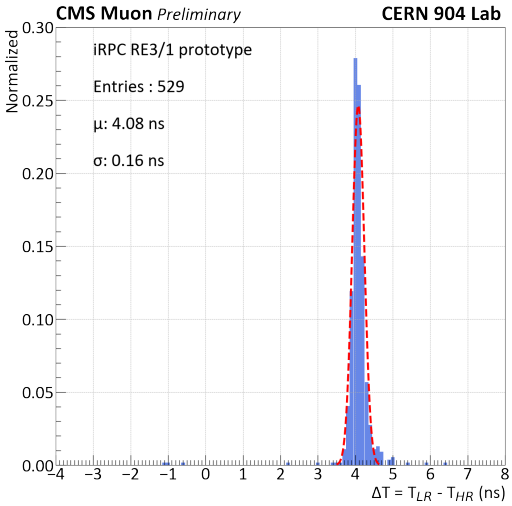

FIGURE 3.14: The distribution of the time differences between the two ends of an iRPC strip, with a standard deviation (σ) of 160 ps after filtering out the noise [131].

tion (σ) of the distribution is 160 ps. This translates to a position resolution of 1.5 cm along the strip, calculated using the formula: $(\Delta y = (v \times \Delta T)/2)$, where v represents the signal velocity on the strip ($0.69c$). Figure 3.15 (left) depicts the distribution of ΔT between the test and reference channels with zero delay. The RMS value of this distribution is approximately 23 ps. By dividing this value by $\sqrt{2}$, the time resolution of one iRPC channel can be estimated, which is around 16 ps. Figure 3.15 (right) illustrates how ΔT changes concerning the delay line's value. With an increase in

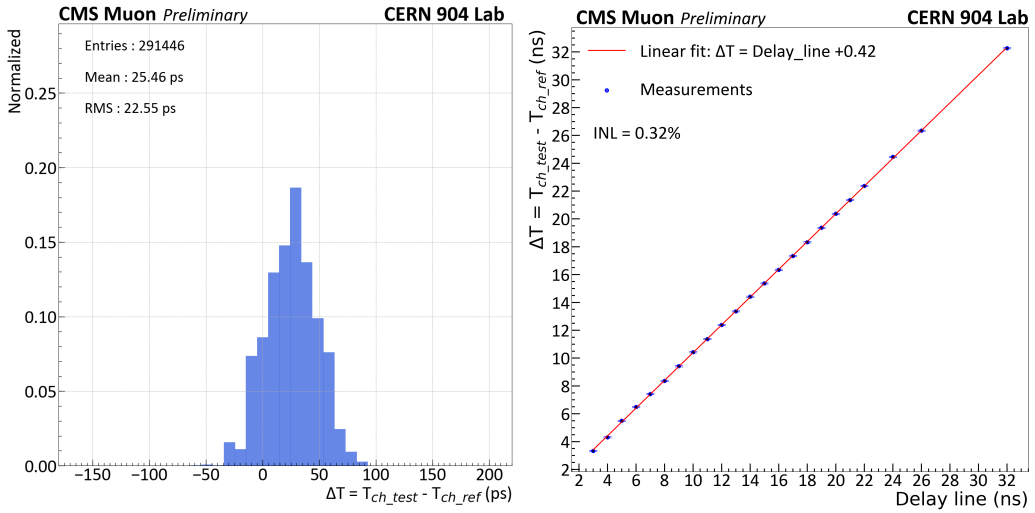

FIGURE 3.15: Left: The distribution of time differences between two iRPC channels without a delay line (RMS ∼23 ps). Right: The time difference for different values of the delay line. As the value of the delay line increases, the time difference between the two channels also increases linearly [131].

the delay line value, ΔT linearly increases, exhibiting a maximum deviation of 0.1 ns and an integral non-linearity (INL) of 0.32% [131].

My primary involvement centred on the production, qualification, and the performance studies of the iRPC chambers with the new front-end electronics FEB v2.2

and the subsequent sections provides the details of these activities and the results achieved.

3.4 The iRPC Demonstrator Project

As explained in the previous section, the iRPC chambers has an improved layout compared to the present RPCs and before starting the production of the chambers for the installation at CMS, its very crucial to validate the proposed new technical layout, the performance of the iRPC and validation of the new front-end electronics. The major efforts towards this started at UGent on 2019.

To validate the chamber mechanics, technical layout, and conduct studies with FEBv2.2, two RE3/1 prototype chambers were constructed at UGent (Belgium) in January 2020. The CMS RPC project team members from Institut de Physique Nucléaire de Lyon (France), Universidad Iberoamericana (Mexico), and Benemerita Universidad Autonoma de Puebla (Mexico) joined the UGent RPC team for the prototype production. Figure 3.16 displays an image of the prototype chamber developed at CMS RPC lab at UGent and the team involved in the assembly. As this

FIGURE 3.16: The iRPC RE3/1 prototype chamber developed at UGent and the CMS RPC team members participated in the assembly.

marked the first assembly of an iRPC detector, several parameters requiring refinement and scrutiny were identified, including cable layouts, gas connectors, honeycomb panel design, strip PCB layout, and assembly procedures. One of the prototypes remained in the Ghent laboratory for mechanical tests, while the other was dispatched to the CMS RPC electronics team at Institut de Physique Nucléaire de Lyon for tests with FEBv2.2. The validation process spanned nearly one year, culminating in the development of a efficient strategy for iRPC assembly and data collection with FEBv2.2 by the end of 2020.

After the successful validation of the chamber layout and mechanics, iRPC demonstrator project was launched on 2021 January to study the detector behaviour under real LHC conditions (background, noise, B field etc.), to validate the iRPC FEB and backend electronics and to integrate the new RPC stations into the CMS Detector Control Software (DCS) and DAQ. The production center of HPL plates for iRPCs as well as RPCs is the Riva Laminati company (Milan, Italy), and the gaps are produced at the Korean Detector Laboratory (KODEL). As part of the project, eight

demonstrator chambers (5 RE3/1 and 3 RE4/1) were assembled at UGent. All the QC procedures for the RPC components as well as chambers are standardised and documented since 2010. During the demonstrator project period, all these procedures were performed and re-validated for the iRPCs at the respective sites of each activity. Figure 3.17 (top) displays an inside view of one of the RE3/1 iRPC demonstrator chambers produced at the CMS RPC lab at UGent, along with the RPC team at Ghent. Figure 3.17 (bottom) provides a closed view of the same iRPC chamber.

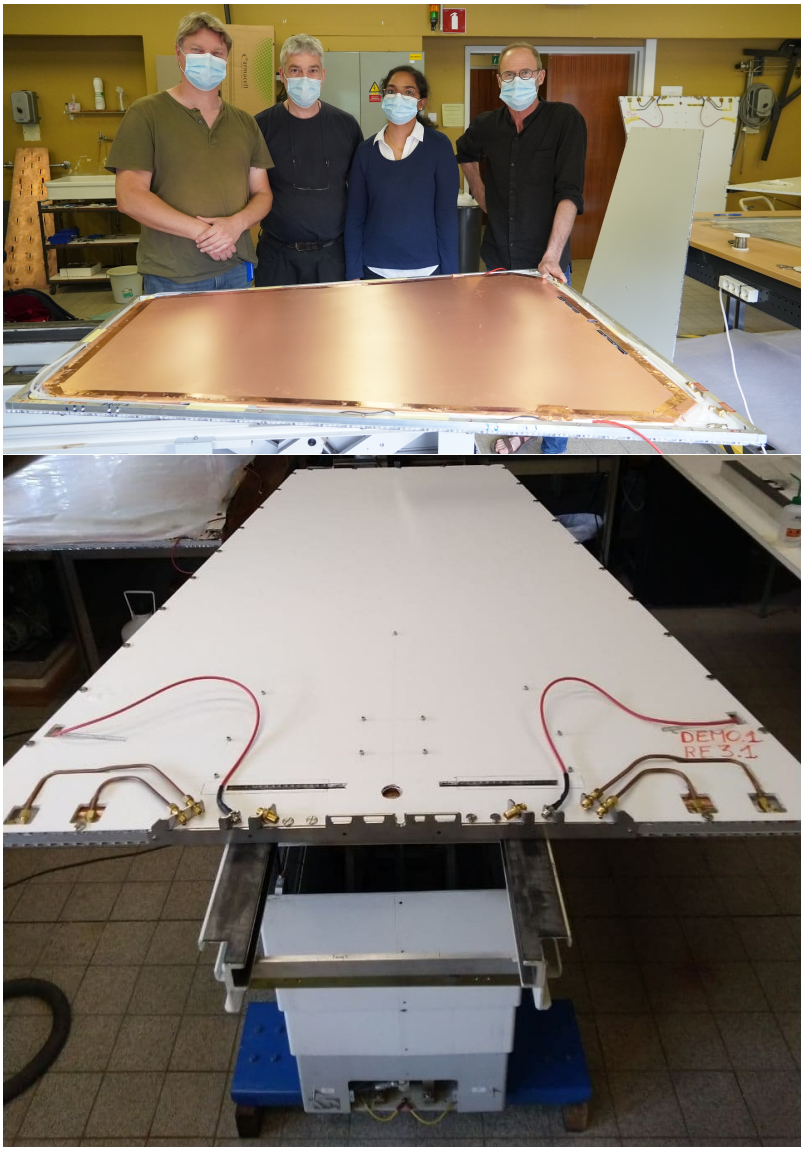

FIGURE 3.17: Top: Inside view of one of the RE3/1 iRPC demonstrator chamber produced at the CMS RPC lab at UGent with the RPC team there. Bottom: Closed view of the same iRPC chamber

The detailed information of the production of the iRPC components, QC procedures and the detector assembly are explained in this section.

3.4.1 QC1 for Detector Components

The initial stage of QC, referred to as QC1, focuses on inspecting and validating all the components essential for detector assembly. The QC1 procedures are conducted at the procurement sites where these components are sourced. Key components subject to QC1 evaluation include the detector electronics, strip PCB, and copper cooling panels.

Regarding the iRPC FEBs, its QC1 procedure entails assessments of each electronic module within the FEB. This assessment covers individual components such as the SCA, GBTx, power supplies, test points, and more. Additionally, the QC1 process involves verifying the integrity of data transmission within the system, assessing the functionality of the FEB firmware implemented on the FPGAs, testing the operation of TDCs and ASICs integrated into the FEB. FEB performance and functionality are validated using injection boards. These boards generate signals that simulate the behavior of iRPCs, which are then injected into the FEBs. The responses of the FEBs are examined and calibrated during this phase. The iRPC FEBv2.2 undergoing QC1 tests at IP2I, Lyon is shown in Fig. 3.18 (left).

The QC1 process for the strip PCB also includes several steps. The electrical continuity of each individual strip is verified to ensure that there are no breaks or interruptions in connectivity. Additionally, it is checked that there is no significant cross talk between the neighbouring strips. The impedance value (54 Ω) of all the 96 strips are verified if they are same. Furthermore, cross talk evaluations are repeated after soldering the ERNI connectors, since the soldering irregularities can lead to contact between adjacent strips. The picture of performing QC1-continuity test to the strip PCB is shown in Fig. 3.18 (right).

FIGURE 3.18: Left - QC1 tests being conducted on the iRPC FEBv2.2. Right - QC1 continuity test being performed on the strip PCB. The pictures are taken from the electronics lab in IP2I, Lyon.

The copper cooling panels for the FEBs are manufactured at the Georgian Technical University in Tbilisi, Georgia. The QC1 process for these cooling panels is straightforward and includes a dimensional and mechanical shape verification. Additionally, to ensure the integrity of the cooling system, a leak test is conducted on the copper pipes at a pressure of 20 bars, considering that the cooling water is supplied at 10 bars.

All other detector components including, gas pipes, connectors, tapes, screws etc. are directly bought from companies. Therefore, the quality procedure of these components includes only visual inspection. Of course, the important parameters like radiation hardness and ageing effects are already tested before finalising the components.

3.4.2 Gap Production and QC2

HPL plate qualifying and cleaning

As previously mentioned, the HPL plates are manufactured by an Italian company and subsequently undergo gas gap production at KODEL. The construction of the gas gaps involves several key steps, including the evaluation of the HPL plate quality, which is assessed as follows:

- **Visual Inspection (QC1):** Panels are examined for any significant defects, damage to the surface, periphery, or corners. Scratches on the panels are common, but those without or with only barely visible microscopic scratches are deemed acceptable.
- **Cleaning Process:** To remove any grease or dirt adhering to the HPL surface (grease is used during the Bakelite production), all panels undergo machine washing using MEK (Methyl Ethyl Ketone) and water. This cleansing step is vital to prevent issues such as condensation bubbles or the absence of the linseed oil layer within the iRPC gas gaps.

The washing procedure for the HPL plates is a two-step process:
1. **Initial Cleaning:** The panels are subjected to two rounds of washing using both metal and Polyethylene (PE) brushes. Each panel undergoes a 3-minute cleaning cycle at a rotation speed of 1000 RPM.
2. **Final Rinse and Drying:** In the second step, the panels are rapidly rinsed for 10 seconds and then thoroughly dried at 90°C temperature. This process effectively removes dirt and grease, ensuring the uniformity of the linseed oil layer in the gas gap side and ensuring good spacer bonding. The steps in the HPL washing procedure is shown in the Fig. 3.19.

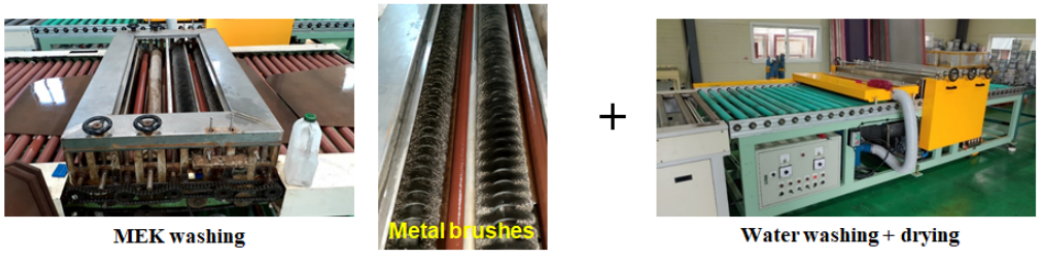

FIGURE 3.19: The washing procedure of the HPL plates. In the first step, the HPL plates undergo a MEK wash with the application of both metal and PE brushes for thorough cleaning. In the second step, the plates are washed once more with water and then subjected to a drying process.

Graphite coating

After the HPL plates have been qualified and cleaned, the electrodes are constructed by applying a graphite layer to one side of the HPL plates. This graphite

layer application follows the same silk screen printing method used in existing RPCs. The graphite paint mixture used for printing consists of a blend of conductive carbon and resistive black carbon resin. This mixture results in a bulk resistivity of 100 Ω and a surface resistivity ranging from 300-700 $k\Omega/\square$, with a mean value of 500 $k\Omega/\square$. The silk screen mesh (mesh #300), with a thickness of 20 μm, is utilised, resulting in a resistive layer of approximately 10 μm thickness. In contrast, the surface resistivity of electrodes in existing RPCs is slightly lower, ranging from 60-250 $k\Omega/\square$, with a mean value of $100k\Omega/\square$. For iRPCs, a slight increase in surface resistivity is implemented to suppress cluster sizes in high particle rate scenarios. Following the silk screen printing process, the plates are dried at $90^{\circ}C$ for 10 minutes. The washing and coating procedure is carried out by Damia, a private company in Korea, and they are able to efficiently process approximately 150 sheets per day. The different stages of the silk screen-based coating procedure are presented in Fig. 3.20. Subfigures (a), (b), (c), and (d) depict the silk screen printer, the silk mesh with mesh number 200, the printing process on one RE3/1 HPL plate, and the plate after drying, respectively.

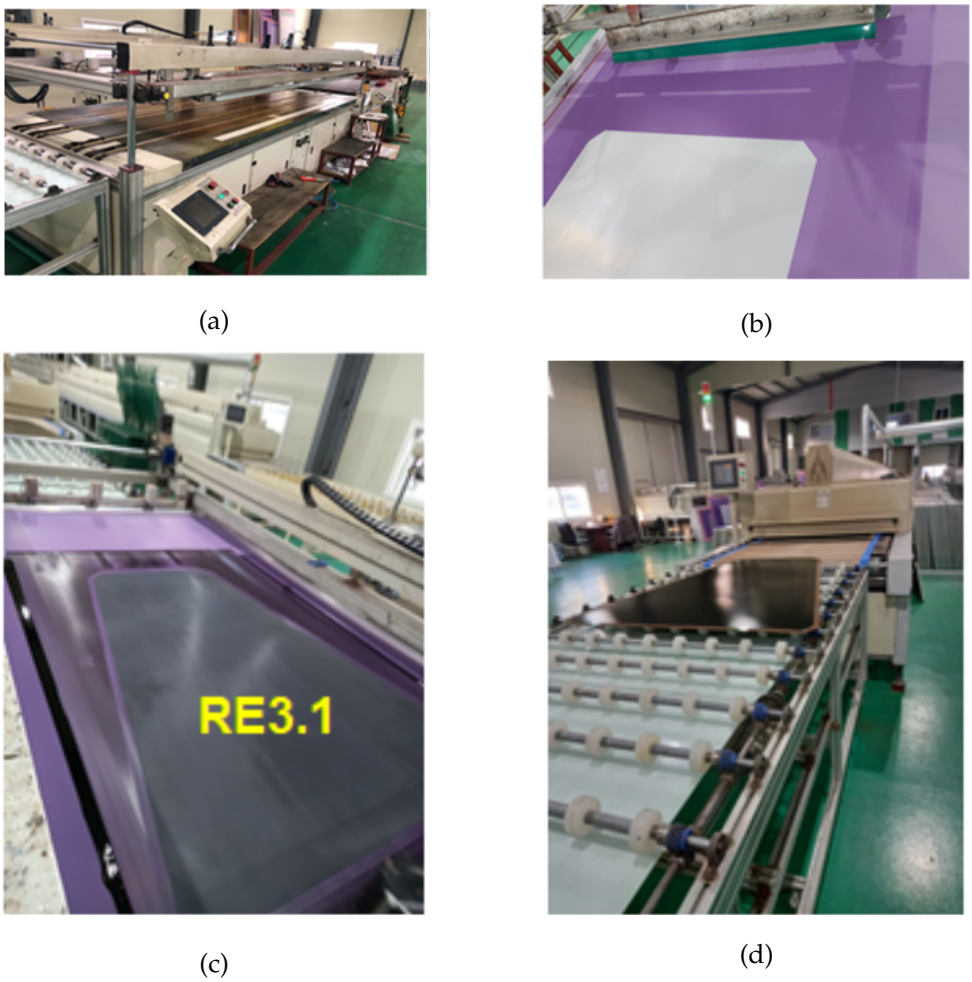

FIGURE 3.20: Various stages involved in the silk screen-based coating procedure for HPL plates used in the iRPC production. Subfigures (a) showcase the silk screen printer, (b) display the silk mesh with mesh number 200, (c) depict the printing process on a single RE3/1 HPL plate, and (d) exhibit the plate after drying.

As part of the QC procedure QC2, after the coating procedure, the surface resistivity at six different locations of the HPL plate is measured and the plates whose surface resistivity is outside the desired range is rejected.

PET film coating on electrodes

The polyester (PET) film is affixed to the graphite-coated side of the HPL plates to effectively prevent the radiation current leaks. As the chambers will be operated at approximately 8 kV, a 250 μm thick PET film with dielectric strength exceeding 10 kV is employed. Unlike existing RPCs, where PET coating was done at the KODEL lab, iRPCs utilise a new facility at a private company in Ilsan, Korea. This facility offers enhanced adhesiveness of PET films to graphite-coated electrode surfaces, reducing defects like air bubbles between the coating and the PET film. The major steps involved in PET film coating are as follows (see Fig. 3.21 for the coating procedure):

- Glass plates with a thickness of 5 mm are placed at the bottom of a vacuum pouch (Fig. 3.21-top left).
- Graphite-printed HPL plates are positioned on top of the glass plates (Fig. 3.21-top middle).
- A layer of Ethylene-Vinyl Acetate (EVA) glue is applied on top of the HPL plates (Fig. 3.21-top right).
- After stacking up to 5 HPL plates, the vacuum pouch is sealed (Fig. 3.21-bottom left).
- The vacuum pouch is then inserted into an oven (Fig. 3.21-bottom middle).
- The oven temperature gradually increases for 20 minutes and is maintained at 110$^{\circ}C$ for 50 minutes until the EVA films on the HPL plates completely melt (Fig. 3.21-bottom right).
- After heating, the vacuum pouch in the oven is allowed to cool down to below 50$^{\circ}C$ in approximately one hour.

It is crucial to attach the PET film to the melted EVA glue layer to minimise the formation of air bubbles caused by the inherent humidity of the HPL plates. The corner PART of the PET film-coated HPL electrode is illustrated in Fig. 3.22.

Gas gap construction

The gas gap is constructed by gluing the HPL electrodes together. The uniform gap gap is maintained by using circular spacers of thickness: 1.39 $mm \pm 10\ \mu m$ and diameter of 10 mm (refer Fig. 3.23-left). The diameter of the bonding area to the electrode is 8 mm. There are also peripheral spacers in the edges of the HPL plates. The gas inlet/outlet profiles are attached in the four corners of the gap. Figure 3.23-right shows the picture of the profile. The total outer thickness of this profile is 5 mm and the thickness of the part between the HPL plates is 1.4 mm. The circular and peripheral spacers and the gas inlet/outlet profiles are made of polycarbonate. An epoxy glue, 3M model DP460, is used for gluing the HPL plates together.

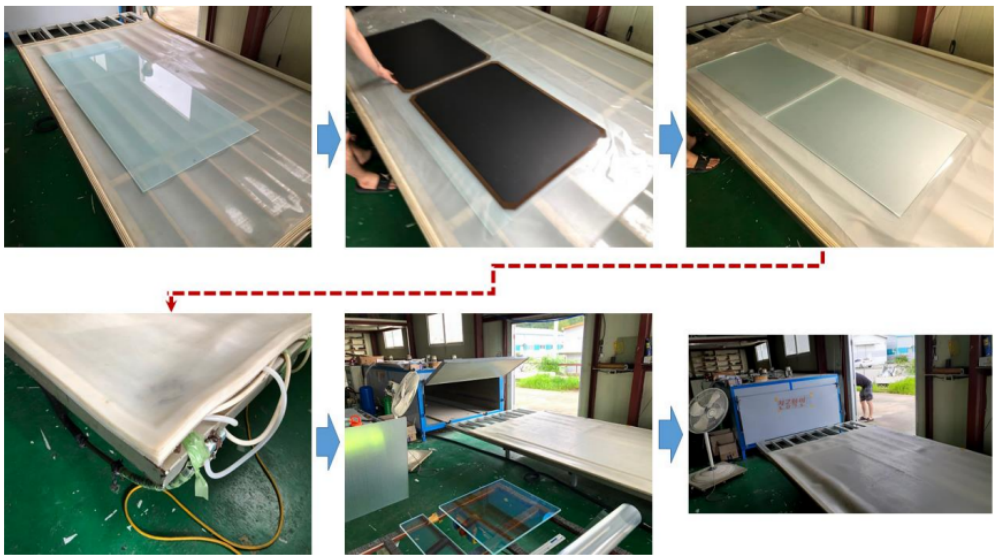

FIGURE 3.21: The procedure of the PET film coating for the HPL electrodes. Key steps include placing graphite-printed HPL plates in a vacuum pouch, applying EVA glue, heating, and cooling to ensure proper PET film adhesion and minimise air bubble formation.

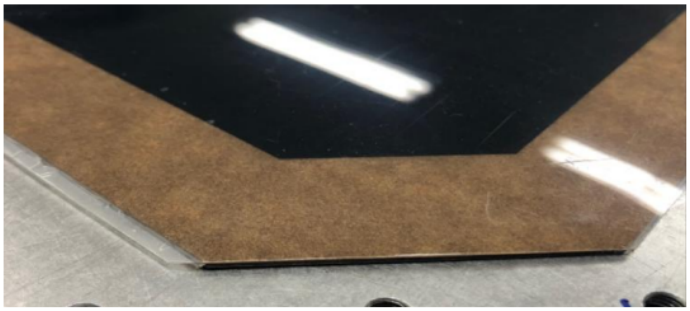

FIGURE 3.22: corner view of an iRPC electrode with PET film coating, highlighting the successful adhesion and minimal air bubble formation achieved through the coating process.

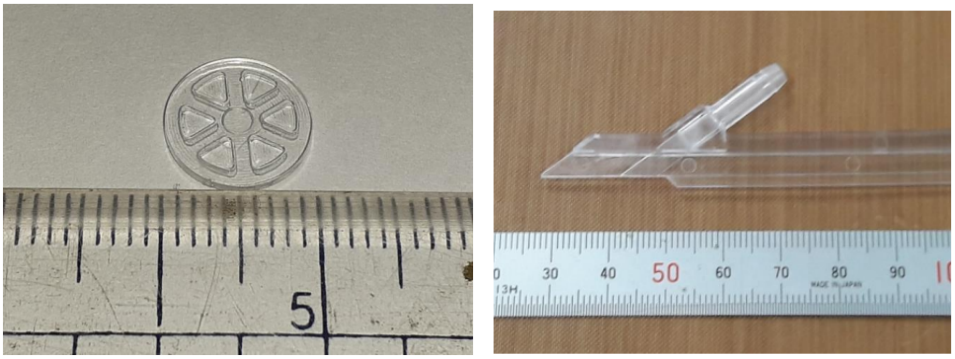

FIGURE 3.23: The circular spacer that is used to construct the gas gap (left). The gas inlet/outlet profile to connect the gas pipes to the gas gap (right).

Following are the major steps involved in the gas gap construction:

- The inner side of the HPL plates (the other side of the graphite+PET coated surface) are cleaned thoroughly with Iso-Propyl Alcohol (IPA).

- The HV side of the electrode is placed on a metric table and the plate is fixed with eight aluminum jigs.
- A spacer jig made of 3 mm thick Plexiglas (Fig. 3.24) of dimensions identical to the HPL plate is placed on the inner surface of the HPL plate. This spacer jig has 12 mm holes machined into it, allowing for precise placement of the circular spacers.
- Epoxy glue is applied to one side of the circular spacers, and the spacers are placed on the HPL plate through the holes of the spacer jig.
- Epoxy glue is applied to the bottom side of peripheral strip spacers and four gas corner pieces, which are then placed at their respective positions along the periphery of the HPL plates.
- Epoxy glue is applied to the top sides of the circular spacers, peripheral strip spacers, and gas corner pieces.
- The second HPL plate is placed on top of the HPL plate fixed on the table and is properly aligned within the aluminum jigs.
- Extra epoxy glue is applied near the corners of the gap to avoid possible gas leaks.
- The glued gap and the metric table are inserted into a glue-curing slot for drying the glue for 24 hours. In each glue-curing slot, an air pouch uniformly presses the whole surface of the gap with a pressure of 30 hPa (equivalent to 300 kgm^{-2}). Figure 3.25 (left) shows a picture of the gluing of gaps, and Fig. 3.25 (right) shows the glued gaps on the metric tables placed in the glue-curing slots.

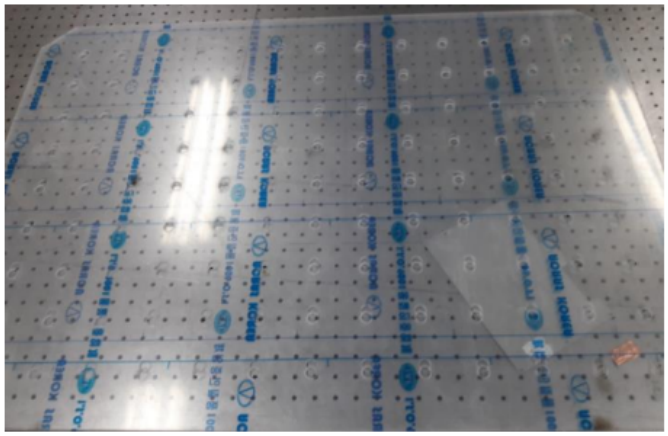

FIGURE 3.24: Spacer jig made of 3-mm-thick Plexiglas used for precise placement of circular spacers during the gas gap construction process.

Following gas gap construction, a series of QC checks (QC2) is carried out, encompassing visual inspection, gas leak testing, and spacer bonding assessment. The visual inspection is the examination of various aspects, including the condition of the gas inlet and outlets, the edge and corner pieces of the gap, the PET coating on both sides of the gap, and the verification of bar code labels on the gap.

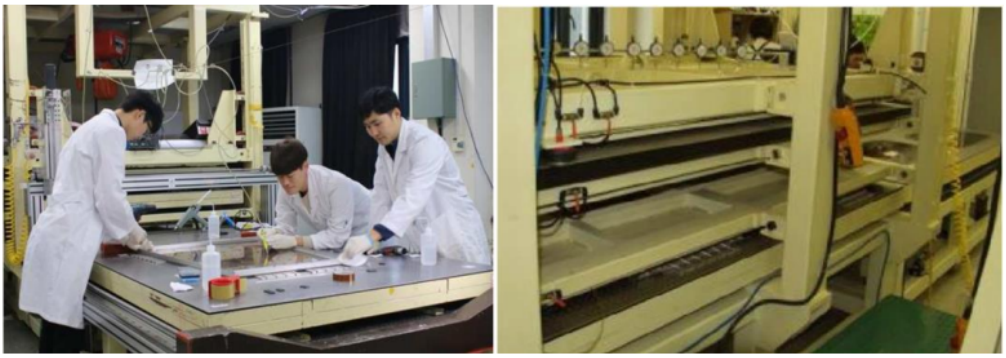

FIGURE 3.25: Left: A picture showing the gluing process of gaps. Right: Glued gaps placed on metric tables in glue-curing slots.

The leak test is done with Argon gas, and the pressure inside the gas gap is raised to 15 hPa while monitoring the pressure drop over time. If the pressure drop exceeds 0.4 hPa per 10 minutes, the gap is rejected. Subsequently, the spacer test is performed as a continuation of the gas leak test. At KODEL lab, this test employs an instrument in which a cylindrical probe with a 1 cm diameter, positioned by a 2-dimensional moving gantry, exerts vertical pressure on each spacer position of the gap with a 1 kg weight. The pressure increase when the cylindrical probe presses on a well-bonded spacer position is typically less than 0.5 hPa. In contrast, the pressure increase measured on a detached spacer is generally greater than 3 hPa. Considering a safety factor of two, meaning that if the pressure increase exceeds 6 hPa, the spacer is considered detached. Even a single detached spacer within the gap results in immediate rejection.

Linseed oil varnishing

The step after the gas gap construction involves applying a 3 μm thick linseed oil varnish layer to the inner surfaces of the gaps. This process is crucial for reducing the stochastic detector noise rate to approximately 1 Hz/cm^2 (detailed in Sec. 2.4.2). The varnish mixture consists of a 50% linseed oil and 50% heptane blend. To apply this mixture, the gas gap is slightly tilted and the varnish is introduced through the gas inlet. Compressed air is then employed to facilitate the drying of the oil layer.

To ensure the effectiveness of the varnishing procedure, a QC check (QC2) is performed. In this process, one gap from each batch ($\sim$ 24 gaps) is opened and inspected for surface condition. If issues such as poor polymerisation of the varnish layer, resulting from excessive thickness or insufficient drying, are observed, it can lead to an increase in the Ohmic current and potentially affect the detector's performance. As part of the QC procedure, if the opened gap displays multiple problematic areas, one or two additional gaps are opened for further verification. If the issues persist across these samples, the entire batch is rejected.

Cabling

The final stage in gas gap production involves the cabling of both the high-voltage (HV) and ground cables. The coaxial HV cable is of outer diameter 4.8 mm and inner diameter 2.7 mm. The diameter of the conductive copper core is 0.8 mm. The HV threshold of the cable is 15 kV. The grounding cable is a black single-enamel coated

wire of diameter 3 mm. The diameter of the conductive copper core in this case is 1 mm. The HV and ground cables are connected to the cathode and anode sides of the gas gap, respectively, at the diagonal corners of the gap. These connections are made 26 cm away from their respective corners. During the chamber assembly, the grounding cable is linked to the ground of the HV connection. The HV connection on the HPL plate is insulated with a rectangular polycarbonate insulator block shown in Fig. 3.26.

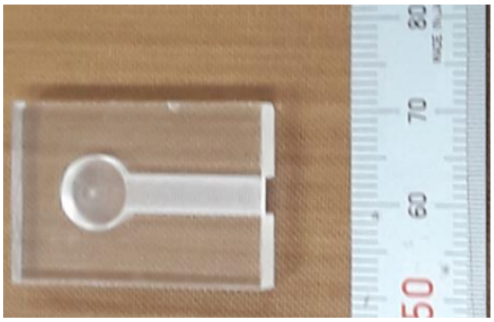

FIGURE 3.26: The rectangular polycarbonate insulator block for the insulation of the high-voltage connections.

Efficient biasing in iRPCs is employed to minimise the voltage difference between the HV and ground connections, particularly in high-rate scenarios. Conductive lines running along the cathode as well as anode sides of the HPL panels enable radiation current to flow transversely from the HV section to the ground, thereby reducing the distance of current flow. In iRPCs, where the mean surface resistivity is around 500 $k\Omega/\square$, the voltage difference between HV and ground is limited to 10 V when the induced current is approximately 100 μA.

The HV test is the final step of QC2, conducted at the KODEL laboratory. During the test the gaps are flushed with RPC standard gas mixture and this test involves both short-term and long-term evaluations for each gas gap. During the short-term test, current measurements are taken at 16 HV points, with the HV varying from 0 to 7.6 kV. In the long-term test, the gap is operated at 7.3 kV for 168 hours. In both case the maximum acceptable current value is 3 μA at 7.3 kV. If a gap exceeds this current value in either of the tests or shows a potential increase in ohmic current after the long-term test, it is rejected. As part of the QC, the connection of the HV as well as the grounding cable to the gap is also verified and its thoroughly checked that the HV connection point on the HPL plate is properly insulated.

All gas gaps produced for the iRPC demonstrator chambers, following the process described in this section (Sec. 3.4.2), were sent to the RPC lab at UGent for detector assembly.

3.4.3 CMS RPC Laboratory at Ghent University

The CMS RPC lab at UGent is a major production site of the CMS RPC project, boasting a rich history of detector production. Previously, this facility was used in producing a substantial number of existing RPCs (RE4/2-3; approximately 50 chambers). From that time all the setups necessary for the QC procedures and

chamber assembly exists in place and all these setups were re-validated during the iRPC demonstrator assembly. These setups include dedicated spaces for detector assembly, controlled environments with regulated temperature and humidity (AirCo room), storage areas for gas gaps and chambers, a crane for heavy lifting (5 tons), convenient access for truck transportation, a fully-equipped mechanical workshop, a gas mixing unit, a leak test setup, etc.

Lab Infrastructure

Figure 3.27 presents a schematic diagram of the CMS RPC lab at UGent, explaining the locations of these test setups for iRPC assembly, each meticulously detailed. Further details of the facility can be observed from the images of the RPC lab and the

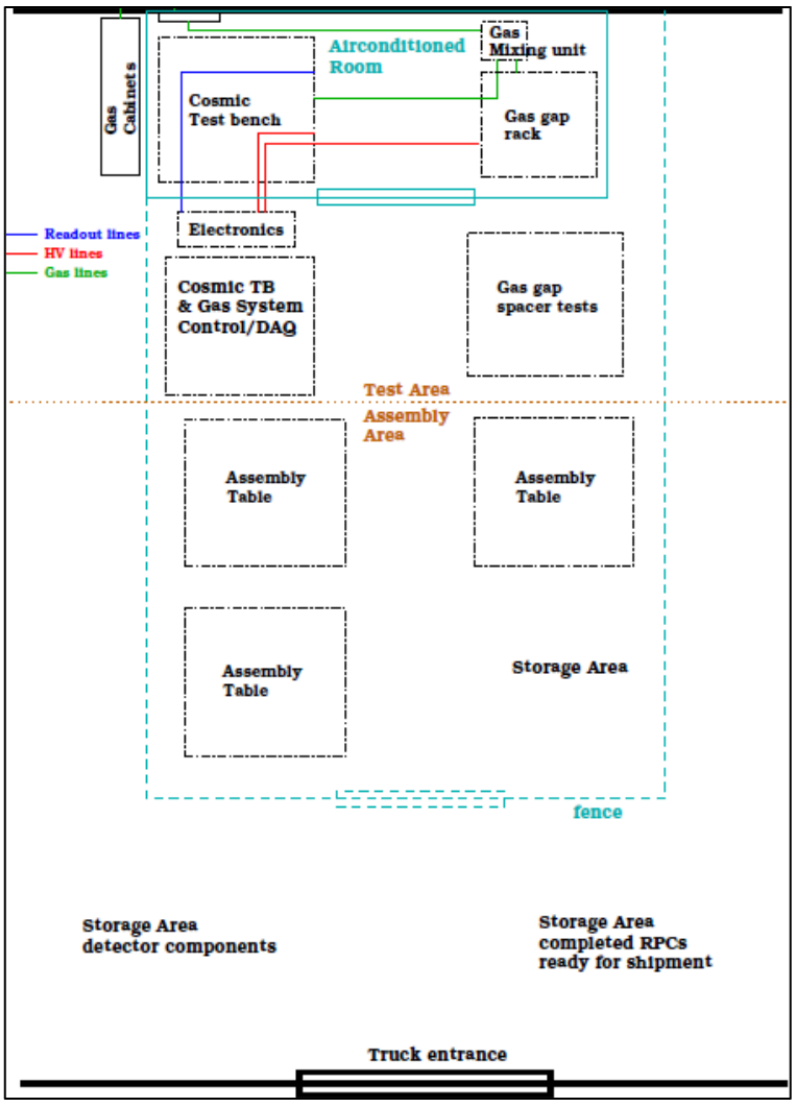

FIGURE 3.27: Schematic diagram of the CMS RPC lab infrastructure at UGent, highlighting key test setups for iRPC assembly and QC procedures.

AirCo room, as illustrated in Fig. 3.28 (a) and (b), respectively. Additionally, a dedicated chamber assembly room was prepared for construction of the iRPC demonstrator chambers, shown in Fig. 3.28 (c).

(a) (b)

(c)

FIGURE 3.28: (a) - View of the CMS RPC lab at UGent. (b) - The temperature and humidity controlled AirCo room inside the lab. (c) - Dedicated room for iRPC demonstrator chamber assembly.

To prevent the gas gaps from the fluctuations of the environmental parameters, once the gaps are received they are horizontally stacked inside the AirCo room. To monitor environmental parameters within the AirCo room, an Oregon WMR200 weather station [132] is installed in the room. This station is connected to a Windows PC in the lab, allowing continuous monitoring and data logging. The Gent RPC lab has a dedicated stand featuring five racks for storing the gas gaps (maximum limit = 30 gaps). The image in Fig. 3.29 (left) displays the iRPC demonstrator gas gaps securely stored within the stand located inside the AirCo room at UGent lab. All the dark current and performance tests of the gaps as well as the chambers are performed inside this room. Inside the AirCo room, a cosmic test bench, shown in Fig. 3.29 (right), is also installed for conducting cosmic muon tracking studies. This test bench comprises five racks for accommodating three RPC test chambers and two chambers (top and bottom) dedicated to tracking (efficiency measurements). Additionally, the setup includes two planes, one on top and the other on the bottom, each equipped with 10 scintillator paddles measuring 200 $\times$ 10 cm^2. These paddles are coupled to Phillips XP1911/UV PMTs [133] using WLS fibers for particle triggering.

FIGURE 3.29: Left: the five rack stand inside the AirCo room at CMS RPC lab at UGent stacked with the gas gaps for the iRPC demonstrator Assembly. Right: The cosmic test bench installed inside the AirCo room for muon tracking studies.

Gas System

The laboratory is equipped with a gas rack for storing gas cylinders required for tests and a gas mixing and distribution unit responsible for producing the standard RPC gas mixture and delivering it to the gaps and chambers via distribution channels. Figure 3.30 (left) showcases the gas racks constructed in compliance with safety protocols. The gas rack houses the gases R-134a (CH_2FCF_3), Isobutane (C_4H_{10}), and sulfur hexafluoride (SF_6) for the RPC gas mixture. Additionally, it accommodates Argon and Nitrogen for supplementary tests such as resistivity measurement and calibration. The right-side image in Fig. 3.30 depicts the gas mixing unit. The gas mixing unit comprises components, including a mixer tube, three mass flow controllers (XMFC-1106,1206 and 1306), two pressure sensors (PT 1009), a humidifier, various valves for manual gas flow control, rota-meters and gas bubblers associated with the gas channels, etc. The gas system has 12 output channels and an exhaust pipe that the releases the return gas from the gaps/chambers to outside. The mass flow controllers are controlled from a Windows computer using the Bronkhorst FlowView software ([134]). However, the channel by channel flow control is only possible manually. At present, the humidity level in the gas mixture is also manually regulated. If needed, this can also be integrated to the software by using additional mass flow controllers. The temperature and humidity of the gas mixture are continuously monitored and recorded using a Pico EL005 T/H sensor [135]. This sensor is connected to an EnviroMon data logger, which in turn is connected to a Windows PC [136]. This setup enables the logging of temperature and humidity data.

QC Setups

A gas leak test setup is installed in laboratory to for the QC procedures performed on gas gaps as well as chambers. The schematic diagram of the gas leak test setup is shown Fig. 3.31. Argon is used for the leak test, and the setup comprises connection slots for the Argon gas, both input and output connections for gas gaps/chambers, a flow meter for gas flow regulation, and three T connectors for gas distribution as illustrated in the diagram. Additionally, a crucial safety component, the Paraffin-filled bubbler, is integrated into the setup. This bubbler plays a vital role in situations where excess gas pressure, beyond what the gaps can withstand, is supplied by accident. It effectively controls the sudden surge in pressure, safeguarding the

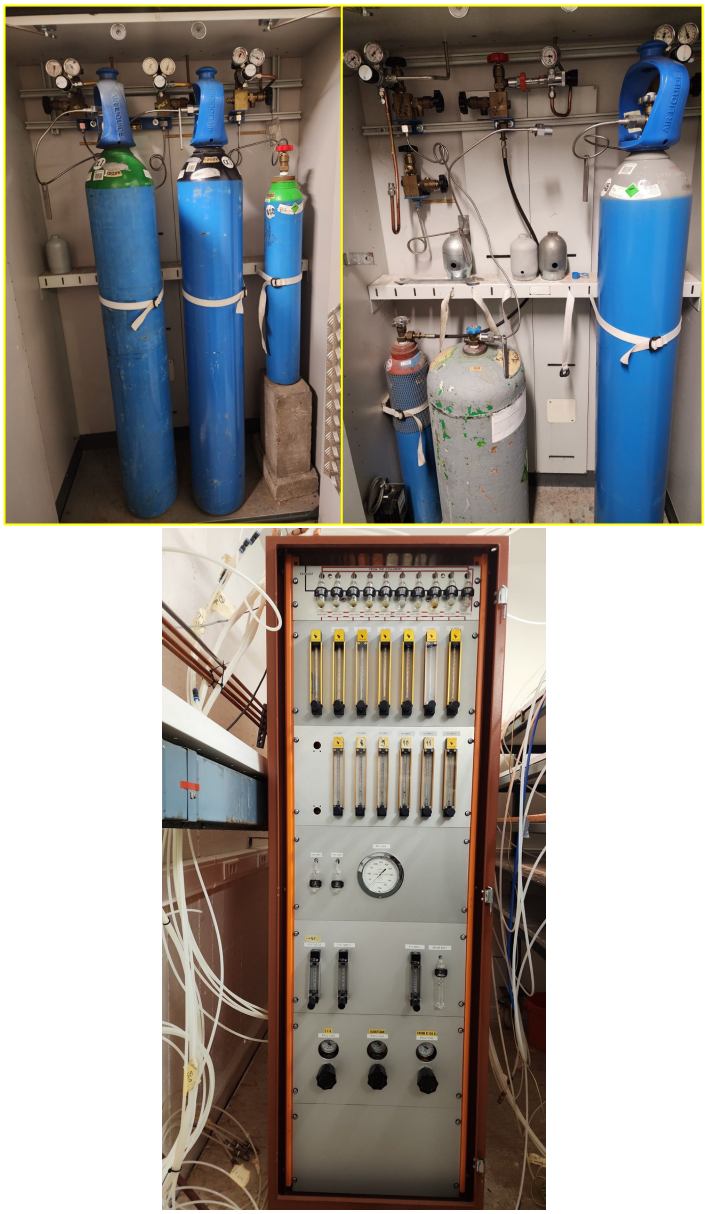

FIGURE 3.30: Gas system setups at RPC lab, UGent. Top-the gas rack housing gases like R-134a, Isobutane, and sulfur hexafluoride for RPC gas mixtures, as well as Argon and Nitrogen for specific tests. Bottom- The gas mixing unit with 12 gas distribution channels.

gaps from potential damage such as detached spacers or cracks. For manual pressure measurement, a water column is included in the setup. To monitor the pressure drop during the leak test, a pressure sensor (SensorTechnics digital pressure sensor) is installed and the setup also comprise of an analog pressure gauge for visual pressure monitoring. The pressure sensor is connected to a Pico ADC-24 data logger, which then connects to a Linux based pc. A low voltage power supply is used to supply the voltage (15 V) to the Pico logger. The data taking during the leak test is done using the Pico logger software. Figure 3.32 shows the picture of the leak test setup. Detailed information about each component within the setup, along with corresponding images, can be found in the document- [137] which I prepared. The details of the leak test procedure are given in Sec. 3.4.4.

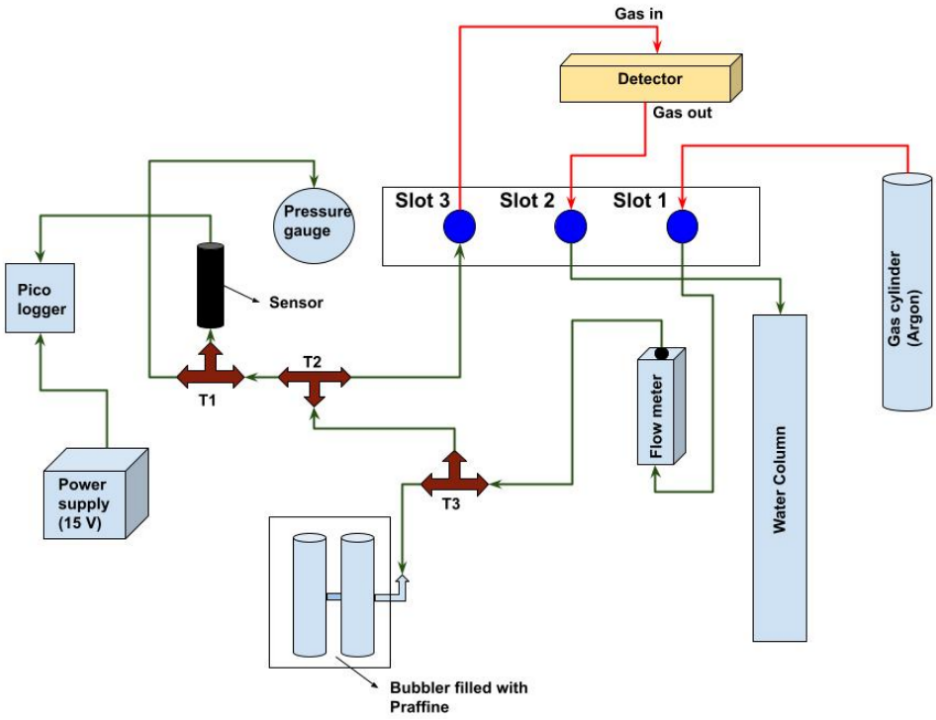

FIGURE 3.31: Schematic diagram of the leak test setup at CMS RPC lab at UGent

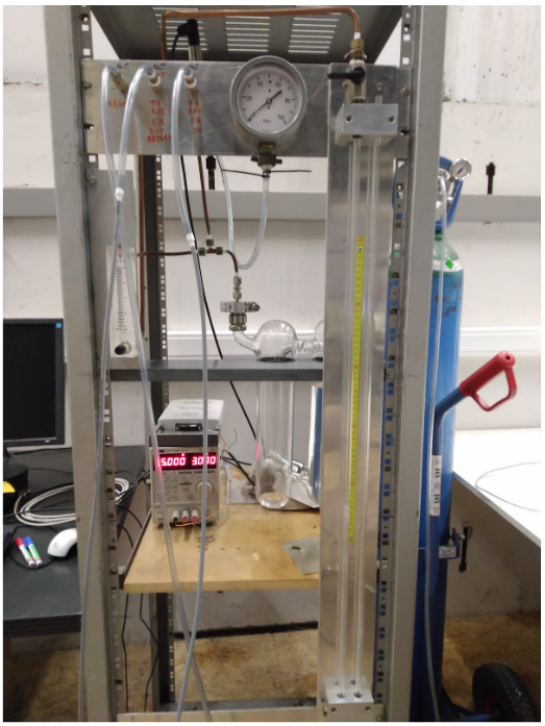

FIGURE 3.32: The picture of the leak test setup at CMS RPC lab at UGent

For conducting the dark current QC tests for the gas gaps and chambers a CAEN SY 1527LC multi-channel power supply system and CAEN A1526 6-channel (15 kV) HV boards integrated into the power supply are used. The HV channels are controlled via the visual interface of the power system. For the dark current tests, specifically in the case of tests conducted for the iRPC demonstrator chambers, an

in-house software linked to the HV boards was used which was the same software used during the RE4 RPC assembly. Additionally, remote access to the power system is also possible using telnet. The CAEN power supply module at the UGent RPC lab is shown in Fig. 3.33.

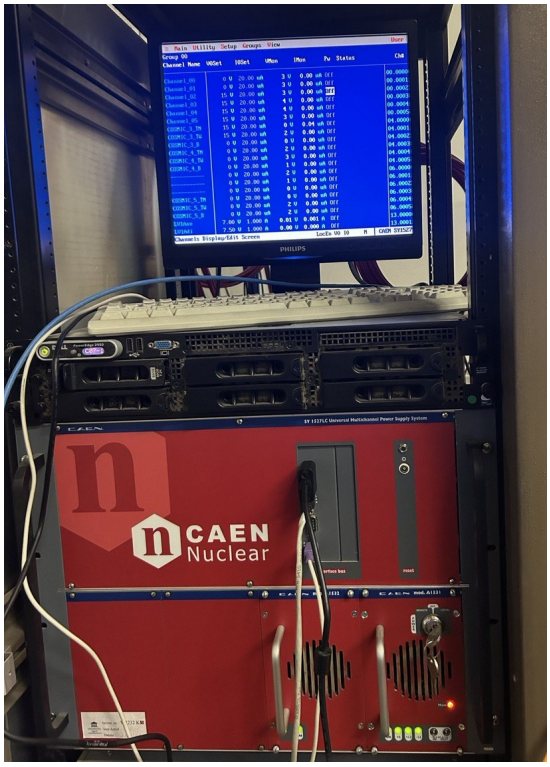

FIGURE 3.33: The CAEN SY 1527LC multi-channel power supply system at the CMS RPC lab at UGent for conducting the dark current QC tests.

Mechanical Workshop and Logistics

In terms of mechanical support and logistics, a fully equipped mechanical workshop is available for constructing, modifying, or repairing iRPC components as required during assembly (Fig. 3.34 - left). The laboratory also features a spacious entrance, allowing trucks transporting large packages of gaps, components, and the detectors produced to enter the building. This setup enables the safe unloading of shipment boxes directly into the laboratory. It's worth emphasising that the unloading process employs a crane designed for heavy lifting, ensuring that gas gaps and chambers are safeguarded against potential damage caused by excessive shocks or vibrations during transportation. Figure 3.34 (right) displays an image taken during the unloading of gas gaps shipped from Korea to the UGent laboratory. In the figure, it can observe that the truck carrying the shipment box was able to reach till the entrance of the lab for unloading.

For the iRPC demonstrator chamber production, the only assembly site was the CMS RPC lab at UGent. Major detector components such as gas gaps, strip PCBs, copper foils for the Faraday cage, etc., were shipped from their respective institutions to the UGent lab. FEBs and cooling pads were still in the production and validation phase. Additionally, all other mechanical components, including honeycomb

FIGURE 3.34: The mechanical workshop at the CMS RPC laboratory site for construction, modification, and repair of iRPC components during assembly (left). The image of unloading the gas gaps shipment from Korea to the UGent laboratory, showcasing the heavy lifting crane installed and the truck reaching the lab entrance for safe delivery (right).

panels, aluminum bars, spacers, screws, gas connectors, etc., were procured at the UGent lab by the assembly team.

3.4.4 QC2 at Assembly Sites

The second part of QC2 is conducted at the detector assembly sites. In the case of iRPC demonstrator production, where UGent was the only production site, the second part of QC2 was carried out at the RPC lab in UGent. Most of the QC2 tests carried out at the assembly sites focus on the gas gaps. While the gaps are carefully packed for transportation from the production site (KODEL), the air travel from Korea to Ghent exposes them to pressure and temperature variations. Moreover, the shipment box undergoes multiple handling processes during transportation until it reaches the assembly site. Therefore, despite passing all QC2 checks at the gap production lab, it is crucial to verify whether the gaps remain in the same condition after the extended journey. The QC2 tests performed on the gas gaps at KODEL are repeated at the assembly site, encompassing visual inspections, spacer condition and gas tightness versification, and dark current tests.

Visual Inspection

During the visual inspection of the gas gaps, the following criteria are thoroughly verified:

- Condition of the barcode labels on the top and bottom HPL plates of the gas gaps: The barcode and the unique gap name assigned should be clearly readable.
- Integrity of the optical HV cable: It should be free from any damage, ensuring proper insulation and the correct length.
- Proper connection of the GND cable to the gap with the required length to connect to the HV side.
- Secure attachment of the polycarbonate HV block to the HV cable without any cracks, ensuring insulation of the HV connection.

- Quality of the Graphite coating on both HV and grounding sides without any significant scratches or damage.
- Inspection of the PET coating on the HPL plates, verifying its condition without defects.
- Thorough examination of the edges and corners of the gas gap to identify any cracks or damage that could lead to a gas leak.
- Inspection of all four gas inlets/outlets to ensure there are no cracks or damage (At times, it is observed that the gas inlets/outlets of the gaps are damaged, a situation not encountered during the QC2 at KODEL. This typically happens due to the fragile nature of these gas profiles and can be damaged during the handling and manipulation of the gaps).
- Recording any bending observed in the gas gap.

In addition to the visual inspection of the gaps, the condition of all other components, including honeycomb plates, various connectors, strip PCB, etc are also verified before chamber assembly. This inspection involves verifying their dimensions and ensuring they are free from any damage.

Gas leak and Spacer bonding Tests

The gas tightness test and spacer test are conducted using the Argon based leak test setup explained in Sec. 3.4.3. To assess gas tightness, the gas inlets/outlets situated in the opposite corners of the gas gap are connected to the input and output slots of the leak test setup. Meanwhile, the gas inlets/outlets in the other two corners of the gas gap are securely sealed with silicon-based stoppers. A pressure of approximately 15 hPa is applied to each gap, and the pressure drop is monitored over time, following the same procedure as in the QC2 test at KODEL. The complete leak test takes 20 minutes to perform, with the initial 10 minutes dedicated to system stabilisation. The leak rate is then calculated based on data collected during the subsequent 10 minutes. If the measured leak rate for this 10-minute period exceeds 0.4 hPa, the gap is considered rejected.

The results of the leak tests conducted as part of the QC on the RE3/1 and RE4/1 gaps, which were utilised in the assembly of the demonstrator chamber, are presented in Fig. 3.35 and Fig. 3.36 respectively. In case of all the plots in both figures the pressure monitored with respect time (20 minutes) is plotted. The blue line represents the actual data, while the red line represents the linear fit applied to the data for calculating the pressure drop. Each gas gap's name and the measured pressure drop are annotated in the respective plot. It is evident all the gaps tested exhibit leak rates below the selection threshold of 0.4 hPa. Across all cases, the leak rates consistently remain well below the specified threshold. The only exception is observed in the case of the CMS-KODEL-DM-RE41-002 gap (Fig. 3.36: row 1, column 2), where the gas leak measures 0.33 $hPa/10\ min$. Nevertheless, it's important to note that this value still falls below the defined threshold.

The spacer bonding test is conducted immediately following the leak test. To perform this test, a Plexiglas spacer map, featuring holes corresponding to the spacer locations within the gap, is positioned atop the gap. Pressure is then applied at each

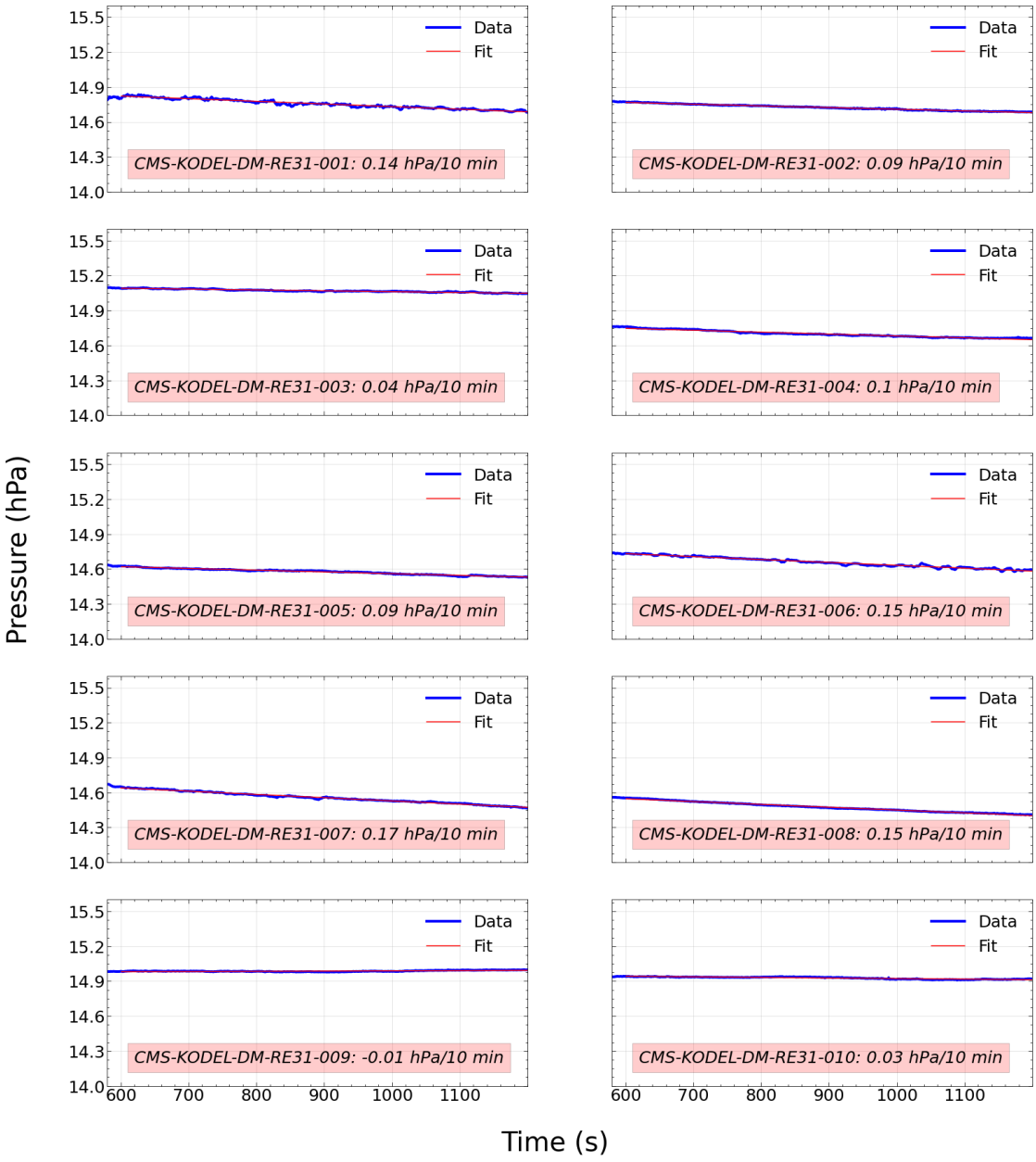

FIGURE 3.35: QC2 Results: Leak rate measured for the RE3/1 gaps used in iRPC demonstrator chamber assembly. The blue line represents the measured pressure over time, while the red line corresponds to the linear fit used to calculate the pressure drop. All gaps exhibit leak rates below the 0.4 hPa threshold.

location using a 15 cm long cylindrical PVC probe with a 1 cm diameter. It's important to note that in contrast to the KODEL test, the pressure is applied manually in the UGent lab by pressing the probe onto the spacer points. This manual process may introduce some minor fluctuations due to variations in individual operators' technique and hand movements. However, this manual approach proves sufficient for detecting any detached spacers. Since the detached spacer can lead to a nearly threefold increase in pressure compared to the normal spacers, even with small fluctuations, this behaviour will be very clear.

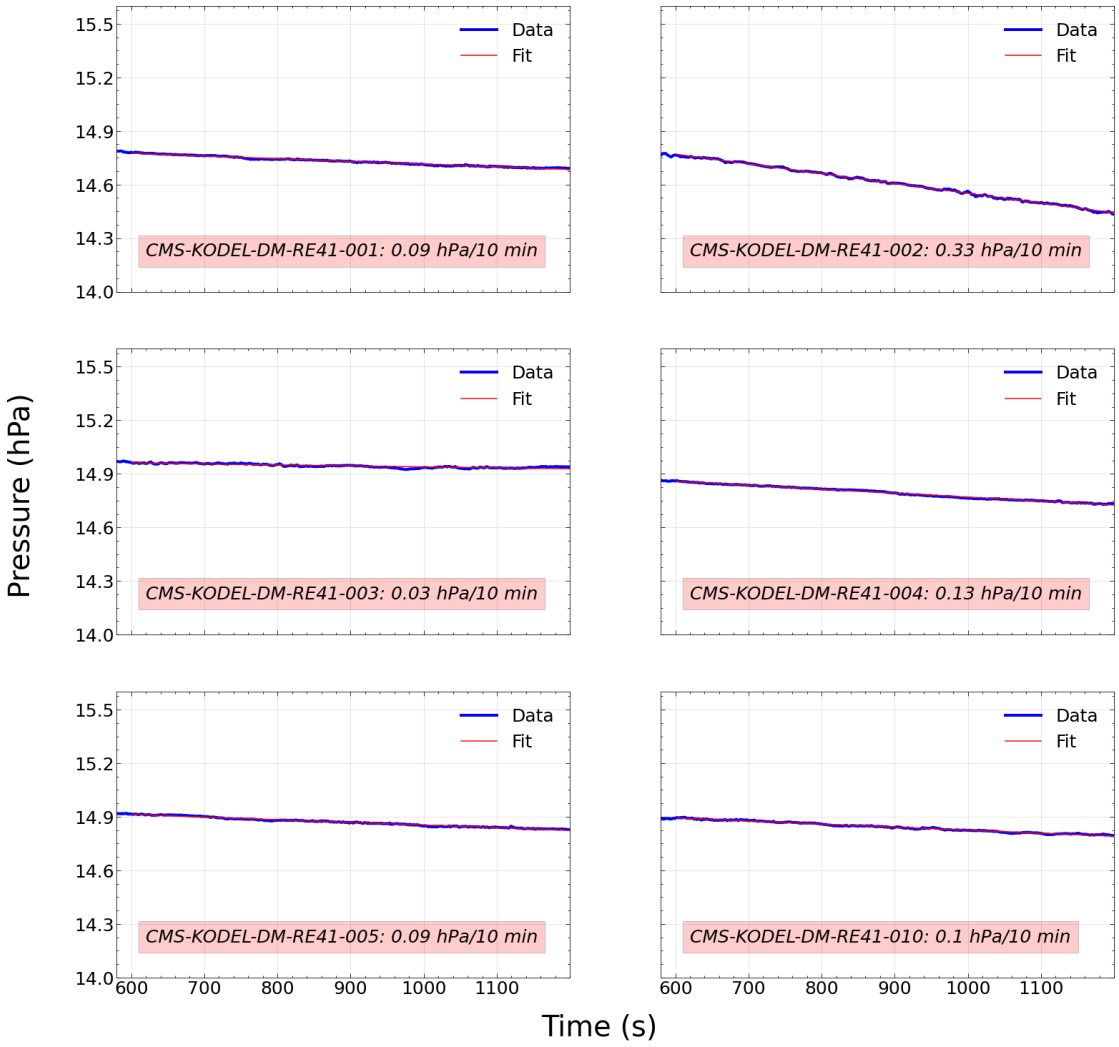

FIGURE 3.36: QC2 Results: Leak rate measured for the RE4/1 gaps used in iRPC demonstrator chamber assembly. The blue line represents the measured pressure over time, while the red line corresponds to the linear fit used to calculate the pressure drop. All gaps exhibit leak rates below the 0.4 hPa threshold.

Figures 3.37 and 3.38 present the results of the spacer bonding tests conducted on the RE3/1 and RE4/1 gas gaps employed in the production of the iRPC demonstrator chamber, respectively. The respective names of each gap are clearly annotated within their corresponding plots in both Fig. 3.37 and Fig. 3.38. In these figures, the blue trend represent the pressure monitored during the test. Each spike visible in the plots corresponds to a spacer within the gap. For all plots, with the exception of CMS-KODEL-DM-RE41-005 (Fig. 3.38: row 3, column 1), the spikes are consistently within the same range, indicating that all spacers are in good condition. However, in the case of the CMS-KODEL-DM-RE41-005 gap, two distinct spikes with amplitudes approximately three times larger than those of the other spacers are marked within the red circle. These spikes correspond to a detached spacer. Two spikes are observed because the spacer was tested twice to cross-check the results. Consequently, this gap was considered as rejected. Although a chamber had been assembled with this particular gap, it was ultimately rejected for installation in the CMS. Nonetheless, as only one spacer was found to be detached, the gap can still be employed for laboratory-based studies.

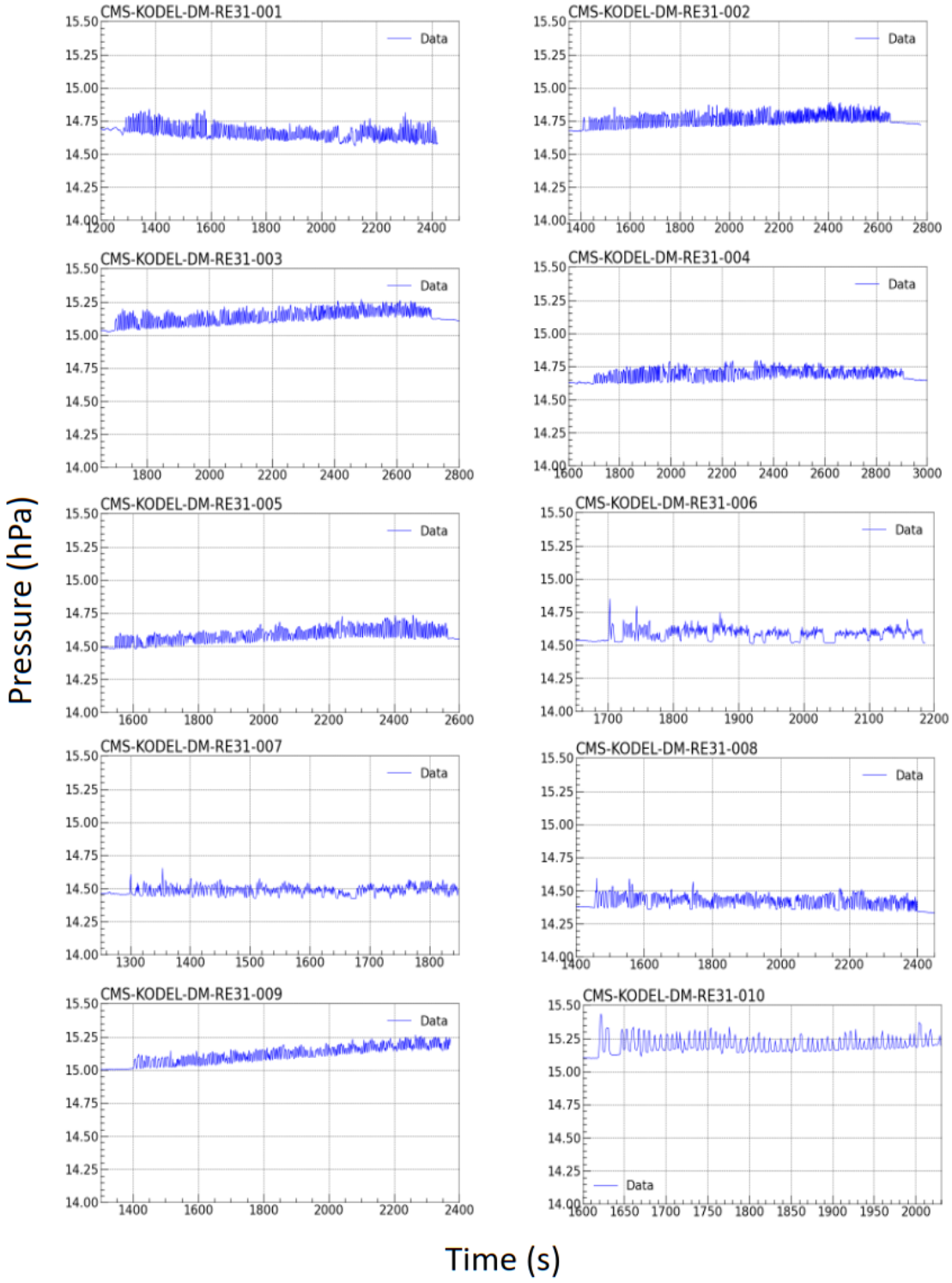

FIGURE 3.37: QC2 Results: Spacer test measurements of the RE3/1 gaps used in iRPC demonstrator chamber assembly. The blue trend corresponds to the pressure monitored during the test. Each spike in the trend corresponds to each spacer inside the gas gap.

I have prepared a manual detailing the procedures for conducting the QC2 leak test and spacer bonding tests and it is available in reference [138].

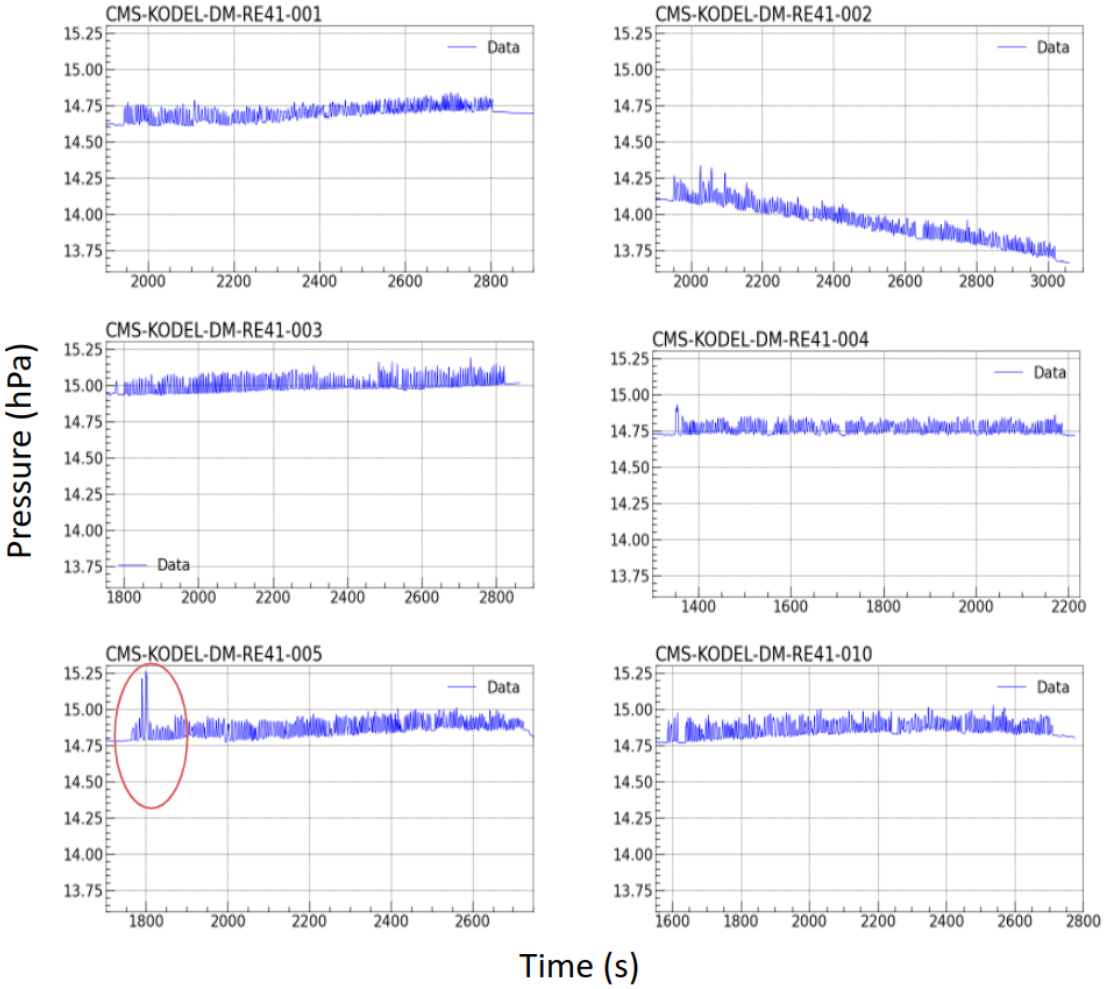

FIGURE 3.38: QC2 Results: Spacer test measurements of the RE4/1 gaps used in iRPC demonstrator chamber assembly. The blue trend corresponds to the pressure monitored during the test. Each spike in the trend corresponds to each spacer inside the gas gap. The two spikes with amplitudes approximately three times larger than the others (marked within the red circle) observed for gap CMS-KODEL-DM-RE41-005 (row 3, column 1) corresponds to a bad/detached spacer inside the gas gap.

Dark Current Test

The final step in the QC2 procedure is the dark current test. Prior to these measurements, all gaps are placed in the AirCo room and flushed with a standard RPC gas mixture for a minimum of 48 hours. This process stabilises the gaps and removes any small dust particles present inside them. The dark current is then measured at 16 high voltage (HV) points using the CAEN HV modules (explained in Sec. 3.4.3).

The results of the dark current measurements for the iRPC RE3/1 and RE4/1 demonstrator assembly gaps are presented in Fig. 3.39 and 3.40. In each figure, the plots display the dark current as a function of effective HV, with the gap names annotated accordingly. The effective HV values are calculated after applying the PT correction (discussed in Sec. 2.4.7).

It is evident from the figures that all the iRPC gaps exhibit ohmic behavior, and the maximum current observed at 7.3 HV is consistently well below the 3 μA dark

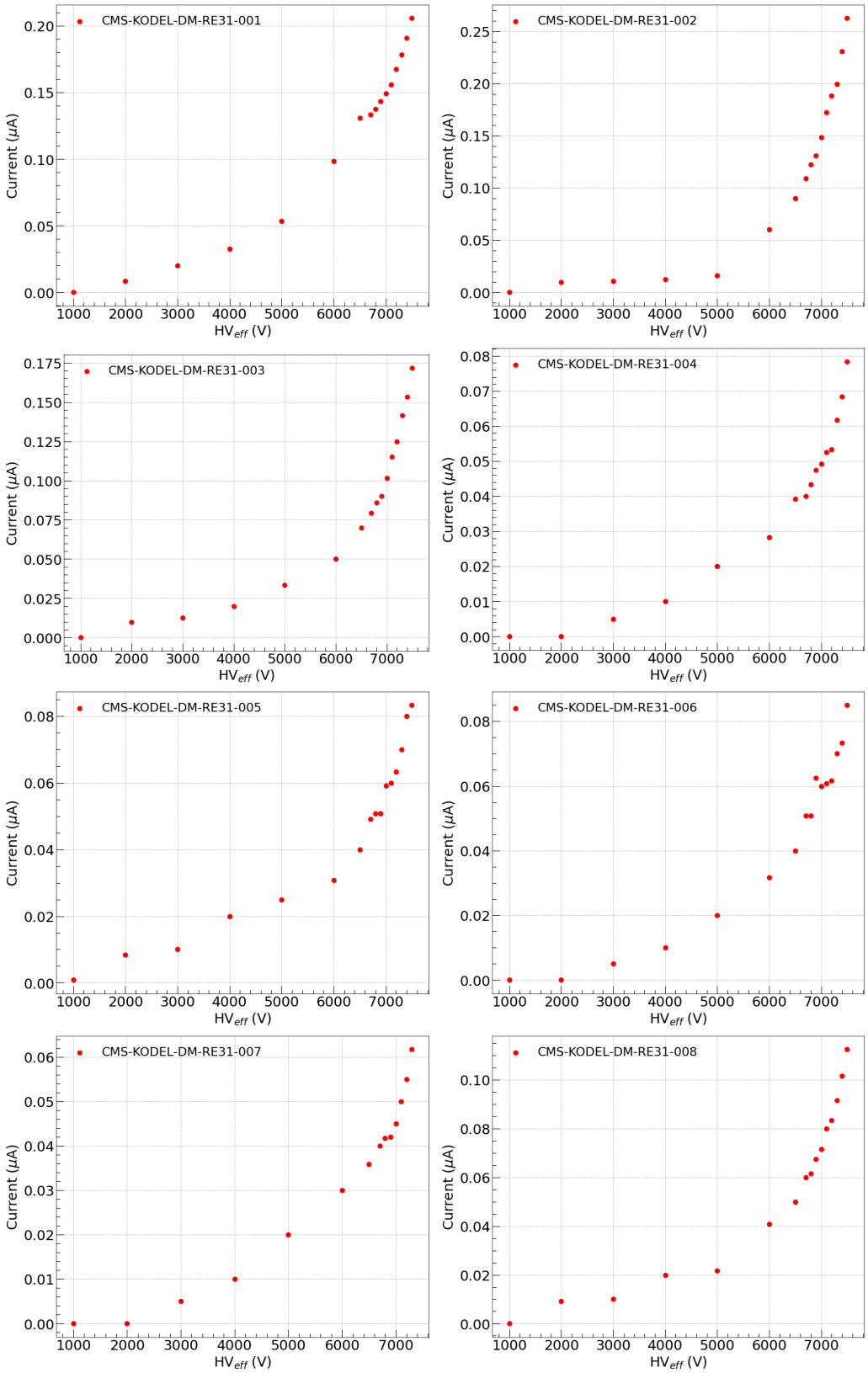

FIGURE 3.39: QC2 Results: Dark current measurements performed for six iRPC RE3/1 gaps used in the demonstrator chamber assembly. The plots display the dark current as a function of effective HV and the name of each gas gaps are labelled in the plots.

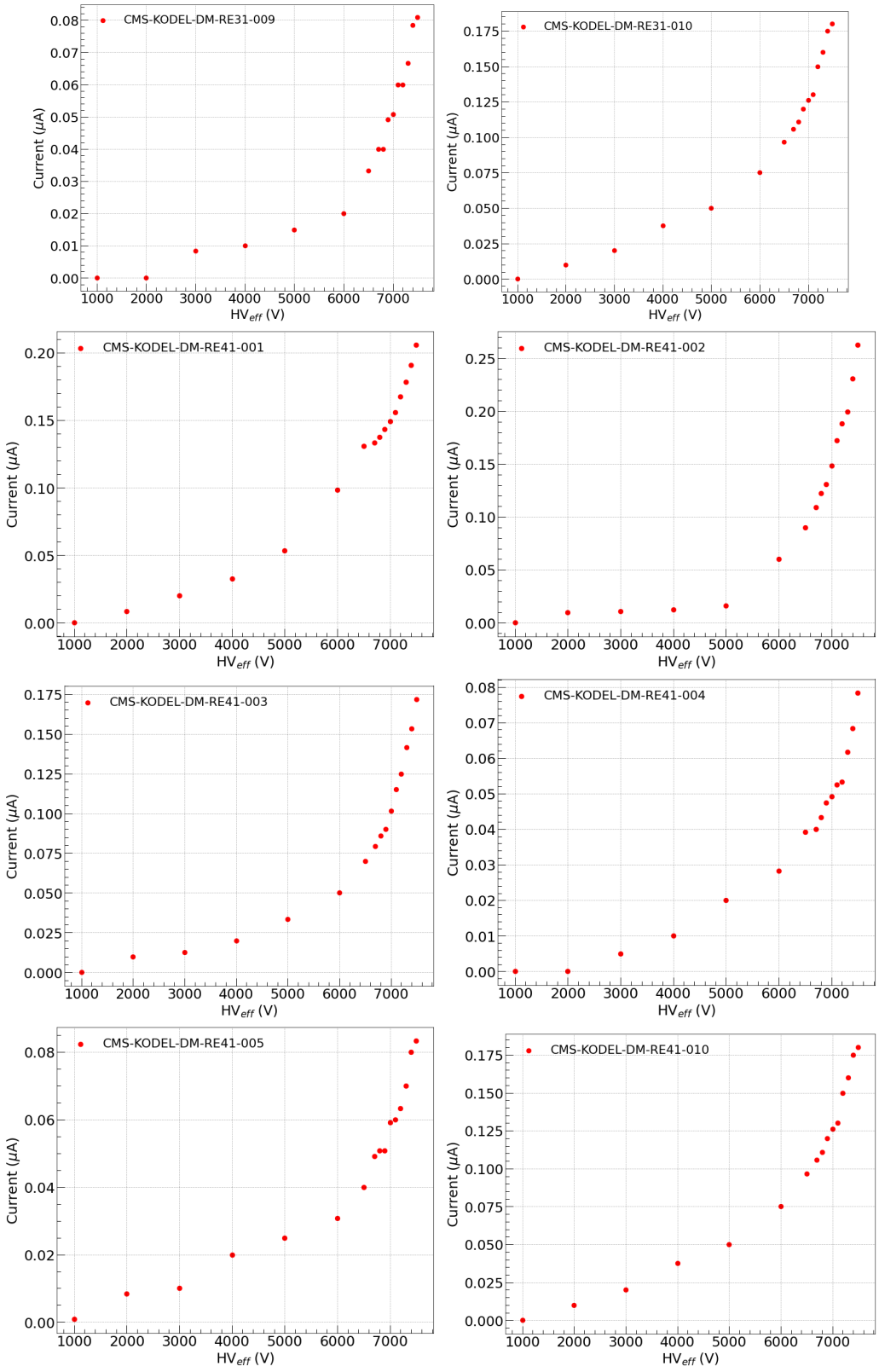

FIGURE 3.40: QC2 Results: Dark current measurements performed for two iRPC RE3/1 and four iRPC RE4/1 gas gaps used in the demonstrator chamber assembly. The plots display the dark current as a function of effective HV and the name of each gas gaps are labeled in the plots.

current threshold required for gap acceptance according to QC protocols. In some instances, when certain gaps were initially tested, fluctuations in the dark current were observed as a result of connection issues with the HV connector and dust present inside the gas gap. To address these problems, connectors were repaired or replaced, and gaps were vertically flushed with argon to remove dust. Most of the gaps were recovered by applying these methods. Despite these efforts, an iRPC RE4/1 gap (CMS-KODEL-DM-RE41-007) continued to exhibit high fluctuations in dark current due to dust accumulation and consequently, it was decided to not use this gap for the assembly or any test until it was recovered.

3.4.5 Detector Assembly

After completing the QC2 procedures, eight iRPC demonstrator chambers were assembled in 2021 in the CMS RPC laboratory of UGent. During the detector assembly process, various strategies and minor modifications were implemented. This assembly phase played a crucial role in establishing the finalised procedure for iRPC assembly, which needs to be followed during mass production. Detailed information on the finalised iRPC assembly procedure is provided in this section.

Following are the major steps of the iRPC assembly:

1. Place the bottom honeycomb panel on the assembly table, aligning the side bars on all four sides to form the box shape. L-shaped spacers are used to secure the gas gaps in position (refer Fig. 3.41-(a)). Ensure the panel is free of dust and any small aluminum particles by vacuuming it. Additionally, clean the inner surface of the bottom panel with alcohol (ethanol/methanol).

2. Prepare the bottom copper plate for constructing the Faraday cage. Clean the plate thoroughly with alcohol using a soft cloth. Attach copper foils, each 60 *mm* wide and 0.050 *mm* thick, to all four sides of the copper plate by soldering. To enhance the connection, use a 12.7 *mm* wide and 0.035 *mm* thick copper tape to link the copper foil to the copper plate. Always wear smooth fabric gloves when handling copper plates and foils to maintain cleanliness and prevent damage.

3. Place the prepared bottom copper plate with attached copper foils onto the bottom honeycomb plate.

4. Clean one side of a Mylar foil with alcohol and place it on top of the copper plate. Then, clean the other side (gap facing side) of the Mylar foil with alcohol. The bottom copper plate as well as the Mylar foil placed inside the honeycomb panel + Aluminum bars box is shown in Fig. 3.41-(b).

5. Position the bottom gas gap on the Mylar foil. Ensure that both sides of the gap are cleaned with alcohol. Accurately adjust the gap's position between the L bars, and route the black grounding cable between the gap and the side bars without stretching the cable (see Fig. 3.41-(c)). To firmly secure the gas gap in place within the layout, insert a Plexiglas plastic filler into the HR section of the chamber between the gas gap and the L spacer (see Fig. 3.41-(d)).

6. To prepare the gas pipes required for the four gas connectors of the bottom gas gap, start by determining the proper length and bending the pipes to fit into the corners of the chamber. Initially, place the pipes on dedicated tools

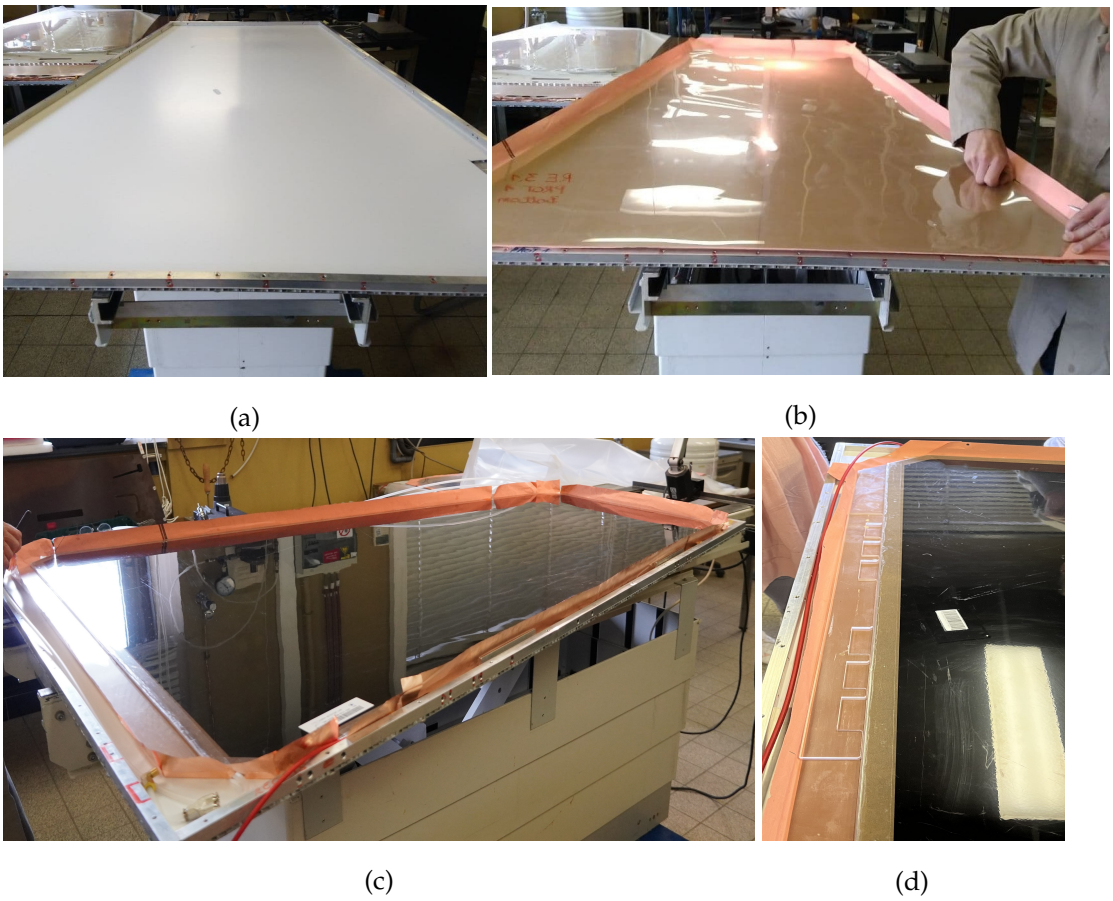

FIGURE 3.41: Pictures of the iRPC assembly procedure explained in steps 1-4.

designed for bending, ensuring they achieve the desired angle (refer Fig. 3.42-left). Next, heat the pipes using either a heat gun or warm water (temperature $< 100^{\circ}$ C). After heating for a few seconds, immediately immerse the pipe in cold water (refer Fig. 3.42-Right). This process makes the bent part of the pipe permanent and robust.

7. Connect the prepared gas pipes to the gas connectors of the gap by gently warming the pipe's edge with a heat gun and immediately attaching it to the gas connectors. Within seconds, it cools down and securely adheres to the connector, preventing any gas leaks. Route the pipes from all the connectors through the sides of the gap, aligning them inside the L-shaped spacers.

8. Prepare the PCB by thoroughly cleaning both sides with anti-static cleaning solutions. Solder two 10×10 *cm* copper foils onto the LR edges of both PCBs for connecting to the Faraday's cage for grounding. Next, use Kapton tape to connect both PCB parts while maintaining a 0.5 *mm* separation between them. This assembly creates a single trapezoidal strip PCB layer. See Fig. 3.43 (left) for the image of the completed PCB layer.

9. Place the PCB layer on top of the bottom gap. Double check there are no visible damages on the ERNI connectors in the both PCB parts.

10. Position the top gas gap atop the PCB layer, following the same procedures as outlined for the bottom gap, including cleaning, gas pipe connection, cable

FIGURE 3.42: Left: Tools for bending gas pipes. Right: Cooling a bent gas pipe in water.

routing and the Plexiglas spacer placement. Fig. 3.43 (right) shows the picture captured during placing the top gap into the chamber.

FIGURE 3.43: Left: PCB layer prepared by merging two PCB parts and soldering copper foils for grounding. Right: Placing the top gas gap into the chamber.

11. Connect all gas pipes from the two gas gaps to the Y, L, and T connectors (for details of the gas connection layout, see Sec. 3.3.1). Arrange the connectors for the bottom gap on the left side and those for the top gap on the right side in the HR region of the chamber. Figure 3.44 - top displays the gas pipes connected to both gaps and the connection layout in the LR region of the chamber, while Fig. 3.44 - bottom illustrates the gas connectors for the bottom gap and the top gap, positioned on the left and right sides of the chamber in the HR region.

12. Place another cleaned Mylar foil on top of the gas gap for insulation.

13. Construct the Faraday cage by positioning the top copper plate over the Mylar foil. Figure 3.45 - left shows the procedure of placing the copper plate. Solder the copper foils attached to the bottom copper plate onto the top copper plate and secure them additional with copper tape. This encloses both the gaps and the PCB layer within the copper Faraday cage.

14. To establish proper grounding, solder two copper foils measuring 16.5×22 cm onto the top copper plate, for the grounding of FEBs. These foils are subsequently routed outside through rectangular slots in the top honeycomb panel and fixed beneath the FEBs. Additionally, solder and connect a larger copper foil (40×16 cm) on the HR side, following the same method, to connect

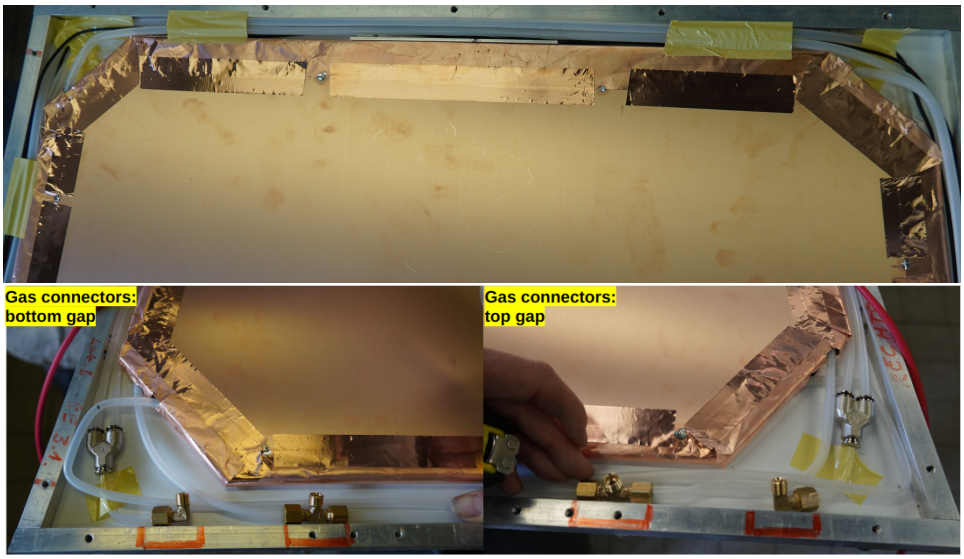

FIGURE 3.44: Gas connection setup for the iRPC chamber assembly. The top image displays the gas pipes connected to both gaps and the connection layout in the LR region of the chamber. In the bottom image, the gas connectors for the bottom gap and the top gap are arranged on the left and right sides of the chamber in the HR region.

the Faraday cage to the grounding bar for improved grounding. Figure 3.45-right shows the inside view of the chamber after closing the Faraday cage and adding all the copper foils necessary for grounding.

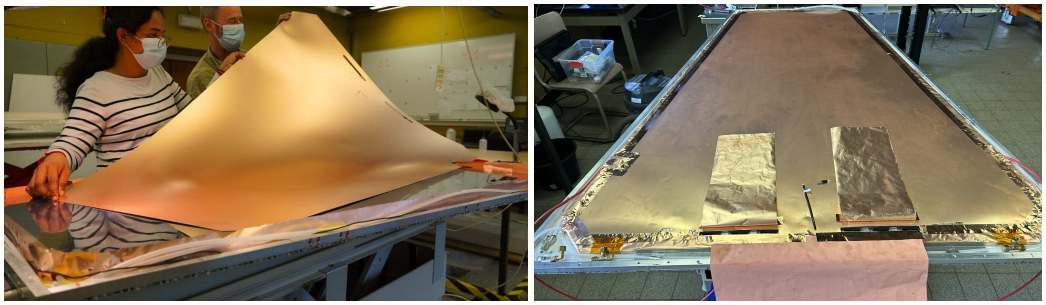

FIGURE 3.45: Left: The process of placing the top copper plate over the Mylar foil to construct the Faraday cage. Right: An inside view of the chamber after the Faraday cage is closed and all necessary copper foils for grounding are added.

15. Put the protection spiral sleeve over the FOS and carefully insert into the chamber through the dedicated hole located in the center of the top copper plate, specifically in the HR region.

16. Close the chamber with the top honeycomb panel. When closing the chamber with the top honeycomb panel, take care to ensure that the HV cables and the FOS are safely guided through their dedicated holes in the panel. Additionally, verify that the positions of the L and T connectors align with and protrude through their respective dedicated holes on the panel.

17. Connect the patch panel to the HR side of the chamber and screw the copper grounding bar to the patch panel. Ensure that the copper foil, which is connected for grounding on the Faraday cage, is sandwiched between the patch panel and the grounding bar. Tighten the screws to secure the connection.

18. Connect the copper gas pipes, which have been prepared in specific shapes using dedicated tools for bending and cutting, to the patch panel. Additionally, connect the HV cables, cooling pipe, and the FOS connectors to the patch panel. After routing the cables and pipes to the patch panel through their dedicated slots, seal the holes and slots with aluminum tape. Figure 3.46 - left displays all the cables and pipes properly aligned in their respective slots and shapes, connected to the patch panel.

19. Install the FEBs onto the top honeycomb panel. Organise all the power and data cables of the FEBs within the aluminum cable router using cable ties, and then guide all the cables to their respective slots in the patch panel.

20. Position the left and right copper cooling pads to cover the FEBs and fasten them to the copper cooling pipes. Figure 3.46 - right illustrates the integration of the FEBs onto the chamber, with all the necessary cables routed through the aluminum cable router to the patch panel, along with the cooling plates placed atop the FEBs.

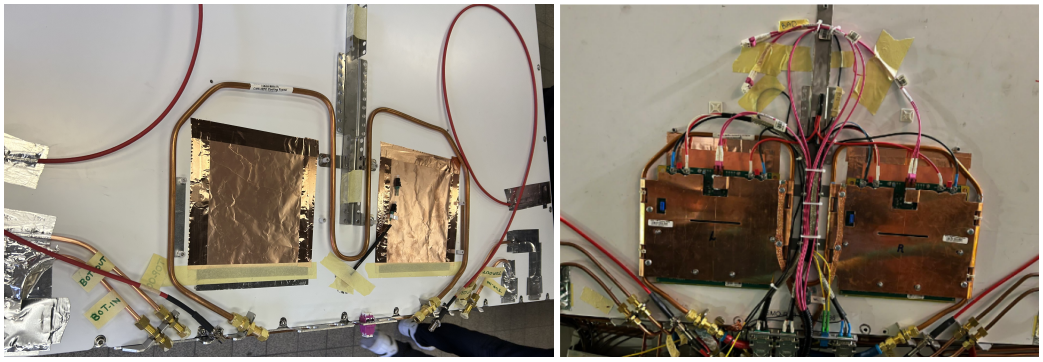

FIGURE 3.46: Left: All the cables and pipes, properly aligned and connected to the patch panel fixed in the HR part of the chamber. Right: The FEBs integrated onto the chamber, with all the essential cables guided through the aluminum cable router to the patch panel. Additionally the copper cooling plates positioned atop the FEBs can also be seen.

21. Secure both FEBs and their associated cables by using the specially designed iRPC cover plate. Figure 3.47 displays an image of the cover plate installed on the chamber and provides the chamber's final look after assembly.

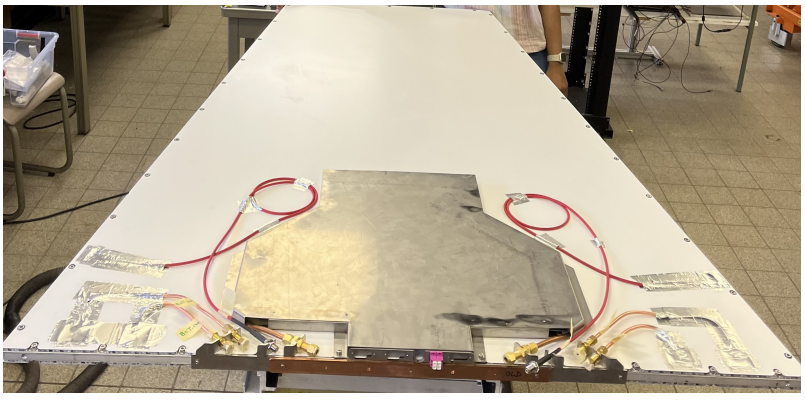

FIGURE 3.47: Installation of the iRPC cover plate on the chamber, providing a final view of the assembled iRPC chamber.

3.4.6 QC3 at Assembly Sites

This section primarily focuses on the QC3 procedures and presents the results of the QC tests applied to the iRPC demonstrator chambers. A summary of the iRPC demonstrator chamber details, along with their respective QC3 results, can be found at the end of this section (Tab. 3.2).

Leak Test

Following chamber assembly, a visual inspection of the chamber mechanics is conducted to ensure the integrity of all external connections, including gas pipes, cooling pipes, HV cables, honeycomb panel screws, sensor cables, and FEB mounting mechanisms. To validate gap condition, the gas leak tests and dark current tests are repeated. This step is crucial due to multiple gap manipulations during assembly and the presence of additional connections such as gas connectors and pipes, which, if not properly secured, can lead to gas leaks.

The expected pressure during the operation of the chamber at CMS is 1.5-2 hPa. Considering a safety factor, the QC3 leak test for the chamber is conducted at 5 hPa. The acceptance threshold for the chamber is 0.4 $hPa/10\ min$ for each of the corresponding gaps. The spacer bonding test is not repeated during QC3, as the chamber is fully closed, and direct access to the spacer locations is not feasible. Figures 3.48 and 3.49 depict the results of the QC3 leak tests conducted on the gaps installed in the iRPC RE3/1 and iRPC RE4/1 chambers, respectively. In all the plots in both figures, the blue line represents the measured pressure over time, while the red line corresponds to the linear fit used for calculating the pressure drop. The name of each gap, along with the corresponding pressure drop measured, is annotated on the plots. It's worth noting that while all the gaps passed the QC test, and in most cases, the pressure remained stable throughout the test duration, there are three exceptions. For CMS-KODEL-DM-RE31-001(Fig. 3.48: row 1, column 1), CMS-KODEL-DM-RE41-003 (Fig. 3.49: row 2, column 1), and CMS-KODEL-DM-RE41-005 (Fig. 3.48: row 3, column 1), the pressure drop is slightly higher, ranging between 0.3 and 0.4 hPa/10 min, just below the selection threshold. This discrepancy could be attributed to minor loose connections of the gas pipe at the gap inlets/outlets. Refer Tab. 3.2 to see which gaps belong to which iRPC demonstrator chamber.

Dark Current Test

The dark current test in QC3 follows the same procedure as in QC2. It involves monitoring the current at 16 different HV points and ensuring that all chambers exhibit the desired ohmic curve behavior. If any chamber's gaps exceed a current of 0.3 μA at 7.3 kV, it is considered as rejected for installation in the CMS detector. Figures 3.50 and 3.51 present the results of the QC3 dark current tests conducted on all gaps installed in the iRPC demonstrator chambers. When comparing the QC3 results to the previously obtained QC2 results (discussed in Sec.3.4.4), it's evident that the I-V curves for all the gaps are quite consistent, with only minor variations in current. These slight discrepancies can be attributed to the 1-2 month gap between the QC2 and QC3 tests, during which operational conditions may have influenced the behavior. All the gaps used for iRPC demonstrator assembly passed the QC3 since the currents at 7.3 kV in all cases were below 3 μA. Notably, in the case of CMS-KODEL-DM-RE41-010, the QC3-I-V curve exhibits slightly more fluctuations

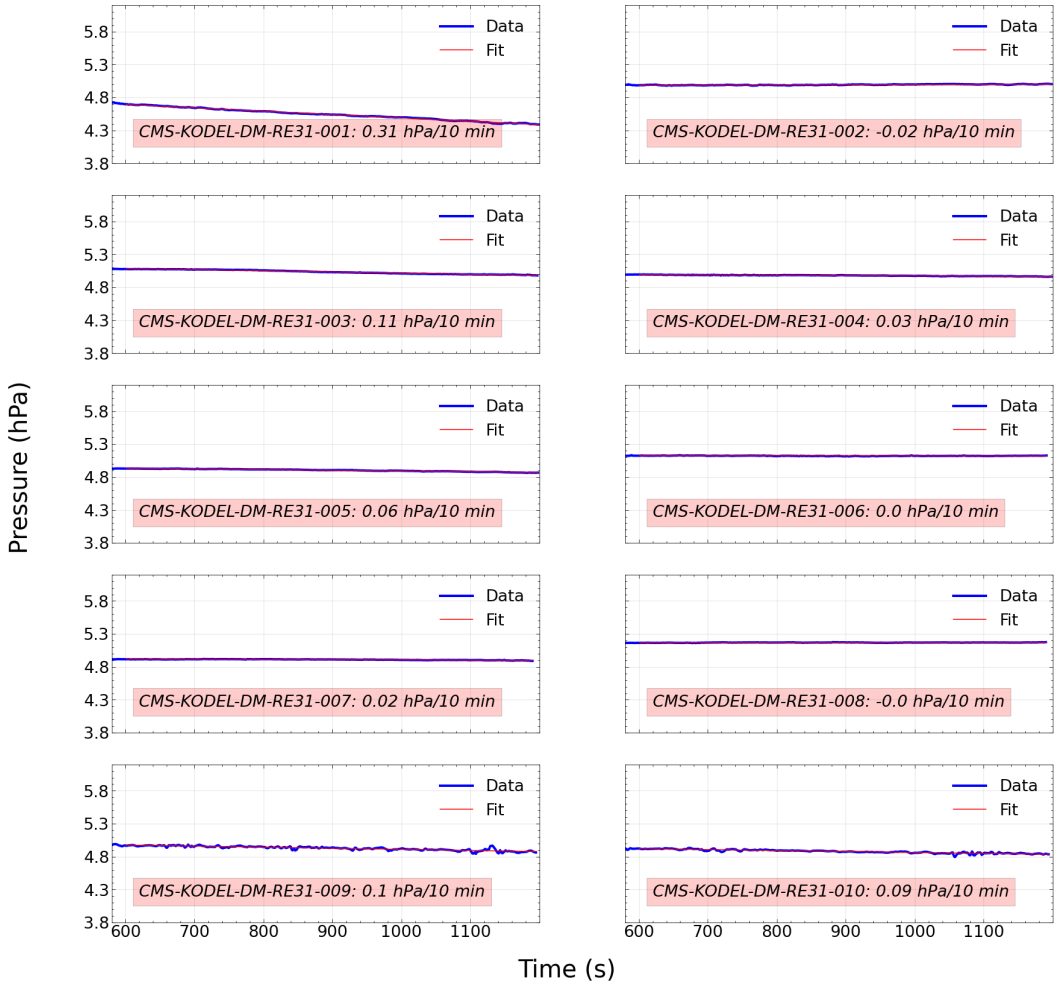

FIGURE 3.48: QC3 Results: Leak rate measured for the RE3/1 gaps installed in the iRPC chambers produced. The test was conducted at 5 hPa pressure. The blue line represents the measured pressure over time, while the red line corresponds to the linear fit used to calculate the pressure drop. All gaps exhibit leak rates below the 0.4 hPa threshold.

compared to the QC2-I-V curve. However, since the behavior remains ohmic, the chamber with that particular gap is not rejected. The details regarding which gaps are installed in each chamber is provided in Tab. 3.2.

Strip PCB Cross-Talk Check

QC3 also encompasses the evaluation of cross-talk within the strip PCB. This evaluation is conducted using a multi-meter to check for any connections between adjacent points on the ERNI connectors located on both the left and right sides of the PCBs. If such a connection is detected between two adjacent strips, the chamber is flagged for repair. During the iRPC demonstrator assembly, this issue was identified in the right-side section of two strip PCBs (refer Tab. 3.2 for specific details).

The QC3 at the assembly sites also includes a long term dark current test(chambers operated at 7.3 kV for 168 hours) and cosmic muon tests where the chamber efficiency and parameters such as cluster size, cluster multiplicity, etc. are studied. But for the iRPC demonstrators, since FEBs for all the chambers were not ready at that time, all these tests were conducted at the CMS RPC lab at CERN. An overview of

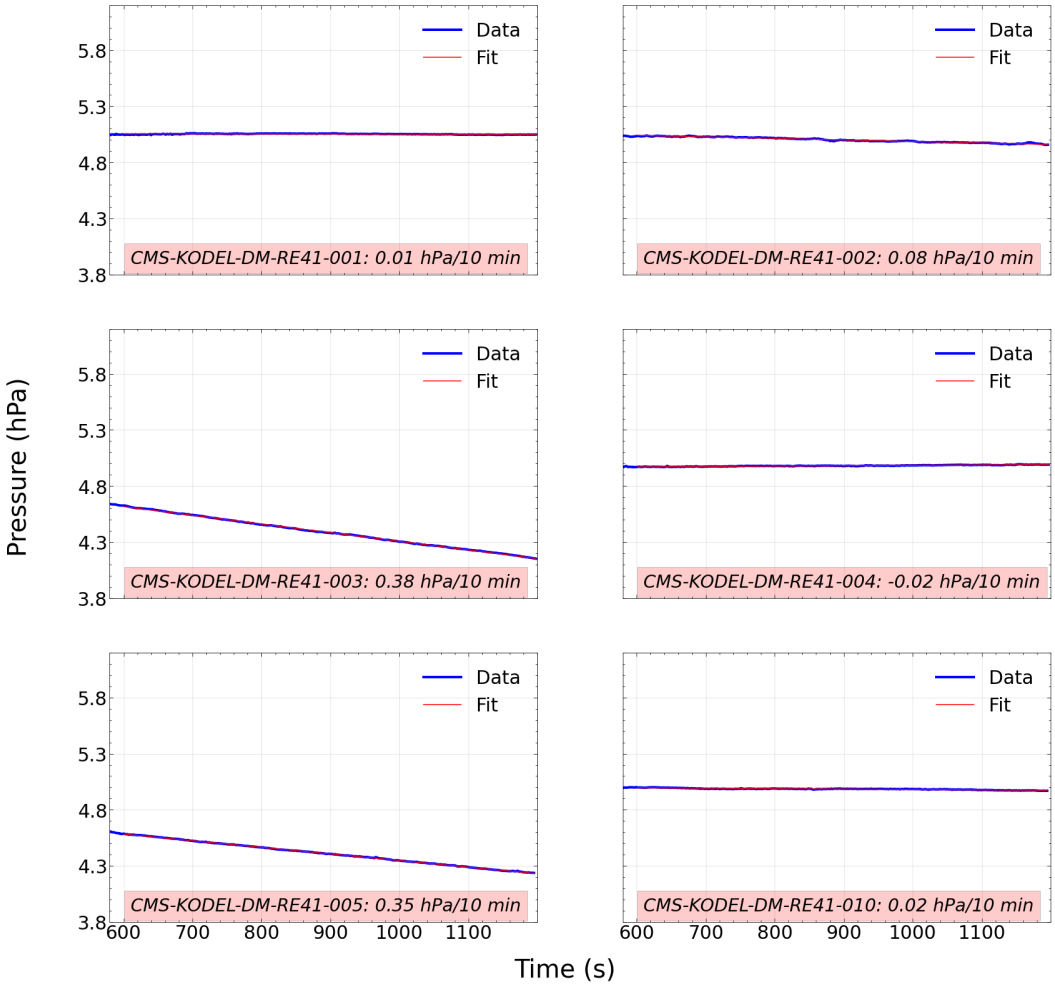

FIGURE 3.49: QC3 Results: Leak rate measured for the RE4/1 gaps installed in the iRPC chambers produced. The test was conducted at 5 *hPa* pressure. The blue line represents the measured pressure over time, while the red line corresponds to the linear fit used to calculate the pressure drop. All gaps exhibit leak rates below the 0.4 *hPa* threshold.

all assembled iRPC demonstrator chambers, including their names, assembly dates, the gaps incorporated within each chamber, and the results of the QC3 assessments performed on them is given in Tab. 3.2.

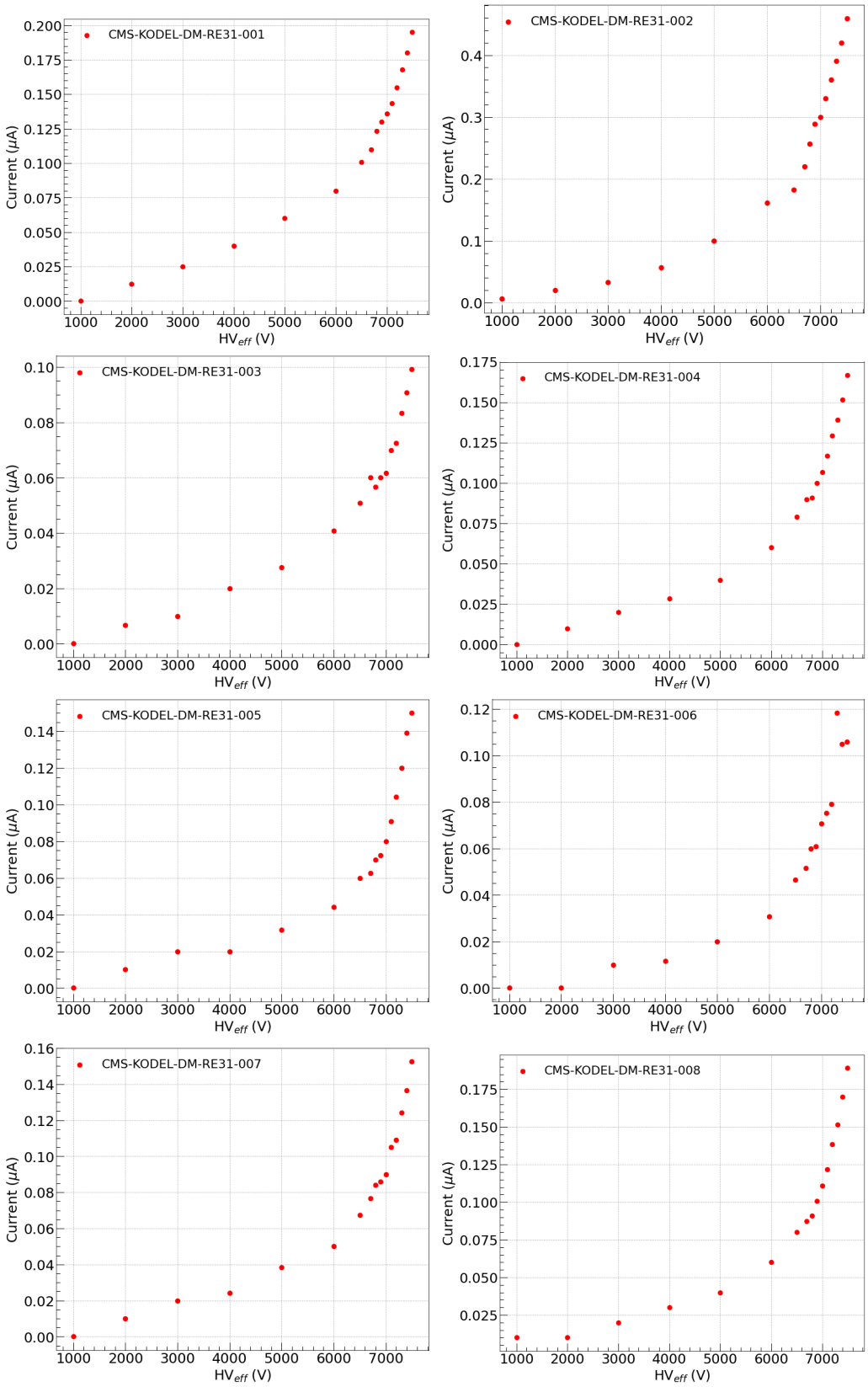

FIGURE 3.50: QC3 Results: Dark current measurements performed for six iRPC RE3/1 gaps installed in the iRPC RE3/1 demonstrator chambers. The plots display the dark current as a function of effective HV and the name of each gas gaps are labeled in the plots.

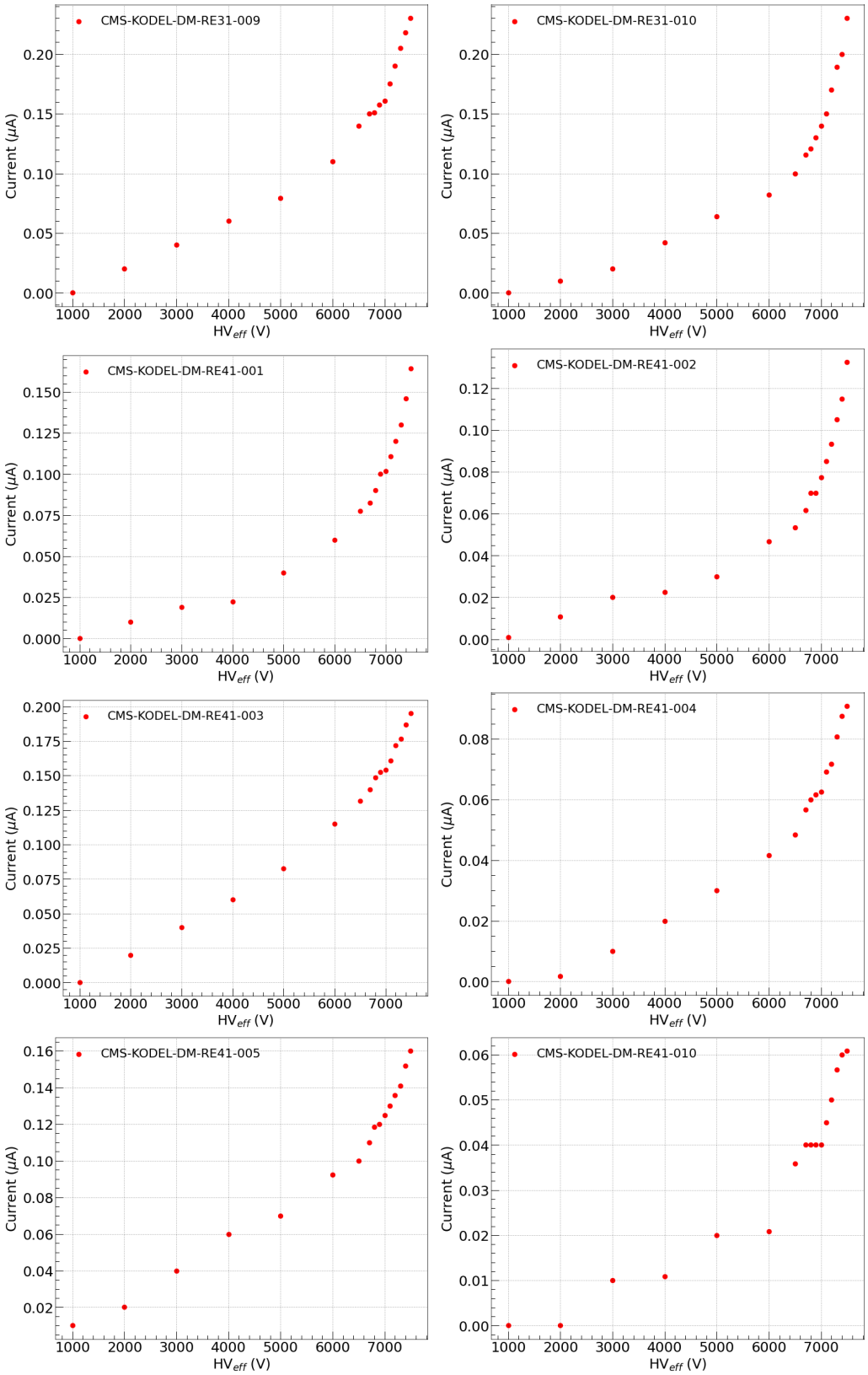

FIGURE 3.51: QC4 Results: Dark current measurements performed for two iRPC RE3/1 and four iRPC RE4/1 gaps installed in the iRPC RE4/1 demonstrator chambers. The plots display the dark current as a function of effective HV and the name of each gas gaps are labeled in the plots.

Chamber Name DEMO-RE3-1-Ghent-	Date	Gap Name CMS-KODEL-DM-		ERNI Connectors:		Gap Spacer	Leak Rate ($mbar/10\ min$)		Dark Current at 7.3 kV (μA)	
		Bottom Gap	Top Gap	Left PCB	Right PCB		Bottom Gap	Top Gap	Bottom Gap	Top Gap
185	12/05/2021	RE31-003	RE31-004	OK	OK	OK	0.11	0.03	0.09	0.16
186	20/05/2021	RE31-006	RE31-005	OK	OK	OK	0.00	0.06	0.11	0.14
187	27/05/2021	RE31-007	RE31-008	OK	OK	OK	0.02	0.00	0.14	0.17
188	1/06/2021	RE41-010	RE41-004	OK	OK	OK	0.02	0.00	0.06	0.087
189	3/06/2021	RE41-001	RE41-002	OK	OK	OK	0.01	0.08	0.15	0.12
190	1/06/2021	RE41-005	RE41-003	OK	ERNI 3: short on pin 15 and 16	1 popped spacer in bottom gap	0.35	0.38	0.15	0.19
191	24/07/2021	RE31-009	RE31-010	OK	ERNI 3: short on pin 15 and 16	OK	0.1	0.09	0.22	0.2
192	27/07/2021	RE31-001	RE31-002	OK	OK	OK	0.31	0.02	0.18	0.42

TABLE 3.2: Summary of the details of the five iRPC RE3/1 and three RE4/1 iRPC demonstrator chambers produced at CMS RPC lab UGent and the associated QC3 results.

3.4.7 QC4 at 904-CERN

After chamber production and QC3 tests, all qualified chambers are transported to the CMS RPC lab at CERN, located in building 904. The QC4 tests essentially repeat all QC3 steps to ensure that the shipment from the assembly site to CERN did not cause any damage to the chambers. Additionally, a long-term dark current stability test and a cosmic muon test to measure chamber efficiency are performed. The cosmic test bench in the lab, used for QC4 cosmic muon tests, is equipped with five scintillator + SiPM paddles positioned on the top and bottom of the stand for triggering purposes. Additionally, the test bench includes seven racks designed to accommodate iRPC chambers. In Fig. 3.52, both the CMS RPC lab at 904 (on the left) and the cosmic test bench (on the right) are shown.

FIGURE 3.52: The image on the left shows the CMS RPC lab at 904-CERN and the image on the right showcases the cosmic test bench in the lab used for QC4 cosmic muon tests.

During the iRPC demonstrator assembly, all QC procedures were successfully validated in view of iRPC mass production at their respective sites. A summary of the QC procedure, including the details of the major steps involved and the locations where they need to be performed, is provided in Tab. 3.3. The results of all QC procedures conducted for the iRPC demonstrator chambers have been uploaded to the CMS Construction Database (Construction DB) [139].

Initially, the Construction DB was compatible only with the data of the RPCs produced in the past and installed at CMS. During the iRPC demonstrator project period, it was adapted for the QC tests and settings of the iRPCs and subsequently validated.

	QC Protocols	Location	Validation
QC 1	Applied to basic chamber components: on-detector electronics, PCB and connectors, HPL electrodes, pipes, unions, HV/LV/signal connectors/cables, cooling pipes/elements	Pavia, Italy (HPL), Lyon (PCB, electronics), 904 lab at CERN	Completed
QC 2	Applied to chamber elements: gas gaps, PCB and cooling circuit For gas gaps: visual inspection (flatness, surface quality etc.), gas leak test (at 15 hPa), resistivity measurements, spacer test, dark current tests	KODEL laboratory at Korea University, Production labs (Gent, Mexico)	Completed
QC 3	Applied to chambers after production: gas leak test (at 5 hPa), electronics tests, PCB test, cooling circuit tightness, dark current tests, chamber performance tests with cosmics	Production labs (Gent, Mexico)	Completed
QC 4	Applied to chambers after shipment to CERN (final validation tests): Repetition of QC3, cosmic validation with final FEB, beam tests (background up to 2 KHz/cm^2)	904 lab at CERN, GIF++ at CERN	Completed

TABLE 3.3: Summary of the QC procedures that were validated during the iRPC demonstrator project in view of the iRPC mass production.

3.4.8 Installation and Integration at CMS

After the completion of the final QC (QC4) procedures, four iRPC demonstrator chambers were successfully installed and commissioned at CMS. Specifically, iRPC RE4/1 chambers DEMO-RE4-1-Ghent-188 and DEMO-RE4-1-Ghent-189 were installed in the CMS positions RE + 4/1/15 and RE + 4/1/16, respectively, on December 3, 2021. Additionally, iRPC RE3/1 chambers DEMO-RE3-1-Ghent-186 and DEMO-RE3-1-Ghent-187 were installed in CMS positions RE+3/1/15 and RE+3/1/16, respectively, on January 27, 2022. These chambers were equipped with two validated FEBs each and connected to all necessary components, including gas pipes, HV cables for power supply, cooling circuits, and LV cables for powering the FEBs. Leak and cooling tightness tests were conducted after installation for revalidation. This installation marked a significant milestone, as it was the first installation of iRPC chambers in the CMS, serving as a validation of the installation procedures and mechanics. Figure 3.53 (left) depicts two RE4/1 chambers installed on the fourth endcap disk of CMS, while Figure 3.53 (right) showcases the two RE3/1 chambers installed on the third endcap disk of CMS. The iRPC chambers in both images are indicated with a blue rectangle.

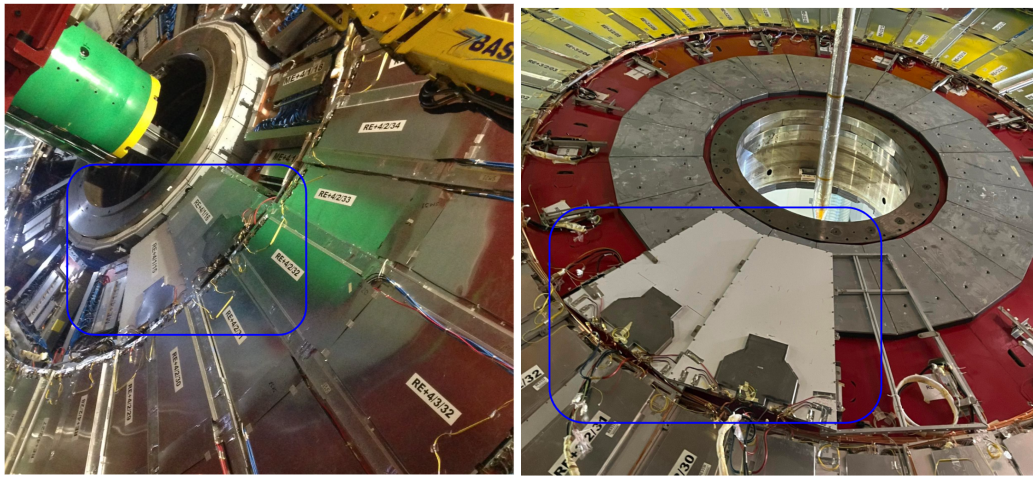

FIGURE 3.53: Installation of iRPC demonstrator chambers at CMS: Left - Two RE4/1 chambers (DEMO-RE4-1-Ghent-188 and DEMO-RE4-1-Ghent-189) installed on December 3, 2021, in CMS positions RE+4/1/15 and RE+4/1/16, respectively. Right - Two RE3/1 chambers (DEMO-RE3-1-Ghent-186 and DEMO-RE3-1-Ghent-187) installed on January 27, 2022, in CMS positions RE+3/1/15 and RE+3/1/16, respectively.

Commissioning the chambers verified their operational integrity within the CMS-endcap closed mode, with the CMS endcap water cooling and normal magnet operation at a magnetic field strength of 3.8 T. The noise level in case of all the chambers were measured as part of commissioning and all four chambers exhibited low noise levels, with a maximum of 1 Hz/cm^2 in both LR and HR regions, even with final CMS endcap disk grounding. Figure 3.54 displays noise rate measured on the strips in the HR and LR regions of the DEMO-RE3-1-Ghent-186 chamber, demonstrating an average noise rate of 0.2 Hz/cm^2, with a maximum reaching only 1 Hz/cm^2. The final DAQ setup for the iRPCs has not yet been installed in the CMS service area. Consequently, the chambers were not actively involved in data acquisition during the CMS Run-3 period. Instead, they remained continuously powered, aligning with

the CMS beam automation matrix, which facilitated the monitoring of current levels and their stability. Periodically, the chambers were tested using a portable DAQ system.

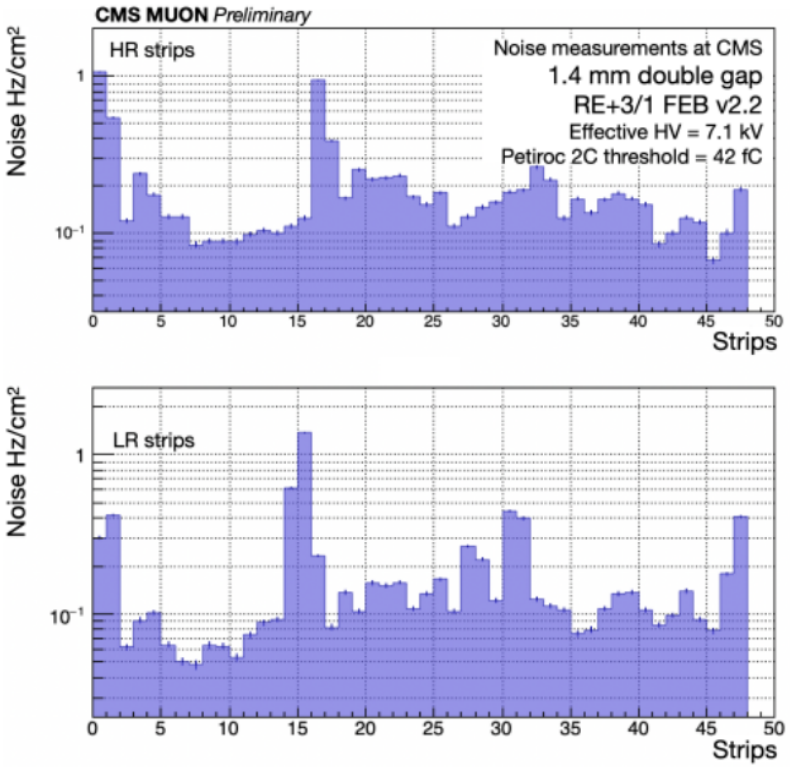

FIGURE 3.54: Noise rate measurements of the iRPC DEMO-RE3-1-Ghent-186 chamber installed at CMS in the strips in both HR and LR regions. The chamber exhibits an average noise rate of 0.2 Hz/cm^2, with the maximum rate peaking at only 1 Hz/cm^2. Similar behaviour is observed in case of all chambers [140].

3.5 iRPC Performance Studies at GIF++

To validate the performance of the iRPC detector, one of the iRPC RE4/1 demonstrator chamber- iRPC DEMO-RE4-1-Ghent-189 was installed at GIF++, where its performance was thoroughly studied under various irradiation conditions during different test-beams. I mainly participated in the activities of the iRPC in the July 2022 test-beam, and the results obtained from the data collected during this specific test-beam are elaborated upon in this section.

3.5.1 Experimental Setup at GIF++

Performance studies involving iRPC demonstrator chambers were carried out using the 150 GeV muon beam available from the SPS beam lines, as well as the 13 TBq ^{137}Cs gamma source at GIF++. The detector was exposed to various levels of gamma background, including the expected level during the HL-LHC phase. Details of the GIF++ facility and how the irradiation levels are adjusted were previously discussed in Sec. 1.4.4. Figure 3.55 presents an image captured inside GIF++, showcasing the installation of the iRPC demonstrator chamber, which is indicated by a red circle in the photograph. The picture also shows the gamma irradiator and

the chamber is installed on Trolley 3 which is the trolley at 3 m distance from the source.

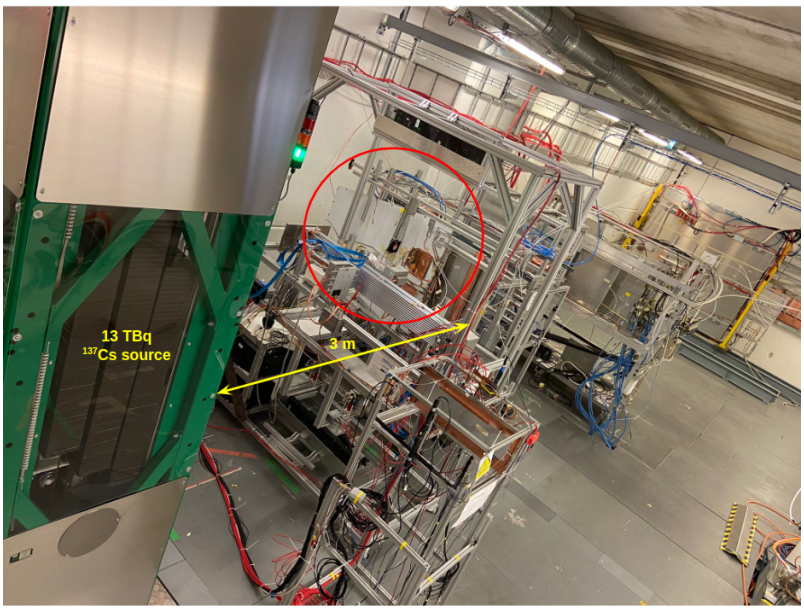

FIGURE 3.55: An interior view of the GIF++ facility, featuring the installation of the iRPC demonstrator chamber, marked by a red circle in the photograph. The image also shows the gamma irradiator and the chamber is installed on Trolley 3, positioned at a distance of 3 m from the radiation source.

The trigger for data taking is provided by the scintillators specifically installed at GIF++ for the CMS RPC RE1/1 which was already installed at GIF++ for environmental friendly gas mixture studies and the scintillators provided by the GIF++ facility. Both detectos were installed on the same trolley during the test beam. The same trigger strategy employed for the CMS RE1 / 1 was adapted to the iRPC. Detailed information on trigger setup is available in the subsequent chapter, Sec. 4.4.3, which elucidates the operation of the RE1/1 chamber at GIF++. Data acquisition was carried out using FEBv2.2, connected to a μTCA-based DAQ system. A signal selection threshold of approximately 33 fC was applied to the FEB for data collection.

The data acquisition is conducted remotely using the WEBDCS software [33], initially developed for RPCs and subsequently adapted for iRPCs. The DAQ as well as the CAEN power supply module is integrated with WEBDCS and this enables remote chamber powering and data collection. Moreover, the software records the environmental parameters, pressure, temperature, and humidity within the GIF++ facility, alongside monitoring the source's status. WEBDCS offers a user-friendly visual interface, allowing users to generate preliminary plots from the collected data and qualify runs without the need to download the data. All data files are stored as root files and are accessible to users remotely through a connection to the WEBDCS server.

3.5.2 Results

During the test beam period in July 2022, as part of the iRPC chamber performance studies, all key parameters such as detector working point, muon cluster size, avalanche charge, position resolution, and muon efficiency were studied. All the results achieved are described in the section.

All the important parameters are studied as a function of the gamma cluster rate measured in kHz/cm^2. It denotes the number of gamma clusters observed within a unit area. A gamma cluster consists of the strips activated within the same time window when the particle passes through. When particles such as muons and gammas pass through the iRPC detector, it can fire multiple strips at a time. Therefore a clustering routine is performed to estimate the time and the position information associated with the particle. The clustering routine involves three steps: 1) A strip is chosen only if there is a LR signal corresponding to an HR signal, 2) the set of signals obtained from HR side and LR side are clustered separately, called "one-side clusters". For this, the strip from which the earliest signal is obtained in the HR (LR) side is selected ($strip_{reference}$) and the neighboring strips ($strip_{neighbour}$) are considered as part of the cluster if $|\Delta T(strip_{reference},\ strip_{neighbour})| < 3\ ns$. The one-side cluster's time and position are calculated by taking the average of that of the signals from the strips involved in the cluster and 3) To build the final cluster, the set of one-side clusters from HR and LR side are taken if the difference of their strip number position is less than one ($|\Delta Strip(HR, LR)| < 1$). The final strip number is estimated as the average of the HR and LR one-side clusters, while the time associated is the difference between the HR and LR one-side cluster time. The number of strips involved in the final size is defined as the cluster size.

Fig. 3.56 shows detector working point (WP) measured as a function of the gamma cluster rate. The WP is determined as the knee voltage (HV_{knee}), derived from the

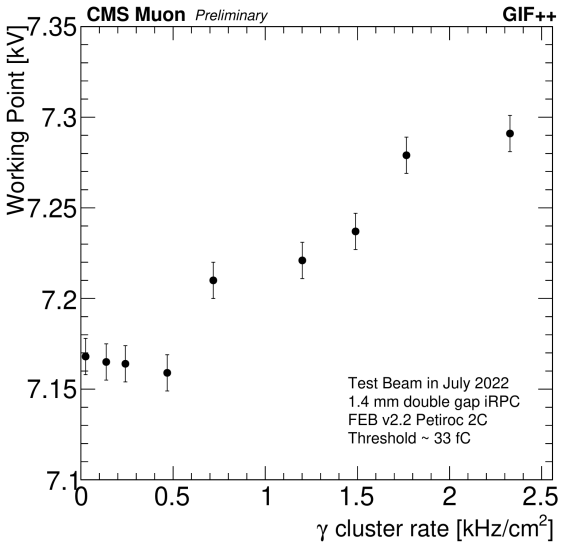

FIGURE 3.56: Variation of the detector's working point (WP) with respect to the gamma cluster rate. The plot shows an increase at WP as the gamma cluster rate exceeds 0.5 kHz/cm^2, with the WP shift remaining below 300 V even at maximum background rates.

sigmoidal fit applied to the efficiency plateau plus 120 V, with HV_{knee} representing the point corresponding to 95% of the maximum efficiency [141]. As the detector's

performance is influenced by the background rate, operating the chamber at the estimated WP is essential for achieving optimal detection efficiency. In the plot, it is evident that the WP increases as the gamma cluster rate exceeds 0.5 kHz/cm^2. However, even at maximum background rates, the WP shift remains below 300 V.

Figure 3.57 (left) illustrates the relationship between gamma cluster size measured and the gamma cluster rate both measured at WP. As the gamma cluster rate in-

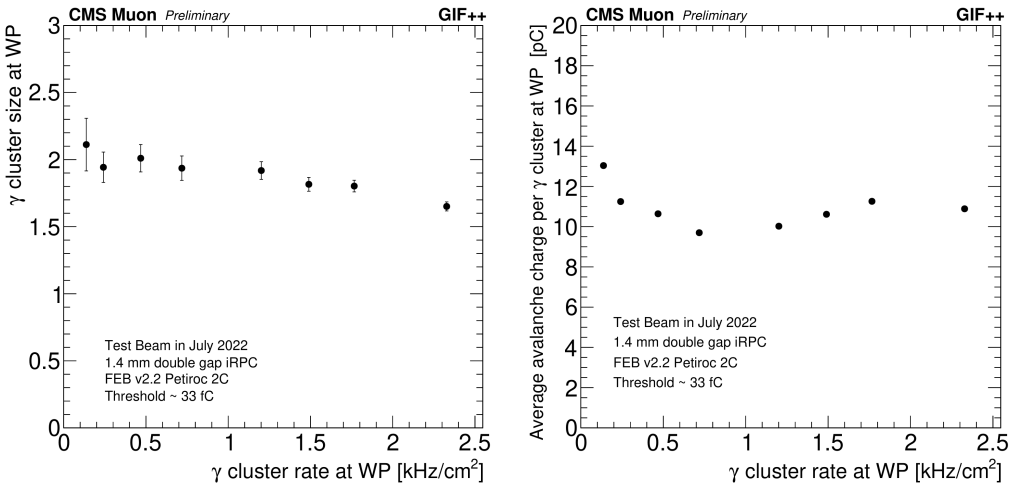

FIGURE 3.57: Left: Gamma cluster size as a function of the gamma cluster rate measured at the WP. A slight decrease in cluster size is observed as the cluster rate increases due to a decrease in effective gain. Right: Average avalanche charge per gamma cluster relative to the gamma cluster rate measured at WP. The charge remains relatively consistent beyond a cluster rate of 0.5 kHz/cm^2 [1].

creases, there is a slight decrease in gamma cluster size. This phenomenon can be attributed to the decrease in effective gain, resulting in reduced efficiency as the gamma cluster rate rises. Figure 3.57 (right) displays the average avalanche charge per gamma cluster concerning the gamma cluster rate measured at WP. The average avalanche charge is calculated as follows:

$$< q >= \frac{(I_{TOP} + I_{BOT})/2}{\text{rate}_{\gamma\,CLS} \cdot A_{GAP}} \tag{3.1}$$

Here, I_{TOP} and I_{BOT} represent the current in the top and bottom gaps, respectively. $\text{rate}_{\gamma\,CLS}$ signifies the rate of gamma clusters, and A_{GAP} denotes the area of the iRPC gap. It is evident that, while a slight decrease is observed for initial data points, the charge remains within a consistent range with minor fluctuations after the rate of the gamma cluster exceeds 0.5 kHz/cm^2.

Figure 3.58 shows the cluster position resolution as a function of the gamma background rates for two different trigger scintillator positions close to HR (red) and close to LR (black). The scintillators are of width 2 cm and were aligned orthogonal to the strips. The results showed that even at higher background rates, a position resolution of less than 3 cm is achievable.

The muon detection efficiency of the chamber was also measured without and with different levels of gamma background. The muon efficiencies (ϵ) are calculated

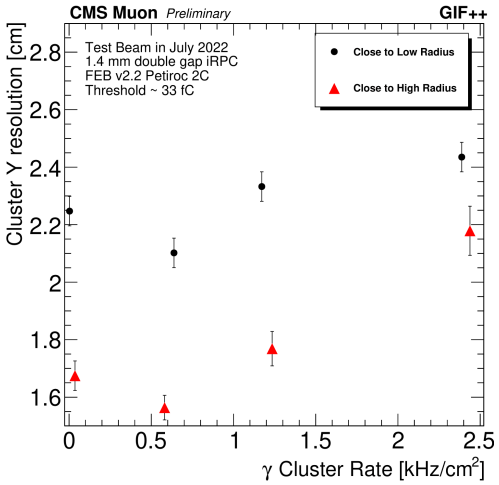

FIGURE 3.58: Cluster position resolution as a function of gamma background rates for two different trigger scintillator positions – one close to HR (in red) and the other close to LR (in black). The results indicate that, even at higher background rates, a position resolution of less than 3 cm is achievable [1].

after subtracting the estimated gamma background obtained using the events falling outside the muon window, using the equation 3.2 where N is the number of muon events detected, N_{trg} is the number of muon triggers and N_{bkg} is the number of gamma background events expected in the time interval [140].

$$\epsilon = \frac{\frac{N}{N_{trg}} - \frac{N_{bkg}}{N_{trg}}}{1 - \frac{N_{bkg}}{N_{trg}}} \tag{3.2}$$

Fig. 3.59 (left) shows muon efficiencies as a function of effective HV (HV_{eff}) without the presence of the background source and at different background rates varying from 0.7 kHz/cm^2 to 2.3 kHz/cm^2 in steps of 0.5 kHz/cm^2. The HV_{eff} is calculated by applying the PT correction explained in Sec. 2.4.7. The first efficiency curve corresponds to the source-off case, followed by multiple efficiency curves corresponding to different gamma rates at which the chamber was tested. The corresponding gamma rates and the estimated WPs for each case are annotated on the plot.

From the plot, it's evident that both the detector's HV_{eff} values and the WP shift to higher voltage values as the gamma rate increases. This shift is attributed to the rise in irradiation current within the detector as the gamma rate rises. The increased irradiation current reduces the voltage across the electrodes, effectively lowering the supplied HV. Consequently, this reduction in the HV applied to the gaps results in a reduced gain for the detector. The shift observed is proportional to the irradiation current on the electrodes. The shift in the WP has been discussed in Fig.3.56, and in Fig.3.59 (right), the efficiency measured at the working point as a function of the gamma cluster rate clearly shows the drop in efficiency due to the decreased gain as the gamma rate increases. At 0.7 kHz/cm^2 (the expected background rate of HL-LHC), the chamber maintains a 96% efficiency (at WP= 7.21 kV), while at 2.3 kHz/cm^2 (above the 3-times safety factor of background radiation), the efficiency drops to 89%.

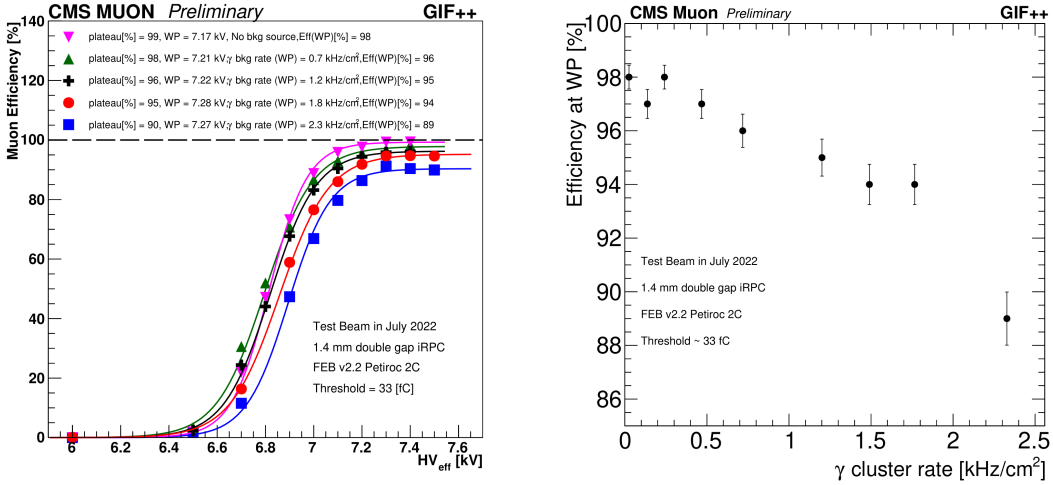

FIGURE 3.59: Left: muon efficiencies plotted as a function of effective HV (HV_{eff}) at various background rates and without the presence of the background source. The initial efficiency curve corresponds to the source-off scenario, followed by the efficiency curves corresponding to different gamma rates. Right: muon efficiency measured at WP as a function of gamma cluster rate [1].

To assess the uniformity of chamber operation across its active area, muon efficiency measurements were conducted at five distinct regions of the detector without background source. Figure 3.60 illustrates the muon efficiencies plotted against HV_{eff} for regions located at specific y positions relative to the HR region, 20, 40, 50, 60, and 80 cm, respectively. It can see that the efficiency measured at WP in all cases is 98$\pm$1 %. The efficiencies calculated at the WP for each case are provided in the figure.

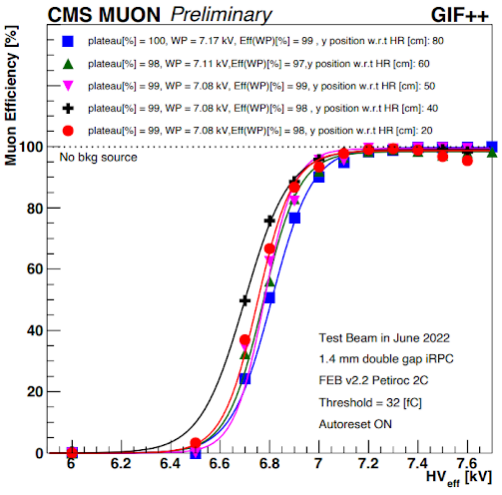

FIGURE 3.60: Muon efficiencies plotted as a function of HV_{eff} for regions located at specific y positions relative to the HR region: 20, 40, 50, 60, and 80 cm, respectively. The efficiencies measured at the WP for all cases are consistently 98$\pm$1%. The calculated efficiencies at the WP for each case is annotated on the plot [1].

The muon efficiency measurements were conducted in both single-gap and double-gap modes to assess the uniformity of behavior between the two gaps. The results

of this comparison are presented in Fig. 3.61.

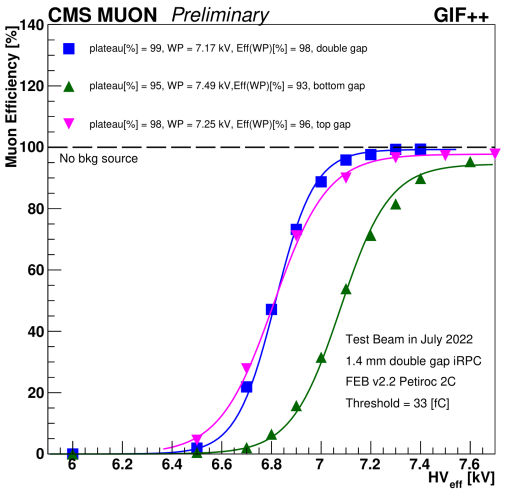

FIGURE 3.61: Comparison of muon efficiency in single-gap and double-gap modes. The blue curve represents measurements taken with the chamber operating in double gap mode, while the green and pink curves correspond to measurements with only the bottom gap and top gap turned on, respectively.

The maximum efficiency (98 %) at WP is achieved when the chamber operates in double gap mode. Comparatively, the efficiency curve of the top gap closely resembles that of the double gap, with only a 2% drop at WP. However, for the bottom gap, the efficiency curve is shifted to the right, resulting in a 5% lower efficiency at the WP compared to the double gap mode. Since this study was conducted with a single iRPC chamber, the results cannot be used to generalise the performance of all iRPC gaps. The unusual trend observed in the bottom gap may be attributed to potential ambiguities within the gap, such as gas flow or spacer-related issues.

To determine the operational threshold of PETIROC 2C, muon efficiencies were measured by varying the threshold from 0 to approximately 10^3 fC. The muon efficiencies, measured at the working point (7.2 kV), are depicted as a function of the PETIROC threshold at both the HR (red) and the LR regions of the chamber in Fig. 3.62. A cumulative gamma distribution was used to fit the curve, with error bars disappearing behind the data points when the statistical uncertainty was less than 2%. This analysis revealed an optimal operational threshold for the Petiroc 2C at approximately 33 fC.

3.6 iRPC Mass Production

After the successful validation of the iRPC chamber, its major components, and the QC protocol, mass production of the iRPC detectors commenced in early 2023. A total of 80 iRPC chambers will be constructed: 40 RE3/1 and 40 RE4/1 chambers. The critical components for these chambers, including HPL panels, gas gaps, strip PCBs, FEBs, and more, are manufactured at the dedicated production sites explained in Sec. 3.4. These components are dispatched in batches to the assembly sites

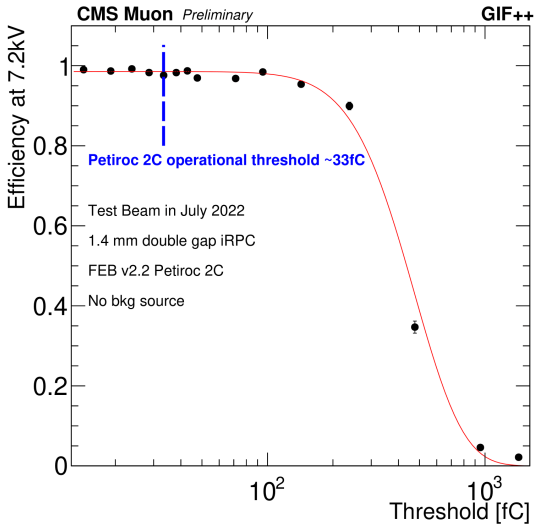

FIGURE 3.62: Efficiency measurements at the working point (7.2 kV) for the HR (red) and LR regions of the chamber as a function of PETIROC threshold, spanning from 0 to approximately 10^3 fC. The determined optimal operational threshold for the Petiroc 2C is approximately 33 fC [1].

where the chambers are produced. Details of the iRPC assembly sites are given in the following section.

3.6.1 Assembly Sites

For the iRPC prototype production and demonstrator project, UGent served as the sole production site. However, for iRPC mass production, additional assembly sites have been established at CERN (CMS RPC lab in building 904) and Ibero-American University (UIA), Mexico. Section 3.4.3 has already provided details about the RPC lab at UGent. The RPC team at CERN already have experienced members who have been involved in RPC production and operation for several years. To facilitate the mass production process, an additional assembly lab has been constructed alongside the existing RPC lab at CERN (equipped with QC4 setups), equipped with all necessary setups for QC2 and QC3. Production is now simultaneously progressing at both UGent and CERN.

Members of the RPC team from Mexico participated in the prototype production at Ghent to gain experience on detector construction and QC tests and also received training at CERN for chamber operation and data collection. The iRPC assembly lab at UIA is fully equipped with all the necessary setups for QC2 and QC3. Chamber production will start at UIA after the final qualification of the lab. Figure 3.63 (left) shows the inside view of the newly constructed static lab at CERN, dedicated to mass production activities, while the right-hand image shows the fully prepared iRPC assembly lab at UIA.

3.6.2 Activities at UGent

This section outlines the mass production activities taking place at the RPC lab within UGent. Starting in August 2022, I was primarily responsible for coordinating

FIGURE 3.63: The images on the left and right depict the dedicated iRPC assembly labs at Building 904, CERN, and UIA, Mexico, specifically built for the mass production of iRPCs respectively. Both labs are fully equipped with all the facilities required for the chamber assembly and QC procedures.

these activities, which involve troubleshooting and setting up all necessary QC setups, and managing the logistical aspects required for mass production. I have prepared a complete list of all the major and minor components required for producing 80 iRPC chambers, providing details such as the number of units per component, manufacturers, delivery dates at assembly sites etc.. The list can be accessed in the document- [142]. For the mass production, additional personnel, including new students, have joined the team. During the initial months, dedicated training sessions were organised to familiarise these new team members with QC testing procedures, chamber construction processes, and the documentation of QC results within the CMS RPC construction DB.

In early 2023, the initial batch of iRPC RE3/1 gas gaps and honeycomb panels for production was received in Ghent from the respective production sites (refer Fig. 3.64. This was the beginning of the production phase, but it was not without its challenges.

FIGURE 3.64: Honeycomb panels (left) and gas gaps (right) received at CMS RPC lab at UGent for the iRPC mass production.

Notably, issues with dimensions and the placement and size of screw holes in the honeycomb panels were identified, necessitating corrective measures. To address these concerns, the panels were sent back to the manufacturer for necessary adjustments and retrofitting. After repair, a detailed panel-by-panel investigation of the honeycomb panels was carried out, resulting in the qualification of all panels for production.

Regarding the gas gaps, bending was observed (1-3 *cm*) in the majority of them, particularly in the corners of the HR region. Figure 3.65 shows the bending observed in one of the iRPC RE3/1 gas gap. To ensure proper chamber assembly and achieve

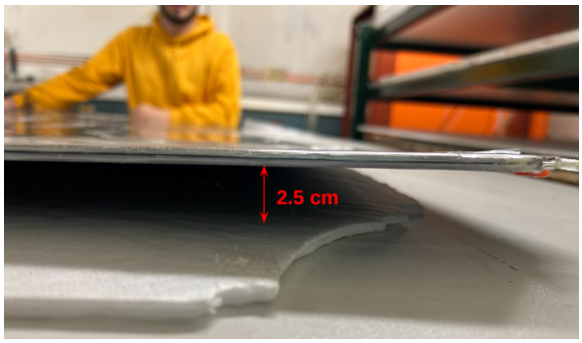

FIGURE 3.65: Bending observed in one of the iRPC RE3/1 gas gap.

consistent performance across the entire active area, it was necessary to minimise any bending in the gas gaps and acquire a horizontal orientation. Increased bending over time can also result in cracks in the peripheral spacers, potentially leading to gas leaks. To prevent further bending and reduce the existing bending, all the gas gaps were placed inside an air-conditioned room, maintaining a humidity level between 30% to 40 % using a portable humidifier. Additionally, heavy aluminum plates were placed on top of the gap stacks to minimise further bending. After nearly a month, most of the gaps showed a reduction in bending and, to prevent further deformations, the gaps were kept inside the humidified environment. All subsequent batches of gaps received at both Ghent and CERN did not exhibit any bending issues.

QC2: Gas Gaps

After receiving the gas gaps, the QC2 tests were performed on each gap, and the results of the first batch of gas gaps are provided in this section. Of the initial batch of 33 received iRPC RE3/1 gaps, the following outcomes were observed:

- 24 gas gaps passed all QC tests (leak test, spacer test, and HV test).
- 3 gas gaps passed the leak and spacer tests but failed the HV test due to sparks and fluctuations in dark current.
- 1 gap was rejected during visual inspection due to a broken gas inlet.
- 3 gaps were rejected due to a high leak rate.
- 2 gaps were rejected due to popped spacers.

Based on these results, the survival rate of gas gaps after transportation from the production site to the assembly site is 73%.

The summary of the QC2 test results for the first batch of gaps is presented in Fig.3.66. The left plot displays the pressure drop calculated for all gaps that passed the leak+spacer QC tests, while the right plot shows the dark current observed at 7.3 *kV* for these gaps. The X-axis of the plots displays labels of the gaps tested. As explained in Sec. 3.4.2, the acceptance criteria are a pressure drop below 0.4

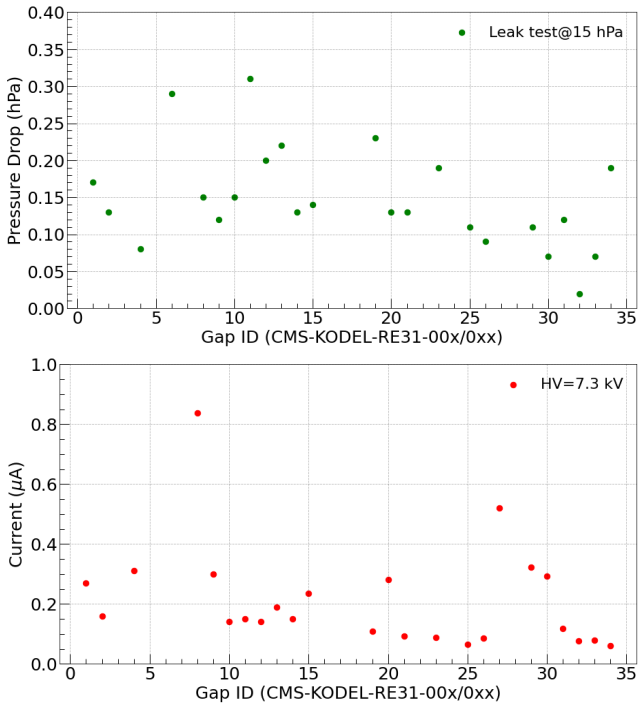

FIGURE 3.66: QC2 results for the first batch of iRPC RE3/1 gas gaps received at the RPC lab at UGent. Left: Pressure drop calculated for gaps that passed leak and spacer tests as a function of gap identification labels. Right: Dark current measured at 7.3 kV as a function of gap identification labels.

$hPa/10\ min$ and a current of less than 3 μA at 7.3 kV. The majority of the qualified gaps showed results well below the selection thresholds. Detailed information on how gaps should perform during leak test, spacer test, and HV test was previously discussed with accompanying plots in the section covering the QC results of iRPC demonstrator chambers (Sec. 3.4). Due to the large number of gaps tested for mass production, a summarised overview is provided here. All QC test results, including data files, are uploaded and can be accessed in the CMS RPC construction DB.

Chamber Production

After the completion of the QC2 testing for gas gaps, detector. To ensure the effectiveness of the finalised assembly procedure and to demonstrate it to the new team members, a trial iRPC assembly was conducted. The step-by-step iRPC assembly procedure, which was revalidated during the trial assembly, can be found in [143].

Starting from April 2023, the iRPC production has been in continuous operation at UGent RPC Lab. Figure 3.67 (left) shows the picture of the first iRPC chamber produced as part of the mass production and the members of the RPC team participated in assembly. The iRPC components are received in batches, undergo QC tests, and one chamber is produced every week. Periodically, all the qualified chambers are transported to CERN in batches where each batches consists of 10 chambers. The transportation process is carried out by RPC team members themselves using specially designed shipment trolleys and boxes, ensuring the safety of the chambers and minimising the risk of any possible damage (refer Fig. 3.67-right).

FIGURE 3.67: Left: The first iRPC chamber produced at CMS RPC lab at UGent as part of the mass production and the team members participated in the assembly. Right: 10 iRPCs produced at RPC lab UGent packed in the trolley and loaded in the truck to ship to CERN.

3.7 Summary and Conclusions

In preparation for the HL-LHC phase, the CMS experiment at the LHC is undergoing substantial upgrades. These enhancements aim to improve sensitivity, address higher background rates, and adapt to increased luminosity conditions. One challenge is the lack of redundancy in the high pseudo-rapidity (η) region of CMS, which affects muon triggering and measurements. To address this, the RE3/1 and RE4/1 iRPCs are introduced, extending the RPC coverage to high η regions.

An overview of the CMS iRPC upgrade is provided in this chapter focusing on my contributions. The iRPC upgrade project and the motivation behind it are introduced in the first two sections (Sec. 3.1, 3.2). Detailed information on the improved technical layout of the iRPC and the new front-end electronics is provided in the third section (Sec. 3.3).

The last three sections focus on the major activities conducted and the significant results achieved. As part of the iRPC project several prototype and demonstrator chambers were constructed and studied. In Sec. 3.4, an overview of the iRPC demonstrator project and the activities conducted are presented. All the QC procedures required at various levels, from component-level testing to detector-level assessments at production sites, assembly sites, and ultimately at CERN that were validated during the iRPC demonstrator project. The section also provides a step-by-step guide to the iRPC assembly procedure and details the installation of the iRPC demonstrator chambers at CMS conducted in early 2022.

Section 3.5 provides the details and results of the performance studies conducted with the iRPC detector at the GIF++ facility during the July 2022 test beam. Notably, the investigation of the detector's working point in relation to the gamma cluster rate reveals that even under maximum background rates, the WP shift remains within an acceptable range, staying below 300 V. Moreover, the chamber's muon detection efficiency is examined both in the absence of and in the presence of varying levels of gamma background. At the anticipated background rate of HL-LHC of 0.7 kHz/cm^2, the chamber maintains an efficiency of 96% at the WP (7.21 kV). Even at background rates exceeding three times the safety factor, efficiency decreased, but still it is $\sim$90%. The uniformity of chamber operation across its active

area is also assessed, showing consistent efficiencies. Additionally, a comparison between single-gap and double-gap modes is presented, revealing differences in efficiency trends. The determination of the operational threshold of PETIROC 2C is also discussed, with an optimal threshold of approximately 33 fC identified.

Section 3.6 offers an overview of the iRPC mass production that commenced in April 2023. Details of the iRPC assembly sites and their readiness for iRPC mass production is detailed. This section also discusses the specifics of ongoing mass production activities at UGent RPC lab and presents the latest results in this regard.

At present, iRPC mass production is progressing at the assembly labs at UGent and CERN. Simultaneously, the production of essential detector components, including major elements like gas gaps and front-end electronics, is progressing at their respective production sites/institutes. Few iRPC chambers will be installed at CMS during January-February 2024 and the installation of the reamining chambers will be conducted during the next EYETS (2024-2025).

Chapter 4

Exploring Eco-Friendly Gas Mixtures for RPCs

This chapter gives detailed information of the activities of the ECOgas@GIF++ Collaboration and highlights my significant contributions to the project. The collaboration is dedicated to the exploration of eco-friendly gas mixtures for the RPCs used in the LHC experiments. Throughout my PhD, I actively participated in majority of activities conducted by the collaboration. I was engaged in a series of test beam studies conducted at GIF++, CERN for evaluating the performance of various RPCs when operated with different eco- friendly gas mixtures under varying irradiation conditions. My principal responsibilities included the preparation of experimental setups in GIF++, managing data acquisition during beam tests, and subsequently conducting in-depth data analyses. My primary focus during the test beam studies was directed towards the CMS RPC chamber, and consequently, all the test beam results discussed within this chapter correspond to this specific chamber.

Furthermore, I had a major role in a year-long ageing (2022-2023) campaign conducted by the collaboration, to qualify the use of an HFO-based gas mixture named ECO2 for the operation of RPCS. My substantial involvement in this campaign includes the continuous monitoring and testing of all the RPCs considered for the ageing studies that are installed at GIF++. This commitment extended to my active participation in weekly shifts dedicated for data taking, organising training sessions for fellow shifters, and performing the data analysis. The results derived from the extensive data collected during this ageing campaign are also thoughtfully presented in this chapter, providing valuable information on the suitability of ECO2 for RPC operation under the present and future conditions of the LHC.

4.1 Introduction

RPCs find extensive application in high-energy physics experiments. These detectors typically operate using a gas mixture (detailed in Sec. 2.4.6) that comprises two types of fluorinated gases: Tetrafluoroethane ($C_2H_2F_4$), commonly referred to as R134a or freon, and sulfur hexafluoride (SF_6). It's important to emphasise the environmental impact associated with these gas mixtures. In the standard RPC gas mixture ($C_2H_2F_4$ /C_4H_{10}/SF_6=95.2%/4.5%/0.3%), which is also utilised in experiments at LHC, including the CMS experiment, the predominant gas is R134a, with a GWP of 1400. Although SF_6 comprises only 0.3% of the mixture, it has a significantly higher GWP of 22800. These gases introduces a high risk to the environment due to their negative impact on global warming. EU has introduced strict regulations to

control high GWP gases and reduce their availability in the market. These regulations involve a phasedown plan aiming to limit the sale of key F-gases to one-fifth of the 2014 levels by 2030. Figure 4.1 shows the progress of the EU HFC phasedown up to 2030. They also encompass restrictions on the use of high-GWP F-gases in new equipment and require mandatory checks, servicing, and gas recovery for existing equipment at the end of its operational life [144]. While research facilities are currently not prohibited from using these gases, the global phasedown of their production is expected to pose challenges in terms of availability and cost. Therefore, there is a pressing need to explore eco-friendly alternatives for RPC operations, not only to align with regulatory changes but also to reduce costs and simplify the sourcing of materials.

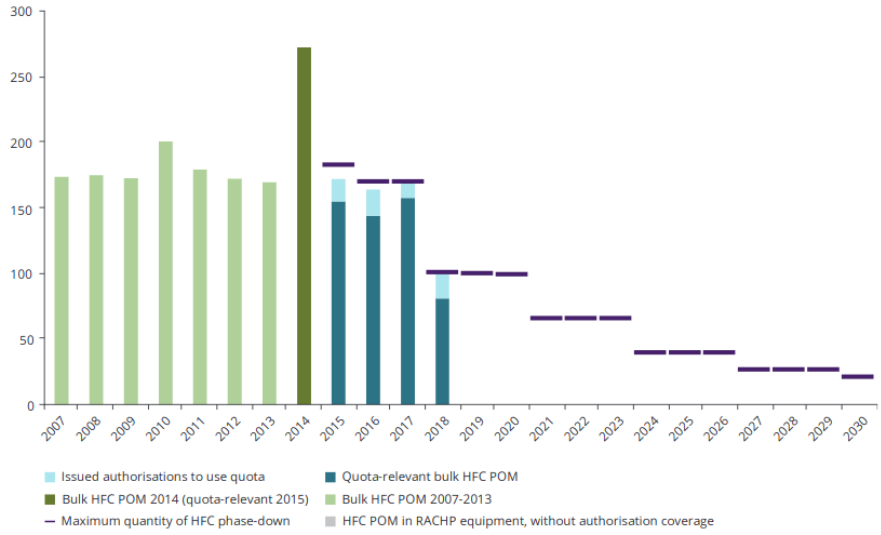

FIGURE 4.1: The progress of the EU-wide phase-down for HFCs implemented according to the EU Regulation on F-gases (No 517/2014), which started in 2015, with the aim of cutting emissions by two thirds by 2030 in the EU compared with 2014 [144].

To align with the European regulations and to explore eco-friendly alternatives, the collaborative effort known as ECOgas@GIF++, involving the ALICE, ATLAS, CMS, LHCb/SHiP[1], and Experimental Physics Department-Detector Technologies (EP-DT) communities at CERN, has undertaken an extensive R&D program. A leading alternative under investigation is HFO-1234ze, notable for its remarkably low GWP value of merely 6, a substantial improvement over the conventionally used R134a. In recent years, RPC detectors with slightly different characteristics and electronics have been studied using gas mixtures based on HFO and CO_2 at GIF++, CERN. These investigations encompass a multifaceted analysis, including the study of detector ageing with the proposed alternative gas mixtures and an in-depth evaluation of detector performance under different irradiation conditions.

Within this chapter, the driving motivations behind this research at CERN and the meticulous selection process of alternative gases are explained. Additionally, analysis results of detector performance under diverse irradiation conditions, with particular emphasis on the CMS RPC detector, are included. Moreover, detailed insights

[1]Search for Hidden Particles (SHiP) and the associated SPS Beam Dump Facility at CERN is a new general-purpose experiment proposed at the SPS to search for "hidden" particles [145].

into the outcomes of ageing campaigns involving RPC detectors, representing the collaborative contributions of the research groups mentioned earlier, are presented.

4.2 Motivation

4.2.1 GHG Emission: LHC Experiments

Within the CERN LHC experiments, a variety of gaseous detectors are deployed, each serving specific functions and operating with distinct gas mixtures. Some of these detectors utilise GHGs with high GWP. Notably, the RPCs, GEMs, and CSCs are among the major detectors that employ fluoride-based GHG gases such as $C_2H_2F_4$, CF_4, and SF_6. Figure 4.2 (left) illustrates the greenhouse gas (GHG) emissions contributed by each LHC experiment during Run-1 (2010-2013). Different colors in the bars represent three distinct GHGs indicated in the legend. The ATLAS and CMS experiments account for the highest emissions, mainly due to their substantial detector volumes (up to 100 m^3). ALICE and LHCb each contribute approximately 12%. On the right side plot of the same figure, the GHG emissions of individual detectors during the same period are displayed. It is evident that a significant majority (over 70%) of emissions are attributed to RPCs, while all the other detectors shown in the plot, including LHCb's Ring-imaging Cherenkov detector 2 (RICH 2), CMS's CSC, LHCb's Multi Wire Proportional Chamber (MWPC), and LHCb's GEM detectors, collectively contribute only 20% of the total GHG emissions. The results serve as the primary motivation for conducting R&D efforts to replace the current RPC gas mixture with more eco-friendly alternatives [146].

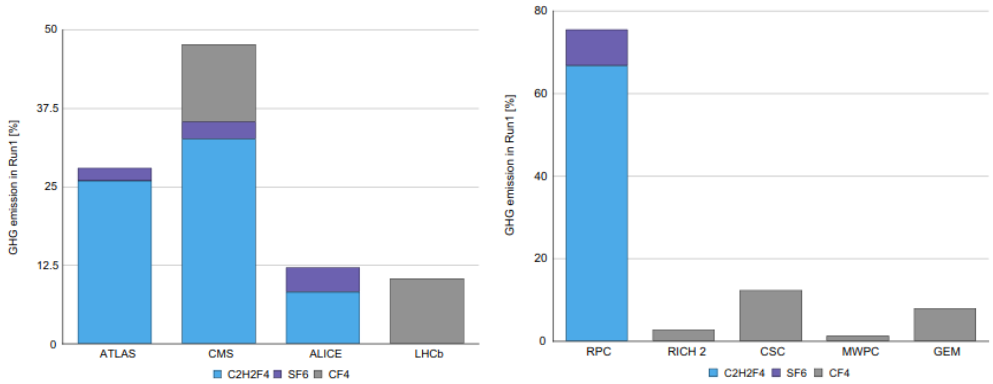

FIGURE 4.2: Greenhouse Gas Emissions from LHC Experiments: Left - Contribution of greenhouse gas (GHG) emissions by various LHC experiments during Run-1 (2010-2013). Right - GHG emissions by individual detectors within the experiments during the same period. RPCs are the primary contributors to GHG emissions, accounting for over 70% of the total [146].

4.2.2 GHG Emission: Current Measures

To mitigate GHG emissions, CERN has implemented both short-term and long-term strategies. Although the complete elimination of F-gases is currently unfeasible, short-term objectives primarily focus on reducing gas consumption. During the extended LHC shutdown in 2013-2014, several gas recirculation systems underwent upgrades to enhance gas recirculation efficiency, resulting in a 40% reduction in GHG emissions per system. However, maintaining efficiency after multiple recirculation cycles poses challenges due to impurity accumulation. To address this

issue, purifiers designed to remove impurities like O_2 and H_2O have been integrated into the recirculation process to sustain performance and prevent impurity buildup. Consequently, all gas circulation systems are now equipped with purifier modules to maintain low impurity levels in the recycled gas.

During the Long Shutdown-2 (LS2) period from 2019 to 2021, the CMS experiment prioritised the consolidation of its RPC gas system. This consolidation effort aimed to minimise gas leaks and implement a newly developed gas front recuperation system. It included the repair of gas leaks across all five barrel wheels of the experiment, with the distribution of these repaired gas leaks (as of June 2022) illustrated in Fig. 4.3. The total number of leaky chambers in each barrel wheel is also shown in the picture. The most vulnerable components in the RPC chambers responsible for gas leaks were the fragile gas inlets and outlets within the gas gaps. A total of 122 gas leaks were identified in the RPCs installed in the barrel region during the three-year LS2 period, mainly due to cracked or broken inlet/outlet components and pipes.

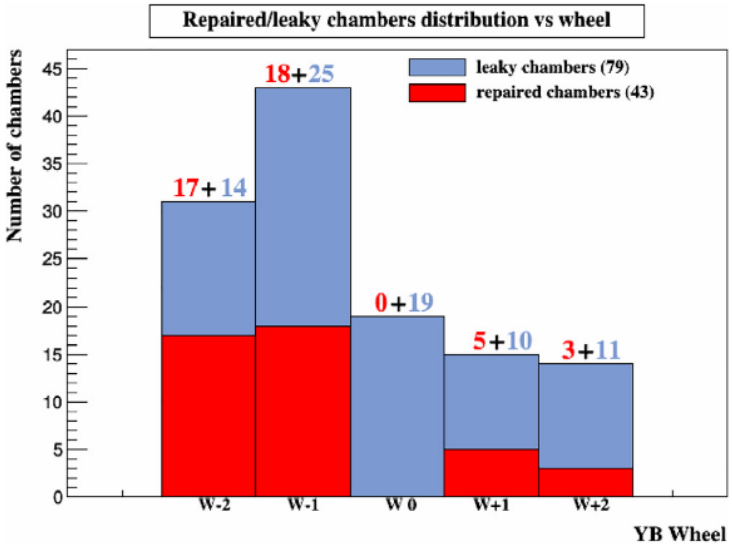

FIGURE 4.3: Distribution of the leaking chambers and the repaired chambers in each of the CMS barrel wheel as of June 2022. [147].

Out of these 122 leaks, 43 chambers have already been repaired and reinstalled, while the remaining 79 chambers have been disconnected from the gas distribution system. As of June 2022, 108 chambers in the barrel region remain disconnected, including 14 with non-repairable leaks, 60 operational but leaking chambers, and 31 operational, non-leaking chambers sharing channels with leaking chambers. This totals 96 operational chambers disconnected, equivalent to nearly 8.9% of the CMS RPC system. This decision aligns with the CMS gas reduction policy, necessitating the disconnection of all leaky chambers, even if they remain operational. Due to this proactive approach, during Run 3, the total expected leak rate will reduce from 900 l/h to 200 l/h and approximately 1000 l/h of gas will be restored to the exhaust [147].

Additionally, a recuperation system for R134a, developed with an efficiency of approximately 80% by the EP-DT team at CERN, was tested and is currently connected

to the exhaust of the CMS RPC gas system. Figure 4.4 illustrates the gas supply strategy at CMS, incorporating the newly implemented recuperation system. The process of injecting recuperated R134a began in early August, with an initial mixture of 15% (60 l/h) recuperated gas and 85% (400 l/h) fresh gas. The schematic diagram of the

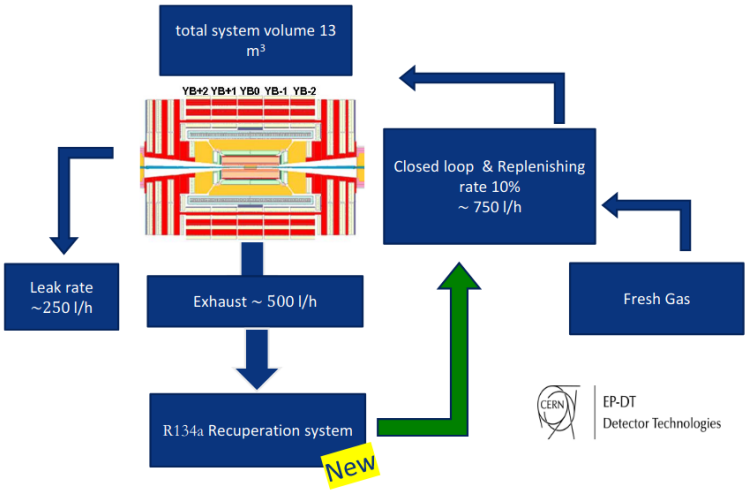

FIGURE 4.4: The gas supply strategy at CMS, which includes the newly implemented recuperation system for R134a. The system started operation in early August, with an initial mixture of 15% (60 l/h) recuperated gas and 85% (400 l/h) fresh gas.

recuperation system is shown in Fig. 4.5.

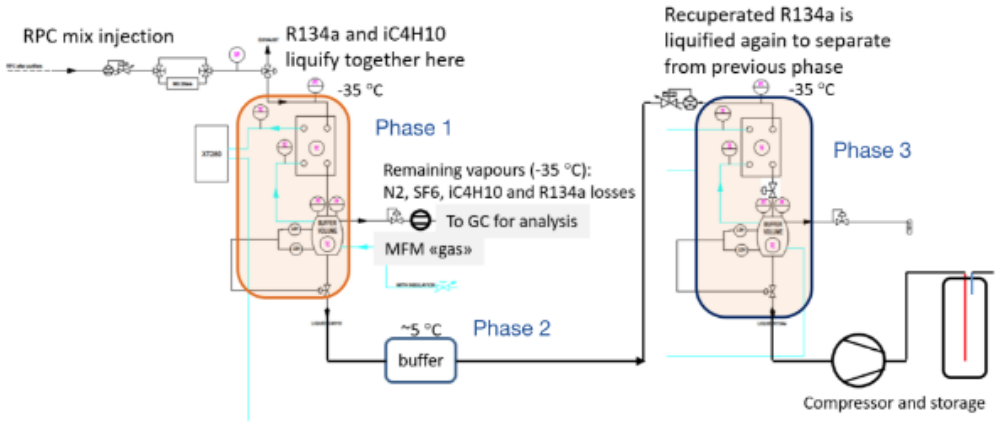

FIGURE 4.5: The schematic diagram of the operation of the first R134a recuperation prototype system [148].

This system operates in three distinct phases:

- **Phase 1**: The gas mixture in buffer 1 is cooled to approximately $\sim -35^{\circ}\ C$. During this phase, R134a and iC_4H_{10} are liquefied together, while the remaining gases (N_2, SF_6, iC_4H_{10} losses, and R134a losses) remain in the vapor phase. The vapor phase, which consists of N_2 and SF_6, is removed through a simple distillation process.
- **Phase 2**: To separate R134a and iC_4H_{10}, the liquid mixture is slowly heated to around $\sim 5^{\circ}\ C$, causing R134a to remain in liquid form while iC_4H_{10} transitions back into vapor. The vaporised iC_4H_{10} is then returned to buffer 1.

- **Phase 3**: In the final phase, R134a is once again liquefied (at $\sim -35^{\circ}\ C$) to separate it from the previous phase. It is then compressed and transferred to a storage cylinder.

Throughout the process, the vapor phase becomes increasingly enriched in iC_4H_{10} at each step, while the liquid phase becomes progressively enriched in R134a. When utilising high-quality R134a, the system achieves a recuperation efficiency of approximately 80% [148].

4.3 Search for Alternatives

The primary objective of the search for eco-friendly gases for RPCs at LHC is centred on the replacement of the main gas mixture component, R134a. Although numerous alternatives exist and are utilised in various industries, finding a suitable substitute for RPCs presents unique challenges due to their specific operational requirements. To ensure a high detection efficiency, such as that of freon, the new gas must possess a high density of primary electrons and ions. Additionally, it should exhibit high electronegativity to facilitate charge localisation and serve as a quenching gas, thereby reducing photon emission and transmission. Crucially, the chosen gas must not pose any health risks to humans (non-toxic). Furthermore, the detector should maintain or enhance its efficiency at a similar operating WP, and the generated signals should remain detectable using existing electronics. This consideration is vital since replacing all the current power systems and electronics to accommodate a new gas mixture would be both inconvenient and cost-prohibitive.

One of the main alternatives with a low GWP currently under study is hydrofluoroolefin, commonly known as HFO. Compared to R134a, HFO contains the same number of fluorine atoms but has one additional carbon atom, resulting in a higher WP for RPCs. Among the various isomers of HFO, the most commercially available options are HFO-1234yf (2,3,3,3-tetrafluoropropene) and HFO-1234ze (1,3,3,3-tetrafluoropropene), which have GWPs of 4 and 6, respectively. Due to concerns about flammability, HFO-1234ze has been chosen as the preferred alternative for further studies [149]. Figure 4.6 shows the chemical composition of R134a (left) and HFO-1234ze (right). The green, black, and white circles correspond to fluorine, carbon, and hydrogen atoms, respectively.

Preliminary tests involved completely replacing R134a with HFO in the RPC gas mixture, resulting in a significant shift in the WP to more than 13 kV. To achieve a suitable compromise, carbon dioxide (CO_2) was introduced alongside HFO. This combination helps to limit the WP while maintaining control over the streamer probability, making it a promising solution for RPC gas mixtures. Figure 4.7 (a) displays the efficiency (solid line) and streamer probability (dashed line) as functions of effective HV for various HFO+CO_2-based gas mixtures, along with the RPC standard gas mixture (in black). In Fig. 4.7 (b), the time resolution concerning effective HV is illustrated for the same set of gas mixtures, with the RPC standard gas mixture included (in black). The plot reveals that as the proportion of CO_2 increases, the WP shifts to lower values. However, if the CO_2 content exceeds 80%, the efficiency drops below 95% and more isobutane is also required to improve quenching. Therefore, utilising approximately 60% CO_2 appears to be an optimal choice. Given that HFO is less electronegative than R134a, it is necessary to maintain around 1% SF_6 in the mixture for charge localisation. Furthermore, despite the WP exceeding 10 kV, the plot

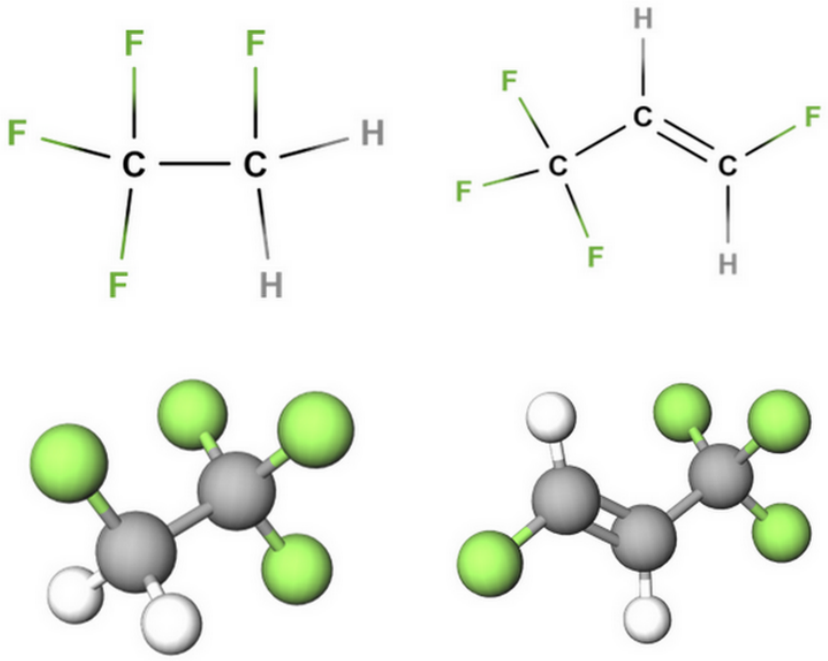

FIGURE 4.6: The chemical composition of R134a (left) and HFO-1234ze (right). The green, black and white circles corresponds to fluorine, carbon and hydrogen atoms respectively.

demonstrates that the mixture with 31% HFO has a controlled streamer probability. Additionally, it indicates that slightly better time resolution can be achieved with HFO compared to the standard gas mixture when the voltage exceeds 10.5 kV [150].

4.4 The ECOgas@GIF++ Collaboration: Experimental Setups

Several studies have been conducted by various research groups to assess the performance of RPCs using HFO-1234ze + CO_2-based gas mixtures (ecogas mixtures), yielding promising results (for references, see [83, 149–153]). However, for the RPCs intended to operate during the HL-LHC period, it is important to investigate how the detectors with the new gas mixtures behave under prolonged irradiation and the subsequent ageing effects on the detectors. To address this critical need, the ECOgas@GIF++ Collaboration was established in 2019, bringing together teams from the ALICE, ATLAS, CMS, LHCb/SHiP experiments, together with the EP-DT gas group at CERN. This collaboration involves RPCs with varying layouts and designs contributed by each participating group. Conducting tests with HFO-1234ze/CO_2 gas mixtures simultaneously on detectors featuring diverse layouts and front-end electronics from different groups provides detailed insights into both gas performance and detector behavior. All the detector systems are installed and the tests are conducted at GIF++, CERN. A detailed description of the GIF++ layout, including information about the radiation source and the strategy employed to adjust irradiation levels can be found in Sec. 1.4.4. Subsequently, the following subsection within this section provides in-depth details of the gas system and detectors that have been installed for the ecogas studies.

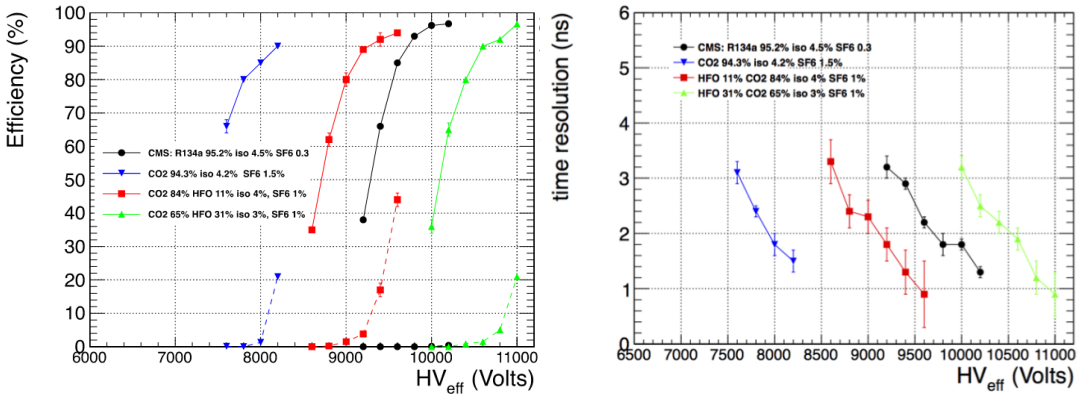

(a) (b)

FIGURE 4.7: (a) Efficiency (solid line) and streamer probability (dashed line) as function of effective HV for various HFO + CO_2-based gas mixtures are shown, along with the RPC standard gas mixture (in black). (b) The time resolution with respect to effective HV for the same set of gas mixtures, with the RPC standard gas mixture included (in black) [150].

4.4.1 Gas System

The gas system for the studies conducted by the ECOgas@GIF++ Collaboration is located within the GIF++ service zone on the second floor. Common gases like R134a, Isobutane, and Argon are provided by the GIF++ team through a general distribution system. However, user-specific gases like HFO are set up by the respective groups. For this experiment, an HFO bottle[2], equipped with a leak detection system and pressure regulator, is installed in the gas distribution room.

The gas system comprises a mixer to create the required gas mixture according to the specified composition. The gas system installed in the service zone is depicted in Fig. 4.8. The figure displays the four rotameters and the control knobs of each of the gases used in the mixture. The gas mixture then passes through a humidifier in the system. Each gas line is connected to a Mass Flow Controller (MFC) to adjust the desired flow rate. Additionally, there are two extra MFCs to manage the humidity level in the gas. The output line of the gas mixture is split into two lines: one is directed to the humidifier tank where the gas is humidified by mixing with water vapor, controlled by one of the MFCs. The other line carries the dry gas mixture, and the second MFC manages this portion. Subsequently, the two lines are combined, and the humidity level is monitored using a dew point sensor. The gas mixture's humidity is fine-tuned by regulating the dry gas and humidified gas lines. All MFCs are controlled through dedicated software called FlowDDE, which allows adjustments of gas volume, composition, flow rate, and humidity level.

Following the dew point sensor, the gas output is channeled to the GIF++ bunker, where it is divided and distributed in parallel to all ECOgas@GIF++ detector systems. The gas flow for each RPC is adjusted using variable area rotameters installed in series with the chamber, and the input flow is measured through a flow cell located in the input line of each detector. Considering the total number of detectors, their volume, and the required volume changes per hour, the gas flow rate needed

[2]The bottle contains approximately 3,000 liters of gas, and under normal usage conditions, one bottle typically lasts for about 30 days.

FIGURE 4.8: The gas system for the studies of the ECOgas@GIF++ Collaboration, installed in the GIF++ service zone, featuring four rotameters and individual control knobs for each gas component used in the mixture.

for the setup is approximately 10 l/h [154]. After the detectors are flushed, the output lines from all systems are merged into a common return line, which joins to the exhaust of the gas distribution area, venting the gas into the atmosphere.

4.4.2 Detectors

The ECOgas@GIF++ Collaboration has deployed detectors from various groups onto two trolleys, designated as Trolley 1 (T1) and Trolley 3 (T3), situated within the GIF++ bunker. These trolleys are positioned at distances of 6 meters and 3 meters from the ^{137}Cs source, respectively. T1 accommodates chambers from the ALICE and LHCb/SHiP groups, while T3 hosts chambers from the ATLAS, CERN EP-DT, and CMS groups. For a detailed overview of the layout, see Fig. 4.9, where the positions of T1 (in red), T3 (in red), the ^{137}Cs source (in yellow), trigger scintillators (s1 and s2 in red; S1 and S2 in blue), and the direction of the muon beam (indicated by the green arrow in the middle) are elucidated. The image in Fig. 4.10 depicts the two trolleys housing the detectors installed within the GIF++ facility.

As previously mentioned in the introduction of this section (Sec. 4.4), it's important to note that the RPCs provided by each group for the experiment are not identical. Specifically, the chambers from ALICE, ATLAS, CERN EP-DT, and LHCb/SHiP are single-gap RPCs with a rectangular shape. In contrast, the chamber from CMS is a double-gap RPC with a trapezoidal shape, similar to the iRPCs discussed in Sec. 3.3.1.

All of these chambers employ copper strips for signal readout. However, there are differences in the strip configurations among the chambers. The CMS and CERN EP-DT chambers are equipped with horizontally oriented strips, while the ALICE and

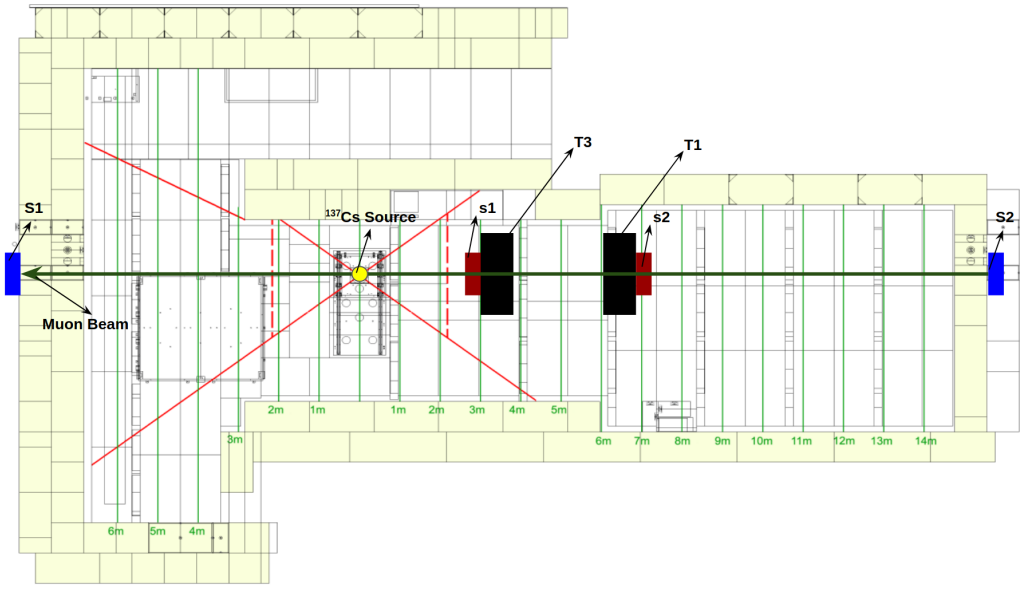

FIGURE 4.9: The layout of the GIF++ facility, showcasing the arrangement of Trolley 1 (T1) and Trolley 3 (T3) in red, the ^{137}Cs source in yellow, trigger scintillators (s1 and s2 in red; S1 and S2 in blue), and the direction of the muon beam indicated by the green arrow.

LHCb/SHiP chambers feature two sets of strips positioned orthogonally, one on top and one on the bottom of the gaps. This configuration allows for 2D hit information. On the other hand, the ATLAS chamber utilises a single central strip. The width of the strips is consistent among all chambers except for the CMS chambers, where the trapezoidal shape leads to varying strip widths in the horizontal direction. The details of the layout of each chamber, encompassing dimensions, gas gap thickness, electrode thickness, and copper strip characteristics (total number and strip pitch), are concisely presented in Tab. 4.1.

Group	Trolley	Size (cm×cm)	Gap thickness (mm)	Electrode thickness (mm)	No of strips	Strip pitch (mm)
ALICE	T1	50×50	2	2	16 + 16	30
ATLAS	T2	55×10	2	1.8	1	N/A
CMS	T2	(41.5÷23.9)×100.5	2+2	2	128	5.5÷11
EP-DT	T2	70×100	2	2	7	21
LHCb/SHiP	T1	70×100	1.6	1.6	32+32	10.6

TABLE 4.1: The summary of chamber specifications, including dimensions, gas gap thickness, electrode thickness, and copper strip characteristics, of different RPC chambers of the ECOgas@GIF++ Collaboration [155].

The required high voltage for all systems is supplied through CAEN HV modules, utilising a setup comprising a CAEN main frame (A1526N) and two HV boards (A1526P: H.V. channels -15 kV 1/0.1 mA - CPE Conn. (6 ch), A1526N: H.V. channels +15 kV 1/0.1 4 - CPE Conn. (6 ch) connected to the main frame. This HV setup is located in the service area of the GIF++. HV cables are routed to the bunker through a dedicated path constructed beneath the floor for cable routing, ultimately connecting to the detectors via an opening within the bunker. All other components, including low-voltage supplies and readout electronics, are specific to each detector.

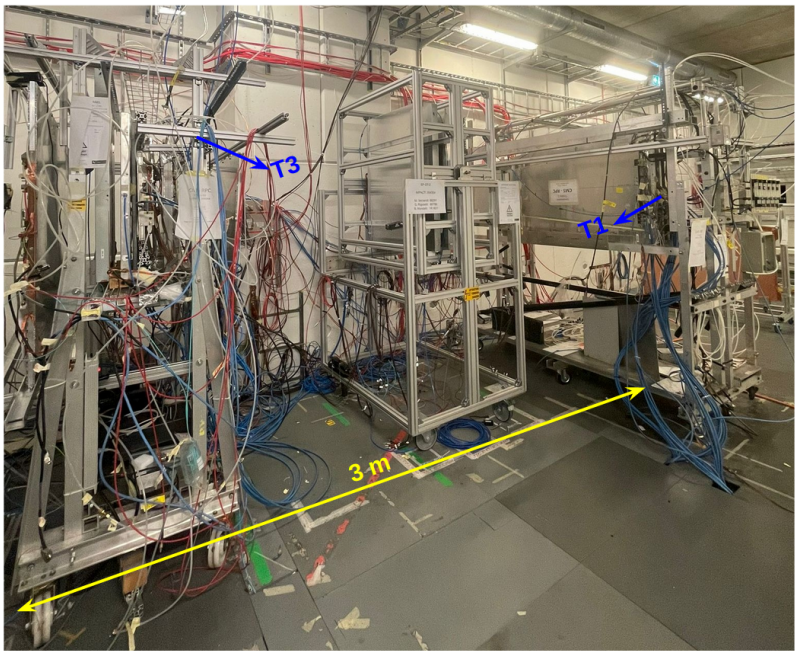

FIGURE 4.10: This figure shows the trolleys T1 and T3 housing the detectors of the ECOgas@GIF++ Collaboration installed inside the GIF++ facility.

4.4.3 Trigger and DAQ

At GIF++, the main feature of the facility is its capability to combine the muon beam with the ^{137}Cs source to replicate the high radiation background encountered in LHC experiments. All detector systems follow the same trigger logic, with muon triggers provided by four scintillators coupled with photomultipliers installed within the facility. Unlike the typical two-scintillator muon trigger configuration, the intense gamma background necessitates the use of additional scintillators. To mitigate false triggers due to irradiation, two outer scintillators, S1 and S2 (each measuring 30×40 cm^2), are positioned outside the bunker, detecting only muon signals and provided by the GIF++ team. Additionally, the ECOgas@GIF++ team installed two inner scintillators, s1 and s2 (each measuring 10×40 cm^2), within the bunker. These inner scintillators are placed orthogonally on T3 and T1, respectively and create a reduced trigger area of 10×10 cm^2. The muon trigger is generated using a standard NIM coincidence module, which takes the input of all four scintillators and provides the AND of the signals as the output. The inner scintillators are located approximately 3.5 m apart from each other, while the outer scintillators are situated at a distance of about 25 m apart from each other [154]. The layout of GIF++ in Fig. 4.9 includes the positions of the trolleys, the source, and all four trigger scintillators (S1, S2, s1, and s2).

In ALICE, CMS, and LHCb/SHiP chambers, the signals obtained from the readout strips undergo amplification, discrimination, and shaping through dedicated front-end electronics. These electronic systems are connected to Time-to-Digital Converters (TDCs) for signal processing. On the other hand, in ATLAS and the CERN EP-DT chambers, signal processing is achieved using digitiser modules which directly capture and store waveform data from the readout strips for subsequent analysis. Each experiment employs custom analysis algorithms to interpret the data, whether obtained from TDCs or digitisers. Table. 4.2 provides an overview of certain electronic

characteristics for each chamber, encompassing details such as the Front-End (FE) electronics chip type, FE equivalent threshold, and the DAQ setup (TDC or Digitiser). The ALICE, CMS, and LHCb/SHiP chambers utilise front-end electronics

Group	FE chip	FE equivalent threshold	DAQ type
ALICE	FEERIC ASICs	-200 mV for horizontal strips, 106mV vertical strips (after amplification)	TDC
ATLAS	N/A	130 fC	Digitiser
CMS	CMS/RPC standard electronics	220 mV $=$ 150 fC (after amplification)	TDC
$EP-DT$	N/A	2 mV	Digitiser
LHCb/SHiP	FEERIC ASICs	70 mV for horizontal strips, 80 mV for vertical strips (after amplification)	TDC

TABLE 4.2: The summary of characteristics of the electronics of each detector of ECOgas@GIF++ Collaboration, including the Front-End (FE) electronics chip type, FE equivalent threshold, DAQ (TDC or Digitiser) [155].

with signal amplification. Therefore, the threshold after amplification is indicated in the table (for details of the front-end electronics used, see [156, 157]). The ALICE and LHCb/SHiP chambers are equipped with two sets of readout strips positioned orthogonally. Hence both thresholds are provided.

This section provides a concise overview of the DAQ systems for all detectors. Since the performance studies discussed in this thesis focuses on the CMS chamber, more details regarding the CMS chamber is given in Sec. 4.5, where the test beam results are discussed in depth.

4.4.4 Online Monitoring and Controlling

All RPCs included in the study undergo continuous monitoring of the logged data using an open-source software, Grafana [158]. Key parameters, including environmental conditions (pressure, temperature, and humidity), gas flow rates for each component of the gas mixture, total gas consumption from the HFO bottle, source status, applied HV, and detector current, are continuously tracked. The software provides a user-friendly visual interface featuring a dashboard with graphical representations of all monitored parameters, facilitating the rapid identification of any potential issues. Additionally, the software is equipped with automatic alarm systems that trigger alerts in the event of issues, such as gas depletion, leading to the automatic shutdown of detectors for safety. A picture of a part of the Grafana dashboard is shown in Fig. 4.11. Data acquisition for all detectors is conducted using the WEBDCS software, originally developed for CMS RPCs, as elaborated in the third chapter of this thesis (Sec. 3.5.1) [33]. The software has been adapted according to the electronic modules of the detectors within the ECOgas@GIF++ Collaboration. It provides an online interface and also enables remote operation of all detector systems. Additionally, the software is equipped to monitor and log various detector parameters during operation.

4.5 Performance Tests Under Irradiation

Since 2019, testing with different ecogas mixtures has been conducted on all detector systems within the ECOgas@GIF++ Collaboration during several test beam

FIGURE 4.11: A part of the Grafana dashboard illustrating the continuous monitoring of RPCs. The software monitors key parameters, including environmental parameters (pressure, temperature, and humidity), gas flow rates, total gas consumption, source status, applied HV, and detector current.

periods at GIF++. Taking into account the preliminary test results obtained with ecogas mixtures, as discussed in Sec. 4.3, the collaboration has primarily concentrated its efforts on testing three specific ecogas mixtures alongside the standard gas mixture for comparison studies. The composition and GWP of all the gas mixtures tested are tabulated in Tab. 4.3. The table includes the standard gas mixture, denoted as STD mix, while the ecogas mixtures are labeled as ECO1, ECO2, and ECO3 for convenience.

Mixture	$R134a$ (%)	$HFO-1234ze$ (%)	CO_2 (%)	$i-C_4H_{10}$ (%)	SF_6 (%)	GWP
STD mix	95.2	0	0	4.5	0.3	1485
ECO1	0	45	50	4	1	438
ECO2	0	35	60	4	1	476
ECO3	0	25	69	5	1	527

TABLE 4.3: Summary of the gas mixtures used in the tests conducted by the ECOgas@GIF++ Collaboration since 2019, including the composition of each gas mixture and the calculated GWP.

The initial tests involved ECO1 and a comparison with STD mix. It was observed that in the case of ECO1, the knee voltage is approximately 1.8 kV higher than the STD mix, and its WP exceeded LHC standards at higher irradiation rates. Notably, the average cluster charge for ECO1 was nearly five times higher than that of the STD mix, with values of 25-30 pC for the STD mix and approximately 150 pC for ECO1. Furthermore, the dark current increased significantly within just one week of irradiation, reaching four times its initial level after two weeks. These effects were observed in all the RPCs under test. Consequently, the decision was made to halt ECO1 irradiation and initiate new tests with ECO2 and ECO3. Even after stopping irradiation and flushing the chambers with STD mix, the dark current continued to

increase over four days and then later started to drop. For the details of the measurements and results of the studies conducted with ECO1, the reader is referred to [159] and [120].

In the context of performance studies of the RPCs with ecogas mixtures conducted during test beam periods at GIF++, I was primarily involved in the hardware activities and the analysis of the CMS RPC detector. Therefore, this section mainly focuses on the test beam results obtained with the CMS RPC, with a significant emphasis on findings from the 2023 test beam.

4.5.1 Detector Parameters: CMS RPC RE1/1

A brief summary of the geometric characteristics of the CMS RPC chamber, RE1/1 (name of the CMS RPCs installed in the first endcap disk of the experiment), has already been provided in Sec. 4.4.2. However, for the purpose of elucidating the performance studies in this section, additional details of the detector are given here.

The detector comprises two 2 mm Bakelite gas gaps (double-gap detector). The lower layer constitutes a single continuous gap, referred to as the bottom gap (BOT), while the upper layer consists of a single gap divided into two parts, named as Top-Narrow (TN) and Top-Wide (TW). Each part features a separate HV connection, with gas supplied separately to the bottom and top layers. Furthermore, the two segments within the top layer are interconnected for gas flow. The strip layout of the chamber is also trapezoidal in shape, comprising a total of 128 strips distributed across four sectors, each containing 32 strips. The signals from these four sections are readout through four modules of CMS RPC front-end electronics [157]. For a visual representation of the CMS RE1/1 chamber and its layout, see Fig. 4.12 (a) and (b), which respectively depict the 3D models of the interior view of the CMS RE1/1 chamber and the arrangement of the FEBs installed on the chamber to readout the signals from the four strip partitions. Additionally, Fig. 4.12 (c) provides a schematic of the strip layout, with measurements in millimeters and the four partitions denoted as A, B, C, and D [160].

As explained in Sec. 4.4.2, the CMS RE1/1 chamber is installed in the T3 at GIF++. The exact distance between the source and the chamber is 3.51 m. To maintain consistency and uniform measurement conditions throughout the testing period, the chamber is kept in the same location within the trolley. While the detector and trolley positions remain constant, it's important to note that various setups and trolleys for other experiments may intermittently occupy the space between the radiation source and T3. These changes occur in response to activities conducted by respective groups and may lead to minor variations in measurements obtained during different times of the year. However, it is worth emphasising that such minor alterations typically do not result in significant deviations. Figure 4.13 shows the closer view of the CMS RE1/1 chamber installed in T3 within the GIF++ bunker. The key details and components of the chamber are annotated in the figure.

4.5.2 Data Taking Strategy

Two types of measurements are performed during the data taking. These measurements are based on the two operational states of the muon beam: the spill cycle

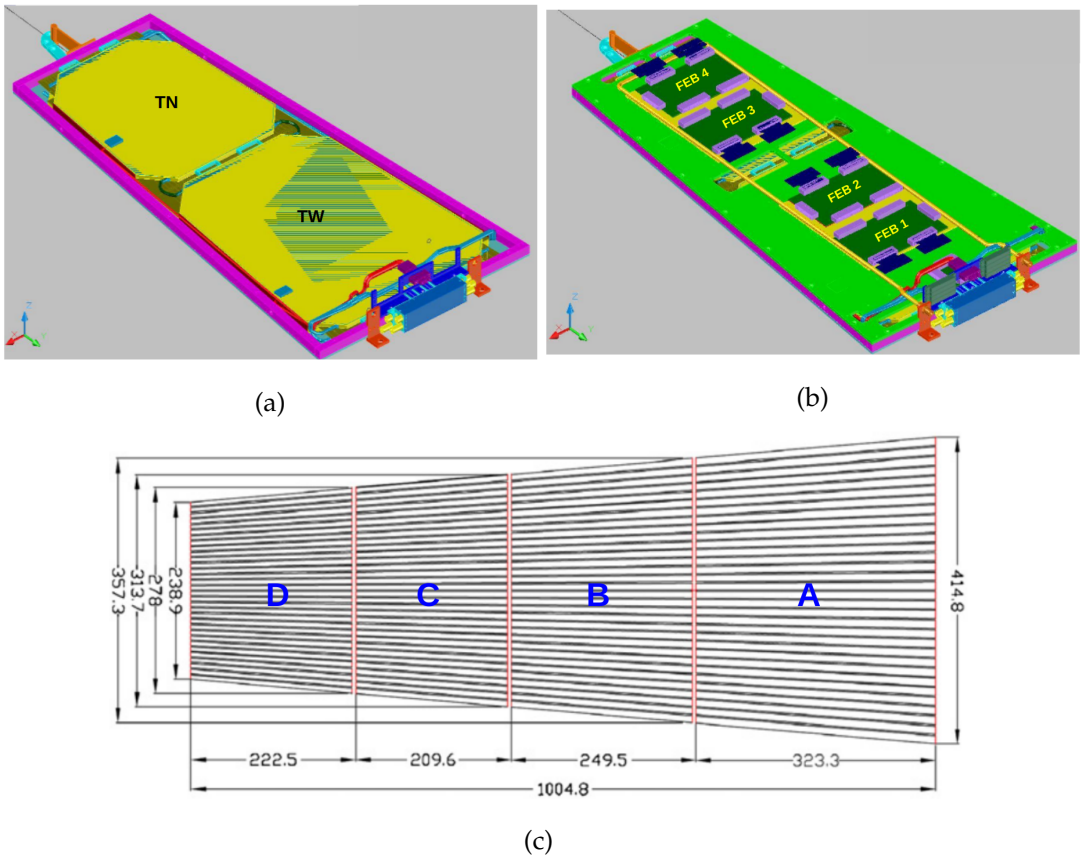

(a) (b)

(c)

FIGURE 4.12: (a) and (b) are the 3D models showcasing the interior of the CMS RE1/1 chamber and the arrangement of FEBs to collect the signals from the strips, respectively. (c)-Schematic representation of the strip layout, including measurements in millimeters and the partitions named A, B, C, and D [160].

and the non-spill cycle. During the spill, the muon beam passes through the bunker and the non-spill cycle corresponds to the period when there is no muon beam. In the first case, the trigger is generated with the four scintillators installed in the GIF++ bunker (explained in Sec. 4.4.3). The generated trigger signal is fed as a trigger input to the TDC (V1190) and the acquisition window is set to 600 ns. The second case is used to trigger the gamma background events. During the non-spill cycle, random triggers are created using a dual timer (model-N93B) with the frequency set to 50 Hz/cm^2 and the generated trigger is fed into the TDC. In this case, the acquisition window is set to 10 μs.

The raw signals generated by the chamber are processed by the FEBs before being sent to the TDCs. These output signals from the FEBs are in the form of Low-Voltage-Differential-Signals (LVDS). Each FEB is responsible for reading data from 32 strips through two 16-pin connectors, and the FEB outputs are subsequently transferred to the TDCs via two 16-channel flat cables. As per the RE1/1 chamber's position, the muon beam predominantly impacts Partition B. However, it's important to note that the beam halo extends to some portions of Partitions A and C as well. All partitions of the chamber are situated within the zone of gamma irradiation. The data acquired by the TDCs are further processed by the DAQ software and subsequently stored in root files, which are conveniently accessible for direct download by users through the WEBDCS software. Notably, the WEBDCS is also configured to perform

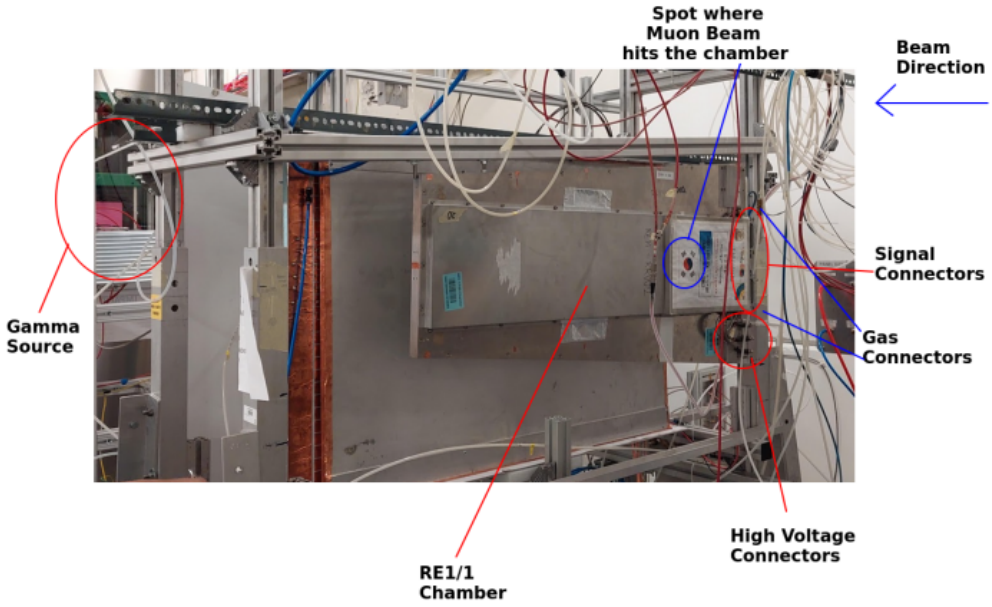

FIGURE 4.13: A close-up view of the CMS RE1/1 chamber installed in T3 within the GIF++ bunker at a precise distance of 3.51 meters from the ^{137}Cs source. The chamber remains consistently positioned within the trolley for uniform measurement conditions.

data analysis, generating distributions related to hit patterns, cluster sizes, efficiency, gamma radiation rates, and more. This feature greatly simplifies the process of run qualification for users.

4.5.3 Data Analysis

During the test beams conducted in July and August 2023, all the detector systems were tested with STD mix, ECO2 and ECO3. The details of the major parameters studied with data collected with the CMS RE1/1 chamber are detailed in this section.

High Voltage: Each run encompasses data corresponding to HV points within the range of 9000 V to 12500 V, depending on the gas mixture. As the final voltage measured across the gaps may vary due to environmental factors such as pressure and temperature, the PT correction method detailed in Sec.2.4.7 is applied. This correction yields the effective HV (HV_{eff}), as described in Eqn.2.30, which is utilised throughout the analysis. Temperature fluctuations can lead to a reduction in the surface resistivity of the electrodes and both temperature and pressure can influence the drift and multiplication processes within the gas gaps. The parameters also affect the dark current and count rates. Therefore, it is crucial to apply the PT correction factor, especially in comparative studies. In this study, the WP is estimated in the same manner as explained for the CMS iRPC detectors in Sec. 3.5.2, where WP is determined as WP = HV_{knee} + 120 V, with HV_{knee} representing the point corresponding to 95% of the maximum efficiency.

Current: The current absorbed by the detector is consistently measured in all runs. Current measurements are logged at two-second intervals, and the mean value of the resulting histogram distribution is determined, corresponding to a specific HV_{eff} value. Under normal operating conditions, the current flowing across all gaps of the CMS RE1/1 chamber, without any background source or muon beam, remains

within the range of a few microamperes. To facilitate meaningful comparisons between detectors with slightly varying geometries within the group, instead of current the current density is considered for the study. The calculation of the current density (J_{mon}) is explained by the following equation:

$$J_{mon} = \frac{I_{mon}^{TN} + I_{mon}^{TW} + I_{mon}^{BOT}}{A_{TN} + A_{TW} + A_{BOT}}, \tag{4.1}$$

Where, I_{mon}^{TN}, I_{mon}^{TW} and I_{mon}^{BOT} are the current measured in the three gaps of the detector and A_{TN},A_{TW} and A_{BOT} are the corresponding active areas.

Cluster Size: A clustering procedure is employed in the analysis. In this context, a cluster is defined as a collection of adjacent strips that were triggered within the same time window, with a time difference of less than 15 ns between them. The cluster size refers to the number of strips involved in the cluster. It essentially quantifies the spatial extent of the avalanche formed within the gas gap. Smaller cluster sizes indicate higher spatial resolution.

Gamma Rate and Gamma Cluster Rate: The background gamma radiation to which the detector is exposed is quantified by measuring the gamma cluster rate (expressed in Hz/cm^2). This measurement is conducted during the non-spill cycle, the period when the muon beam is absent. To calculate the gamma rate, the total number of hits detected during the non-spill cycle is counted, and this count is divided by the acquisition time and the active area of the detector. Similar to the estimation of the muon clusters, the clustering routine also computes the gamma clusters. The total number of gamma clusters detected corresponds to the gamma cluster rate, which provides a reliable estimate of the background radiation level in the active area of the detector.

Efficiency: The efficiency (ϵ) is calculated as the ratio of the number of hits recorded in the detector to the number of muon triggers detected by the scintillator system. To determine the muon efficiencies, the estimated gamma background, obtained from events falling outside the muon window (as outlined in Eqn. 3.2 and detailed in Sec. 3.5.2), is subtracted. A sigmoidal fit is applied to the efficiency curve using the following equation:

$$\epsilon(HV_{eff}) = \frac{\epsilon_{max}}{1 + e^{-\lambda(HV_{eff} - HV_{50})}} \tag{4.2}$$

In this equation, ϵ_{max} represents the maximum efficiency of the detector, λ denotes the slope of the curve before reaching the plateau, and HV_{50} corresponds to the HV point at which the efficiency reaches 50% [161].

Absorption Factors During the July and August 2023 test beam sessions, the CMS RE1/1 chamber, in conjunction with other detectors, was subjected to various absorption factors, hence different irradiation rates. To facilitate better comparison studies, data was selected for analysis, specifically focusing on four common absorption factors for all three gas mixtures. Additionally, data collected with the background source turned off (source-off) was included in each case. The table in Tab. 4.4 provides a list of the irradiation conditions utilised in these tests.

Irradiation conditions
Source-off
100
22
6.9
3.3

TABLE 4.4: List of absorption factors corresponding to the data selected for the July and August 2023 test beam data analysis.

4.5.4 Test Beam Results

The results presented in this section are based on data collected during the July and August 2023 test beam at GIF++. Detailed information about the tested gas mixtures, the CMS RE1/1 detector, and the relevant parameters considered for the study are provided in earlier subsections of this section.

Working Point

Figure 4.14 shows the comparative WP trends for the three gas mixtures with respect to gamma rates. The graph provides a precise visualisation of the variations in WPs between STDmix and ECO2, as well as between STDmix and ECO3. Notably, all three gas mixtures exhibit a linear increase in WP as gamma rates rise. It's important to highlight that ECO2's WP trend appears to have a steeper slope than the other two, suggesting a faster increase in ECO2's WP compared to the other two gas mixtures.

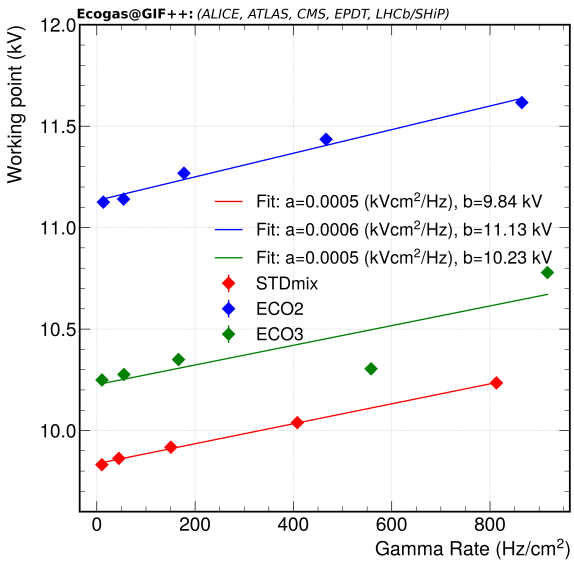

FIGURE 4.14: The plot illustrates the linear increase in WPs (WPs) for the three gas mixtures (STDmix, ECO2, and ECO3) as the gamma rate rises. Notably, the slope of ECO2 appears slightly steeper than the other two, indicating a faster increase in its WP compared to the other two gas mixtures.

Current Density

Figure 4.15 presents the current density as a function of HV_{eff} for the three gas mixtures under different irradiation conditions. Subplots (a), (b), and (c) correspond to STDmix, ECO2, and ECO3, respectively. The first curve in each case corresponds to the source-off condition and last curve corresponds to the lowest absorption factor (3.3). Each subplot provides details about the WP and the gamma cluster rate (CLR) measured at the WP. Notably, the cluster rate indicated for the source-off case represents noise, as no gamma background is present.

For the HL-LHC period, considering a three times safety factor it was decided to study the performace of the detector up to gamma rate 2000 Hz/cm^2. However, it's essential to acknowledge that the data collected at such high rates are currently insufficient for comparison, necessitating additional test beam campaigns. For this analysis, the data obtained at a gamma rate of approximately 900 Hz/cm^2 was considered.

Across all three cases, a similar trend is observed in the current density, but both ECO2 and ECO3 exhibit higher current density compared to STDmix. The current density in STDmix and ECO3 falls within a similar range due to the minimal difference in HV points. It's important to note that the in all three cases, HV_{eff} corresponding to each curve varies as the HV points are adjusted to attain the efficiency plateau.

In these plots, the initial two or three points within the curves exhibit a more linear behavior, while the subsequent behavior becomes more exponential due to gas amplification. This difference in behavior is particularly pronounced in the curves corresponding to higher rates. Comparison of current density of the three tested gas mixtures as a function of the gamma rate under varying irradiation conditions is depicted in Fig. 4.16. These values are determined at the WP for each respective gas mixture. The data DAQ focuses on partition B of the detector, thus the gamma rate and currents are considered specifically for this section. The current measurements from partition B encompass the currents measured in both TW and BOT gaps, as outlined in Sec. 4.5.1 for more details about the partitions and involved gaps. Consequently, the current density for partition B (J^B_{mon}) is calculated using the following equation:

$$J^B_{mon} = \frac{I^{TW}_{mon} + I^{BOT}_{mon}}{A_{TW} + A_{BOT}} \tag{4.3}$$

The current densities for the three gas mixtures exhibit closer agreement when the gamma rate is below 200 Hz/cm^2. However, after reaching 300 Hz/cm^2, discrepancies between the current densities of STDmix, ECO2, and ECO3 become more pronounced. The increase in current density relative to the rate displays a linear relationship for all three gas mixtures. Nonetheless, it is evident that both ECO2 and ECO3 require higher current at their respective WPs to achieve rates similar to that of STDmix. Notably, the third point in the ECO3 curve does not align well with the overall trend, suggesting that further analysis is needed, and this particular run may need to be repeated during upcoming test beams.

Cluster Size

The Fig. 4.17 presents the cluster size as a function of HV_{eff} for the detector tested with the three gas mixtures across varying irradiation rates. It's evident that, for all three gas mixtures and at all rates, the cluster size linearly increases within the

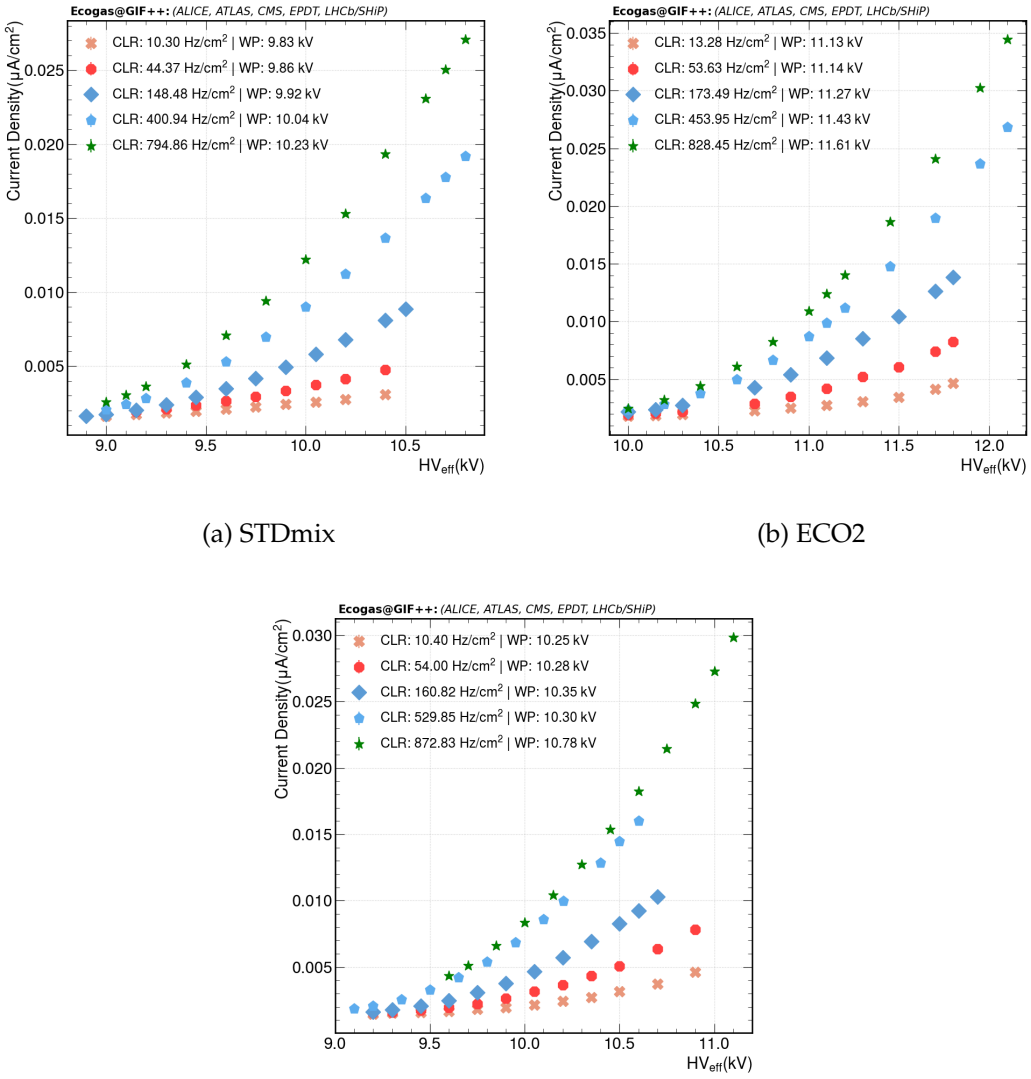

(a) STDmix

(b) ECO2

(c) ECO3

FIGURE 4.15: Current density trends for STDmix, ECO2, and ECO3 under various irradiation conditions, including the source-off condition and the lowest absorption factor (3.3). The plots show that ECO2 and ECO3 exhibit higher current density compared to STDmix. Each subplot provides details about the WP (WP) and the gamma cluster rate (CLR) measured at the WP.

HV range corresponding to gas amplification. This behavior arises from the proportional increase of the electric field within the gas, resulting in an enhancement of the induced signals. Additionally, in the initial segment of each trend, a slight decrease is noticeable, particularly at higher rates. This decrease could be attributed to a voltage drop in the electrodes when the rate is higher, leading to a minor reduction in HV_{eff} and efficiency at that point. Detailed explanations of this voltage drop effect can be found in the subsequent section on efficiency measurements (Sec. 4.5.4). Moreover, it is notable that, in all cases, the cluster size of ECO3 is quite similar to that of STDmix, and sometimes even smaller. This primarily occurs due to the lower efficiency of ECO3 compared to STDmix. Conversely, in all scenarios, the cluster size in ECO2 is slightly larger than that of STDmix and ECO3.

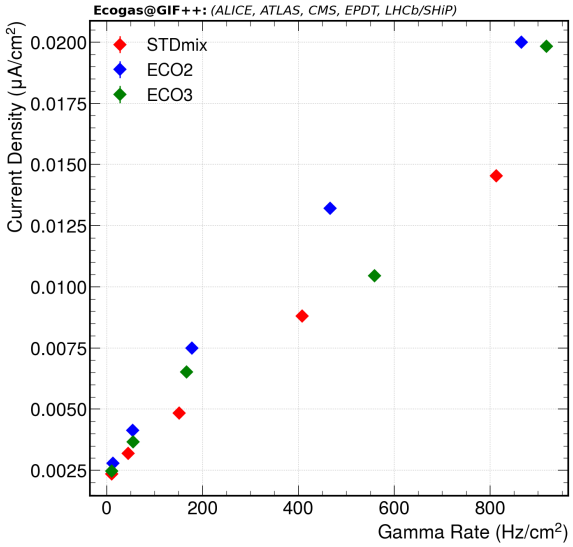

FIGURE 4.16: Comparison of the current densities of the three gas mixtures as a function of gamma rate. The current densities observed with the three gas mixtures are similar at rates below 200 Hz/cm^2 and the disparities increases at higher rates.

The relationship between cluster size at the working point and the measured gamma rate is depicted in Fig. 4.18. It is evident that an increase in the gamma rate leads to a decrease in cluster size for all three gas mixtures. This primarily occurs because as the gamma rate rises, the effective gain of the detector, and consequently its efficiency, decreases, resulting in reduced cluster sizes. Notably, ECO3 exhibits the most significant reduction in cluster size, closely correlated with its efficiency drop. Further details on efficiency measurements are discussed in the following section.

Muon Efficiency

Figure 4.19 displays the muon efficiency, calculated for three different gas mixtures, as a function of HV_{eff}. Plots (a), (b) and (c) correspond to STDmix, ECO2 and ECO3, respectively. Each curve in the plots corresponds to varying irradiation rates, except for the first curve. The initial curve on the plot corresponds to the source-off data, while the last curve represents the lowest absorption factor (3.3), resulting in the highest gamma cluster rate. The WP and the gamma cluster size (measured at the WP) are annotated on the plots.

The plots make it evident that at a specific HV point, an increase in the gamma rate leads to a decrease in efficiency. The detector's HV_{eff} values as well as the WP gets shifted to higher voltage values. This occurs because the exposure to gamma radiation elevates the circulating current in the detector. The subsequent rise in current causes a drop in the voltage across the Bakelite electrodes, diminishing the supplied HV across the gaps (discussed in Sec. 2.4.5). Consequently, this reduction in the HV across the gaps, which is responsible for the charge multiplication process, results in decreased gain. If this effect is substantial, it will shift the efficiency plateau to higher voltages, as demonstrated in the results. This shift will be proportional to the absorbed current.

The voltage drop across the electrodes, which mentioned earlier, can be estimated by considering the total current measured within the gaps (I_{tot}) and the equivalent

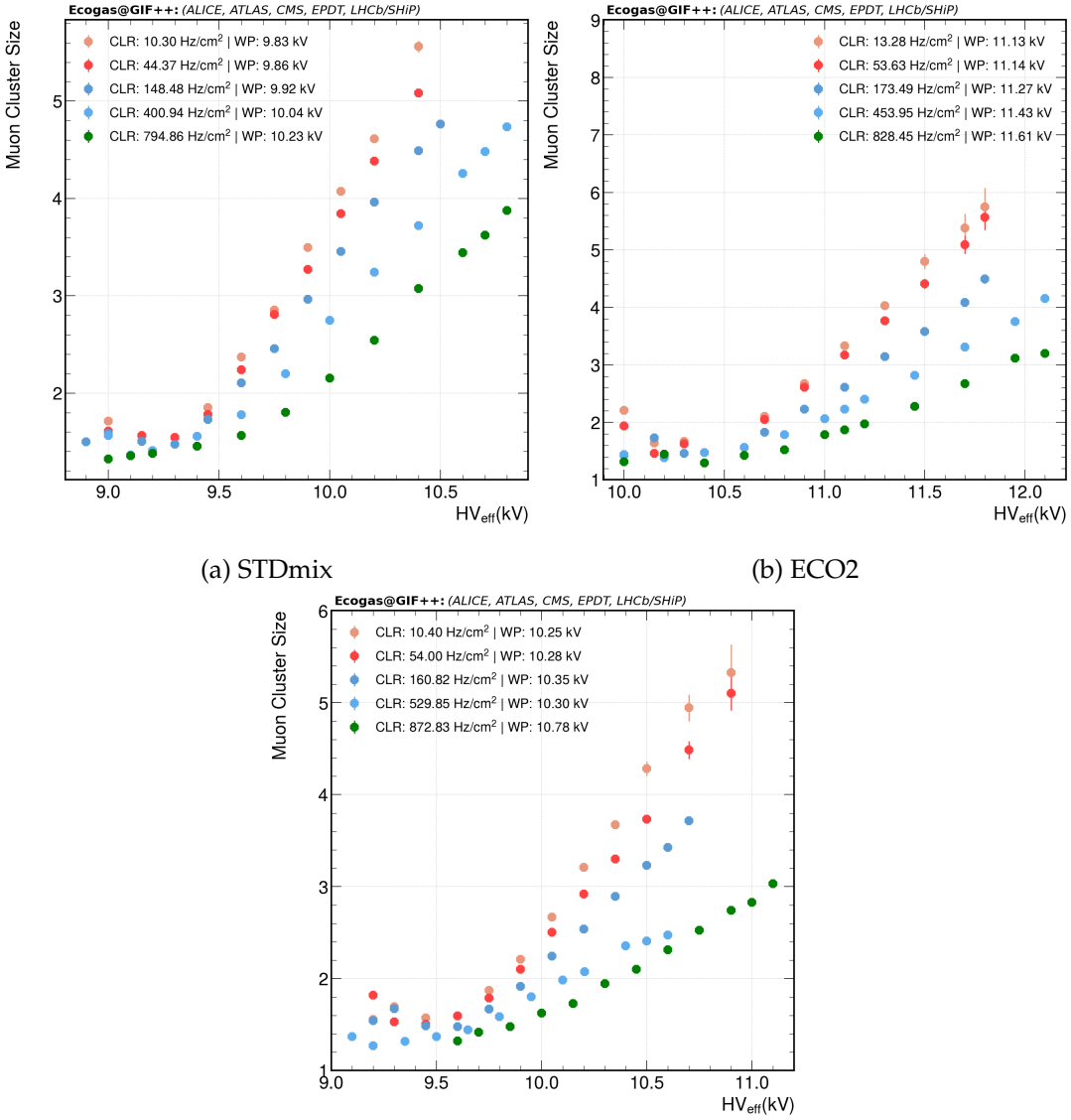

(a) STDmix (b) ECO2

(c) ECO3

FIGURE 4.17: Cluster size as a function of HV_{eff} for the detector tested with three different gas mixtures under varying irradiation rates. Plot (a), (b) and (c) corresponds to STDmix, ECO2 nad ECO3 respectively. The WP as well as gamma cluster rate (CLR) measured at WP in each case is annotated in the plots.

resistance of the electrodes (R_{eqv}). This voltage drop is directly proportional to both the current and the gap resistance. By quantifying this voltage drop, the actual voltage across the gas gap can be derived, obtained by subtracting the voltage drop from the HV_{eff}. This derived voltage is referred to as HV_{gas} [162].

The total current,

$$I_{tot} = I_{TN} + I_{TW} + I_{BOT} \tag{4.4}$$

Where, I_{TN}, I_{TW} and I_{BOT} are the current monitored in the TN, TW and BOT gaps of CMS RE1/1 chamber respectively.

The equivalent resistance,

$$R_{eqv} = \frac{R_{TN} \cdot R_{TW} \cdot R_{BOT}}{R_{TN} \cdot R_{TW} + R_{TW} \cdot R_{BOT} + R_{TN} \cdot R_{BOT}} \tag{4.5}$$

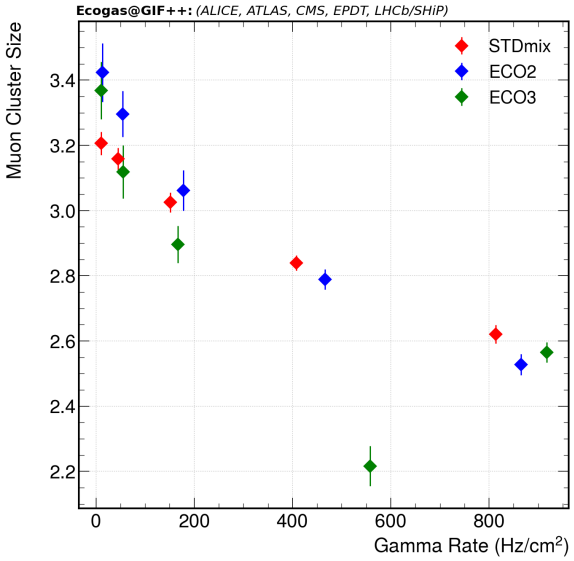

FIGURE 4.18: Cluster size measured at the working point for the three gas mixtures with respect to the measured gamma rate. As the gamma rate increases, cluster size decreases for all gas mixtures. This decrease is more pronounced in ECO3, closely linked to its reduced efficiency.

To calculate the R_{eqv}, it is considered that all the three gaps are in parallel. The resistance values for each gap, denoted as R_{TN}, R_{TW}, and R_{BOT}, are determined through an Argon scan conducted with the detector. At lower voltages, approximately 2-3 kV, Argon's high Townsend coefficient causes the formation of plasma in the gas gap, effectively reducing the resistance between the electrodes. Beyond this transition voltage, the current increases linearly, and the slope of the current-voltage (I-V) curve provides the electrode resistance [162]. I have performed resistance measurements for the CMS RE1/1 chamber, along with other chambers of the ECOgas@GIF++ Collaboration. Table 4.5 presents the resistance values obtained for the CMS RE1/1 chamber's gaps and the equivalent resistance calculated in this context. After estimating the total current and the equivalent resistance, the HV_{gas} can

Electrode	Resistance (Ω)
TW	3.99×10^7
TN	3.15×10^7
BOT	1.26×10^7
R_{eqv}	7.34×10^6

TABLE 4.5: The resistance values for the CMS RE1/1 chamber's gaps: Top Narrow (TN), Top Wide (TW), and Bottom (BOT) and the equivalent resistance estimated (R_{eqv}) is tabulated. These measurements were derived through an Argon scan.

be estimated using the following equation:

$$HV_{gas} = HV_{eff} - I_{tot} \cdot R_{eqv} \tag{4.6}$$

The efficiency of the chamber with respect to HV_{gas} under various irradiation conditions tested with the three gas mixtures is depicted in the Fig. 4.20. Unlike the plots in Fig. 4.19, most of the curves in all three plots largely overlap. Comparing the plots in Fig. 4.19 with those in Fig. 4.20, it becomes evident that when plotted

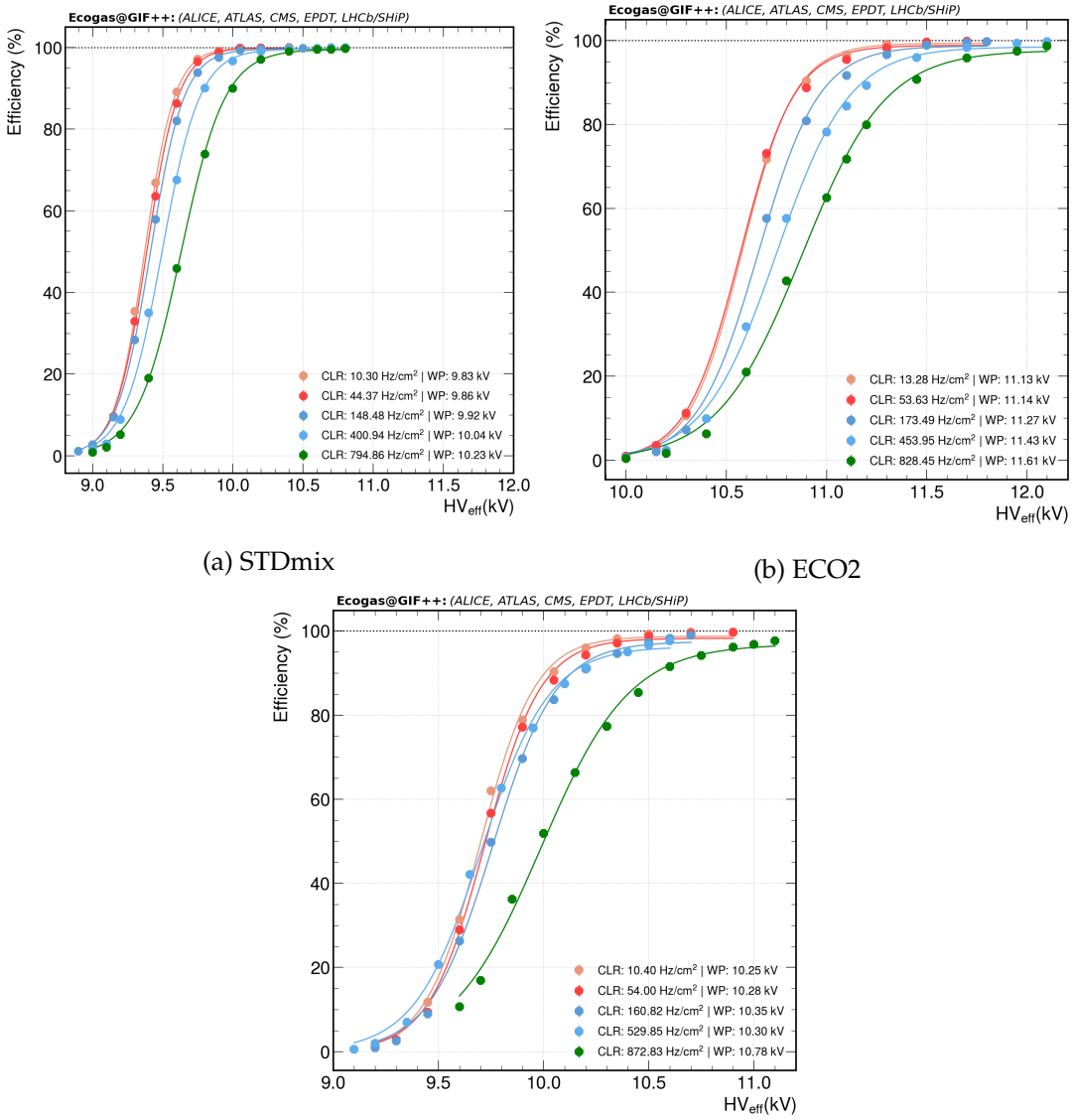

(a) STDmix

(b) ECO2

(c) ECO3

FIGURE 4.19: Muon efficiencies as a function of HV_{eff} for the three gas mixtures tested at different absorption factors. Each curve in the plots represents various gamma rates, with the initial curve showing results for the source-off data and the final curve corresponding to the lowest absorption factor (3.3). The WP of the detector in each case and the gamma cluster rate measured at that point are annotated in the plots.

against HV_{eff}, the efficiency plateau is reached at higher efficiency levels, which is not observed when plotted against HV_{gas}. This difference arises because as HV_{eff} increases, the voltage drop across the electrodes also increases. As a result, the incremental increase in HV_{gas} becomes very small, making it not possible to discern a clear plateau in the HV_{gas} plot at high rates keeping the same x axis conditions of the HV_{eff} case. The points within the efficiency plateau of the HV_{eff} plots are still within the rising section of the efficiency curve in the HV_{gas} plot due to the lower voltage across the gas that the applied voltage, resulting in lower gas gain within the detector.

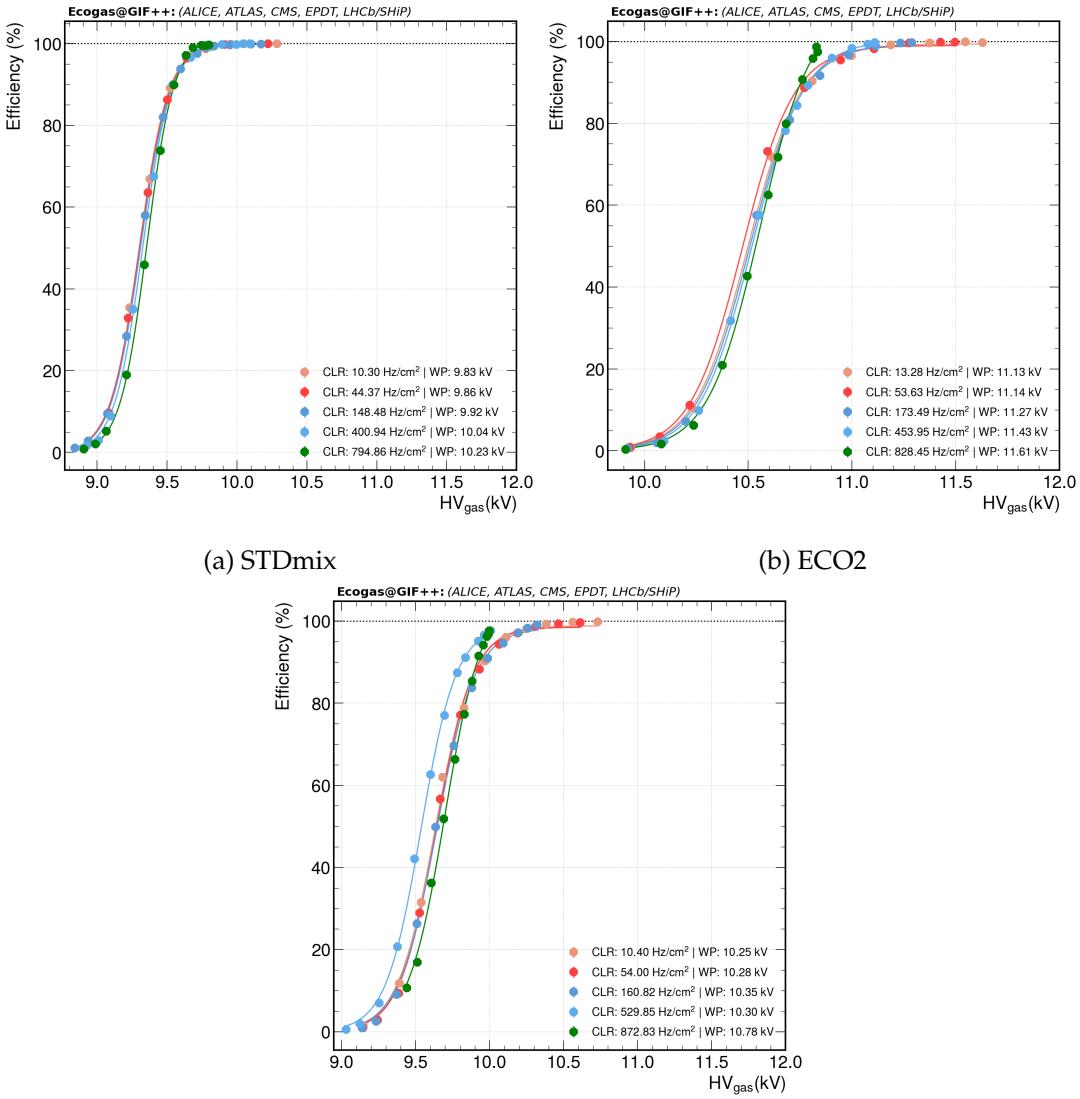

(a) STDmix (b) ECO2

(c) ECO3

FIGURE 4.20: Muon Efficiencies as function of $HV_{gas}(HV_{eff} - I_{tot} \cdot R_{eqv})$ for the three gas mixtures tested at different absorption factors. Each curve in the plots represents various gamma rates, with the initial curve showing results for the source-off data and the final curve corresponding to the lowest absorption factor (3.3). The WP of the detector in each case and the gamma cluster rate measured at that point are annotated in the plots.

In order to conduct a better comparison between the gas mixtures, the muon efficiency is analysed and plotted separately for the source-off condition and each absorption factor for the three gas mixtures. Figure 4.21 illustrates the efficiency as a function of HV_{eff} for the three gas mixtures under the source-off condition. The distinctive shifts in the efficiency curves reveal the differences between the gas mixtures. Notably, the difference in WP is 1.3 kV between STDmix and ECO2 and roughly 0.42 kV between STDmix and ECO3. Consequently, the difference in the working points (WP) between ECO2 and ECO3 is approximately 0.9 kV. So, it becomes evident that reducing the HFO percentage in the mixture from 35% to 25% results in a nearly 9% reduction in the WP.

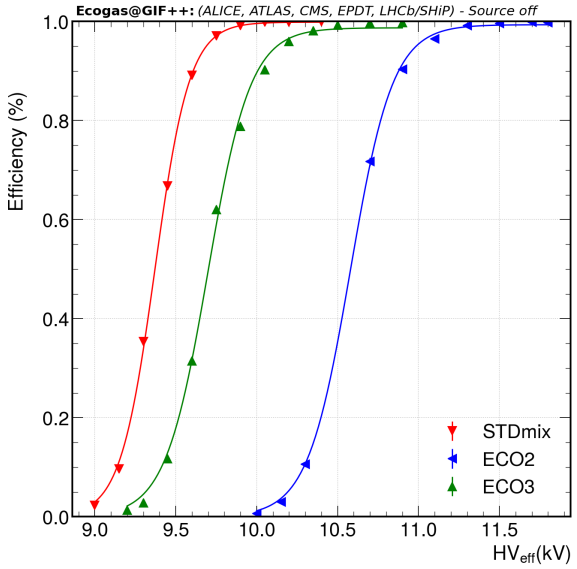

FIGURE 4.21: Muon efficiencies as a function of HV_{eff} for the three gas mixtures under source-off conditions.

The comparison plots of efficiency measurements for the three gas mixtures under four different irradiation conditions are depicted in Fig. 4.22. The subplot captions indicate the absorption (ABS) values of the gamma source, which are also annotated within the plots. Notably, while the WP is consistently shifted as the gamma rate increases, the difference in WP between STDmix and ECO2, as well as STDmix and ECO3, remains within a similar range with a very slight increase. Specifically, at the maximum rate (ABS=3.3), the differences in WP between STDmix and ECO2 and STDmix and ECO3 are 1.38 kV and 0.55 kV, respectively. Observing the efficiency curves in all the cases, including the source-off case, reveals that as the gas mixture's density increases, achieved by raising the HFO percentage, the maximum efficiency tends to align more closely with that of the STDmix (ECO2 consists of 10% more HFO than ECO3). This trend is more pronounced in Fig. 4.23, which displays efficiencies calculated at the working points (WP) corresponding to the three gas mixtures as a function of the measured gamma rate.

The results clearly demonstrate that as the gamma rate increases, the difference in efficiency at WP for STDmix and ECO2, as well as for STDmix and ECO3, grows. Up to a rate of 200 Hz/cm^2, these differences remain relatively small, but they become more significant as the rate reaches approximately 1000 Hz/cm^2. In general, the efficiency at the WP of ECO3 is lower than that of ECO2. Notably, the third point for ECO3 deviates from the trend, indicating a need for further investigation in upcoming test beams to better define this point.

4.6 Ageing Studies with ECO2

Conducting an ageing campaign is a fundamental step in the certification of a gas mixture for Detectors. RPCs operating at the LHC are subjected to extended periods of irradiation. Thus, to consider replacing the standard gas mixture, it is important to thoroughly examine the effects on detectors operating with alternative gas mixtures over prolonged durations. Common ageing effects include increased

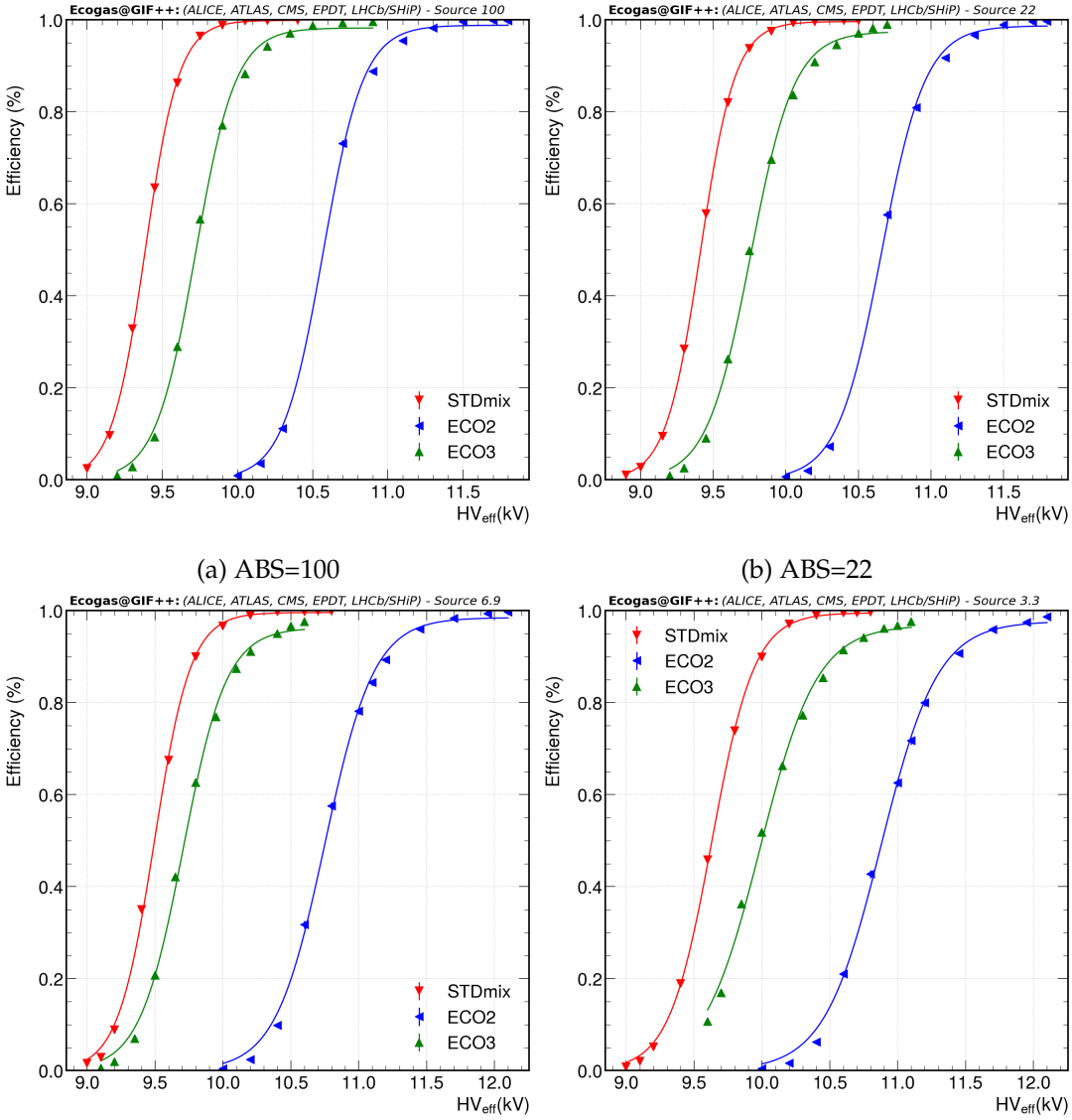

(a) ABS=100

(b) ABS=22

(c) ABS=6.9

(d) ABS=3.3

FIGURE 4.22: Comparison plots of efficiency measurements for the three gas mixtures under four different irradiation conditions. The subplot captions provide information about the absorption (ABS) values of the gamma source, which are also annotated within the plots. Remarkably, while the working point (WP) consistently shifts as the gamma rate increases, the difference in WP between STDmix and ECO2, as well as STDmix and ECO3, remains within a similar range with a minimal increase. Analysing the efficiency curves, including the source-off case (refer Fig. 4.21), reveals that as the gas mixture's density increases, by increasing the HFO percentage (ECO2 contains 10% more HFO than ECO3), the maximum efficiency tends to align more closely with that of the STDmix.

dark current, elevated noise rates, and a reduction in detection efficiency over time. These deteriorations primarily result from the production of impurities within the gas gap. Upon examination of the RPCs after a long term irradiation, both macroscopic and microscopic imperfections on the electrodes, as well as traces of polymer deposits, are observed. Ageing is a complex process, involving multiple simultaneous chemical reactions, making it challenging to understand the underlying mechanisms fully [79]. For more in-depth information on the ageing effects of RPCs, the reader is referred to Sec. 2.4.8.

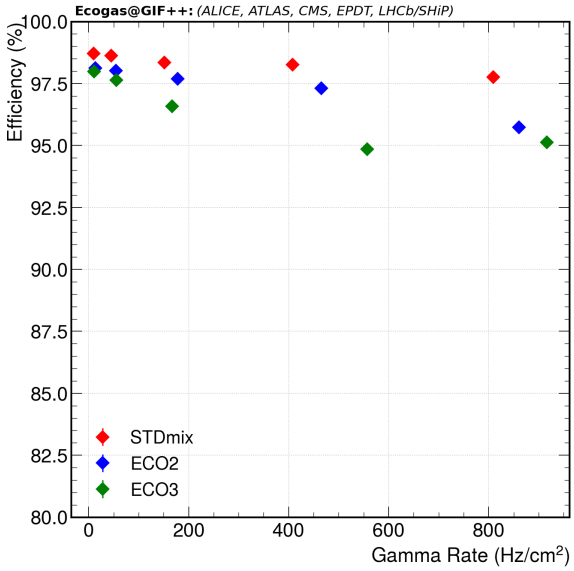

FIGURE 4.23: The efficiencies at the WPs corresponding to three different gas mixtures (STDmix, ECO2, and ECO3) as a function of gamma rates. As the rate rises, the efficiency difference between STDmix and ECO, as well as STDmix and ECO3, becomes more prominent, particularly beyond 200 Hz/cm^2. Despite ECO3 having a lower WP than ECO2, the efficiency at ECO3's WP consistently remains lower than ECO2's.

The ECOgas@GIF++ Collaboration initiated a series of ageing campaigns in 2019 to investigate potential ageing effects associated with both the STDmix and ecogas mixtures. The list of the gas mixtures and the details are given in Tab. 4.3. Testing with the STDmix served as a reference for facilitating comparison studies. As previously detailed in Sec. 4.5, the first gas mixture considered, ECO1, did not yield promising results. Consequently, the ageing campaign began with ECO2, chosen over ECO3 due to ECO2's higher efficiency, which closely approached that of the STDmix, despite ECO2 exhibiting a greater shift in the WP. This choice was consistently validated through the results obtained from the 2021, 2022, and 2023 test beam studies. In July 2022, the ECOgas@GIF++ Collaboration launched the ageing campaign with ECO2 and the findings from nearly a year-long ageing campaign are presented in this section.

It is also noteworthy to investigate the ageing effects of ECO3, given its lower WP and an efficiency exceeding 95% even at high irradiation rates, as indicated in Sec. 4.5.4. Thus, the collaboration will conduct an ageing campaign with ECO3 in the upcoming years, to facilitate comparisons with both the STDmix and ECO2.

4.6.1 Experimental Setup

The ECOgas@GIF++ Collaboration is conducting the ageing campaign using the ECO2 gas mixture at GIF++. The campaign involves all the detectors listed in Tab. 4.1. The detectors are installed on two trolleys, T1 and T3, positioned at distances of 6 m and 3 m from the ^{137}Cs source, respectively. Additional information regarding the experimental setup, gas system, detector geometry, power supply, and other relevant details have been previously discussed in Sec. 4.4.

The primary objective of this study was to investigate the long-term stability of detector current when operating all detectors with ECO2 under high irradiation rates for a minimum duration of one year. The high irradiation rates available at the GIF++ facility (ABS values less than five), exceeding those anticipated for the HL-LHC, will significantly accelerate the ageing process. This acceleration enables the attainment of results within relatively short time frames, typically ranging from one to two years.

Since the detectors are positioned on two trolleys at varying distances from the source, the gamma rates they experience differ. To ensure more accurate comparisons of the results obtained from all detectors, measurements of the actual gamma ray doses at both trolley locations were taken. This was accomplished using a dosimeter, model MIRION RDS-31iTx S/R [163]. The dose measurements were taken at the 3 m and 6 m positions as functions of the ABS values and are illustrated in Fig. 4.24 [155]. The plot clearly indicates that as the ABS value increases, the absorption dose decreases. Notably, the dose also decreases significantly when moving from 3 m to 6 m at a specific ABS value.

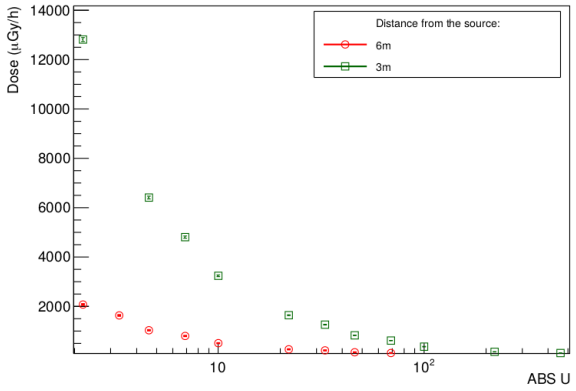

FIGURE 4.24: Dose measurements at two trolley locations (3 m and 6 m from the ^{137}Cs source) at the GIF++ bunker as functions of ABS values [155].

4.6.2 Data Collection and Analysis

For the ageing studies, the data collection primarily involves recording the current absorbed while operating the detectors at the respective WPs chosen. The absorption values at GIF++ is usually set to 2.2 or 4.6, which was decided together with the GIF++ team. Continuous gas flushing is maintained, with each detector receiving a gas flow rate of 1 vol/hour. Environmental parameters, including pressure and temperature within the bunker, are constantly monitored to enable PT corrections to maintain stable HV supply. Current is measured using the CAEN HV modules of each system, detailed in Sec. 4.4.2. These parameters, which encompass HV, absorbed current, temperature, pressure, gas flow, source status, and more, are stored in a centralised database and monitored through the Graphana live monitoring system, explained in Sec. 4.4.4. To support the extended duration of data collection during the ageing campaign, Grafana's alarm feature proves highly beneficial. In cases of major issues, such as changes in gas composition due to the depletion of certain gases, Grafana sends alerts to all users. Furthermore, Grafana is integrated with WEBDCS, allowing it to send a kill command to WEBDCS in such situations.

This command terminates all ongoing data collection and powers down all operating detectors. In the following paragraphs of this section, different types of data collected for the ageing studies and the important parameters considered for the analysis are explained.

Stability Run: A stability run is a continuous data taking process during which the detector operates under irradiation. The absorbed current, high voltage (HV) readings and the time of each measurement in epoch time format are recorded every 30 seconds. Typically, a stability run has a maximum duration of six days.

Source-Off Scan: Every Wednesday, the gamma source at GIF++ is turned off. On these days, a source-off high-voltage (HV) scan is performed as a reference scan for the week's stability run. During this scan, the current is measured at 21 voltage points. The voltage ranges from 0 to specific maximum values depending on the type of chamber: between 11,000 and 12,000 V for ALICE, ATLAS, CMS, and EPDT chambers, and between 9,500 and 10,000 V for the SHiP chamber. This scan essentially provides the I-V curve without any irradiation effects.

Current and Current Density: All detectors, except for the CMS RPC (RE1/1), are single-gap RPCs. Therefore, the recorded current corresponds to a single gap's current, and the current density (J_{mon}) is calculated by dividing the current by the active area of the detector. In the case of the CMS RPC, which is a double-gap RPC consisting of three parts (TW, TN, BOT) as explained in Sec. 4.5.1, the total current and total current density are computed using the currents measured in these three gap regions (total current: Eqn.4.4 and total current density: Eqn.4.1). The current density is mainly studied as it allows for a meaningful comparison across all detector systems, given their varying active areas and geometries. More information regarding the gaps and active areas of each detector is provided in Tab. 4.1.

Integrated Charge: Typically, when evaluating long-term current measurements, the integrated charge (Q_{int}) over time is analysed, expressed in units of mC/cm^2. This parameter represents the integral of current within the detector over time, considering a unit area. In simpler terms, it reflects the average current density accumulated in the detector over a specific time period.

The integrated charge is calculated using the following equation:

$$Q_{int} = \int_{t_i}^{t_f} J_{mon}\, dt \tag{4.7}$$

Where t_i and t_f are the start time and end time respectively.

The current, current density, and the integrated charge over time were studied using the data collected during the one-year irradiation campaign with the ECO2 gas mixture. The results of this analysis are presented in the following section.

4.6.3 Results

This section presents all the results obtained from the 2022-2023 ageing campaign conducted by the ECOgas@GIF++ Collaboration.

4.6.4 Current/Current Density

Figure 4.25 illustrates the current/current density as a function of time for all the RPCs in the ECOgas@GIF++ Collaboration. Each subplot's caption contains the name of the corresponding RPC. In each case, HV values in the ohmic region (3 and 4 kV) and two HV values near the WP are selected. The presented current/current density data is obtained from source-off scans conducted over the course of one year, reflecting the current monitored when the gamma source is not present. The gaps in the plots indicate periods when the detector was offline for maintenance or troubleshooting.

The data presented covers data up to September 2023 for all detectors except the EPDT chamber. Due to high currents observed in the EPDT chamber, as seen in the corresponding plot, the detector was replaced with a new one in April 2023. In general, it's evident that for all chambers, especially at higher HV points, the current/current density has increased over time. However, in the case of the

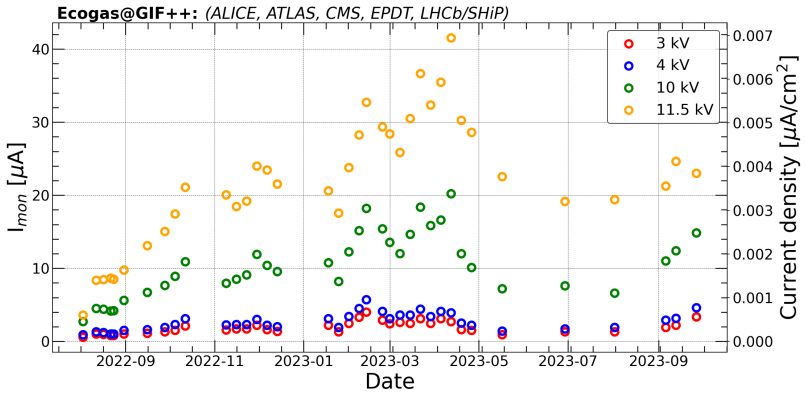

(a) CMS RE1/1

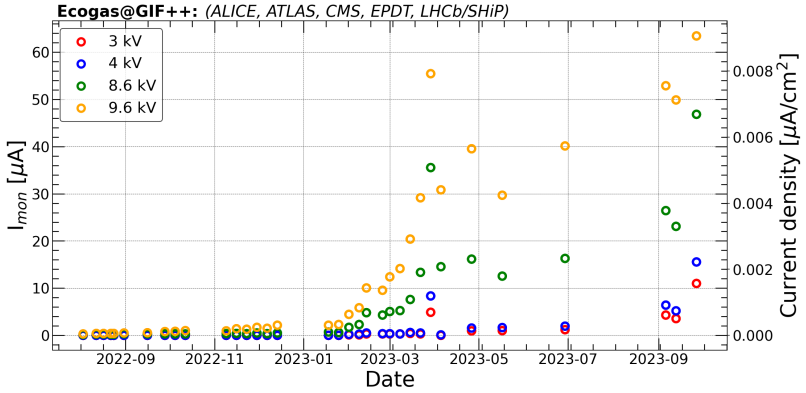

(b) SHiP 1-6

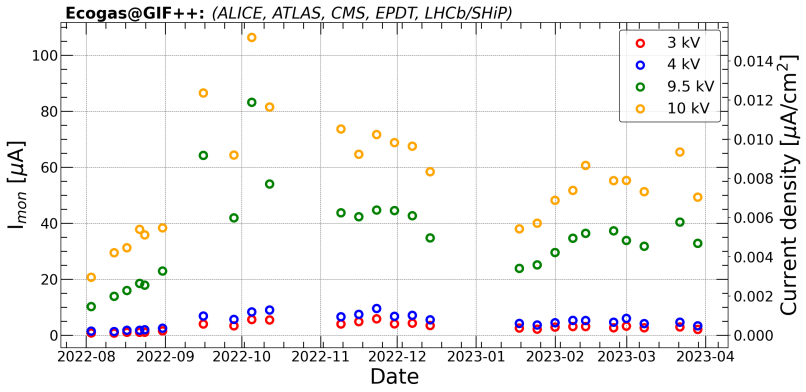

(c) EPDT-RPC6

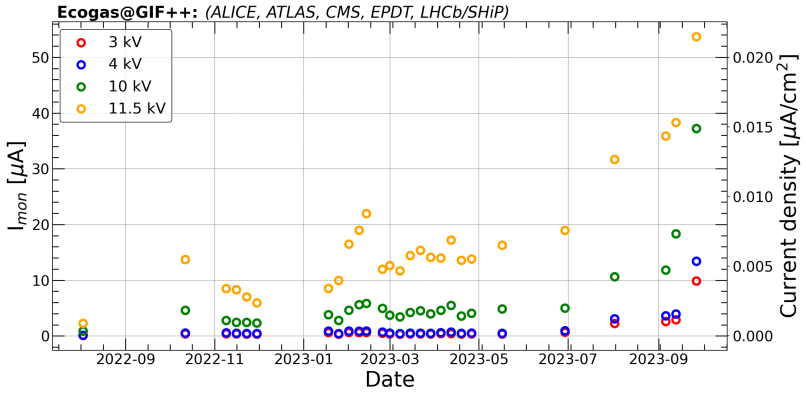

(d) ALICE-2-0

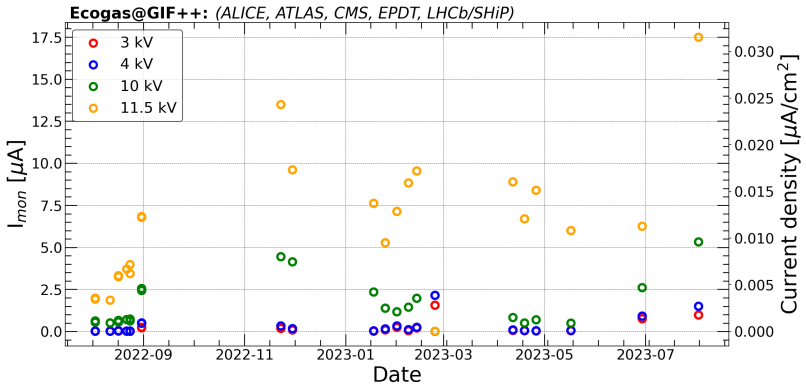

(e) ATLAS-small

FIGURE 4.25: Current and current density as a function of time for the RPCs of the ECOgas@GIF++ Collaboration. Each subplot corresponds to a specific RPC, with sub captions indicating their names. The data in each case includes HV values within the ohmic region (3 and 4 kV) and two HV values close to the WP. The presented current/current density data is derived from source-off scans conducted over the course of one year (2022-2023), reflecting the current monitored in the absence of the gamma source. Gaps in the plots represent periods when the detector was offline for maintenance or troubleshooting.

CMS RE1/1 RPC, the current/current density at the two higher HV points fluctuated over time instead of showing a consistent increase. As a response to this behavior, the detector underwent various treatments, including continuous flushing without irradiation and flushing the gas at a slightly higher rate to remove impurities. These treatments temporarily reduced the current/current density after May 2023 but appeared to increase again gradually.

The ShiP 1-6 RPC exhibited stable current/current density at all four HV points during the first six months. After that, mainly in the higher HV points, the current/current density started increasing more exponentially than linearly. This behavior seems to be more related to a detector issue than ageing.

In the case of the EPDT-RPC6 chamber, the current/current density at the high HV points increased in the initial months and then remained relatively stable until April 2023. However, the current/current density observed at these points was very high and not suitable for the detector's operation. Hence the detector was removed.

For the ALICE chamber, the current/current density at 10 kV remained stable until July 2023 and then started gradually increasing. At 11.5 kV, the current/current density showed an increase from the beginning with slight fluctuations, and the rate of increase escalated after July 2023.

As for the ATLAS-small chamber, the current/current density trend at 10 kV resembled that of the ALICE-2-0 chamber. However, at 11.5 kV, the current/current density exhibited significant fluctuations. The lower number of data points for the ATLAS-small chamber is due to various maintenance-related issues, as the chamber was taken out from the tests several times.

In all chambers, the current/current density in the ohmic part remained stable until August 2023 (April 2023 for the EPDT chamber). At the same time some large

fluctuations of the current at the WP need to be investigated. The recent rise in the current/current density in both the ohmic part need to be studied carefully to see if its due to detector or any hardware related issue or a sign of ageing. Study should continue for at least six more months to determine if the current/current density continues to rise.

Figure 4.26 displays the I-V curves of all the tested detectors, using data acquired from source-off scans. Sub-captions of each subplot specify the detector's name. For each detector, one or two source-off scans per month over the one-year period are used for the analysis, and the date corresponding to the scans considered are provided in the legends of all plots. Notably, all curves exhibit ohmic behavior without any fluctuations, with an upward shift in the curves toward higher y-values (current/current density).

This shift is less within the ohmic region and as the ionisation phase begins, the shift between the curves become increasingly significant. While the fundamental message conveyed by Figure 4.26 parallels that of Figure 4.25, it offers a more detailed perspective on the current shift at all HV points. Additionally, it highlights that the observed fluctuations over time are not confined to specific HV points but to the complete ohmic curves.

In case of the CMS RE1/1 chamber, it's evident that the curve with the highest current/current density value does not correspond to the HV scan conducted at the later date. This discrepancy arises from the chamber's history: due to the increased current/current density trend, the chamber was powered off and subjected to gas flushing for almost a month. After the chamber was re-powered, currents decreased significantly (post-May 2023), and the ohmic part nearly aligned with the initial scans. However, the data indicates a gradual increase in current over time.

The rapid increase in current/current density in the SHiP 1-6 chamber is evident in the respective plot. Ohmic curves consistently overlap in the case of scans from the first six months after that the I-V curves starts to shifts to higher y-values.

The EPDT-RPC6 chamber curves appear to follow an order based on the dates but exhibit some intermixing. In case of some scans, the maximum current is exceeding 300 μA. These plots underscore the necessity of replacing the EPDT-RPC6 chamber, as its effects could lead to misinterpretation of ageing results.

Regarding the ALICE-2-0 chamber, comparing the plot to Fig. 4.25 reveals a significant shift to lower current/current density values after the chamber remained un-powered for almost a month following a current increase on October 12, 2022. However, following continuous irradiation, the current/current density gradually increased again.

For the ATLAS-small RPC, the shifts between curves resemble those of other detectors. In this case, although current/current density increases over time, the shifts in the ohmic curves do not strictly align with chronological order and exhibit fluctuations in some instances.

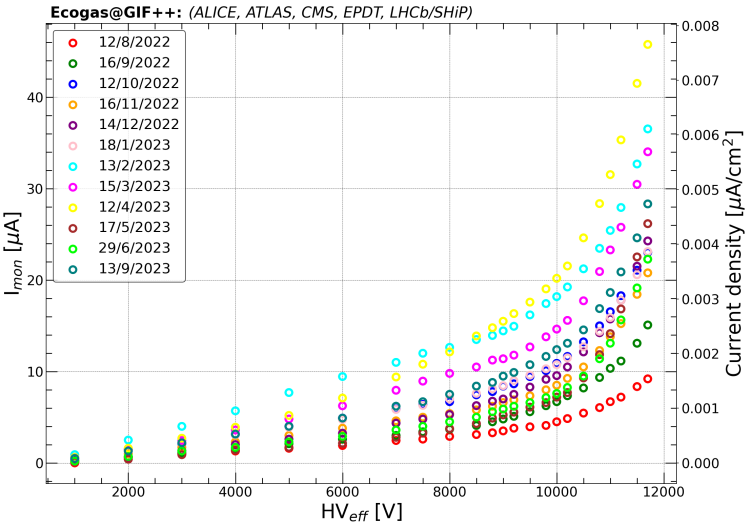

(a) CMS RE1/1

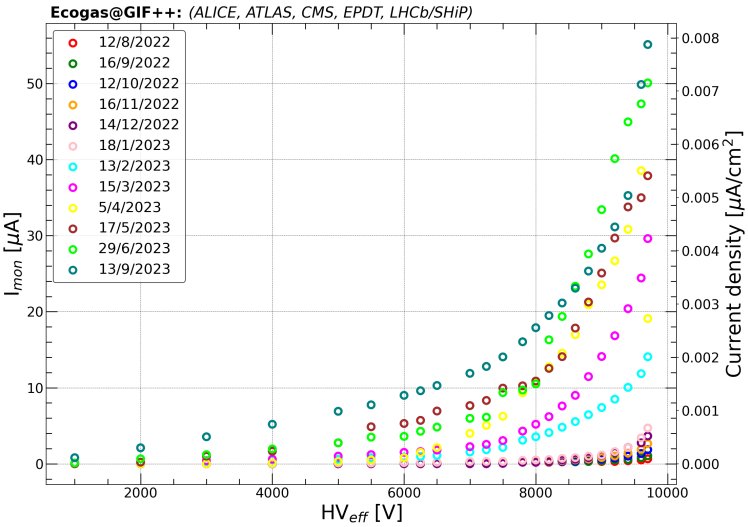

(b)SHiP 1-6

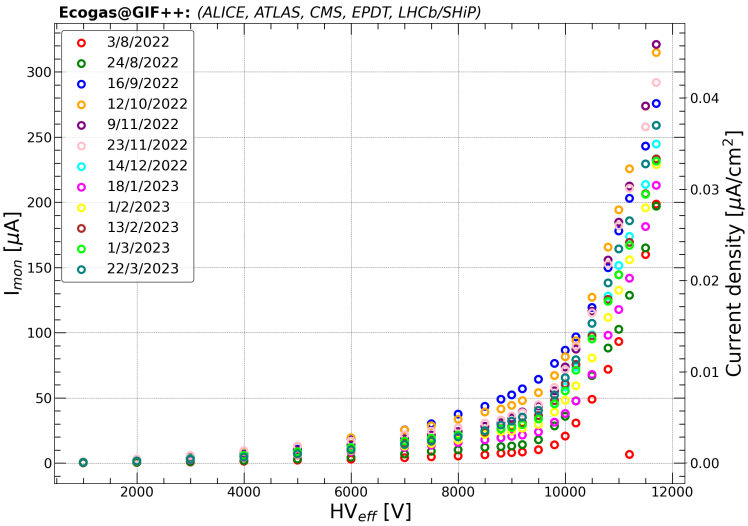

(c) EPDT-RPC6

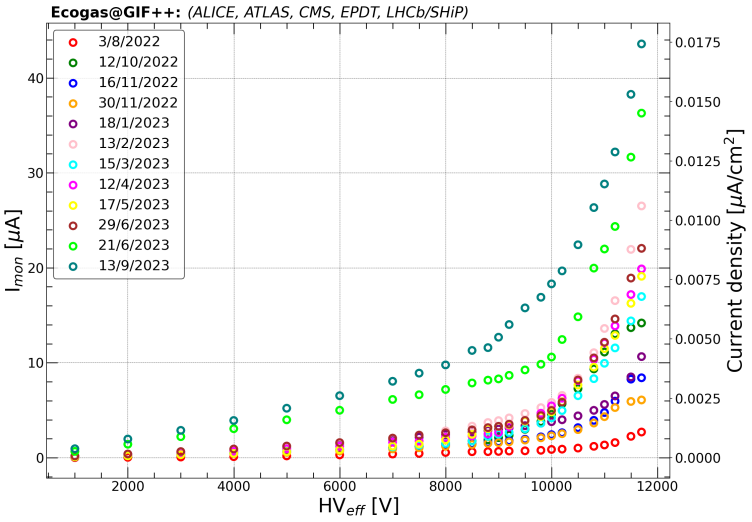

(d) ALICE-2-0

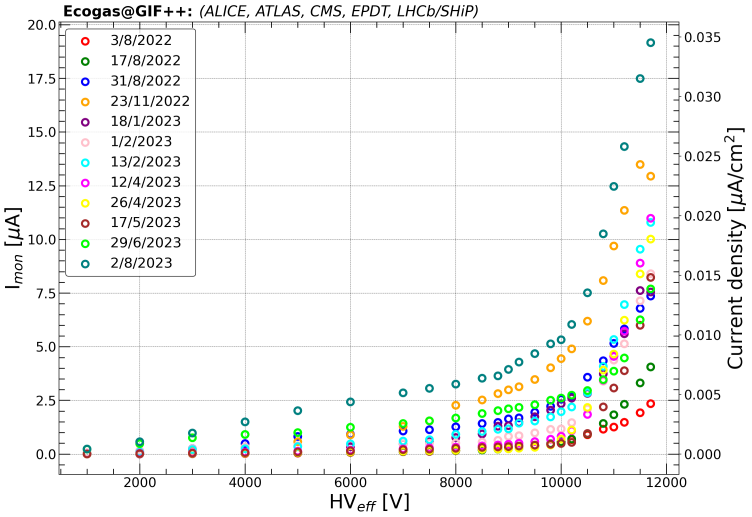

(e) ATLAS-small

FIGURE 4.26: I-V curves for all tested detectors obtained using the data of the source-off scans. Each subplot's caption specifies the detector's name. One or two source-off scans per month during the one-year observation period is considered for the analysis, with corresponding scan dates detailed in the legends of all plots. Notably, all curves exhibit ohmic behavior without any fluctuations, but they display an upward shift towards higher y-values (current/current density values).

4.6.5 Charge Integrated Over Time

The primary objective of the ECOgas@GIF++ Collaboration's long-term irradiation campaign is to accumulate the equivalent charge anticipated under HL-LHC conditions and analyse how detector parameters evolve in response to this integrated charge. This investigation aims to identify any signs of ageing and validate the performance of the RPC systems with ecogas mixtures for prolonged operation in HL-LHC conditions. This section explains the results obtained from integrated charge measurements obtained with operating chambers with ECO2 and the variations observed in key parameters concerning the integrated charge.

The irradiated current in the RPCs is continuously monitored during stability runs. To investigate ageing effects, the current in relation to the integrated charge is compared. Three stability runs conducted during different periods (July 2022, February 2023, and June 2023) of the year, each spanning three to five days of data collection were considered for the study.

The analysis of the variation in irradiated current concerning the integrated charge, is not a very straightforward method. Careful estimation of the ohmic current, present in the irradiated current, is required. If a detector exhibits a significant ohmic component in its dark current, this component is also present in the irradiated current measurements. However, as this ohmic current does not correspond to the charge released in the gas gap, it necessitates subtraction. The correction of the ohmic current in the collected data is applied as follows:

- Each stability run (irradiation run) is associated with a corresponding reference source-off scan to estimate the ohmic current specific to that irradiation period
- A linear fit is applied to the data points up to 5000 V (well below the multiplication threshold) and extrapolated to the WP at which detectors operate during irradiation
- The extrapolated current value is subtracted from the irradiation current measured at the WP during the stability run, yielding the current solely attributable to the ionisation of particles within the gas gap

Figure 4.27 depicts the estimation of the ohmic component for all five detectors, based on one of the source-off scans considered for this study (scan 455: 17th February 2023). Each subplot in the figure corresponds to an individual detector. The blue data points represent the current measurements as a function of the HV_{eff}, while the red line illustrates the extrapolated linear fit.

The estimated ohmic components for all the detectors, derived from the data of reference source-off scans 259, 455, and 483 corresponding to the stability runs 98, 143, and 169, respectively, are summarised in Tab. 4.6. The date corresponding to the scans and the WP of the detector at which the ohmic components are estimated are also tabulated. For most of the detectors, there is a noticeable increase in the ohmic component over time. In scan ID 483 and the corresponding stability run 169, the EPDT-RPC6 chamber is excluded as it was replaced with a new detector in April 2023. In Figures 4.28, 4.29, and 4.30, the current density is displayed as a function of integrated charge for all detectors during scans 98 (3-days; 01/07/2022-04/07/2022), 143 (4.5-days; 17/02/2023-22/02/2023), and 169 (3-days; 12/06/2023 to 15/06/2023), respectively. For the sake of better comparison, current density is used instead of current. In all three figures, blue data points represent the current density, including the ohmic component, while green data points represent the current density after subtracting the ohmic component. Additionally, the WPs at which the detectors operated are marked in each plot. Furthermore, the date corresponding to the start of each scan is also annotated in the plots.

Analysing Fig. 4.28, several key observations emerge. Initially, during the early stages of the ageing campaign with the ECO2 gas mixture, the current density, both with and without the ohmic component, closely aligns for most detectors, with one notable exception—the EPDT-RPC6 chamber. This alignment suggests that, during

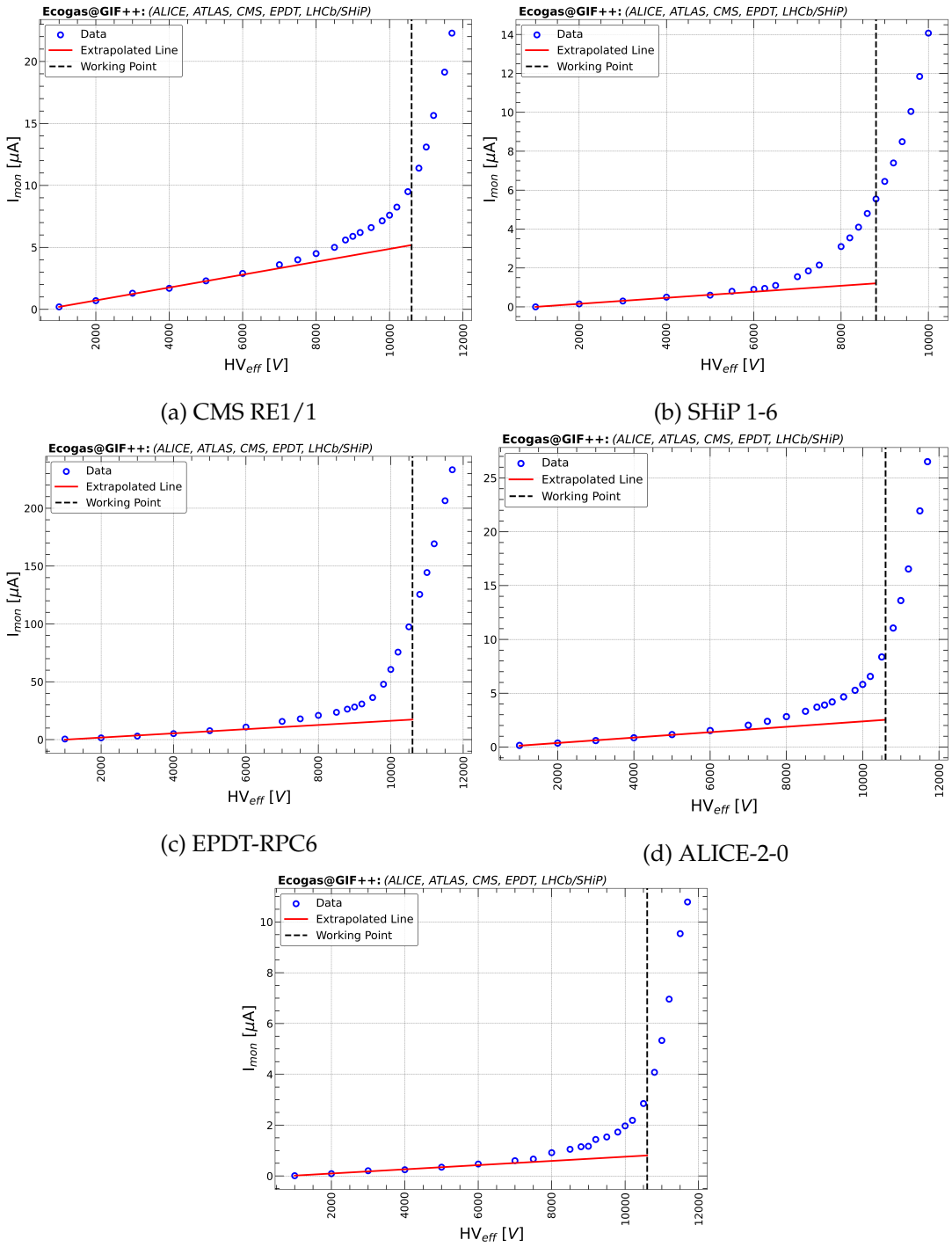

(a) CMS RE1/1

(b) SHiP 1-6

(c) EPDT-RPC6

(d) ALICE-2-0

(d) ATLAS-small

FIGURE 4.27: Estimation of the ohmic component for all five detectors based on a selected source-off scan (scan 455: 13th February 2023) used in the ageing study. Each subplot in the figure corresponds to an individual detector. The blue data points showcase current measurements as a function of HV_{eff}, while the red line represents the extrapolated linear fit.

the three days of irradiation, the ohmic component either remained stable or exhibited minimal increase. Notably, the overlap is excellent across the SHiP 1-6 and ATLAS-small detectors.

Detector	Scan ID	Date	Working Point (V)	Ohmic Component (μA)
CMS RE1/1	259	01/07/2022	10600	2.41
	455	13/02/2022	10600	16.91
	483	14/06/2023	10600	5.19
SHiP-1-6	259	01/07/2022	9600	0.01
	455	13/02/2022	9600	1.21
	483	14/06/2023	8800	5.15
EPDT-RPC6	259	01/07/2022	10600	20.74
	455	13/02/2022	10600	17.33
ALICE-2-0	259	01/07/2022	10600	0.36
	455	13/02/2022	10600	2.53
	483	14/06/2023	10600	2.66
ATLAS-small	259	01/07/2022	10600	0.04
	455	13/02/2022	10600	0.81
	483	14/06/2023	10600	2.17

TABLE 4.6: The estimated ohmic components for all the detectors, derived from the data of reference source-off scans corresponding to the stability runs 98, 143, and 169. The scan ID within the WEBDCS system, the corresponding date, and the WP of each detector are also given. There is a noticeable increase in the ohmic component of most of the detectors over time.

Conversely, the EPDT-RPC6 chamber presents a significant difference between the current density with and without the ohmic component. This discrepancy hints at an increase in the ohmic component when the chamber is under irradiation, even during the initial campaign phase. It is worth considering that this discrepancy may be attributed to pre-existing defects within the chamber rather than being a direct result of ECO2 irradiation. Otherwise, the effect should be observable for all detectors, which is not the case.

The noticeable drop in current density observed at the beginning and end of the irradiation run for all detectors can be attributed to shifts in the source's status. Specifically, the source underwent multiple on/off cycles at the beginning of the run and similarly experienced another cycle as the run concluded. The status of the source during the scan corresponding to Fig. 4.28 is shown in Fig. 4.31-(a).

During the 3-day irradiation run conducted in the initial phase of the ageing campaign, the CMS RE1/1, SHiP 1-6, EPDT-RPC6, ALICE-2-0, and ATLAS-small chambers integrated approximately 3.7, 0.95, 5.2, 2.4, and 6.2 mC/cm^2 of charge, respectively.

Regarding Fig. 4.29, there is a significant increase in the difference between current density with and without the ohmic component, particularly evident in CMS RE1/1, ALICE, and ATLAS chambers. Conversely, the EPDT-RPC6 chamber shows a consistent difference, while the SHiP 1-6 chamber exhibits only a slight variation compared to the run in Fig. 4.28.

The stability run (143) corresponding to Fig. 4.29 was taken nearly after six months of irradiation period operating chambers with ECO2 gas mixture. The results clearly

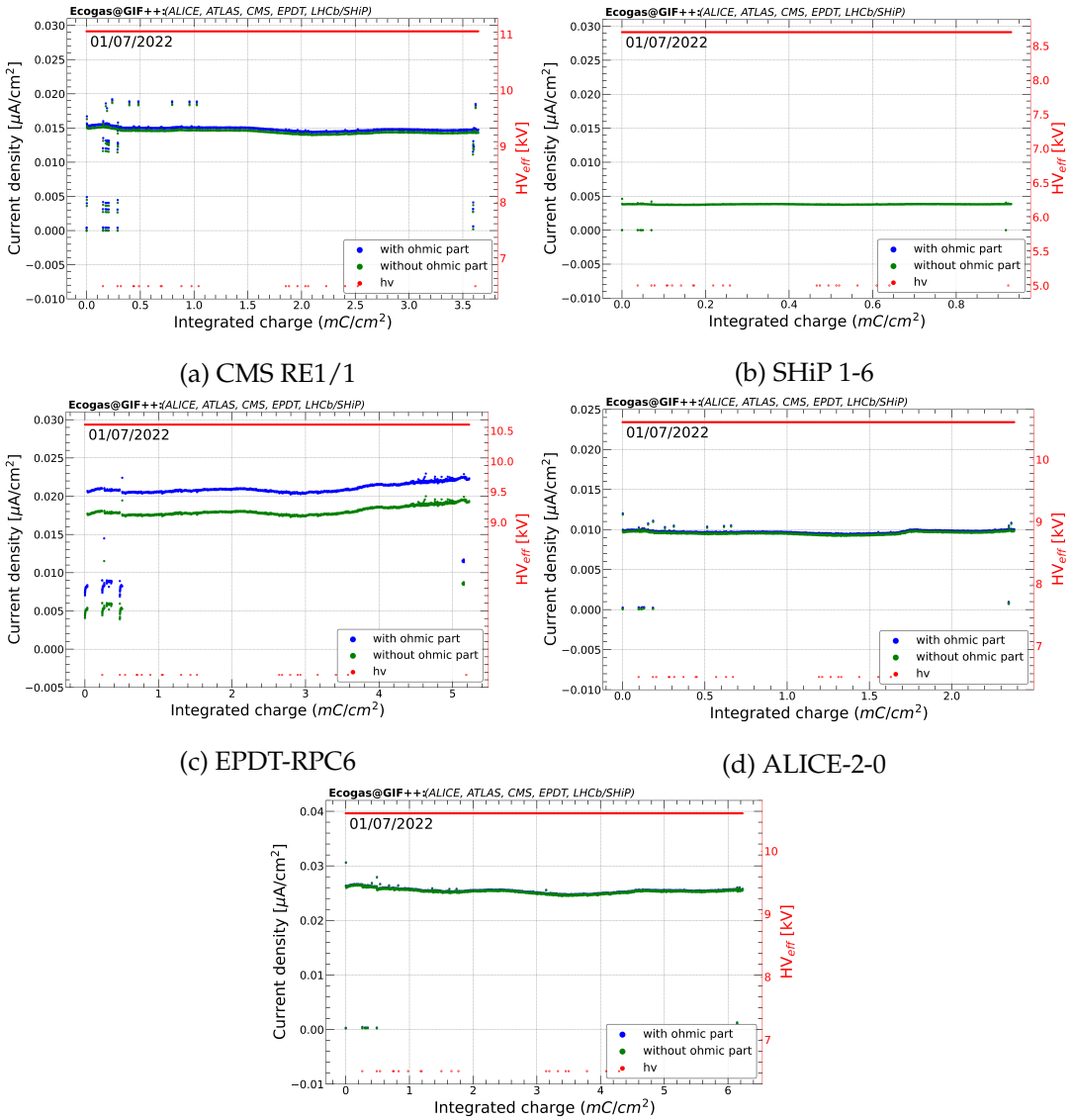

(a) CMS RE1/1

(b) SHiP 1-6

(c) EPDT-RPC6

(d) ALICE-2-0

(d) ATLAS-small

FIGURE 4.28: Current density, with and without the ohmic component as a function of the charge integrated for all the detector systems, during the irradiation period in the starting period of the ageing campaign of ECO2 gas mixture. Most detectors show a close alignment between current density with and without the ohmic component, suggesting the stability of ohmic current. However, the EPDT-RPC6 chamber exhibits a significant discrepancy, possibly due to pre-existing defects. The red data points in the plots correspond to the WP at which the detectors were operated during the run. The drop in current density at the start and end of the irradiation run is linked to the change in the source status. The data corresponds to the stability run 98 (WEBDCS id) conducted from 01/07/2022-04/07/2022.

indicate that after this extended irradiation period, the ohmic component increases when the chamber is under irradiation. During stability run 143, the source remains constantly active (ABS=2.2), resulting in a steady current and WP without fluctuations. The status of the source corresponding to scan 143 is shown in Fig. 4.31-(b).

During the 4.5-day irradiation run (17/02/2023-22/02/2023) conducted after the first six months of the ageing campaign, the CMS RE1/1, SHiP 1-6, EPDT-RPC6,

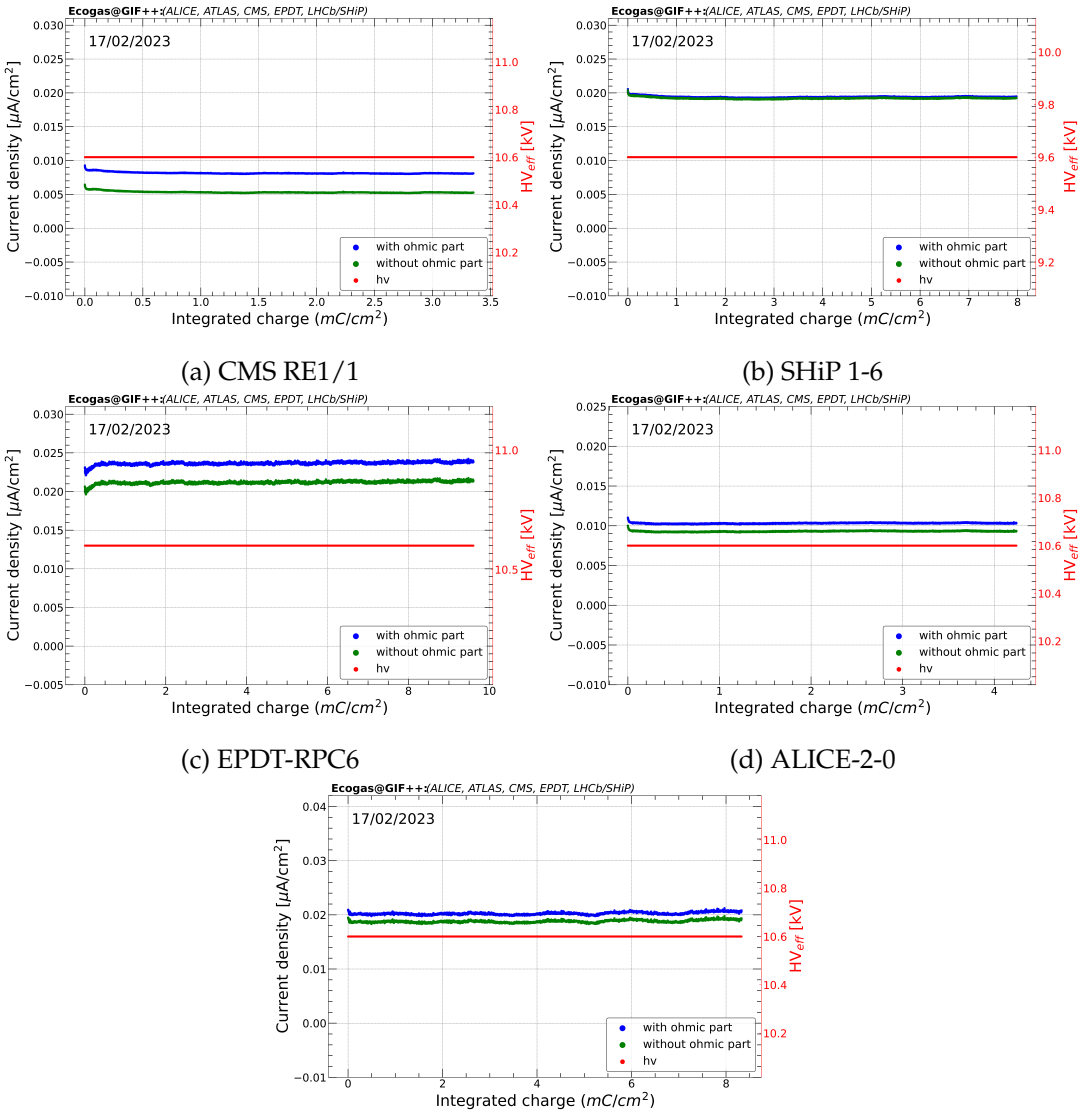

(a) CMS RE1/1

(b) SHiP 1-6

(c) EPDT-RPC6

(d) ALICE-2-0

(d) ATLAS-small

FIGURE 4.29: Current density with and without ohmic components as a function of integrated charge for all the detectors under test. The data corresponds to the 4.5-day (17/02/2023-22/02/2023) irradiation run conducted after approximately six months of the ageing campaign of the ECO2 gas mixture. The source remains constantly active during this period (ABS=2.2), ensuring steady current and stable WPs without fluctuations.

ALICE-2-0, and ATLAS-small chambers integrated approximately 3.3, 8, 8.9, 4.5, and 8.15 mC/cm^2 of charge, respectively.

Figure 4.30 presents the results of a 3-day irradiation run (scan id: 169) conducted from 12/06/2023 to 15/06/2023, following the one-year irradiation campaign during which the detectors were operated with ECO2 gas mixture. The observed fluctuations in both current density and WPs in the plots can be attributed to changes in the source status. During the scan, the source was turned off twice. The periodic fluctuations correspond to the data collected when an HV scan was performed during the first source-off period. The status of the source corresponding to scan 169 is shown in Fig. 4.31-(c).

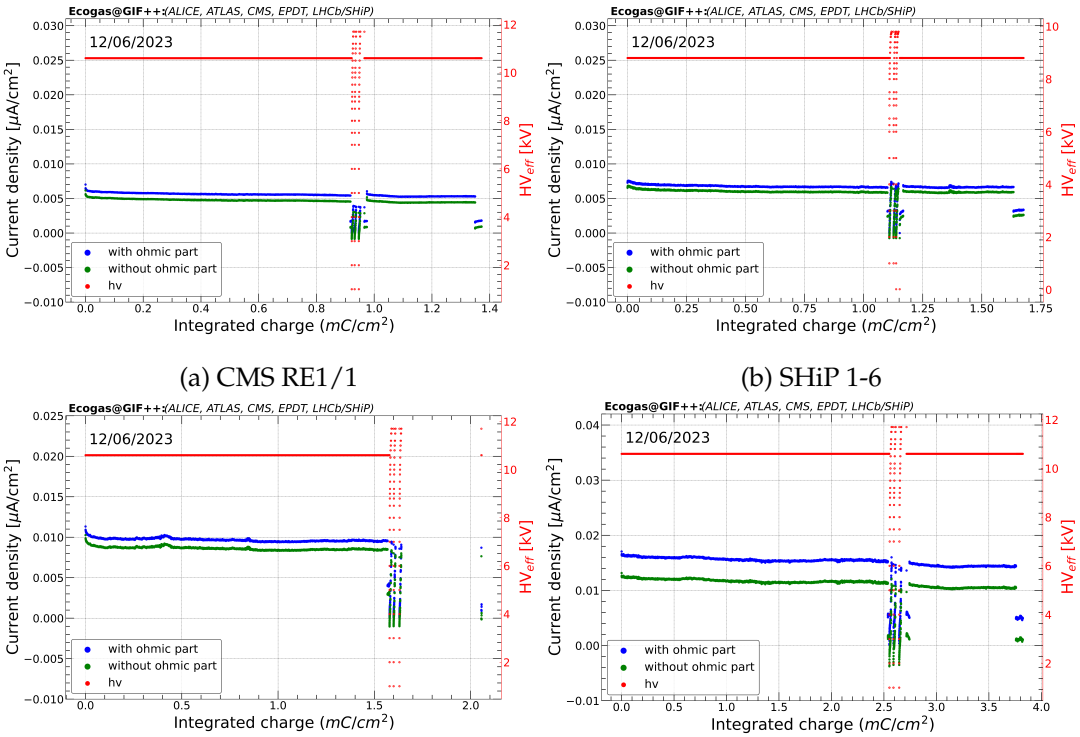

(a) CMS RE1/1

(b) SHiP 1-6

(c) ALICE-2-0

(d) ATLAS-small

FIGURE 4.30: The results of 3-day irradiation run (scan id: 169) carried out from 12/06/2023 to 15/06/2023, following a year-long irradiation period during which detectors operated with the ECO2 gas mixture. The plots illustrate the current density, both with and without the ohmic component, as a function of integrated charge for all detectors in operation during the scan. Distinct fluctuations are noticeable in the current density trends for all detectors due to two source interruptions during the scan and an HV scan performed during the source-off.

In the case of SHiP 1-6, ALICE-2-0, and ATLAS-small chambers, the difference between current density with and without the ohmic component has increased when compared to the results from irradiation runs in the initial and mid-phases of the ageing campaign. For the CMS RE1/1 chamber, both the difference and current density decreased in the last scan compared to the scan conducted six months earlier. This decrease can be attributed to the detector being offline for nearly a month during the period between the last two scans due to necessary repairs. This extended offline period significantly reduced the detector's current (explained in Sec. 4.6.4). The results for the EPDT-RPC6 chamber are not shown for scan 169, as it had been replaced before the scan.

Over time, while the difference between current density with and without the ohmic part widens, it's noteworthy that the current density of all chambers with the ohmic part remains within a similar range over the year. There is no substantial increase in any of the detectors. Additionally, based on the results of the source-off scans for all detectors until September 2023 (see Fig. 4.25), the ohmic part exhibits remarkable stability. So, just the increase observed in the ohmic component over time (in case of stability run) cannot be considered as a sign of ageing. But it is also not something that can be ignored. To precisely understand this effect, further study is required, extending over a longer duration.

(a) Stability Run: 98

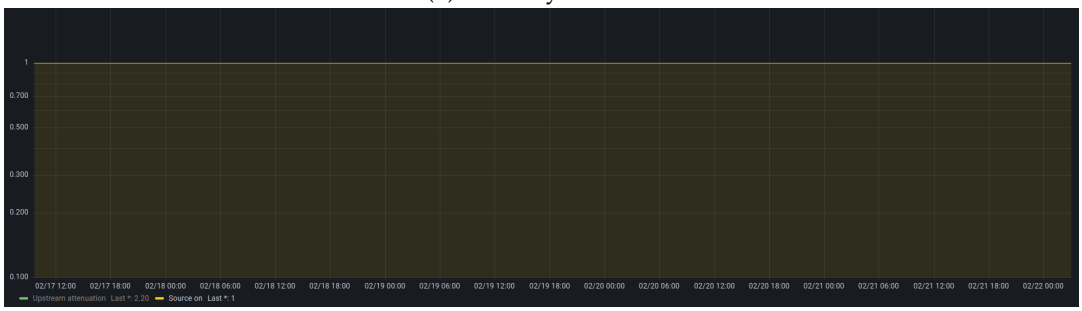

(b) Stability Run: 143

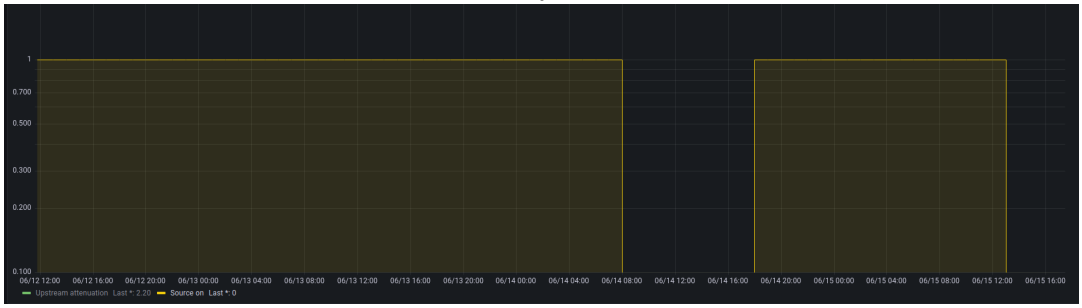

(c) Stability Run: 169

FIGURE 4.31: These plots display the operational status of the ^{137}Cs source at GIF++ during the three stability runs conducted for ageing studies of the ECO2 gas mixture. The scan IDs are given in the sub-captions of each plot. The source status is represented by binary values: '1' indicates the source is active ('on'), and '0' indicates it is inactive ('off'). These plots were generated using the Graphana tool.

The charge integrated by all detectors over the course of the one-year irradiation period has been estimated and is presented in Fig. 4.32. The horizontal parts in the curves corresponds to the time when detectors were powered off. It's important to note that the source activity at GIF++ remains consistently below 5 ABS throughout this period. As a result, all the detectors are exposed to gamma radiation levels at least three times higher than what is expected during HL-LHC operation except in the case of LHCb detector.

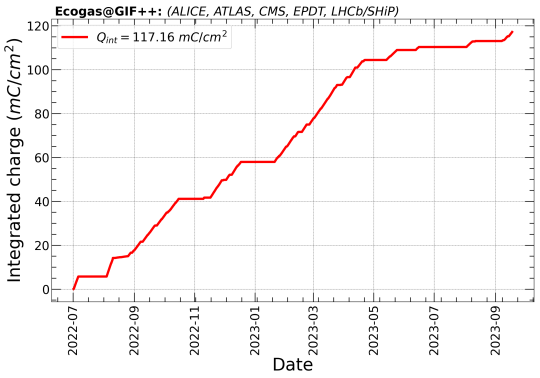

(a) CMS RE1/1

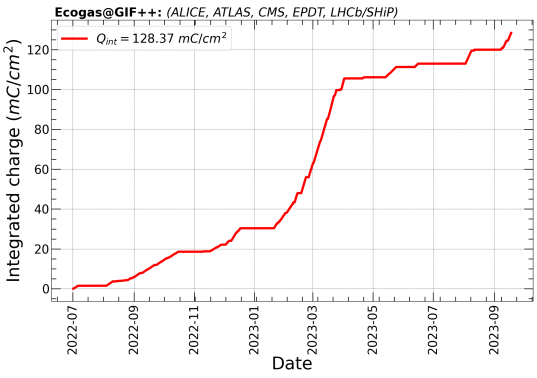

(b) SHiP 1-6

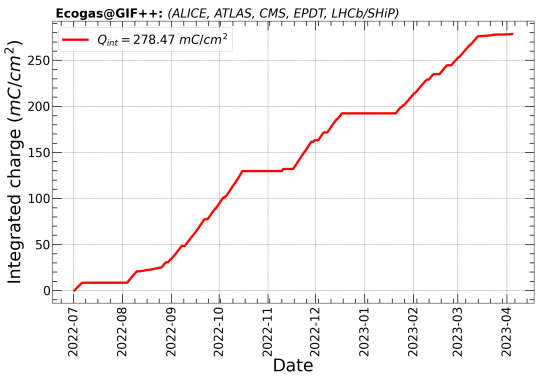

(c) EPDT-RPC6

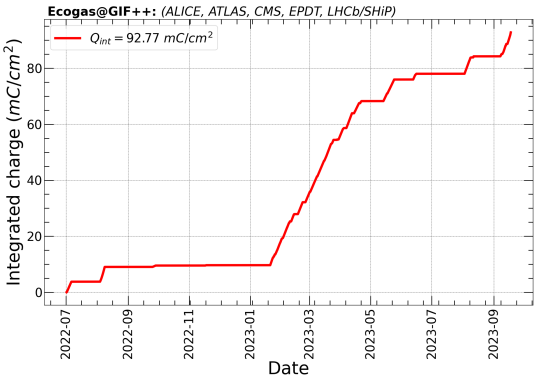

(d) ALICE-2-0

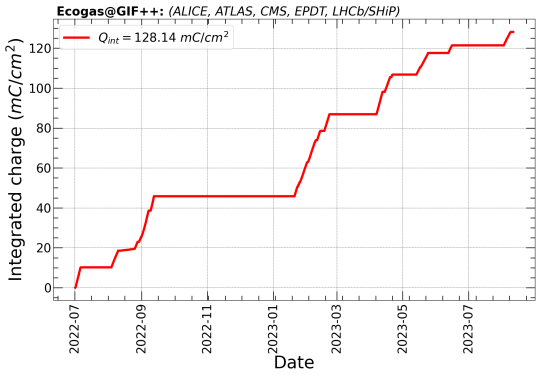

(d) ATLAS-small

FIGURE 4.32: Integrated charge over time for all detectors during the one-year irradiation period with ECO2. Horizontal segments represent periods when detectors were powered off.

In the case of CMS RPCs, the maximum anticipated rate per unit area during HL-LHC is 200 Hz/cm^2, with an expected maximum integrated charge of 280 mC/cm^2

by the end of HL-LHC. However, based on the 2023 test beam data, it is evident that the gamma rate at the WP for ECO2, even at the lowest ABS value tested, is approximately 850 Hz/cm^2. Thus, when the ABS value is below five, the gamma rate for CMS chambers is roughly three times higher than the expected rate during HL-LHC operation [164].

The expected particle rate for ATLAS RPCs during the HL-LHC phase is slightly higher than that of CMS RPCs. Currently, ATLAS RPCs are certified to operate at a rate of 100 Hz/cm^2, with an estimated total integrated charge of 300 mC/cm^2. However, during the HL-LHC phase, the particle rate within the RPC region is expected to increase to around 300 Hz/cm^2, and the final integrated charge is estimated to reach approximately 480 mC/cm^2 [165].

The RPCs at LHCb are situated in the outermost station of the muon system, and the maximum expected rate in these regions is approximately 10 kHz/cm^2, which is significantly higher compared to the RPCs at ATLAS and CMS. The anticipated maximum integrated charge is few C/cm^2 [166].

For the ALICE experiment, the HL-LHC phase won't significantly impact particle rates since the experiment won't have head-on collisions. In the case of ALICE RPCs, particle rates are notably low, with an expected maximum hit rate of approximately 90 Hz/cm^2 and an estimated integrated charge for Run3+Run4 at around 60 mC/cm^2 [154, 167].

All the particle rates and integrated charge values mentioned earlier are in the case where RPCs are operated with the standard gas mixture. However, upon comparing the results in Fig. 4.15, it becomes evident that the current density at high rates for ECO2 is approximately 30-40 % higher than that of the standard gas mixture. Consequently, the integrated charge in the case of ECO2 will also be higher by the same percentage. The total integrated charge for all the detectors is indicated in the respective plots in Fig. 4.32 and is summarised in Tab. 4.7. Analysing the values in

Detector	Q_{int} **(**mC/cm^2**)**
CMS RE1_1	117.15
SHiP-1-6	128.37
EPDT-RPC6	278.46
ALICE-2-0	92.77
ATLAS-small	128.14

TABLE 4.7: Total charge integrated for all detectors during the one year irradiation period with ECO2.

the table, it becomes evident that, for the CMS RE1/1, SHiP-1-6 and ATLAS-small chambers, the total integrated charge during the one-year irradiation campaign is less than 50% of what is anticipated at the end of the HL-LHC period. Although no significant signs of ageing have been observed in the results thus far, it is crucial to continue irradiating and operating the chambers with ECO2 for at least one or two additional years. This extended period is crucial for the thorough qualification of the ECO2 gas mixture for RPC operation at the LHC during the HL-LHC phase. In the case of ALICE-2-0, even though the total integrated charge surpasses what

is anticipated for the end of Run 4, it is advisable to qualify the gas mixture for an integrated charge of at least three times the expected value for safety. Therefore, it is essential to continue testing the ALICE chamber with ECO2 at GIF++.

4.7 Summary and Conclusions

RPCs are gaseous detectors widely used in high-energy physics experiments, particularly for particle tracking and triggering. The environmental impact of the standard gas mixture employed for RPCs is a growing concern, given the high GWP of R134a SF_6. In recent years, the EU has implemented stringent regulations to phase down high-GWP GHGs and reduce their market availability, aiming to achieve one-fifth of 2014 levels by 2030. Although research facilities are not currently prohibited from using these gases, the global phasedown is expected to pose challenges in terms of both availability and cost. Therefore, there is a compelling need to explore eco-friendly alternatives for RPC operations, both to align with regulatory changes and to reduce costs while simplifying material sourcing.

To address these challenges, the ECOgas@GIF++ Collaboration, which includes the ALICE, ATLAS, CMS, LHCb/SHiP, and EP-DT communities, is conducting an extensive R&D program. One prominent alternative under investigation is HFO-1234ze, notable for its remarkably low GWP value of just 6, representing a significant improvement over the conventionally used R134a. RPC detectors with slightly different characteristics and electronics, utilising gas mixtures based on both HFO and CO_2, are being studied at GIF++. The major activities of the collaboration include in-depth evaluations of the performance of the detectors under various irradiation conditions operating with the HFO-based ecogas mixtures and a study of detector ageing by conducting long-term irradiation campaigns.

This chapter provides a detailed overview of the ECOgas@GIF++ Collaboration's work and the major results achieved in recent years focusing on my contributions.

The first three sections of the chapter explore the motivation behind establishing the collaboration for conducting ecogas researches for RPCs. They also provide insight into the details and reasons for choosing HFO-based alternatives.

Section 4.4 offers the overview of the experimental setups of the ECOgas@GIF++ Collaboration at GIF++. This includes details about the gas system, the geometry and technical specifications of all the detectors, the DAQ setup, and the control and long-term monitoring of all the systems.

The performance tests of RPC detectors conducted as part of the ECOgas@GIF++ Collaboration discussed in the thesis focus on the CMS RE1/1 chamber. The Sec. 4.5 summaris the key findings from the 2023 test beam results of this chamber when operated with three different gas mixtures: STDmix, ECO2, and ECO3. The analysis includes the investigation of WP trends, variations in current density, behavior of cluster sizes, and muon efficiency under varying irradiation conditions. Notably, all three gas mixtures display a linear increase in their WPs as gamma rates rise, with ECO2 showing a steeper trend, indicating faster WP growth. In terms of current density, ECO2 and ECO3 exhibit higher values than STDmix at their respective WPs

for rates exceeding 200 Hz/cm^2. Cluster sizes increase linearly with higher voltage in the gas amplification range, with ECO3 often displaying cluster sizes similar to or smaller than STDmix due to its lower efficiency. As gamma rates increase, cluster sizes decrease for all mixtures, with ECO3 experiencing the most significant reduction due to its reduced efficiency. Overall, the findings highlight the growing differences in performance among gas mixtures as gamma rates rise, with ECO3 consistently exhibiting lower efficiency compared to ECO2 and STDmix. The impact of voltage drop across the electrodes on efficiency is also identified as a critical factor.

The 2022-2023 ageing campaign was conducted to investigate the long-term ageing effects of the ECO2 gas mixture when RPC detectors are exposed to high levels of gamma irradiation. This year-long campaign tracked variations in the dark current across all detectors, providing valuable insights into their performance. No evidence of ohmic current increase has been seen so far. At the same time, some large fluctuations of the current at the WP was observed which better investigated. One key observation is the increase in the ohmic component at WP over time. This increase, however, is not uniform across detectors, which hints at potential pre-existing issues in certain chambers. Although the difference between current density with and without the ohmic component widened during different phases of the irradiation campaign, the current density with the ohmic component stayed within a consistent range. Considering all these results achieved, its clear that, there in no clear evidence of ageing in any of the detectors tested. The integrated charge measurements obtained during this year-long campaign are lower than the anticipated values for the HL-LHC period. So, it is crucial to continue testing and monitoring the chambers with ECO2 for at least one or two additional years to study ageing effects and ensure the qualification of the gas mixture for RPC operation during the HL-LHC phase.

Part II

Cosmic Rays for Imaging: Muography

Chapter 5

Fundamentals of Muography

5.1 Introduction

Muon radiography also refereed as muography is an imaging method that uses cosmic-ray muons to study the interior structure of natural or man-made large-scale objects. This technique exploits the penetration capability of muons, with imaging executed through measurements of muon absorption profiles during their traversal through materials. The roots of muography trace back to E.P. George's 1955 endeavor, where he employed a Geiger detector to measure the overburden of a tunnel within the Snowy Mountains Hydroelectric Scheme (Australia) [168]. Pioneering advancements by Alvarez in 1975 marked a significant milestone, producing the first muographic image of the Chefren pyramid [169]. This breakthrough not only validated the viability of muography for probing large structures but also opened up new possibilities for archaeological research, offering a unique perspective into the hidden mysteries of ancient structures.

Since the 1990s, muography has seen widespread applications across diverse domains [170, 171], including volcanology [172], archaeology [173], geosciences [174], nuclear waste characterisation [175], etc. More recently, an emerging technique in muography involves muon deflection and is known as muon tomography. In muography, detectors are positioned on one side of the target to measure the absorption of the muons in the matter and the measured number of muons is used to estimate the density distribution within the target. In muon tomography, used for relatively smaller objects (thickness not exceeding tens of meters), detectors capture muons before and after they enter the target, and the subsequent analysis involves studying muon scattering or deflection. Muon tomography finds applications in border controls [176], nuclear warhead verification in the context of nonproliferation treaties [177], and industrial monitoring and maintenance [178].

The choice of detector technologies for muography depends on factors such as the size and density of the targets, practical considerations such as the required resolutions, experimental budgets and planned durations. This results in a diverse range of muon detectors, tailored to specific applications in the field of muography.

Since this thesis discusses R&D activities conducted for muography, including the development of muon detectors specifically designed for this purpose (Chapter 6), as well as the studies conducted for the MURAVES experiment (Chapter 7), this chapter is dedicated to providing in-depth insights into the details of muography-based imaging. It emphasizes the scientific principles and methodologies employed

in the field. Section 5.2 provides brief details of cosmic rays, cosmic ray air showers, the generation of cosmic muons, and their interactions with matter. The physics underlying muography-based imaging is addressed in Sec. 5.3, encompassing both two-dimensional (2D) and three-dimensional (3D) imaging, along with a discussion on the challenges encountered in the application of muography. Section 5.4 discusses the major detector technologies employed in muography across various applications, providing specific details. Furthermore, Section 5.5 offers a detailed exploration of the diverse applications where muography plays an important role.

5.2 Cosmic Rays and Muons

5.2.1 Cosmic Rays

Cosmic radiation was first observed in 1912 when the Austrian physicist Victor Hess ascended in a hydrogen-filled balloon to altitudes above terrestrial radiation. Surprisingly, he found that radiation levels increased with altitude rather than decreased, suggesting an extraterrestrial origin for these energetic particles [179]. This groundbreaking discovery earned Hess the Nobel Prize in Physics in 1936. Subsequent years saw significant advancements in cosmic ray understanding, including the identification of charged primary particles through observations like Clay's latitude effect in 1927 [180]. Bruno Rossi's 1930 theory predicted an east-west effect if cosmic rays were predominantly charged, a hypothesis independently confirmed by Johnson and Alvarez-Compton in 1933 [181]. Further discoveries in the 1940s and 50s provided deeper insights into the origin and particles involved in cosmic rays.

Currently, it is known that cosmic rays are composed of about 90% protons and 9% alphas, the rest being essentially electrons and some small fractions of heavier ions up to iron (Fe). Most cosmic rays are determined to be generated by supernova explosions, where these violent events release immense energy, propelling particles to relativistic speeds. Furthermore, contributions to the cosmic ray population are made by active galactic nuclei, pulsars, and the Sun [182].

The measured kinetic energy of cosmic rays spans a wide range of energy ranging from several MeV to 10^{12} GeV, as shown in Fig. 5.1 [183]. The plot illustrates the particle flux reaching Earth, presented in terms of the energy carried per unit interval of $ln(E)$ or $E^2J(E)$, where $J(E)$ signifies the number of particles arriving per unit interval of time, area, solid angle, and kinetic energy, E. At lower energies, the fluxes of various nuclei, with protons being the most abundant, can be measured. Common nuclei exhibit nearly identical spectrum shapes relative to rigidity (momentum/charge $\propto$ to energy/charge at relativistic energies). For clear particle identification, detection is crucial before the decay into secondaries, possible through the detectors installed on balloons or satellites. Beyond the 10^5 GeV threshold, where the flux becomes too minimal, air shower experiments are used to measure the overall flux of all particles. The well-established power-law spectrum, $J(E) \propto E^{-2.7}$, holds reasonably well before the "knee", the downward bend near $10^{6.5}$ GeV. The decrease below 10 GeV represents a highly localized effect within the solar system. Across three energy decades above the knee, the flux undergoes a steeper decline, reaching the "ankle," where the rate of descent briefly moderates and, eventually, statistics and flux diminishes near 10^{11} GeV. For more details on each region of the spectrum, the reader is referred to [183].

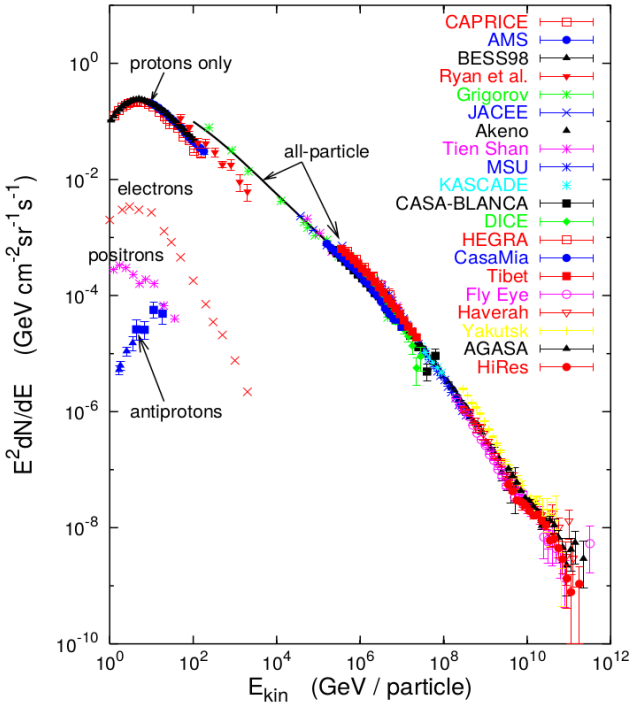

FIGURE 5.1: Cosmic ray energy spectrum obtained from the measurements of different experiments, produced by Gaisser [183].

5.2.2 Extensive Air Shower

When primary cosmic rays penetrate Earth's atmosphere, their interaction with atmospheric nuclei initiates a complex cascade of secondary particles known as an Extensive Air Shower (EAS). This cascade comprises three primary components: a hadronic component, an electromagnetic component, and a muonic component. The hadronic component encompasses a diverse array of high-energy mesons and baryons, generated in various hadronic interactions, including the initial interaction of the cosmic ray with the atmosphere. This component governs the overall development of the shower. High-energy hadrons continuously contribute to the electromagnetic component, primarily through the decay of neutral pions and eta particles into photons, which constitute their dominant decay channel. Each sufficiently energetic photon triggers electromagnetic sub-showers, evolving through processes like positron-electron pair production and bremsstrahlung. Furthermore, high-energy hadrons may further interact with atmospheric nuclei, intensifying the hadronic cascade. Lower-energy charged mesons, particularly pions and kaons, fuel the muonic component through their decay into muons and neutrinos [184].

The longitudinal development of the various particle species in a cascade is described by a system of equations known as cascade equations [183]. These equations take the form:

$$\frac{dN_i(E,X)}{dX} = -\frac{N_i(E,X)}{\lambda_i} - \frac{N_i(E,X)}{d_i} + \sum_j \int_E^\infty \frac{F_{ji}(E,E_j)}{E} \frac{N_j(E_j,X)}{\lambda_j} dE_j \tag{5.1}$$

Here, $N_i(E,X)dE$ represents the flux of particles of type i at slant depth X within the energy interval E to $E+dE$. The probability of interaction of a particle of type i

when traversing an infinitesimal slant depth element (dX) is given by $\frac{dX}{\lambda_i(E)}$, with λ_i as the interaction length in the air. Similarly, the probability of a particle decaying in dX is $\frac{dX}{d_i(E)}$, where d_i represents the decay length. Both the interaction and decay lengths are expressed in g/cm^2, as is X. The function $F_{ji}(E, E_j)$ denotes the particle yield for a particle of energy E_j colliding with an air nucleus to produce a particle i with energy $E < E_j$, derived from the inclusive cross section for the process.

In the calculation of particle fluxes and energy spectra, a critical parameter to consider is the decay probability. Many secondary particles generated from hadronic interactions are inherently unstable and possess the ability to decay during their transit through the atmosphere. Understanding these decay probabilities is of paramount importance for accurately modeling and analysing the behavior of particle cascades initiated by primary cosmic rays in the atmosphere [182]. Following equation explains the decay probability:

$$W = 1 - exp\left(-\int \frac{m_0}{\rho\tau_0 p} dX\right) \simeq \frac{m_0 X}{\rho\tau_0 p} \tag{5.2}$$

Here, m_0 denotes the rest mass of the unstable particle (GeV/c^2), X represents the traversed thickness (g/cm^2), ρ signifies the density of the medium (g/cm^3), τ_0 stands for the mean life at rest (s), and p denotes the momentum (GeV/c). The equation corresponds to a vertical incidence where the zenith angle is $\theta = 0^\circ$. If this is not the case and $\theta > 0^\circ$, the probability of decay along its prolonged path to a particular atmospheric depth X is enhanced by the factor $sec(\theta)$ and the equation becomes:

$$W \simeq \frac{m_0 X sec(\theta)}{\rho\tau_0 p} \tag{5.3}$$

This formula clearly indicates that, for a given column of air traversed, the decay probability of a particle is contingent upon factors such as its mean life, momentum (or energy), density (or altitude), and zenith angle of propagation in the atmosphere.

5.2.3 Cosmic Muons

Pions (π^+, π^0, π^-) and kaons (K^+, K^0_S, K^0_L, K^-) are the sub-nuclear particles most abundantly produced in the EAS, and when charged, their dominant decay modes produce muons [185].

$$\pi^\pm \rightarrow \mu^\pm + \nu_\mu(\bar{\nu_\mu}) \tag{5.4}$$

$$K^\pm \rightarrow \mu^\pm + \nu_\mu(\bar{\nu_\mu}) \tag{5.5}$$

The decay mode in Eqn. 5.4 results in muons $\simeq$ 99.99% of the time, while Eqn. 5.5 leads to muons around 64% of the time. Charged kaons, if not directly decaying into muons, typically undergo two or three-pion decays ($\pi^\pm\ \pi^0$, $\pi^\pm\ \pi^\pm\ \pi^\mp$ *or* $\pi^\pm\ \pi^0\ \pi^0$). Subsequently, these pions are likely to decay into muons if they are charged. The short-lived K^0_S particle predominantly decays into pion pairs ($\pi^+\ \pi^-$ or $\pi^0\ \pi^0$), while the long-lived K^0_L are likely to decay into pion triplets ($\pi^+\ \pi^-\ \pi^0$ or $\pi^0\ \pi^0\ \pi^0$). Moreover, K^0_L contributes to muon production in approximately 27% of its decays through the channel:

$$K^0_L \rightarrow \pi^\pm + \mu^\mp + \bar{\nu_\mu}(\nu_\mu) \tag{5.6}$$

In addition to the previously mentioned favorable decay modes, muons have a high probability of surviving the atmosphere and reaching sea level mainly due to two key reasons:

- **Extended Mean Lifetime:** Muons exhibit a longer mean lifetime ($\approx 2.2\ \mu s$) compared to other unstable particles such as mesons. This extended lifetime is further influenced by a well-known relativistic effect, which dilates their observed lifetime according to the Lorentz factor:

$$\gamma \equiv \frac{1}{\sqrt{1-\beta^2}} = \sqrt{1+\left(\frac{p}{m_\mu}\right)^2} \tag{5.7}$$

  where $\beta = v/c$ is the relativistic speed and m_μ is the rest mass of muon.

- **Relatively large mass:** Muons have a significantly greater mass compared to electrons (about 207 times). This substantial mass difference is crucial in their energy loss characteristics. Bremsstrahlung-induced energy loss, which is proportional to $1/\gamma^2$, results in values approximately 40,000 times smaller for muons than for electrons at a given energy. Consequently, ionisation and excitation processes dominate the energy loss of muons to energies on the order of 500 GeV.

In Fig. 5.2, the vertical fluxes of particles with momenta greater than 1 GeV, originating from cosmic rays, are presented as a function of atmospheric depth [173]. The plot illustrates that at sea level, the combined flux of positive and negative muons dominates the overall charged particle flux. While the neutrino flux is higher, its low interaction rate renders it negligible for muographic measurements. The muon flux is approximately $70/(m^2\ s\ sr)$ on the vertical axis, exhibiting a rough $cos^2(\theta)$ dependence, where θ represents the angle to this axis. As θ increases, the longer path muons traverse in the atmosphere favors the decay of low-energy muons, resulting in a higher mean energy. A semi-empirical estimation of the mean flux at sea level for high-energy muons ($E > 100\ GeV/cos\theta$) is provided by Eqn. 5.8 introduced by Gaisser [183].

$$\frac{dN}{dEd\Omega} = \frac{0.14E^{-2.7}}{\text{cm}^2\ \text{s sr GeV}} \times \left(\frac{1}{1+\frac{1.1\times E\cos\theta}{115\text{GeV}}} + \frac{0.054}{1+\frac{1.1\times E\cos\theta}{850\text{GeV}}}\right) \tag{5.8}$$

At lower energies, determining the mean muon flux becomes complex due to non-negligible muon decay probabilities and various atmospheric and solar effects. However, systematic measurements and parametrisations are available, as detailed in [186] and [187] respectively.

Various factors influence muon flux, encompassing altitude, Earth's magnetic field, solar activity, atmospheric pressure, and upper atmospheric temperature [188]. Simulation tools, such as CORSIKA (COsmic Ray SImulations for KAscade) [189], as well as tools like MUSIC (MUon SImulation Code) [190]and TIERRAS [191], aid in propagating muons through dense matter. More details of using CORSIKA can be found in Sec. 7.6.1.

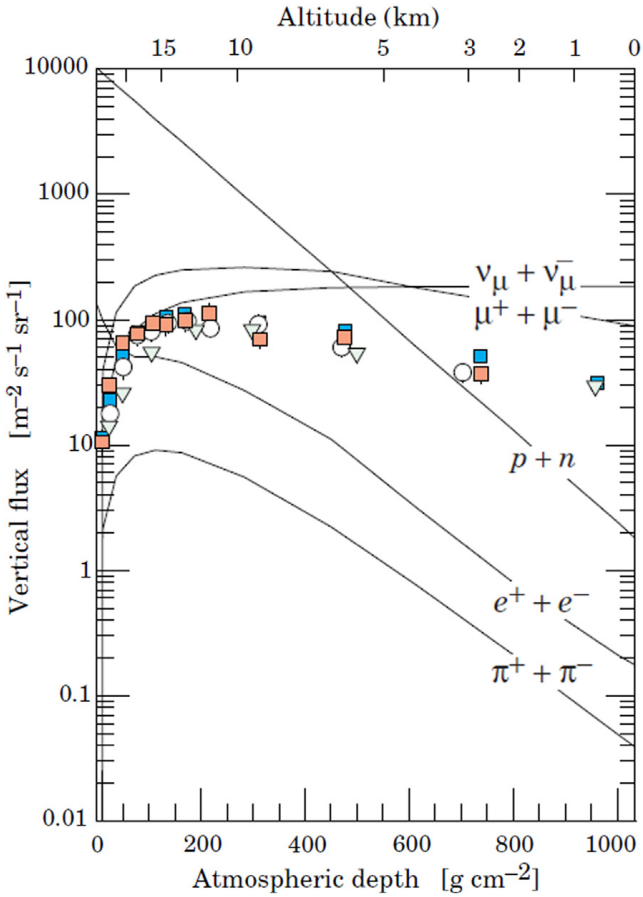

FIGURE 5.2: Vertical fluxes of particles of momenta greater than 1 GeV, originating from cosmic rays, as a function of depth in the atmosphere [173].

In muography experiments, accurately estimating the flux of incident cosmic muons is essential to assess the attenuation caused by the target material. Achieving precise density measurements relies on providing a highly accurate model of this muon flux. In addition to MC simulations, alternatives include utilising measured fluxes as a reference or employing an analytical model to estimate the sea-level muon flux, as exemplified by Gaisser's formula (Eqn. 5.8) mentioned earlier. Gaisser's standard formula holds true when the curvature of the Earth can be disregarded ($\theta < 70°$) and muon decay can be considered negligible. However, for numerous muography experiments where the relevant muon directions are predominantly horizontal, a modified parameterisation becomes necessary.

A novel parameterisation has been introduced by M. Guan, et al. [192], considering the curvature of the Earth. In this scenario, the observed zenith angle θ on the ground differs from the zenith angle at the production point of muons in the atmosphere, denoted as θ^* [193, 194]. The relationship between $cos(\theta^*)$ and $cos(\theta)$ can be expressed as in Eqn. 5.9.

$$\cos\theta^* = \sqrt{\frac{(\cos\theta)^2 + P_1^2 + P_2(\cos\theta)^{P_3} + P_4(\cos\theta)^{P_5}}{1 + P_1^2 + P_2 + P_4}} \tag{5.9}$$

Where P1, P2, P3, P4 and P5 are parameters provided in Tab. 5.1. The equation in Eqn. 5.8 is adapted by incorporating an additional term to the $E_\mu^{-2.7}$ factor. As the

P1	P2	P3	P4	P5
0.102573	-0.068287	0.958633	0.0407253	0.817285

TABLE 5.1: Parameters used in Eqn. 5.9

muon energy rises, this added term becomes insignificant, reverting the formula to its original form. The modified equation is presented below:

$$\frac{dI_\mu}{dE_\mu} = 0.14\left[\frac{E_\mu}{GeV}\left(1+\frac{3.64GeV}{E_\mu\left(\cos\theta^*\right)^{1.29}}\right)\right]^{-2.7} \times \left[\frac{1}{1+\frac{1.1E_\mu\cos\theta^*}{115\text{GeV}}}+\frac{0.054}{1+\frac{1.1E_\mu\cos\theta^*}{850\text{GeV}}}\right] \tag{5.10}$$

The parameters 3.64 and 1.29 are determined through fitting. Further insights into the comparison between the muon flux derived from the equation and the measured flux, along with the validation of the results through comparison with MC simulations, can be found in [192].

5.2.4 Muon Interaction with Matter

Muons, distinguished by their considerable mass and prolonged mean lifetime, exhibit exceptional penetration capabilities, enabling them to traverse extensive distances, even through several hundred meters of rock. This intrinsic property positions muons as powerful tools for muography, especially in imaging large-scale structures. In general, when charged particles passes through matter, two significant factors characterize their behavior: (1) energy loss by the particle and (2) the deflection of particles from their original direction. These phenomena occur primarily because of inelastic collisions with the atomic electrons of the material and elastic scattering from the nuclei. These processes occur multiple times per unit length as the particles traverse the matter, leading to the two principal effects observed. Although relatively rare, other processes include the emission of Cherenkov radiation, nuclear reactions, and bremsstrahlung.

According to [74], the probability that a muon will not interact over a distance x is expressed as $e^{-x/\lambda}$. Here, λ denotes the mean absorption length, defined as $\lambda = (\rho\sigma)^{-1}$, dependent on the density of the material (ρ) through which the muon penetrates and the cross section denoted as σ. The σ is commonly represented as a function of the particle's energy (E), signifying the probability of a particular process occurring. In the case of muons, the thickness x crossed is significantly larger than the mean absorption length λ, and the number of interactions with matter is on the order of x/λ. Consequently, one can meaningfully work with the average energy loss per unit path length often called as stopping power. Bohr initially calculated this using classical arguments, and later, Bethe, Bloch, and others refined the calculation using quantum mechanics. [74, 195].

The mean stopping power of high-energy muons in a material can be expressed as follows:

$$\langle\frac{-dE}{dx}\rangle = a(E) + b(E)E \tag{5.11}$$

Here, $a(E)$ accounts for ionisation and atomic excitation, while $b(E)$ corresponds to radiative processes such as bremsstrahlung, pair production, and photo-nuclear

interactions ($b = b_{brems} + b_{pair} + b_{nucl}$). Bethe-Bloch formula further defines the first part a(E) which dominates at low energies (<100 GeV). The Bethe-Bloch equation for muons is (for more details, the reader is referred to [196]):

$$\left\langle -\frac{dE}{dX} \right\rangle = Kz^2 \frac{Z}{A} \frac{1}{\beta^2} \left[\frac{1}{2} \ln \frac{2m_e c^2 \beta^2 \gamma^2 W_{max}}{I^2} - \beta^2 - \frac{\delta(\beta\gamma)}{2} \right] \tag{5.12}$$

Equation 5.12 describes the energy loss for ionisation and atomic excitation per unit opacity-X (refer next paragraph for definition of opacity). In the equation, K is a proportional coefficient, z is the charge number of the incident particle (z=1 for muons), Z and A are the atomic and mass numbers of the absorber material, I is the mean excitation potential in electron volts, m_e is the electron mass ($m_e = 511, \text{keV}$), W_{max} is the maximum energy transfer in a single collision, and $\delta(\beta\gamma)$ is a correction factor (correction factor that adjusts the calculation of energy loss to better match experimental observations, especially in materials of high density) related to the density effect.

The range of a muon is determined by inverting and integrating Eqn. 5.12 from the energy at the entry point (where $\beta \simeq 1$) up to where the muon is at rest ($\beta = 0$). In practical terms, a muon detector directly measures the muon flux arriving from various directions within its acceptance. Comparing this flux to the "free-sky" flux provides the probability for a muon to be absorbed along a specific line of sight, known as "muon transmission." This forms the basis for absorption-based muography. This probability can be directly interpreted in terms of "opacity" along that line of sight, defined as the density integrated along a path length: $X = \int_0^x \rho(x')dx'$. A convenient unit for opacity is meters water equivalent (mwe), with a conversion factor of 1 $mwe \simeq 100\ g/cm^2$. The energy loss of an energetic muon is approximately 0.2 GeV/mwe [197].

In certain scenarios, the thickness of the target area is known (e.g. from geographical data). The opacity in that specific direction then allows for the measurement of the average density of the material along that path. However, in other applications, the process can be reversed. For instance, when the objective is to measure the boundaries of a volume, such as the overburden of a tunnel, an initial estimate of the average density of the material is employed as the input.

In the year 1911, experiments conducted by Rutherford using exceedingly thin targets demonstrated that charged particles entering a material undergo deflection due to Coulomb scattering caused by the intense electric field near nuclei [198]. The probability distribution of the angular deflection $\Delta\theta$ for a single scattering event adheres to Rutherford's Law, $P(\Delta\theta) \propto 1/sin^4(\Delta\theta/2)$. When the average number of scatterings exceeds 20 and the energy loss is minimal, a common scenario in muography applications, most deflections are of a small magnitude. Consequently, while traversing a substantial amount of material, the actual distribution demonstrates an approximately Gaussian core, aligning with expectations from the central limit theorem. This Gaussian approximation effectively characterizes about 98% of the actual distribution [199], with a standard deviation that, within a wide range of Z and for targets that are not very thin, is accurately estimated by the expression (explained

by G. R. Lynch, et al. in [200]):

$$\sigma(\Delta\theta) = \frac{13.6\text{MeV}}{\beta c p}\sqrt{\frac{x}{X_0}}\left[1 + 0.038\ln\frac{x}{X_0\beta^2}\right] \tag{5.13}$$

where p represents the muon momentum, x is the total path length traversed, βc denotes the velocity, z stands for the charge, and X_0 represents the radiation length. A concise expression for radiation length (with an accuracy better than 2.5% for all elements except helium [201]) is provided as follows:

$$\frac{1}{X_0} \propto \frac{Z(Z+1)}{A}\ln\left(\frac{287}{\sqrt{Z}}\right) \tag{5.14}$$

For accurate estimations of $1/X_0$, the reader is referred to [202].

5.3 Radiographic Imaging with Muons

5.3.1 Two-dimensional Imaging

As outlined in the introduction section of this chapter (Sec. 5.1), muon imaging is carried out through various methods, utilising muon absorption and multiple scattering, known as muography and muon tomography, respectively. Given that the projects discussed in the second part of this thesis (the reader is referred to Chapter 7 and Chapter 6) are centred around muography, this section provides an in-depth information of the technique of muography.

Muography, through the absorption method, quantifies the degree of absorption of muons within a given volume. This approach indirectly provides the mean density of the materials traversed and identifies density anomalies, such as void regions or high-density deposits, reflected as an excess or deficit of muons. Comparing with traditional X-ray radiography, muography employs natural cosmic muons as a fixed, non-unidirectional source. Crucially, muons, with their exceptional ability to penetrate hundreds of meters of rock, outperform X-rays, which are limited to the decimeter range. This unique property positions muons as ideal for scanning larger structures.

In muography experiments, the measurement of the muon flux from the area of interest is performed as a function of direction (α, ϕ), where α and ϕ represent the elevation and azimuth angles, respectively. The recorded number of muons, denoted as N^u, in the muon detector within any specific angular region (α, ϕ) can be expressed as:

$$N^u(\alpha,\phi) = T^u_{acq} \cdot S^u_{\text{eff}}(\alpha,\phi)\int_{E_{\min}}^{\infty}\Phi(\alpha,\phi,E)\mathrm{d}E \tag{5.15}$$

where T^u_{acq} is the total data acquisition time, $S^u_{\text{eff}}(\alpha,\phi)$ is effective area of the detector and $\Phi(\alpha,\phi,E)$ is the differential muon flux with respect to the muon energy E, in the given angular region. The effective detector area $S_{\text{eff}}(\alpha,\phi)$ depends on different factors and it can be written as follows:

$$S_{\text{eff}}(\alpha,\phi) = S \cdot A(\alpha,\phi) \cdot \epsilon_{\text{trig}}(\alpha,\phi) \cdot \epsilon_{\text{DAQ}}\left(v_{\text{trig}}\right) \cdot \epsilon_{\text{an}}(\alpha,\phi) \tag{5.16}$$

where S represents the sensitive area of the detector, $A(\alpha,\phi)$ denotes the geometrical acceptance, $\epsilon_{\text{trig}}(\alpha,\phi)$ accounts for the trigger efficiency, $\epsilon_{\text{DAQ}}\left(v_{\text{trig}}\right)$ reflects the data

acquisition efficiency and $\epsilon_{\text{an}}(\alpha, \phi)$ denotes the analysis efficiency. The lower limit of the integral in Eqn. 5.15, denoted as E_{min}, signifies the minimum energy required for muons to traverse the target, reach the detector, and depends on the opacity of the target in a specific direction (α, ϕ).

Additionally, the density distribution within the target volume is estimated by evaluating the transmission of muons. Two types of transmission can be distinguished: measured transmission and expected transmission. Measured transmission refers to the ratio of the muon flux measured by the detector from the target area to that in calibration mode. The calibration flux, often referred to as the free-sky flux, is measured when the detector points toward the open sky, collecting data in the same manner as during the measurement of muon flux from the target direction. Equation 5.15 represents the muon flux from the target direction and similar to that the free-sky muon flux is defined as follows:

$$N^{\text{fs}} = T^{\text{fs}}_{acq} \cdot S^{\text{fs}}_{\text{eff}}(\alpha, \phi) \int_{E_0}^{\infty} \Phi(\alpha, \phi, E) \mathrm{d}E \tag{5.17}$$

In the given equation, the parameters are the same as described for Eqn. 5.15, with the distinction that it corresponds to free-sky data collection. Here, E_0 represents the minimum energy of the muon in the specific direction (α, ϕ) in the free-sky mode. Using Eqn. 5.15 and Eqn. 5.17 the measured transmission $T_{meas}(\alpha, \phi)$ can be defined as:

$$\frac{N^u(\alpha, \phi)}{N^{\text{fs}}(\alpha, \phi)} = \frac{T^u_{acq} \cdot S^u_{\text{eff}}(\alpha, \phi)}{T^{\text{fs}}_{acq} \cdot S^{\text{fs}}_{\text{eff}}(\alpha, \phi)} \frac{\int_{E_{\text{min}}}^{\infty} \Phi(\alpha, \phi, E) \mathrm{d}E}{\int_{E_0}^{\infty} \Phi(\alpha, \phi, E) \mathrm{d}E} \tag{5.18}$$

Here, the ratio $T^u_{acq}/T^{\text{fs}}_{acq}$=1, when normalising the time to the free-sky data-taking time. It is assumed that the geometrical acceptance, trigger efficiency and analysis efficiency are very similar in both data samples, with the only significant change occurring in the data acquisition efficiency $\epsilon_{\text{DAQ}}(v_{\text{trig}})$, which depends on the trigger rate (v_{trig}) that is much lower in the case of the target direction. The ratio between the DAQ efficiencies remains constant: $\epsilon^u_{\text{DAQ}}(v_{\text{trig}}) / \epsilon^{\text{fs}}_{\text{DAQ}}(v_{\text{trig}}) = C$, simplifying the equation to:

$$T_{meas}(\alpha, \phi) = \frac{N^u(\alpha, \phi)}{N^{fs}(\alpha, \phi)} = C \cdot \frac{\int_{E_{\text{min}}}^{\infty} \Phi(\alpha, \phi, E) \mathrm{d}E}{\int_{E_0}^{\infty} \Phi(\alpha, \phi, E) \mathrm{d}E} \tag{5.19}$$

The expected transmission is estimated by numerical methods or MC simulations, using the known muon flux impinging the Earth's surface at free sky and accounting for the known absorption properties of matter [203]. The expected transmission is defined as:

$$T_{exp}(\rho, \alpha, \phi) = \frac{1}{C} \frac{N^u(\alpha, \phi)}{N^{fs}(\alpha, \phi)} \tag{5.20}$$

To measure the density distribution within the target volume, it is essential to conduct a comparison with simulations. The simulations must encompass a realistic muon flux that describes both the angular and energy spectra at ground level. Additionally, these simulations need to account for the detailed external geometry of the volume under examination as observed from the detector's viewpoint, along with an estimated average value of the volume density. By comparing the measured transmission with various simulations, each conducted under different assumptions

of the average density, a 2D average density map can be generated from the detector's perspective. In the case of the MURAVES experiment, the density evaluation is performed by estimating T_{meas} from the detector data and T_{exp} using PUMAS based backward MC simulations. The detailed explanation of the procedure followed is provided in Sec. 7.7.1.

The relative transmission, $R(\rho, \alpha, \phi)$, is expressed as the ratio of measured transmission to expected transmission, as indicated by Eqn. 6.9 and Eqn. 5.20.

$$R(\rho, \alpha, \phi) = \frac{T_{meas}(\alpha, \phi)}{T_{exp}(\rho, \alpha, \phi)} \tag{5.21}$$

In case there is no region in the target with density anomalies and the density ρ inserted in the numerical calculation performed to estimate the expected transmission is correct , the resulting value of $R(\rho, \alpha, \phi)$ is equal to 1. In contrast, if $R(\rho, \alpha, \phi) > 1$, it means that muons that traverse that specific direction encounter a region of lower density, such as a cavity. s a result, an excess of muons is measured compared to the expected muon count. Conversely, instances of $R(\rho, \alpha, \phi) < 1$ suggest the existence of a denser material in that specific direction, leading to a reduced muon flux from that particular direction.

5.3.2 Three-dimensional Imaging

In muography, data from multiple viewpoints can be correlated to infer a 3D distribution of the scanned target. This involves either simultaneous observation of the target from different viewpoints or the movement of a single tracker around the target. The latter approach minimizes cost and logistical complexity but assumes no significant evolution during the measurement period. Figure 5.3 shows two configurations of installation of muon telescopes to obtain 2D and 3D images of an overburden, respectively [197]. Typically, objects are sliced into a 3D voxel matrix with initial densities assigned. An iterative minimisation procedure adjusts voxel densities until the best fit to the data is achieved, presenting a classic inversion problem. Regularisation algorithms, based on minimum-squares formulations [204, 205] or Bayesian approaches [206], help mitigate instabilities and convergence issues. Muography has found diverse applications, showcasing numerous examples in which it has been employed to obtain 3D density images of volcanoes and to measure tunnel overburdens, especially in the context of mining explorations [207–211].

While imaging by a single muography telescope is inherently 2D, recent work explained in [212] demonstrates deriving 3D information from a single observation point. Imaging is performed using a back-projection algorithm developed to capture the target from various angles. The method relies on geometric constraints, where a detector, positioned below the object, achieves a stereoscopic view of the object due to different parts of the detector observing the object along varied directions. This holds as long as the object's distance from the detector is not excessively large compared to the detector's size. The back-projection method is then implemented, involving internal triangulation of data based on muon transmission maps obtained separately for each part of the detector. This method allows for a sort of stereoscopic vision of the object, enabling the reconstruction of muon tracks and the identification of anomalous regions, representing the projection of the hidden object's shape. The angular width of these regions provides information on the object's distance from

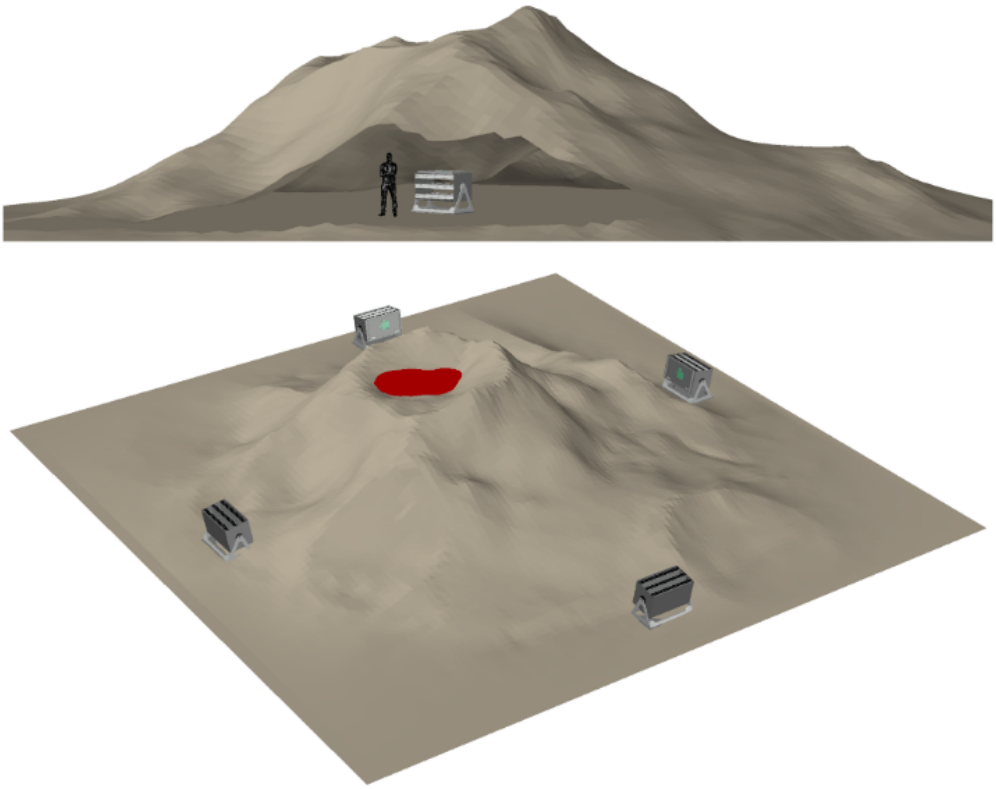

FIGURE 5.3: The top and bottom images shows the configurations of installation of muon telescopes for obtaining 2D and 3D images respectively [197].

the detector, and the linear extension of the anomalous region gives insights into the hidden object's size. Thus, this method, using single muon radiography, provides three-dimensional information for characterising an unknown object in the instrument's field of view, and it can guide the optimisation of detector installation points for triangulation of the detected object. This method is suitable for locating volumes with vastly different densities from the surrounding material, such as empty cavities or metal deposits within a rocky layer.

Additional Data Sources

In enhancing the 3D imaging process, collateral measurements play a crucial role, particularly in geosciences, archaeology, and civil engineering applications. These fields often utilise various geophysical tools for surveys, each offering complementary advantages. In volcano imaging, additional data sources such as gravimetry, seismic noise, seismic waves, and geoelectric data are commonly employed. However, these methods face challenges due to strong model assumptions and nonlinear inversion problems. Muographic data, with its directional nature, naturally addresses these challenges by breaking degeneracies. Ground-penetrating radars (GPRs) and magnetometers are frequently employed tools in near-surface surveys, notably in archaeology.

In this context, the combination of gravimetry with muography is particularly advantageous, as both methods directly respond to the density distribution of the rock. A gravimeter is specifically designed to measure the local acceleration of gravity (g), influenced by the nearby mass density distribution. Since a single gravimeter lacks

directionality due to the spherical symmetry of the gravitational field, it is primarily sensitive to distance (the effect of an object with density ρ and volume V at a distance r from the gravimeter is given by $\Delta g = G\rho V/r^2$, where G is Newton's constant). Gravimetry campaigns are based on arrays of measurements, and the inverse dependence on r makes the method less sensitive to increasingly distant volumes of interest. Although muography faces similar challenges with large target depths that reduce available statistics, its key advantage lies in not requiring surface installation on the target itself. Successful examples of combining gravimetric and muographic data involve using gravimetric data as initial seeding for the 3D voxel density matrix, refined later with muographic data. The study in [213] provides a detailed quantitative comparison of the merits of muography alone, gravimetry alone, and their combination. The comparison is conducted using simulations of realistic density distributions as benchmarks.

In cases where traditional methods, such as gravimetry and seismic tomography, yield discordant results, muographic data can serve as an independent source to help determine the correct solution during the inversion process. For instance, conflicting outcomes about the deep structure of Mt. Vesuvius [214, 215] from gravimetry and seismic tomography highlight the potential of muography for resolving such discrepancies. Similarly, traditional methods may suggest the presence of a large dike within Mt. Stromboli [216], but lack the precision to provide accurate estimates of its dimensions. In such scenarios, muography, with its target resolution of 10 meters or less, can offer significant insights.

5.3.3 Major Challenges

Background Effects

In muography experiments, addressing the challenge of background interference is crucial for accurate muon flux measurements. Various types of backgrounds contribute to this issue. Intrinsic detector noise introduces random hits across detector layers, infiltrating the muon trigger window. These hits can be mitigated by employing a restricted muon trigger window and applying cuts based on data selection from detector calibration data. Another type of background arises from muon-like hits produced by charged hadrons or $e^{\pm}$ particles that manage to reach sea level despite their large interaction cross sections. The abundance and spectrum of these hits depend on factors affecting real muons, necessitating in situ estimation due to location-dependent variations. Such hits are commonly referred to as fake muon hits [217]. Low-momentum muons (commonly referred to as soft muons) entering the detector's acceptance range can contribute to image blurring [218]. This phenomenon presents challenges, particularly for large targets such as mountains and volcanoes, where scattered soft muons, resulting from significant-angle scattering, become predominant [197].

A highly effective passive method for mitigating fake muon background involves incorporating an absorber, such as iron or lead slabs, into the detector setup [169]. This leverages the likelihood of hadrons and $e^{\pm}$ particles undergoing a destructive interaction, either nuclear or electromagnetic. The absence of hits in the detection plane following the absorber or the detection of multiple hits, indicative of nuclear

or electromagnetic showers resulting from interactions in the absorber material, indicates that the track corresponds to soft muons. The absorption in the passive material introduces an effective momentum cut-off, and any remaining soft muons exhibit distinctive kinks in their trajectories, aiding identification during offline analysis. MC simulations serve as another valuable tool for studying the track properties of fake or soft muons, particularly to understand energy deposits and hit distribution in the detector. Cuts on the data based on simulation studies can be instrumental in eliminating these background hits. In the case of the MURAVES experiment [185], a 60 cm thick lead wall is installed between the last and next-to-last layers of the detectors for background rejection (see Sec. 7.3.1 for details). Additionally, simulation studies conducted as part of this thesis's research quantifies the possible fake muon tracks in the MURAVES detector and explores the track properties of fake muon hits, with detailed results provided in Sec. 7.6.6. Usage of high time resolution detectors (refer Sec. 5.4.3) with particle identification (PID) capabilities can also be implemented for rejecting background particle tracks based on PID.

In addition to the previously mentioned cases, another source of background in muography experiments is presented by backward-going muons—muons that enter from the back side of the detector and traverse all detector layers. A common method for rejecting such muon tracks relies on the time-of-flight measurement [219]. To implement this, the detector's time resolution needs to be in the order of a few nanoseconds. The specific value depends on the geometry of the muon telescope.

Certain experiments employ Cherenkov detectors for background rejection, as elaborated in Sec. 5.4.4. The Cherenkov detectors function as absorbers, offering an intrinsic momentum threshold to discard soft muons. Simultaneously, they provide PID information based on the Cherenkov ring's shape, enabling the elimination of fake muons.

Momentum Estimation

The absorption process as well as the scattering process depends on the muon momentum. The interplay between these processes introduces nuisances such as image blurring due to large-angle scattering of low-momentum muons and selective biases on the momentum spectrum [220]. Accurate momentum spectrum description relies on various factors, including location [221], altitude, latitude, longitude, and geomagnetic conditions [222]. Seasonal variations, solar activity, and atmospheric pressure fluctuations further impact muon spectra. To address these challenges, muography teams employ methods like magnetic spectrometers or absorption in known materials to select momentum ranges. Reference data from dedicated detectors and advanced techniques, such as those involving absorbers, contribute to minimising model dependencies. Achieving in situ momentum measurements remains an ideal goal for enhancing accuracy and reducing background in absorption muography, offering significant benefits for signal significance. In certain specific applications of muography, such as volcanology, the need arises to measure muon momentum up to several tens of GeV. This level of measurement precision can be attained by incorporating a magnetic spectrometer in conjunction with high-resolution detectors [186, 223].

Monte Carlo Issues

The comparison of data with MC simulations is integral to the imaging process in muography. The simulation chain initiates with the generation of muons, incorporating realistic angular and momentum distributions. Various simulation methods exist, ranging from ab initio simulations like CORSIKA to parametrisations based on existing data. Simulating the geometry and response function of the detector, either as a point in space or with detailed efficiency parametrisations, is crucial. The most pertinent simulation step for muography involves the propagation of particles through the target material. While tools like Geant4 or FLUKA offer accurate but time-consuming simulations, specialized codes like MUSIC provide parametric simulations. MUSIC considers main electromagnetic interactions, using stochastic processes for energy loss and a continuous approximation below a user-defined threshold. Backward MC programs like PUMAS address efficiency issues by exclusively sampling the final state, making them suitable for specific muography applications, such as volcano studies [197].

In the context of the MURAVES experiment, a detailed examination of track properties is conducted using Geant4, despite its time-consuming nature, considering the relevance of the study. While assessing the feasibility of employing CORSIKA for cosmic shower generation, it became evident that the substantial computational time required by CORSIKA, especially when integrated with Geant4, could significantly extend the simulation process. To address this challenge, the cosmic ray generator CRY [224] is adopted. Despite its limitations compared to CORSIKA, CRY proves sufficient for a diverse range of studies discussed in Chapter 7. A comparison between CRY and CORSIKA is presented in Sec. 7.6.1. Furthermore, in addition to challenges posed by the detector setup, incorporating the geometries of large structures such as volcanoes into Geant4 simulations proves impractical due to the anticipated computational burden. Consequently, for the MURAVES experiment, the backward MC technique PUMAS is deemed more convenient, and detailed information can be found in Sec. 7.6.2.

In addition to the above mentioned aspects, there are practical challenges inherent in muography experiments, primarily due to the often remote and diverse environmental conditions of the experimental sites. Selecting appropriate experimental locations and establishing the necessary logistical support for various detector setups present substantial challenges. These practical difficulties can vary from one detector type to another, and specific challenges related to each type of detector are discussed in the following section.

5.4 Detector Technologies

Muon detectors designed for muography applications need to meet diverse requirements, distinct from the mainstream particle physics detectors, reflecting the wide range of muography applications. These detectors must be durable and capable of remote operation with minimal intervention, considering the often challenging deployment sites. Power consumption is a crucial consideration, depending on the location of the experiment. The low event rate characteristic of muography applications reduces concerns about data rate, data acquisition speed, and front-end electronics performance. The specific requirements of muography applications lead

to variations in detector geometries and detection technologies. Over the past few decades, numerous muon detectors have been proposed and constructed, showcasing a variety of features. This section provides the details of the major detection techniques employed in muography.

5.4.1 Scintillator Detectors

Scintillators emit flashes of light (scintillations) when exposed to ionising radiation. The process begins with the interaction between ionising radiation and the scintillator material, resulting in the excitation of atoms within the material. As these excited atoms return to their ground state, they release energy in the form of photons, constituting the scintillation light. To capture and quantify this light, photo-detectors are used. These devices convert the optical signals into electrical pulses. The intensity and timing of these pulses offer valuable information about the incident radiation, enabling measurements of energy levels and tracking of the paths of particles.

Plastic scintillators offer an excellent solution, especially in scenarios where precise spatial and angular resolution is not a primary concern, as seen in applications such as muography. Durable muon trackers, designed for challenging environments, can be created using fast-response plastic scintillator materials, maintaining a reasonable cost-performance. The attractiveness of these detectors has increased with the introduction of silicon photomultipliers (SiPM), which replace traditional, more expensive photomultipliers (PM) while operating on a lower cost and power budget. The adaptability of plastic scintillators to various geometries, such as square, rectangular, or triangular bars, enables the creation of position-sensitive detection layers with a relatively low number of readout channels. The customisation of detector geometry is illustrated in Fig. 5.4, which showcases configurations with arrays of long plastic scintillator bars [197]. These bars, when placed side by

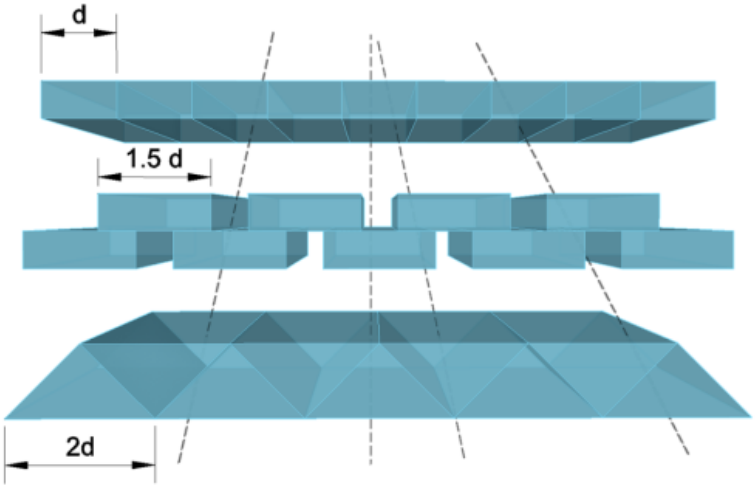

FIGURE 5.4: Three different configurations of detector plane construction using scintillator bars [197].

side, produce a simple detection layer (Fig. 5.4-top). The configurations, like the second and third ones in Fig. 5.4, introduce partial overlap to enhance spatial resolution without increasing the readout channels significantly. The second was tested by the MIMA collaboration [225] and the third solution, the detection plane with triangular

scintillator bars was tested by Fermi National Accelerator Laboratory (USA) and has been used for muography experiments MU-RAY [226], MURAVES (Chapter 7) and MIMA [225]. The advantage of using this triangular configuration and calculating the position of the particle hit using a centre of gravity algorithm is explained in Sec. 7.5.2. Regardless of the geometry, the scintillation photons emitted along the particle's path can be collected using either a light guide, a Wavelength Shifter Fiber (WLS) typically enclosed within the scintillator bar, or through SiPMs (or PMs) directly linked to the scintillator bars. The use of the WLS approach enables the use of compact SiPMs with dimensions as small as 1 mm^2, resulting in reduced costs for front-end electronics. For the detectors in the MURAVES experiment, signal extraction is achieved using WLS fibers embedded in triangular scintillator bars and coupled to SiPMs. The details of the construction of the MURAVES detector planes in this configuration, along with the pictures, is provided in the corresponding chapter in Sec. 7.3.

A drawback of scintillators detectors with SiPMs is, SiPMs exhibit a notable temperature dependent behavior, impacting gain, dark count rate, and reverse current. To mitigate this effect, precise and continuous temperature monitoring is essential, necessitating adjustments to the operating voltage. Taking this into account a dedicated temperature stabilisation system is implemented for the MURAVES detectors, the details can be found in Sec. 7.3.3.

One of the recent interesting development is the scintillator based borehole detector systems [227, 228]. These systems adopt novel design configurations to optimize angular acceptance, a crucial aspect given the compact size of these detectors. Borehole detectors face demanding criteria, which require compactness, robustness, impermeability, and reliable performance under diverse environmental conditions.

5.4.2 Nuclear Emulsion Detectors

A widely employed muography technique involves the use of nuclear emulsion plates. The detector operates on the same principle as analog photography, with silver halide crystals mixed in gelatin and coated on a glass substrate. This detector is of a limited cost and does not require any power supply. When muons interact, they initially reduce silver ions to metallic silver. Following exposure, the emulsion undergoes development to promote the reduction reaction around previously reduced sites. In the final step, the remaining silver halides are dissolved (fixation), resulting in a plate darkened at the muon positions, as shown in Fig. 5.5.

Nuclear emulsions, thicker than standard photographic films, enable 3D reconstruction of muon trajectories with high granularity, achieving sub-micron resolution. This surpasses blurring from multiple scattering within the object, allowing for compact instruments with large acceptance. The track pattern analysis, along with alternating emulsions with Lead or Iron plates, aids in distinguishing high-energy muons from low-energy ones or electrons. Notably, this passive instrument is ideal in scenarios without an available energy source. A notable example of a large-scale application is the OPERA neutrino experiment [229], which has led to recent developments in muography [230–232].

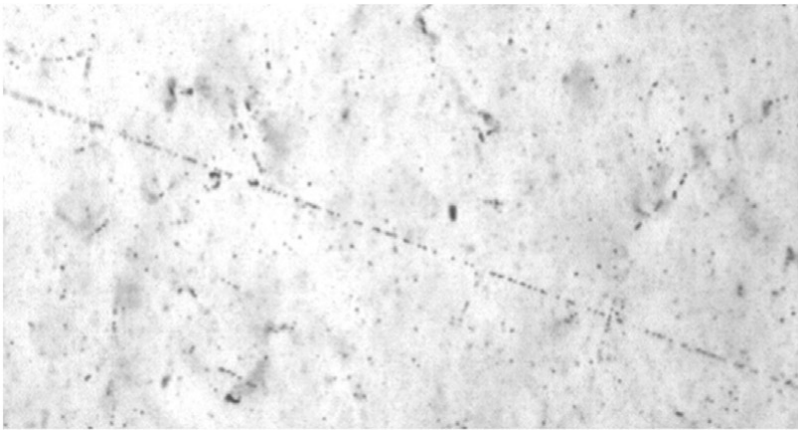

FIGURE 5.5: Transmitted light image through an optical microscope showing the track of a cosmic ray muon on an emulsion film. The track is visible as a sequence of tightly aligned grains after development, with a resolution typically better than 50 nm. The average size of grains is about 0.5 μm [173].

There are also some issues related to this detector type [173]. The useful life of emulsions is typically limited to a few months and decreases further at high humidity or temperatures exceeding approximately $25°C$. Furthermore, data analysis is deferred until after exposure, requiring a time-consuming automated scanning process for track reconstruction and image formation. Importantly, the plates lack time information, as they accumulate muons throughout the entire exposure, hindering dynamic structural monitoring.

Despite these limitations, emulsion films have proven effective in numerous muography experiments, showcasing exceptional performance in diverse environments, including alpine tunnels [233, 234], hot sand deserts [232], and Mediterranean volcanoes [232]. These experiments extended over several months of measurement periods.

5.4.3 Gaseous Detectors

In the case of gaseous detectors, the muon detection relies on the interaction with a gas mixture, causing ionisation along the muon trajectory. In this process, electrons drift towards an anode (plane or wires) under proper electric fields and are subsequently accelerated to further ionise the gas. The acceleration leads to a charge avalanche in the vicinity of the anode. The resulting movement of electron–ion pairs induces a charge collected on readout elements (wires, strips, pixels) connected to dedicated electronics.

The development of gaseous detectors for muography projects has been driven by numerous advantages. Notably, they can achieve resolutions on the order of a few hundred microns, which is at least a factor of 10 better than scintillators, all while maintaining reasonable costs. Unlike emulsions, gaseous detectors allow for dynamical studies, combining the advantages of both historical technologies. Various solutions also exist to limit the number of electronic channels.

Wire Chambers

Multi-Wire Proportional Chambers (MWPCs) and Drift Tube Chambers (DT) are two types of wire chambers commonly used in various muography experiments (eg [177, 235–237]). MWPCs feature parallel cathode strip planes with an array of thin anode wires in between. The induced signal from the electrode avalanche (for details of the electron avalanche, the reader is referred to Sec. 2.2.3) is collected through the anode wires, while the signal corresponding to the positive ions is collected in the cathode strips. DTs, inspired by MWPCs, consist of narrow tubes (with dimensions on the *mm* scale in height and width) called drift tubes, with anode wires placed in the middle. The particle's position can be correlated with the time measurement, given the approximately constant drift velocity in the tube volume. Unlike MWPCs, the narrow tubes in DTs confine the electron drift path, reducing electron diffusion and improving spatial resolution [80]. Figure 5.6 depicts the schematic diagrams of the MWPC and the schematic diagram of DT was are already provided in Sec. 1.3.5. While MWPCs and DTs provide commendable spatial and angular resolution, a no-

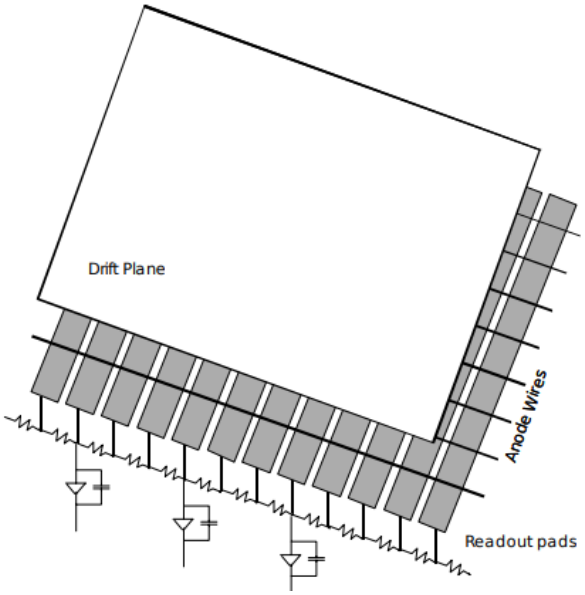

FIGURE 5.6: Schematic diagram of an MWPC chamber [238]

table drawback is their limited time resolution, typically in the order of microseconds.

MicroMegas

MicroMegas, a subset of Micro Pattern Gaseous Detectors (MPGDs) designed for precision tracking in muography, functions through gas amplification within a meticulously segmented structure [239]. The detector comprises a micro-mesh layer positioned between two layers, typically serving as the anode and drift electrode. Electrons undergo amplification within the microholes of the mesh, and this structure effectively localizes the resulting avalanches, providing exceptional position resolution, potentially reaching tens of micrometers. Historically, their application in muography faced challenges due to a substantial amount of required readout electronics. However, the introduction of genetic multiplexing and large-area 2D detectors with 2000 strips, operated efficiently with only two 64 channel connectors, has addressed this issue [240]. Notably, the ScanPyramids project is among the

prominent experiments using MicroMegas-based muon telescopes [232]. While this technology excels in spatial resolution, it is essential to acknowledge its limitation in terms of time resolution, similar to wire chambers.

RPCs

RPCs represent another category of gaseous detectors capable of addressing the time resolution limitations faced by the aforementioned detectors. The advanced multi-gap RPCs can offer time resolutions even in the picosecond range. The operational principles and mechanisms behind the superior time resolution provided by RPCs are elaborately discussed in the chapter dedicated to the physics of RPCs (Chapter 2). While the position resolution of RPCs is not as exceptional as that of MicroMegas, it still falls within the range of a few hundred micrometers. RPCs are relatively straightforward to construct, and their production costs are quite low, making them suitable for large-scale deployment. Consequently, RPCs can be employed as a cost-effective solution for constructing extensive surface trackers. The details of glass RPCs used for the imaging of the Puy de Dôme, a dormant volcano near Clermont–Ferrand (France) can be found in [73].

One of the primary challenges associated with working with RPCs is the requirement for a high operational voltage (approximately 8-10 kV), coupled with their operation using a gas mixture of high GWP, primarily composed of R134a and a small amount of flammable isobutane. This issue is addressed in this thesis through extensive studies to identify eco-friendly gas mixtures for RPCs (Chapter 4). While alternative solutions, as discussed in Chapter 4, may exhibit ageing effects, it is not a serious concern in muography applications since the detectors are exposed to relatively lower particle rates. In addition, the upcoming plans for the portable RPC project outlined in Chapter 6 includes the testing of RPCs with eco-friendly gas mixtures specifically tailored for muography applications.

Another notable challenge encountered with RPCs and other gaseous detectors is their reliance on continuous gas flow, necessitating gas bottles, associated logistics, and installations like gas pipes at experiment sites. Chapter 6 discusses the efforts conducted to mitigate this challenge by developing gas-tight, small-scale portable RPCs, yielding promising results. Although implementing a gas-tight layout for large-area detectors poses additional challenges, the technology applied to the small-scale portable RPCs has the potential to significantly reduce gas consumption, requiring only minimal volumes of gas bottles for controlled flow. In the work presented in Sec. 6.5, significant research and development efforts have been undertaken to progress the development of an advanced gaseous detector telescope for muography. The conceptual design involves the utilisation of gas-tight multi-gap RPCs with dimensions of $1 \times 1\ m^2$. A successful small-scale test prototype has already been developed. The telescope configuration will further incorporate gas-tight Thick Gas Electron Multipliers (THGEMs), representing another type of gaseous detector known for providing excellent position resolution.

Additionally, the drift velocity is intricately linked to the electric field, the gas pressure ratio, and the temperature variations, especially crucial in the dynamic conditions of muography experiment locations compared to controlled laboratory settings. In response to this challenge, the RPC detectors developed as part of the

research discussed in this thesis (Sec. 6.3.1) feature strategically positioned sensors for monitoring environmental parameters within the chambers.

5.4.4 Other Technologies

Semiconductor detectors, like silicon microstrips or pixels, have been underexplored in muography due to their higher cost per unit area compared to other detector technologies, despite their outstanding spatial resolution (around 10 μm). However, their potential lies in specific applications where radiation hardness and compact design are critical, such as nuclear plants, radioactive waste management [241], etc. Another innovative approach involves using Cherenkov imaging techniques for muography. This has been already proposed for muography applications in volcanology [242–244]. This method captures the Cherenkov light emitted when charged particles, like muons, surpass the speed of light in a dielectric medium (e.g., water). Although construction is costly, preexisting telescopes, originally designed for fundamental physics research, can be utilised for muography of nearby targets. Furthermore, the MuTe project in Colombia [245] explores the Cherenkov effect for particle identification, combining traditional scintillator-based telescopes with water Cherenkov detectors to discriminate muons from electrons and positrons, showcasing its potential for background discrimination.

5.5 Applications

Muography, which uses the absorption characteristics of muons, is widely used in diverse scientific applications. This section provides information on the major applications along with examples.

5.5.1 Geophysics

Muography, a technique suitable for investigating large geophysical targets, complements traditional survey methods by providing directional sensitivity to the in-depth structure of such objects. However, challenges arise when attempting to resolve narrow structures within large targets, especially at low elevation angles where the muon flux is less intense. Under these conditions, both the signal strength and the survival rate of muons passing through substantial material can be compromised by background interference. Effectively reducing these backgrounds is a primary concern in muography experiments for geophysical applications. The details of the background effects and possible solutions were already discussed in Sec. 5.3.3.

One prevalent application of muography is in volcano imaging, with established collaborations between physicists and volcanologists. The choice of target is often influenced by opportunities such as geographical proximity to institutions of particle physics and volcanology. Noteworthy activities in this field are observed in countries like Japan [246], Italy [247], France [208, 248], and more recently, Colombia [249, 250].

In 1994, Japanese scientists pioneered the application of muography to scan the internal structure of a volcano, specifically Mt. Tsukuba. Using a straightforward

tracking system comprising plastic scintillator bars to measure muon flux, they discovered that muography had the potential to offer higher spatial resolution in deciphering a volcano's internal structure compared to traditional geophysical techniques. Subsequently, other Japanese volcanoes, including Mt. Asama [251], were explored using muography with ECC emulsion detectors, marking early evidence of the efficacy of muography in volcanological applications. In Fig. 5.7-A (left), the muographic image of the summit region of Mt. Asama is depicted, while Figure 5.7-B (right) illustrates the reconstructed average density distribution along each path line. Two primary observations emerged: Firstly, the area of relatively strong muon absorption aligns with the position and shape of the newly formed lava mound on the original crater floor, dating back to the pre-2004 eruption (as indicated by the blue dotted line in Fig. 5.7-A). This suggests that the original crater is now covered with solidified or partially solidified dense lava. Second, the region exhibiting relatively weak muon absorption implies a lower density beneath the original crater from the pre-2004 eruption [252].

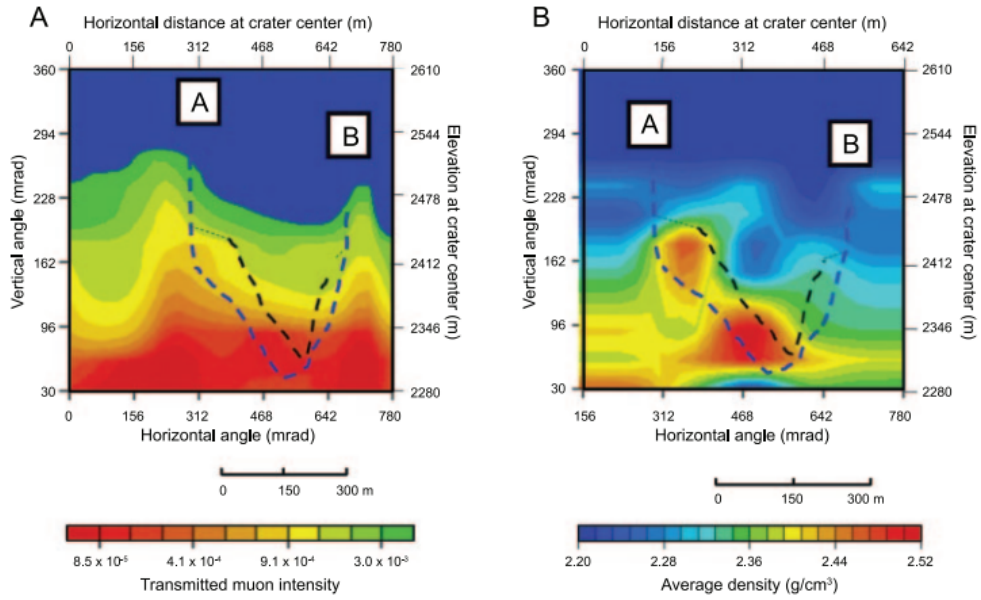

FIGURE 5.7: Major results of the muography conducted to study the interior structure of Mt. Asama. (a) Muographic image of the summit region of Mt. Asama. (b)- The reconstructed average density distribution for each path line [252].

Understanding eruption patterns often involves visualising magma dynamics with in a conduit. In 2013, groundbreaking evidence of magma dynamics in a volcanic conduit was presented through muography data [253], indicating the potential of muography as a tool to detect pre-eruption signs. The experiment took place at the Satsuma-Iwojima volcano in Japan. Satsuma-Iwojima volcano, situated on the northeastern rim of the Kikai caldera, is part of a mostly submerged caldera formed 7300 years ago. Although the Kikai caldera was the origin of the Akahoya eruption, one of the largest Holocene eruptions, magma activity at Satsuma-Iwojima's summit crater ceased 600–500 years ago. Intensive degassing at the Iwodake summit crater has persisted for at least 40 years. The muographic imaging revealed a low density anomaly region (shown in Fig. 5.8), suggesting densities similar to those of liquid water, highly altered rocks with porosity, or rhyolitic magma with porosity. Considering the ongoing emission of volcanic gases, the presence of a large amount

of liquid water beneath the crater is unlikely. The rock composition, formed by acid leaching of rhyolitic lava over 500 years ago, does not support long-term preservation of porosity. Therefore, the muographically observed low-density magma indicates recent emplacement at the shallow depth of the volcano's crater [246].

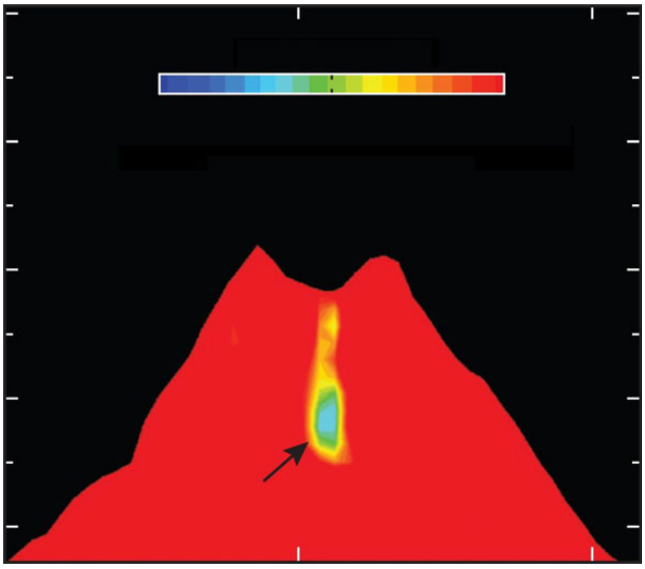

FIGURE 5.8: Muographic image of Satsuma-Iwojima volcano. The arrow indicates the low-density bubbly magma [246].

Muon data integrated over months can be effectively employed to generate static images for investigating a volcano's internal composition, providing crucial insights into the distribution of rocks with varying densities. A notable example is the muographic imaging of Mt. Stromboli, a stratovolcano in the Aeolian archipelago, Italy, characterised by frequent gas emissions and continuous "Strombolian" eruptions [231]. Using emulsion detectors, specifically chosen for logistical reasons, the study spanned five months and identified a substantial low-density zone (30-40% contrast with bedrock) at the volcano's summit. Density uncertainty was estimated at 18%, with 10% statistical and 15% systematic components.

The investigation of Mt. Vesuvius, a renowned stratovolcano near Naples, Italy, is strongly motivated by hazard concerns. This volcano gained global recognition because of its catastrophic eruption in 79 CE, which led to the destruction of the ancient Roman cities of Herculaneum and Pompeii. The initial investigations were carried out under the MU-RAY project, and subsequently, with a modified and enhanced detection setup, the research continued under the MURAVES project. The detailed information on the muography of Mt. Vesuvius is provided in Chapter 7.

The Puy de Dôme, standing at a height of 1465 m as a part of an extensive volcanic chain, serves as an exceptional case for testing muography detectors and methods. Its suitability arises from the wealth of reference data obtained through conventional geophysical methods and the logistical convenience it offers. The TOMUVOL telescope, developed for this purpose, is composed of glass RPC detectors, originally designed within the context of the particle physics CALICE collaboration. The joint

measurement campaign conducted in 2013 by the TOMUVOL and MU-RAY collaborations, utilising two different detector technologies, proved instrumental in assessing challenges and guiding further developments. Both telescopes were stationed at a distance of 1.3 km from the summit, featuring 1 m^2 detector layers with a few millimeter position resolution and an energy threshold in the range of hundreds of MeV. Figure 5.9 shows the results of the measurement campaigns. In Fig. 5.9-(a) and (b), the measured and expected transmissions throughout the entire mountain are presented. The measurements reveal that, for rock thicknesses exceeding 1 km, a

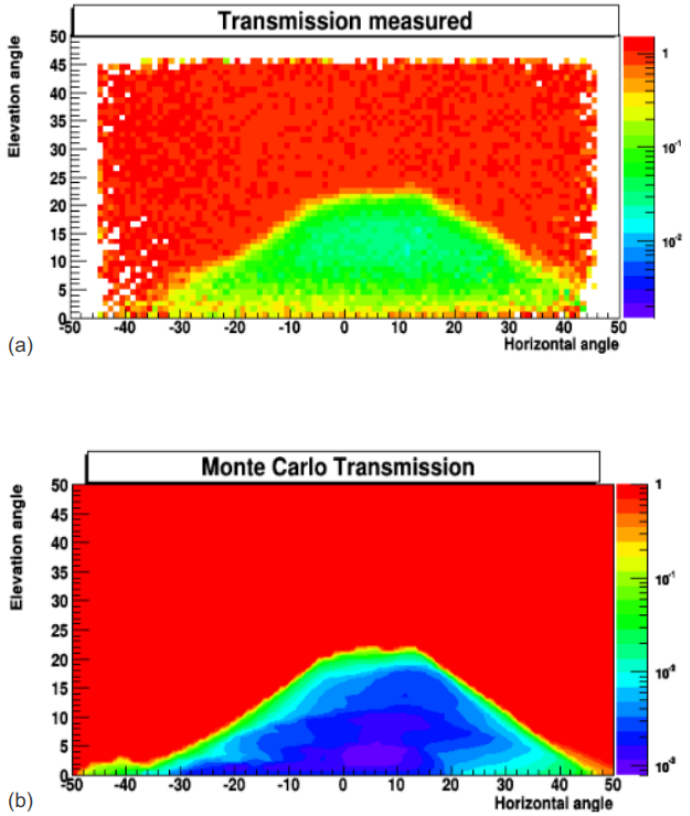

FIGURE 5.9: Results of the muography conducted for the Puy de Dome volcano: The figures (a) and (b) shows the measured and transmitted muon flux respectively [254].

significant background influences the data. This background, likely originating from low-energy muons (soft muons) scattered in the rock, deviates from their initial direction or encompasses stray particles. These muons traverse the detector, imitating muons from various regions of the mountain, thereby generating a uniform residual background [254].

In addition to the examples mentioned above, muography is actively applied in various volcano-based studies that include the investigations of Soufrière de Guadeloupe, an active volcano in the Lesser Antilles (France) [255], Mt. Etna near Catania (Italy) [256], Cerro Machn volcano in Tolima Department, Colombia, and others [257].

In addition to its application in volcanology, muography has been investigated for various other geoscience purposes. These encompass the surveillance of groundwater and saturation levels in bedrocks prone to landslides [258], the analysis of

hydro-geological rock density variations [259], assessment of river banks affected by animal activity [260], exploration of ice-filled cleft systems in steep bedrock permafrost [261], examination of carbon capture storage sites [262], as well as the investigation of natural caves [263, 264] and mineral exploration [211, 265, 266].

5.5.2 Archaeology and Civil Engineering

Muography finds common ground in its applications in archaeology and civil engineering. In both scenarios, the focus is on man-made structures, and frequently the research inquiries addressed by muography pertain to the identification of voids, although this is not always the case. The usual dimensions of the targets make absorption based muon imaging the preferred method [203, 267].

The pioneering application of muography in archaeology began with Alvarez et al.'s investigation of Chephren's pyramid in Egypt [169]. The study aimed to determine if there were unknown upper chambers above the Belzoni Chamber in Chephren's pyramid. The data, compared to a MC simulation, excluded the existence of significant upper chambers. Subsequently, the Pyramid of the Sun at Teotihuacan in Mexico was surveyed with muography to search for inaccessible chambers [268]. The preliminary results suggested a large volume of low density on the southern side, raising concerns about structural stability. Muography was also employed at the Mayan site of La Milpa in Belize and [269], more recently, as part of the ScanPyramids project in Egypt. The ScanPyramids project, utilising various non-invasive techniques, including muography, revealed an unexpected large void inside the Great Pyramid of Giza, providing valuable insights into the internal structure of this iconic ancient monument [232] Three muography teams contributed to this discovery, utilising different detector technologies (nuclear emulsions, scintillator telescope and MicroMegas), and their complementary data allowed for a precise 3D localisation of the void within the pyramid. The findings resulted from the data analysis of the all the three detectors systems reported an excess in muon flux originating from the same position in space, with statistical significance in excess of 5 standard deviations away from the null hypothesis (no void), as shown in Fig. 5.10. In Fig. 5.10-left, an illustration depicts the correlation between the muography image, obtained using the MicroMegas detector positioned outside and the Great Pyramid's face. The yellow and red angular regions correspond to the unknown void and the Grand Gallery, respectively. In Fig. 5.10-right, event counts (depicted by black points with error bars) are plotted against the horizontal angle within the yellow-indicated angular area on the left. The solid curve represents a model of homogeneous material. The peak in the plot signifies an unexpected excess of muons in the data, quantified as 141.3 ± 28.3 counts based on the best-fit result, with the uncertainty attributed to statistical considerations.

Mt. Echia, the initial settlement site of Naples, boasts a rich history with a complex network of underground tunnels and cavities carved into its soft volcanic rock. Accessible through the Bourbon Tunnel, excavated in the 19th century, these cavities hold diverse historical information. The first muographic studies at Mt. Echia with the MU-RAY telescope hinted at hidden underground cavities [270]. Recognising the challenges posed by the intricate system of cavities, a new approach to 3D muography was pursued [271]. This innovative method directly combines 2D muographies collected by placing MU-RAY detector at two different locations and MIMA portable telescope at a third location to create a high-resolution 3D image,

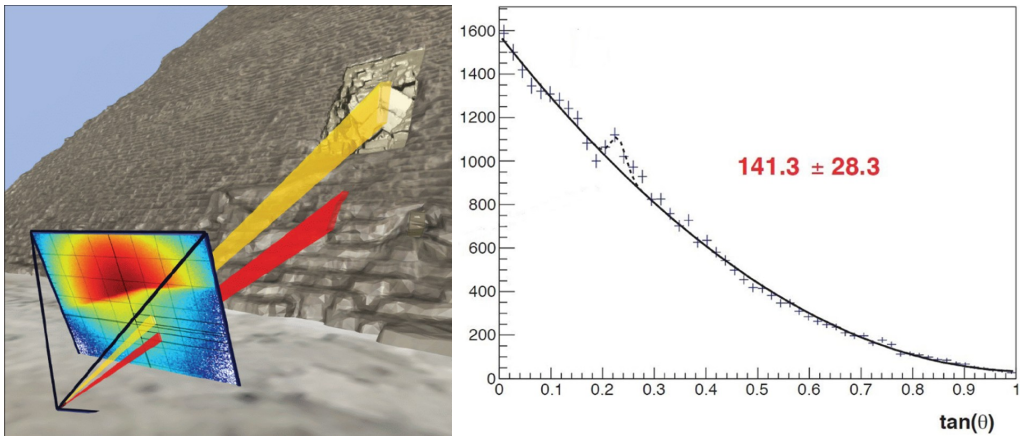

FIGURE 5.10: Left: Illustration demonstrating the correlation between the muography image obtained using the MicroMegas detector positioned outside and the face of the Great Pyramid or the Khufu's Pyramid. The yellow and red angular regions represent the unknown void and the Grand Gallery, respectively. Right: Event counts (black points with error bars) plotted against the horizontal angle within the yellow-indicated angular area on the left. The solid curve represents a model of homogeneous material. The peak in the plot indicates an unexpected excess of muons in the data, quantified as 141.3 $\pm$ 28.3 counts based on the best-fit result, with the uncertainty attributed to statistical considerations [232].

enabling the localisation and reconstruction of cavity shapes. The success in identifying a hidden cavity at Mt. Echia demonstrated the enhanced discovery potential of the 3D muography approach, particularly in complex underground environments, without requiring prior information about cavity locations or density distributions. Figure 5.11 illustrates the known cavities within Mt. Echia and the muon tracker locations: *A*, *B*, and *C*, each situated at an altitude of approximately 10 *m* above sea level. In Fig. 5.12: *a*–*c*, relative transmissions measured at these locations pro-

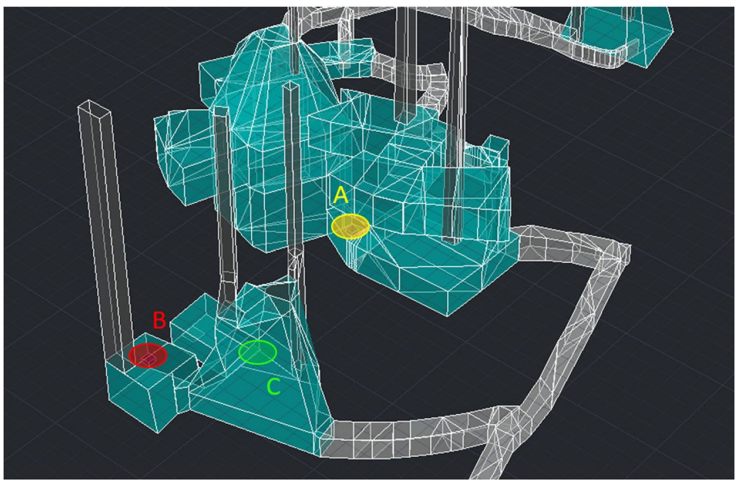

FIGURE 5.11: The CAD model of known cavities inside Mt. Echia and the three detector installation locations (*A*, *B* and *C*) for conducting muography [271].

vide projective muographic images. High relative transmission regions (depicted in green) suggest potential cavity locations. Data from location *A*, obtained with the MU-RAY muon tracker, revealed a region of interest (green) near the bottom-left corner, indicating a hidden cavity (marked inside red rectangle). The same tracker was then moved to location *B*, where a similar region of high transmissivity confirmed

the presence of the hidden cavity. Subsequently, the MIMA tracker, positioned at location *C* with a tilted view axis, captured data showing a signal for the hidden cavity within an angular region consistent with the observations from locations *A* and *B*. Although the chosen tracker locations were dictated by logistical constraints, they provided adequate information for a 3D muographic study. The outcomes of

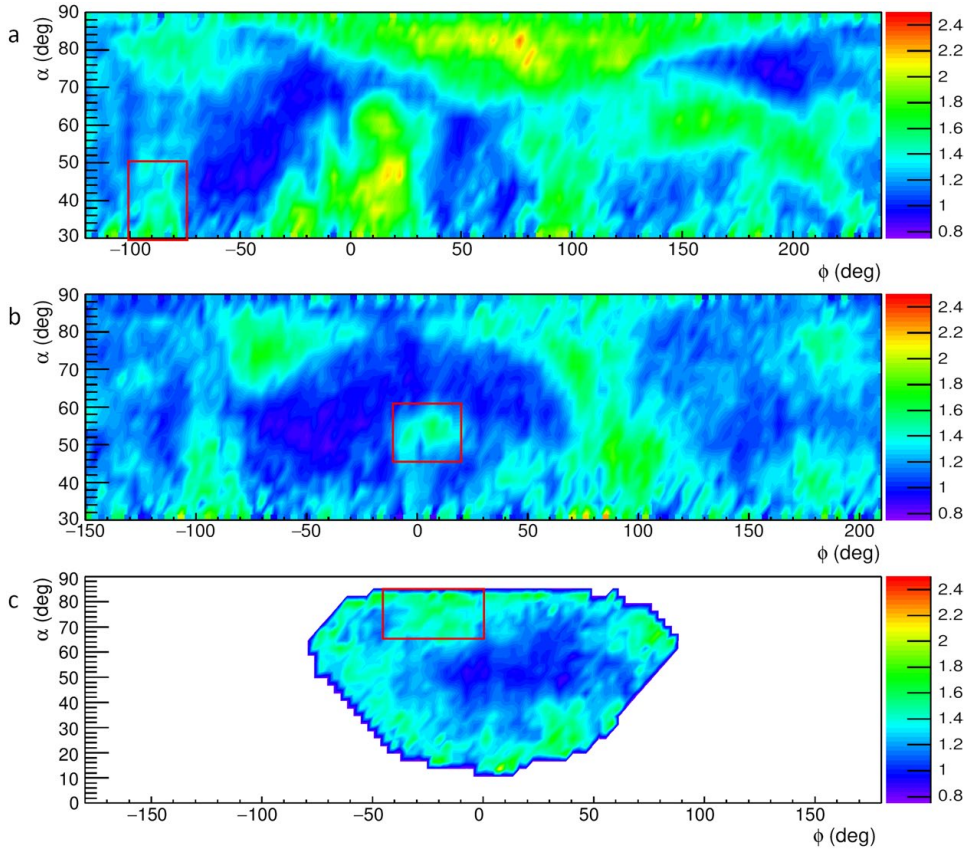

FIGURE 5.12: *a*, *b* and *c* illustrates the relative transmission observed at locations *A*, *B* and *C* (in Fig. 5.12), respectively, measured by the corresponding muon trackers. Rectangles highlight the angular regions linked to the presence of the hidden cavity [271].

the 3D muographic investigation, displaying two perspectives of the reconstructed hidden cavity in a coordinate system centered at the MIMA muon tracker at location *C*, are depicted in Fig. 5.13.

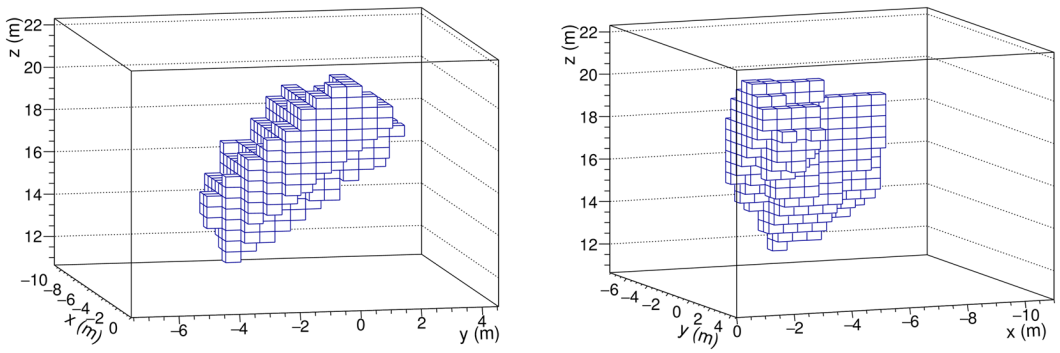

FIGURE 5.13: Two perspectives of the 3D reconstruction of the hidden cavity inside Mt. Echia, with origin at the centre of the MIMA muon tracker at location *C* [271].

Other applications of muography in archaeology and civil engineering encompass the examination of infrastructure degradation [272], exploration of tunnel overburden structures in Changshu, China [168], and imaging the entire overburden of a railway tunnel in the UK [273], among others.

Muon imaging also finds applications in nuclear safety, homeland security, and industrial process control (e.g., blast furnaces [274]) [275–284]. In these applications, scattering-based muography is commonly employed.

Chapter 6

Development of Small-Scale RPCs for Muography

In this chapter, a summary of the instrumentation efforts carried out applying RPC technology for muography is given. As part of the activities, I have developed a novel spray-gun coating technique for fabricating glass resistive electrodes for RPCs, yielding promising results. Additionally, I designed and evaluated single-gap and double-gap glass RPC prototype detectors, demonstrating the feasibility of constructing a compact, leak-tight, and portable RPC muon telescope with high detection efficiency. In view of constructing an advanced gaseous muon telescope, I built and studied a multi-gap RPC prototype detector, showcasing successful preliminary tests. Furthermore, I developed a Geant4-based mRPC telescope simulation setup to explore the potential of utilising TOF information for PID. Detailed insights into the projects, developed detectors, and achieved results are provided.

6.1 Introduction and Motivation

Muography is an imaging technique that uses freely available cosmic-ray muons to study the interior structure of natural or man-made large-scale objects .Applications of muography are becoming ubiquitous [170, 171], ranging across archaeology [285], volcanology [172], geosciences [174], nuclear waste characterisation [175], border controls [176], nuclear warhead verification in the context of non-proliferation treaties [177], and industrial monitoring and maintenance [178]. The selection of the experimental setup and site depends on factors like the size and structure of the object, as well as practical considerations related to its location. Most muography projects are based on large-area detectors, e.g. in order to surround volumes of the size of a cargo container or to collect large statistics to study huge targets such as volcanoes or pyramids; moving such large detectors is very complex, and in most cases, unnecessary. However, some important use cases demand detector set-ups that are small and portable. This is often the case in archaeological or geophysical explorations, where the detectors may need to be located in narrow and confined environments such as tunnels or underground chambers [286]. Use cases for portable detectors can also be found in cultural heritage preservation, e.g. statues hosted in crowded museum spaces and which are too heavy or too fragile to be transported to a laboratory [287]. A portable muon detector is also necessary for a new type of positioning system based on cosmic muons [288, 289], for use in places (e.g. underground) where more standard navigation techniques such as GPS are unavailable.

Muon telescopes in muography typically utilise technologies based on nuclear emulsions, scintillators, or gaseous detectors (see e.g. [173] and Chapter 5). Each

technology offers distinct features and advantages, and the choice depends on the specific application, the nature of the target object, and its environmental context. Among them, gaseous detectors are often chosen when real-time information is necessary (which excludes nuclear emulsions) and spatial resolution is important. RPCs, in particular, have been utilised by several teams because of their trade-off between performance and cost [290].

The muography groups at UGent and the Catholic University of Louvain (UCL) are involved in the development and investigation of small-scale glass RPC-based (gRPC) portable detectors designed for muography applications in confined environments. The RPC technology is chosen due to its aforementioned detector-specific advantages, cost-effectiveness, and the extensive experience of the participating groups in RPC detector development. The ongoing efforts involve the construction and study of several prototype detectors. The primary objectives include optimising an efficient portable detector layout, refining detector electronics, and addressing logistical considerations.

The RPCs typically operate using a standard gas mixture composed of 95.2% $C_2H_2F_4$, 4.5% i-C_4H_10, and 0.3% SF_6. However, the high GWP of this mixture, particularly due to the significant R134A ($C_2H_2F_4$) component, has led to increasing restrictions in European regulations regarding the usage and emission of greenhouse gases (detailed in Sec. 4.1). Considering this, a fully leak-tight design is proposed for the RPC detectors and the goal is to create detectors that not only minimise gas consumption but also operate effectively without the need for continuous gas flow in a closed mode, all while maintaining portability.

Sections 6.2, 6.3 and 6.4 provides a detailed account of the major activities conducted and the significant results attained. An in-house coating technique was developed for the creation of glass resistive electrodes, and detailed information on the procedure and the achieved results can be found in Sec. 6.2. Two types of gRPC portable detectors were developed: a basic version with a single gas gap and an advanced version with a double gap design. The construction details of these prototypes, the results of their quality assurance tests, and the outcomes of performance studies with cosmic muons are covered in Sec. 6.3 and Sec.6.4 respectively.

Recently, R&D efforts at UGent have also been initiated to construct an advanced gaseous detector-based muon telescope for muography. The aim is to exploit the advantages offered by specific technologies by incorporating multiple detector types into a single, highly-performing muon telescope. For now, mRPCs and Thick Gas Electron Multipliers (THGEMs) are being considered to improve the muon telescope's performance in terms of time and spatial resolution simultaneously. The work discussed in the thesis primarily focuses on the mRPC part. The details of the initial version (small-scale) of the mRPC prototype detector constructed, the related Geant4 simulation studies conducted, and the achieved results are presented in Sec. 6.5.

6.2 Development of Resistive Plates

The resistive coating applied in the glass plates plays a very crucial role in the operation of the RPCs. The surface resistivity of the coating should be within a specific

range that allows the bias voltage required for the operation of the RPC to be applied to the coating, and since the induced charge is measured as the signal output, it should be transparent to the electric pulses induced due to the displacement of the charge produced in the gas volume. If the surface resistivity is too low, it causes the induced charge to spread across the coated surface, leading to the activation of multiple strips (resulting in an increased cluster size) and crosstalk, which degrades spatial resolution. Conversely, if the surface resistivity is too high, it decreases the rate capability as well as the amplitude of the generated pulses. Therefore, a specific range of surface resistivity (0.4 to 4 $M\Omega/\square$) is selected for the fabrication of the plates where the cluster size is low with a uniform detection efficiency across the active area [291]. In large-scale experiments like CMS, resistive plates are typically mass-produced by industries. However, since our project focuses on creating small-scale RPC detectors, an exploration of the possibility of producing most components within our laboratory was undertaken. As a result, an in-house method was developed for the production of resistive plates. This section presents a detailed account of the process, including the results achieved. The details of using glass based electrodes for RPCs is discussed in Sec. 2.4.2.

6.2.1 Coating Procedure

Preparation of glass plate: The coating process involves a series of steps. It begins with the preparation of float glass (see Sec. 2.5.2 for details of the float glass) plates (30×30 *cm*). These glass plates must undergo thorough cleaning using acetone, glass cleaner spray (Bohle glass cleaner [292]) and a microfiber cloth to ensure the removal of all dust particles and chemicals. Proper cleaning is crucial to achieve uniform coating thickness. After the glass plates are cleaned, a piece of copper tape (measuring 2.5×7 *cm*) is affixed to one edge of the glass plate for HV or ground connections. This ensures a secure HV connection to the coating, with the adhesive side of the tape facing the glass plate. It's important to ensure that all sides of the tape are firmly attached to the glass plate. Any detachment of the tape can lead to cracks in the coating around the tape, affecting the HV distribution. A 9 *mm* wide masking tape is applied to all four borders of the glass plate to prevent the coating from being applied to the edges. The steps involved in the preparation of the glass plate are shown in Fig. 6.1.

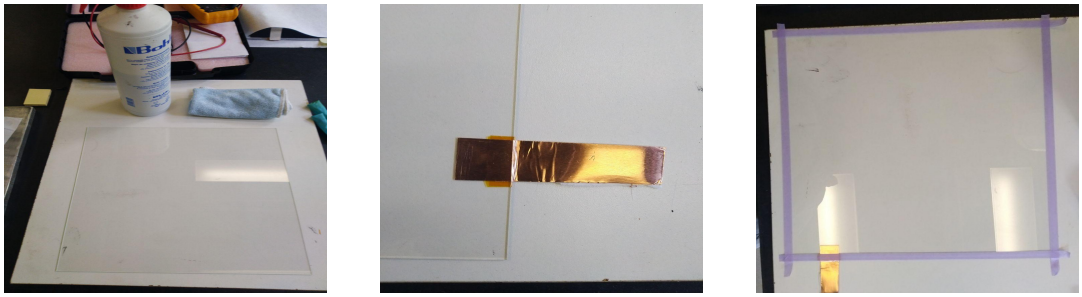

(a) (b) (c)

FIGURE 6.1: Glass plate preparation steps: (a) cleaned glass plate with glass cleaner and micro fibre cloth, (b) copper tape for HV connection and (c) masking tape for preventing the edges from coating.

Spray Painting

For this resistive coating, a mixture of Electrodag 6017SS conductive and Electrodag PM-404 resistive paint is used [293]. A solvent 2-butoxy ethyl acetate (diluter) is also added to the paint mixture to dilute and fine-tune the resistivity values (discussed in Sec. 6.2.2). The paint mixture is sprayed onto the glass plates via a hand-held painting gun (ASTUROMEC-SERIES OM-IMIM/SP [294]) operated under a nearly constant pressure of 4.5 to 5 *bar* supplied by an air compressor. To prevent cracks in the coating and to ensure uniformity, the painting process always follows a single direction, either vertical or horizontal. Since the coating is applied using a spraying technique, even after one layer is applied, some tiny spots may remain without coating. To address this issue, glass plates are placed on a specially designed wooden light box during painting. This light box features a rectangular hole on top (28×28 *cm*) where the glass plates are positioned. Inside the wooden box, three tube lights are installed. When the coating is applied, the plate is placed atop the rectangular hole, exposing the coating area to the bright light below. The painting is performed in a dark room and the thick black paint makes any unpainted spots highly visible due to the intense illumination. Multiple layers (usually 3 to 4) of coating are applied to the plates until all the spots are completely covered. After painting, the glass plates are immediately baked in an oven for 20 minutes at $100^{\circ}C$ to allow the coating to dry. When painting is conducted outside the clean room environment, it is crucial to immediately transfer the plates to the oven. Failure to do so can lead to the adherence of tiny dust particles to the paint, resulting in coating irregularities and bumps. Figure 6.2 displays the wooden light box (left) designed for the coating process and an image of plate baking in the oven at $100^{\circ}C$ (right). A uniform resistive layer in terms of thickness as well as resistivity was achieved and the front and back side view of an example resistive plate developed is shown in Fig. 6.3.

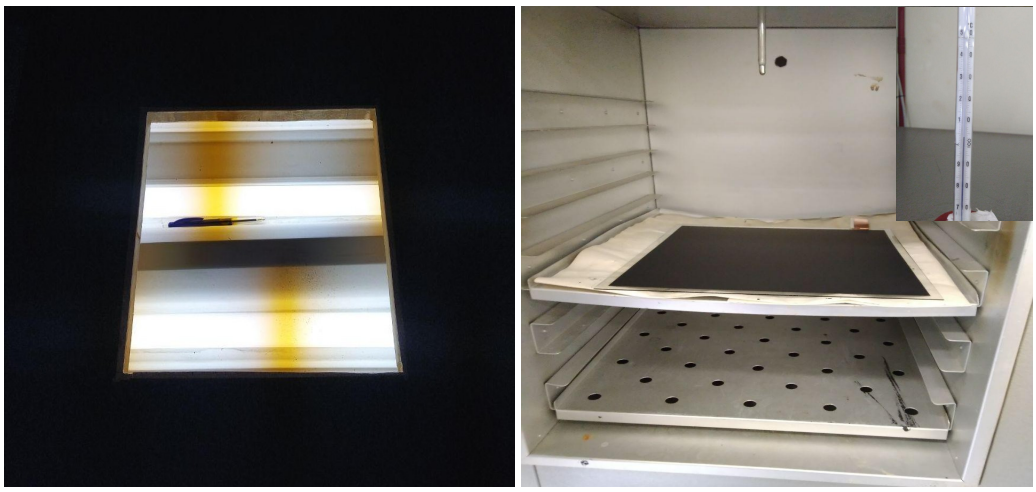

FIGURE 6.2: (Left) Wooden light box used for the coating procedure, and (Right) Baking the plate in the oven at $100^{\circ}C$.

One significant challenge encountered in the early stages of this study was the occurrence of cracks in the glass plates. It was identified that various factors contribute to these cracks, with one prominent cause being the baking temperature. Plates baked at temperatures below 90 $^{\circ}C$ exhibited severe cracking throughout

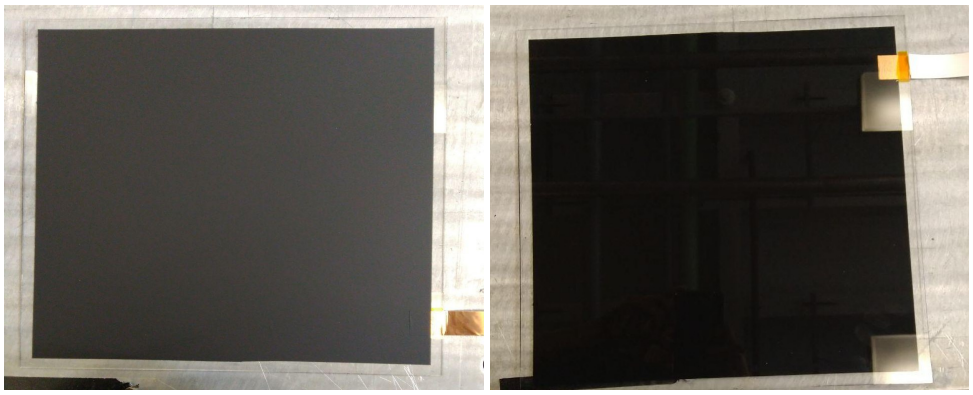

FIGURE 6.3: The front and back views of the resistive plates produced using the in-house spray gun-based coating technique.

FIGURE 6.4: Left: Glass plate with extensive cracking due to low-temperature baking. Maintaining a baking temperature between 100-110°C is crucial for optimal results. Right: Application of silver conductive paint on the edges of the copper tape to ensure proper HV connection on the electrode.

the coating. Figure 6.4-left displays a glass plate with extensive cracking due to low-temperature baking. Therefore, maintaining a temperature range between 100-110°C is critical for optimal results.

Another factor contributing to cracks is the copper tape used for HV connection. If the corners of the tape is not firmly adhered to the glass, it may protrude and cause cracks in the coating around the tape. This affects not only the coating but also the HV connection to the electrode. To mitigate this, the copper tape must be securely affixed to the glass plate, and for additional assurance, silver conductive paint (SCP silver conductive paint [295]) is applied to the three corners of the tape after the coating process. Figure 6.4-right illustrates the application of silver conductive paint on the edges of the copper tape.

Inadequate cleaning of the plates is yet another potential cause of cracks. During the float glass manufacturing process, molten glass floats on a pool of tin, leaving traces of tin and tin oxide on the glass surface. These residues can negatively affect

the coating. Therefore, thorough cleaning with acetone followed by a glass cleaner is essential.

Additionally, prolonged exposure to varied environmental conditions can induce cracks. To counteract this, an insulator spray (URETHAN 71 [296]) is applied on top of the coating, providing a protective barrier against external variations. Further measurements and results are elaborated upon in the following section.

6.2.2 Measurements and Results

Mass Ratio Estimation

As mentioned earlier, the resistive coating is created by combining resistive and conductive paints. The conductive paint contains carbon particles within a thermoplastic resin, while the resistive paint consists solely of the thermoplastic resin. The required proportions of conductive and resistive paint are determined by the mass ratio, denoted as r_c, calculated using the following formula:

$$r_c = \frac{m_c}{m_c + m_r} \tag{6.1}$$

In this equation, m_c represents the mass of the conductive paint, and m_r represents the mass of the resistive paint. According to the percolation model, as described in [297], the paint mixture undergoes a phase transition towards higher conductivity as the concentration of carbon particles increases. Each carbon particle in the mixture acts as a conductive region, and the fraction of conductive regions is correlated with the mass ratio r_c. When the relative quantity of resistive paint increases, the likelihood of conductive pathways decreases, leading to an increase in resistivity. Once a critical point is reached, no conductive pathways remain in the coating. This behavior is commonly described using a power law [297].

The manufacturer's product data sheet provides values for m_c, m_r and the achievable resistivity (R_{tot}) using the corresponding mixture, ranging from 34 $\Omega/\square$ to 1 $G\Omega/\square$ with a coating thickness of 25 μm. Initially, an attempt was made to fit a power law curve to the data from the datasheet to estimate the precise composition of m_c and m_r required to achieve the desired resistivity values within the range of 0.4 to 4 $M\Omega/\square$. However, the resistivity of the coating obtained with these estimated values did not align with the expected values, showing a difference of several hundred $k\Omega/\square$ from the measured value. This discrepancy could be attributed to the age of the paint used in the experiment, which had been stored for several months, potentially undergoing changes such as evaporation and alterations in properties over time. Consequently, a calibration study was conducted to ensure the attainment of the required surface resistivity in the coating. Considering the data given in the datasheet, a constant quantity of conductive paint (m_c=11 g) was maintained while varying the quantity of the resistive paint. Several sample plates for the calibration study were developed with the mixtures with varying m_r. The first plot in Fig. 6.5 illustrates the surface resistivity measurements plotted against the computed mass ratio r_c, with a power law fit depicted by the red line. In the second plot, resistivity measurements are displayed as a function of the varying quantity of resistive paint in grams. Subsequently, these calibration results were used to develop the resistive electrodes for all the gRPC detectors.

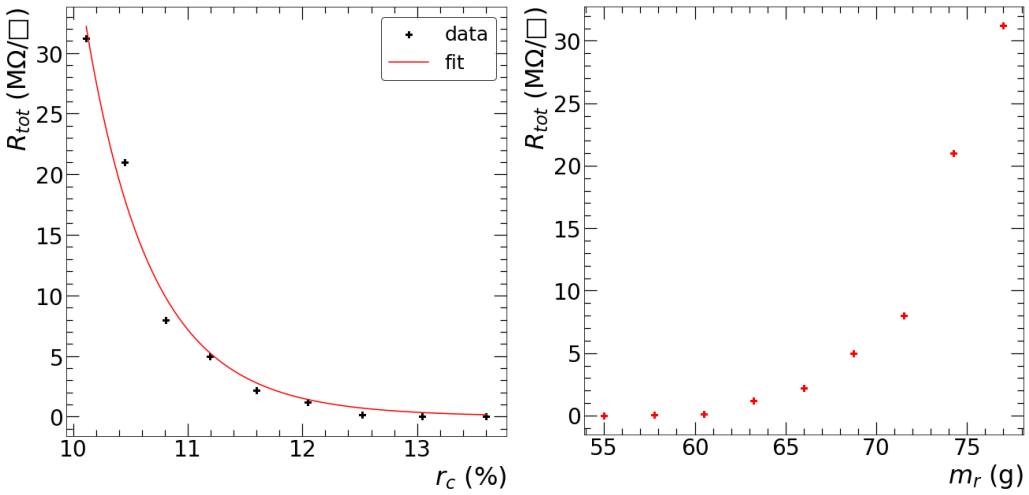

FIGURE 6.5: The first plot depicts surface resistivity as a function of the computed mass ratio r_c with a power law fit (red line). The second plot showcases resistivity measurements based on the varying quantities of resistive paint in grams.

Surface Resistivity Measurements

The surface resistivity of the developed resistive plates is assessed using a concentric ring probe. This specialised device comprises of metallic concentric rings, offering a distinctive approach. Unlike traditional measurements between two points, it measures the resistance between two circular areas. The outer circular region has a diameter of 63 mm, while the inner one measures 30 mm. With a weight of approximately 2.6 kg, the probe ensures robust contact with the resistive surface. A digital multimeter reads the resistance from the banana jack adapter. The probe is designed by the manufacturer (Desco Europe [298]) in a way that the measured resistance multiplied by 10 $\square^{-1}$ gives the surfarce resistivity in units of $\Omega/\square$. In Fig. 6.6 (left), the concentric ring probe and the two metallic circular regions for resistance measurement are depicted.

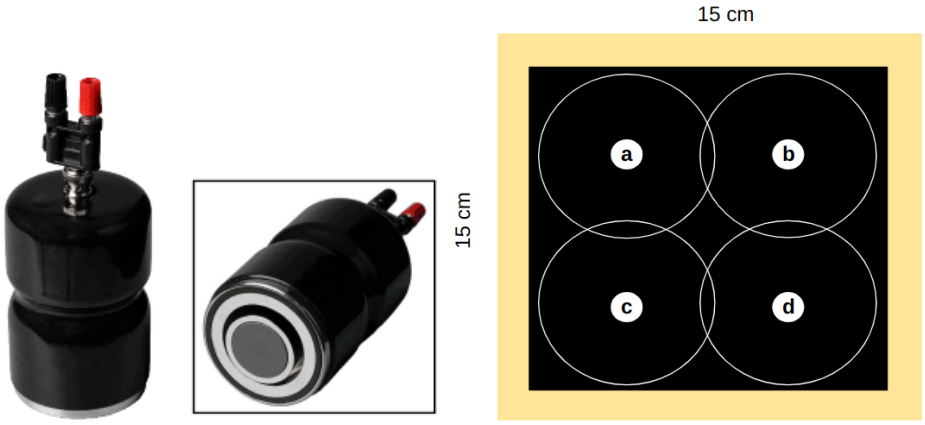

FIGURE 6.6: Left: Image of the concentric ring probe depicting the metallic circular regions used for resistance measurement [298]. Right: Schematic representation of the four distinct measurement locations (a, b, c, and d) on the 15 $\times$ 15 cm sample resistive plates, monitored for long-term surface resistivity stability measurements.

To ensure the long-term stability of surface resistivity in the resistive plates, a continuous monitoring approach was employed. Four sample resistive plates, each measuring 15 $\times$ 15 cm, were developed for this purpose. The surface resistivity at four distinct locations on the plates, labeled as a, b, c, and d were measured using the circular probe. A schematic illustrating these measurement locations is provided in Fig. 6.6 (right). The time-dependent surface resistivity of all glass plates is presented in Fig. 6.7, where each color in the plots corresponds to a specific measurement location. In the case of all the glass plates, slight variations in surface resistivity values

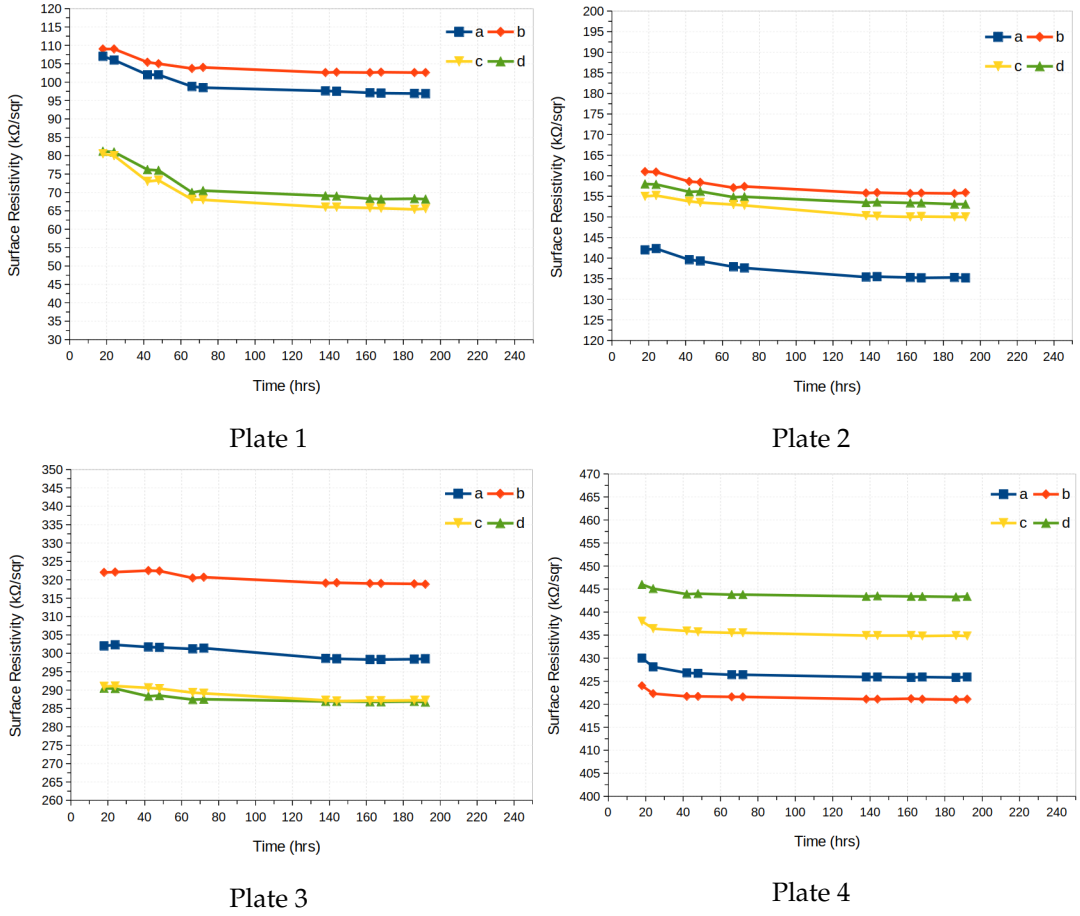

FIGURE 6.7: Surface resistivity variation over time for four sample glass plates. Minor differences in coating thickness result in slight variations among the four locations (a-d). The resistivity initially drops and then stabilises, remaining stable even a week after painting.

among the four locations are observed, attributed to minor differences in coating thickness. It is evident that, in all cases, surface resistivity initially drops and then stabilises over time. Even a week after painting, the resistivity remained very stable. The observed drop in surface resistivity for Plate 1 is slightly higher compared to other cases. This variation could be attributed to environmental factors or aspects related to the coating procedure, such as the baking temperature.

The surface resistivity values are different in the case of all plates. This is associated with the use of these plates to quantify the amount of diluter (2-butoxy ethyl acetate) needed in the paint mixture to increase surface resistivity in small steps. (in steps of 50-150 $k\Omega/\square$). Figure 6.5 demonstrates that even a slight increase in the amount of resistive paint leads to surface resistivity increments in steps of $M\Omega/\square$.

Therefore, the use of the diluter plays a crucial role in achieving slight increases. In this study, the values of m_c and m_r were fixed at 11 g and 61 g, respectively, while the amount of diluter was varied. The table below presents the quantity of diluter used in each case along with the corresponding mean surface resistivity achieved. The results demonstrate that fine-tuning the surface resistivity values is achievable

Glass Plate	Diluter: 2-butoxy ethyl acetate (ml)	Mean Surface Resistivity ($k\Omega/\square$)
1	10	83.3
2	7	148.5
3	4	297.8
4	1	431.3

TABLE 6.1: The table provides details of the amount of the diluter (2-butoxy ethyl acetate) used in case of each glass plate and the corresponding mean surface resistivity achieved.

by slightly adjusting the amount of diluter.

To assess the long-term effects, the resistivity of a 30×30 cm glass plate, also used in constructing one of the detectors, was monitored for over six months. Figure 6.8 depicts the resistivity measurements conducted from September 2021 to May 2022 [3]. The stable nature of the surface resistivity over such an extended period underscores the quality and durability of the coating procedure. In the plot, Loc1 to Loc4 represent four distinct locations on the plate where measurements were taken using the concentric probe.

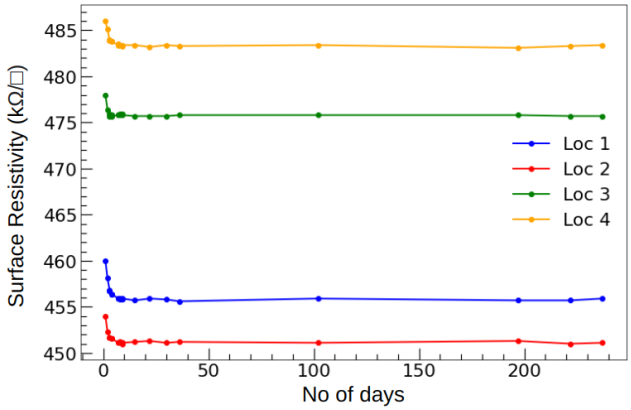

FIGURE 6.8: Result of long-term resistivity monitoring of a 30×30 cm resistive electrode used in detector construction. The plot shows resistivity measurements conducted from September 2021 to May 2022, emphasising the stability and durability of the surface resistivity over this six-month period. Loc1 to Loc4 indicate four specific locations on the plate where measurements were performed using the concentric probe [3].

Thickness measurement

To ensure the uniformity of the coating thickness on glass plates, an equipment named PWB SWISS TOOL MASTER 2D [299] was initially used for measurements. The tool utilises a conical metallic probe, initially placed on an uncoated area of the glass plate to establish the zero point. Subsequently, the probe is positioned on a

region with coating, and the instrument accurately measures the difference between these points in micrometers, providing the coating thickness. With a precision of 1 μm, the tool ensures highly accurate measurements. Figure 6.9-left visually demonstrates the process of measuring coating thickness on a sample plate. Conducting measurements at various locations on different sample plates consistently yielded values between 25-30 μm, affirming the uniformity achieved through this manual coating method.

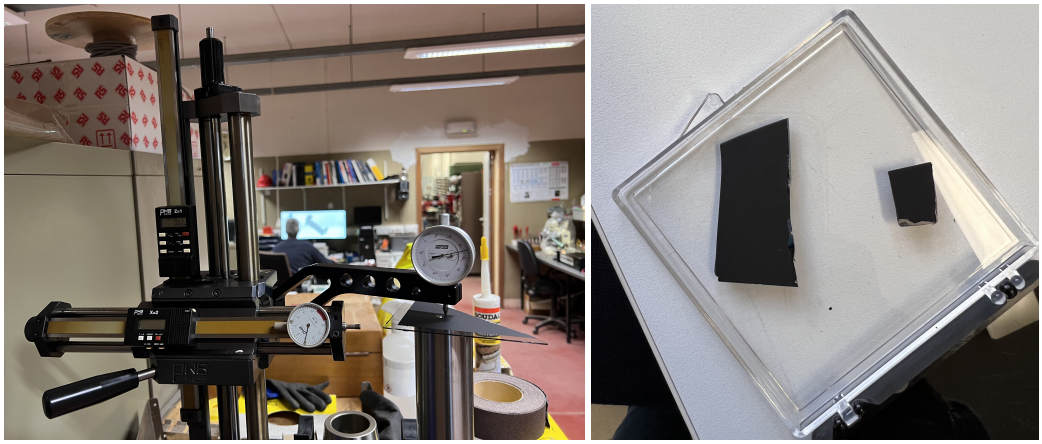

FIGURE 6.9: Left: procedure of thickness measurement of the coating on the glass plates. Measurements conducted at different locations on various sample plates consistently show values between 25-30 μm, confirming the uniformity achieved through the manual coating method. Right: resistive layer coated silicon wafer samples prepared for SEM-based thickness measurements.

For a more in-depth analysis, the thickness and uniformity were examined using a Scanning Electron Microscope (SEM) [300]. To facilitate SEM-based measurements, specific samples were prepared on silicon wafers, positioned at various locations on the glass plates during the coating process. The measurements were carried out at the Department of Solid State Sciences, UGent[1]. Figure 6.9-right shows a depiction of the samples prepared for this investigation, and the corresponding SEM images are presented in Fig. 6.10 [3].

Figure 6.10, (a) showcases the SEM image of a section of the resistive layer coated on the silicon wafer, with a scanned part width of 200 μm. The uniformity in coating thickness is evident in this image. Subsequent images (b), (c), and (d), show different sections of the samples, each with a width of approximately 20 μm. The measured thickness in each case is annotated on the figures, revealing that the overall deviation in thickness is minimal (a few μm) when employing this coating technique. Given that variations in thickness can influence surface resistivity, achieving such an industrial level precision through a manual technique is a noteworthy accomplishment.

The results from both surface resistivity and thickness measurements indicate that this manual coating technique is comparable to industrial methods, such as silk

[1]Special thanks to Dr. Nithin Poonkottil (Department of Solid State Sciences, UGent) for his help and suggestions for conducting the SEM measurements.

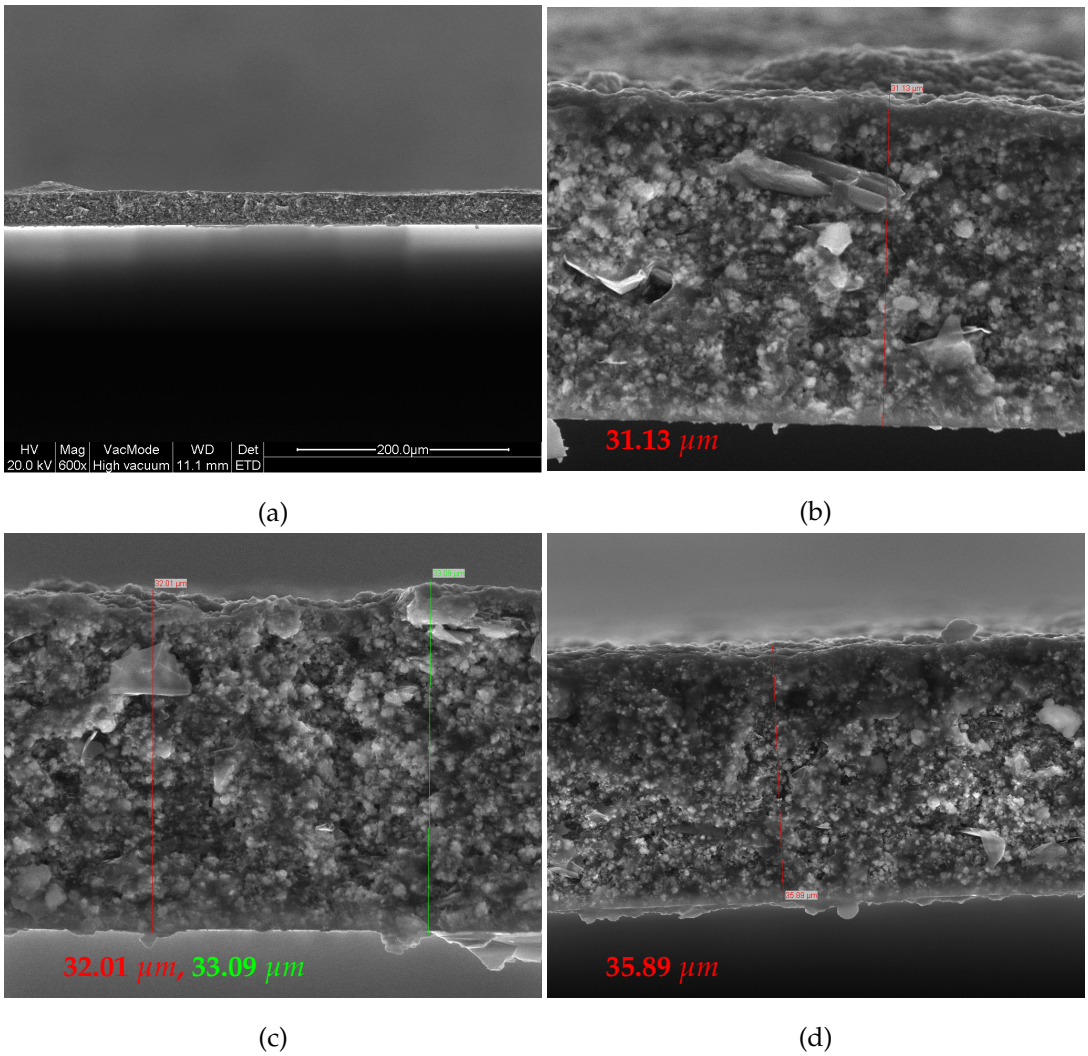

(a) (b)

(c) (d)

FIGURE 6.10: SEM images of the resistive layer coating for the thickness measurement. (a) SEM image of the coating with a scanned width of 200 μm, demonstrating uniform thickness. (b), (c), and (d) showcase SEM images of different sections of the samples with a width of approximately 20 μm, each annotated with measured thickness values. The consistent measurements affirm the precision of the in-house coating technique, revealing minimal overall thickness deviation (a few μm) [3].

screen printing. The implementation of this in-house coating method not only reduces the production cost of electrodes but also speeds up the process, eliminating delays associated with ordering electrodes from external suppliers.

6.3 Single-gap gRPC

The initial phase of the project involved the development of a single-gap gRPC detector. As this was the first attempt to construct a gRPC prototype, it served as a valuable learning experience aimed at optimising technical design for a portable gRPC-based gaseous detector. This phase included understanding the logistics required and studying the detector's operation.

The resulting detector represents a fundamental version, constructed using materials readily available in the workshop, ensuring a minimal production cost. The

subsequent subsections in this section detail the construction process, major challenges encountered, and the results achieved.

6.3.1 Detector Construction

This section provides a comprehensive step-by-step guide to the construction of the single-gap gRPC prototype. It can also be used as a manual for easily developing a small-scale RPC using low-cost components and basic mechanical workshop facilities.

To ensure the portability of the detector, a gas-tight layout was adopted with the possibility to operate the chamber without continuous gas flow. All detector components, including electrodes and strip PCB, are assembled inside a sealed detector box, which is subsequently filled with the gas for operation. Differing from the iRPCs discussed in Chapter 3, instead of sealing the sides of the gas gap and flushing the gas only between the electrodes, in this case the gas is filled inside the entire box. Dedicated gas connectors are attached to the box to facilitate chamber filling and refilling, while the HV and signal readout connections are established through slots made on the sides of the detector box.

Following are the details of the steps involved in detector construction:

Step 1: The detector box is constructed using plates based on polyvinyl chloride (PVC). A rectangular PVC plate serves as the base, with PVC sidebars affixed to all sides and corners sealed with glue. Figure 6.11 (left) illustrates the constructed PVC box. The top PVC bar features a flat cable connector, a PTH sensor (pressure, temperature and humidity sensor), and a gas connector secured through slots in the bar. The bottom bar accommodates an HV connector and a gas connector. The channel carved in the top part of all sidebars holds O-rings (made of Nitrile rubber) with a diameter of 2 mm, ensuring gas tightness when closing the chamber. Additionally, screw holes are added in this area to fix the top plate for chamber closure. Long copper tapes are affixed to three corners of the box to construct the Faraday cage.

Step 2: A copper foil with a thickness of 200 μm is placed at the bottom, stretching to cover the sides for the construction of the Faraday cage (see Fig. 6.11 (right)). On all three sides of the box, plastic bars (yellow bars in Fig. 6.11 (right)) are affixed to the copper foil to secure the cylindrical spacers in place. These cylindrical spacers, made of Bakelite, serve to hold the glass plates and PCB in position and are also used for the construction of the gas gap. A Mylar foil of thickness 200 μm is also added on top of the copper foil for insulation.

Step 3: For the signal readout, a strip PCB is positioned atop the Copper+Mylar foils. The strip PCB comprises 16 strips, each with a width of 15 mm and separated by 1.6 mm. Signal cables are soldered to each strip. The continuity of the strips and the potential for cross-talk between adjacent strips are verified using a digital multimeter. The arrangement of the strip PCB within the detector box is depicted in Fig. 6.12 (left).

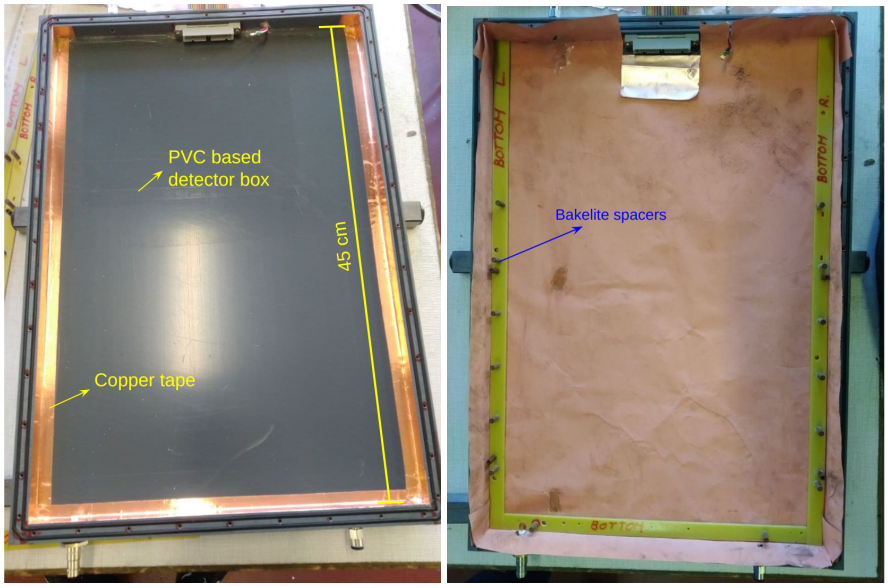

FIGURE 6.11: **Step 1&2-**Left: The PVC box with a rectangular base plate, sidebars, and corner seals. Right: A 200 μm copper foil covers the bottom and sides for the construction of Faraday cage. Plastic bars (yellow) secure cylindrical Bakelite spacers, used for holding glass plates and PCB on position, and for gas gap construction.

Step 4: A Mylar foil ($30 \times 30\ cm$) is placed on top of the PCB layer for insulating and avoiding direct contact of the resistive plate to the PCB strips. After placing the Mylar foil, the first resistive plate is placed in the chamber between the cylindrical spacers facing the resistive coating side to the Mylar foil (shown in Fig. 6.12 (right)).

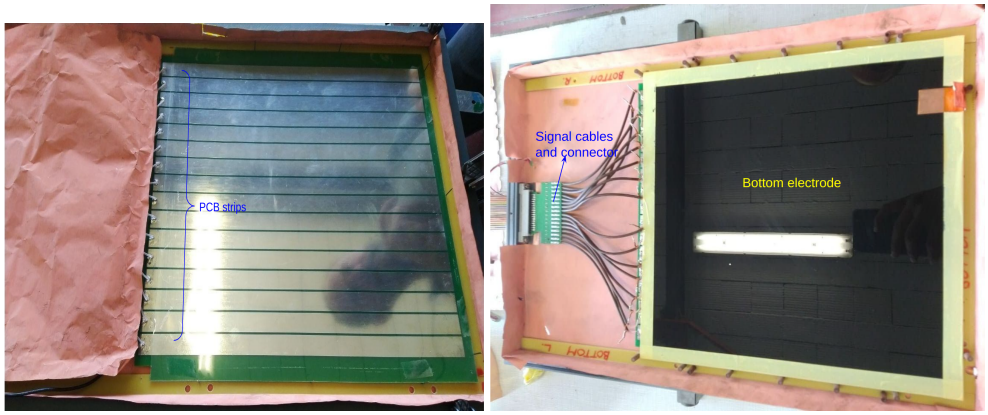

FIGURE 6.12: **Step 3&4-**Left: Strip PCB placed within the detector box. Right: Placement of the first resistive plate in the chamber between cylindrical spacers, facing the resistive coating side toward the Mylar foil.

Step 5: The 1 mm gas gap is created using 1 mm diameter fish wire. To ensure a consistent gas gap across the entire active area, the fish wire is arranged in a configuration depicted in Fig. 6.13-left. It is securely fastened to the cylindrical circular spacers with small screws, as illustrated in Fig. 6.13-right. In particular, the fish wire is not glued, allowing for easy disassembly of the chamber if repairs are required.

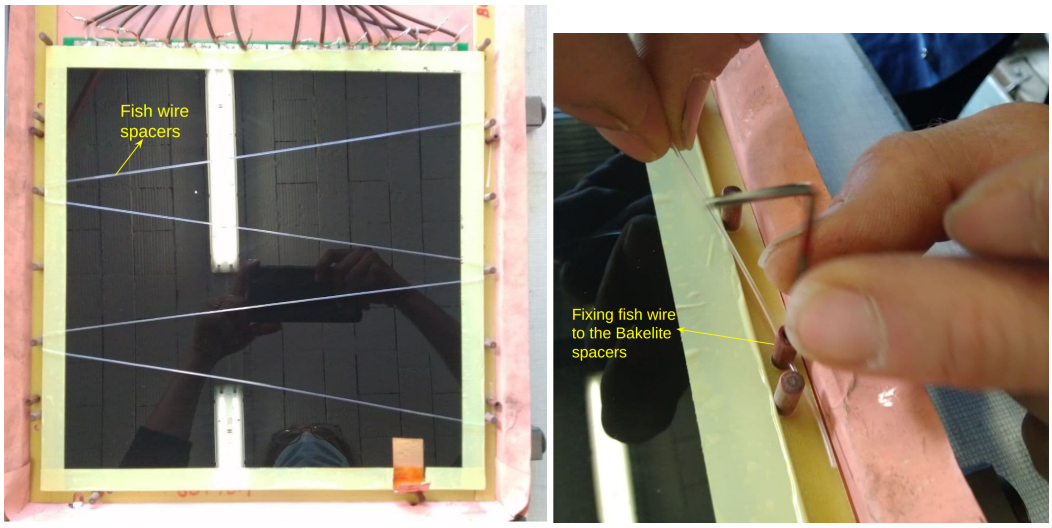

FIGURE 6.13: **Step 5-**Arrangement of fish wire to create the 1 *mm* gas gap (left) and the procedure for fixing the fish wire to cylindrical spacers (right).

Step 6: The second electrode is positioned on top of the fish wire, as depicted in Fig. 6.14(left), thereby completing the construction of the gas gap. Both electrodes used in this case have surface resistivity values ranging from 600-700 $k\Omega$. Additionally, a Mylar foil is placed on the second electrode for insulation.

Step 7: HV is linked to the upper electrode, while the bottom electrode is connected to the ground. The Jupiter HV connector is attached to the side bar with its pin extending into the detector box. A wire is soldered from the HV point to the top plate, as illustrated in Fig. 6.14 (right) for the HV connection (red cable). To prevent sparks

FIGURE 6.14: **Step 6&7-**Left: The second electrode positioned on top of the fish wire, completing the construction of the gas gap. Right: Procedure of implementing the HV connection.

due to the close proximity of the HV connection to the copper foil, it is properly insulated with Kapton tape. The bottom electrode is connected to the copper Faraday cage foil, and the foil is connected to the grounding part of the HV connector via a black insulated cable.

Step 8: To ground the signal cables, the grounding part of all 16 cables is soldered to a copper foil positioned on top of the upper Mylar foil. This foil is then connected to the primary Faraday cage foil. Each signal cable is securely fixed in place using a PVC bar. The connectors on the other ends of the signal cables are attached to the flat cable connector fixed on the PVC side bar. Both sides of this connector are insulated with taped Mylar foils to prevent contact with the Faraday cage. These steps are illustrated in Fig. 6.15 (left).

Step 9: To close the Faraday cage, an additional piece of foil is added on top of the section containing the signal cables. All foils are interconnected using copper tapes, resulting in the final configuration as depicted in Fig. 6.15 (right).

FIGURE 6.15: **Step 8&9-**Left: Image of grounding the signal cables to a copper foil atop the upper Mylar foil, connected to the primary Faraday cage foil. Each signal cable is fixed in position using a PVC bar. Right: Inside view of the chamber after closing the Faraday cage.

Step 10: The upper section of the detector box is sealed using a honeycomb panel. Prior to closure, vacuum grease is applied between the O-rings and the honeycomb panel. To ensure a secure seal and prevent gas leaks, four aluminum bars with screw holes are affixed to each side of the detector. The screws through the aluminum bars connect to the PVC side bar, effectively closing the chamber.

An exploded view of the chamber layout with the thickness of each material used is shown in Fig. 6.16. It is crucial to note that throughout all assembly steps, every component, including resistive electrodes, strip PCB, copper, and Mylar foils, undergoes a thorough cleaning using ethanol or methanol.

6.3.2 Leak Test and Dark Current Test

After chamber assembly, a leak test at 20 *mbar* over-pressure was conducted to assess the chamber's gas tightness. The same leak test setup used for CMS iRPCs, as explained in Sec. 3.4.3, was used in this case as well. The chamber was filled with argon and the leak rate was monitored. Within the first few minutes, a substantial

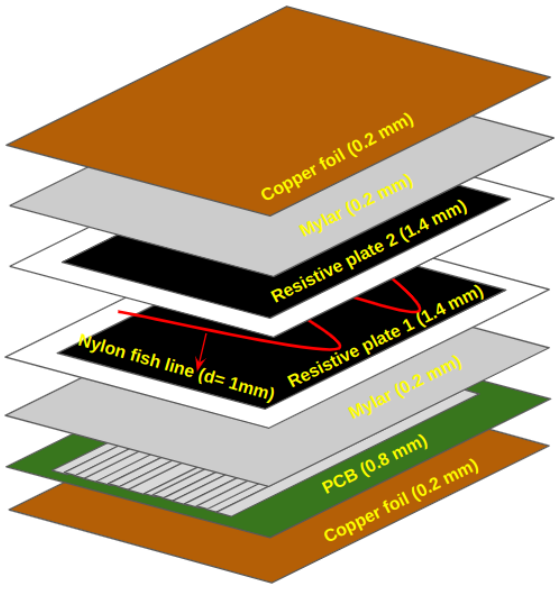

FIGURE 6.16: An exploded view of the single-gap gRPC chamber.

leak was observed in the chamber (approximately 1 $mbar/\ 5\ s$). Given the significantly high leak rate, it became crucial to identify the cause and perform repairs. To address this, the chamber was continuously flushed with Argon at an increased pressure of 25 $mbar$, and a soap water solution was applied to all four sides. The procedure and observations are detailed in Fig. 6.17.

Upon inspection, it was observed that the chamber exhibited leaks in the four sides at the bottom where the PVC bars were affixed to the bottom PVC panel. Additionally, leaks were identified in the regions where slots were made on the bars for sensor cables, flat cables, and HV connections. The good news was no leaks were detected in the honeycomb panel sides, affirming the effectiveness of the O-ring strategy. Consequently, it was decided that, for the next iteration of prototypes, O-rings would be employed both in the top and bottom parts, eliminating the need for glued sections. Furthermore, it became evident that an improved strategy is essential to eliminate holes in the side bars for cables.

The leaking spots were repaired by adding additional epoxy glue, but still the leak rate was quite high because of which, continues gas flow was required to operate the chamber.

Before testing the chamber's operation, it was flushed for 48-hours with a standard RPC gas mixture to eliminate any residual Argon and potential dust particles. As a crucial first step to validate chamber operation, the HV test was performed and the result is illustrated in Fig. 6.18. Monitoring the dark current at HV points ranging from 0 to 12000 V showed the chamber's successful operation. The chamber showed an ohmic behavior up to 5000 V. Beyond this point, the current showed exponential growth, indicative of ionisation within the gas gap. Taking into account these results and after checking the raw signal on the oscilloscope, it was determined that operating the chamber within the voltage range of 7500 to 8000 V was optimal. Beyond 8000 V, signals exhibited increased fluctuations and also a significant rise in current,

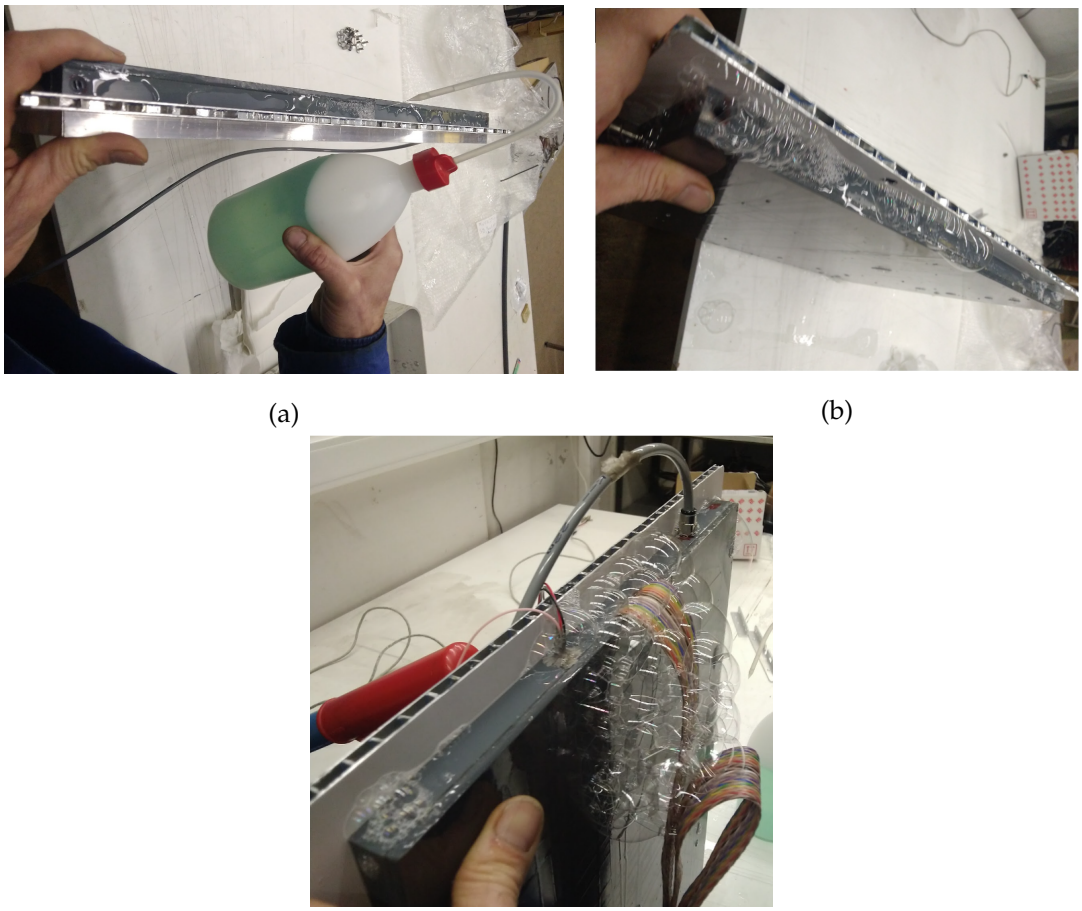

(a) (b)

(c)

FIGURE 6.17: The procedure for identifying leaks in the single-gap RPC: (a) applying soap water solution along the sides of the chamber for leak detection. Pictures (b) and (c) show soap bubbles formed, indicating gas leaks along the lateral sides of the chamber and through the slots for the cables.

indicating the chamber's transition from the avalanche region to the streamer region. For powering the chamber, CAEN-based HV modules are used, as explained in Sec. 3.4.3.

6.3.3 Performance Studies and Results

Cosmic muon tests were performed to calculate the detection efficiency of the chamber. The details of the experimental setups and results are described here.

Trigger Setup

A scintillator-based trigger setup was employed for triggering, comprising two scintillator modules coupled to Photo Multiplier Tubes (PMTs). Each module consists of a scintillator bar with dimensions of $5\times5\times1$ cm, and four Wave-Length Shifting Fibers (WLS) embedded on it connected to the PMT. Both PMTs are operated at 1300 V. During data collection, these two identical scintillator setups were aligned on the top and bottom of the chamber within a cosmic stand. Given that the width of the scintillator is 5 cm, it covers only three strips of the strip PCB (width=1.5 cm; separation=0.16 cm). Figure 6.19, illustrates the experimental setup featuring

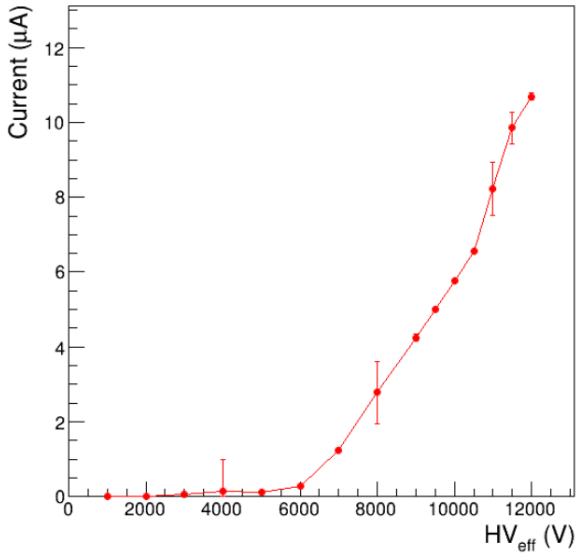

FIGURE 6.18: HV test results for the single-gap RPC. The dark current was monitored at HV points ranging from 0 to 12000 V. The chamber exhibited successful operation with ohmic behavior up to 5000 V, beyond which the current showed exponential growth, indicating ionisation within the gas gap.

the gRPC single-gap chamber with the two trigger scintillators and the top view of the configuration. The raw signals originating from the PMTs undergo initial pro-

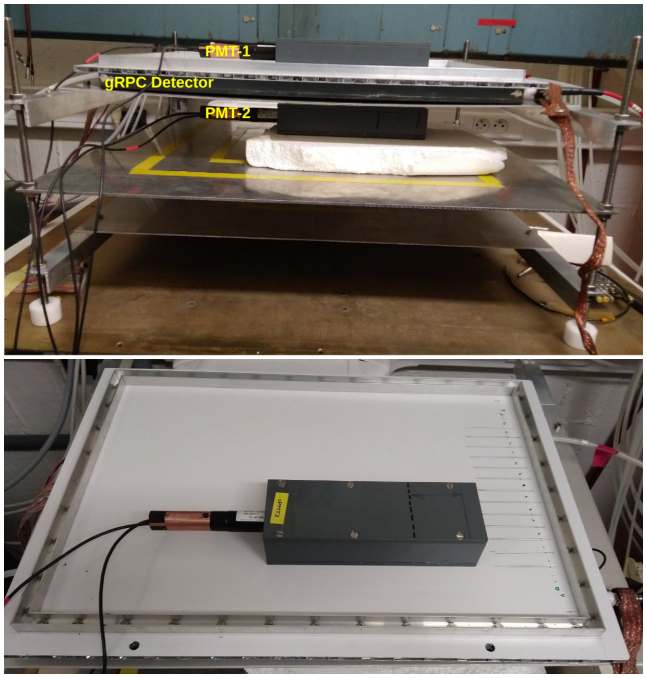

FIGURE 6.19: Top: Experimental setup featuring the single-gap gRPC chamber with two trigger scintillators. Bottom: The top view of the setup displaying the scintillator's coverage.

cessing through NIM discriminator modules. Subsequently, they are directed to a coincidence module, where the output signal (coincidence AND signal), indicative of a simultaneous event in both scintillator modules, serves as the trigger input for a CAEN QDC module (v792) [301]. The block diagram of the trigger generation is shown in Fig. 6.20.

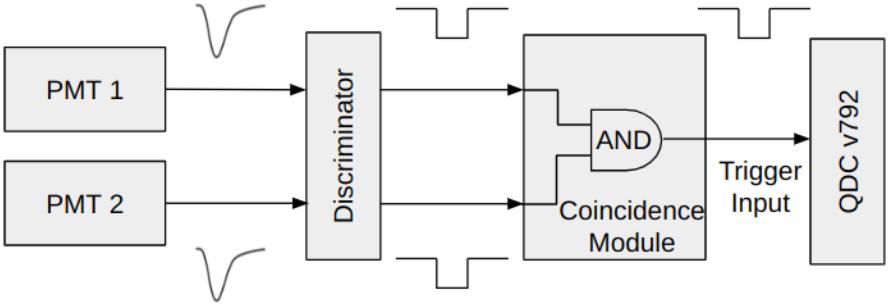

FIGURE 6.20: Block diagram illustrating the trigger generation process for data collection. The analog signals from the PMTs undergo initial processing through a discriminator, followed by further processing in a coincidence module. The AND coincidence output from this module serves as the trigger input for the CAEN QDC.

Data Taking

The detector's signal is collected and routed to a CAEN impedance adapter (A992) that accommodates 16 channels for 50 Ω impedance matching, which is then connected to the QDC module. The connection diagram of the signal cable from the detector (source) to the QDC module is shown in Fig. 6.21.

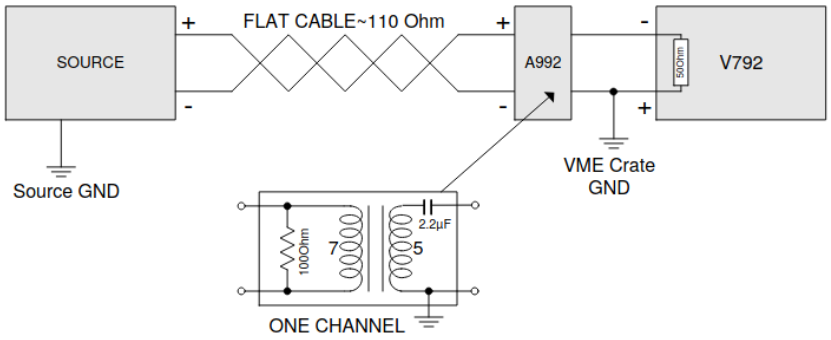

FIGURE 6.21: Connection diagram of the signal flat cable from the detector to the CAEN QDC module (v792). An impedance adapter (CAEN A992) is used in between for 50 Ω impedance matching

It is noteworthy that the detector signal consistently precedes the trigger signal. This is because the second PMT signal is generated after the detector and also the pre-processing of PMT signals to generate the coincidence output introduces delays. This delay, measured with an oscilloscope, is estimated to be approximately 50 ns. A 50 m long flat cable is used to delay the gRPC signal so that it falls inside the coincidence time window. A threshold of 100 mV is established on the QDC for signal selection. Whenever the QDC receives a trigger signal, it records the signals from all 16 gRPC channels.

Before each cosmic run, a pedestal run with random triggers is taken. During the pedestal run, the chamber is operated at 7.4 kV and the trigger is generated by keeping the scintillators in overlap with each other but away from the active area of the chamber resulting in a trigger that is not related to a physical effect, hence

dubbed the random trigger method. Using the collected pedestal data, a channel-by-channel threshold is estimated for event selection in efficiency estimation.

The threshold for a specific channel (Ch^i_{thr}) is determined as the mean (μ_i) of the pedestal distribution for that channel plus three times the standard deviation (σ_i) as illustrated in Eqn. 6.2.

$$Ch^i_{thr} = \mu_i + 3 \cdot \sigma_i \tag{6.2}$$

Here i is the number of the channel and for the single-gap gRPC i varies from 0 to 16.

Efficiency Measurements

For the muon efficiency calculation, given that the scintillator covers only three strips, the data collected from these specific strips are considered for the estimation of efficiency. A signal in a given channel is considered only if it surpasses the channel threshold (Ch^i_{thr}) estimated from the corresponding pedestal data. In the case of a single event, if adjacent strips are fired, they are considered as muon clusters. The muon efficiency is then calculated as the ratio of the number of gRPC events to the number of triggers collected (Eqn. 6.3).

$$E_\mu = \frac{N_{gRPC}}{N_{trigger}} \tag{6.3}$$

Figure 6.22 shows the results of the muon efficiency study conducted with the single-gap gRPC chamber. The muon efficiencies are depicted as a function of the

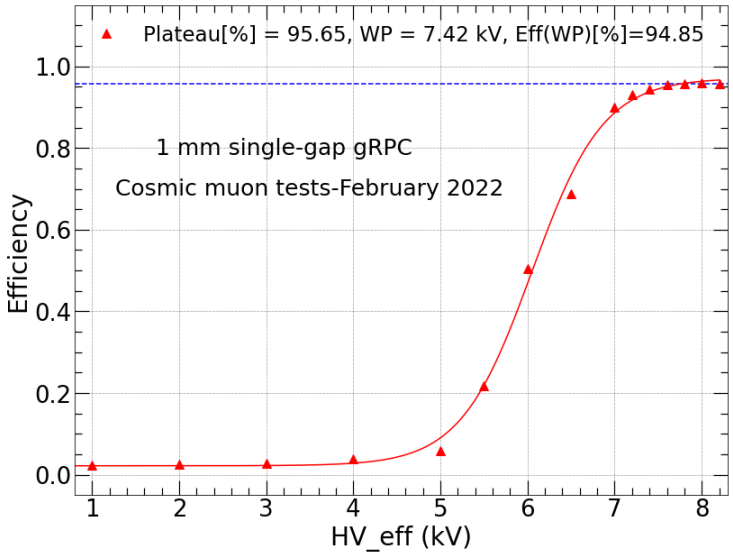

FIGURE 6.22: The muon efficiencies as a function of the effective HV values estimated for the single-gap gRPC chamber. As per the results, ionisation in the gas gap starts after 5 kV and the efficiency plateaus at 95.65% is achieved after reaching 7 kV.

corresponding effective high voltage (HV_{eff}). HV_{eff} is determined by the PT correction (detailed in Sec.2.4.7 for an explanation of the PT correction), using the pressure and temperature values obtained from the PTH sensor within the chamber. The results indicate that the ionisation region starts after HV reaches 5 kV, and the efficiency plateau at 95.65% is achieved after HV reaches 7 kV. The slight decrease in

the efficiency of 100% for a few points could be attributed to the gas leak observed in the chamber. The working point of the detector is estimated using the HV knee voltage, calculated as explained in Sec.3.5.2, and the determined value for the single-gap gRPC chamber is 7.42 kV. At WP, the chamber shows an efficiency$\sim$95%.

Comparison Studies

The performance of the single-gap RPC (A1) developed at UGent RPC lab was compared with another gas-tight single-gap RPC (B1) developed by the UCL team with slightly different characteristics. Given the slight differences in technical layout and geometric characteristics between the two cases, the primary aim of this comparative study was to identify and optimise the best features for a portable gRPC detector. The geometric details of A1 were previously discussed in Sec. 6.3.1.

Similar to A1, B1 comprises two resistive electrodes, each with a thickness of 1.1 mm and a gas gap of 1 mm. For B1, the resistive plates are developed using Serigraphy and the gas gap is formed by nine round-edge spacers crafted from polyether ether ketone (PEEK). B1 is a comparably smaller detector, featuring an active area of 16 $cm \times 16$ cm when contrasted with the A1 detector of active area. The readout board of B1 consists of sixteen copper strips, each 9 mm wide and separated by a 1 mm gap. The gas gap + PCB assembly is enclosed in an airtight aluminum box and the detector weighs approximately 6.5 kg. The rate of gas leakage for B1 under vacuum conditions was measured using helium and found to be 10^{-9} $mbar^{-1}$ [302]. A comparison of the geometrical properties of the gRPCs A1[2] and B1 are given in Tab. 6.2. The inside view of the B1 detector is shown in Fig. 6.23 (left).

Detector	gRPC-A1	gRPC-B1
Active Area	28×28 cm^2	16×16 cm^2
Box type	Honeycomb based	Aluminum casket
Weight	2.8 kg	6.5 kg
Readout strips	16-1D	16-1D
Strip pitch	15 mm	10 mm
Gas gap	1 mm Single gap	1 mm Single gap
Thickness of electrodes	1.1 mm	1.1 mm
Resistive coating	Spray-gun ($\sim$650 $k\Omega/\square$)	Serigraphy ($\sim$4 $M\Omega/\square$)
Gas mixture	95.2% Freon, 0.3% SF6, 4.5% isobutane	
Portability	No	Yes

TABLE 6.2: Overview of the geometric characteristics of the two single-gap gRPCs, A1 and B1 [2].

[2]gRPC-A1 is not portable due to minor gas leakage. This necessitates the connection of the detector to the gas supply and operation in gas flow mode to ensure optimal detection efficiency. The second version of gRPC developed is completely gas tight.

The activities of the project also includes the development of portable electronics and the comparison studies were carried out using the first version of the portable DAQ developed by the UCL team. This portable DAQ comprises two FEBs borrowed from the RPC group of the CMS experiment [157, 303]. Each FEB has the capacity to handle 32 analog input channels, featuring an amplifier with a charge sensitivity of 2 mV/fC, a discriminator, a monostable, and a Low Voltage Differential Signaling (LVDS) driver. The LVDS outputs of all the FEBs are interconnected to a System-on-Chip (SoC) module, situated on a carrier board with wireless connectivity, ensuring operational autonomy [304]. Figure 6.23 (right) shows the picture of the portable DAQ box mounted on a VME stand for tests.

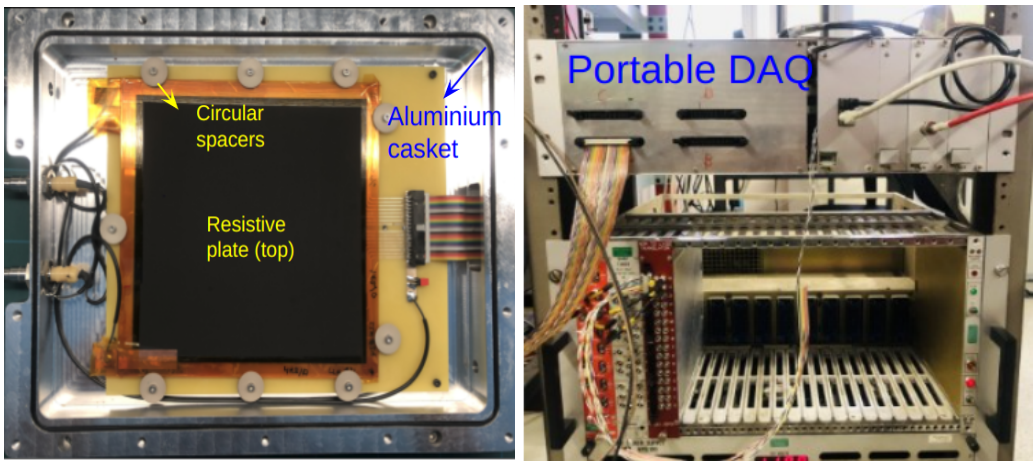

FIGURE 6.23: Left: Inside view of the airtight aluminum casket of the gRPC detector B1 showing the top resistive plate, the circular edge spacers, and the PCB board connected to the flat cable connector. Right: The portable DAQ setup developed for the gRPCs at UCL [2].

For the data-taking of the comparison studies, two scintillators with an active area of $16\times16\ cm^2$, coupled to PMTs, were employed to generate the trigger. The left image in Fig. 6.24 illustrates the placement of gRPC-B1 between the trigger scintillators, while the right side image in the same figure presents a schematic inside view. The schematic depicts the top trigger scintillator and the gRPC-B1 detector, showcasing the scintillator covering the entire active area of the detector. In the case of gRPC-A1, the scintillators only cover a portion of the chamber, as the active area of the detector exceeds that of the trigger scintillators.

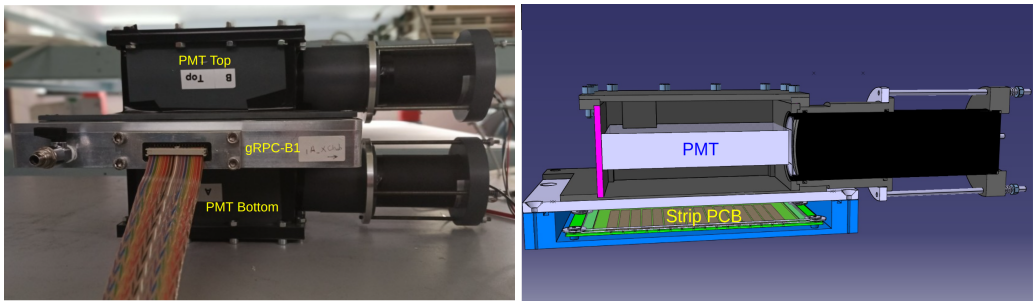

FIGURE 6.24: The left image illustrates the placement of gRPC-B1 between the trigger scintillators, while the right side image presents a schematic inside view. The schematic shows the top trigger scintillator covering the entire active area of the detector.

The primary outcomes of the joint data-taking involving the two gRPC prototypes are illustrated in Fig. 6.25. Both detectors were operated in avalanche mode at their respective working points, with gRPC-A1 set at 7.3 kV and gRPC-B1 at 7 kV. Due to the scintillator's coverage limitation, only the last eight strips of both gRPC-A1 and gRPC-B1 were considered for the study. The first half of the gRPC-A1 was also excluded due to some cross-talk issues occurred in three strips in that region during the period of data-taking. Later this issue was resolved through repairs. The threshold value of discriminator of DAQ was set to 90 DAQ units. In Fig. 6.25, the left side displays the strip occupancy, representing the frequency of each strip firing throughout the run, while the right side shows the cluster size, denoting the number of strips fired per event. The occupancy distributions in both cases exhibit similar behavior, indicating comparable performance between the detectors. Although the cluster sizes are nearly within the same range, gRPC-B1's cluster size appears slightly higher, as anticipated due to its narrower strip width compared to gRPC-A1.

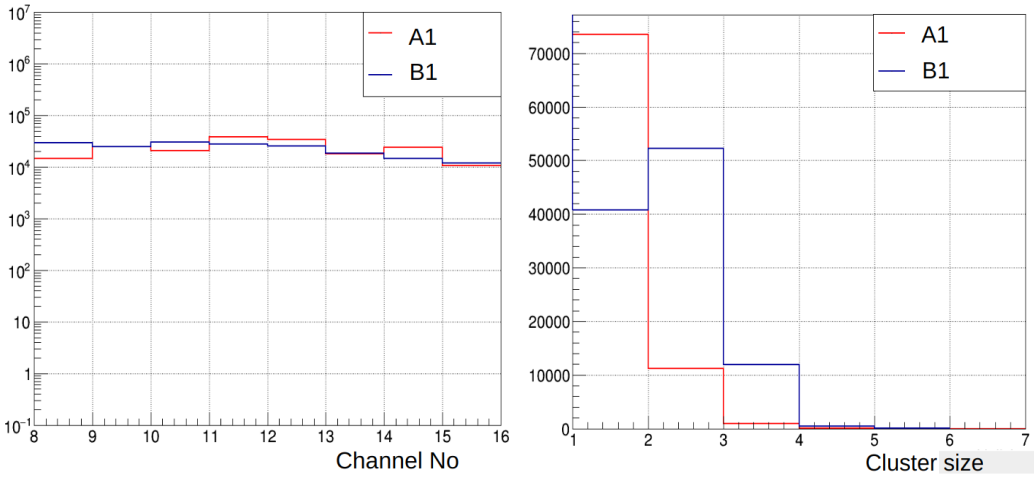

FIGURE 6.25: Joint data-taking results of gRPC-A1 and gRPC-B1. The left plot shows the comparison of strip occupancy, while the right plot displays the cluster size of both chambers [304].

6.4 Double-gap gRPC

The successful construction and validation of the single-gap gRPC chamber led to the development of an advanced double-gap gRPC chamber. Challenges encountered in the single-gap version, including issues such as gas leaks, cross talk, and signal reflections, were addressed and resolved in the double-gap configuration. Moreover, the double-gap chamber features a more compact layout, with two gas gaps, provides 2D position information, and incorporates an improved PCB design. This section discusses the details of the detector components, the assembly process and the results of the performance studies conducted on the double-gap chamber

6.4.1 Detector Components

Resistive Plates

As the coating technique using the spray gun demonstrated highly promising results, the development of resistive electrodes for the double-gap gRPC followed the

same proven technique and procedures outlined in Sec. 6.2. The construction of the two gas gaps involved the use of four resistive electrodes. The bottom and top glass plates in the lower gas gap exhibit mean surface resistivity values of 948 $k\Omega/\square$ and 750 $k\Omega/\square$, respectively, while the bottom and top glass plates in the upper gas gap possess mean surface resistivity values of 1740 $k\Omega/\square$ and 1454 $k\Omega/\square$, respectively.

Strip PCB

A new strip PCB, featuring advanced characteristics, was designed for the double-gap gRPC and manufactured through the services of ELTOS, an esteemed PCB company based in Italy [305]. In contrast to the basic version used for the single-gap gRPC, this iteration incorporates a doubled number of strips (32 strips) with a narrower strip width of 0.8 *cm*, all integrated onto the PCB. The design includes slots for two 17-pin flat cable connectors and a BNC connector for the HV connection. To guide signals from the strips to the flat cable connectors, 32 signal traces are integrated on the PCB, eliminating the need for separate signal cables soldered onto the strips. The presence of a solder mask that covers all the traces prevents cross-contact between neighboring strips, mitigating potential cross-talk issues. Dedicated slots for adding 50 Ω resistors between the signal trace and the grounding slots of flat cable connectors significantly reduce possible signal reflections. In addition to the signal traces, the PCB features traces for HV, ground connection, and a PTH sensor. All the connection slots on the PCB, intended for linking the flat cable and HV connectors, sensor, resistors, etc., are left uncovered without solder mask, facilitating direct soldering. The PCB also includes 36 M3 screw holes with a diameter of 3.2 *mm* for fastening the PCB to the detector frame. Additionally, there are four mounting holes positioned at the corners, which are reserved for future integration with muon hodoscope mechanics. The backside of the PCB is coated with a 35 μm thick layer of copper to construct the Faraday cage. This copper coating is safeguarded by a protective layer applied during manufacturing. Notably, the backside of all connection slots is left uncoated, creating a clear separation from the copper section to avoid any interference. Figure 6.26-top shows the technical drawing of the PCB, while the bottom picture provides a zoomed view of the section that highlights the connection slots for the flat cable connectors and the resistors for termination. Pictures and further details of the PCB assembly inside the chamber and the corresponding connections are provided in the section dedicated to detector construction (Sec. 6.4.2).

3D Printed Detector Frame

Drawing upon insights gained from the initial single-gap prototype, a new improved layout is proposed for the detector frame. This frame was specifically designed and developed as part of an independent R&D project at UGent [3], as discussed in Sec. 6.5 and the idea was adapted for the double-gap gRPC detector and tested. The frame is manufactured using polyamide powder and as a single piece utilising laser-based 3D printing technology. Since the frame is a single piece, it mitigates the risk of junctions, eliminating potential gas leaks at the corners. 3D printing was carried out through PolyBull [306], a Belgium-based 3D printing company.

The frame design incorporates slots for gas inlet and outlet, along with a gas channel that divides the gas input/output into four lines, ensuring uniform gas distribution within the detector volume. Additionally, slots in the top and bottom parts of

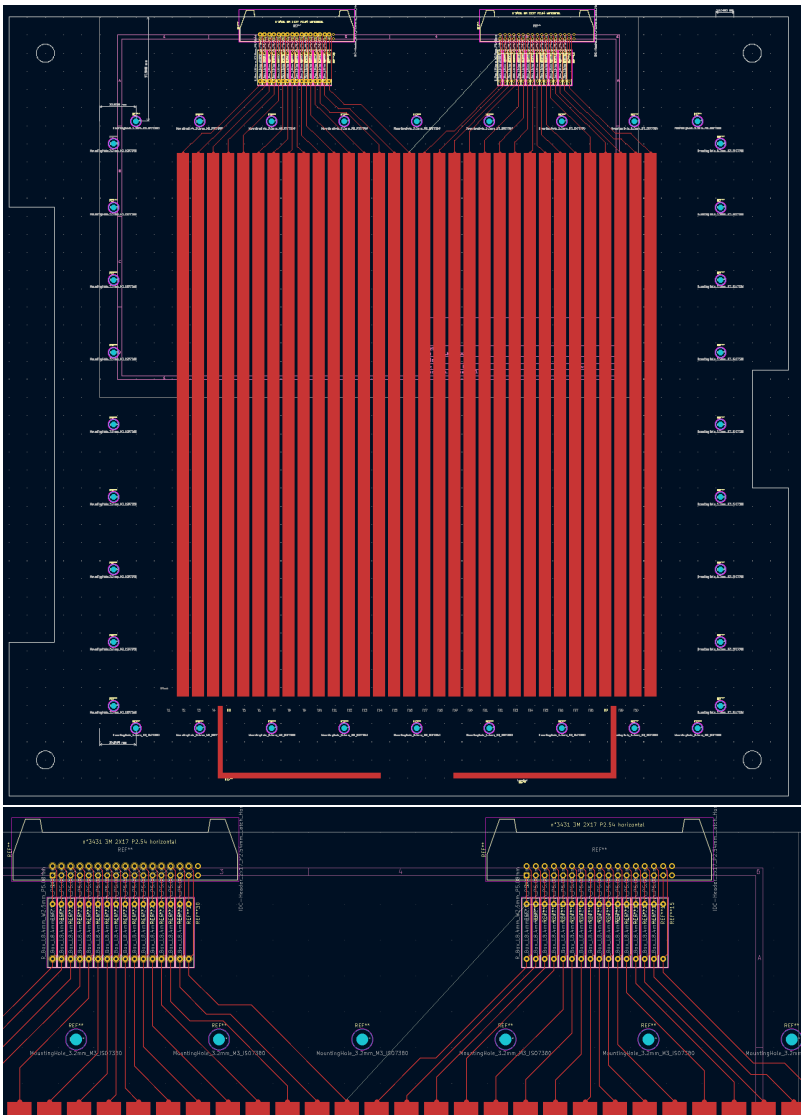

FIGURE 6.26: The top picture shows the technical drawing of the PCB and the bottom offers a close-up, emphasising the connection slots for flat cable connectors and resistors for termination. Notably, the PCB incorporates 36 M3 screw holes for secure attachment to the detector frame and includes four corner mounting holes. These corner holes are designed for potential integration with the mechanics of the muon hodoscope.

the frame accommodate O-rings and M3 screw holes are provided to attach the top and bottom PCBs to the frame. On two opposite sides, rectangular spacers secure the electrodes in position, while on the other two opposite sides, six rectangular blocks fix the 3D printed spacers that secure the fish wires and hold the electrodes in place.

Figure 6.27 (a) shows the Computer-Aided Design (CAD) model of the frame, highlighting the rectangular spacers on all four sides, the O-ring channel, and the M3 screw slots. In (b), the interior view reveals the gas channel with a specially designed slot in the central part of the frame to connect the gas connector. Gas enters the elongated channel within the frame, distributing uniformly through four slots connected to this channel. For a better understanding of the gas distribution, (c) offers a detailed view of four slots on one side of the channel. Notably, the two slots adjacent to the central part are intentionally made slightly smaller than the other two

to ensure an even gas flow rate through all four slots. The same design principle is mirrored on the opposite side of the frame.

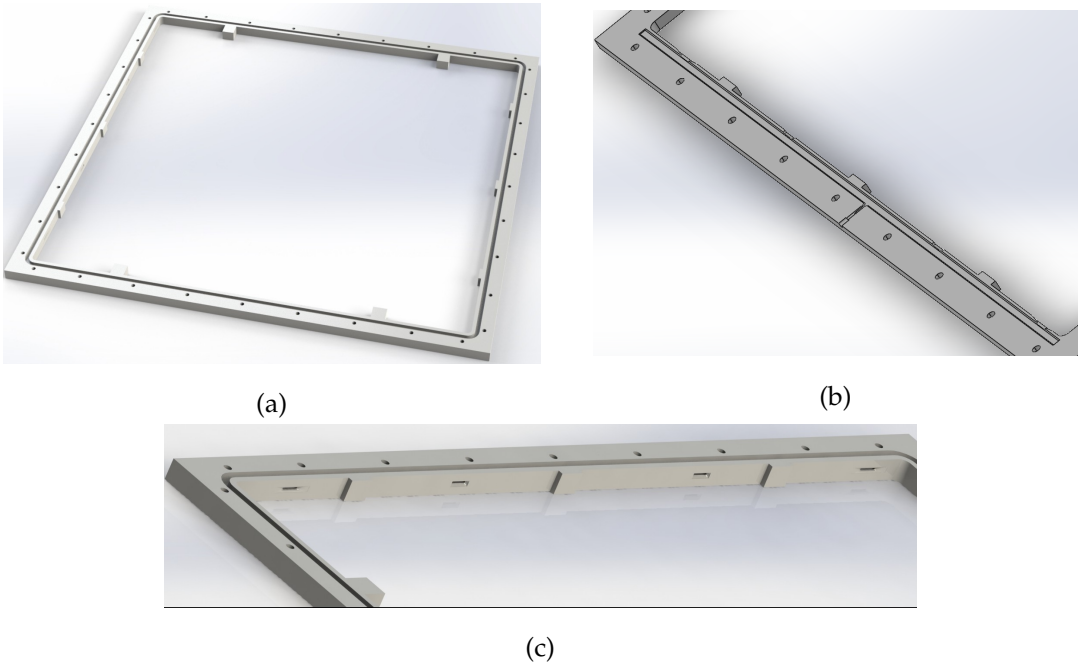

(a) (b)

(c)

FIGURE 6.27: The CAD models of the 3D printed detector frame, depicting the (a)-full frame design, (b)-gas channel interior, and (c)-gas distribution slots [2].

Figure 6.28 illustrates the CAD model of the 3D printed rectangular blocks designed for securing fish wires for the gas gap construction. The cut in the central part on the left side is intended for fixing the block to the rectangular block in the frame. Small slots labeled as a and b are designated for inserting fish wires corresponding to the top and bottom gaps, respectively. Additionally, slightly larger slots labeled as A and B are slots for inserting screws to tighten the fish wires inserted into slots a and b, respectively. The spacers also hold the glass electrodes in position inside the detector box.

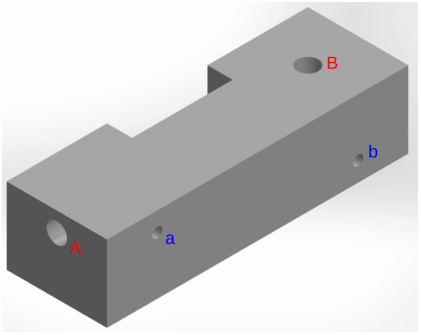

FIGURE 6.28: The CAD model of the 3D printed spacer designed for securing fish wires during gas gap construction. The 3D printed detector frame features six dedicated slots to firmly secure these spacers in place. Small slots a and b are for inserting fish wires corresponding to the top and bottom gaps, respectively and the slightly larger slots A and B are for inserting screws to tighten the fish wires inserted into slots a and b, respectively.

6.4.2 Detector Construction

This section provides the details of the construction of the double-gap gRPC. The procedures for constructing the gas gaps, establishing internal connections within the chamber, and the overall structure of the detector, including the placement of electrodes, insulation layers, and other components are similar to that of the single-gap gRPC. The key distinction lies in the incorporation of an additional gap in the detector and a slightly modified layout featuring newly designed components.

To achieve a compact and lightweight detector, the honeycomb panel+PVC-based detector box is completely eliminated in this configuration. The detector comprises two PCBs for 2D dimensional readout, attached to the top and bottom parts of the 3D printed detector frame. This integrated arrangement serves as a closed detector box, eliminating the need for any additional external detector box.

The initial phase of construction involves preparing the PCB boards, where all the components that require soldering are affixed. Figure 6.29 displays an image of the PCB prepared for chamber assembly. The connector labeled as A is the BNC connector for HV connection, while the traces marked as B represent the HV and ground traces that extend into the chamber from the HV connector to establish connections with the electrodes. The area marked as C shows the 32 readout strips integrated on the PCB. The resistors embedded on the PCB for 50 Ω termination are outlined in region D, each in their designated slots. Additionally, the connectors marked as E are the flat cable (male) connectors for signal collection.

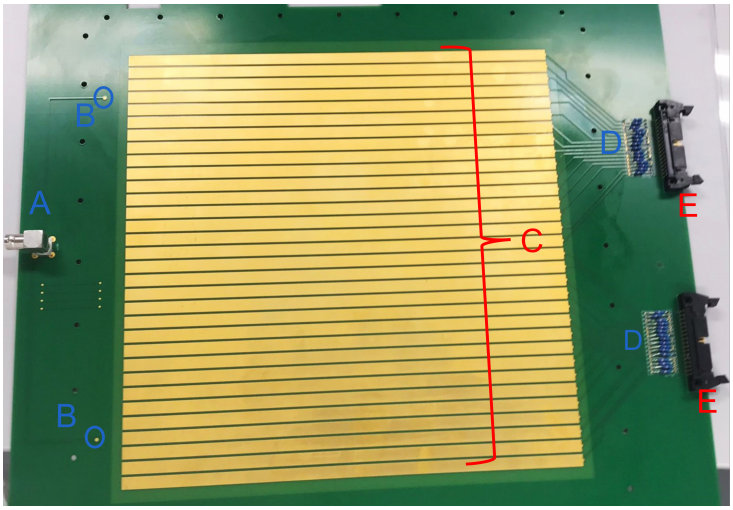

FIGURE 6.29: Strip PCB used in the double-gap gRPC assembly, showcasing the BNC connector (labeled as A) for HV connection and HV/ground traces (labeled as B) extending into the chamber to establish connections with the electrodes. Region C and D highlights the 32 strips integrated on the PCB and the resistors embedded on the PCB for 50 Ω termination, respectively. Connectors marked as E are the flat cable (male) connectors for signal collection.

After preparing the PCBs, the bottom PCB is positioned on a flat table. The 3D printed detector frame is secured on the PCB by inserting M3 screws into the corners. O-rings are added to the top and bottom of the detector frame and the gas

inlet and outlet connectors are attached. Six 3D printed spacers are fixed to the detector frame. A Mylar foil, measuring 30 cm $\times$30 cm with a thickness of 200 μm, is placed on the PCB between the spacers. On top of the Mylar foil is the bottom resistive electrode. Three fish wires (diameter=1 mm) are tightly secured on top of the electrode, connected to the 3D printed spacers, using screws to construct the gas gap. The PTH sensor is soldered to the respective connection points and placed on the side of the detector between the detector frame and the electrode. The bottom electrode is connected to the ground trace via a wire, and another wire is connected to the HV trace to link to the top plate of the bottom gas gap. All the HV, ground and sensor connections are insulated and protected using Kapton tape. All these details are illustrated in Fig. 6.30.

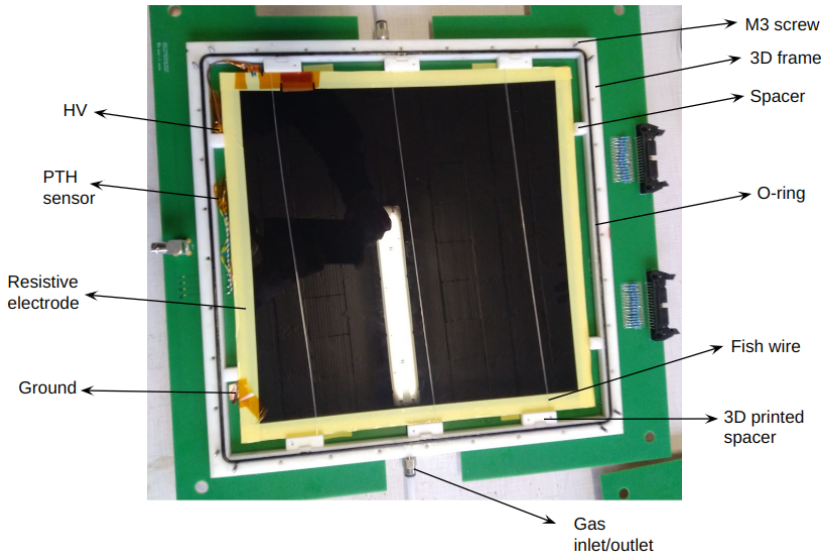

FIGURE 6.30: Inside view of the double-gap gRPC chamber showing the layout, major components and construction of the gas gap.

After constructing the first gas gap, the top electrode of the first gas gap is positioned on top of the fish wires, connected to the HV wire that was already prepared. Similarly, the second gas gap is constructed by placing two resistive electrodes and placing fish wires between them on top of the first gas gap structure. In this construction layout, where the electrodes connected to HV face each other, a thicker Mylar foil with a thickness of 350 μm is placed between the HV electrodes for proper insulation. The inside view of the chamber after placing the final fourth electrode is presented in Fig. 6.31-left.

After placing the final electrode, an additional Mylar foil, identical to the one used at the bottom, is placed on top of the electrode for insulation. Before closing the chamber, it is crucial to double check and verify that all necessary connections inside the chamber are properly established. The chamber is sealed by attaching the top PCB to the detector frame. The closed view of the double-gap gRPC chamber is depicted in Fig. 6.31-right. The copper coating applied on the backside of the PCB is clearly visible in the picture. Four aluminum brackets are positioned on both the top and bottom PCBs between the M3 screws and the PCBs to ensure a tight closure. Additionally, vacuum grease is applied to the O-rings on the top and bottom of the detector frame. All open slots in the top and bottom PCBs are sealed and insulated

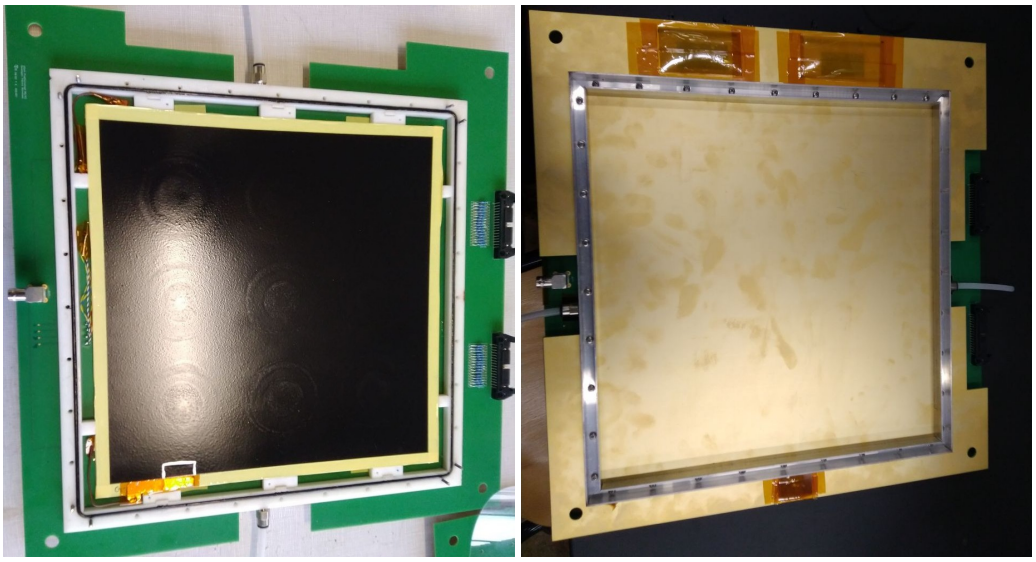

FIGURE 6.31: Left: Inside view of of the double-gap gRPC chamber after the placement of the fourth resistive electrode, completing the construction of the second gas gap. Right: Closed view of the chamber, featuring the copper coating on the backside of the PCB, four aluminum brackets positioned between the M3 screws and the PCB to ensure a secure closure, and the sealed connection slots on the PCB.

with rectangular pieces of Mylar foils and Kapton tapes, as illustrated in the closed view of the chamber. After completing the detector assembly and conducting preliminary tests, all four sides of the chamber are closed by connecting the bottom and top PCBs with copper foils. This configuration serves as a Faraday cage, providing protection against electromagnetic noise. The schematic of the double-gap gRPC developed is shown in Fig. 6.32.

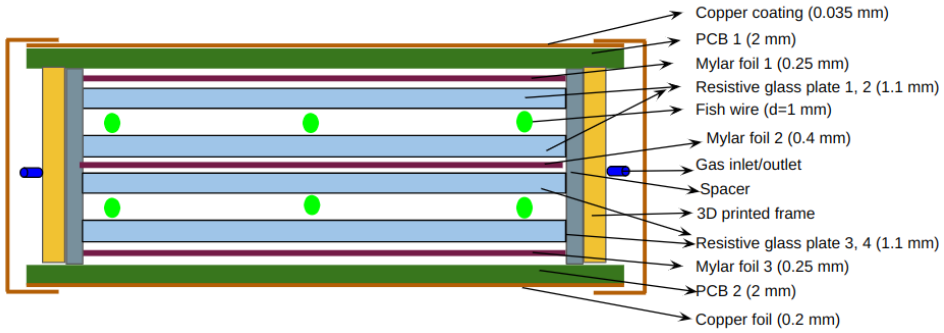

FIGURE 6.32: Schematic of the technical layout of the double-gap gRPC.

As evident in the assembly images, the integration of power, grounding, and signal traces directly onto the PCB eliminates the need for any external cables entering the detector through the detector frame. Together with the single-piece construction of the detector frame, this design achieves a compact and fully gas-tight detector. Eliminating the external detector box reduces the overall volume of the detector and hence results in a decrease in gas consumption. Qualification tests for the chamber, including leak tests and dark current tests, were conducted. The results of these tests and the results of the performance studies are discussed in the next sections.

6.4.3 Qualification Tests

X-ray Test

Since it was the first time the 3D printing technology was used for the detector frame construction project, it was crucial to validate the structural integrity of the frame and confirm its adherence to the design specifications. External components such as M3 screw holes, spacers, and O-ring channels precisely matched the dimensions and shapes specified in the design. To verify the structure of the central and lateral gas channels integrated inside the detector frame, areas that are not visible to the naked eye, an X-ray scanning procedure was used. The X-ray tests were conducted with the X-ray scanner [307] at the Center for X-Ray Tomography (UGCT) at UGent [308][3], which is located in the same building of the RPC lab.

In Fig. 6.33, the X-ray scanner and the scanning procedure for the frame are illustrated. The frame was securely positioned on a vertical stand, with the X-ray gun directed towards the gas inlet location. Figure 6.34 shows the X-ray image of the

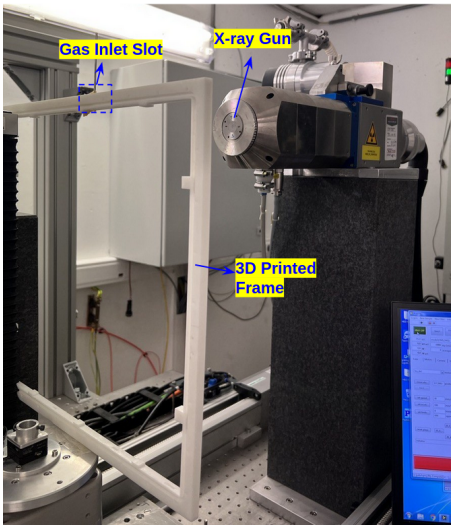

FIGURE 6.33: The X-ray scanner and the scanning procedure for the frame. The frame was securely positioned on a vertical stand, with the X-ray gun directed towards the gas inlet location.

scanned portion of the frame, highlighting the gas channel within the central part of the frame connecting the gas inlet/outlet connector and extending into the lateral channel. The scale given in the plot indicates the photon absorption(normalised). The cylindrical stick in the middle of the image is a reference stick placed during scanning for marking the gas channel location. However, the thinner part of the frame between the O-ring channels obscures the structure of the lateral channel in the X-ray results. It is noteworthy that the gas inlet, crafted inside the frame using 3D printing is the same as the design outlined in the CAD model. Hence, the scan results for these components validated the efficiency of the 3D printing technique.

Despite the 3D printed structure meeting expectations, there were instances of deposits of polyamide powder discovered within the lateral channel. These deposits

[3]Special thanks to Caori Organista Castelblanco (UGCT, UGent) and Ruizhi Tang (UGCT, UGent) for their assistance and suggestions regarding the X-ray test.

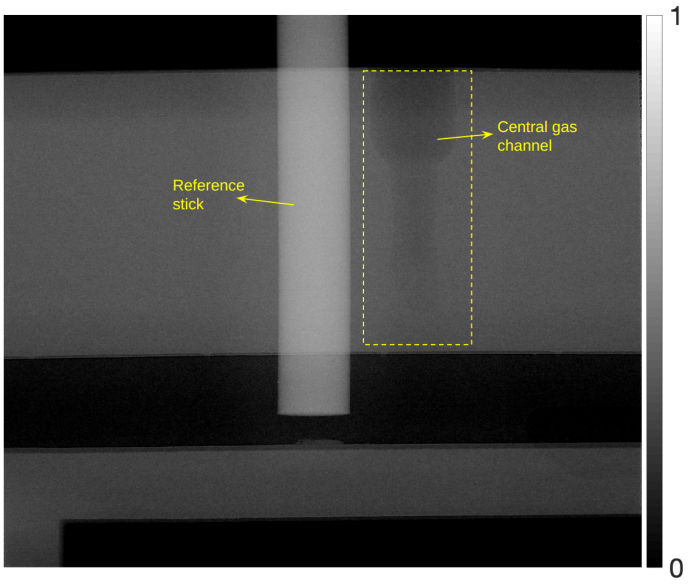

FIGURE 6.34: X-ray image of the complete scanned section of the frame, revealing the gas channel within the central part of the frame that connects the gas inlet/outlet connector and extends into the lateral channel. The cylindrical stick in the middle of the image is a reference stick placed during scanning for marking the gas channel location.

can slightly affect the gas flow to the four slots. Fortunately, addressing this issue was straightforward – the deposits were effectively cleared by inserting a flexible metallic wire into the slots.

Leak Test and Dark Current Test

To validate the gas tightness of the 3D printed frame, a leak test was performed using the argon-based leak test setup at 22 *mbar* overpressure. The results of the leak test are presented in Fig. 6.35. Continuous pressure monitoring for 10 hours revealed no significant variations, affirming the robust leak-tight construction of the detector. To further confirm, the chamber was left undisturbed overnight, and subsequent pressure checks the next day and two days later consistently showed that the pressure level remained unchanged at 22 *mbar*.

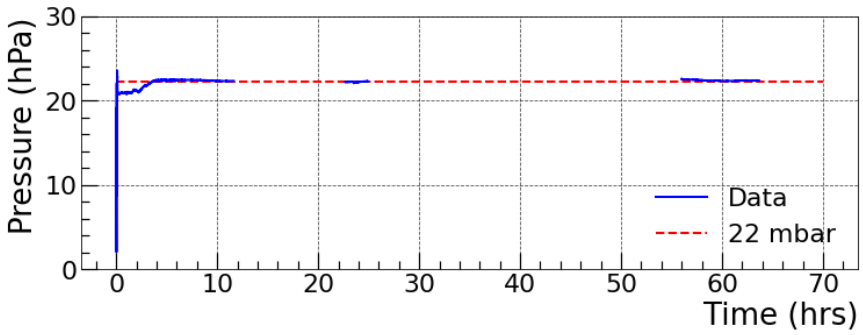

FIGURE 6.35: The result of the gas leak test of the double-gap gRPC conducted using Argon gas at 22 *mbar* over pressure. The blue line corresponds to the measured data and the red dotted line corresponds to the applied pressure.

Figure 6.36 presents the outcomes of the dark current test conducted on the double-gap chamber. Both HV electrodes were parallel connected to the same HV point and ground during the test (the technical layout of the chamber also offers the possibility to operate the gaps separately). The total dark current, measured from both gaps, is plotted as a function of the effective HV. The effective HV (HV_{eff}) was determined by applying PT correction to the applied HV using the data collected from the PTH sensor. The results indicate that up to 5000 V, the detector exhibits linear ohmic behavior. Beyond this point, the current increases exponentially due to ionisation in the gas gap. The observed ohmic curve confirms that the chamber is functioning as anticipated.

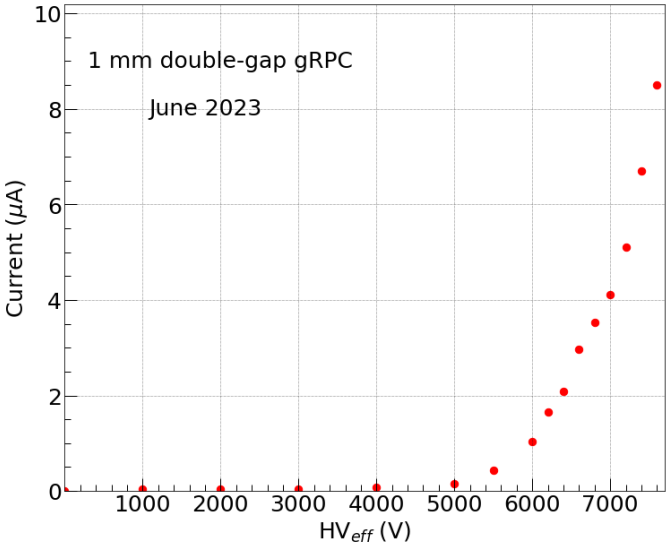

FIGURE 6.36: Dark current test results for the double-gap gRPC chamber. The obtained ohmic curve validates the successful operation of the detector [3].

6.4.4 Performance Studies and Results

Upon the successful completion of the chamber qualification tests discussed above, the double-gap gRPC underwent performance studies. The same trigger setup and signal collection procedure used for the single-gap gRPC tests were employed. The details and connection diagrams (Fig. 6.20, Fig. 6.21) were previously explained in Sec. 6.3.3. In total, the detector consists of 64 channels, considering channels from both PCBs. For these preliminary detector performance studies, only one PCB was considered, with 32 channels connected to two flat cables, utilising all 32 channels of the CAEN QDC module. Figure 6.37 shows the experimental setup for data collection with the double-gap gRPC, positioned between two trigger scintillators. The two flat cables employed for signal collection are also visible in the image. The trigger scintillators used for the performance studies were the 16 $cm \times$ 16 cm scintillators used in the single-gap gRPC comparison studies explained in Sec. 6.3.3. Due to the reduced active area of the scintillators, only 18 strips of the detector out of 32 were covered.

The data-taking procedure mirrors that of the single-gap gRPC, as explained in Sec. 6.3.3. Prior to each cosmic run, a pedestal run is conducted, and the QDC threshold for each channel is determined from the pedestal distribution using Eqn. 6.2.

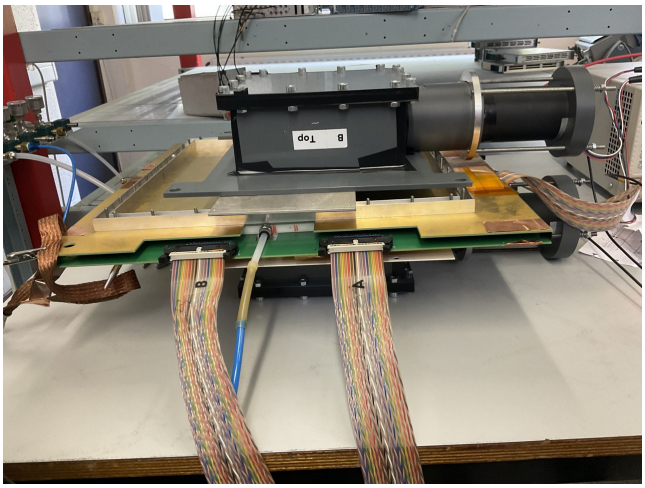

FIGURE 6.37: Experimental setup for data collection with the double-gap gRPC. The detector is positioned between two trigger scintillators. Two flat cables used for signal collection can also be seen.

Subsequent analysis focuses on the strips with signals that exceed their respective QDC thresholds.

Chamber Occupancy: Figure 6.38 illustrates the occupancy distribution within the chamber during operation at 7000 V (the working point estimated from the dark current results) based on data collected from 10000 triggers. The observed shift to the right is ascribed to the off-center placement of trigger scintillators. Additionally, the lower statistics in the initial and final strips result from the difference in the active area of the detector compared to that of the trigger scintillators.

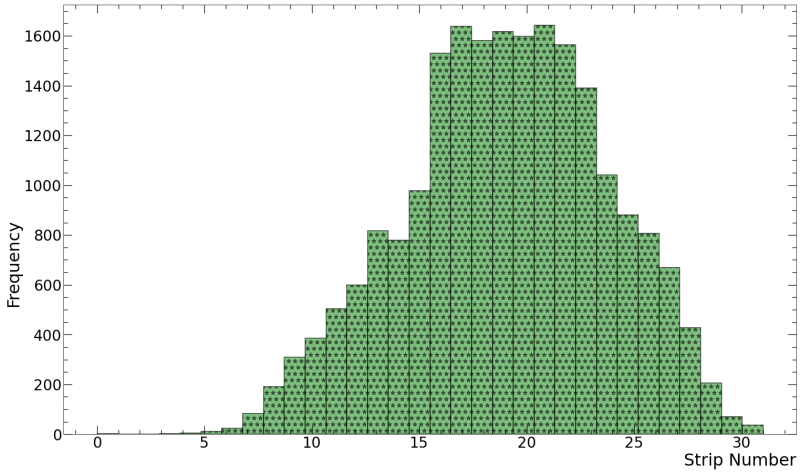

FIGURE 6.38: Occupancy distribution in the double-gap gRPC chamber at an operational voltage of 7000 V, using data from 10000 triggers. The observed rightward shift is attributed to the off-center positioning of the trigger scintillators. Lower statistics in the initial and final strips are due to the variation in the active area between the detector and the trigger scintillators [2].

Cluster Size: Figure 6.39 displays the distribution of cluster sizes, representing the number of strips fired per event, based on data collected at three distinct voltage values (7000 V, 7300 V and 7600 V) with 10000 triggers. The plot indicates a marginal

rise in cluster size with increased applied voltage, aligning with expectations. Notably, the majority of events exhibit a cluster size ranging from 0 to 4.

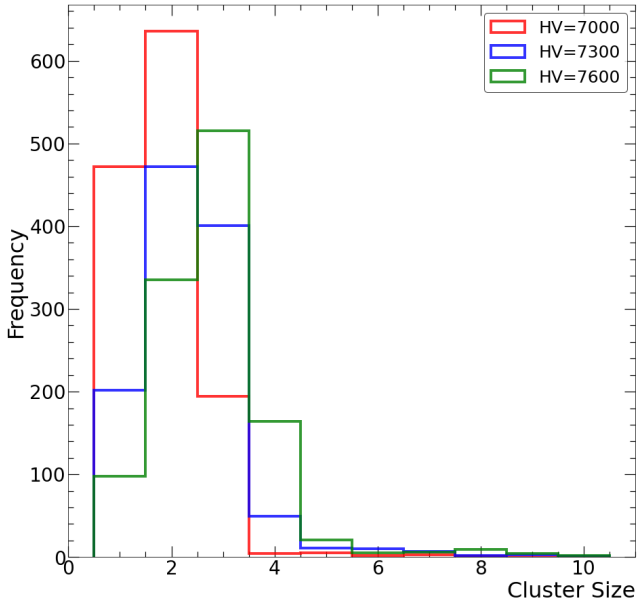

FIGURE 6.39: Distribution of cluster sizes in the double-gap gRPC (number of strips fired per event) obtained from data collected at three distinct voltage values within the avalanche region (7000 V, 7300 V, and 7600 V) with 10000 triggers [2].

Charge Measurements: One of the primary reasons for utilising the CAEN QDC in the performance studies was its capability to investigate the charge generated in the detector. According to the QDC manual, 1 QDC corresponds to 0.098 pC [301]. The pulse charge measured in the detector at three different HV values within the avalanche region is depicted in Fig. 6.40-left. Clearly, the charge exhibits an upward trend with the applied HV. Charge per cluster is determined by adding the charge collected from the strips within the cluster. Fig. 6.40-right illustrates the average cluster charge (the average charge of all clusters in the data collected at a specific HV point) as a function of HV. The cluster charge demonstrates a linear increase in response to HV.

Muon Efficiency: Muon efficiency measurements were conducted by collecting data at HV points ranging from 0 to 8.3 kV. Each data file corresponds to 1000 triggers, and the event selection procedure and efficiency calculation are the same as explained in the single-gap gRPC (Sec. 6.3.3). Efficiency is estimated using Eqn. 6.3. Figure 6.41 illustrates the results of this study. The efficiency begins to increase after 6 kV, reaching a plateau at $\sim$97% after the HV value of 7.5 kV. The estimated WP for the double-gap gRPC is 7.38 kV, and the efficiency at the WP is 96%.

6.5 Advanced Gaseous Detector Muon Telescope

In order to construct an advanced gaseous detector based muon telescope for muography, a telescope configuration incorporating mRPCs and THGEMs (a multi-detector telescope) is considered. This integration aims to enhance the muon telescope's performance in terms of both time and spatial resolution. mRPCs may play

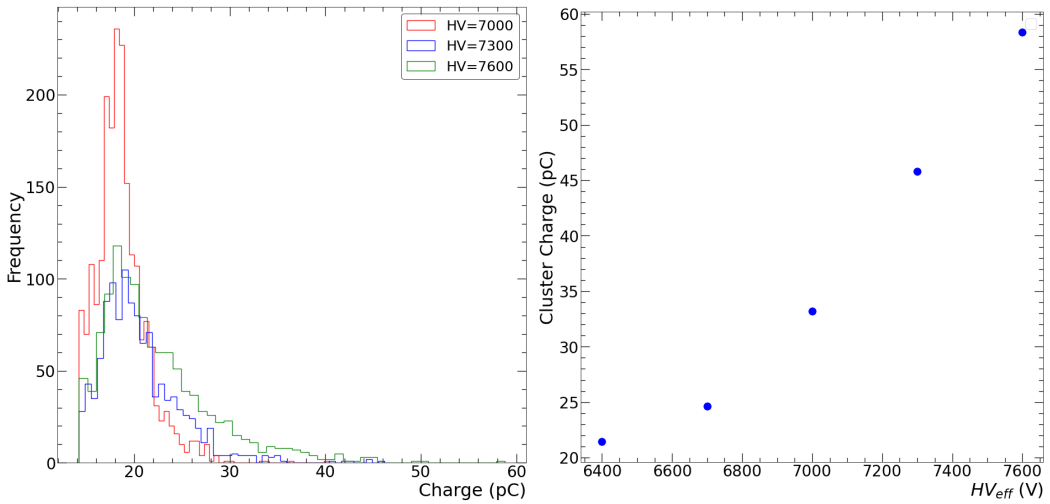

FIGURE 6.40: Left: Pulse charge distributions in the double-gap gRPC at three different HV values within the avalanche region. Right: Cluster charge as a function of the effective HV [2].

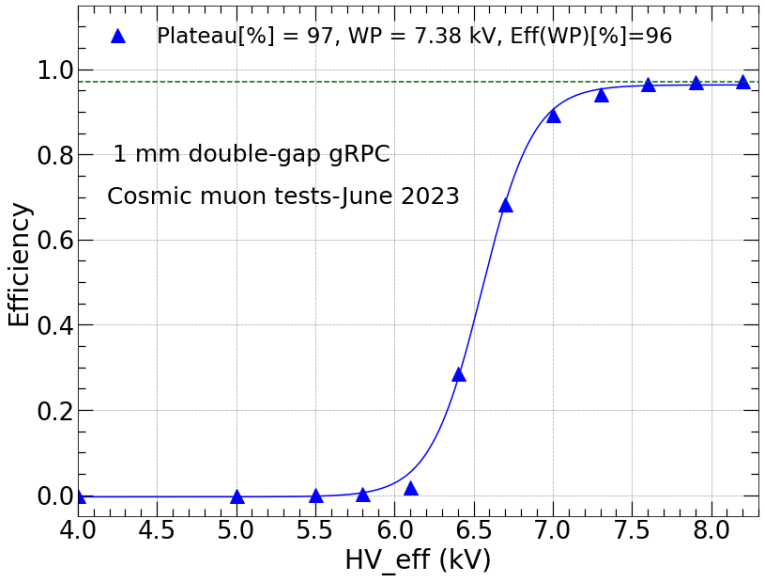

FIGURE 6.41: The muon efficiencies as a function of the effective HV values estimated for the double-gap gRPC chamber. Efficiency starts to increase exponentially after 6 kV and the efficiency plateaus at ∼97% is achieved after reaching 7 kV.

a crucial role in detector in detector background rejection (detector noise, backward-going muons, etc.) due to their ability to provide sub-nano second timing information. THGEMs, on the other hand, offer excellent position resolution in the 100 μm range which will enhance the muographic image resolution. Compared to standard GEMs, their design is more robust and allows manufacturing in an economical way. Compared to RPCs, they can be operated using simple gas mixtures or even mono-gases, greatly simplifying their operation in outdoor environments [3].

At UGent, prototype detector planes using each of the aforementioned technologies are being designed, constructed and their performance is being evaluated in

the lab using cosmic-ray muons and/or X-rays. In addition, a Geant4-based simulation of a generic 4-plane muon telescope is being developed to fine-tune the detector and telescope geometry and to study the effectiveness of using improved time information in the background rejection. Finally, a Garfield++-based [309] simulation of THGEM is being used to study and optimise the detector performance in terms of e.g. hole dimensions, detector gap sizes, field values, gas mixtures.

As I was majorly involved in the development and study of the mRPC prototype, Geant4-based mRPC simulation studies, the details and major outcomes of these activities are discussed in this section.

6.5.1 mRPC Prototype Development

A first mRPC prototype chamber is developed targeting a detector with a 2D position readout that reaches a spatial resolution well below 1 mm, in combination with a time resolution below 100 ps. The operational principles of the mRPC and its ability to achieve improved time resolution, measured in picoseconds (ps), compared to single-gap or double-gap RPCs (measured in nanoseconds, ns), have been thoroughly discussed in Sec. 2.5.2.

The chamber is designed with a low volume leak-free gas compartment, which in principle allows the detector to operate in a sealed zero-flow mode. The constructed mRPC prototype has an active area of 28×28 cm^2 and shares components nearly identical to the double-gap gRPC, such as resistive electrodes created with the spray gun method, 32 channel PCBs with enhanced designs, resistors for impedance matching, BNC HV connectors, flat cable connectors, etc. Notably, the major exceptions were the omission of the 3D-printed frame and spacers, as well as the fish wire spacers used in the double-gap gRPC.

While the 3D printed design and detector frame was designed explicitly for the advanced gaseous detector project and it showed highly successful results when it was tested with the double-gap gRPC prototype, the mRPC prototype opted for a PVC frame developed in-house. This choice was made for pragmatic reasons, as it represents the first mRPC prototype developed in the project. The primary focus was to finalise the multi-gap layout of the detector and assess its operational efficiency. Consequently, a leak-tight PVC frame was sufficient for the prototype, offering cost savings in the production phase. Once the performance and layout of the mRPC protype are validated, future plans involve advancing to the development of 1×1 m^2 mRPC hodoscope planes. This will incorporate the finalised technical layout and the 3D printed detector frames.

Detector Layout and Construction

The mRPC prototype comprises a stack of 7 glass plates, corresponding to six gas gaps. The top and bottom glass electrode plates have a thickness of 1.2 mm, while the intermediate plates between those electrodes are floating glass plates with a thickness of 0.5 mm. The assembly steps for the mRPC prototype are similar to those of the double-gap gRPC explained in Sec. 6.4.2. The detector frame is sandwiched between the top and bottom PCBs, and the electrodes, floating glass plates, and top and bottom insulation layers are assembled inside the detector box. The cross-sectional view of the mRPC prototype detector is shown in Fig. 6.42.

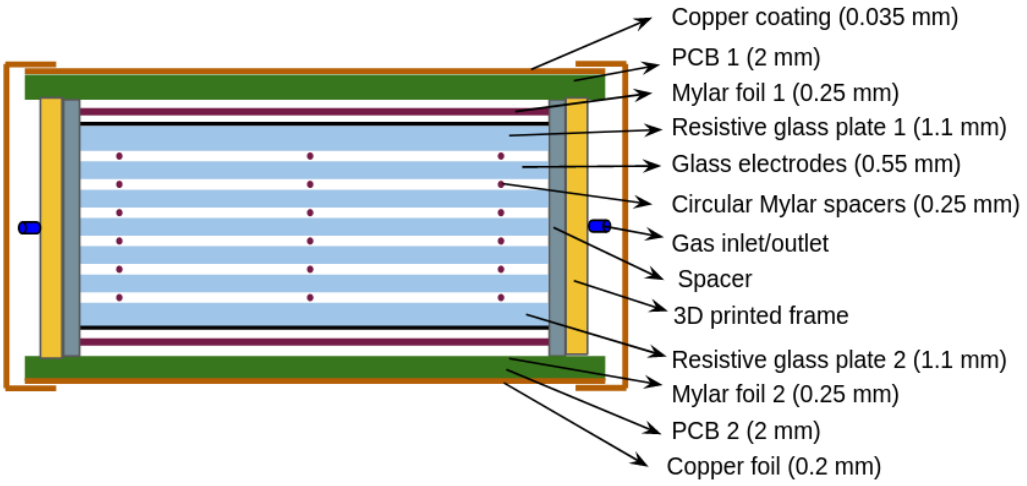

FIGURE 6.42: Cross-sectional view of the mRPC prototype detector [3].

Detector Frame: As previously mentioned, a PVC-based detector frame was constructed in the laboratory workshop using a CNC machine, specifically for this prototype. The drawing of the mRPC prototype frame is depicted in Fig. 6.43-left, while the right side illustrates the process of constructing the frame using the CNC machine. The frame layout closely resembles that of the 3D-printed frame, featuring

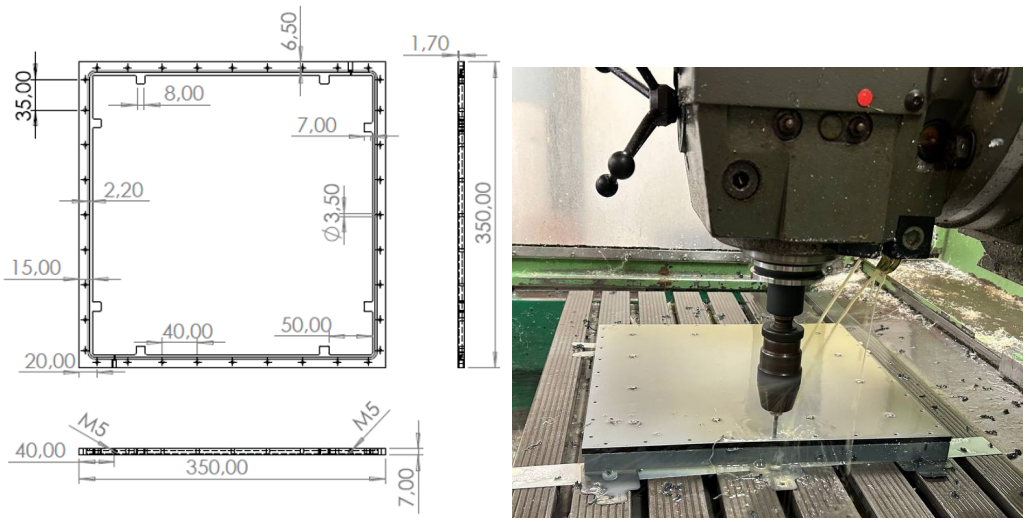

FIGURE 6.43: mRPC prototype frame, with the left side displaying the drawing of the frame, and the right side showcasing the construction process using a CNC machine.

M3 screw holes for PCB fixation, channels on the top and bottom for O-rings and spacers to secure the glass plates in place. The primary distinction lies in the absence of internal gas channels and distribution slots for efficient and uniform gas circulation when the chamber is operated in gas flow mode. Constructed as a single piece, the frame exhibits minimal leak issues, unlike the single-gap gRPC case. However, compared to the results of the 3D printed frame, a slight leak was detected (approximately 1.5 *mbar* over four days). Since this leak rate corresponds to test with 22 *mbar* and in real scenario the pressure will be almost same as the atmospheric pressure, it is not anticipated to significantly impact the prototype's performance studies.

Gas Gap Construction: In the mRPC prototype, the gas gaps are constructed with circular pieces of Mylar foil, each with a thickness of 250 μm and a diameter of 5 mm, replacing the use of fish wires. The fish wires were mainly eliminated due to the complexity of adding wires to construct six or more gas gaps, and their susceptibility to breakage at the required diameter of 250 μm. Introducing this alternative technique using Mylar foil-based spacers proves to be more convenient, eliminating the need for 3D-printed spaces to secure the fish wires. The Mylar spacers are made by attaching double-sided adhesive tape to both sides of a Mylar foil. Circular spacers are then obtained by punching holes in this tape-covered Mylar foil sheet with a hole puncher. These spacers are subsequently adhered to designated locations on the glass plates during the assembly process. Figure 6.44-left displays an image of two glass plates with circular Mylar spacers attached prepared for mRPC assembly. Figure 6.44-right shows the side view of the chamber after completing the assembly of the glass plates highlighting the six 250 μm gas gaps.

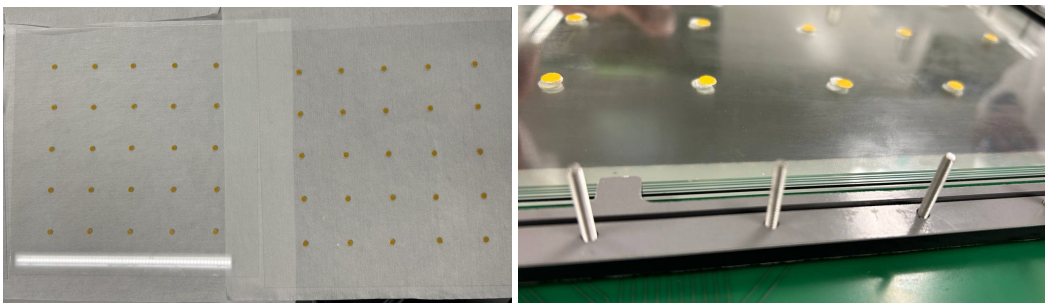

FIGURE 6.44: Left: Glass plates with circular Mylar spacers (diameter=5 mm; thickness=200 μm) attached for assembly of the mRPC prototype. Right: Side view of the chamber after assembly, highlighting the 250 μm gas gaps constructed.

Detector assembly: The assembly of the mRPC detector requires a more delicate procedure compared to the single-gap or double-gap detectors. The gas gaps are nearly four times smaller, which makes it crucial to prevent the entry of dust into the chamber and to maintain the utmost cleanliness of the components. Consequently, the entire assembly process is conducted inside the clean room section of the lab. Similar to the previous assembly, all components undergo thorough cleaning with alcohol, and a vacuum cleaner with a cleaning brush is employed for additional dust removal. The assembly process for the mRPC prototype closely follows the steps outlined for the double-gap gRPC, with the exception of the mRPC prototype detector frame and gas gap construction (already discussed in this section). A concise summary of the crucial steps is provided in Fig. 6.45 and illustrated in the following steps:

(a) Installation of the detector frame onto the bottom PCB.

(b) Cleaning the interior of the detector box using a vacuum cleaner.

(c) Placement of the bottom Mylar layer for insulation.

(d) Proper positioning of the bottom resistive electrode and the first floating glass plate between the spacers on the frame, with the first gas gap constructed using circular Mylar spacers.

(e) Completion of the interior assembly, featuring the top resistive electrode and the top Mylar layer for insulation.

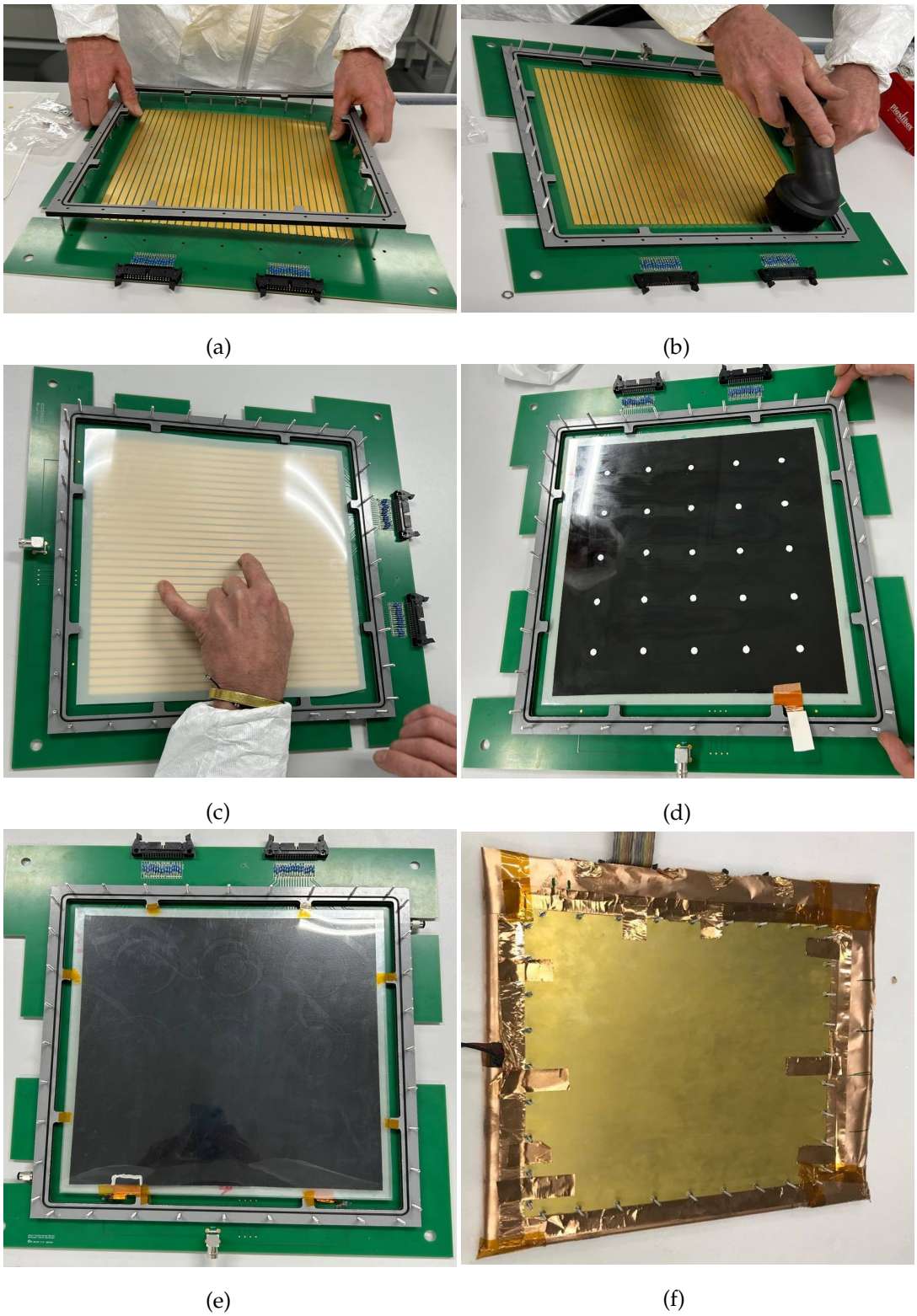

(a) (b)

(c) (d)

(e) (f)

FIGURE 6.45: Major steps involved in the construction of the mRPC prototype detector.

(f) The final appearance of the mRPC detector after sealing the Faraday cage by connecting the top and bottom PCBs on all four sides of the chamber with copper foils.

Figure 6.46 showcases a picture taken during the mRPC assembly (left), followed by a picture (right) featuring the team members participated in the assembly alongside the fully assembled prototype detector.

FIGURE 6.46: Pictures of the mRPC prototype detector construction along with the team members participated in the assembly.

6.5.2 Preliminary Tests

The results of the preliminary tests conducted with the mRPC prototype is discussed here.

Figure 6.47 illustrates the outcomes of the dark current scan performed on the mRPC. The dark current was measured at various HV values spanning from 1000 to 8000 V. Despite exhibiting an overall ohmic trend, there was a noticeable linear rise in current. Even at lower HV values (1000-4000 V) the dark current is few μA and this may be due to detector-related issues. The initial rise in current to a few micro amperes prompts the need for further investigation of the possible detector-related issues.

In order to assess the operational capability of the detector, a series of preliminary tests were conducted to examine the raw signals generated within the detector. New trigger scintillators, each with a 28×28 cm^2 active area, were specifically developed for the mRPC tests. The triggers generated by these scintillators were used for the signal tests conducted with the detector.

In Fig. 6.48-left, the mRPC detector under test is depicted, with trigger scintillators positioned on top and bottom, effectively covering the entire active area of the detector. The scintillators were powered at 1300 V, and the trigger signals were generated by processing them through the NIM discriminator and the coincidence

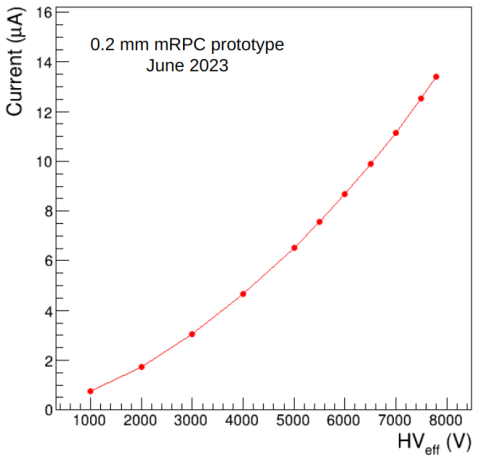

FIGURE 6.47: Dark current behavior in the mRPC with respect to the effective HV. Notably, the dark current exhibited a linear increase, initiating from the initial HV points.

module, following the same procedure detailed in Sec. 6.3.3. The discriminated signals from both PMTs, along with the coincidence trigger signal, were connected to an oscilloscope, along with a single signal cable from the top PCB of the detector.

Figure 6.48-right presents the outcome of this test. The yellow and blue channels represents the discriminated signal pulses from the PMTs, the pink channel corresponds to the coincidence trigger signal, and the green channel displays the signals collected from the mRPC detector channel. The pulses are recorded in the oscilloscope's overlap mode, where all signals detected within one hour are captured. The detector signal pulses falling within the coincidence trigger window provide confirmation that the detector is operational and capable of detecting signals in the multi-gap configuration.

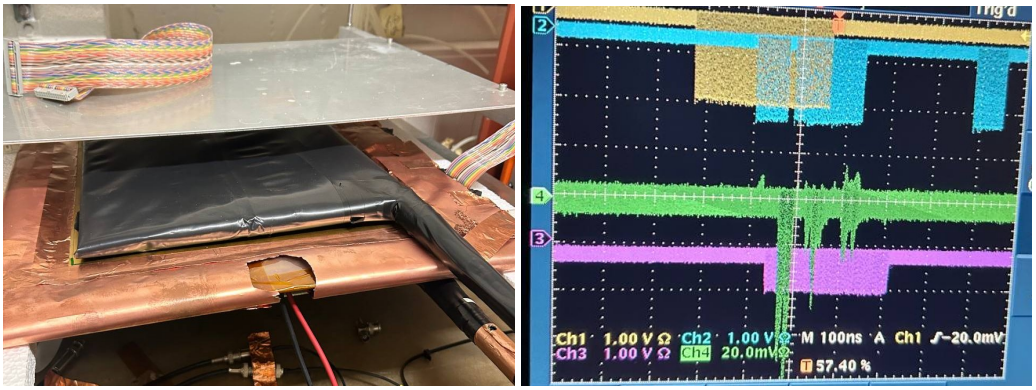

FIGURE 6.48: Left: The mRPC detector positioned in the cosmic stand with trigger scintillators aligned at the top and bottom for chamber performance tests. Right: Results of the one-hour data collection and monitoring conducted with the mRPC detector. The yellow and blue oscilloscope channels correspond to the top and bottom trigger scintillators, respectively. The pink channel corresponds to the coincidence trigger output, and the green channel shows the signal collected from one strip of the detector.

Although the detector was operational, few issues were identified. Compared to previous gRPC prototype detectors, the mRPC detector exhibited a high noise level. Additionally, due to the multi-gap configuration necessitating a higher electric

field, the detector needed to be tested at HV values up to 12000 V for efficiency measurements. Beyond 8500 V, sparks were observed on the PCB where the HV connector was soldered. These issues were addressed by implementing repairs in the chamber.

To mitigate the noise level and secure the signal connectors, the soldering part of the flat cable connectors, as well as 50 Ω resistors, on the PCB were thoroughly sealed with a thick special type PET film insulation tape. Subsequently, these regions were covered with copper tape. Figure 6.49 illustrates the signal connection regions on the PCB sealed with PET film tapes and then the copper foil and tapes. Additionally, the Faraday cage was cross checked and any small openings were covered as much as possible.

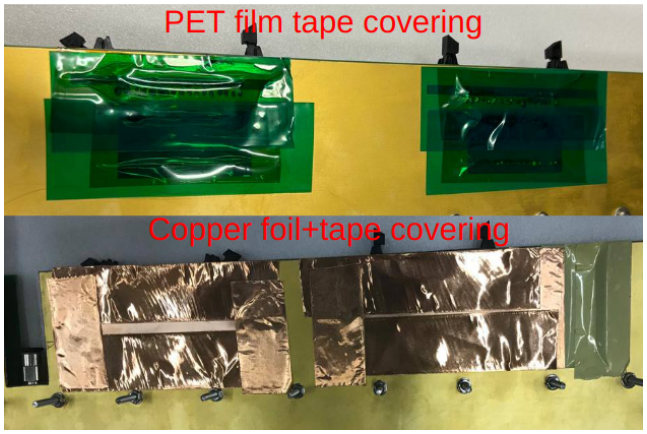

FIGURE 6.49: Images showing the insulation and secure sealing of the signal connection zones on the mRPC PCB first using PET film tape and then with copper foil and tapes on top.

To address the high current and spark issues, the HV connector on the PCB was removed, and the HV and ground cables were directly connected to the corresponding slots in the PCB. The area around the HV connection was protected with Teflon tape, known for its excellent insulation properties and additionally covered with Kapton tape. The part connecting the HV and ground cables to the PCB was thoroughly covered and sealed with liquid electric tape [310], allowing 24 hours for drying. In Fig. 6.50-left, the HV and ground connections sealed with liquid electric tape are showcased, while in Fig. 6.50-right, the other side of the connection in the PCB demonstrates the HV pin well covered with Teflon and Kapton tapes.

After implementing the aforementioned repairs, a substantial reduction in the noise level and fluctuations observed in the raw detector signal was achieved. Moreover, the issues related to high current and sparks linked to the HV connection were successfully resolved. The next steps of the project will include the efficiency scans using cosmic muons and performance studies in terms of position and time resolution. Finally, the chamber will also be tested with more eco-friendly gas mixtures and with low gas flow or sealed mode, where the latter is of particular interest for muography applications.

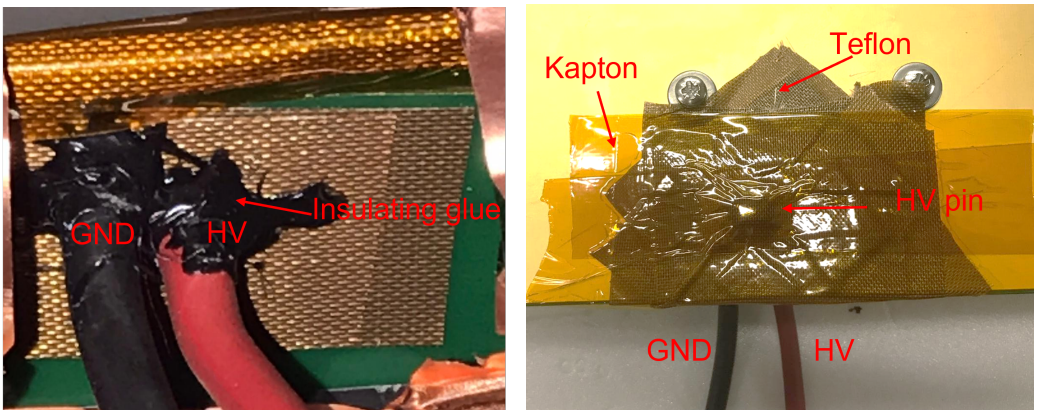

FIGURE 6.50: Left: HV and ground connections on the PCB sealed with insulation glue. Right: The other side of the PCB connection, showcasing the well-covered HV pin with Teflon and Kapton tapes.

6.5.3 Geant4 simulation studies

To optimise the detector and telescope geometry and investigate the role of time resolution in background rejection, a Geant4 simulation for the planned 4-plane mRPC-based muon telescope is being developed. This simulation will eventually be fine-tuned with actual telescope data and will be necessary for effective muography image reconstruction once the setup is fully operational. In the simulation setup, each mRPC station is composed of a stack of seven glass plates, each measuring $1 \times 1\ m^2$ and separated by gas gaps of 250 μm. The composition of the standard gas mixture is included in the simulation, along with all the remaining elements, such as Mylar foils, Copper plates, etc. The interaction of ten muons with an energy of 800 MeV in the simulation setup is shown in Fig. 6.51.

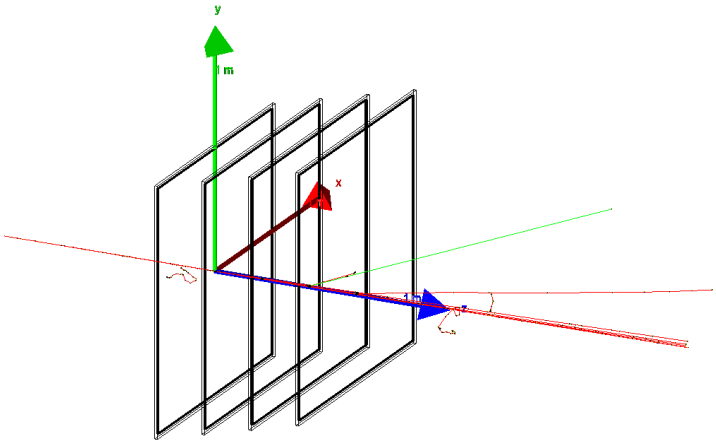

FIGURE 6.51: Interaction of ten 800 MeV muons with the mRPC muon telescope in the Geant4 simulation. The red, green and blue axes in the figure represent the X, Y and Z axes in Geant4, respectively [3].

In the telescope setup, the detector planes are arranged vertically in parallel, maintaining an inter-station distance of 20 cm. Each station is shifted upwards by 5 cm relative to the previous one, allowing the telescope to be oriented slightly upwards.

In the very first preliminary study, 10^5 mono-energetic muons of 4 GeV, i.e. about the average cosmic-ray muon energy were shot at the telescope in the direction perpendicular to the planes, and the detector responses were analysed. Since each plane has six gas gaps, multiple hits per plane are produced. The first plot in Fig. 6.52 shows the global time distribution associated with the hits generated in each plane. A threshold of 100 MeV is applied for hit selection to eliminate the hits induced by the low-energy secondary particles. The second plot in Fig. 6.52 shows the global time distribution after applying this threshold.

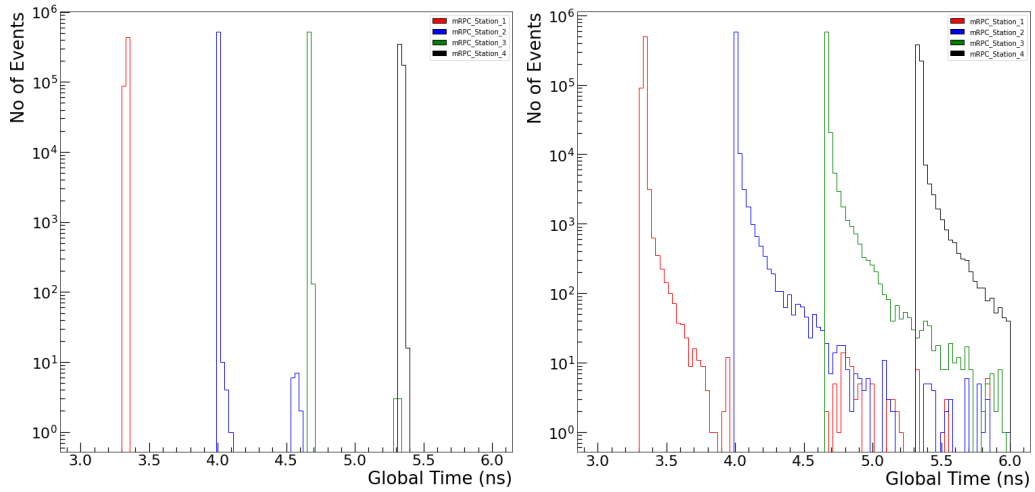

FIGURE 6.52: The global time distribution of Geant4 raw hits in four mRPC planes. Left: data without applying any energy thresholds. Right: data selected after applying an energy threshold of 100 MeV. The red, blue, green and black distributions correspond to stations 1, 2, 3 and 4, respectively [3].

The results explain that a separation of 20 cm between the planes can already offer a time difference of $\sim$0.5 ns. For further analysis, the particle generator software CRY will be used to generate cosmic muons. CRY provides cosmic-ray particle shower distributions at one of three elevations (sea level, 2100 m, and 11300 m) for input to detector simulation [224]. To compare with the performance of the real mRPC detector, the Geant4 raw hit level data will be digitised. In the simulation, the possibility of adding the actual detector effects in terms of noise and factors affecting time resolution needs to be studied.

6.6 Summary and Conclusions

Muography is an imaging technique relying on freely available cosmic-ray muons to probe the internal structure of microscopically large objects. 2D or 3D density profiles of a target can be obtained via measurements of the transmitted muon flux through the object. The UGent muography group is actively involved in intensive R&D efforts, focusing on the development of compact and portable RPCs together with RPC team at UCL. Additionally, the group is working on an advanced gaseous detector muon telescope for muography. This chapter thoroughly details my significant contributions to these activities and presents the achieved results.

An in-house spray-gun based coating technique was developed that offers uniform and stable surface resistivity within the desired range (Sec. 6.2). Challenges,

such as cracks in glass plates, have been effectively addressed through optimal baking temperatures and additional measures. Continuous monitoring of the sample electrodes construed proved the long-term stability of the surface resistivity. Precision measurements, both in terms of resistivity and coating thickness, validate the efficacy of the manual coating method, showcasing its comparability to industrial processes. Overall, these results mark a significant advancement in cost-effective and efficient electrode production for small-scale RPC detectors.

Two gRPC prototypes detectors were built and studied. The initial iteration, a basic single-gap gRPC version, was constructed using cost-effective materials with the primary goal of learning and refining the technology. Section 6.3 provides all the details of the chamber's construction and the tests conducted. Although the detector showed gas leak problems, with the implemented repairs, it was operational and showed a detection efficiency of 94.85% at WP (7.42 kV). Comparison studies with another single-gap gRPC prototype (developed by the UCL team) highlighted similar performance trends in strip occupancy and cluster size, affirming the viability of the portable detectors developed.

Addressing challenges encountered in the single-gap version, such as gas leaks and signal reflections, the second iteration, the double-gap gRPC discussed in Sec. 6.4 features a compact layout with two gas gaps, providing 2D position information. The strip PCB, and 3D printed detector frame underwent significant enhancements. The strip PCB design incorporated advanced features to eliminate cross-talk issues. The 3D printed detector frame, a single-piece structure, ensured gas-tight integrity, and the assembly process involved effective way (usage of 3D printed spacers) of gas gap construction, placement of electrodes, and integration of components. The qualification tests, including X-ray validation, leak tests, and dark current tests, confirmed the structural integrity, gas-tight construction and successful operation of the double-gap gRPC. As part of the performance studies the chamber as well as muon cluster properties such as occupancy, cluster size, cluster charge etc. were studied. The efficiency measurements with cosmic muons showed a muon efficiency plateaued at approximately 97% after 7.5 kV, with the estimated working point at 7.38 kV. As per the results achieved, the double-gap gRPC exhibits enhanced features and promising performance, showcasing its potential for applications in muography.

In view of developing an advanced gaseous detector muon telescope, a six gap mRPC prototype was constructed and preliminary tests were performed. A new strategy using Mylar foils based spacers was implemented to construct the gas gaps. Preliminary tests indicate operational capability, though noise levels were higher compared to previous prototypes. Repairs, including sealing signal connectors and HV connections, resulted in noise reduction. Geant4-based simulation setup for the mRPC-based muon telescope was also developed and some preliminary studies were conducted. Initial studies show significant time differences between the planes leading to particle identification possibilities. This need to be verified after incorporating the mRPC time resolution to the Geant4 raw time information.

Chapter 7

The MURAVES Experiment

This chapter presents an overview of the MURAVES experiment, focusing primarily on my contributions. I was majorly involved in the simulation studies and the analysis of data collected from the MURAVES detectors (mainly for actual data vs MC comparison). I compared various hadronic interaction models of the cosmic muon generator CORSIKA to identify the optimal model for MURAVES simulations. Additionally, I created a CORSIKA-Geant4 interface to perform the cosmic shower generation and Geant4 simulation in a single step. I also conducted a thorough comparison study between CORSIKA and CRY. As a next step, I developed the clustering, digitisation and tracking algorithm for the MURAVES Geant4 simulation. This algorithm converts the raw Geant4 particle hit data into particle cluster information, encompassing essential details such as energy, position, and cluster properties. Given that the energy deposited by the particle in the detector cannot be measured directly and the detector is readout using SiPMs whose response correlates with the particle's deposited energy, the digitisation segment of the algorithm transforms Geant4 cluster data into the specific MURAVES detector data format (SiPM response). Following digitisation, the tracking component of the algorithm reconstructs muon tracks, employing the same methodology applied in real data scenarios, including trigger conditions, cluster selection thresholds, and more. The analysis extended to real data, focusing on understanding muon cluster and track properties, followed by a comparison with simulated data. I also explored the properties of non-muon particle tracks to enhance the current background rejection strategy. Another significant aspect of the study involved introducing noise effects into the simulated data to align the simulation more closely with real-world conditions. I developed an advanced 3D tracking algorithm, demonstrating its potential for more effective tracking and background rejection compared to the current 2D tracking method employed in the MURAVES analysis algorithm. During my PhD, I also visited the MURAVES experimental site multiple times and participated in some of the hardware activities related to the detector. Detailed insights into each study conducted and the results achieved are provided in the respective sections of this chapter.

7.1 Introduction and Motivation

Italy is renowned as a captivating land that is home to several active volcanoes, each contributing to its unique geological and cultural landscape. Among the notable active volcanoes in Italy, four major ones stand out: Etna, Stromboli, Vulcano, and Vesuvius. These volcanoes have captured the attention of scientists and researchers to undertake extensive studies and investigations using various methodologies, including the cutting-edge technique of muography. A map indicating the

location of Vesuvius and other major volcanoes in Italy are shown in Fig. 7.1 [311].

FIGURE 7.1: Map indicating the location of Mt. Vesuvius on the west coast of Italy. The other prominent volcanoes in Italy-Campi Flegrei, Stromboli, Etna, Vulcano, Panarea, and Campi Flegrei del Mar di Sicilia are also shown [311].

The MURAVES experiment[1] was proposed in 2012 with the objective of conducting muographic measurements on Mt. Vesuvius. The primary focus of the experiment is to study the summital cone of Mt. Vesuvius by measuring its density profile through muon flux attenuation. The following subsections outline the primary motivations of conducting muography-based studies of Mt. Vesuvius and the specific details of monitoring Mt. Vesuvius. A comprehensive overview of the MURAVES experiment is presented in Sec.7.2, while the intricacies of the detectors and electronics are elaborated upon in Sec.7.3. The procedures for data collection and analysis are detailed in Sec.7.4 and Sec.7.5, respectively. Section 7.6 explains the specifics of all the MC simulation studies conducted and the corresponding results achieved. Finally, Sec. 7.7 provides a summary of the initial of the density evaluation conducted with the MURAVES data.

Motivation

Mt. Vesuvius, an iconic stratovolcano located near the city of Naples, Italy, holds a storied history and a remarkable geological significance. It is considered as one of the world's most dangerous volcanoes mainly due to its history of catastrophic eruptions. Its close proximity to densely populated areas, including the city of Naples, places millions of people at risk in the event of a major eruption. Furthermore, Mt. Vesuvius is known for its explosive eruptions, generating pyroclastic flows, ash clouds, and volcanic projectiles.

[1]The Italian Ministry of Research approved the MURAVES proposal in 2015. This approval came under the framework of the Progetto Premiale, specified in the decree MIUR n.949/ric dated December 19, 2012.

Over the past 17,000 *years*, Mt. Vesuvius has experienced eight major eruptions. The most infamous eruption occurred in 79 AD, burying the cities of Pompeii and Herculaneum under layers of ash, mud, and rocks. The eruption is believed to have caused the demise of over 16,000 individuals. This led to the collapse of a large portion of the volcanic edifice, forming the Mt. Somma caldera, from which the Mt. Vesuvius cone now emerges [312]. Over the years, the eruptive activity has altered the morphology of the volcano. In particular, several explosive eruptions led to the collapse of the crater, as depicted in Fig. 7.2 [313]. The most recent eruption occurred

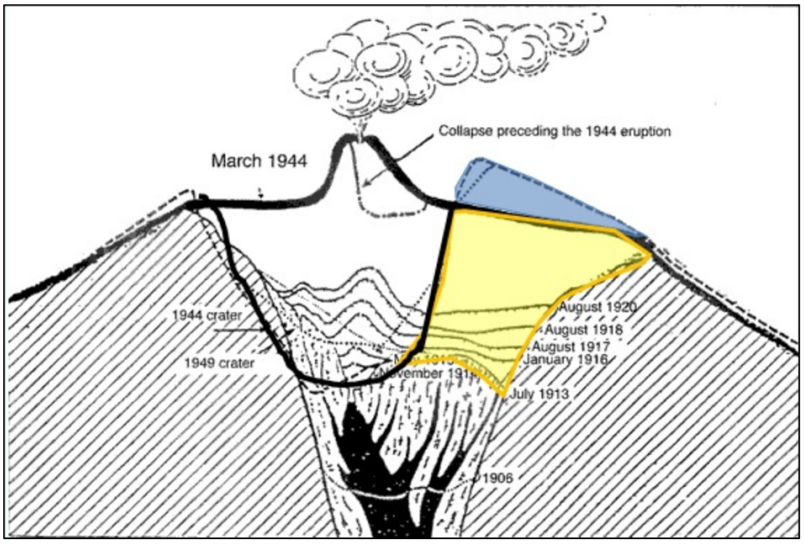

FIGURE 7.2: The schematic of the evolution of the Mt. Vesuvius crater between 1906 and 1944. After the eruption in 1944, the width of the crater was reduced (yellow: lava, blue: pyroclasts)

in 1944, initially displaying effusive activity with lava overflow, followed by an explosive eruption. In Fig. 7.3, the appearance of the crater before the 1944 eruption is shown in the left image, while the transformation after the eruption, which represents the current status, is depicted in the right image [314, 315]. The significant changes caused by the eruption are clearly illustrated by the pictures. The explosive eruption deposited high-density lava on the northeastern side of the volcano, while an incoherent and low-density deposit formed on the volcano's summit. The measurement of these density distributions is of great interest as it helps us gain insights into past explosive dynamics and aids in understanding potential future activity.

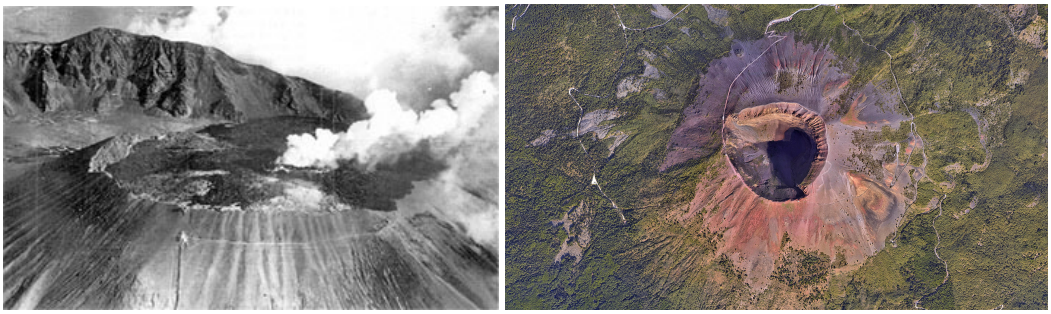

FIGURE 7.3: A comparison of the crater's appearance before the 1944 eruption (left) and its transformation after the eruption, representing the current status (right).

There are several ongoing studies on the density structure of the summital cone of Mt. Vesuvius with conventional geophysical techniques such as seismic surveys, gravimetric measurements, petrological and geochemical analysis, etc. These methods face major challenges due to the volcano's active nature, making direct access to the cone difficult and hazardous. Additionally, The steep slopes and rugged terrain make it difficult to place geophysical instruments or sensors in the desired locations for accurate measurements. Moreover, during periods of active gas emissions through fumaroles, accessing the crater becomes extremely perilous due to the presence of toxic gases, high temperatures, etc. The images in Fig. 7.4 illustrate the steep slopes (left) and gas emissions from a vent (right) in the Vesuvius crater [314].

FIGURE 7.4: The first image illustrates the steep and hazardous slopes, and the second image shows gas emissions through a fumarole vent in the Vesuvius crater, making direct access challenging.

What makes muography particularly interesting is its ability to provide non-invasive imaging of the volcano's internal structure. More details are explained below:

- Muons can penetrate through hundreds of meters of rock, providing valuable information about the internal density variations and structures (presence of the magma chambers, magma pathways, etc.) without any drilling, excavation, or physically accessing the hazardous areas unlike the conventional methods.
- With cosmic-ray muons being a continuous source, muography enables ongoing and continuous monitoring of Vesuvius.
- As it is non-intrusive, it has a minimal environmental impact, making it particularly suitable for protected or ecologically sensitive areas.

Hence, muography can complement other monitoring methods by providing additional data on the internal dynamics of the volcano. By continuously monitoring the density variations over time, it is expected to detect changes that might indicate volcanic unrest or potential eruption scenarios.

Monitoring of Mt. Vesuvius by INGV

Currently, Vesuvius remains in a quiescent state, exhibiting relatively mild volcanic activity. This is evident through the presence of low-temperature fumaroles, with temperatures below 100° C, and moderate seismic activity, averaging around 100 earthquakes per year with magnitudes ranging from 0.5 to 3.6 on Richter scale.

However, the timing and likelihood of a future explosive eruption from Vesuvius are difficult to predict. The volcano's behavior can evolve unexpectedly, highlighting the need for continued monitoring and research to improve our understanding of its activity. Considering this, the INGV Vesuvius Observatory has employed a network of monitoring instruments to track the volcano's activity and assess potential risks as described below:

- seismic sensors are installed around the volcano to detect even the slightest ground vibrations and monitor seismicity patterns
- GPS stations and satellite measurements are utilised to monitor ground deformation, providing insights into magma movements and potential volcanic unrest
- gas monitoring stations track the composition and flux of volcanic gases emitted by Vesuvius, aiding in eruption forecasting

The first image in Fig. 7.5 shows the control room of the INGV Vesuvius Observatory, where the signals from all the permanent monitoring networks of the Campania volcanoes (Vesuvius, Campi Flegrei, Ischia) and the Stromboli seismic network are collected. The second image showcases the monitoring panels of Vesuvius. The data

FIGURE 7.5: (left) Monitoring Room of the INGV Vesuvius Observatory in Naples, serving as the operational center for collecting signals from all the permanent monitoring networks of the Campania volcanoes (Vesuvius, Campi Flegrei, Ischia) and the Stromboli Seismic Network. (right) Monitoring panels of Vesuvius in the monitoring room.

collected by the observatory's monitoring network is analysed in real-time, allowing scientists to promptly identify any changes or anomalies in the volcano's behavior[2]. Figure. 7.6 shows the stamen terrain map of seismic events that occurred over a period of two years in the Vesuvius region. The color and size of the data points correspond to the period when the event occurred and the magnitude of the event, respectively. Additionally, the plot marks the positions of seismic stations installed throughout the region [316].

The live monitoring leads to the timely dissemination of information to civil protection authorities and the local population, particularly in high-risk and emergency situations. The Italian 'Protezione Civile' has developed an evacuation plan (accessible at [317]) to address the potential risks associated with an eruption of Mt. Vesuvius. This plan operates under the assumption of a 2-week to 20-day warning period prior to an eruption. It encompasses the emergency evacuation of approximately 700,000 individuals, primarily consisting of residents within the 'zona rossa' or red zone, where the threat of pyroclastic flows is most significant [247]. Figure. 7.7

[2]The pictures were taken during the visit to the observatory.

presents the risk zones in the Vesuvius region, classified by the Italian Civil Defense Authority. Apart from the red zone, which poses the highest hazard and volcanic risk due to pyroclastic flows, there is also the yellow zone, at risk of fall-out deposits, and the blue zone, susceptible to mud flow and lahar deposits. Additionally, the figure indicates the location of the largest civil hospital in southern Italy, the Hospital of the Sea (Ospedale del Mare), situated 7.5 kilometers away from the crater to handle emergency risk situations [318].

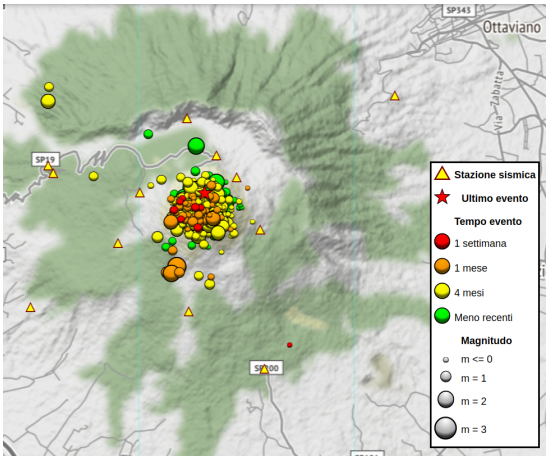

FIGURE 7.6: The stamen terrain map featuring seismic events recorded in the Vesuvius region over a span of two years. Data points on the map are represented by varying colors and sizes, indicating the event's time period and magnitude. The locations of the seismic stations installed in the region are also shown [316].

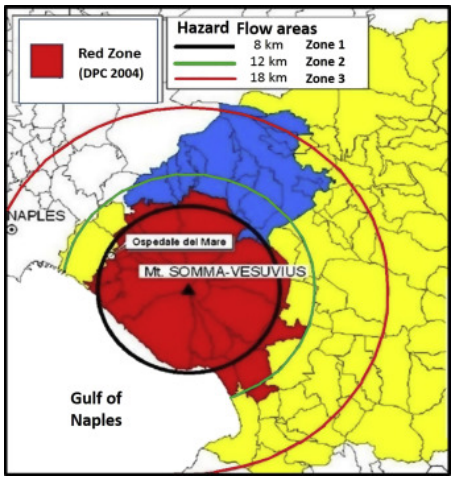

FIGURE 7.7: Vesuvius red, yellow, and blue risk zones delimited by the Italian 'Protezione Civile', along with the location of the Ospedale del Mare. The areas delimited at 8, 12, and 18 *km* have been drawn based on the distribution of pyroclastic flows in the past [318].

7.2 The MURAVES Experiment

The MURAVES experiment aims to study the density distribution in the summital cone of Mt. Vesuvius by measuring the muon flux from the direction of the area of interest. The details of the technique of muography used to estimate the density distribution is discussed in Sec. 5.3. The muography data, when combined with information gathered from gravimetric and seismic measurement campaigns, will contribute to a better understanding of the structure of the volcanic plug located at the base of the crater. This plug serves as a seal, preventing magma ducts from the caldera below from reaching the surface.

The MURAVES collaboration involves a diverse team of physicists, geologists, and volcanologists from University of Florence, University of Naples, University of Gent, Vrije Universiteit Brussel, Université catholique de Louvain, Istituto Nazionale di Geofisica e Vulcanologia (INGV), and Istituto Nazionale di Fisica Nucleare (INFN). The experiment was built upon baseline ideas and the expertise gained from the INFN R&D project Mu-Ray, which began in 2009 [217]. The MU-RAY detector, a plastic scintillator detector with a 1 m^2 surface area, served as a prototype to assess the feasibility of the technology and functioned as a hodoscope during short data-taking campaigns [226, 319]. Since 2019, the MURAVES experiment has been

actively collecting data. The preliminary results from the analysis of the initial data sample have already been published, reflecting the experiment's progress and contributions to the field [320].

7.2.1 Experiment Site Selection

Site Selection: Selecting the optimal location for a laboratory poses significant challenges, and the MURAVES laboratory was no exception. Due to the requirement of imaging the bottom of the crater, only a few sites with a sufficiently low altitude around Vesuvius could be considered. Moreover, the surrounding area falls within the boundaries of the Vesuvius natural park, under the management of the park authority "Ente Parco Nazionale del Vesuvio," responsible for safeguarding and authorizing activities within the park region. Among the promising options, "Casino Imbo" initially appeared favorable due to its logistical ease and power line availability. However, its proximity to the mountain can introduce a non-negligible fraction of low-energy muons undergoing multiple scattering on the outer layers of the mountain, causing deflection and falling within the detector's acceptance range. In contrast, "Casina Amelia," situated on the southwest slope of Vesuvius at an altitude of 600 m and a distance of 1500 m from the crater, proved more favorable in terms of background events as it is far more distant from the crater compared to "Casino Imbo". Despite the absence of electrical power lines, this site offers a significantly lower fraction of background events. Optimising background effects involved MC simulations using the custom software PUMAS Reverse Muon Simulation, leading to the selection of "Casina Amelia" as the ideal location for the laboratory installation [185, 321]. In Fig. 7.8, the top image depicts the location of the MURAVES observatory, with the city of Naples also indicated. The bottom image captures the view of the Vesuvius crater as seen from the laboratory, with the telescope's central line of sight clearly marked by the green arrow. Both Images are created using the Google Earth software [322].

7.2.2 Laboratory Setups

The laboratory is housed within a metal container of area 45 square meters, accommodating the MURAVES muon hodoscopes and all experimental logistics, as illustrated in Fig. 7.9. The detection setup consists of three fully operational and identical tracking hodoscopes named NERO, ROSSO, and BLUE. The acceptance range for all three detectors is set to the same values ($60^\circ < \phi < 200^\circ$; $14.8^\circ <$ elevation $< 22^\circ$). The use of three hodoscopes, as opposed to one, enhances statistics and reduces the overall data collection time. The region below an elevation of 14.8° is excluded due to increased thickness (> 1500 m), which may result in prolonged data collection periods. For detailed information on Mt. Vesuvius rock thickness, experiment data collection duration to achieve the targeted density resolution, etc., refer to Sec. 7.4.3.

Each hodoscope comprises four tracking stations, with a thick lead wall acting as a passive filter for low-momentum muons placed between the third and fourth stations. The telescope's geometries and the component's details are described in Sec. 7.3.1. Inside the container, four designated spots are arranged for the installation of the hodoscope, each equipped with a concrete platform specifically designed to house the lead wall. These platforms are placed directly on the ground to avoid affecting the container floor due to the weight of the lead wall. The first three stations of each hodoscope are mounted on an iron-based stands, allowing for

FIGURE 7.8: Top image: The MURAVES observatory location (red marker) on Google Earth, with the city of Naples (blue marker) also indicated. Bottom image: View of the Vesuvius crater seen from the laboratory, showcasing the hodoscope's central line of sight denoted by the green arrow. Both Images are created using the Google Earth software.

FIGURE 7.9: The container housing the MURAVES hodoscopes situated inside the Vesuvius national park.

distance adjustment between stations, elevation fixing from the floor, and easy mobility from one spot to another while maintaining relative geometry. The schematic of the four spots to host the detectors inside the container are shown in Fig. 7.10. The schematic illustrating the placement of the detectors inside the container is presented in Fig. 7.10. Three spots, represented by blue, red, and black rectangles, are

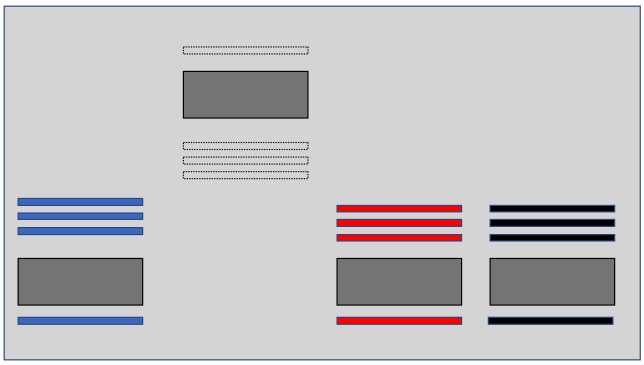

FIGURE 7.10: Schematic representation of the installation slots of the MURAVES hodoscopes inside the laboratory. Three spots (blue, red and black rectangles) are dedicated to hosting the hodoscopes, pointing toward the volcano, while the fourth spot (dotted rectangles) serves for operating detectors in open sky calibration mode. The dark gray boxes represent the lead wall [323].

specifically designated for hosting the hodoscopes, oriented towards the volcano. The fourth spot, indicated by dotted rectangles, is used for operating detectors in open-sky calibration mode. In this mode, the cosmic muon flux from the open sky is estimated, providing valuable data absent in the volcano-directed observations. The dark gray boxes in the figure depict the lead wall. During calibration, the detector orientation is reversed, pointing towards the sky. Figure 7.11 shows the MURAVES hodoscopes NERO pointing towards the volcano and ROSSO in the open sky calibration mode. The images also display the lead wall installed between the last two stations and the iron base effectively holding the stations in position.

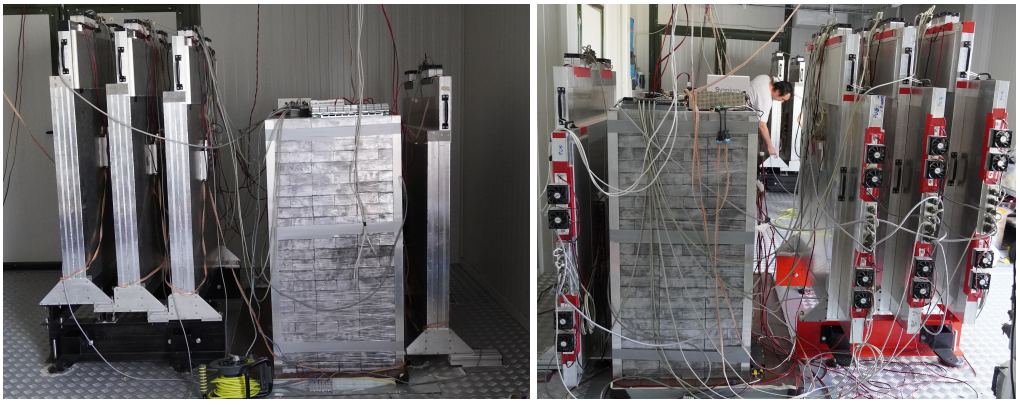

FIGURE 7.11: (Left) MURAVES hodoscope NERO positioned to capture data from the Vesuvius. (Right) MURAVES hodoscope ROSSO operating in open sky calibration mode, estimating cosmic muon flux from the open sky. The lead wall between the last two stations and the iron base holding the stations in position can also be observed in the images.

Solar-Powered Operation: The entire laboratory operates using solar panels installed on the container's roof. The hodoscopes are remarkably energy-efficient, with each hodoscope requiring approximately 30 watts for its full functioning. These solar panels are connected to an array of batteries, ensuring continuous operation even during night-time hours and cloudy days. The first and second images in Fig. 7.12 displays the first image with the solar panels installed on the container's roof, while the second image highlights the batteries linked to the solar system.

FIGURE 7.12: The left-side image shows the solar panels installed on the container's roof and the right-side image displays the array of batteries connected to the solar panel system, ensuring continuous operation even during night-time and cloudy days.

Remote Monitoring and Control : Due to the remote location of the MURAVES laboratory, daily access presents challenges. To address this, remote monitoring and control systems have been implemented for the MURAVES hodoscopes and their supporting systems. Continuous monitoring of environmental parameters such as temperature, pressure, and humidity is established. In particular, the temperature of the hodoscopes, the SiPM working points, the trigger rates, and other critical parameters are meticulously recorded, allowing the supervision of hodoscope operations. Moreover, the power supply system status is effectively monitored through a dedicated website provided by Victron Energy Enterprise, the energy system supplier [324]. This platform offers insights into battery charge levels, power generated using the solar panels, power consumption details, and more. Figure 7.13 showcases a month-long summary of power system monitoring, illustrating solar energy production, consumption, and battery charging status.

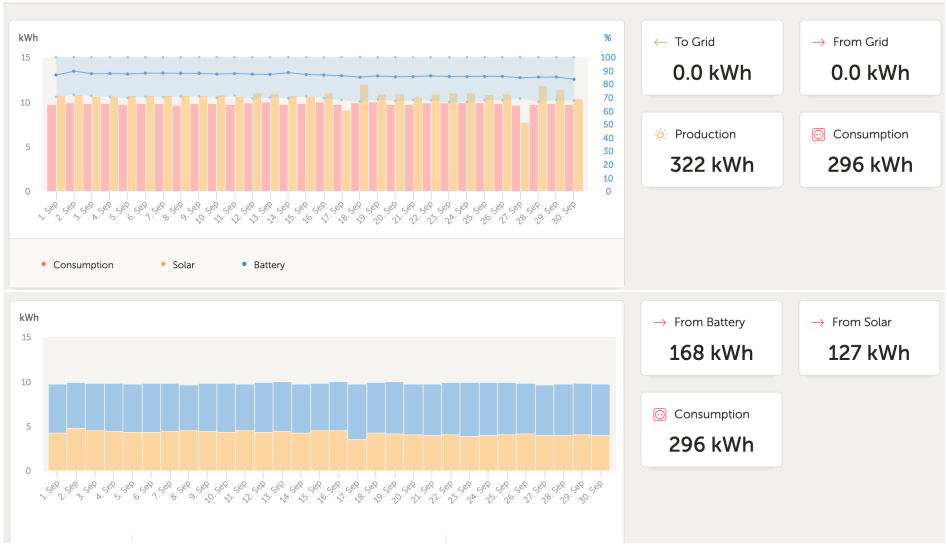

FIGURE 7.13: One-month summary of the remote power supply monitoring system at the MURAVES laboratory. It presents solar energy production, battery charging status, and power consumption patterns over the period.

7.3 The MURAVES Detector and Electronics

7.3.1 Design and Components

The MURAVES detection setup comprises of three identical and independent tracking hodoscopes, namely NERO, ROSSO, and BLUE, drawing upon the experience gained from the MU-RAY prototype detector. Each hodoscope includes four tracking stations, with each station featuring two planes (X and Y) comprising 64 adjacent plastic scintillator bars. These bars, covering a sensitive area of 1 m^2, are placed orthogonally to each other, allowing the extraction of bi-dimensional information from muon hits. To maximise the geometrical acceptance of particles arriving from the observation point, the tracking stations are vertically arrayed at distinct elevations above the ground. Specifically, the stations 3, 2, and 1 are elevated by 20 cm, 25 cm, and 30 cm, respectively, compared to the station 4. Concerning horizontal alignment, the first three stations are separated by around 25 cm, while the last two stations has a wider separation of approximately 120 cm. A schematic view of the MURAVES hodoscope design is shown in Fig. 7.14. Additionally, the pictures of the three fully assembled and operational MURAVES hodoscopes (NERO, ROSSO and BLUE) are depicted in Fig. 7.15.

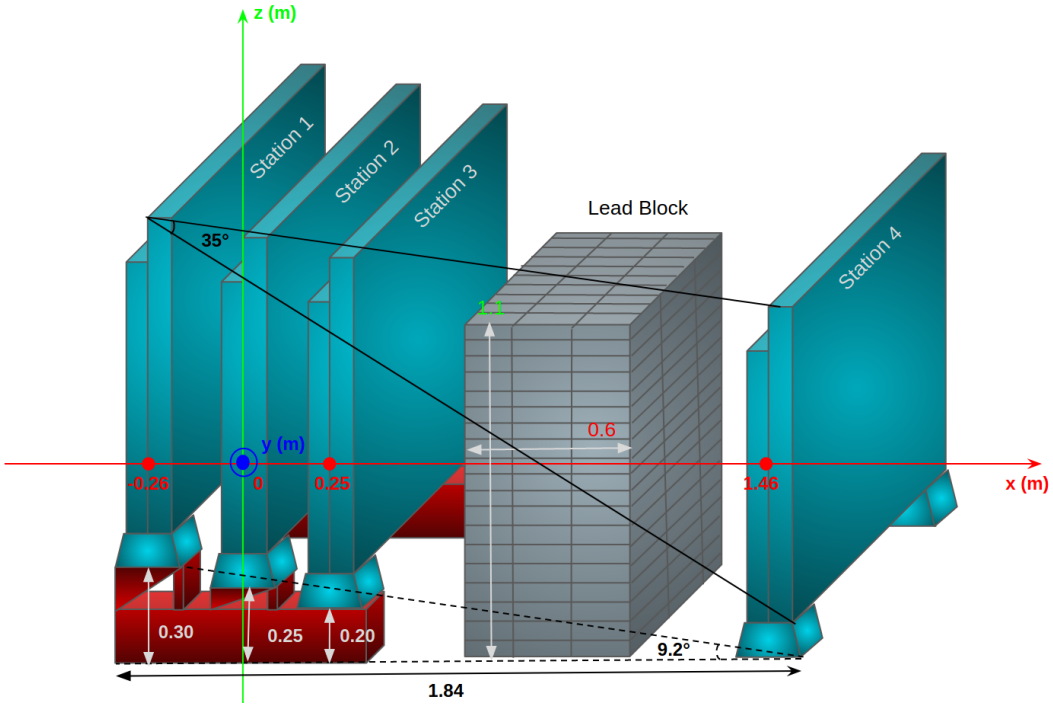

FIGURE 7.14: The schematic diagram of MURAVES hodoscope.

Background Rejection Strategy: The hodoscopes will suffer background from low-energy muons, as well as electrons, positrons, and gammas. The background events enters the hodoscopes from both backward and forward (volcano direction) directions. The rejection of backward-background can be addressed via time-of-flight measurements. The major source of background in the forward case are the muons, undergoing multiple scattering within the volcano and subsequently exiting with low energy and the muons that scatter off the outer layer of the crater and reach the

hodoscope's acceptance region (for more details, see Sec. 5.3.3). To mitigate this issue and counteract low-energy tracks from various particles at ground level, a lead wall measuring 110 *cm* in length, 60 *cm* in width, and 110 *cm* in height is placed between last two stations. This lead wall serves a dual purpose in filtering out low-energy muons from the volcano direction. Firstly, particles below a specific energy threshold ($\sim$1 *GeV*) are unable to traverse the lead wall. Secondly, as the scattering angle of muons within the lead wall correlates directly with their energy, measuring this angle aids in the rejection of low-energy particles [217].

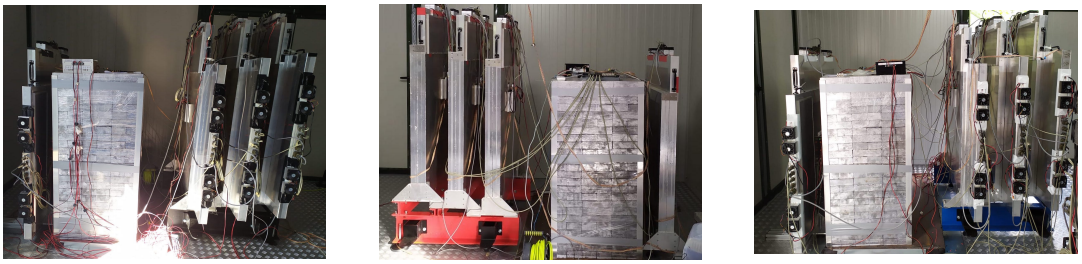

(a) (b) (c)

FIGURE 7.15: The three MURAVES hodoscopes fully operational installed at the laboratory: (a) NERO, (b) ROSSO and (c) BLU.

Scintillator Bars: The scintillator plastic is made of polystyrene infused with 2,5-Diphenyloxazole (PPO) and 1,4-bis(5-phenyl-2- oxazolyl)benzen (POPOP) scintillation dopants, emitting light in the blue wavelength region centred at 420 *nm* with an emission time of 3 *ns*. The bars are of isosceles triangular shape, measuring 33 *mm* in base width, 17 *mm* in height, and 1 *m*in length, and are placed side by side in alternating orientations (upward and downward triangular tips, as depicted in Fig. 7.16 (top)) to construct the detection plane. This configuration enables muons entering the plane to traverse at least two adjacent bars, allowing precise hit position reconstruction using a barycenter-like algorithm, leading to enhanced spatial resolution.

Signal Extraction: For scintillator signal readout, a central hole with a diameter of 1.5$\pm$0.1 *mm* is created along the length of each bar's axis. Through these holes, wavelength shifting fibers (WLS) with a diameter of 1.2 *mm* are inserted to efficiently collect light signals induced by muons. The WLS fibers are of multiclad Kuraray Y11 S-35 type, exhibiting an absorption spectrum within the wavelength range of 400-470 *nm* and an emission spectrum spanning 470-550 *nm* with a peak in the green region. To further enhance internal reflectivity and shield the fibers from environmental light, they are coated with a layer of TiO_2 measuring 0.2 *mm* in thickness. Fig. 7.16 (bottom) shows a half-tracking plane featuring 32 scintillator bars equipped with wavelength-shifting fibers (WLS) [185].

7.3.2 Photo Sensor and Front-End Electronics

In the MURAVES hodoscopes, the light signals collected by the WLS fibers are channeled to the photosensors, specifically the ASD-RGB1C-P Silicon Photomultipliers (SiPMs), manufactured by AdvanSiD [325]. The choice of this specific SiPM model was driven by its advantages, including a low operating voltage of 30 *V* and cost-effectiveness. Despite having a slightly higher Dark Count Rate (DCR) ($<$ 100

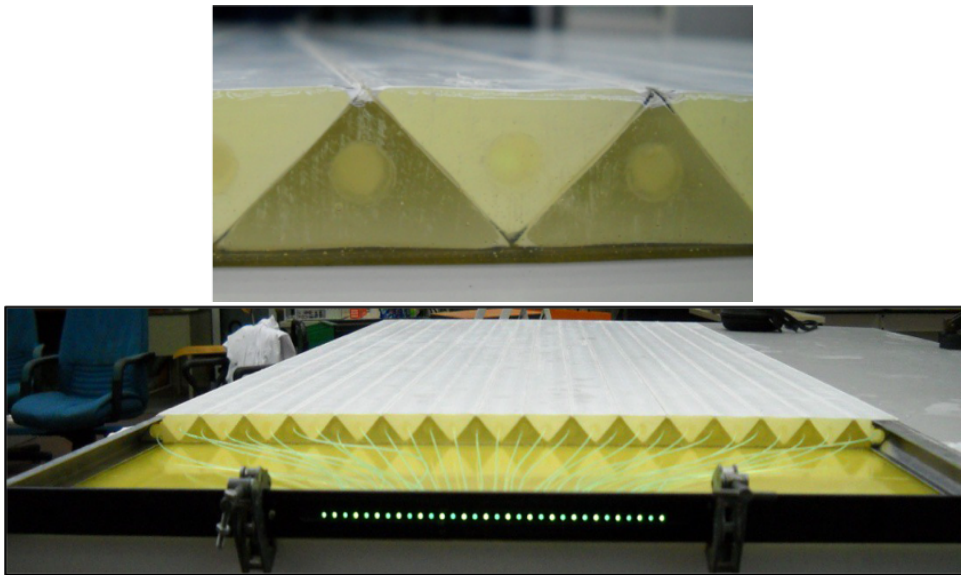

FIGURE 7.16: Top: a close-up view showcasing the side-by-side alignment of the triangular bars within the detector plane. Bottom: a half-tracking plane with 32 scintillator bars, each equipped with wavelength-shifting fibers, integrated into an aluminum frame.

$kHz/\ mm^2$) and a slightly lower Photon Detection Efficiency (PDE) (32.5 %) compared to standard Hamamatsu photo sensors (DCR: 50 to 60 100 kHz/mm^2; PDE 40-45 %), the ASD-RGB1C-P SiPMs emerged as the optimal choice due to their remarkable temperature stability. This temperature stability is crucial since the detectors operate in an environment characterised by significant temperature variations throughout the year. The SiPMs are integrated into a PCB designed to host 32 elements (see Fig. 7.17). Each hodoscope plane is equipped with two of these PCBs.

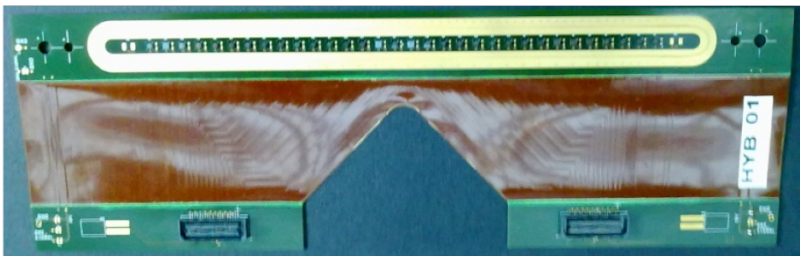

FIGURE 7.17: PCB used in MURAVES hodoscopes, incorporating 32 ASD-RGB1C-P SiPMs. Each hodoscope plane utilises two of these PCBs.

Considering the constraints on electricity availability, the MURAVES hodoscopes employ low-power-consuming front-end electronics for signal processing and DAQ. Each hodoscope, consisting of 16 PCBs, is connected to 16 corresponding SLAVE boards, each capable of reading 32 SiPM channels, which are equipped with an EASIROC ASIC [326]. The utilisation of this dedicated ASIC offers several essential functionalities, including SiPM gain adjustment, signal shaping, charge measurements, and high and low gain multiplexed outputs, as well as a TDC providing TOF measurements with a 0.1 ns time resolution. The power consumed by each board is only approximately 2.5 W.

The SiPM signals are amplified and converted into ADC counts, allowing precise measurements of the charge deposited. Moreover, a local trigger signal is generated by the SLAVE board, achieving this by performing a logical OR operation on all 32 SiPM signals (OR32). The resulting trigger signal is then transmitted to the MASTER board to generate the global trigger.

The outputs of all SLAVE boards are sent to the MASTER board, which houses an FPGA and a Raspberry-Pi computer. When the MASTER board receives signals from the SLAVE boards, it checks for trigger requirements set by the FPGA. If the criteria are met, the data is collected and stored in the storage device. Figure 7.18 shows the images of the SLAVE board and the MASTER board, respectively.

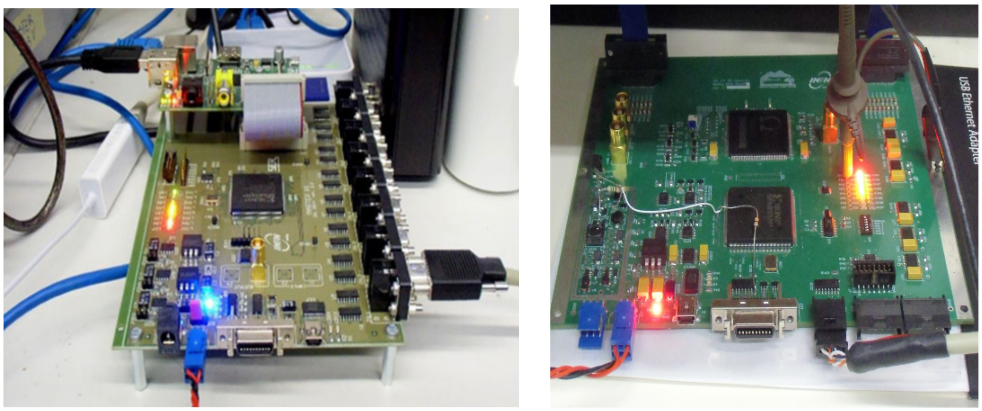

FIGURE 7.18: The SLAVE board (left) and MASTER board (right) of the MURAVES hodoscopes' front-end electronics. The SLAVE boards send their outputs to the MASTER board, which houses an FPGA and a Raspberry-Pi computer for data processing and triggering.

A significant feature of the MURAVES front-end electronics is its ability to measure the TOF of muon tracks in the hodoscopes. This capability allows the rejection of muons entering the telescope from the backside of the hodoscope and the muons that scattered upwards after reaching Earth's surface and enter the hodoscope's acceptance. Each SLAVE board contains a time expansion system based on the charge and discharge of a capacitor. When a local trigger occurs on the SLAVE board, the capacitor starts charging, and it begins to discharge upon receiving a trigger signal from the MASTER board. The discharge time ($T_{discharge} \sim E \cdot T_{charge}$, where E is the expansion factor ≈ 50) is measured by the SLAVE clock operating at 50 MHz, providing an effective resolution of about 400 ps [323].

7.3.3 Temperature Stabilisation System

The MURAVES experiment experiences varying environmental temperatures due to the seasonal changes in the region. In addition, it is also influenced by the mountain's elevation and its proximity to the Mediterranean sea. Summer temperatures can reach 30-35°C (86-95°F), while winter temperatures can drop to 5-10°C (41-50°F) or lower. To ensure reliable data collection over the extended duration of the experiment, which spans several months, a sophisticated temperature stabilisation system has been developed to regulate the operating temperature of the SiPMs. These SiPMs are highly sensitive to temperature changes, and their performance can be

affected by fluctuations in the breakdown voltage, quantified by the Breakdown Voltage Temperature Coefficient (BDTC). In this setup, the BDTC of the SiPMs is measured to be BDTC = $27mV/^{\circ}C$.

The temperature stabilisation system relies on the Peltier effect, enabling both cooling and heating of the SiPMs. For each array of SiPMs, two Peltier cells are employed, along with a copper rectangular bar to ensure uniform temperature distribution and a pair of cooling fans per board. The configuration can be visualised in Fig. 7.19, showcasing the white board housing the Peltier cells and the copper bar, atop which the cooling fans are positioned. A custom-made circuit equipped with Pulse Width Modulation drivers efficiently controls the thermoelectric coolers, and the entire system is connected to a PC through a USB and CAN-bus interface.

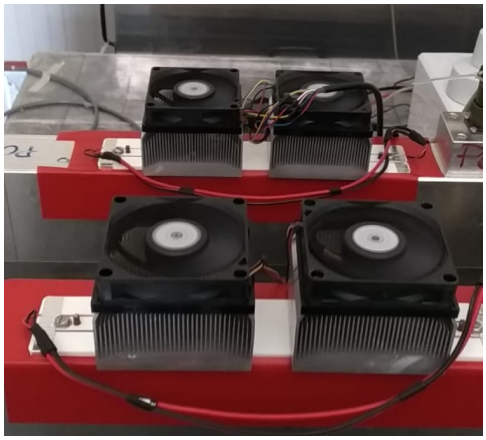

FIGURE 7.19: The temperature stabilisation system components, including the white board hosting the Peltier cells and a copper rectangular bar, and cooling fans.

To achieve optimal performance, the working point temperature of the SiPMs is modulated in a specific manner, ensuring a maximum difference of $5^{\circ}C$ between the sensor temperature and the ambient environment. When this difference exceeds $5^{\circ}C$, the SiPM temperature is adjusted to maintain the desired margin. This approach significantly reduces power consumption from 15-20 W to 4 W per plane. In addition to temperature, the laboratory's humidity levels are continuously monitored, and the SiPM temperature is carefully set to remain distant from the dew point. This prevents condensation, which could potentially damage the sensor [323].

7.4 Data Collection

7.4.1 Trigger Logic

To perform a rigorous event selection, the hodoscope system employs a trigger logic (T_{logic}). This logic records an event only if sequential signals are detected in the first three stations of the hodoscope, encompassing both the y and the z planes. Taking into consideration the SiPMs' gain, a threshold on photoelectron (*phe*) counts (threshold=6) is set, which can be adjusted accordingly. A scintillator bar is considered part of the event only if the number of photoelectrons ($nPhE$) surpasses this threshold.

The trigger logic can be explaind through the equation:

$$T_{logic} = \bigcap_{i=1}^{3} M_z^i \cap M_y^i \tag{7.1}$$

Here, M_z^i and M_y^i represent the logical OR of the 64 scintillator bars in the z and the y planes respectively for the i^th station, where i ranges from 1 to 3. The trigger logic then operates as the logical AND of M_z^i and M_y^i. Data acquisition occurs in runs comprising 40000 triggers, each associated with a unique run number that corresponds to the respective data file. Figure 7.20 displays the trigger rates measured for the NERO (top) and ROSSO (bottom) detectors as a function of the run number. Both plots depict the measured values (black points), with the red line representing

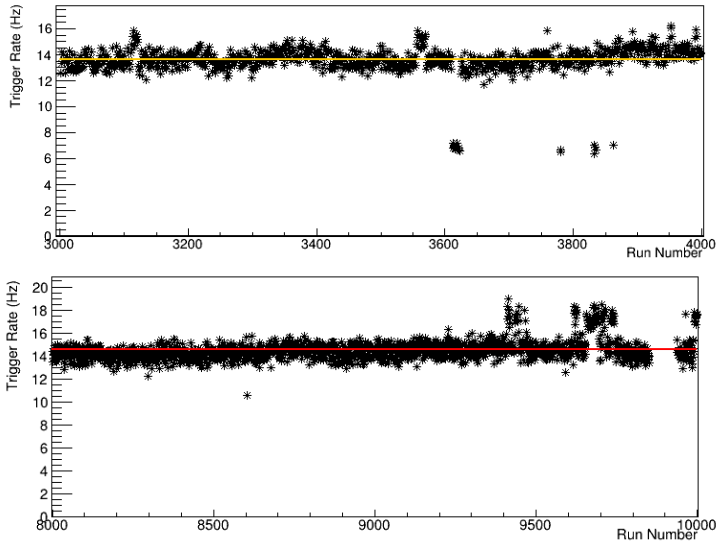

FIGURE 7.20: Trigger rates measured as function of the run number for the NERO (top) and ROSSO (bottom) detectors. The red lines in both plots corresponds to the mean trigger rates in both cases: NERO= 13.6 Hz; ROSS0= 14.5 Hz [323].

the mean value. The mean trigger rate for NERO is 13.6 Hz, while for ROSSO, it is 14.5 Hz. The first quality selection applied to the data is based on the trigger rate measured. Ideally, all runs should exhibit similar trigger rates. However, if certain runs deviate significantly from the average trigger rate of a specified number of runs, as indicated by the plots, this might be due to hardware or electronics issues during data collection. Consequently, such runs are excluded from analysis, considering the data associated can be corrupted.

7.4.2 SiPM Working Points

As discussed in Sec. 7.3.3, the MURAVES experiment is designed for an extended data acquisition period spanning several years. During this duration, the detector systems will be exposed to a wide range of environmental conditions, including variations in pressure, humidity, and temperature. Even within a single day, these parameters can exhibit significant fluctuations. Given the temperature-sensitive nature of the SiPMs used in the detectors, ensuring consistent performance over this

prolonged period is crucial. To achieve this, a strategy involving different temperature working points for the SiPMs is devised, and a temperature stabilisation system is employed to align these working points according to the observed variations.

The working point here denotes a specific combination of temperature and bias voltage (V_{bias}) applied to the SiPMs. This combination is carefully adjusted, maintaining a range of 5-7 degrees in relation to the external temperature. This approach not only minimises power consumption but also ensures that the working point remains considerably distant from the dew point, avoiding the potential for condensation. The breakdown voltage (V_{bd}) of the SiPMs is directly proportional to temperature, and fluctuations in this parameter can lead to variations in SiPM performance. To uphold consistent detection efficiency and stable gain, the overvoltage ($V_{ov} = V_{bias} - V_{bd}$) is maintained at a constant level. This is achieved by dynamically altering the V_{bias} either upwards or downwards in response to changes in V_{bd}.

While the SiPMs' operating points are adjusted based on the environmental temperature, they constitute a range of values rather than a fixed parameter. Notably, variations in detector performance were noted across these distinct working points. Taking account of these variations, the data analysis conducted so far has been carefully separated into different datasets, each corresponding to a specific working point.

7.4.3 Data Taking Period

Vesuvius stands as one of the world's largest volcanoes, with its horizontal thickness at its summit measuring several meters and extending to about 4 to 5 km at its base. Figure 7.21 shows the Digital Elevation Model (DEM) of the mountain derived using the data from [327]. As the volcano's thickness increases, the likelihood of

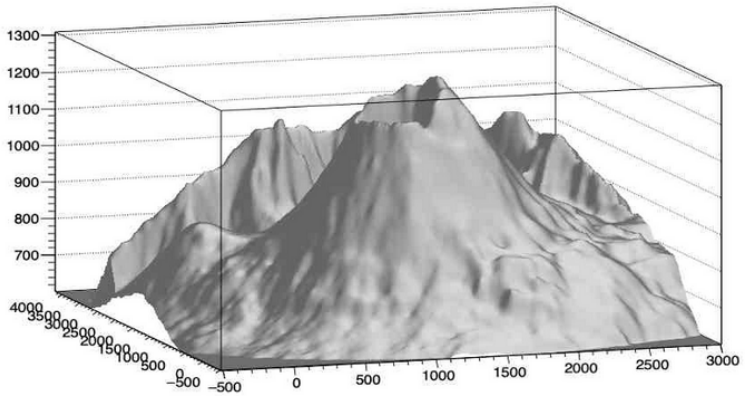

FIGURE 7.21: Digital terrain model of Vesuvius crater. Based on data from [327].

muons successfully traversing its body and reaching the MURAVES detector's acceptance area diminishes. Additionally, the detector is positioned at an inclination towards the volcano, approximately 20 degrees relative to the ground. Within this lower zenith angle, the muon flux is notably lower than in vertical directions. These combined effects necessitate an extended data collection period to acquire the statistics necessary for achieving the desired spatial and density resolutions. The rock thickness map of Vesuvius that needs to be traversed by muon evaluated using the DEM is shown in Fig. 7.22 [320]. As the mountain's thickness differs at various ele-

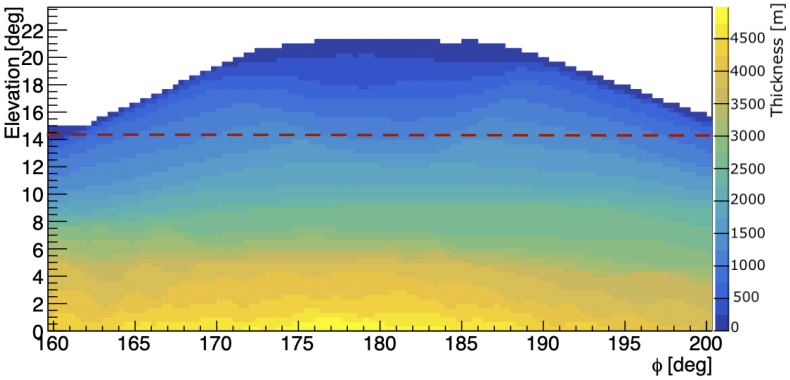

FIGURE 7.22: The rock thickness map of Vesuvius as a function of elevation and horizontal angles. The region above the horizontal red line corresponds to the detector's acceptance range [320].

vations, specific parts of the mountain demand varying data collection durations to achieve the same density resolution. To precisely understand this data-taking timeframe, the MURAVES team at the University of Naples Federico II in Naples, Italy, conducted an in-depth study, and the significant findings of this study are summarised in the following paragraph [323].

The minimum data-taking time period is estimated for different thicknesses and spatial resolution values considering the density is uniform $\rho = 2.65\ g\ cm^{-3}$ and the density resolution achievable is 10% (obtained from Lesparre et al. in [328]). With the spatial resolution and thickness held constant, the variation in the density measurement of 10%, $\delta\rho$ =0.1ρ, arises from the variation in the observed number of muons. This variation, $\Delta N(\rho, \delta\rho)$, is defined as the difference between the counts at densities $\rho + \delta\rho$ and ρ:

$$\Delta N(\rho, \delta\rho) = N(\rho + \delta\rho) - N(\rho) \tag{7.2}$$

The muon count, $N(\rho)$, is directly related to the acquisition time (T_{acq}):

$$N(\rho) = \Phi(\rho)\Delta T_{acq} \tag{7.3}$$

Here, $\Phi(\rho)$ represents the muon flux measured for density ρ.

To achieve the desired density resolution, ΔN must exceed the uncertainty in the muon count ($\sqrt{N}$):

$$\Delta N > \delta N = \sqrt{N} \tag{7.4}$$

Consequently, the minimum time (T_{acq}^{min}) required to achieve the specified resolution is determined by:

$$T_{acq}^{min}(\rho, \delta\rho) = \frac{\sqrt{N}}{\Phi(\rho, \delta\rho)} \tag{7.5}$$

Figure 7.23 shows the minimum time period of data collection necessary to achieve the desired density resolution for different spatial resolutions (Δx) as a function of the mean thickness of the mountain. The time periods shown are calculated considering the total sensitive area of the telescope (3 m^2). The effects in muon flux measurements due to detector inefficiencies are not taken into account. The results indicate that using the current detection system, it would take over 2 years to achieve

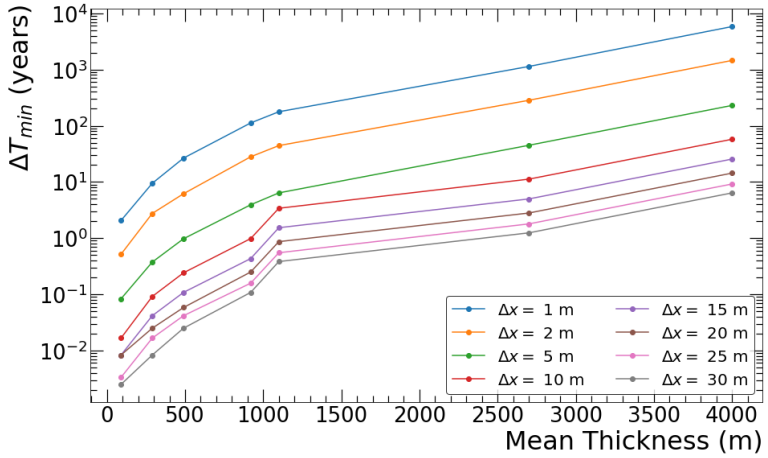

FIGURE 7.23: Minimum data-taking period required to attain the targeted density resolution (10%) for varying spatial resolutions (Δx). The calculations consider the total sensitive area of the telescope (3 m^2), while potential effects of detector inefficiencies on muon flux measurements are not taken into account. The figure is generated using the data taken from [323].

a spatial resolution of 1 m and a density resolution of 10% for thickness around 100 m, corresponding to the volcano's summital part at elevations greater than 20 degrees. For measurements on the lower slopes with a thickness of about 4000 m, a minimum of 7 years would be needed to achieve a spatial resolution of 30 m. Given these outcomes, the experiment is currently focusing solely on the mountain's summital region.

7.5 Data Analysis

To perform the density measurements, the raw data collected needs to undergo several stages of data processing. Initially, raw data collected in hexadecimal format is converted into more user-friendly decimal form, including key details like board number, ADC values, time stamps, and temperatures for each of the 40000 trigger events in a run.

Next, data quality is assured by checking trigger rates, ADC count distributions, and related factors. Qualified data is then reconstructed, converting detector hits into clusters. Tracking is performed, and optimal tracks are selected based on a chi-square threshold. All major processes involved in the data analysis are detailed in this section.

7.5.1 SiPM Response and Photoelectron Counting

When a muon interacts with a scintillator material, the number of emitted photons is proportional to the energy deposited by the muon. The emitted scintillation photons are detected by the SiPM. Each photon that strikes the SiPM can trigger the release of a photoelectron. The number of released photoelectrons is proportional to the number of detected photons, which, in turn, is proportional to the energy deposited by the muon in the scintillator.

In the MURAVES apparatus, the SiPMs are read out and their signals are digitised using ADCs. The energy of the interaction, measured in terms of the number of photoelectrons produced, can be inferred from the collected ADC data. However, the ADC spectrum, representing the range of ADC counts corresponding to different signal strengths, exhibits varying behaviors across different SiPMs. Factors such as detection efficiency, crosstalk, and after-pulses contribute to these variations. Moreover, real-time factors like atmospheric conditions and operational variations can introduce fluctuations in the SiPM response, impacting the ADC data. To counteract these influences and refine the collected data, a control run consisting of 50,000 events is executed using a random trigger mode before each data acquisition run.

Within the ADC spectrum, the highest peak (H_{peak}) corresponds to the baseline signal level when the SiPM is not exposed to incident photons, often referred to as the 'pedestal' and adjacent peaks (P_{peak}) to the right of this pedestal signify specific numbers of photoelectrons. These peaks will be at integer multiples of the average pulse height corresponding to 1 photoelectron (1 *phe*). This 1 *phe* represents the ADC counts corresponding to one photoelectron. Figure 7.24 illustrates an example of an ADC spectrum derived from a channel in a control run dataset. In this plot, the key parameters, namely H_{peak}, P_{peak}, and 1 *phe*, are marked for reference. By

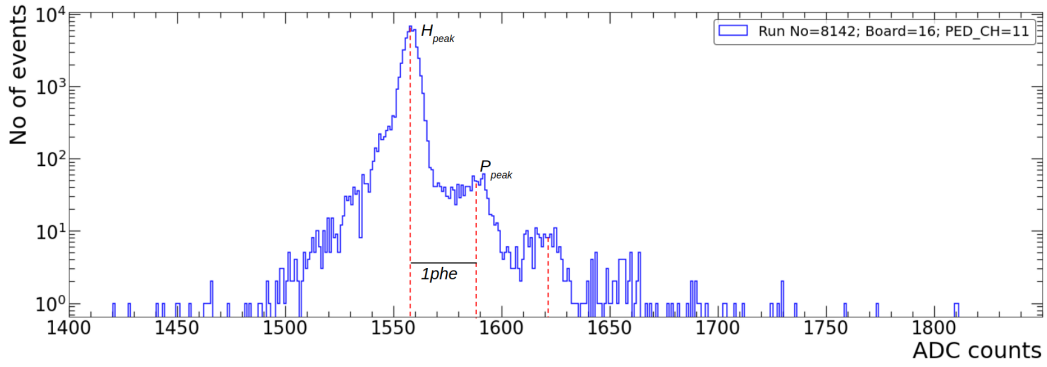

FIGURE 7.24: ADC spectrum obtained from a specific channel in a control run dataset. The primary characteristics of the spectrum, including the baseline signal level (H_{peak}), the adjacent photoelectron peaks (P_{peak}), and the value corresponding to 1 photoelectron (1 *phe*), are highlighted.

calculating the difference between the P_{peak} and H_{peak} values and then dividing the result by the 1 *phe* value, the corresponding count of photoelectrons for each peak can be estimated. This calculation is summarised by Eqn. 7.6. More details can be found in [328].

$$N_{phe} = \frac{P_{peak} - H_{peak}}{1phe}^{3} \tag{7.6}$$

Due to the potential variations observed in SiPM response, the control runs are regularly conducted before each data acquisition run. Parameters such as pedestal and 1 *phe* values are determined on a per-channel basis. These channel-specific corrections are then applied across all 1536 channels, comprising 32 boards across 3 hodoscopes.

[3]Calibration tests on SiPMs have indicated a linear relationship between SiPM response and the number of photoelectrons.

The plots presented in Fig. 7.25 exhibit the ADC distributions of two distinct channels across various runs conducted between September 2020 and July 2022. The upper plot (channel 3) illustrates an SiPM with consistent behavior over time. In contrast, the lower plot exemplifies an SiPM with variations in its ADC spectrum observed during the same period.

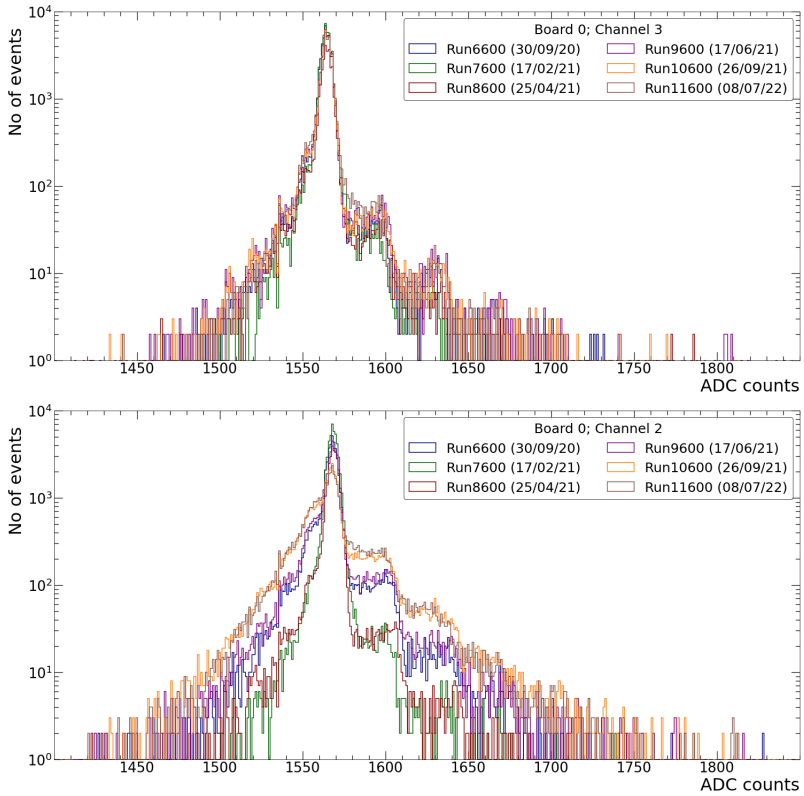

FIGURE 7.25: ADC distributions of two distinct channels for various runs conducted between September 2020 and July 2022. The top plot showcases the stable behavior of an SiPM over this time frame, while the bottom plot provides an example of an SiPM exhibiting fluctuations in its ADC spectrum throughout the same period.

Figure 7.26 presents the ADC spectra for a selection of 16 random channels from a single board. Among the displayed channels, channel 11 and channel 22 exhibits malfunctions.

7.5.2 Clustering and Tracking

The accuracy of mountain imaging depends on the precise reconstruction of muon tracks. Starting from the collected raw data, the scintillator bars impacted by muons are identified, and their associated energies (measured in terms of the number of photoelectrons) are determined. This information is then utilised in an energy-weighted approach to calculate the muon cluster position and their corresponding cluster energies. Through this method, a thorough understanding of the exact muon hit positions and the total energy deposited by specific events in the detection plane can be attained. The subsequent section provides a detailed explanation of the clustering procedure. To evaluate the performance of the simulation chain, the tracking method applied to real data is replicated for the simulation. A comparison is made between the χ^2 values and all the cluster properties associated with the tracks of

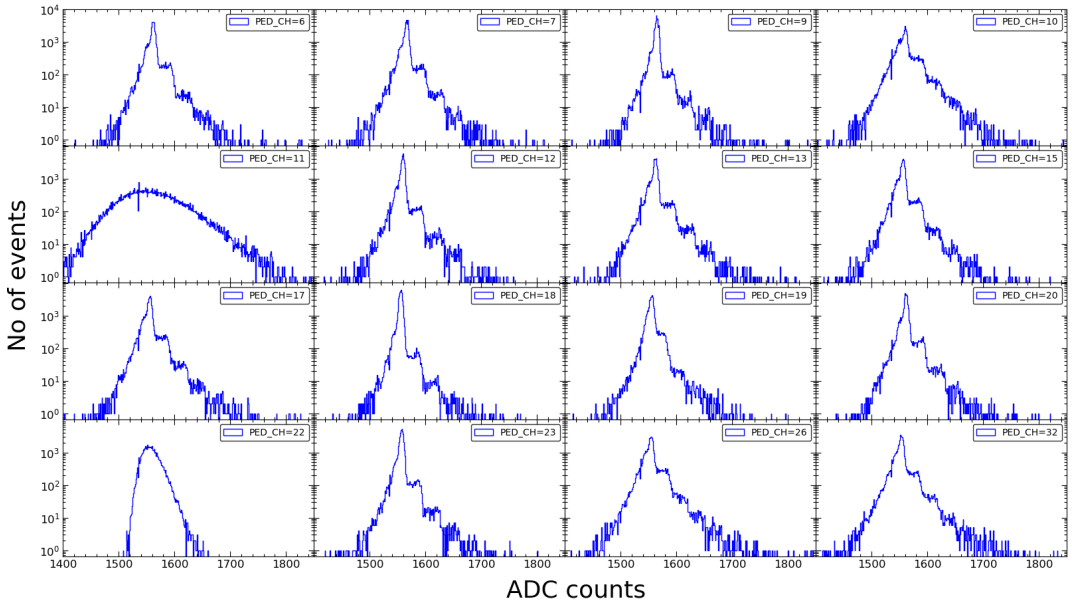

FIGURE 7.26: ADC responses of 16 randomly selected channels from one of the readout boards. Among the displayed channels, channel 11 and channel 22 exhibits malfunctions.

the simulated data and those of the real data. Similar trends are observed in both cases, but slight differences are present due to the simulation not taking into account experimental effects such as dark noise and electronics effects.

When a muon interacts with a scintillator bar, it generates a distribution of light that is collected by the SiPMs. The barycenter position, effectively the center of mass of the light distribution, provides an estimate of where the particle interaction transpired along the scintillator bar's length. Consequently, the muon hit positions in the scintillator bars correspond to their barycenter positions, with the measured photoelectron count indicating the associated energy.

Clusters consist of adjacent bars whose signals surpass a defined threshold. Figure 7.27 presents a schematic illustration of example clusters that are formed when muons traverse through the detection planes. Due to the triangular shape of the scintillator bars and their alignment side by side, the majority of clusters comprise a minimum of two bars (Refer Sec. 7.3.1). In the case of MURAVES, a bar is considered part of a cluster only if its energy exceeds 6 *phe*. Clusters can also consist of single bars, in which case, however, a higher threshold of 10 *phe* is applied. This differentiation helps eliminate signals attributed to dark counts. For clusters involving a single bar with energy exceeding 10 *phe*, the adjacent bar is included in the cluster if its energy exceeds 2 *phe*.

When a cluster encompasses multiple bars, the cluster's position is determined through their barycenter positions. This entails calculating the weighted average of the bar positions involved, where the weights correspond to the number of photoelectrons, as described by Eqn. 7.7. Furthermore, the energy associated with the cluster is straightforwardly calculated as the sum of the number of photoelectrons

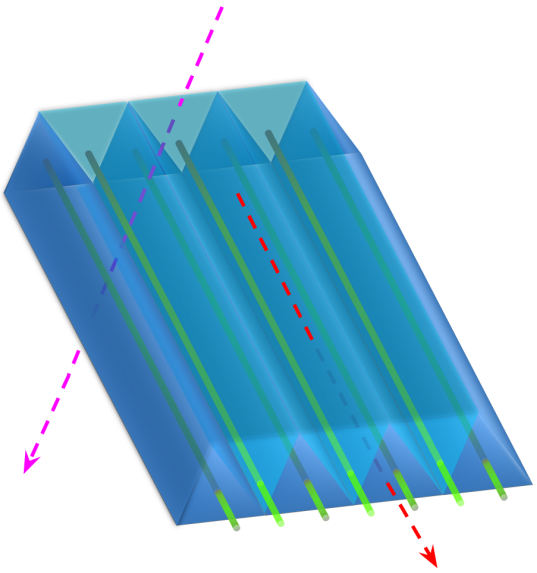

FIGURE 7.27: Schematic of muon tracks in the scintillator bars. The red track passes through two scintillator bars, resulting in a cluster size of two. In contrast, the purple track passes through three scintillator bars, leading to a cluster size of three.

of all the bars involved in the cluster.

$$X_{cluster} = \frac{\sum_{i=1}^{n} X_i E_i}{\sum_{i=1}^{n} E_i} \tag{7.7}$$

Here, X_i denotes the position of the i^{th} bar in the cluster, E_i stands for the energy of that bar and n denotes the total number of bars involved in the cluster.

To gain more detailed understanding of the energy deposits and clusters, several key properties are presented in the following part of this paragraph. Figure 7.28 displays the cluster size distribution based on a dataset of 3.79×10^6 recorded events in the ROSSO detector's y-planes, with each distribution representing data from individual y-planes. Figure 7.29 displays the distributions of strip energies (a), cluster energies (b), and cluster multiplicities (c) based on the same data of the ROSSO detector mentioned above. Each distinct color in these plots corresponds to data collected from individual y-planes, as indicated in the accompanying legends. However, it's important to note that the histograms for cluster size, strip energy, and cluster energy plots are not directly comparable. This discrepancy arises from variations in the total number of strips fired per event and the number of clusters formed per event, even though the total number of recorded events remains the same. Besides some minor fluctuations at various working points, all planes across the three hodoscopes display a similar behavior as shown in the plots.

After clustering, the tracking process begins. This tracking procedure is two-dimensional, constructing tracks separately for the y-z and x-z planes. Here are the key steps involved:

- A cluster in the y or z plane is considered for tracking only if there is at least one cluster present in the corresponding orthogonal z or y plane.

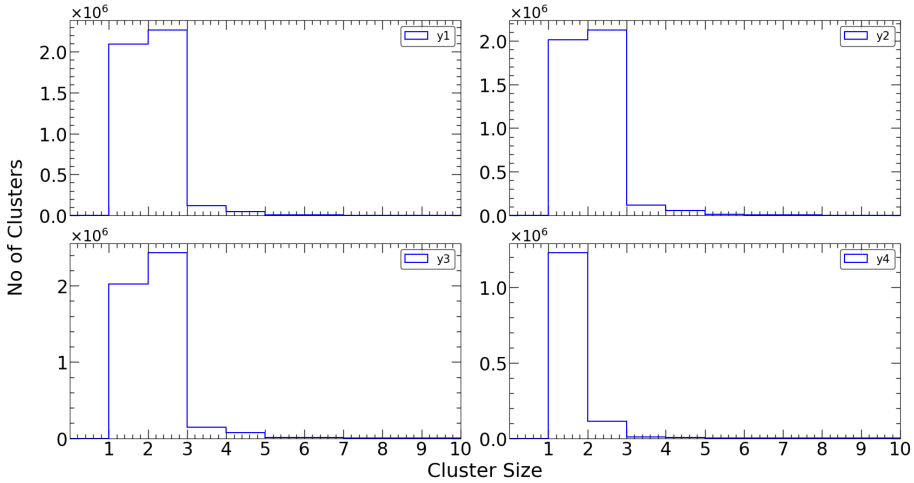

FIGURE 7.28: Cluster size distribution based on a dataset of 3.79×10^6 recorded events in the ROSSO detector's y-planes, with each distribution representing data from individual y-planes.

- All combinations of clusters in the first and third planes are considered, and a linear fit is applied.
- The coordinates in the second plane corresponding to each linear fit are estimated.
- The cluster in the second plane that is closest to the estimated coordinates, within 5 cm from the estimated location, is selected. A linear fit involving this cluster is then applied.
- Once tracks in all three planes are established, each track is extrapolated to the fourth plane. The track is considered valid only if the extrapolated coordinates fall within the sensitive area of the fourth plane.
- In the fourth plane, the cluster with the lowest scattering angle closest to the expected coordinates is chosen.
- A linear fit is performed using all the points, resulting in the final track.

It is typically observed that the majority of events yield only a single track. However, in instances where multiple tracks are present, the selection of the best track is determined based on a parameter known as the chi-square (χ^2), as described by the following equation:

$$\chi^2 = \sum_{i=1}^{n} \frac{(y_i^{data} - y_i^{pred})^2}{\sigma_y^2} \tag{7.8}$$

In this equation, y_i^{data} and y_i^{pred} represent the measured and predicted cluster positions, respectively. The term σ_y^2 in the denominator accounts for the uncertainty in the measurement of the cluster positions. The best track is determined as the one with the lowest chi-square value.

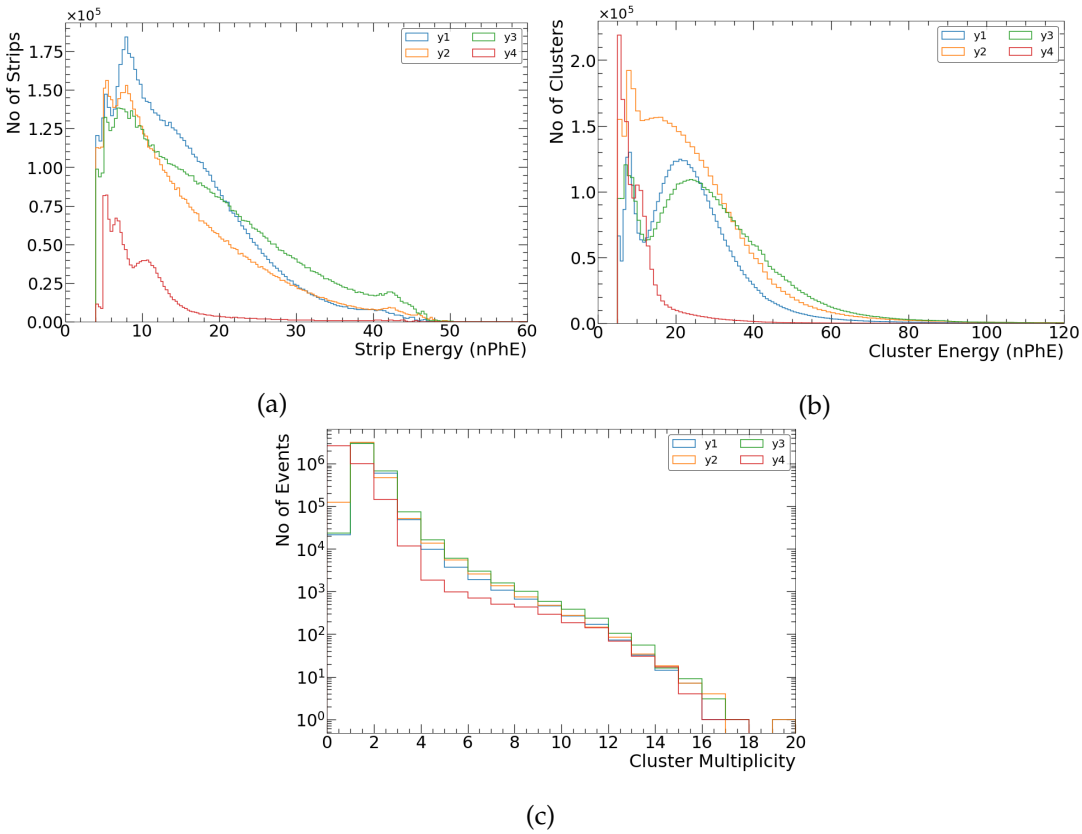

FIGURE 7.29: The figure illustrates the energy distributions of the strips (a) and clusters (b), as well as the distribution of cluster multiplicity (c) based on data obtained from 3.79×10^6 events recorded in the y-planes of the ROSSO detector. Each distinct color in the plots corresponds to data collected from individual y-planes, as indicated in the legends.

In the case of four-plane tracks, it's important to consider that particles may follow a straight trajectory in the first three planes before being deflected due to the presence of the lead wall between them. So, the chi-square value for the four-plane tracks is calculated as follows:

$$\chi^2_{4planes} = \chi^2_{3planes} \cdot |y_4^{data} - y_4^{pred}| \tag{7.9}$$

In this equation, $\chi^2_{3planes}$ corresponds to the chi-square of the three-plane track, while the second part of the equation accounts for the deviation of the measured cluster in the fourth plane.

As the chi-square parameter serves as an indicator of track quality, it is essential to establish a chi-square value threshold to qualify tracks. Data collection at MURAVES encompasses calibration data and mountain data acquired during different periods throughout the year, reflecting varying environmental conditions and changes in working parameters. Consequently, distinct chi-square thresholds are estimated for each system by dividing the data into separate sets based on hodoscopes and working points.

To determine the appropriate chi-square threshold value for each case, a specific strategy is employed. The strategy assumes that the flux measured from open sky

directions overlying the volcano must be consistent with the flux measured in calibration mode from the corresponding directions. To validate this assumption, a designated region defined by $\Delta\phi$ and $\Delta\theta$ is chosen to satisfy the following condition:

$$\frac{\phi_{\mu}^{Ves}(\Delta\phi, \Delta\theta)}{\phi_{\mu}^{Calib}(\Delta\phi, \Delta\theta)} = 1 \tag{7.10}$$

A range of chi-square threshold values is explored for both Vesuvius and calibration data sets, and all possible combinations are examined to assess if the condition outlined in Eqn. 7.10 is met. The chi-square threshold values for Vesuvius and calibration data determined for the datasets used for the density evlaution is detailed in Sec. 7.7 where the density evaluation procedure and results are discussed.

7.6 Simulation Studies

Comparison of experimental data with MC simulations is crucial for the imaging of a target. A popular approach is to compare various density hypotheses with the observed transmission map to identify the one that best fits the data. In other research scenarios, the focus is on detecting anomalies in relation to the expected map. However, it's crucial to acknowledge that various factors can introduce biases into these expectations. Consequently, it becomes imperative to assess the impact of these factors by testing a range of modeling assumptions in MC simulations.

The simulation chain starts from the generation of muons with realistic angular and momentum distributions. This can be accomplished through diverse methods, spanning from simulations that replicate the entire cosmic shower in the atmosphere, encompassing background particles like electrons, positrons, and hadrons (e.g., CORSIKA [189]), to parameterisations based on existing empirical data.

When dealing with the cosmic cascade at the receiving end, it is essential to simulate both the geometry and the response function of the detector. The extent of this simulation can vary depending on the specific circumstances. In muography, for instance, relatively straightforward parametrisations of the detector's efficiency are commonly utilised. However, as MURAVES data collection progresses and high statistical precision becomes a realistic expectation over the years, it becomes essential to perform more comprehensive simulations of the detector's response

In between the source and the detector, the most crucial simulation step is the particle propagation through the target material, where absorption and scattering effects need to be accurately modeled. General-purpose tools like Geant4 or FLUKA provide accurate models of the muon interaction with the traversed material, but take a very long computation time at each simulation step. To mitigate this, ongoing research is exploring parametric or semi-parametric simulations that aim to reduce CPU time while maintaining reasonable accuracy (e.g., [190, 329]).

In this section, the development of a MC simulation setup, following the steps outlined in Fig. 7.30 is detailed. The major focus of this section (marked with "✓" in Fig. 7.30) lies in the cosmic muon generation, the Geant4-based detector simulation and a series of simulation studies that are conducted to investigate the effects of the experimental constraints and to perform comparisons with the actual observations.

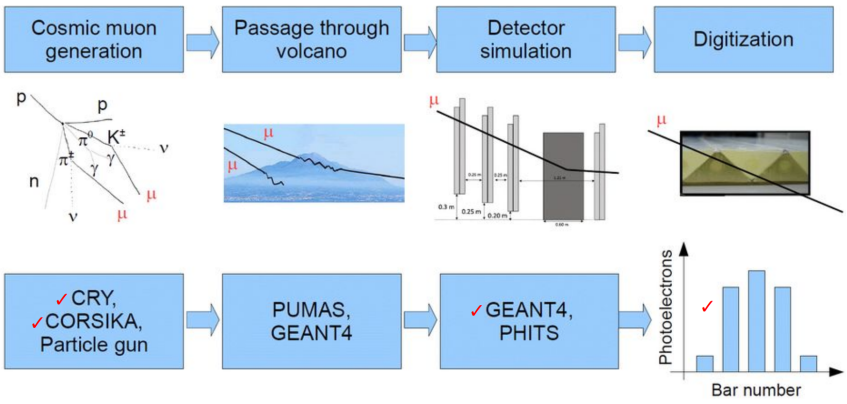

FIGURE 7.30: A schematic representation of the MURAVES simulation chain [4]. The points marked with "✓" highlights the topics discussed in this thesis.

7.6.1 Particle Generation

In this stage of the simulation process, muons and background particles, including electrons, positrons, and hadrons, are generated using a realistic model. A comparative analysis of two distinct MC tools (CRY and CORSIKA), each characterised by unique philosophies and complementary advantages, was conducted.

CRY functions as a parametric single-particle simulator, while CORSIKA undertakes a comprehensive, step-by-step modeling of cosmic showers. Notably, a significant difference in computational speed is observed. It was determined that, for the generation of 10^5 muons, CRY requires approximately 1.4 minutes, whereas CORSIKA necessitates around 9 hours on a standard CPU (tested with Intel Core^{TM} i7-9750H CPU @ 2.60 GHz per core) for the same task. Consequently, these tools are suited for distinct applications, with CRY being preferred for scenarios where speed takes precedence over precision, while CORSIKA excels when precision is of greater importance. The two simulations complement each other in the possibility to address various systematic effects. CRY's parametrisation, based on the MCNPX simulation [330], takes into account geomagnetic effects on the cosmic flux, depending on time (solar cycle), latitude and altitude. On the other hand, in CORSIKA the user can choose across various low-energy and high-energy hadronic interaction models.

Hadronic interactions in CORSIKA are simulated using different models depending on the energy range. For the simulation of high-energy hadron-nucleus and nucleus-nucleus collisions, four models that are DPMJET, QGSJET, EPOS and VENUS were considered and compared. For lower energy ranges, two available models are GHEISHA and ISOBAR. The model ISOBAR enables fast calculations. However, GHEISHA was preferred because its routines implemented in CORSIKA are adapted from the widely used detector simulation code GEANT3 [331], making it a more widely accepted and validated choice within the field. Furthermore, the high-energy models, namely DPMJET, QGSJET, and VENUS, require (and automatically force) the use of the GHEISHA routine. This necessity arises because the baryons with strangeness ± 2 and ± 3 generated by models cannot be treated with the ISOBAR model [189].

To conduct the comparative studies, 100 showers were generated for each of the high-energy models employed in CORSIKA, as mentioned in the preceding paragraph. The low-energy interaction model was set to GHEISHA across all cases. The primary particle was set to proton of energy 10^5 GeV. The zenith angle was systematically varied from 0°to 70°, and the azimuthal angle covered the full range from -180°to 180°. Additionally, the elevation level was set to match that of the MURAVES laboratory, which stands at an altitude of 600 meters above sea level. For each simulation of 100 showers, it took 10 hours CPU time. The resulting energy distributions of muons, generated from the 100 showers for each high-energy model, are illustrated in Fig. 7.31 (top subplot), with each model distinctly labeled in the legend. Each distribution encompasses approximately 2.2×10^3 muons. From the comparison plot, it becomes evident that the muon energy spectra produced by the considered models exhibit a similar trend. For a better understanding all models are compared with each other by plotting the difference of distributions in Fig. 7.31 (bottom subplot). The muon charge ratio for each model was evaluated, and the

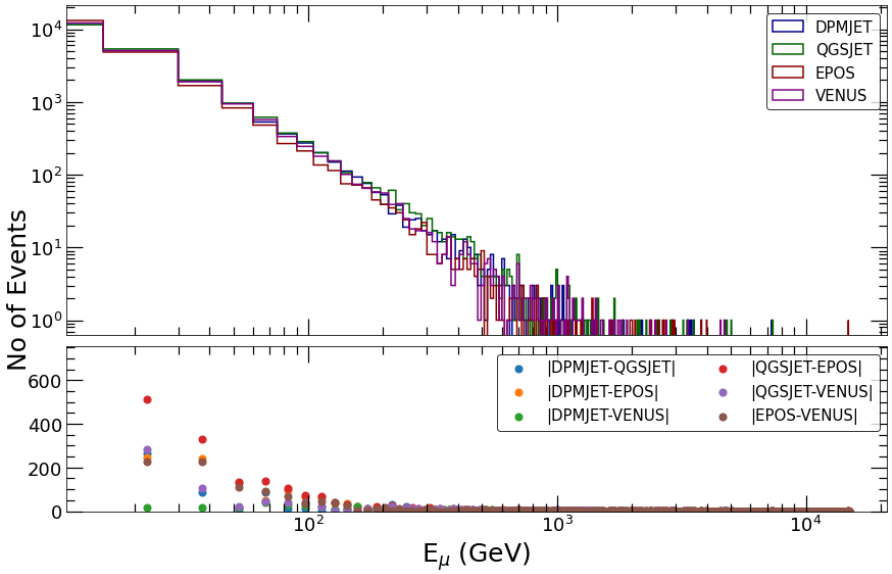

FIGURE 7.31: Top subplot: energy distribution of muons generated from 100 showers for each high-energy model in CORSIKA, with the low-energy model consistently set to GHEISHA. The primary particles are protons with an energy of 10^5 GeV. Zenith angles varied from 0°to 70°, azimuthal angles covered the full range (-180°to 180°), and the simulations were conducted at an elevation level matching that of the MURAVES laboratory (600 m). Each distribution represents approximately 2.2×10^3 muons. Bottom subplot: Comparison of all models with each other by plotting the difference of the respective distributions.

results, along with the calculated statistical uncertainties, are presented in Fig. 7.32. For the generation of these plots, the data for μ^+ and μ^- were divided into 20 bins, and the charge ratio represents the ratio of the number of μ^+ to μ^- in each bin, with each bin having a width of 100 GeV. The data points beyond 500 GeV are not shown in the plots due to low statistics in these bins (refer Fig. 7.31). The analysis reveals that the charge ratio, calculated for each model across different energy ranges, consistently falls within the same range. When compared to measurements obtained from various experiments, it's evident that the atmospheric muon charge ratios for energies below 500 GeV typically range from 1 to 1.4 [332, 333]. The results obtained from all models in this study align with this range, with some points falling between 0.6 and 1.

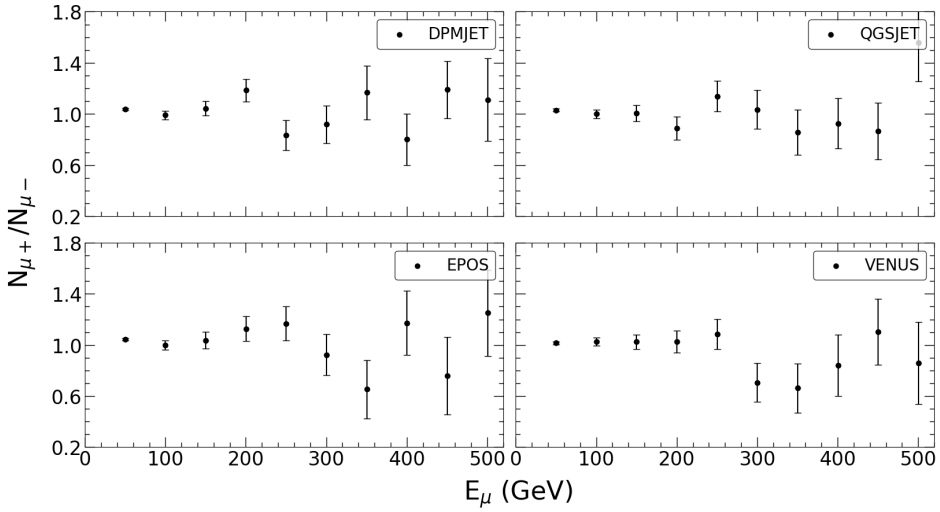

FIGURE 7.32: The plot shows the muon charge ratio, calculated as the ratio of μ^+ to μ^-, categorized into 20 energy bins, each with a width of 100 GeV. Data points beyond 500 GeV are omitted due to low statistics in those bins. The results displayed for various energy ranges and models aligns with the typical atmospheric muon charge ratio range of 1 to 1.4 (reported by previous experiments [332, 333]) with some points falling between 0.6 and 1.

The comparison between muon fluxes generated using CORSIKA and CRY was also conducted. Figure 7.33 displays the particle flux as a function of energy generated using CRY and the three distinct high-energy hadronic interaction models of CORSIKA. The plot reveals that across the energy spectrum (1 MeV to 10^7 MeV) shown, all models exhibit qualitatively similar shapes and peak positions. For MU-

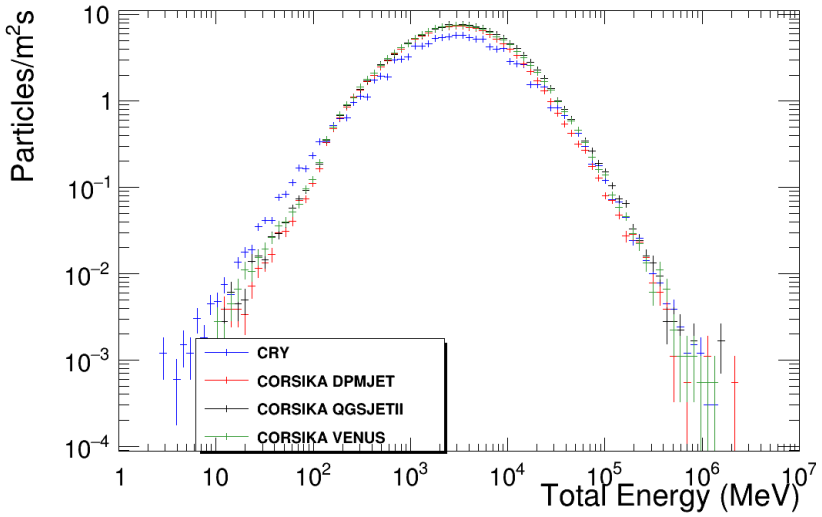

FIGURE 7.33: Comparison of muon fluxes generated using CRY and three different high-energy hadronic interaction models in CORSIKA.

RAVES simulations, the decision was made to primarily utilise CRY as the event generator while retaining CORSIKA for assessing systematic uncertainties associated with physics modeling. The choice of CRY as the default generator was primarily motivated by its speed and its ease of integration with Geant4, in the detector simulation described in Sec. 7.6.3. CRY is linked to Geant4 directly in a way that the particle generation and detector simulation can be performed in a single step and linking

process is quite straightforward. In contrast, integrating CORSIKA with Geant4 is significantly more complex. The algorithm to interface CORSIKA to Geant4 is also developed and tested to use when it is required. The interface is implemented using the G4HEPEvtInterface class available in Geant4. Most event generators, including CORSIKA, are traditionally written in FORTRAN. However, Geant4 does not allow direct linkage with FORTRAN programs or libraries due to potential limitations regarding the utilisation of object-oriented C++ features. Instead, Geant4 provides an ASCII file-based interface for communication with such event generators. The G4HEPEvtInterface reads an ASCII file generated by an event generator, typically following the HEPEVT format [334]. HEPEVT is a standardised format widely employed by various event generators written in FORTRAN. CORSIKA's default output particle data file is in binary format (though root file format is also possible with CORSIKA installed in express mode). CORSIKA offers FORTRAN routines to convert binary files into the required ASCII format. The G4HEPEvtInterface takes the provided ASCII file and translates the information stored in the HEPEVT common block into an object-oriented data structure compatible with Geant4. Additionally, it necessitates the specification of the interaction point's coordinates, as event generators do not inherently provide this information to Geant4. Given the extended computation time required by CORSIKA and the desire to maximise the reuse of its generated events (while modifying other parameters down the simulation chain), the simulation is executed in two distinct steps. Initially, the generated events are saved in ASCII files and then these files serve as input for Geant4 in the subsequent step. While CRY can simulate multiple muons within a single event, CORSIKA is anticipated to offer a more realistic representation of multi-muon events, a scenario not uncommon for large-area detectors like those used in MURAVES. Generating simulated events with multiple muons will also facilitate the development of tracking algorithms capable of handling such situations. Currently, in real-data analysis, two-muon events are either excluded or a single-muon ansatz is imposed in the reconstruction.

There are plans to explore and investigate additional event generators in the future. For instance, a newly developed parametric generator called EcoMug [335] has been introduced. EcoMug prioritises computational efficiency and offers the flexibility to generate muons from various types of surfaces, in contrast to CRY and CORSIKA, which are limited to flat surfaces. While these are appealing features, EcoMug does not simulate background particles differently from both CRY and CORSIKA.

7.6.2 Muon Transport Through Vesuvius

The probability of muons penetrating an object relies on the object's opacity (χ), which quantifies the density integrated over the muon path, and the initial energy of the muons. To deduce information about the target's density, one can measure the transmitted flux of atmospheric muons passing through it from various directions. This measurement offers a two-dimensional projection of the target's structure from the detector's perspective. By utilising the equation $\chi = x\rho$, where x represents the muon path length or material thickness, the average density (ρ) of the target can be determined based on the known opacity. The Vesuvius crater's thickness distribution is assessed using its DTM discussed in Sec. 7.4.3 and illustrated in Fig. 7.21.

The simulation of the expected muon flux through Vesuvius is carried out using PUMAS [321], a muon transport library based on a Backward Monte Carlo (BMC) technique, which is integrated with TURTLE [336] for the navigation of the DTM. Figure 7.34 shows the expected muon flux per year, considering the geometrical acceptance of the detector achieved using PUMAS. The BMC technique involves run-

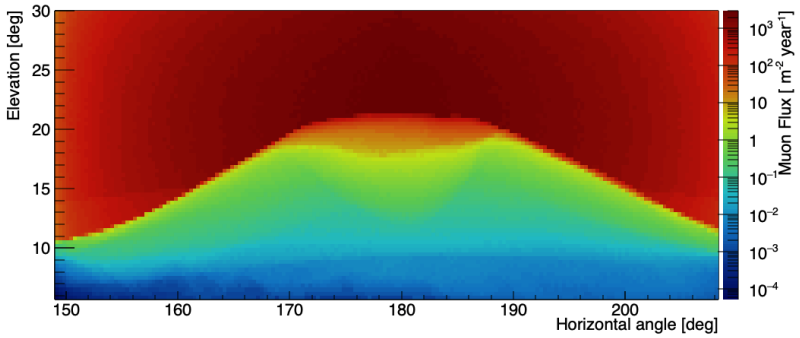

FIGURE 7.34: Expected muon flux per year considering the geometrical acceptance of the detector simulated using PUMAS [4].

ning the MC simulation backward, from the detector to the sky. It addresses the same problem as the forward case and generates the final observable states, significantly reducing computation time. In this study, PUMAS considers muon scattering as they pass through the mountain, simulating the muon flux based on material thickness and average density. In regions near the mountain, a substantial number of low-energy muons are expected to experience multiple scattering near the surface and deflect into the hodoscope's acceptance at spurious angles. Accounting for these background effects, the PUMAS simulation assists in selecting the optimal observation point for the MURAVES detector. Due to PUMAS's substantially higher computational efficiency compared to forward MC programs, it was chosen as the primary program for this simulation step, but it was also validated against a "golden standard."

To validate PUMAS, a comparative study of muon energy loss and scattering in rock using both PUMAS and Geant4 was conducted. The simulations covered muons in the energy range from 0 GeV to 100 GeV, with a fixed muon path length of 50 m in standard rock. Figure 7.35 illustrates the distribution of energy loss (left) and scattering angle (right), evaluated using PUMAS (red line) and Geant4 (blue line), showing nearly identical results between both methods.

7.6.3 Detector Response

Geant4 stands as the preeminent MC particle transport simulation tool, with extensive applications spanning particle and nuclear physics, medical sciences, and space exploration. In the context of MURAVES simulation research, a detailed model of a MURAVES hodoscope was developed. As explained in the previous section, this model is interfaced with CRY as the source for all signal and background particles. For specific studies, single muons are simulated at specific energies and incident positions using the 'Particle Gun' and 'General Particle Source' classes available in Geant4.

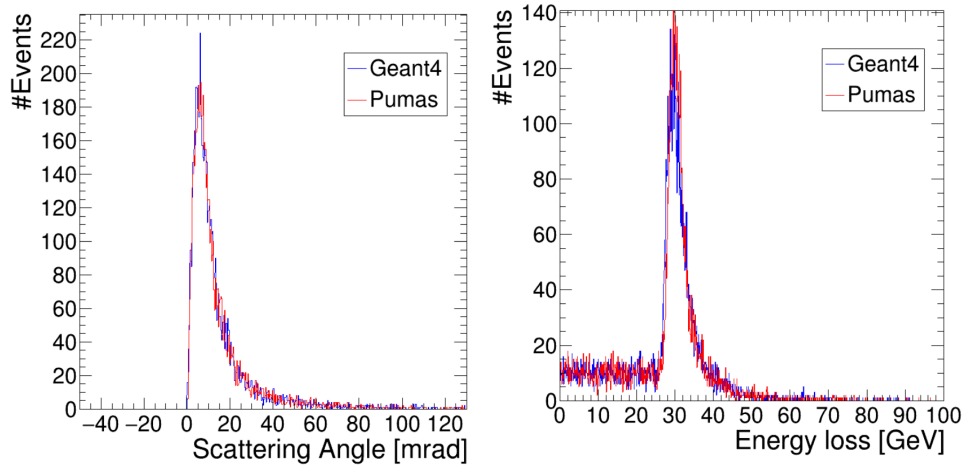

FIGURE 7.35: Comparison of energy loss (left) and scattering angle (right) distributions for muons in the energy range from 0 GeV to 100 GeV simulated using PUMAS (red line) and Geant4 (blue line) in standard rock. The results from both simulation methods exhibit close agreement [4].

The MURAVES setup consists of an array of three identical and independent tracking hodoscopes, constituted of scintillator bars coupled to SiPM, which are already installed on Vesuvius and fully operational(as detailed in Sec. 7.3). Considering that all these hodoscopes are strictly identical, the hodoscope in the simulation setup is built exactly mimicking the geometry of the hodoscopes in the real case. Within the simulated hodoscope, four tracking stations have been included, with a thick lead wall of 60 cm in thickness positioned between the 3^{rd} and 4^{th} stations, serving as a passive filter for low-momentum muons. In each station, two planes (X and Y) with 64 adjacent scintillator bars and a sensitive area of 1 m^2 are placed orthogonally to each other to extract bi-dimensional information about the muon hits. The scintillator bars have a triangular shape with a base width of 33 mm and a height of 17 mm, and they alternate between upward and downward pointing tips. These scintillator bars are constructed using Geant4 material, specifically "G4_PLASTIC_SC_VINYLTOLUENE", which has a density of 1.032 g/cm^3. The layout of the scintillator bars in all planes is situated inside aluminum boxes, each measuring 1.1 meters in width, 1.1 meters in length, and 0.1 meters in height, with a uniform thickness of 2 mm, mirroring the real setup. The entire assembly is situated within a world volume of air material, which spans dimensions of $400 \times 400 \times 400$ m of material air. In Fig. 7.36 (top), the simulation depicting the interaction of a 1 GeV muon with the MURAVES hodoscope. The alignment of the scintillator bars, stations, and other components is prominently displayed in this image. The lower part of Fig. 7.36 presents the interaction of 100 muons with energies ranging from 0 to 1 GeV. The selection of the low-energy range enhances the visibility of scattering and track deviation as the muons traverse the hodoscope, as illustrated in the figure.

A study was conducted to examine the probability of a muon reaching the 4^{th} station of the detector (after traversing the lead wall) using the Geant4 particle gun. This probability is defined as the ratio of the number of events that reached the 4^{th} station to the number of events that crossed the first 3 stations. As depicted in Fig. 7.37, it was observed that the 50% survival probability is achieved at 0.9 GeV (indicated by the dotted red line), and nearly 100% survival probability is attained at 1.2 GeV (represented by the solid green line).

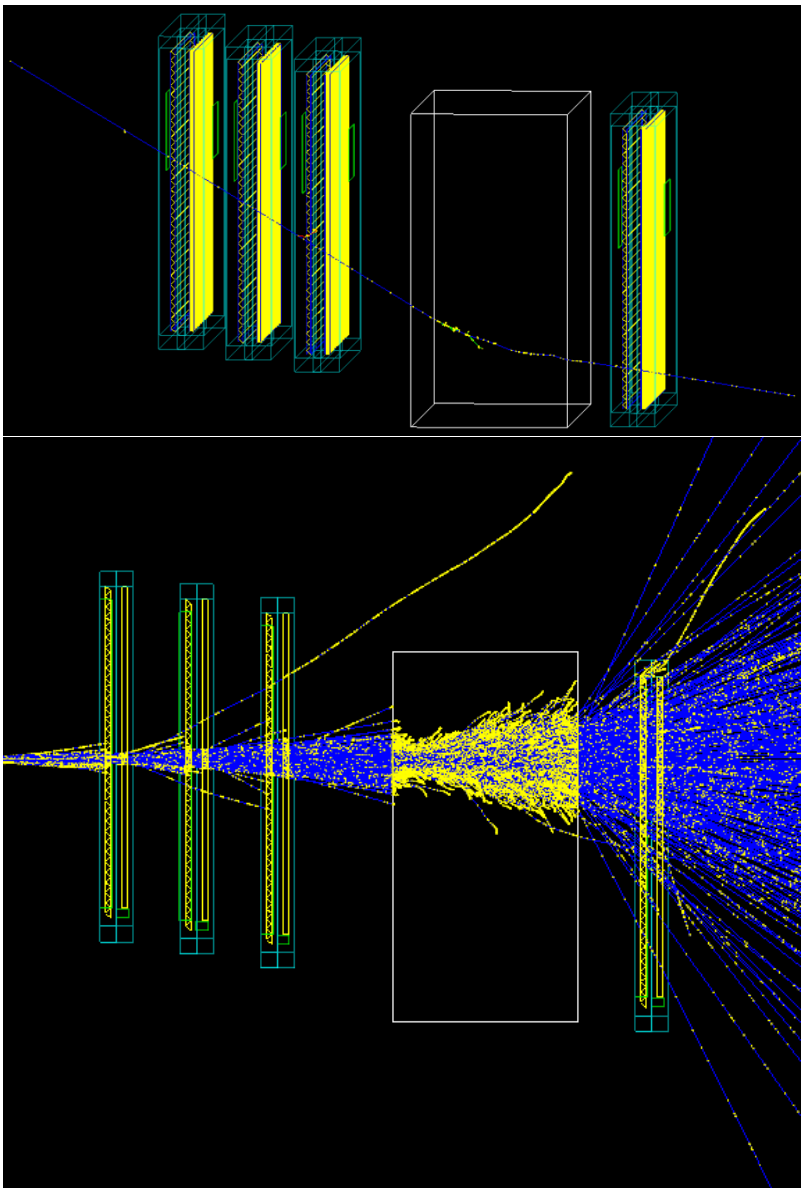

FIGURE 7.36: (Top) Simulation illustrating the interaction of a 1 GeV muon with the MURAVES hodoscope, highlighting the alignment of scintillator bars and stations [4]. (Bottom) Simulation depicting the interaction of 100 muons with energies ranging from 0 to 1 GeV, emphasizing track scattering and deviation in the low-energy range as they pass through the hodoscope.

7.6.4 Digitisation, Clustering and Tracking

The Geant4 output contains information of "hits", corresponding to each simulation step for each particle (e.g., a hit may correspond to the interaction of a charged particle that leads to the emission of a photon). These hits are characterised by their 3D position, time, energy deposition, and the particle's identity involved. Typically, when a particle traverses a detector plane in Geant4, it generates multiple hits in the scintillator bars. These hits encompass those produced by the primary particle as well as its secondaries. Figure 7.38 shows the event displays for three example events generated in the simulation. In plots (a), (b), and (c), the total number of hits are 131, 201, and 84, respectively. In these plots, muons (μ^+ or μ^-) are depicted in blue, while electrons or positrons are shown in red. For all three cases, the primary

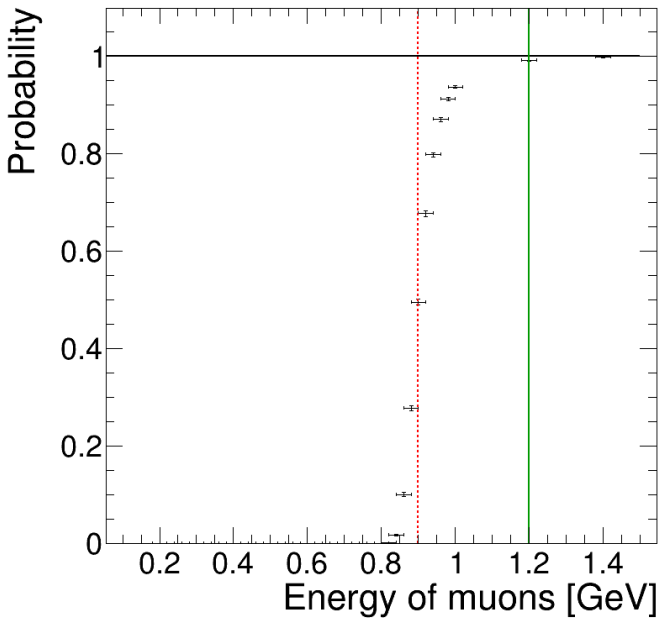

FIGURE 7.37: Survival probability of muons reaching the 4^{th} station of the detector, following their passage through the lead wall. The study, conducted using the Geant4 particle gun, demonstrates that a 50% survival probability is achieved at 0.9 *GeV* (dotted red line), while nearly 100% survival is attained at 1.2 *GeV* (solid green line) [4].

particle is a muon, and the electrons are secondary particles produced during the simulation. However, in reality, only a single signal per bar is obtained. Consequently, the output data from the simulation must undergo a series of steps to transform Geant4's raw data into a data format that is comparable to real experimental data.

The digitisation process for the GEANT4 raw hits involves quantising their positions and energy deposits. The energy deposits for a given event are summed for each scintillator bar, and the position for each bar is represented by its midpoint. This total energy deposit is then converted into the number of photoelectrons. The conversion factor is determined through a comparison between the energy deposited in the simulated data and that in real cases. The energy deposits per bar in the NERO and ROSSO hodoscopes of the MURAVES experiment were studied for each plane, and the average energy deposit per plane in both cases was found to be within the same range. This data was then compared with the energy deposits per bar in the simulated setup for all planes which was approximately 18-23 *MeV*, allowing the determination of the conversion factor. According to estimations, 10 photoelectrons are equivalent to 1.4 *MeV*, and this conversion factor is subsequently applied in the algorithm.

The clustering procedure is initiated as the next step. A cluster is a collection of adjacent bars whose signals pass a certain threshold; clusters may also be constituted of a single bar, in which case however the signal must pass a stricter threshold. When a cluster contains more than one bar, the cluster position is calculated from their barycenter, i.e. the weighted average of the positions of the bars involved, where the weights are given by the number of photoelectron (refer Eqn. 7.7). It is noteworthy

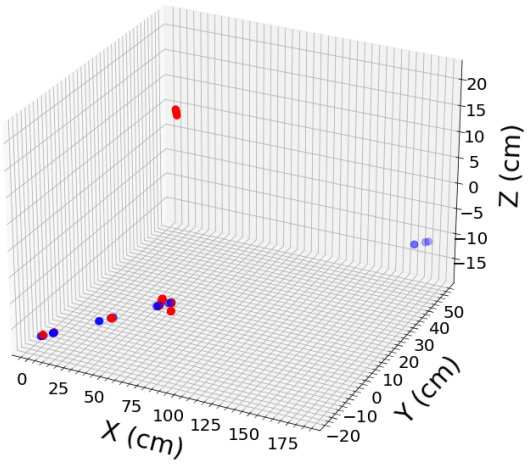

(a)μ^-=24; e^-=107

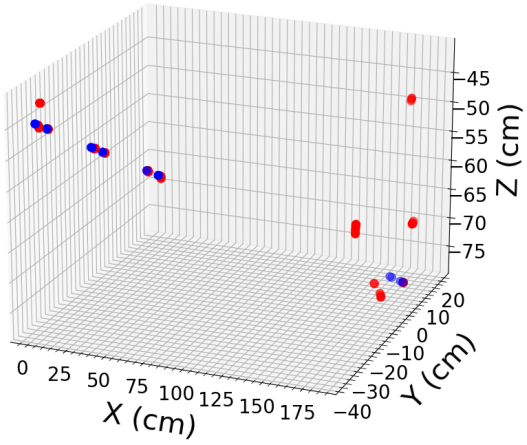

(b)μ^-=26; e^-=163; e^+=12

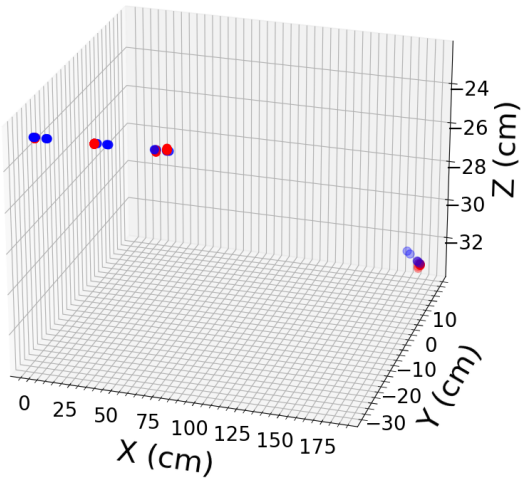

(c)μ^-=22; e^-=62

FIGURE 7.38: Event display of three example events generated in the simulation. Plots (a), (b), and (c) exhibit a total of 131, 201, and 84 hits, respectively. Muons (μ^+ or μ^-) are represented in blue, while electrons or positrons are shown in red.

that the specific thresholds in use are continuously evolving. Nevertheless, it is important to emphasise that the same algorithm and threshold criteria applied to real data are consistently employed in the MC simulations at all times. For a detailed understanding of the complete clustering procedure, including the cluster thresholds adhered to in real data, which are replicated in the simulation, see Sec. 7.5.2. Figure 7.39 illustrates the energy deposition distributions per bar (a&b) and the energy distributions of clusters (c&d) for all y and z planes. Notably, for all planes, the energy deposition per bar and the cluster energy distributions exhibit consistent patterns within their respective scenarios. In the majority of cases, the energy deposited per bar remains below 20 $nPhE$, while the cluster energy distributions typically peak at around 25 $nPhE$.

The simulated clusters are subsequently processed by the tracking algorithm, which is rigorously applied in a manner consistent with real data procedures. A detailed

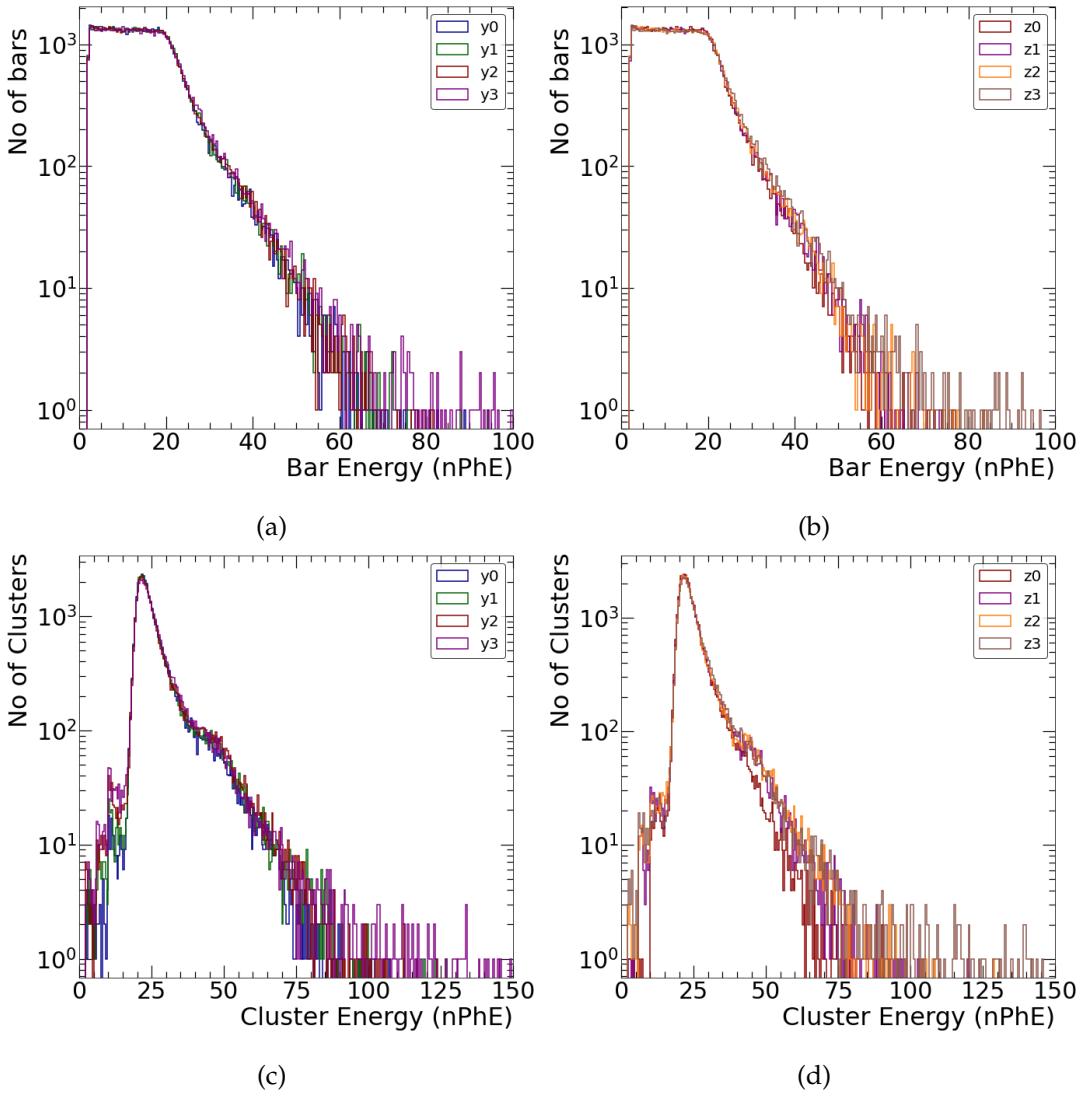

FIGURE 7.39: Distributions of energy deposited per bar (a&b) and energy of clusters (c&d) for all y and z planes. The graphs show consistent patterns in both energy deposition per bar and cluster energy distributions across all planes. Energy deposited per bar predominantly remains below 20 $nPhE$, while cluster energy distributions typically peak at around 25 $nPhE$.

description of the tracking procedure can be found in Sec. 7.5.2. Tracking is independently conducted for X planes and Y planes, with track quality assessed through the calculation of χ^2 (see Eqn. 7.8). Additional information regarding track properties and associated cluster properties is available in the following section.

7.6.5 Comparison Studies: Monte Carlo vs Real Data

To validate the detector response simulated using Geant4, a comparison with experimental data is necessary. This section discusses the major findings from the conducted comparison studies. The χ^2 values of the generated tracks, along with essential properties of the associated clusters, such as cluster size, cluster multiplicity, cluster energy, etc., were compared across all Y and Z planes within the four stations.

In order to perform the comparison, the 4-plane (tracks which crossed through all the x and y planes) tracks reconstructed from the NERO detector were considered.

Since the simulation doesn't involve tracks that traverse through the mountain for the moment, the data set corresponds to opensky data. For the simulation, approximately 1 million events were generated using CRY, among which 36,407 events were recorded as having traversed all the planes, including the lead wall. All 36407 events include clusters that adhere strictly to the reconstruction thresholds applied in the real data. In the subsequent sections where the results are elaborated, the term "best track" refers to tracks with the lowest chi-square values. It's important to note that in certain events, multiple tracks are reconstructed.

Figure 7.40 presents a comparison of cluster energies of the clusters that are part of the best track in the case of real data and simulated data for all the Y (PlaneY1-Y4) and Z (PlaneZ1-Z4) planes of the hodoscope. The red and blue distributions correspond to the real and simulated data, respectively. Each plot includes equal numbers of clusters from both datasets, with bin ratios displayed as subplots beneath the main plots. It is evident that the cluster energies in both real and simulated data fall within the same range (10-100 $nPhE$), with both distributions peaking around 30 $nPhE$. However, while the distributions are similar in range, they do not exhibit a perfect mirror symmetry. This discrepancy may arise from the absence of detector effects in the simulated data, such as dark noise, SiPM inefficiencies, variations in environmental parameters, etc.

Figure 7.41 displays a comparison of cluster sizes (number of scintillator bars involved) for clusters belonging to the best track in all Y (PlaneY1-Y4) and Z (PlaneZ1-Z4) planes. The number of clusters considered for comparison is consistent between both cases, with bin count ratios shown in subplots. In all cases, the majority of clusters have a size of 2 due to the triangular shape of the scintillator bars. However, in real data, the maximum cluster size for all planes is higher than in the simulated data. This suggests that, in reality, some events involve more scintillator bars than seen in the simulation, particularly in the last planes. This effect may be due to real-time factors unique to experimental data.

Figure 7.42 presents a comparison of cluster multiplicity, i.e., the number of clusters per event in each plane (PlaneY1-Y4 and PlaneZ1-Z4), for real and simulated data. The number of events in both distributions for each plot is consistent, and bin-by-bin ratios are displayed in subplots. In all cases, the maximum number of clusters per event per plane is 4 or 5 in simulated data, compared to 10 or 12 in real data. The additional clusters observed in real data could be attributed to scintillator bars that are not part of the event, possibly caused by noisy channels that consistently produce signals above the threshold. Implementing cluster multiplicity cuts is essential for improving data quality, as demonstrated by this comparison study.

The chi-square values for 4-plane tracks reconstructed in real data were compared with those in the simulated dataset, as illustrated in Fig. 7.43. The plots correspond to the comparison in the case of Y (χ^2-Yplane) and Z (χ^2-Zplane) plane tracks respectively. To facilitate this comparison, all best-fit tracks with chi-square values less than 15 were selected. Both plots display an equal number of events for real and simulated data. The results reveal that, in comparison to real data, the simulated dataset contains tracks with lower chi-square values. In the simulated data, the majority of tracks exhibit chi-square values below 4, while in real data, the chi-square

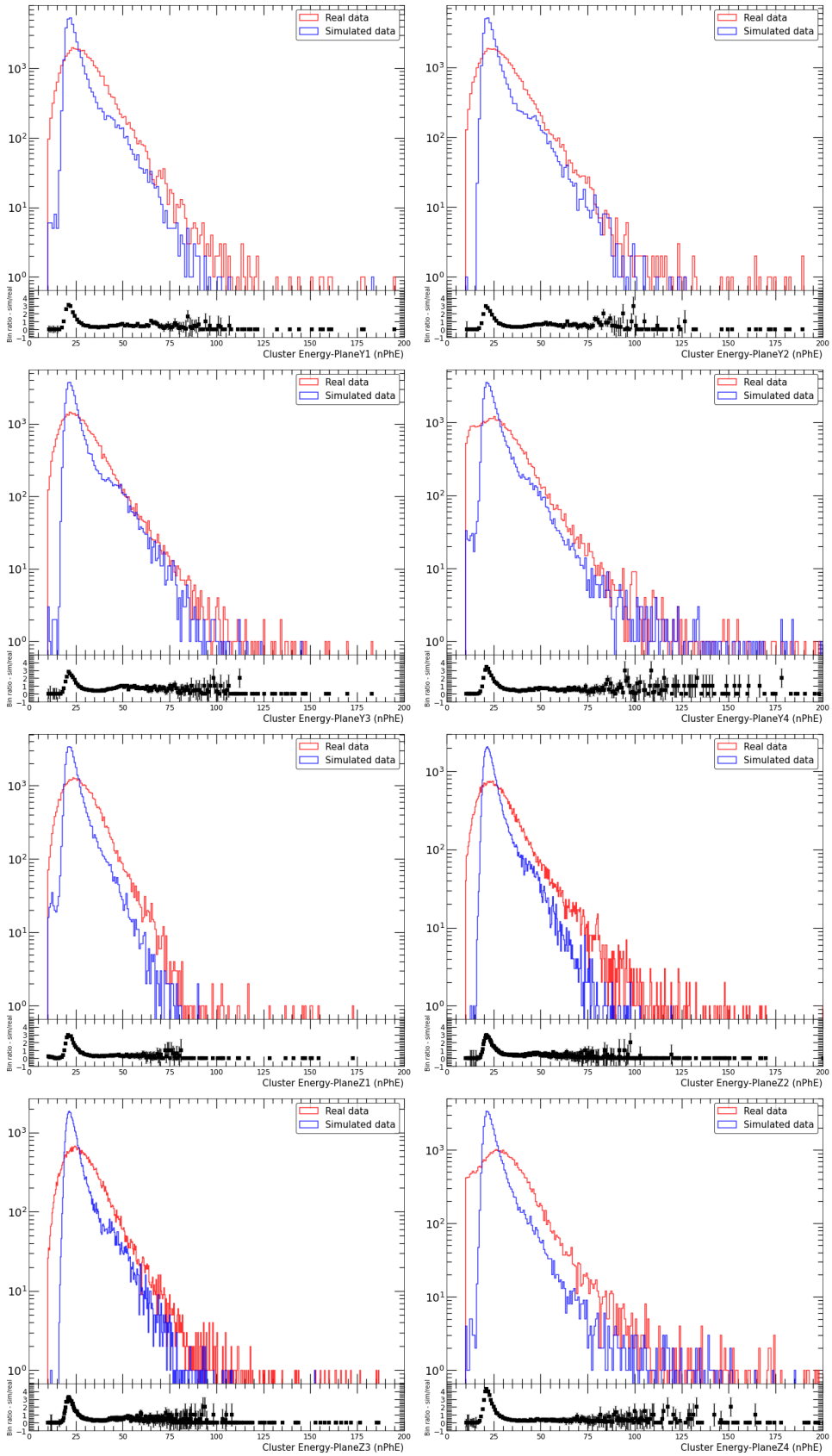

FIGURE 7.40: Comparison of cluster energies (measured in nPhE) between real (red) and simulated (blue) data for all Y (PlaneY1-Y4) and Z (PlaneZ1-Z4) planes in the hodoscope. Each plot includes an equal number of clusters from both datasets, with bin ratios displayed below. Both distributions peak around 30 *nPhE*, although some differences are observed, likely due to the absence of detector effects in the simulated data.

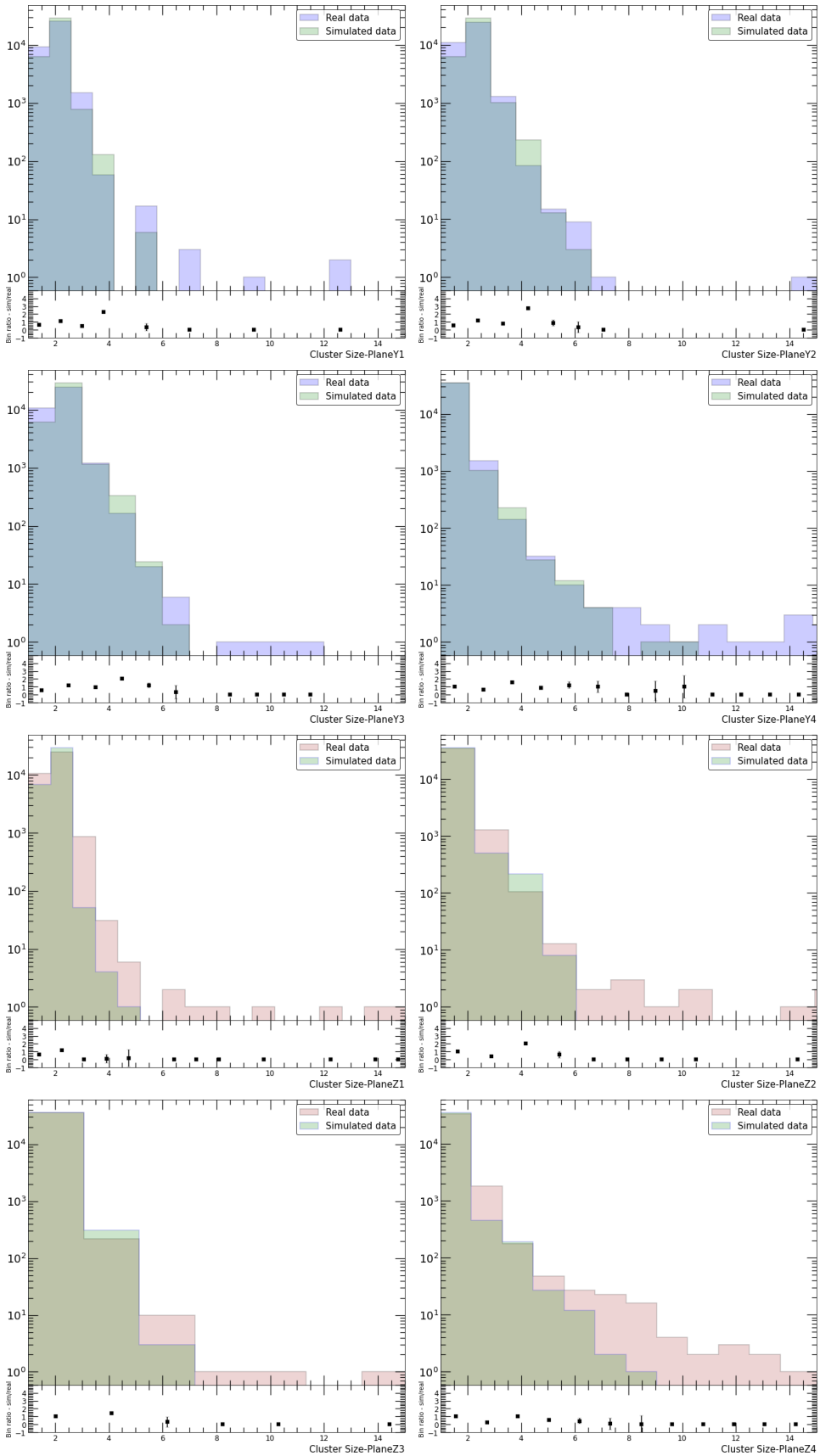

FIGURE 7.41: Comparison of cluster sizes (number of scintillator bars involved) for clusters belonging to the best track in all Y (PlaneY1-Y4) and Z (PlaneZ1-Z4) planes. Each plot includes an equal number of clusters from both real and simulated datasets. Bin count ratios are displayed in subplots. In all cases, the majority of clusters exhibit a size of 2 due to the triangular shape of the scintillator bars. However, real data consistently shows a higher maximum cluster size for all planes compared to the simulated data. This may result from real-time factors unique to experimental data.

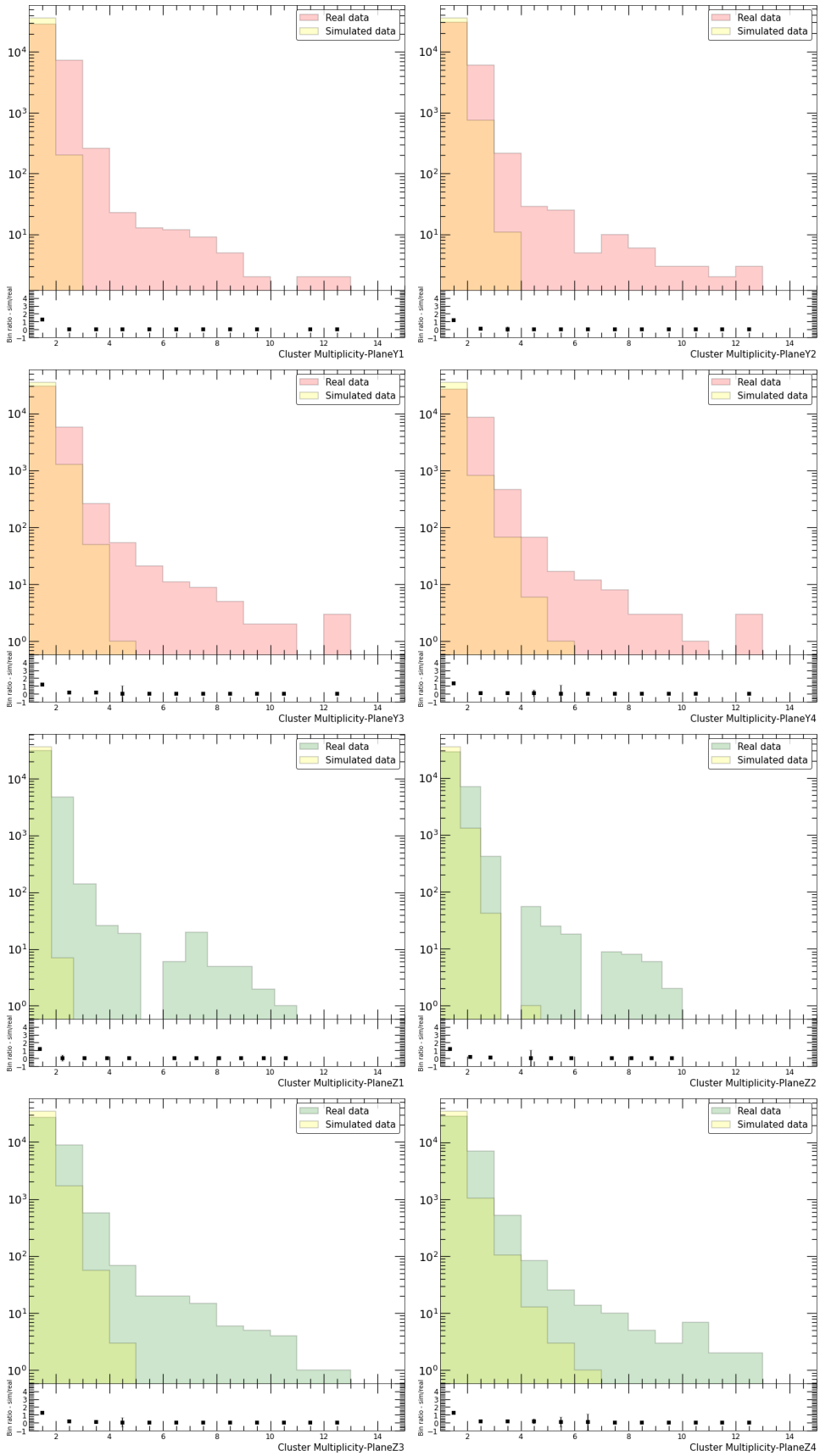

FIGURE 7.42: Comparison of cluster multiplicity between real and simulated data for all Y (PlaneY1-Y4) and Z (PlaneZ1-Z4) planes. Each plot presents an equal number of events from both datasets, with bin-by-bin ratios shown in subplots. In all cases, the maximum cluster multiplicity per event per plane is 4 or 5 in simulated data, whereas real data exhibits higher values, ranging from 10 to 12 clusters. The additional clusters observed in real data may be attributed to scintillator bars not associated with the event, possibly due to noisy channels consistently producing signals above the threshold. This comparison highlights the importance of implementing cluster multiplicity cuts to enhance data quality.

values for most tracks extend up to 8. In both cases, tracks with chi-square values greater than 8 but less than 15 are present in almost similar quantities.

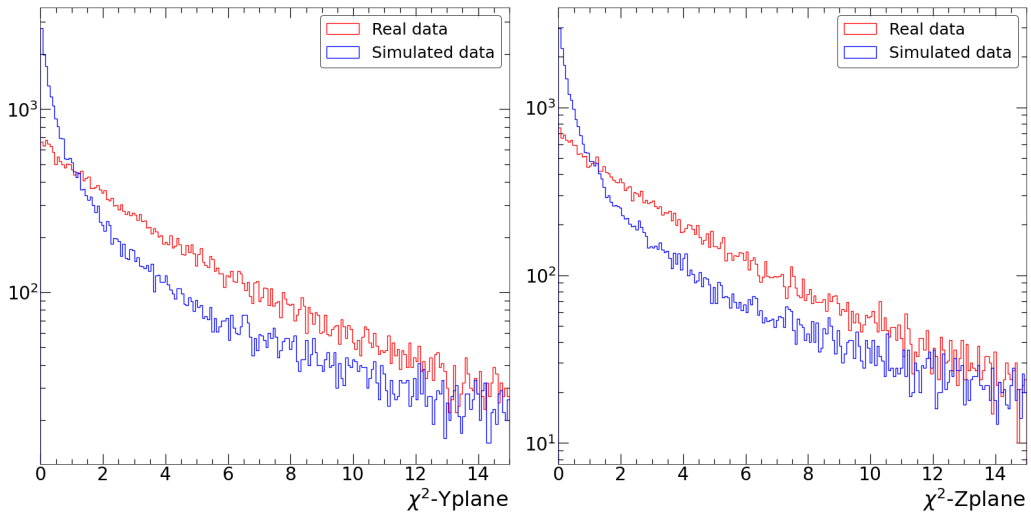

FIGURE 7.43: Comparison of chi-square values for 4-plane tracks reconstructed in real data and simulated data. The plots correspond to the comparison in the case of Y (χ^2-Yplane) and Z (χ^2-Zplane) plane tracks respectively. The comparison is limited to the best tracks with chi-square values below 15. The number of events in both datasets is identical. The results reveal that simulated data tends to produce tracks with lower chi-square values in comparison to real data. In the simulated data, the majority of tracks exhibit chi-square values less than 4, while in real data, chi-square values for the majority of tracks extend up to 8.

The comparison of chi-square values was also extended to the 3-plane tracks obtained from both real data and simulated data. Out of the 1 million events generated, approximately 95,000 events resulted in three-plane tracks, which reduced to approximately 36,000 when the 4-plane condition was applied. Similar to the 4-plane case, only tracks with chi-square values less than 15 were considered for comparison. The results are presented in Fig. 7.44. Notably, in this case, the distributions in the first half of the plot for both the Y and Z planes exhibit a higher degree of agreement compared to the 4-plane tracking case.

7.6.6 Tracing Back to the Parent Particles

In the MURAVES hodoscopes, it's possible for particles other than muons to leave tracks. However, most of these non-muon tracks are expected to be filtered out due to the lead wall positioned between the last two stations. Only high energy muons (energy> 1 GeV) reach the fourth station. To assess the impact of non-muon particle tracks, a comprehensive study was conducted. The particle generator CRY generates all the possible particles in the cosmic ray that can reach the altitude specified. The simulation process does not just involve muons; instead, all the particles that are generated by CRY. Following the simulation, as explained in the previous section, clustering and tracking are performed. Then, a dedicated algorithm developed for this study traces back the primary particles responsible for generating 3-station tracks and 4-station tracks in the hodoscope.

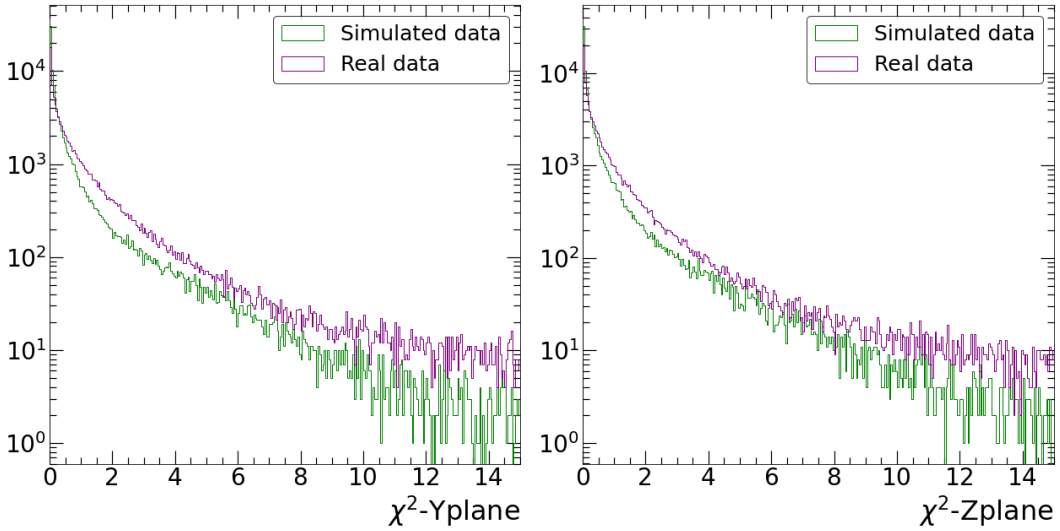

FIGURE 7.44: Comparison of chi-square values for 3-plane tracks between simulated data (green) and real data (purple). The distributions show a higher degree of agreement compared to the 4-plane tracking case, particularly in the first half of the plot for both the Y and Z planes.

Table. 7.1 presents data of the particles generated within the cosmic shower by CRY, detailing how many of them were able to produce tracks within three or four stations. The first row of the table enumerates the quantity of each particle type generated by CRY. In the second row, it is indicated how many of these generated particles successfully traversed the first three stations of the hodoscope. As expected, muons dominate this category, yet a noteworthy number of electrons and positrons also managed to cross the first three stations. In the last row, the table provides the count of particles that successfully crossed all four stations in each case. It is evident that the presence of the lead wall filtered out the majority of particles, excluding muons. Only a minimal number of protons and a single neutron successfully traversed all four stations. This table underscores the substantial role played by the lead wall in screening out tracks of particles other than muons. The results are also

	μ^+	μ^-	e^+	e^-	γ	n	p^+	p^-	π^+	π^-	**Total**
CRY data	175367	163599	32528	54968	481460	76805	5518	1	27	45	990318
3 station events	87947	81420	8774	11269	990	95	2267	0	18	21	192801
4 station events	18653	17736	0	0	0	1	17	0	0	0	36407

TABLE 7.1: Summary of particle generation with CRY and their traversal through the first three and all four tracking stations.

graphically depicted in Fig. 7.45, where the first plot (a) corresponds to the CRY-generated data, the second plot (b) represents data for particles that crossed the first three hodoscope stations, and the last plot (c) displays data for particles that successfully traversed all four stations.

To study the variations between clusters created by muons and those generated by other particles, a comparison was conducted on the cluster energy, cluster multiplicity and chi-square values of events involving muons and events with other particles.

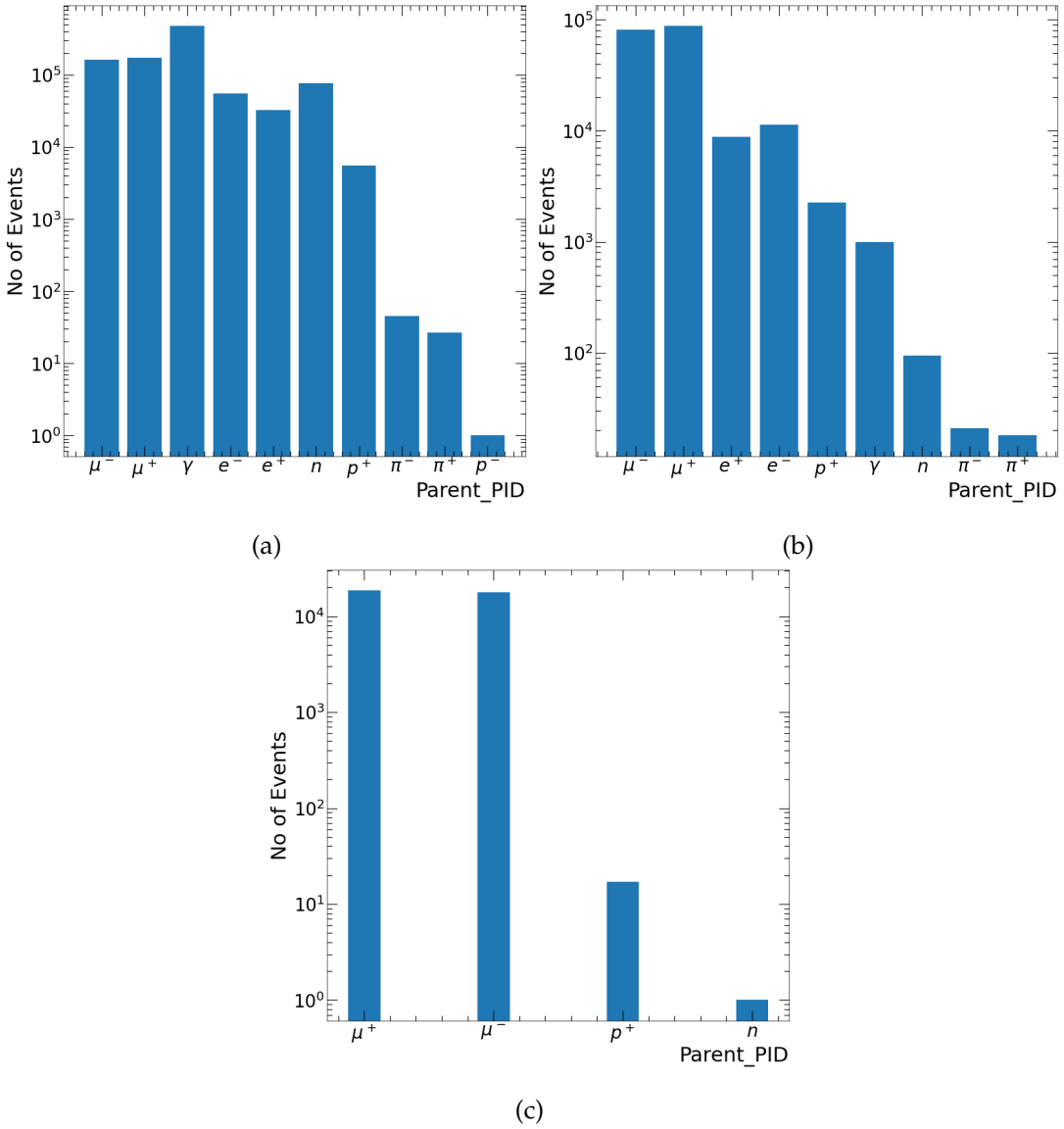

FIGURE 7.45: Summary of the particle tracking study using CRY-generated particles. (a)All generated particle types. (b) Particles that passed through the first three tracking stations. (c) Particles that successfully crossed all four tracking stations. The lead wall effectively filtered out non-muon particles, with only a few protons and a neutron reaching all four stations.

Given the limited presence of tracks from other particles in the 4-station dataset, the comparison was carried out using the 3-station data.

The top row in Fig. 7.46 illustrates the energy distribution of clusters within muon events in the Y and Z planes of the first three stations of the hodoscope. Conversely, the bottom row of the same figure displays the energy distribution of clusters of non-muon events in the Y and Z planes of the first three stations. The distributions in all plots contain the same number of events selected with random sampling. It is evident from the plots that muon clusters are predominantly found within the 0-100 *nPhE* range. While the cluster energy distribution for non-muon events also peaks around 30 *nPhE* (same as muon events), it extends up to 200 *nPhE*. These findings underscore the potential to implement an upper energy threshold for cluster selection, effectively eliminating clusters originating from non-muon events.

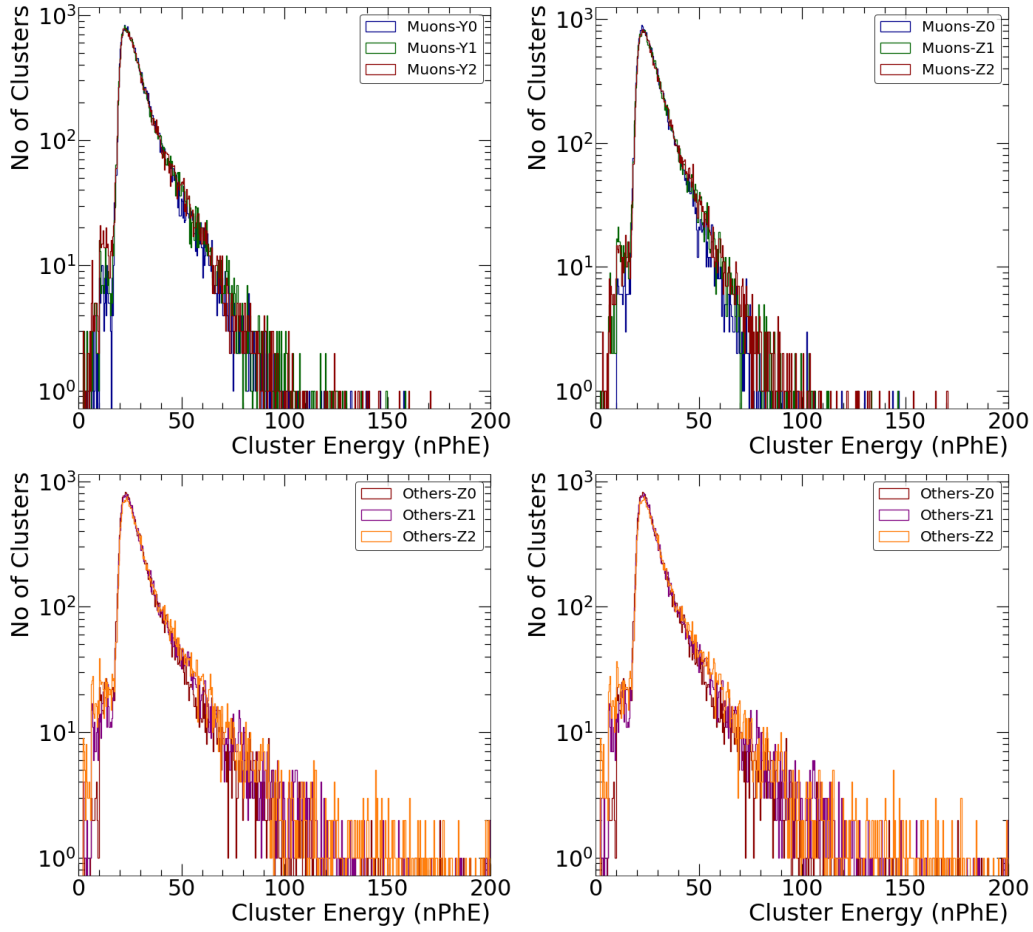

FIGURE 7.46: Comparative analysis of cluster energies within the hodoscope for different event types. The top row displays energy distributions of clusters within muon events, while the bottom row shows clusters from non-muon events. Both distributions are shown for the Y and Z planes of the first three stations in the hodoscope. Muon clusters primarily fall within the 0-100 *nPhE* range, while non-muon event clusters extend up to 200 *nPhE*. This highlights the potential for implementing an upper energy threshold to filter out non-muon clusters.

Figure 7.47 shows the comparison of cluster multiplicity in muon (top row) and non-muon (bottom row) events across the Y and Z planes of the hodoscope. To

ensure equitable comparisons, an equal number of events were randomly sampled for all distributions, given the unequal number of muon and non-muon events in the dataset. Results indicate that muon events exhibit a maximum cluster multiplicity of 4, while non-muon events show cluster multiplicities extending beyond 4 up to 8. Therefore, an additional cluster multiplicity threshold can effectively discriminate non-muon events.

To assess the quality of non-muon tracks and conduct a comparison with muon tracks, a chi-square analysis was performed for both types of tracks. Figure. 7.48 depicts chi-square distributions for muon tracks in the Y (blue) and Z (red) planes, as well as for non-muon tracks in the Y (green) and Z (orange) planes. The same number of events were considered for all distributions through random sampling. A clear distinction is observed in the plot: the majority of muon tracks exhibit chi-square values below 10, indicating tracks of high quality. In contrast, significantly higher chi-square values are evident for non-muon tracks. Although the chi-square value of some non-muon tracks lie within the range of that of the muon tracks, the implementation of an effective chi-square threshold, such as 4 to 6, can efficiently eliminate the majority of non-muon tracks. For understanding the behavior leading to high cluster multiplicity and elevated chi-square values in non-muon particles that traversed either three or four layers, a detailed examination was carried out. In Fig. 7.49, event displays featuring a proton (left) and an electron's (right) tracks within the hodoscope are showcased. All the Geant4 hits involved in the track clusters are plotted in both cases. It can be observed that, in contrast to the muon tracks displayed in Fig. 7.38, the hits induced by non-muon tracks exhibit significant scattering and deviation due to their lower energy, thereby resulting in the formation of multiple clusters and the generation of higher chi-square values.

7.6.7 Noise Implementation

In the preceding sections, the details of the outcomes of the comparison studies between real experimental data and simulated data and the characteristics of tracks originating from different primary particles were discussed. It's noteworthy that, in the simulation process, meticulous attention was given to ensuring precise fidelity to real-world conditions. This included the replication of the detector geometry in Geant4, the digitisation of Geant4 hits to emulate realistic SiPM responses and the complete adaptation of all real data algorithm thresholds into the clustering and tracking algorithm utilised in the simulation study. Despite these rigorous efforts, it was observed that there were some disparities between the results obtained from experimental data and Geant4 simulations (refer Sec. 7.6.5). The observed differences can be attributed to the absence of various experimental effects in the simulated data, such as electronic noise, SiPM efficiency, and detector responses influenced by environmental factors. To address this and assess whether incorporating these effects in the simulation could yield results closer to real data, a study was conducted to introduce noise into the simulated data. Achieving a better agreement between simulation and real data results could lead to estimating more accurate density measurements achievable using the actual hodoscopes. Additionally, the simulation algorithm can distinguish between original particle clusters and introduced noise, enabling the training of machine learning-based models for noise identification. Once adequately trained, these models can be applied to real data for noise-filtering purposes.

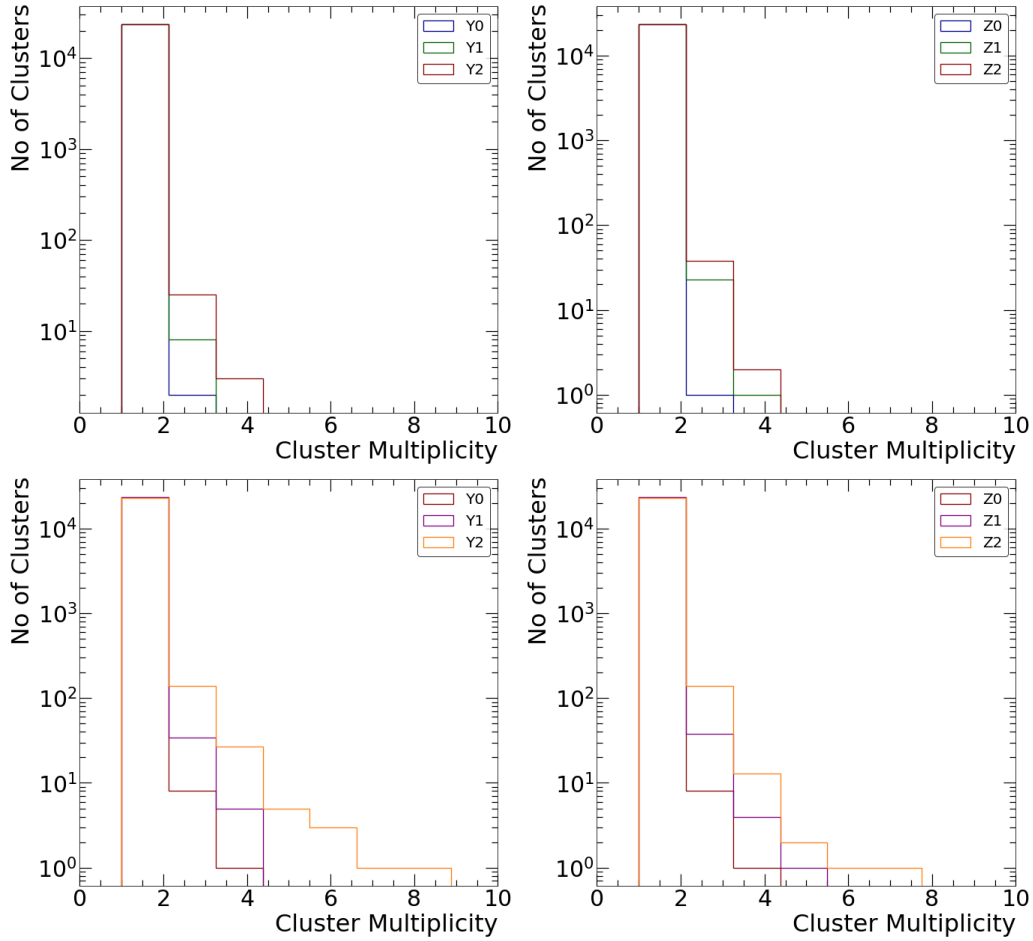

FIGURE 7.47: Comparison of cluster multiplicities in muon (top row) and non-muon (bottom row) events across the Y and Z planes of the hodoscope. Random sampling ensures an equal number of events for all distributions. Muon events exhibit a maximum cluster multiplicity of 4, while non-muon events display cluster multiplicities extending beyond 4 up to 8. Implementing an additional cluster multiplicity threshold can effectively discriminate non-muon events.

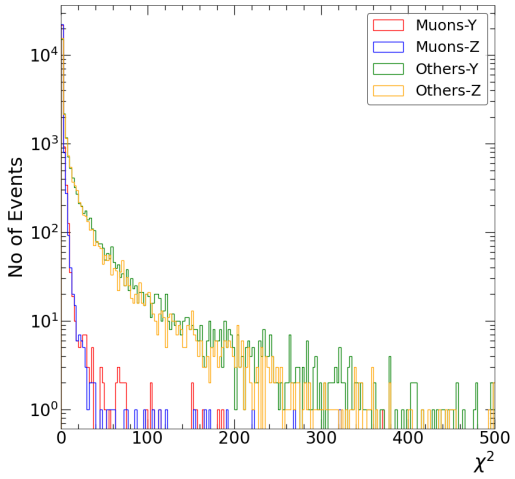

FIGURE 7.48: Comparison of chi-square values for muon and non-muon tracks in the Y and Z planes of the hodoscope. Blue and red represent muon tracks in Y and Z planes, while green and orange are non-muon tracks in Y and Z planes. An equal number of events were randomly sampled for all distributions. The plot shows that the majority of muon tracks have lower chi-square values (< 10), whereas non-muon tracks have higher values. Applying a chi-square cut between 4 and 6 can effectively eliminate most of the non-muon tracks.

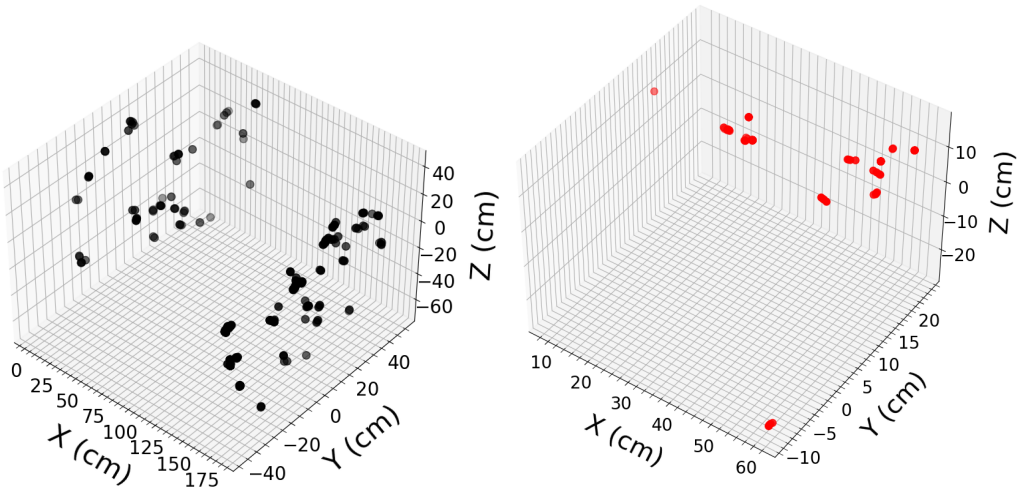

FIGURE 7.49: Event displays of proton (left) and electron (right) tracks within the hodoscope. These non-muon particles exhibit scattered and deviated hits due to their lower energy, leading to the formation of multiple clusters and higher chi-square values, in contrast to the muon tracks shown in Fig. 7.38.

As a first stage for the noise implementation, the scenario after reconstructing the data and applying all thresholds is considered. While noise level optimisation is feasible to some extent using PEDESTAL data, this approach is adopted because, during the reconstruction process, each run is adjusted and refined by filtering out the pedestal distribution specific to that run. Consequently, the discrepancies observed in the comparison studies can be attributed to effects that persist even after this filtering process.

To introduce noise effects into the simulated data, the essential information required includes the positions to which they should be assigned, the frequency of noise clusters per event, and the energy associated with the noise clusters. In general, electronic noise, which encompasses factors like thermal noise and amplifier noise, is often represented as Gaussian noise. Gaussian noise serves as a suitable model for capturing the random, uncorrelated variations in the detector's output arising from electronic and instrumental sources. Consequently, a Gaussian distribution for the position of the noise clusters is generated by defining the minimum and maximum possible ranges for each Y and Z plane.

To estimate the frequency of the noise clusters, the probability distribution describing the difference between the multiplicity distribution in real and simulated data for each Y and Z plane was analysed. Figure 7.42 illustrates these multiplicity distributions in both real and simulated data. The distribution that best fits the difference in these distributions is the Landau distribution. Therefore, datasets for each plane, following the Landau distribution, were created. This was achieved by specifying the minimum and maximum values, mean, and spread estimated from the difference distributions of each plane. Figure 7.50 provides an example of a Gaussian-based position distribution and a Landau-based frequency distribution, which were created using the estimations mentioned earlier for creating noise clusters. For esti-

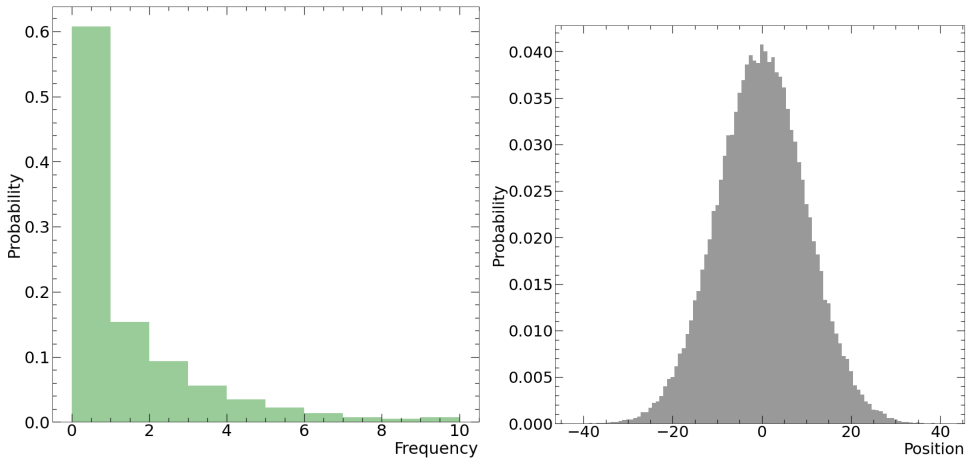

FIGURE 7.50: Example of Gaussian-based position and Landau-based frequency distributions used for assigning positions and frequencies to noise clusters during the noise implementation process.

mating the energy of the noise clusters, an analysis was performed on clusters that were not part of the tracks but still met all the defined thresholds using real data. Figure 7.51 displays the probability distribution of non-track cluster energy in all Y and Z planes of the NERO detector, using the same real data as in the comparison studies, consisting of 1000 runs from the NERO detector. It's notable that in

the case of all planes, the data follows a Landau function. Consequently, Landau-based distributions were generated based on the parameters estimated from these distributions for each plane. With all the necessary datasets generated, a dedicated algorithm for noise implementation selects events from the simulated data one by one. Using a randomiser function, it randomly chooses a position, frequency, and energy value for each plane from the created noise datasets. It then generates noise clusters with the selected attributes and adds them to the events. For example, if the randomiser selects a frequency of two for a particular plane, the algorithm creates two clusters with positions and energy values chosen from the Gaussian-position and Landau-energy distributions generated for the noise clusters. This process is repeated for all events in the simulated data.

After incorporating noise into the simulated data, a comparison of track chi-square values was conducted with pure simulated data (data without noise) and real data. Figure 7.52 illustrates the results of this comparison, with the first and second plots depicting the chi-square comparison for the Y and Z planes, respectively. In the plots, the red trend represents real data, blue corresponds to pure simulated data, and green corresponds to simulated data with added noise. It can be observed that the simulated data with the inclusion of noise aligns more closely with the real data compared to the pure simulated data. However, a notable difference from the real data still exists. This difference may arise from the fact that noise is currently added at the cluster level, and further investigation, possibly at the individual bar level, is required for a deeper understanding. Cluster positions are calculated from the barycenter positions, so exploring and implementing noise effects at the bar level could provide clearer insights. Additionally, applying weights to the bars based on the SiPM efficiency of the bars in the real case could further refine the simulation.

7.6.8 Introducing 3D Tracking

In the current MURAVES tracking algorithm (detailed in Sec. 7.5.2), muon tracks are reconstructed separately for the Y and Z planes. Various track characteristics are evaluated independently, and track quality is assessed based on individual Y and Z chi-square values. This approach is adopted due to a fundamental reason: when a muon traverses the four stations of the hodoscope and interacts with both Y and Z planes, the number of bars it intersects and the resulting clusters in the X and Y planes of each station are not equal. For example, as a muon passes through the Y and Z planes of the first station, there may be two clusters in the Y plane and three in the Z plane. In such a scenario, it becomes challenging to determine the correspondence between Y clusters and Z clusters. Therefore, X-Y and X-Z tracking are conducted independently. Furthermore, when an equal number of clusters are formed in both the Y and Z planes, but this number exceeds one, it becomes challenging to establish a one-to-one correspondence between Y clusters and Z clusters.

To improve the existing technique and to define a better track selection scheme, a new 3D tracking algorithm was developed. The steps involved in the algorithm are as follows:

1. **Cluster Selection**:
    - Clusters that are part of an event in all planes in all stations are considered.

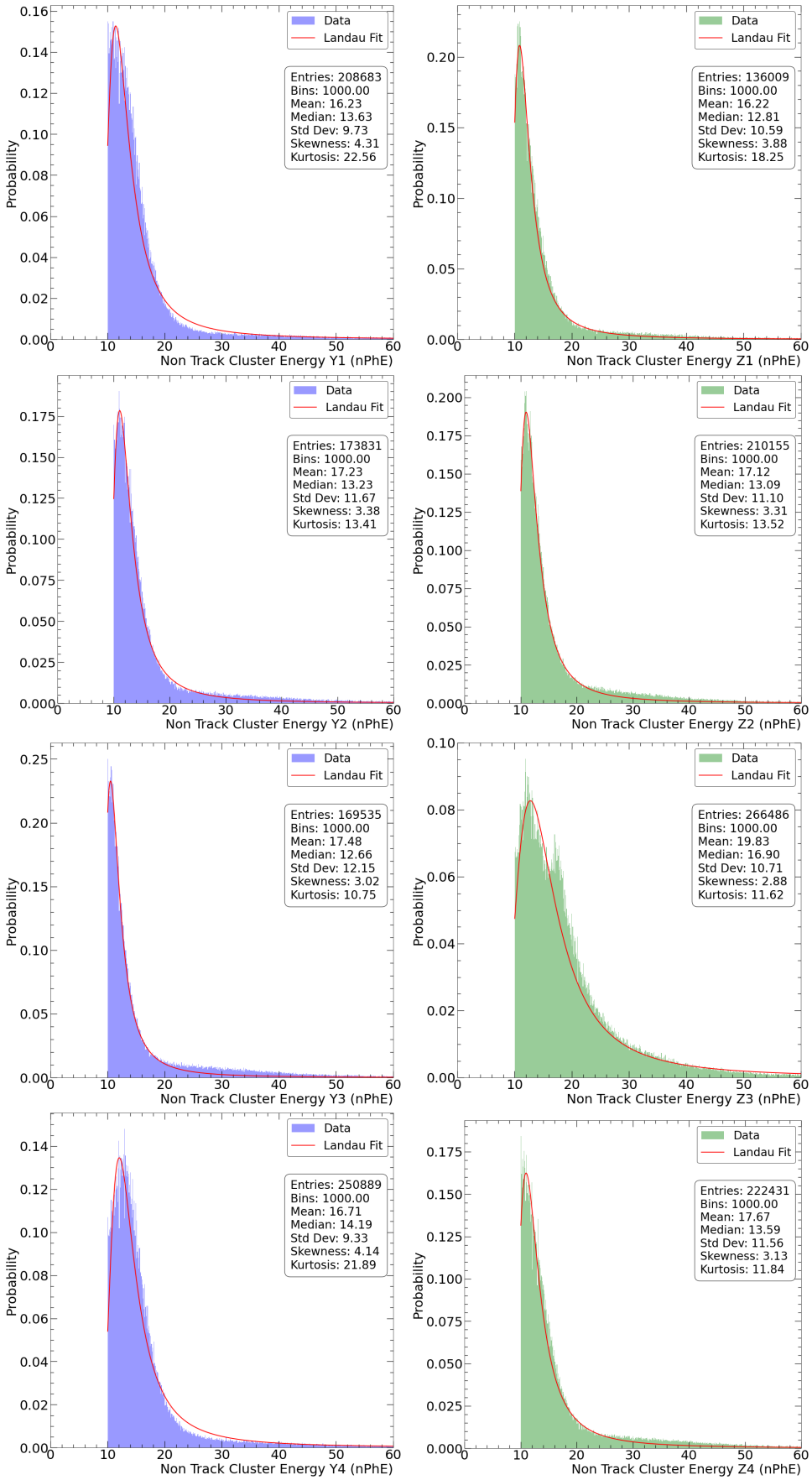

FIGURE 7.51: Probability distribution of non-track cluster energy in all Y and Z planes of the NERO detector, illustrating the Landau-based distributions used for estimating noise cluster energies during the noise implementation process.

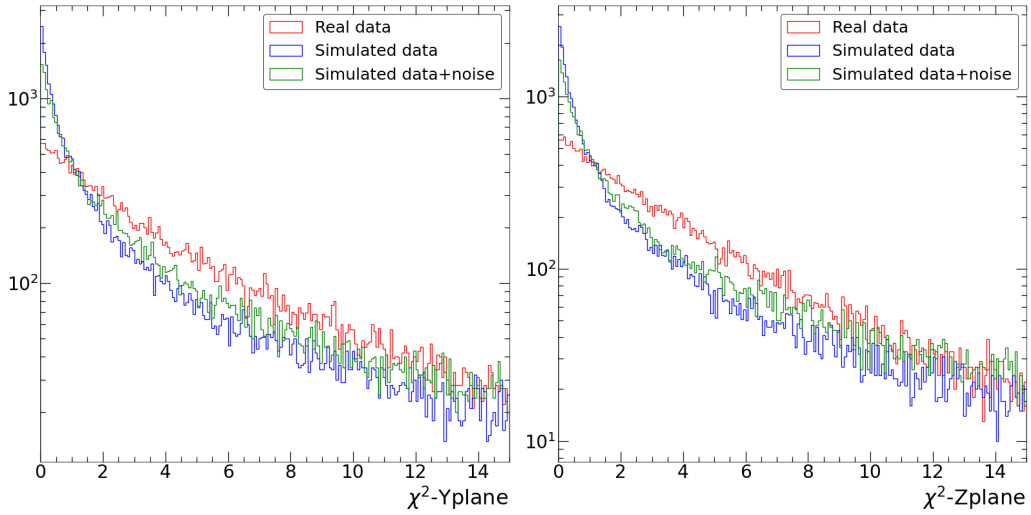

FIGURE 7.52: Comparison of track chi-square values between different datasets. The first and second plots represent the chi-square comparison for the Y and Z planes, respectively. Red corresponds to real data, blue corresponds to pure simulated data, and green corresponds to simulated data with added noise. The alignment of the green trend with real data suggests that the noise implementation brings simulated data closer to real observations, although discrepancies still exist. Further investigation at the bar level and considering SiPM efficiency could provide insights for refining the simulation.

2. **X-Y-Z Cluster Combination**:

   - Combinations of X-Y-Z clusters in all stations are constructed. For instance, in the case of the first station, where there are two clusters in Y_1 (b_1, b_2) and two clusters in Z_1 (c_1, c_2), the possible [X, Y, Z] combinations are $[a_1, b_1, c_1]$, $[a_1, b_1, c_2]$, $[a_1, b_2, c_1]$, and $[a_1, b_2, c_2]$, with a_1 representing the X-coordinate of the first station.

3. **Combinations Count**:

   - If there are N_y clusters in a Y plane and N_z clusters in the corresponding Z plane, the total number of three-point combinations in that particular station will be $N_y \cdot N_z$.

4. **Track Combinations**:

   - After constructing X-Y-Z cluster combinations in all planes, all possible tracks with these combinations are considered. Each track consists of one $[X, Y, Z]$ combination from each station. The number of tracks that can be reconstructed is equal to the product of the number of combinations ($N(xyz)_i$) in all stations:

$$N_{\text{tracks}} = \prod_{i=1}^{n} N(xyz)_i \tag{7.11}$$

     where n is 3 for three-plane tracking and 4 for 4-plane tracking.

5. **Track Selection with Chi-Square**:

   - To select the best track and the associated 3D coordinates, the chi-square (χ^2) of each track is calculated. The chi-square of the 3D track is calculated

as the sum of the chi-square of the X-Y and X-Z tracks of the 3D track, as given by:

$$\chi^2_{3D} = \sum_{i=1}^{n} \frac{(y_i^{\text{meas}} - y_i^{\text{pred}})^2}{\sigma_y^2} + \frac{(z_i^{\text{meas}} - z_i^{\text{pred}})^2}{\sigma_z^2} \tag{7.12}$$

where y_i^{meas} and z_i^{meas} represent the measured cluster positions, while y_i^{pred} and z_i^{pred} represent the predicted cluster positions, respectively. The terms σ_y^2 and σ_z^2 in the denominators account for the uncertainty in the measurements of the cluster positions.

6. **Best Track Selection**:

   - The 3D track with the least chi-square value is chosen as the best reconstructed track.

This approach has been implemented to enhance track selection by considering the goodness of fit using the chi-square metric, ensuring that the chosen track provides the most accurate representation of the particle's trajectory.

Figure 7.53 provides an overview of the 3D tracking process. The first two images (a and b) display the clusters in the Y and Z planes. The third plot (c) represents the 3D clusters generated from all possible X-Y-Z combinations and illustrates all the tracks that were reconstructed. In this particular example, 24 tracks were reconstructed, taking into account all combinations. The final plot showcases the track with the lowest chi-square value among the 24 reconstructed tracks. The X-Y-Z clusters associated with the track can also be seen in the plot.

To validate the new tracking method and understand track properties in the case of 3D tracking, tests were conducted using simulated data for both 3-plane tracking and four-plane tracking. The comparison involved assessing key track properties such as, residues, chi-square values, and track energies for both the best tracks and the rejected tracks.

Figure 7.54 illustrates the comparison of residue values (Eqn. 7.13) between the rejected and best tracks for both 3-plane and four-plane tracking scenarios. Residue quantifies how well the reconstructed track matches the actual measurements. The smaller the residue, the better the track describes the observed data points.

$$Residue_{3D} = \sum_{i=1}^{n} (y_i^{\text{meas}} - y_i^{\text{pred}})^2 + (z_i^{\text{meas}} - z_i^{\text{pred}})^2 \tag{7.13}$$

In both plots, it is evident that clusters associated with the best tracks exhibit significantly less deviation compared to those associated with the rejected tracks. The residue values for the rejected tracks span a much broader range than those for the best tracks, making it much easier to distinguish the best tracks from the others.

Figure 7.55 shows the outcomes of the chi-square comparison study, providing insights similar to those derived from the residue distributions. Chi-distributions additionally consider statistical uncertainties inherent in measurements. In the first plot (corresponding to 3-plane tracking) and the second plot (corresponding to 4-plane tracking), the chi-square values of the best tracks are shown in red, while

the rejected tracks are displayed in black. In the case of 3D tracking, it's expected that the chi-square of the 3D track will be higher than that of the 2D track, as it encompasses uncertainties from both planes. This higher chi-square value is actually advantageous because it helps distinguish the best track from the alternative tracks, which have higher uncertainties and cluster deviations. The plots clearly demonstrate a substantial difference in the chi-square ranges between the best tracks and the rejected tracks. This significant difference simplifies the process of applying and estimating a chi-square cut for track selection, particularly in the case of 3D tracking.

A parameter called 'track energy' is employed to compare the energies of clusters associated with tracks. Track energy is calculated as the sum of the energies of the Y and Z clusters that constitute the track in all four stations. Figure 7.56 presents a comparison of track energies between the best tracks and rejected tracks in both the 3-plane and four-plane tracking scenarios. These plots suggest that applying both lower (100 $nPhE$ for 3-plane; 150 $nPhE$ for four-plane) and upper (500 $nPhE$ for 3-plane; 350 $nPhE$ for four-plane) energy thresholds can effectively aid in best track selection.

Table 7.2 summarises the key findings discussed in this study. One notable observation is the significant difference in the mean residue and chi-square values between the best tracks and the rejected tracks, underscoring the importance of utilising the 3D tracking algorithm for track qualification. Concerning mean track energy values, despite the means falling within a similar range, it's worth highlighting that there are significant variations in the minimum and maximum values within both cases.

	Mean Residue		Mean Chi-square		Mean Track Energy (nPhE)	
	Best Tracks	Rejected Tracks	Best Tracks	Rejected Tracks	Best Tracks	Rejected Tracks
3-Plane Tracking	1.15	121.63	5.04	443.84	174.69	208.73
4-Plane Tracking	4.68	114.07	20.6	439.47	208.00	232.65

TABLE 7.2: This table provides an overview of the key outcomes from the 3D tracking analysis. Notably, there is a substantial contrast in the mean residue and chi-square values between the best and rejected tracks, emphasizing the utility of the 3D tracking algorithm for track assessment. Although mean track energy values fall within a similar range, it's important to highlight the significant variations in minimum and maximum values within both cases (refer Fig. 7.56).

7.7 Density Evaluation Study

In the previous sections, the data analysis procedure applied in the MURAVES experiment, the current status of ongoing simulation studies, and the obtained results were discussed. The primary objective of the MURAVES experiment is to conduct a density distribution measurement of the summital cone of Vesuvius. A study was conducted to estimate the density at different regions of the mountain cone with the first data collected using the ROSSO and NERO hodoscopes. In this section, the significant outcomes achieved from this study are presented [320, 323]. The third hodoscope BLU is not included in this study since the calibration data collection of the detector was not completed. As discussed in Sec. 7.2.1, the determination of density typically relies on transmission measurements. Transmission is quantified

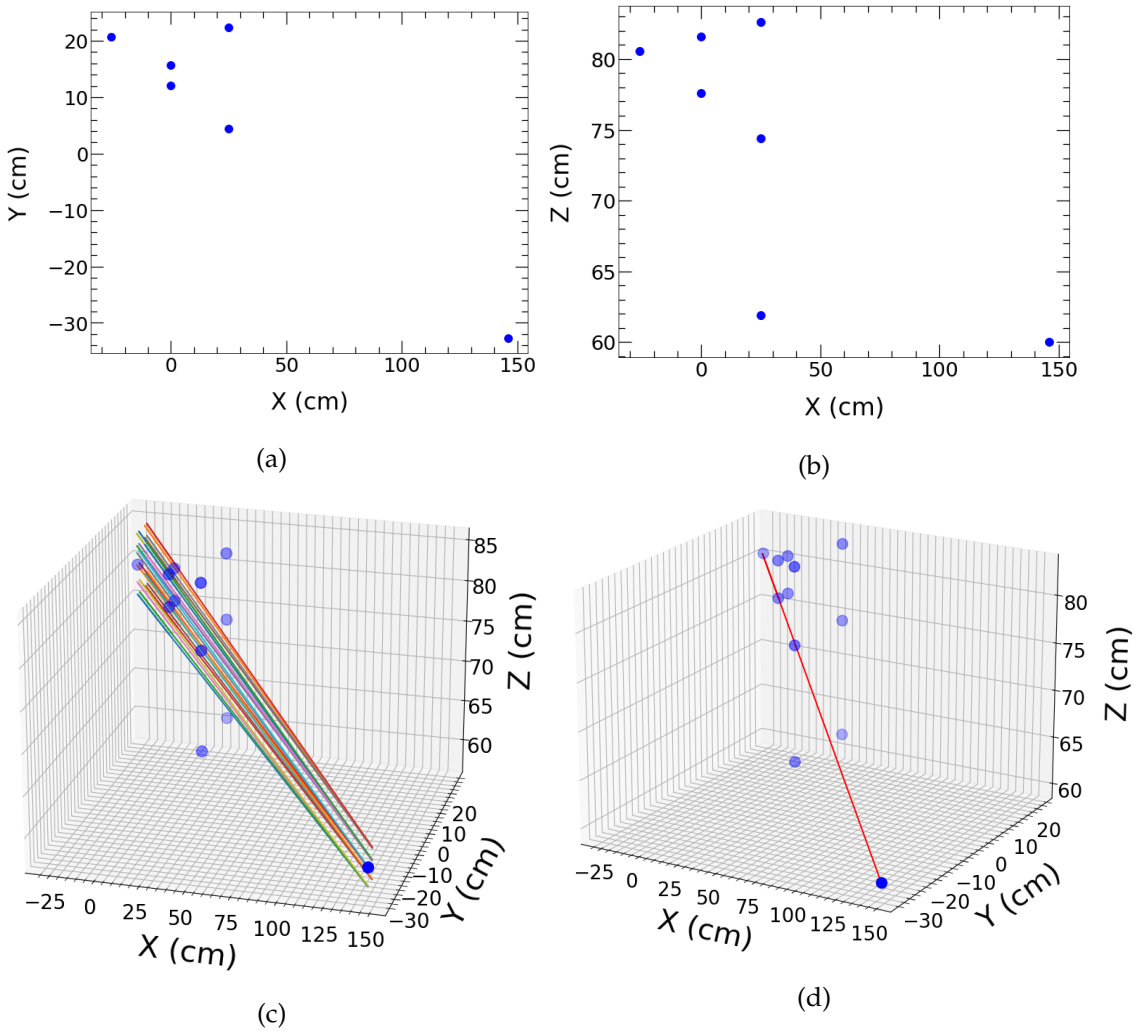

FIGURE 7.53: Illustration of the 3D tracking process. In (a) and (b), clusters in the Y and Z planes are displayed, respectively. Plot (c) showcases the 3D clusters formed from all possible XYZ combinations, revealing multiple reconstructed tracks. In this specific example, 24 tracks were reconstructed, considering all combinations. The final plot presents the track with the lowest chi-square value.

as the ratio of the measured flux from the direction of Vesuvius to that from the open sky. These two flux measurements are acquired separately by rotating the detectors to the opposite direction.

In this study, four datasets from the ROSSO and NERO detectors were analysed. Each detector's datasets corresponded to operating temperatures of 15°C and 20°C. The acquisition times for each dataset for both Vesuvius and open-sky cases are provided in Tab. 7.3. The calibration datasets required less acquisition compared to Vesuvius data. The chi-square cut applied to the data for track selection estimated as explained in Sec. 7.5.2 are also tabulated in the same table.

7.7.1 Density Evaluation: Procedure

The following section describes the procedure for density evaluation, a process that requires the combination of experimental and simulated data. The measured

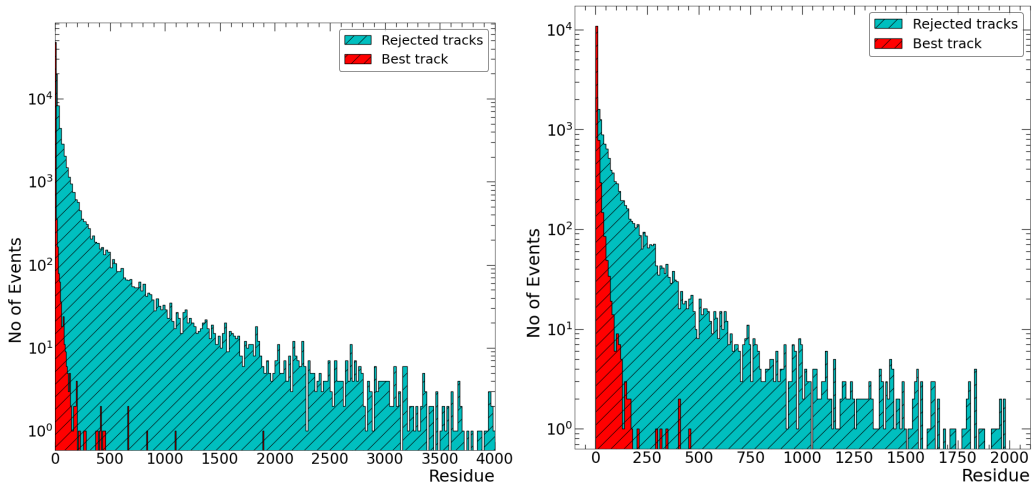

FIGURE 7.54: A comparison of residue values for both 3-plane and 4-plane tracking scenarios. The residue measured for rejected and best tracks are shown in blue and red colour respectively. This comparison highlights the significant deviation observed in clusters associated with rejected tracks, in contrast to the minimal deviation seen in clusters associated with the best tracks.

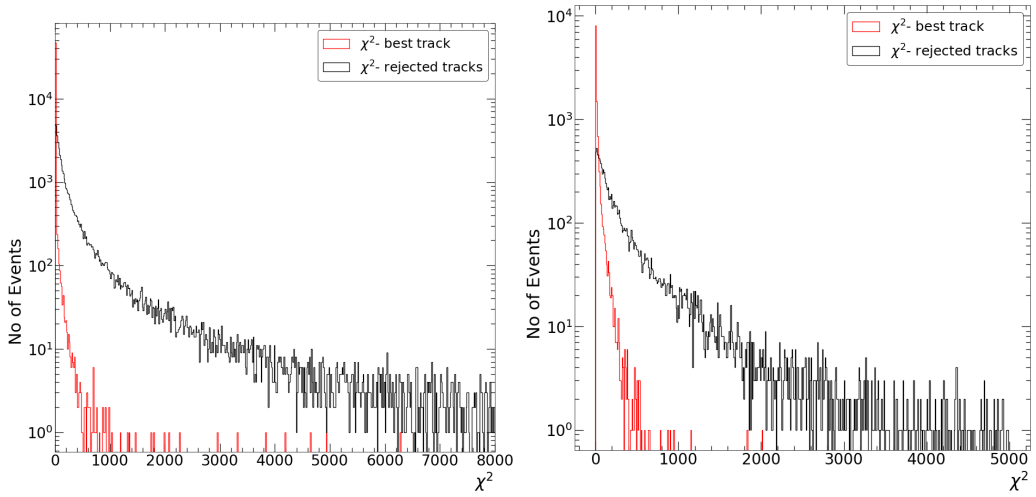

FIGURE 7.55: Comparison of chi-square values for track selection between 3-plane and 4-plane tracking scenarios. The first plot (3-plane tracking) and the second plot (4-plane tracking) display chi-square values for the best tracks (in red) and the rejected tracks (in black). This analysis highlights the effectiveness of using chi-square cuts for track selection, with a notable distinction in chi-square ranges between the best and rejected tracks, particularly in the 3D tracking scenario.

Dataset	Acquisition Time: Vesuvius (days)	Acquisition Time: open sky (days)	Maximum χ^2
ROSSO wp 15°C	51	9.5	5
ROSSO wp 20°C	40	14.3	4.4
NERO wp 15°C	43	10	5.1
NERO wp 15°C	26	17	5.1

TABLE 7.3: The acquisition times for datasets corresponding to the ROSSO and NERO detectors at different operating temperatures. The last column corresponds to the maximum chi-square values applied to the data for event selection [320].

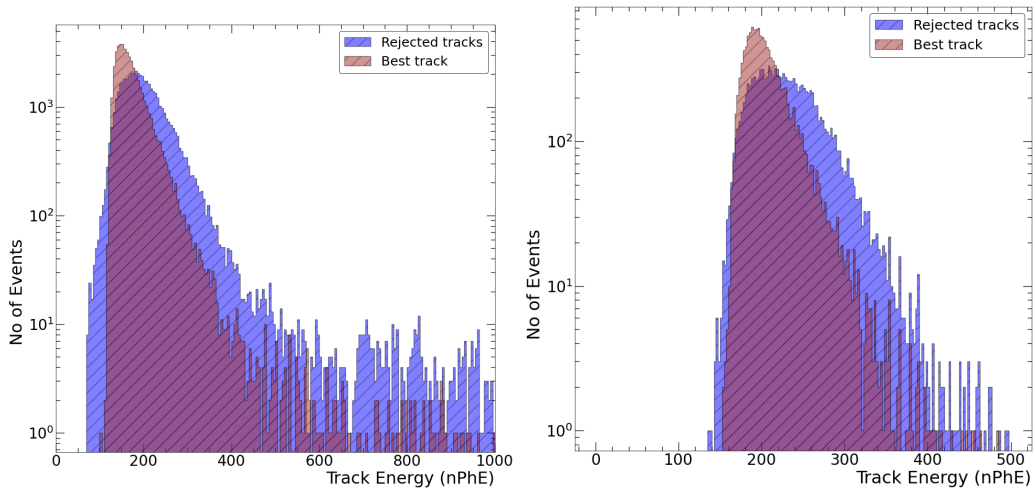

FIGURE 7.56: Comparison of track energies between the best tracks and rejected tracks in the 3-plane and 4-plane tracking cases. Track energy, defined as the sum of energies from Y and Z clusters in all four stations associated with the track, illustrates the clear distinction between best and rejected tracks, indicating the potential for effective track selection based on lower and upper energy thresholds.

fluxes are mathematically represented by the following equations:

$$\Phi^{Ves}_{meas}(\phi,\alpha) = S_{eff}(\phi,\alpha)\cdot\epsilon_{Det}(\phi,\alpha)\cdot\epsilon_{tr}\cdot\epsilon^{Ves}_{\chi^2}\cdot\Phi^{Ves}_{real}(\phi,\alpha)+\delta\Phi^{Ves}_{noise} \tag{7.14}$$

$$\Phi^{os}_{meas}(\phi,\alpha) = S_{eff}(\phi,\alpha)\cdot\epsilon_{Det}(\phi,\alpha)\cdot\epsilon_{tr}\cdot\epsilon^{os}_{\chi^2}\cdot\Phi^{os}_{real}(\phi,\alpha)+\delta\Phi^{os}_{noise} \tag{7.15}$$

These equations consider various factors and parameters that influence flux measurements. The term S_{eff} represents the effective surface of the detector, while ϵ_{Det} and ϵ_{tr} correspond to detector and trigger efficiencies, respectively. The ϵ_{χ^2} is related to the cut applied in the analysis on the χ^2 parameter. When the detector stations' alignments are consistently maintained during orientation inversions and data collection occurs with minimal time gaps, the parameters related to effective surface area and detector efficiency are expected to be equal in Φ^{Ves}_{meas} and Φ^{os}_{meas}. However, if a significant time difference (on the order of months) exists between these measurements, slight changes in detector efficiencies may be anticipated. Trigger rate efficiencies can be considered comparable, as the trigger rates are of similar magnitudes in both data acquisitions.

The efficiency in the measurement of the tracks (ϵ_{χ^2}) cannot be considered equal since the energy range of the muon tracks in the detector can be different in both cases. Estimating these efficiencies solely from measured data is not feasible; they must be derived through realistic simulations of the apparatus and expected fluxes. Currently, the simulation lacks the necessary detail to provide accurate efficiencies. The terms Φ^{Ves}_{noise} and Φ^{os}_{noise} in these equations represent hypothetical contributions from noise and background effects in the measurements. Assuming these effects are negligible, the measured transmission would be:

$$T_{meas}(\phi,\alpha) = \frac{\epsilon^{Ves}_{\chi^2}}{\epsilon^{os}_{\chi^2}}T_{real}(\phi,\alpha) \tag{7.16}$$

The quantity $T_{real}(\phi, \alpha)$ can be estimated using the MC tool mentioned in Sec. 7.6.2, while $\frac{\epsilon^{Ves}_{\chi^2}}{\epsilon^{os}_{\chi^2}}$ is measured through a data-driven approach in the present case. Based on volcanology methods, a density hypothesis is conducted for a specific region of the mountain, assuming an average density ρ_0 in the region $\Delta\Phi_0, \Delta\alpha_0$. Through this hypothesis, the unknown parameter C can be estimated as follows:

$$C = \frac{\epsilon^{Ves}_{\chi^2}}{\epsilon^{os}_{\chi^2}} \approx \frac{T_{PUMAS}(\Delta\Phi_0, \Delta\alpha_0; \Delta\rho_0)}{T_{meas}(\Delta\Phi_0, \Delta\alpha_0)} \tag{7.17}$$

The estimated parameter C can then be used to correct the generic transmission $T_{meas}(\phi, \alpha)$. The corrected transmission $T'_{meas}(\phi, \alpha)$ can be thus used to evaluate the density.

After filtering the muon events in the data that meet the selection criteria, the data analysis proceeded by dividing the angular range corresponding to the upper part of the mountain into regions large enough to contain reasonable statistics. Figure. 7.57 shows the angular regions chosen. These regions were selected to be larger

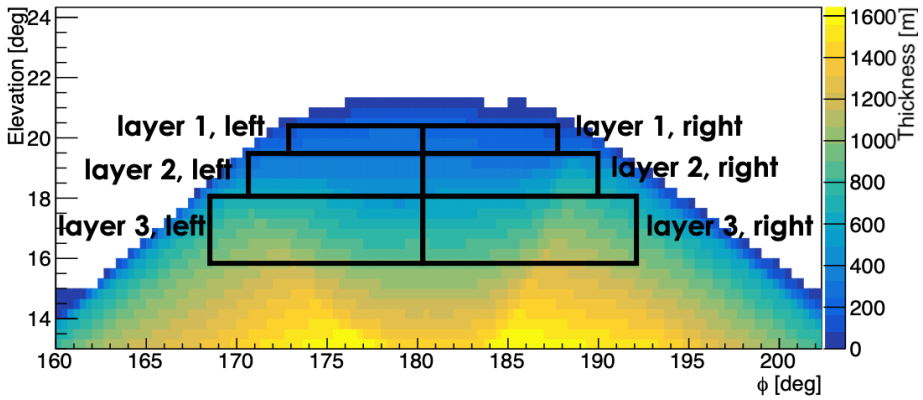

FIGURE 7.57: Angular regions defined for the evaluation of the average density [320].

in azimuthal angle compared to elevation to provide observation coverage over a possible stratification of materials with different densities. For a better balance, the layers cover an increasing range of elevation angles descending from the top of the volcano. The three layers decided upon were further subdivided into left and right sides, as shown in Fig. 7.57 (west and east sides, respectively), to search for possible asymmetries within the mountain's cone.

In the mentioned datasets, the number of events recorded in each of the six angular regions are listed in Tab. 7.4. The statistical uncertainty is generally maintained below 10%, with a few cases exceeding but still remaining below 20%.

The average densities in the angular regions defined are estimated. The following are the steps involved:

- The first step entails simulating the expected transmission by varying the overall density value.

Dataset	No of Events		Stat. unc. (%)	
	Left	Right	Left	Right
Layer 1				
ROSSO wp 15°C	428	439	0.05	0.05
ROSSO wp 20°C	346	323	0.05	0.05
NERO wp 15°C	231	258	0.05	0.05
NERO wp 15°C	128	258	0.07	0.06
Layer 2				
ROSSO wp 15°C	164	140	0.08	0.08
ROSSO wp 20°C	106	109	0.10	0.10
NERO wp 15°C	78	79	0.11	0.11
NERO wp 15°C	61	63	0.13	0.13
Layer 3				
ROSSO wp 15°C	61	76	0.12	0.11
ROSSO wp 20°C	58	63	0.13	0.13
NERO wp 15°C	47	47	0.14	0.15
NERO wp 15°C	27	30	0.19	0.18

TABLE 7.4: Table provides the event counts recorded in each of the six angular regions within the datasets mentioned. In most cases, statistical uncertainty remains below 10%, with a few exceptions where it remains below 20% [320].

- A function, denoted as $T_{\Delta\Phi,\Delta\alpha}(\rho)$, is derived from the distribution of the expected transmission as a function of density.
- Subsequently, the inverted function, $\rho_{\Delta\Phi,\Delta\alpha}(T)$, is employed to estimate the density value corresponding to the measured transmission.
- The measured transmission is corrected by considering the uncertainty, denoted as $\sigma T'$, resulting in $T'_{\Delta\Phi,\Delta\alpha}$.
- The density can be evaluated with two limits corresponding to the 1σ fluctuations of the transmission.
- The upper limit, denoted as $\rho^{up}\Delta\Phi, \Delta\alpha$, is calculated as follows:

$$\rho^{up}\Delta\Phi, \Delta\alpha = \rho_{\Delta\Phi,\Delta\alpha}(T'_{meas} - \sigma T') \tag{7.18}$$

  and the lower limit, denoted as $\rho^{low}\Delta\Phi, \Delta\alpha$, is evaluated as follows:

$$\rho^{low}\Delta\Phi, \Delta\alpha = \rho_{\Delta\Phi,\Delta\alpha}(T'_{meas} - \sigma T') \tag{7.19}$$

This procedure has been applied to each of the chosen angular regions.

7.7.2 Density Evaluation: Results

Profiting the data collected by the volcanologists, density hypotheses for the region denoted as "layer1, left" in Fig. 7.57. The assumed density value in this area was 2.65 g/cm^3, which corresponds to the density of standard rock. Subsequently, the densities were evaluated following the aforementioned procedure for each dataset and within the selected regions. The resulting densities are visually represented in Fig. 7.58. The plots in Fig. 7.58 also illustrate the average density derived from the

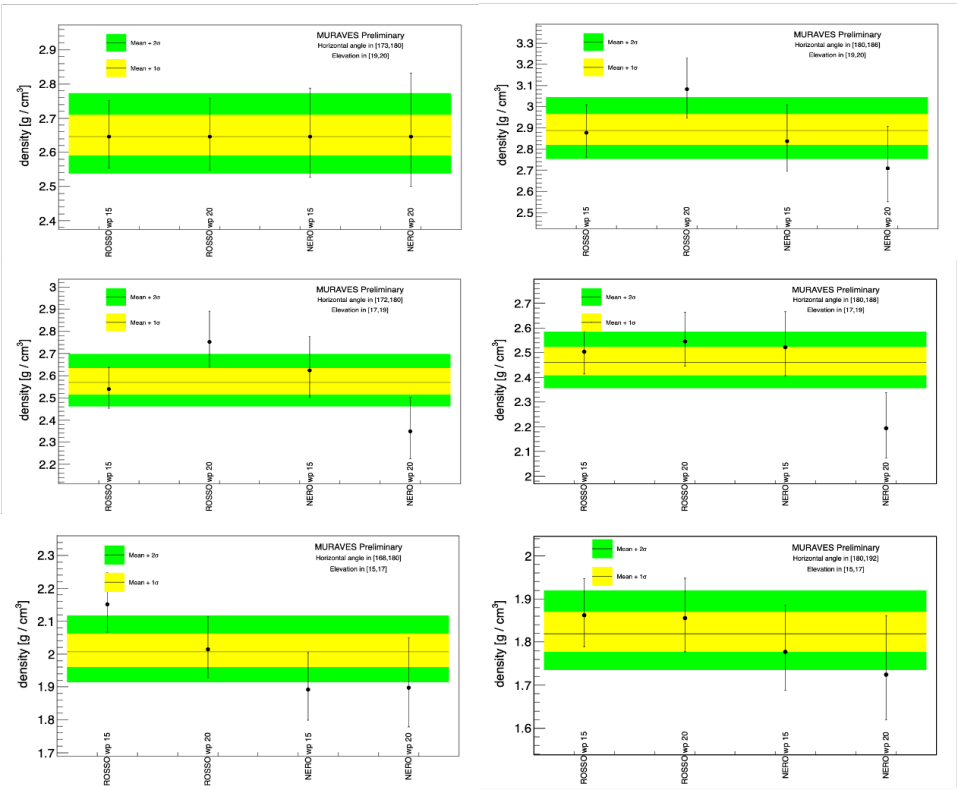

FIGURE 7.58: Densities measured in the six chosen angular regions following the method described in the text. A density of 2.65 g/cm^3 is hypothesised in the region $\Phi\epsilon$[173°,180°] $\alpha\epsilon$[19°,20°]. Only statistical uncertainties have been accounted [323].

combination of all four measurements, along with 1 and 2 σ colored bands for uncertainty. However, it is evident from Fig. 7.58 that the densities obtained from different datasets do not consistently align; in certain instances, the discrepancies exceed 2 σ. This observed variability strongly suggests the presence of systematic errors, which are dataset-specific and contingent upon factors such as the particular detector and working conditions.

To address this issue, a decision was made to assess the relative density between two regions within the same layer. Consequently, the ratio $\frac{\rho_{right}}{\rho_{left}}$ was computed for each layer and for each of the four datasets. The outcomes of these calculations are depicted in Fig. 7.59. The average line and 1-2 σ bands are shown as well. Plots in Fig. 7.59 clearly show a reduction in the disagreement between the various datasets, confirming that the density disagreements, observed in Fig. 7.58, derive particularly from systematic effects related to the detector and the working point. The disagreements in the relative densities between different datasets are confined within the 1 σ range. While the results do show a noticeable difference in the density ratio $\frac{\rho_{right}}{\rho_{left}}$ for the uppermost layer, suggesting a higher density on the right side, it's crucial to note that the significance level of this discrepancy is only 1.5 σ. The same goes for the deeper layers; discrepancies between the two sides are observed, but opposite with respect to the first layer, with significance levels of 0.67 σ and 2 σ in layers 2 and 3, respectively.

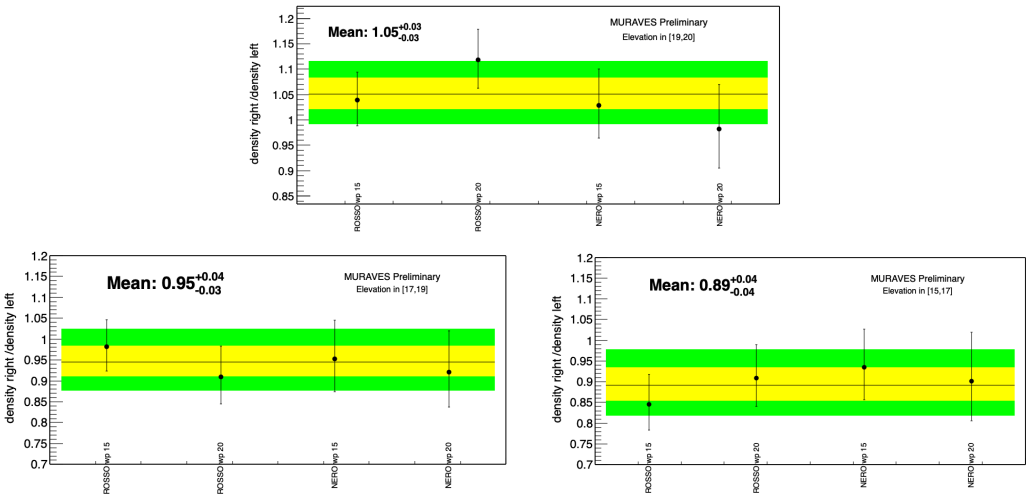

FIGURE 7.59: Right/left asymmetries. From top to bottom: Layer 1, Layer 2, Layer 3 [323].

7.8 Summary and Conclusions

The primary objective of MURAVES experiment is to investigate the density distribution within the upper region of Mt. Vesuvius using muography. This chapter outlines the significant activities carried out as part of the experiment and the corresponding results achieved up to this point. One of the primary challenges of this experiment is the extended data collection period required, spanning several years. This is essential to attain the expected precision in density measurements. Managing and operating three hodoscopes continuously over such an extended period while ensuring their efficiency under harsh environmental conditions presents a substantial challenge.

The in-depth information regarding the logistics of the experiment encompassing aspects such as the laboratory setup, hodoscope design, detector specifications, electronics configuration, temperature stabilisation system, solar-based powering scheme, etc., were discussed in Sec. 7.3.

The raw data from MURAVES detectors undergoes a rigorous series of steps before reconstruction. Starting from the collected raw data, the scintillator bars impacted by muons are identified, and their associated energies (measured in terms of the number of photoelectrons) are determined. This information is then utilised in an energy-weighted approach to calculate the muon cluster position and their corresponding cluster energies. The proprieties of the muon clusters in terms of energy, size, multiplicity, etc., are studied, and the results are presented in Sec. 7.4. After the clustering, the muon tracks are reconstructed and the tracks are qualified based on their associated χ^2 value.

In the simulation part, the status of the implementation of the MC simulation chain for the MURAVES experiment is described. For each step, available software tools striving for a trade-off between accuracy and speed that adequately meets the requirements of an experiment, such as MURAVES, are examined. For the generation of the cosmic muons, CRY is considered in the present scenario due to its short computation time and ease with interfacing to Geant4, but CORSIKA interface is

also set due to the possibility it offers to simulate additional effects and to quantify the effect of different hadronic interaction models.

The problem of efficient simulation of the muon passage through a large body, such as Vesuvius, is approached using PUMAS. To verify the accuracy of this method, a comparison study is conducted between PUMAS and Geant4 by analyzing the energy loss and scattering of muons in rock. The results of both methods were in line with each other. The survival probability of the muons in the MURAVES setup was also studied and as per the results, 50% of muons of energy 0.9 GeV were able to reach the 4^{th} station of the detector and $\sim$100% survival probability was observed at 1.2 GeV. The Geant4 response generated after interfacing with CRY is then digitised into the MURAVES data format that can be directly fed into the standard MURAVES reconstruction code. To evaluate the performance of the simulation chain, the tracking method applied to real data is replicated for the simulation. A comparison is made between the χ^2 values and all the cluster properties associated with the tracks of the simulated data and those of the real data. Similar trends are observed in both cases, but slight differences are present due to the simulation not taking into account experimental effects such as dark noise and electronic effects. All the results are showcased in Sec. 7.6.5.

The study of particle tracks, aside from muons, within the hodoscope was performed using the simulation setup. The study quantified alternative particle tracks within the hodoscope and cluster properties of these events were studied. The results presented in Sec. 7.6.6 revealed that the χ^2 values for these alternative particle tracks and their cluster multiplicities are significantly higher compared to those of muon tracks. In the case of 3-plane tracking, most of these events can be excluded by applying an efficient χ^2 cut for event selection. However, in the case of four-plane tracking, the results demonstrated the effective role of the lead wall in filtering out these alternative particle tracks. Out of all generated events, approximately 34% corresponded to muon events, while the remaining 66% were associated with other particles interacting with the hodoscope's active area. Among the 34% of muon events, 50% crossed all three stations of the hodoscope, and 10% survived by crossing all four stations, overcoming the lead wall. In contrast, out of the 66% of other particle events, only about 3.5% successfully traversed the 3 planes of the detector. In the case of 4 stations, an even smaller fraction, approximately 0.002%, managed to meet the survival criteria. The simulation studies also included the implementation of detector noise, which is observed in real data even after the application of cluster threshold and reconstruction. By studying the noise pattern in real data and incorporating it into simulations, more accurate predictions of density measurement results can be achieved, achievable with real conditions. Additionally, a better understanding of these effects can lead to the development of more effective noise-filtering techniques. The noise was introduced into the simulation through a data-driven procedure conducted using real data, as detailed in Sec. 7.6.7. The results demonstrated that, after the addition of noise, the distribution of χ^2 values for simulated tracks aligns more closely with that of real data. However, further in-depth investigation of these effects is needed for detailed analysis.

A novel three-dimensional tracking method has been developed and evaluated to enhance the existing two-dimensional tracking technique. The results indicate great promise for this method, as it provides a superior strategy for qualifying tracks

based on criteria such as residue, χ^2 value, track energy, etc. The details of these results can be found in Sec. 7.6.8. A significant difference in the mean residue and chi-square values was observed between the best tracks and the rejected tracks when utilising the 3D tracking method. Concerning the mean track energy values, although the means fell within a similar range, significant variations in the minimum and maximum values were observed in both cases.

In the final part of the chapter (Sec. 7.7), the first results of density measurements achieved with the MURAVES data is summarised. Density measurements were conducted in the "layer1, left" region of Mt. Vesuvius, assuming a density of 2.65 g/cm^3, typical of standard rock. These measurements were carried out using data from four datasets, each corresponding to different working conditions. The resulting densities exhibited variability between datasets, with some deviations exceeding 2 σ, suggesting dataset-specific systematic errors. To address this, the relative density between two regions in the same layer was analysed by computing the ratio $\frac{\rho_{right}}{\rho_{left}}$. The results showed a reduction in dataset disagreements within the 1-2 σ range. Although a density discrepancy was observed in the uppermost layer, indicating higher density on the right side, the significance was only 1.5 σ. Similar findings were noted in deeper layers, where discrepancies existed but with opposite tendencies relative to the first layer, having significance levels of 0.67 and 2 σ for layers 2 and 3, respectively.

MURAVES has accumulated a substantial volume of data over the past year. Analysis efforts are now underway to process this new data, aiming to validate prior findings with enhanced statistical confidence. With the expanded dataset, measurement precision is expected to significantly improve. For the analysis of this new data, the reconstruction algorithm will be adjusted based on the outcomes of simulations, promising more accurate results. Additionlly, the new 3D tracking algorithm will be tested for tracking. A series of simulation studies are still under going and the background contaminations are expected to be filtered out in more effective way profiting from thein-depth simulation studies.

Summary and Outlook

Several upgrades of the CMS RPC system are currently being implemented to ensure a highly performing muon system during the upcoming HL-LHC phase, which will have an increased integrated luminosity of 3000 fb^{-1}. The expected experimental conditions in that period in terms of background rates, event pileup, and the probable ageing of the current detectors present a challenge for the entire CMS detection system. The upgrade includes replacing the present system's readout system and installing two new RPC stations (RE3/1 and RE4/1) in the 3rd and 4th endcap disks of CMS. These new stations feature an improved detector layout compared to the present systems and will also be equipped with an enhanced version of front-end electronics.

Several iRPC prototype and demonstrator chambers were developed and studied in the context of the CMS RPC upgrade. These investigations played a crucial role in validating the technical design of the detectors, finalising the requisite QC procedures for both chamber components and the chambers themselves, and certifying the chambers alongside the newly designed front-end electronics tailored for HL-LHC. All constructed demonstrator chambers successfully passed the QC tests, and four of them were installed and commenced at CMS. The irradiation tests with one of the iRPC chambers at GIF++ yielded highly promising outcomes. Under the expected background rate at the iRPC region (0.7 kHz/cm^2) during the HL-LHC, the chambers showed a 96% detection efficiency at the WP. Even under background conditions three times higher than the expected rate, the chamber maintained an efficiency of approximately 90%. Additionally, essential detector parameters such as detector WP, gamma cluster properties, and position resolution were thoroughly examined under varying background conditions. Following the successful completion of the iRPC demonstrator project, the mass production of iRPCs was initiated. To conduct the iRPC mass production, the CMS RPC lab at UGent was prepared, which included the preparation and calibration of QC setups and training of new team members involved in the assembly. The QC tests for the first set of gas gaps received were performed (73% of the gaps received passed all the QC) and the initial iRPC chambers were produced.

In compliance with EU regulations on F-gases, CERN is actively implementing measures to reduce F-gas consumption and emissions from RPCs, which are significant contributors of GHG emission at CERN. The ECOgas@GIF++ collaboration, established in 2019 and involving ALICE, ATLAS, CMS, LHCb/SHiP, and EP-DT communities, focuses on exploring eco-friendly gas mixtures for RPCs at LHC. Currently testing HFO and CO2-based mixtures, the collaboration assesses detector performance and conducts studies on ageing under varying irradiation conditions at GIF++.

The 2023 test beam at GIF++ included testing the CMS RE1/1 chamber and other detectors with three different gas mixtures (STDmix, ECO2, and ECO3). The analysis included the studies of essential parameters such as the detector WPs, current density, cluster sizes, and muon efficiency under varying irradiation conditions for three gas mixtures. The ECO2 gas mixture showed a steeper trend in WP growth, higher current density at rates exceeding 200 Hz/cm^2 and larger cluster sizes than STDmix. The ECO3, with reduced efficiency, exhibited the most significant reduction in cluster sizes as gamma rates increased, consistently showing lower efficiency than ECO2 and STDmix. The voltage drop across electrodes is identified as a critical factor influencing efficiency. Although ECO2 requires a higher WP, it remains within the limits of CMS power supplies. The detection efficiency of ECO2 is comparable to STDmix and better than ECO3. Considering these facts, ECO2 can be considered a promising candidate for replacing STDmix.

The 2022-2023 ageing campaign investigated the long-term effects of the ECO2 gas mixture on the RPC detectors under high gamma irradiation. The data obtained from the tested detector systems has been analysed, and as of now, there is no definitive evidence of ageing observed. Extended ECO2 chamber testing for 1-2 years is required to assess ageing effects and qualify the gas mixture for RPC operation in HL-LHC, as the total charge integrated in the case of all detectors in the one year period (2022-2023) is below the expected values.

In addition to the CMS RPC activities, the RPC group at UGent is involved in the development of compact and portable gRPCs for conducting muography in confined environments together with the UCL group. These detectors address challenges from logistical constraints and spatial limitations in restricted experimental sites. A novel, cost-effective spray gun-based coating technique was developed in-house, ensuring uniform and stable surface resistivity in the desired range. A preliminary single-gap gRPC version was developed, and its performance was studied, with a comparative analysis conducted against a similar gRPC developed by the UCL team. Despite gas leak issues, repairs enabled operational functionality with a detection efficiency of 94.85% at WP, and the comparison studies, particularly regarding muon cluster properties, demonstrated consistent results. The second iteration, a double-gap gRPC, addressed challenges from the single-gap version with enhancements in design and construction. The qualification tests confirmed its structural integrity and successful operation. Performance studies, including muon cluster properties, demonstrated promising results with a muon efficiency plateauing at approximately 97%. Therefore, this work tackled the significant challenge of constructing a portable gaseous detector, accomplished through the development of the double-gap gRPC, which is not only leak-tight and portable but also offers high detection efficiency.

To develop an advanced gaseous detector-based muon telescope, a six-gap mRPC prototype was built and underwent preliminary tests, demonstrating operational capability with initial noise issues. Repairs were successful in reducing noise levels. Additionally, a Geant4-based simulation was developed for the mRPC-based muon telescope, revealing significant time differences between planes that can be used for PID.

Participating in the MURAVES experiment offered valuable insights into the muography technique for exploring the interior of large-scale objects and the associated challenges of conducting experiments in remote outdoor environments. The objective of the experiment is to examine the internal structure of the summital cone of Mt. Vesuvius by measuring the density distribution in that area. The thesis focuses on the critical task of comparing the actual data obtained from MURAVES with the MC simulations for improving the track reconstruction and imaging of the target. Data analysis of the real data was performed to study the muon cluster properties and track properties. For cosmic muon generation, CRY was chosen as the workhorse, while a role was found for CORSIKA due to its capability to simulate additional effects and quantify the impact of different hadronic interaction models. The challenge of efficiently simulating the passage of muons through a large body like Vesuvius was addressed using PUMAS. To ensure the accuracy of this method, a comparison study between PUMAS and Geant4 was conducted, analysing the energy loss and scattering of muons in rock. A simulation chain encompassing Geant4 simulation, clustering, digitisation, and tracking was established. A comparison was conducted by evaluating χ^2 values and various cluster properties related to the tracks in simulated and real data. While similar trends were observed, minor differences emerged attributed to the simulation not considering experimental effects like dark noise and electronic effects. A study on the particle tracks, excluding muons, within the hodoscope was also conducted. The analysis showed that the particle tracks other than muons have significantly higher χ^2 values of the tracks and cluster multiplicity compared to that of muons. A new 3D tracking method has been developed and evaluated, showing great promise in enhancing the existing 2D technique by providing a superior strategy for qualifying tracks based on criteria such as residue, χ^2 value, track energy, etc. After implementing the noise effects, the simulation results aligned more closely to the real data, suggesting the potential for more accurate density evaluation under real experimental conditions with a detailed exploration of detector noise. The initial results of density measurements using MURAVES data were also discussed. In the uppermost layer of the Mt. Vesuvius crater, a density discrepancy suggesting higher density on the right side was observed, with a significance of only 1.5 σ. Deeper layers showed discrepancies with opposing tendencies relative to the first layer, having significance levels of 0.67 and 2 σ for layers 2 and 3, respectively.

Outlook

The research presented in this thesis addresses diverse challenges faced in particle physics experiments, including detector development, high-rate capability requirements, detector ageing effects, portability of gaseous detectors, and conducting experiments in challenging environmental conditions. The study provides answers and innovative solutions to these multifaceted challenges. In addition, the research also explores the use of several MC simulation tools and event generators such as Geant4, CRY, CORSIKA, PUMAS, etc.

The CMS iRPC Upgrade: The iRPC detectors studied in this thesis will be installed at CMS for the HL-LHC phase during the upcoming EYETS (2024-2025) after the detector's mass production phase. This will improve the triggering efficiency in the high $|\eta|$ region of CMS and increase the redundancy in that region by complementing the existing CSCs. Efforts are underway to combine the improved timing and 2D position information from the iRPCs with the information of the CSCs in the CMS

muon reconstruction algorithm. These iRPCs can also serve as general-purpose detectors for HEP experiments, effectively addressing scenarios with higher particle rates and offering efficient particle triggering due to their excellent intrinsic time resolution.

New eco-friendly Gas Mixtures for RPCs: The investigation into new eco-friendly gas mixtures for RPCs addresses the significant challenge faced by the whole RPC community. ECO2, exhibiting characteristics similar to the standard RPC gas mixture, can already be used as a potential solution for low particle rate experiments such as cosmic ray experiments and muography, where the likelihood of ageing issues is minimal. Initial ageing studies of ECO2 haven't shown any evidence of ageing problems. If the results remain consistent, even under high particle rate conditions in accelerator physics experiments, this new gas mixture holds promise for ensuring the long-term sustainability of RPC technology in particle physics.

Small-scale Portable gRPCs: The inherent logistical challenges of gaseous detectors, including the need for gas mixing units, gas pipes, and associated mechanics for gas connections, as well as continuous gas flow for operation, are effectively addressed by introducing a compact, leak-tight gRPC detector. Innovative in-house methods for component development, such as resistive plates, contribute to cost-effectiveness. The technical design, eliminating the need for an extra detector box and utilising the PCB as a detector box, results in a lightweight and easily manipulatable detector. These attributes make it suitable for muography in confined spaces with installation limitations. Another significant challenge, the high voltage requirements (7000-10000 V) in RPCs, can be successfully addressed by using the new compact and portable CAEN and ISEG HV modules. While a basic portable DAQ is already developed, further R&D is needed for an advanced version capable of extracting signal charge and timing properties, while also meeting the demands of harsh environmental conditions and ensuring portability. The future plans of the project also involve testing the current prototypes developed with eco-friendly gas mixtures.

Advanced Gaseous Detector Telescope for Muography: The advanced gaseous detector telescope concept introduces excellent timing and position resolution, enabling precise muographic measurements. In contrast to standard RPCs, mRPCs are more intricate due to narrower gas gaps and delicate glass plates. The successfully developed mRPC prototype features a gas-tight design and a construction strategy that allows easy manipulation and rotation without affecting the gas gaps. In addition, the superior time resolution (30-150 ps) of mRPCs can be used for PID and background rejection. This eliminates the need for filters like lead or Cherenkov blocks, streamlining the detector setup. The mRPC prototype employs Mylar foil-based spacers, mitigating ageing and dark rate issues observed with the usual fish wire spacers. While mRPCs have a more complex design than RPCs, they remain cost-effective, easy to construct, and suitable for large-area instrumentation, up to a few square meters. Beyond muography, these mRPCs find potential applications in future hadron calorimeter experiments, improving time resolution for studying the time evolution of hadronic showers and enhancing background rejection. This aligns with the ECFA (European Committee for Future Accelerators) R&D roadmap's focus on achieving five-dimensional (3D spatial + energy + time) calorimetry for particle shower reconstruction. Integrating THGEMs into the telescope alongside the

mRPCs will significantly enhance position resolution. The project roadmap encompasses studies investigating the construction of large-area mRPCs and THGEMs and advanced Geant4 simulations building upon the existing framework. These simulations aim to explore the usage of timing information for PID and background rejection.

The MURAVES experiment: The MURAVES experiment has accumulated substantial data over the past three years, and efforts are underway to analyse the complete dataset. The new 3D tracking method and background rejection strategies developed as part of the research discussed in this thesis will enhance the quality of density evaluation. The entire simulation chain, except the inclusion of the volcano's structure, is ready. The background simulation studies using PUMAS and MUSIC are progressing, and the most suitable technique will be integrated into the simulation chain. Future plans for the project also involve upgrading the SiPMs in the MURAVES detectors due to issues such as high dark noise and malfunctioning after three years of operation. Additionally, there is a proposal to replace the current lead wall filter with a water Cherenkov detector. Compared to lead wall, the Cherenkov detector provides more detailed information on particle shower properties, enabling the potential for PID and enhanced background rejection based on PID.

Nederlandstalige samenvatting

Deze scriptie verkent toepassingen van deeltjesdetectoren, waarbij de link wordt gelegd tussen fundamentele natuurkunde en interdisciplinaire vakgebieden, en waarbij de veelzijdige impact wordt geïllustreerd van detectortechnologie op het begrip van het universum en op diverse andere gebieden. Het hier gepresenteerde werk omvat studies over detectorontwerp en data-analyse die zijn uitgevoerd zowel voor de Fase-2 upgrade van het CMS experiment op de LHC (Deel I) als voor Muografie (Deel II).

Momenteel worden verschillende upgrades van het CMS RPC-systeem geïmplementeerd om een goede werking van de muondetectoren te garanderen tijdens de aankomende HL-LHC-fase, die een verhoogde geïntegreerde luminositeit van 3000 fb^{-1} met zich mee zal brengen. De verwachte experimentele omstandigheden in die periode, zoals de hoeveelheid ruis, aantal overlappende events en de voorziene degradering van de huidige detectoren, vormen een uitdaging voor het gehele CMS-detectiesysteem. De upgrade omvat het vervangen van het huidige uitleessysteem en het installeren van twee nieuwe RPC-stations (RE3/1 en RE4/1) in de 3e en 4e uiteinde-schijven van CMS. Deze nieuwe stations hebben verbeterde detectoren in vergelijking met de huidige systemen en worden ook uitgerust met een verbeterde versie van de front-end elektronica.

Verschillende prototypes en demonstratiemodellen voor de iRPC zijn ontwikkeld en bestudeerd in het kader van de CMS RPC-upgrade. Deze studies speelden een cruciale rol bij het valideren van het technische ontwerp van de detectoren, het finaliseren van de vereiste QC-procedures, zowel voor detectorcomponenten als voor de geassembleerde detector, en het certificeren van de detectoren samen met de nieuw ontworpen front-end elektronica afgestemd op HL-LHC. Alle gebouwde demonstratiemodellen slaagden met succes voor de QC-tests, en vier ervan werden geïnstalleerd en opgestart in CMS. De bestralingstests met een van de iRPC-detectoren in GIF++ leverden veelbelovende resultaten op. Onder de verwachte hoeveelheid achtergrondstraling op de positie van de iRPC's tijdens de HL-LHC (0,7 kHz/cm^2), vertoonden de detectoren een detectie-efficiëntie van 96% bij het voorziene werkingspunt. Zelfs met een achtergrondstraling die drie keer hoger was dan de verwachte flux, behield de detector een efficiëntie van ongeveer 90%. Daarnaast werden essentiële detectieparameters zoals het werkingspunt, de eigenschappen van de gamma-clusters en positieresolutie grondig onderzocht onder variërende omstandigheden van de achtergrondstraling. Na het succesvol afronden van het iRPC-demonstratieproject werd de massaproductie van iRPC's opgestart. Daartoe werd het CMS RPC-lab aan UGent voorbereid, inclusief de voorbereiding en kalibratie van QC-opstellingen en de opleiding van nieuwe teamleden die betrokken zijn bij de assemblage. De QC-tests voor de eerste ontvangen set van gasholtes werden uitgevoerd (73% van de ontvangen gasholtes slaagde voor alle QC-tests) en de eerste iRPC-detectoren werden geproduceerd.

In naleving van de EU-regelgeving inzake F-gassen implementeert CERN actief maatregelen om het verbruik en de uitstoot van F-gassen in RPC's, die een aanzienlijke bijdrage vormen van de uitstoot van broeikasgassen door CERN, te verminderen. De ECOgas@GIF++-samenwerking, opgericht in 2019 en met deelname van ALICE, ATLAS, CMS, LHCb/SHiP en de EP-DT-gemeenschappen, richt zich op het verkennen van milieuvriendelijke gasmengsels voor RPC's in de LHC. Momenteel worden HFO- en CO2-gebaseerde mengsels getest, waarbij zowel de prestaties van de detector als verouderingseffecten onder variërende bestralingsomstandigheden in GIF++ bestudeerd worden.

Met behulp van de deeltjesflux voor testdoeleinden van 2023 in GIF++ werden de CMS RE1/1 en andere detectoren getest met drie verschillende gasmengsels (STDmix, ECO2 en ECO3). De analyse omvatte studies van essentiële parameters zoals het werkingspunt van de detector, stroomdichtheid, clustergroottes en muonefficiëntie onder variërende bestralingsomstandigheden voor de drie gasmengsels. Het ECO2-gasmengsel vertoonde een steilere trend in verhoging van het werkingspunt, een hogere stroomdichtheid bij fluxen boven 200 Hz/cm^2 en grotere clusters dan STDmix. Het ECO3-mengsel, met verminderde efficiëntie, vertoonde de meest significante vermindering van clustergroottes bij toenemende gammaflux, waarbij het een consistent lagere efficiëntie vertoonde dan ECO2 en STDmix. De spanningsval tussen elektroden is een kritische factor die efficiëntie beïnvloedt. Hoewel ECO2 een hoger werkingspunt vereist, blijft het binnen de limieten van de stroomvoorziening van CMS. De detectie-efficiëntie van ECO2 is vergelijkbaar met STDmix en beter dan ECO3. Gezien deze feiten kan ECO2 worden beschouwd als een veelbelovende kandidaat voor het vervangen van STDmix.

Tijdens een testperiode in 2022-2023 werden de langetermijneffecten onderzocht van het ECO2-gasmengsel op de RPC-detectoren onder hoge gammabestraling. De verkregen gegevens van de geteste detectiesystemen zijn geanalyseerd, en tot nu toe is er geen definitief bewijs van degradering waargenomen. Uitgebreide tests van ECO2-detectors gedurende 1-2 jaar zijn vereist om mogelijke verouderingseffecten in te schatten en het gasmengsel te kwalificeren voor gebruik in de RPC's in de HL-LHC, aangezien de totale geïntegreerde lading in voornoemde tests onder de verwachte waarden ligt.

Naast de CMS RPC-activiteiten is de RPC-groep aan UGent, samen met de groep aan UCL, betrokken bij de ontwikkeling van compacte en draagbare gRPC's voor muografie. Deze detectoren pakken uitdagingen aan van logistieke en ruimtelijke beperkingen op moeilijk toegankelijke experimentele locaties. Een innovatieve, kosteneffectieve spuitpistool-gebaseerde coatingtechiek werd hier ontwikkeld, waardoor een uniforme en stabiele oppervlakteweerstand binnen het gewenste bereik wordt gegarandeerd. Een voorlopige versie van de single-gap gRPC werd ontwikkeld en de prestaties ervan werden bestudeerd in een vergelijkende analyse ten opzichte van een vergelijkbare gRPC ontwikkeld door het UCL-team. Na initiële gaslekproblemen maakten reparaties operationele functionaliteit mogelijk met een detectie-efficiëntie van 94,85% bij het werkingspunt, en de vergelijkende studies, met name met betrekking tot de eigenschappen van de muonclusters, toonden consistente resultaten. De tweede iteratie, een double-gap gRPC, leerde uit de problemen van

de single-gap versie met verbeteringen in ontwerp en constructie. De kwalificatietests bevestigden de structurele integriteit en succesvolle werking. Prestatiestudies, inclusief muonclusterkaraketerisatie, toonden veelbelovende resultaten met een muonefficiëntie die plafonneert op ongeveer 97%. Samenvattend heeft dit werk de aanzienlijke uitdaging aangepakt om een draagbare gasgevulde detector te ontwerpen, culminerend in de ontwikkeling van de double-gap gRPC, die niet alleen lekvrij en draagbaar is, maar ook een hoge detectie-efficiëntie biedt.

Om een geavanceerde muontelescoop gebaseerd op gasgevulde detectoren te ontwikkelen, werd een zes-gap mRPC-prototype gebouwd en aan voorlopige tests onderworpen, waarbij operationele mogelijkheden werden aangetoond ondanks aanvankelijke problemen met ruis. Reparaties slaagden erin om ruisniveaus te verminderen. Daarnaast werd een Geant4 simulatie ontwikkeld voor de mRPC-muontelescoop, waarbij significante tijdsverschillen tussen de verschillende lagen werden gevonden, die kunnen worden gebruikt voor PID.

Deelname aan het MURAVES-experiment bood waardevolle inzichten in de muografietechniek voor het verkennen van de interne structuur van grootschalige objecten en de bijbehorende uitdagingen waarmee het uitvoeren van experimenten in afgelegen buitenomgevingen gepaard gaan. Het doel van het experiment is het onderzoeken van de interne structuur van de topkegel van de Vesuvius door de dichtheidsverdeling in dat gebied te meten. Deze scriptie richt zich op de cruciale taak om de werkelijke gegevens van MURAVES te vergelijken met de MC-simulaties om de reconstructie van tracks en de beeldvorming van het doelwit te verbeteren. De reële data werden geanalyseerd om de eigenschappen van muonclusters en tracks te bestuderen. Voor de generatie van kosmische muonen werd CRY gekozen, terwijl een aanvullende rol werd gevonden voor CORSIKA vanwege zijn vermogen om bijkomende effecten te simuleren en de impact van verschillende hadronische interactiemodellen te kwantificeren. De uitdaging om efficiënt de doorgang van muonen door een groot lichaam zoals de Vesuvius te simuleren, werd aangepakt met behulp van PUMAS. Om de nauwkeurigheid van deze methode te waarborgen, werd een vergelijkende studie tussen PUMAS en Geant4 uitgevoerd, waarbij het energieverlies en de verstrooiing van muonen in rots werden geanalyseerd. Een simulatieketen inclusief clustering, digitalisering en tracking werd opgezet in Geant4, waarmee een vergelijking werd uitgevoerd van de χ^2-waarden en van verschillende clustereigenschappen van gesimuleerde tracks ten opzichte van die uit reële gegevens. Hoewel vergelijkbare trends werden waargenomen, werden kleine verschillen zichtbaar die konden worden toegeschreven aan het feit dat de simulatie geen rekening hield met bepaalde experimentele effecten zoals donkere ruis en elektronica-effecten. Een studie van de tracks van andere passerende deeltjes dan muonen binnen de hodoscoop werd ook uitgevoerd. De analyse toonde aan dat de tracks van andere deeltjes dan muonen aanzienlijk hogere χ^2-waarden en clustermultipliciteit hebben vergeleken met die van muonen. Een nieuwe 3D-trackingmethode werd ontwikkeld en geëvalueerd, met veelbelovende resultaten die laten zien dat deze methode de bestaande 2D-techniek kan verbeteren door een superieure strategie te bieden voor het kwalificeren van tracks op basis van criteria zoals residu, χ^2-waarde, track-energie, enzovoort. Na het implementeren van de ruiseffecten sloten de simulatieresultaten nauwer aan bij de echte gegevens, wat wijst op het potentieel voor een nauwkeurigere evaluatie van de dichtheid onder echte experimentele omstandigheden door middel van het gedetailleerd bestuderen

van detectorruis. De initiële resultaten van de dichtheidsmetingen met behulp van MURAVES-data worden ook besproken. In de bovenste laag van de krater van de Vesuvius werd een dichtheidsverschil waargenomen dat wijst op een hogere dichtheid aan de zuidelijke kant, met een significantie van slechts 1,5 σ. Diepere lagen vertoonden tegenstrijdigheden met tegenovergestelde neigingen ten opzichte van de eerste laag, met significantieniveaus van 0,67 en 2 σ voor respectievelijk lagen 2 en 3.

Uitzicht

Het onderzoek dat in deze scriptie wordt gepresenteerd, behandelt uiteenlopende uitdagingen in de experimentele deeltjesfysica, waaronder de ontwikkeling van detectoren, vereisten voor hoogfrequente metingen, verouderingseffecten van detectoren, draagbaarheid van gasdetectoren en het uitvoeren van experimenten onder uitdagende milieuomstandigheden. De studie biedt antwoorden en innovatieve oplossingen voor deze veelzijdige uitdagingen. Daarnaast verkent het onderzoek ook het gebruik van verschillende MC-simulatietools en event-generatoren zoals Geant4, CRY, CORSIKA, PUMAS, enz.

De CMS iRPC Upgrade: De iRPC-detectoren die in deze scriptie worden bestudeerd, zullen worden geïnstalleerd in CMS voor de HL-LHC-fase tijdens de aankomende EYETS (2024-2025), na de massaproductiefase. Dit zal de efficiëntie van de triggering verbeteren in de hoge $|\eta|$-regio van CMS en de redundantie in dat gebied vergroten door de aanvulling op de bestaande CSC's. Ondertussen worden inspanningen geleverd om de verbeterde timing- en 2D-positie-informatie van de iRPC's te combineren met de informatie van de CSC's in het reconstructiealgoritme voor muonen in CMS. Deze iRPC's kunnen ook dienen als algemene detectoren voor HEP-experimenten, waarbij op effectieve wijze wordt ingespeeld op scenario's met hogere deeltjesfluxen en efficiënte triggering vanwege hun uitstekende intrinsieke tijdsresolutie.

Nieuwe milieuvriendelijke gasmengsels voor RPC's: Het onderzoek naar nieuwe milieuvriendelijke gasmengsels voor RPC's pakt de aanzienlijke uitdaging aan waar-

mee de hele RPC-gemeenschap wordt geconfronteerd. ECO2, met kenmerken vergelijkbaar met het standaard RPC-gasmengsel, kan al worden gebruikt als een potentiële oplossing voor experimenten met een lage deeltjesstroom, zoals kosmischestralingsexperimenten en muografie, waar de kans op verouderingsproblemen minimaal is. Initiële degraderingsstudies van ECO2 hebben geen bewijs van verouderingsproblemen aangetoond. Als de resultaten consistent blijven, zelfs onder omstandigheden van hogere deeltjesstromen in experimenten met deeltjesversnellers, biedt dit nieuwe gasmengsel hoop op de duurzaamheid van RPC-technologie in de deeltjesfysica.

Kleine, draagbare gRPC's: De inherente logistieke uitdagingen van gasdetectoren, waaronder de behoefte aan gasmengeenheden, gasleidingen, en bijbehorende mechanische structuren voor gastransport, evenals een continue gasstroom voor een correcte werking, worden op effectieve wijze aangepakt door de introductie van een compacte, lekdichte gRPC-detector. Innovatieve zelfontwikkelde methoden voor

het produceren van componenten, zoals resistieve platen, dragen bij aan kosteneffectiviteit. Het technische ontwerp, waarbij de noodzaak van een extra detectorbehuizing wordt geëlimineerd en de PCB zelf als een detectorbehuizing wordt gebruikt, resulteert in een lichte en gemakkelijk hanteerbare detector. Deze kenmerken maken de gRPC geschikt voor muografie in moeilijk toegankelijke ruimtes met beperkingen op het installeren van apparatuur. Een andere belangrijke uitdaging, de hoge vereiste elektrische spanning (7000-10000 V) in RPC's, kan succesvol worden aangepakt door het gebruik van de nieuwe compacte en draagbare CAEN- en ISEG-HV-modules. Hoewel er al een basisversie van draagbare DAQ is ontwikkeld, is verder onderzoek en ontwikkeling nodig voor een geavanceerde versie die in staat is om signaallading en timing-eigenschappen te extraheren, terwijl ook wordt voldaan aan de eisen van moeilijke milieuomstandigheden en draagbaarheid. De toekomstplannen van het project omvatten ook het testen van de huidige prototypes ontwikkeld met milieuvriendelijke gasmengsels.

Geavanceerde gasgevulde detector-telescoop voor muografie: Het concept van de geavanceerde gasgevulde detector-telescoop introduceert uitstekende timing- en positieresolutie, waardoor nauwkeurige muografische metingen mogelijk zijn. In tegenstelling tot standaard RPC's zijn mRPC's ingewikkelder vanwege smallere gasholtes en delicate glazen platen. Het succesvol ontwikkelde mRPC-prototype heeft een gasdicht ontwerp en een constructiestrategie die gemakkelijke manipulatie en rotatie mogelijk maakt zonder het risico op het beschadigen van de gasholtes. Bovendien kan de superieure tijdsresolutie (30-150 ps) van mRPC's worden gebruikt voor PID en het verwerpen van achtergrondstraling. Dit elimineert de noodzaak van filters zoals lood of Cherenkov-blokken, waardoor de detectoropstelling wordt gestroomlijnd. Het mRPC-prototype maakt gebruik van Mylarfolies als tussenlagen, waardoor de problemen met degradering en donkerstroom zoals die werden waargenomen bij de gebruikelijke visdraadlagen, worden verminderd. Hoewel mRPC's een complexer ontwerp hebben dan RPC's, blijven ze kosteneffectief, gemakkelijk te construeren en geschikt voor grootschalige instrumentatie, tot een paar vierkante meter. Naast muografie vinden deze mRPC's potentiële toepassingen in toekomstige hadron-calorimeterexperimenten, waarbij ze de tijdsresolutie kunnen verbeteren om de ontwikkeling van hadronische cascades te bestuderen en om het verwerpen van achtergrondsignalen te verbeteren. Dit sluit aan bij de R&D-richtlijnen van het ECFA (European Committee for Future Accelerators), met als doel het bereiken van vijfdimensionale (3D ruimtelijk + energie + tijd) calorimetrie voor de reconstructie van deeltjescascades. Het integreren van THGEM's in de telescoop naast de mRPC's zal de positieresolutie aanzienlijk verbeteren. Het projectplan omvat studies die de constructie van grootschalige mRPC's en THGEM's onderzoeken en geavanceerde Geant4-simulaties ontwikkelen op basis van het bestaande kader. Deze simulaties beogen het gebruik van timing-informatie voor PID en achtergrondverwerping te verkennen.

Het MURAVES-experiment: Het MURAVES-experiment heeft de afgelopen drie jaar aanzienlijke gegevens verzameld, en er wordt gewerkt aan de analyse van de volledige dataset. De nieuwe 3D-trackingmethode en strategieën voor achtergrondverwerping die zijn ontwikkeld als onderdeel van het in deze scriptie besproken onderzoek, zullen de kwaliteit van de densiteitsinschatting verbeteren. De volledige simulatieketen, behalve de inclusie van de structuur van de vulkaan, is gereed. De

studies naar simulatie van achtergrondprocessen met behulp van PUMAS en MUSIC vorderen, en de meest geschikte techniek zal worden geïntegreerd in de simulatieketen. Toekomstplannen voor het project omvatten ook het upgraden van de SiPM's in de MURAVES-detectoren vanwege problemen zoals hoge donkere ruis en gebreken na drie jaar gebruik. Daarnaast is er een voorstel om de huidige loodwandfilter te vervangen door een Cherenkov-detector met water. In vergelijking met de loodwand biedt de Cherenkov-detector meer gedetailleerde informatie over de eigenschappen van de deeltjescascade, waardoor het potentieel voor PID en verbeterde achtergrondverwerping op basis van PID wordt vergroot.

Acknowledgments

I was born and raised in a small village in southern India. Joining this PhD program was a significant turning point in my life. Everything around me was new and different from what I had experienced or seen until then. I was in a new country with a totally different culture and lifestyle. I knew very few people here. I ate food which I had never heard of or seen before. It was a journey both exciting and scary that I had set off. These four years of PhD life have not only refined my skills as a researcher but also transformed me into a better person in several ways. The whole period was very fruitful and joyous due to the support of many individuals in both my professional and personal life. I would like to express my sincere gratitude to all of them.

I begin by thanking Michael, my supervisor, who has shown unwavering support from the very first day of my PhD until now. Michael, you have been a constant presence, guiding me through every major step of my research journey. Your support to engage in diverse research projects and explore my own ideas truly allowed me to blossom into a confident and capable researcher. Moreover, you have been more than just a mentor; you've been a great friend. Thanks a bunch for all the fun and adventures, and for putting up with my hilarious attempts to master skiing ;)

Being involved in various projects allowed me to connect with a wide range of people beyond Ghent University, many of whom have become close friends. I'm grateful to the entire CMS RPC team for the wonderful times we've shared. Gabriella and Salvatore, thank you for your guidance and support throughout my career journey. And to Salvadore, Mehar, Maxime, Anton, Ivan, Kyong Sei, Ece, Mauricio, Mariana, Kevin, Mapse, Cecelia, Reham, and Joao, thank you for your collaboration and teamwork. A special shout-out to Mariana and Ece - our girls' time has always been a highlight, and I deeply appreciate your constant support and friendship. Also, thanks to Jan for his help, dedication, and always being available whenever needed.

I want to express my heartfelt gratitude to the UCL muography team. Andrea and Eduardo, your guidance and our insightful discussions have been invaluable to me. And to Marwa, Ishan, Samip, Maxime, and Vishal, I'm truly grateful for your friendship and all the fun times we've shared.

I also want to thank the entire MURAVES team, with a special mention to Giulio, Gigi, Mariaelena, Giovanni, and Flora. Working alongside all of you has been an incredible experience, and I'm truly grateful for the opportunity. A big thank you for your warm hospitality during our visit to Naples. Exploring Mt. Vesuvius and the national park with your guidance was a privilege, and learning about the volcano's geological insights from each of you was truly fascinating.

I thank the RPC ECOgas@GIF++ team for the great teamwork. Special thanks to Davide, Mapse, Alessandra, Luca, and Dayron for their collaboration and engaging discussions.

I also want to express my gratitude to Deepak, my Master's thesis supervisor from Central University of Karnataka, for introducing the world of particle detectors and inspiring me to aim high and pursue my dreams.

In Ghent, throughout my PhD journey, I was the only PhD student working on RPCs. Despite this, I never felt alone in my work. Michael was there, and alongside him were Patrick and Yves, our dedicated technical staff, who consistently offered their expertise and brainstormed with me to bring our projects to fruition. Patricko and Yveii, you both were not just colleagues but also dear friends with whom I shared many enjoyable moments. Together, the four of us formed an incredible team.

Big thanks to Christos and Yanwen for not only being amazing teammates but also wonderful friends. Christaniiii, the COVID time at INW would have been much more boring without you there, and Yanwen, thank you for sharing so many wonderful moments together.

I'd like to thank Didar for being a wonderful colleague throughout the past four years. Thank you, Didar, for always encouraging me and for organising those nice cooking sessions!

I also want to thank 'BROSONS' - Luka, Liam, Niels, and David - for making our office days so much funnier. And a special thanks to Joscha for being the fun-time coordinator. Luka and Liam, thanks for being great friends, especially during the stressful last period of the PhD journey. Niels, I'll definitely miss your cookies, and even more so, the look on your face when I snatch them up! :D. Also Bob, you were the first person to give me a full tour of Ghent and also thanks a lot for all those good little chit chat time we shared at INW. Thanks for being a nice friend :)

I want to extend a huge thanks to my "biggg" brother Ivan. Your strong support has meant a lot to me, even if you scared me in the corridors over 100 times! But hey, it was all in good fun, right? :D Thank you for being my driving instructor and for making all those "we are gonnaaaa diee" moments so funny!

And to my girls, Caori and Nilufar, thank you both from the bottom of my heart for the wonderful moments we've shared and for always being there for me when I needed support. And also to Ray, Wiebe, Omid, and Yennii, all those dinner and game nights we've all had together are some of the best memories of my PhD life.

I also want to thank my Ghent Family-Ranjithettan, Jiji chechi, Aradhya, Nithin ettan, Vinduja, Femi, and Akhil. You've been the main reason I've never felt lonely in Ghent. Ranjithietta and Jiji chechi, thanks a million for those legendary kanji nights ;D, and always showing endless love and support towards us. Nithin etta and Femi, thank you for all the funny, silly, and crazy times we've shared together and for the dynamic duo I can rely on, no matter how absurd the situation, even if it's in the

dead of night. Also thanks to Manjari chechi and Nikhil ettan for being a part of my Ghent life and for all the good memories.

And a big shout-out to my crazy pack - Rufa, Shiva, and Manju! Who would've thought we'd all end up in Europe together after leaving India? What we had back home was just a taste of the lifetime of friendship we were in for! Thanks for being my partners in crime, my go-to for laughs, and for all the wacky adventures and ridiculous moments we've shared. Here's to many more escapades and belly laughs together! Manju, you have been my rock, my cheerleader, and my cocoon, no matter the ups and downs. Thanks for all those fun and adventures we had and I'm eagerly awaiting many more to come!

Last but certainly not least, Pappa, Amma, and Appu, my "big" little world. Without your love and support, I wouldn't be where I am today. Since childhood, Pappa and Amma, you've encouraged me to chase my dreams, no matter the odds. I feel incredibly lucky to have you all in my life, and I can't thank you enough for simply being yourselves and embracing me for who I am.

Bibliography

[1] A Samalan *et al.*, "Improved resistive plate chambers for hl-lhc upgrade of cms," *Nuclear Instruments and Methods in Physics Research Section A: Accelerators, Spectrometers, Detectors and Associated Equipment*, p. 169 075, 2024.

[2] A. Samalan *et al.*, "Small-area portable resistive plate chambers for muography (submitted)," *Journal of Advanced Instrumentation in Science*, 2023. arXiv: 2311.11451.

[3] A. Samalan *et al.*, "Exploring advanced detector technologies for muon radiography applications," in *2022 IEEE Nuclear Science Symposium and Medical Imaging Conference (NSS/MIC)*, IEEE, 2022, pp. 1–8.

[4] A Samalan *et al.*, "End-to-end simulations of the muon radiography of vesuvius experiment," *Journal of Instrumentation*, vol. 17, no. 01, p. C01015, 2022.

[5] A Samalan *et al.*, "Upgrade of the cms resistive plate chambers for the high luminosity lhc," *Journal of Instrumentation*, vol. 17, no. 01, p. C01011, 2022.

[6] A Samalan, C. Collaboration, *et al.*, "Improved resistive plate chambers for the upgrade of the cms muon detector," in *Journal of Physics: Conference Series*, IOP Publishing, vol. 2374, 2022, p. 012 006.

[7] A. V. Lanyov, C. collaboration, *et al.*, "Cms collaboration results: Higgs boson and search for new physics," *Physics-Uspekhi*, vol. 57, no. 9, p. 923, 2014.

[8] A. Collaboration *et al.*, "Observation of a new particle in the search for the standard model higgs boson with the atlas detector at the lhc," *arXiv preprint arXiv:1207.7214*, 2012.

[9] L. Evans and P. Bryant, "Lhc machine," *Journal of instrumentation*, vol. 3, no. 08, S08001, 2008.

[10] K. Hübner, "Designing and building lep," *Physics reports*, vol. 403, pp. 177–188, 2004.

[11] B. Müller, J. Schukraft, and B. Wysłouch, "First results from pb+ pb collisions at the lhc," *Annual Review of Nuclear and Particle Science*, vol. 62, pp. 361–386, 2012.

[12] C. A. Salgado and J. P. Wessels, "Proton–lead collisions at the cern lhc," *Annual Review of Nuclear and Particle Science*, vol. 66, pp. 449–473, 2016.

[13] M. Schaumann *et al.*, "First xenon-xenon collisions in the lhc," in *9th International Particle Accelerator Conference, p. MOPMF039*, 2018.

[14] M. Darbin, "Stanford accelerator conference 199 report on the ixth international conference on high energy accel erators covering the performance of accelerators and storage rings now in operation, progress in construction of new machines, development work on superconductivity for radio-frequency and," *CERN COURIER*, vol. 14, no. 6, 1974.

[15] M. Q. Barton, "Acceleration of heavy ions in the ags and cba," Brookhaven National Lab., Tech. Rep., 1983.

[16] L Rossi, "The lhc superconducting magnets," in *Proceedings of the 2003 Particle Accelerator Conference*, IEEE, vol. 1, 2003, pp. 141–145.

[17] A Airapetian *et al.*, *ATLAS detector and physics performance: Technical Design Report, 1*. ATLAS-TDR-014, 1999.

[18] G. L. Bayatian *et al.*, *CMS Physics: Technical Design Report Volume 1: Detector Performance and Software* (Technical design report. CMS). Geneva: CERN, 2006, There is an error on cover due to a technical problem for some items. [Online]. Available: `https://cds.cern.ch/record/922757`.

[19] B Abelev *et al.*, "Technical Design Report for the Upgrade of the ALICE Inner Tracking System," Tech. Rep., 2014. DOI: `10.1088/0954-3899/41/8/087002`. [Online]. Available: `https://cds.cern.ch/record/1625842`.

[20] R Antunes-Nobrega *et al.*, *LHCb reoptimized detector design and performance: Technical Design Report* (Technical design report. LHCb). Geneva: CERN, 2003. [Online]. Available: `https://cds.cern.ch/record/630827`.

[21] D. Boussard and T. P. R. Linnecar, "The lhc superconducting rf system," Tech. Rep., 1999.

[22] "Cern accelerator complex," [Online]. Available: `https://commons.wikimedia.org/wiki/File:Cern-accelerator-complex.svg`.

[23] C. Collaboration *et al.*, "The cms experiment at the cern lhc," *Jinst*, vol. 3, S08004, 2008.

[24] S. Chatrchyan *et al.*, "Observation of a new boson at a mass of 125 gev with the cms experiment at the lhc," *Physics Letters B*, vol. 716, no. 1, pp. 30–61, 2012.

[25] T. Sakuma and T. McCauley, "Detector and event visualization with sketchup at the cms experiment," in *Journal of Physics: Conference Series*, IOP Publishing, vol. 513, 2014, p. 022 032.

[26] V Karimäki, "The cms tracker system project: Technical design report," CMS-TDR-005, Tech. Rep., 1997.

[27] K. Z. Gumus, "Search for new physics in the compact muon solenoid (cms) experiment and the response of the cms calorimeters to particles and jets," Ph.D. dissertation, Texas Tech University, 2008.

[28] C. Biino, "The cms electromagnetic calorimeter: Overview, lessons learned during run 1 and future projections," in *Journal of Physics: Conference Series*, IOP Publishing, vol. 587, 2015, p. 012 001.

[29] J Mans, "Cms technical design report for the phase 1 upgrade of the hadron calorimeter," CMS-TDR-010, Tech. Rep., 2012.

[30] A. Benaglia, "The cms ecal performance with examples," *Journal of Instrumentation*, vol. 9, no. 02, p. C02008, 2014.

[31] M. Rieger, "Search for tt–h production in the h→ bb,"

[32] J. Goh *et al.*, "Cms rpc tracker muon reconstruction," *Journal of Instrumentation*, vol. 9, no. 10, p. C10027, 2014.

[33] A. Fagot, "Consolidation and extension of the cms resistive plate chamber system in view of the high-luminosity lhc upgrade," Ph.D. dissertation, Ghent University, 2020.

[34] "Cms rpc plots-twiki page," [Online]. Available: `https://twiki.cern.ch/twiki/bin/view/CMSPublic/RPCPlots`.

[35] T. Bawej *et al.*, "The new cms daq system for run-2 of the lhc," *IEEE Transactions on Nuclear Science*, vol. 62, no. 3, pp. 1099–1103, 2015.

[36] C. collaboration *et al.*, "The cms trigger system," *arXiv preprint arXiv:1609.02366*, 2016.

[37] J. Brooke, "Performance of the cms level-1 trigger," *arXiv preprint arXiv:1302.2469*, 2013.

[38] T. Virdee, A. Ball, and A. Petrilli, "Cms high level trigger," Tech. Rep., 2007.

[39] "The Phase-2 Upgrade of the CMS Muon Detectors," 2017, This is the final version, approved by the LHCC. [Online]. Available: https://cds.cern.ch/record/2283189.

[40] M. Jeitler, "The phase-2 upgrade of the hardware trigger of cms at the lhc," *Journal of Instrumentation*, vol. 15, no. 09, p. C09009, 2020.

[41] S. R. Chowdhury, C. collaboration, *et al.*, "The phase-2 upgrade of the cms outer tracker," *Nuclear Instruments and Methods in Physics Research Section A: Accelerators, Spectrometers, Detectors and Associated Equipment*, vol. 979, p. 164 432, 2020.

[42] D Contardo, M Klute, J Mans, L Silvestris, and J Butler, "Technical Proposal for the Phase-II Upgrade of the CMS Detector," Geneva, Tech. Rep., 2015. DOI: 10.17181/CERN.VU8I.D59J. [Online]. Available: https://cds.cern.ch/record/2020886.

[43] "The Phase-2 Upgrade of the CMS Tracker," CERN, Geneva, Tech. Rep., 2017. DOI: 10.17181/CERN.QZ28.FLHW. [Online]. Available: https://cds.cern.ch/record/2272264.

[44] "The Phase-2 Upgrade of the CMS Endcap Calorimeter," CERN, Geneva, Tech. Rep., 2017. DOI: 10.17181/CERN.IV8M.1JY2. [Online]. Available: https://cds.cern.ch/record/2293646.

[45] "The Phase-2 Upgrade of the CMS Barrel Calorimeters," CERN, Geneva, Tech. Rep., 2017, This is the final version, approved by the LHCC. [Online]. Available: https://cds.cern.ch/record/2283187.

[46] M. Jeitler, "The upgrade of the cms trigger system," *Journal of Instrumentation*, vol. 9, no. 08, p. C08002, 2014.

[47] J. G. Hegeman, "The cms data acquisition system for the phase-2 upgrade," Tech. Rep., 2018.

[48] A. Triossi, "Electronics Developments for Phase-2 Upgrade of CMS Drift Tubes," CERN, Geneva, Tech. Rep., 2018. [Online]. Available: https://cds.cern.ch/record/2645761.

[49] M. B. Kiani, "Upgrade of the Drift Tube (DT) Muon System for the CMS Detector at the HL-LHC," CERN, Geneva, Tech. Rep., 2023. DOI: 10.22323/1.414.0934. [Online]. Available: https://cds.cern.ch/record/2841566.

[50] M. B. Kiani, "The upgrade of the CMS muon system for the High Luminosity LHC," CERN, Geneva, Tech. Rep., 2023. [Online]. Available: https://cds.cern.ch/record/2884268.

[51] Y. Haddad, "Upgrade of the CSC Muon System for the CMS Detector at the HL-LHC," CERN, Geneva, Tech. Rep., 2022. DOI: 10.22323/1.398.0837. [Online]. Available: https://cds.cern.ch/record/2797652.

[52] B Boghrati *et al.*, "New slow control emulator for the CMS phase-2 upgrade RPC link system," *Nucl. Instrum. Methods Phys. Res., A*, vol. 1052, p. 168 268, 2023. DOI: 10.1016/j.nima.2023.168268. [Online]. Available: https://cds.cern.ch/record/2856429.

[53] B Boghrati *et al.*, "Cms phase-ii upgrade of the rpc link system," *Journal of Instrumentation*, vol. 16, no. 05, p. C05003, 2021.

[54] J. G. Layter, *The CMS muon project: Technical Design Report* (Technical design report. CMS). Geneva: CERN, 1997. [Online]. Available: https://cds.cern.ch/record/343814.

[55] F. Bradamante, "The compass experiment at cern: Present and future," *Nuclear Physics B-Proceedings Supplements*, vol. 154, no. 1, pp. 86–98, 2006.

[56] R. Bouclier *et al.*, "The gas electron multiplier (gem)," *IEEE Transactions on Nuclear Science*, vol. 44, no. 3, pp. 646–650, 1997.

[57] A Colaleo, A Safonov, A Sharma, and M Tytgat, "CMS Technical Design Report for the Muon Endcap GEM Upgrade," Tech. Rep., 2015. [Online]. Available: https://cds.cern.ch/record/2021453.

[58] P. Verwilligen, "Gem detectors for the cms endcap muon system: Status of three new detector stations," *arXiv preprint arXiv:2303.17244*, 2023.

[59] L. Malter, "Thin film field emission," *Physical Review*, vol. 50, no. 1, p. 48, 1936.

[60] R Guida, "Gif++: The new cern irradiation facility to test large-area detectors for hl-lhc," in *2015 IEEE Nuclear Science Symposium and Medical Imaging Conference (NSS/MIC)*, IEEE, 2015, pp. 1–4.

[61] D. R. Ferrero *et al.*, "Irradiation aging of the cms drift tube muon detector," *Radiation Physics and Chemistry*, vol. 172, p. 108 747, 2020.

[62] B. Wang *et al.*, "Longevity studies and phase 2 electronics upgrade for cms cathode strip chambers in preparation for hl-lhc," *Nuclear Instruments and Methods in Physics Research Section A: Accelerators, Spectrometers, Detectors and Associated Equipment*, vol. 958, p. 162 279, 2020.

[63] R Aly *et al.*, "Latest results of longevity studies on the present cms rpc system for hl-lhc phase," *Nuclear Instruments and Methods in Physics Research Section A: Accelerators, Spectrometers, Detectors and Associated Equipment*, p. 168 452, 2023.

[64] L. Quaglia *et al.*, "Eco-friendly resistive plate chambers for detectors in future hep applications," *Nuclear Instruments and Methods in Physics Research Section A: Accelerators, Spectrometers, Detectors and Associated Equipment*, vol. 1058, p. 168 757, 2024.

[65] R. Margraf and N. Charitonidis, "Muon beam studies in the h4 beam line and the gamma irradiation facility (gif++)," Tech. Rep., 2018.

[66] D. Pfeiffer *et al.*, "The radiation field in the gamma irradiation facility gif++ at cern," *Nuclear Instruments and Methods in Physics Research Section A: Accelerators, Spectrometers, Detectors and Associated Equipment*, vol. 866, pp. 91–103, 2017.

[67] "The h4 secondary beam line of ehn1/sps," [Online]. Available: https://sba.web.cern.ch/sba/BeamsAndAreas/H4/H4_presentation.html.

[68] Y Hoshi, N Kikuchi, T Nagamine, K Neichi, and A Yamaguchi, "Performance of the endcap rpc in the belle detector under high luminosity operation of the kekb accelerator," *Nuclear Physics B-Proceedings Supplements*, vol. 158, pp. 190–194, 2006.

[69] Y. Xie *et al.*, "First results of the rpc commissioning at besiii," *Nuclear Instruments and Methods in Physics Research Section A: Accelerators, Spectrometers, Detectors and Associated Equipment*, vol. 599, no. 1, pp. 20–27, 2009.

[70] C Bacci *et al.*, "High altitude test of rpcs for the argo ybj experiment," *Nuclear instruments and methods in physics research section a: accelerators, spectrometers, detectors and associated equipment*, vol. 443, no. 2-3, pp. 342–350, 2000.

[71] H. A. Pol *et al.*, "A large area timing rpc prototype for ion collisions in the hades spectrometer," *Nuclear Instruments and Methods in Physics Research Section A: Accelerators, Spectrometers, Detectors and Associated Equipment*, vol. 535, no. 1-2, pp. 277–282, 2004.

[72] A Blanco *et al.*, "Efficiency of rpc detectors for whole-body human tof-pet," *Nuclear Instruments and Methods in Physics Research Section A: Accelerators, Spectrometers, Detectors and Associated Equipment*, vol. 602, no. 3, pp. 780–783, 2009.

[73] C Cârloganu *et al.*, "Towards a muon radiography of the puy de dôme," *Geoscientific Instrumentation, Methods and Data Systems*, vol. 2, no. 1, pp. 55–60, 2013.

[74] W. R. Leo, *Techniques for nuclear and particle physics experiments: a how-to approach*. Springer Science & Business Media, 2012.

[75] F. Sauli, "Principles of operation of multiwire proportional and drift chambers," *Geneva, Switzerland*, 1977.

[76] J. W. Keuffel, "Parallel-plate counters," *Review of Scientific Instruments*, vol. 20, no. 3, pp. 202–208, 1949.

[77] M. Babykin, A. Plakhov, Y. F. Skachkov, and V. Shapkin, "Plane-parallel spark counters for the measurement of small times," *The Soviet Journal of Atomic Energy*, vol. 1, no. 4, pp. 487–494, 1956.

[78] V. Parkhomchuck, Y. N. Pestov, and N. Petrovykh, "A spark counter with large area," *Nuclear Instruments and Methods*, vol. 93, no. 2, pp. 269–270, 1971.

[79] M. Abbrescia, V. Peskov, and P. Fonte, *Resistive gaseous detectors: designs, performance, and perspectives*. John Wiley & Sons, 2018.

[80] G. Charpak and F. Sauli, "Multiwire proportional chambers and drift chambers," *Nuclear Instruments and Methods*, vol. 162, no. 1-3, pp. 405–428, 1979.

[81] R Santonico and R Cardarelli, "Development of resistive plate counters," *Nuclear Instruments and Methods in physics research*, vol. 187, no. 2-3, pp. 377–380, 1981.

[82] S. Altieri *et al.*, "The bakelite for the rpcs of the experiment cms," *Nuclear Instruments and Methods in Physics Research Section A: Accelerators, Spectrometers, Detectors and Associated Equipment*, vol. 456, no. 1-2, pp. 132–136, 2000.

[83] M Abbrescia, E Bisceglie, G Iaselli, S Natali, G Pugliese, and F Romano, "Resistive plate chambers performances at low pressure," *Nuclear Instruments and Methods in Physics Research Section A: Accelerators, Spectrometers, Detectors and Associated Equipment*, vol. 394, no. 3, pp. 341–348, 1997.

[84] C Gustavino, M D'Incecco, E Tatananni, and G. Trinchero, "A glass resistive plate chamber for large experiments," *Nuclear Instruments and Methods in Physics Research Section A: Accelerators, Spectrometers, Detectors and Associated Equipment*, vol. 457, no. 3, pp. 558–563, 2001.

[85] A Candela *et al.*, "Glass resistive plate chambers in the opera experiment," *Nuclear Instruments and Methods in Physics Research Section A: Accelerators, Spectrometers, Detectors and Associated Equipment*, vol. 581, no. 1-2, pp. 206–208, 2007.

[86] A Abashian *et al.*, "The kl/μ detector subsystem for the belle experiment at the kek b-factory," *Nuclear Instruments and Methods in Physics Research Section A: Accelerators, Spectrometers, Detectors and Associated Equipment*, vol. 449, no. 1-2, pp. 112–124, 2000.

[87] R Cardarelli, V Makeev, and R Santonico, "Avalanche and streamer mode operation of resistive plate chambers," *Nuclear Instruments and Methods in Physics Research Section A: Accelerators, Spectrometers, Detectors and Associated Equipment*, vol. 382, no. 3, pp. 470–474, 1996.

[88] R Cardarelli, A Di Ciaccio, and R Santonico, "Performance of a resistive plate chamber operating with pure cf3br," *Nuclear Instruments and Methods in Physics Research Section A: Accelerators, Spectrometers, Detectors and Associated Equipment*, vol. 333, no. 2-3, pp. 399–403, 1993.

[89] K Doroud, A Moshaii, Y Pezeshkian, J Rahighi, and H Afarideh, "Simulation of temperature dependence of rpc operation," *Nuclear Instruments and Methods in Physics Research Section A: Accelerators, Spectrometers, Detectors and Associated Equipment*, vol. 602, no. 3, pp. 723–726, 2009.

[90] R Arnaldi *et al.*, "Influence of temperature and humidity on bakelite resistivity," *Nuclear Instruments and Methods in Physics Research Section A: Accelerators, Spectrometers, Detectors and Associated Equipment*, vol. 456, no. 1-2, pp. 140–142, 2000.

[91] G. Alkhazov, "Statistics of electron avalanches and ultimate resolution of proportional counters," *Nuclear Instruments and Methods*, vol. 89, pp. 155–165, 1970.

[92] M Abbrescia *et al.*, "Progresses in the simulation of resistive plate chambers in avalanche mode," *Nuclear Physics B-Proceedings Supplements*, vol. 78, no. 1-3, pp. 459–464, 1999.

[93] W. Riegler, C. Lippmann, and R. Veenhof, "Detector physics and simulation of resistive plate chambers," *Nuclear Instruments and Methods in Physics Research Section A: Accelerators, Spectrometers, Detectors and Associated Equipment*, vol. 500, no. 1-3, pp. 144–162, 2003.

[94] W Riegler, "Time response functions and avalanche fluctuations in resistive plate chambers," *Nuclear Instruments and Methods in Physics Research Section A: Accelerators, Spectrometers, Detectors and Associated Equipment*, vol. 602, no. 2, pp. 377–390, 2009.

[95] S Narita *et al.*, "Measurements of induced charge profile in rpc with submillistrips," *IEEE Transactions on Nuclear Science*, vol. 57, no. 4, pp. 2210–2214, 2010.

[96] Q. Li *et al.*, "Study of spatial resolution properties of a glass rpc," *Nuclear Instruments and Methods in Physics Research Section A: Accelerators, Spectrometers, Detectors and Associated Equipment*, vol. 663, no. 1, pp. 22–25, 2012.

[97] G Aielli *et al.*, "The rpc space resolution with the charge centroid method," *Journal of Instrumentation*, vol. 9, no. 09, p. C09030, 2014.

[98] I Crotty, P Fonte, T Francke, V. Peskov, and J Rantanen, "High-rate, high-position resolution microgap rpcs for x-ray imaging applications," *Nuclear Instruments and Methods in Physics Research Section A: Accelerators, Spectrometers, Detectors and Associated Equipment*, vol. 505, no. 1-2, pp. 203–206, 2003.

[99] G Aielli *et al.*, "Improving the rpc rate capability," *Journal of Instrumentation*, vol. 11, no. 07, P07014, 2016.

[100] R. K. Pachauri, A. Reisinger, *et al.*, "Ipcc fourth assessment report," *IPCC, Geneva*, vol. 2007, p. 044 023, 2007.

[101] A. Mota-Babiloni, J. Navarro-Esbrí, Á. Barragán-Cervera, F. Molés, and B. Peris, "Analysis based on eu regulation no 517/2014 of new hfc/hfo mixtures as alternatives of high gwp refrigerants in refrigeration and hvac systems," *International journal of refrigeration*, vol. 52, pp. 21–31, 2015.

[102] M Abbrescia *et al.*, "Resistive plate chambers performances at cosmic rays fluxes," *Nuclear Instruments and Methods in Physics Research Section A: Accelerators, Spectrometers, Detectors and Associated Equipment*, vol. 359, no. 3, pp. 603–609, 1995.

[103] M. Alviggi *et al.*, "Results on long-term performances and laboratory tests of the l3 rpc system at lep," *Nuclear Instruments and Methods in Physics Research Section A: Accelerators, Spectrometers, Detectors and Associated Equipment*, vol. 515, no. 1-2, pp. 328–334, 2003.

[104] C. Lu, "Rpc experience: Belle, babar and besiii," SLAC National Accelerator Lab., Menlo Park, CA (United States), Tech. Rep., 2006.

[105] J. Va'vra, "Physics and chemistry of aging–early developments," *Nuclear Instruments and Methods in Physics Research Section A: Accelerators, Spectrometers, Detectors and Associated Equipment*, vol. 515, no. 1-2, pp. 1–14, 2003.

[106] F Anulli *et al.*, "Performances of rpcs in the babar experiment," *Nuclear Instruments and Methods in Physics Research Section A: Accelerators, Spectrometers, Detectors and Associated Equipment*, vol. 515, no. 1-2, pp. 322–327, 2003.

[107] I. Crotty, J. L. Valverde, G Laurenti, M. Williams, and A. Zichichi, "Investigation of resistive parallel plate chambers," *Nuclear Instruments and Methods in Physics Research Section A: Accelerators, Spectrometers, Detectors and Associated Equipment*, vol. 329, no. 1-2, pp. 133–139, 1993.

[108] G Aielli *et al.*, "New results on atlas rpc's aging at cern's gif," *IEEE transactions on nuclear science*, vol. 53, no. 2, pp. 567–571, 2006.

[109] A. Gelmi *et al.*, "Longevity studies on the cms-rpc system," *Journal of Instrumentation*, vol. 14, no. 05, p. C05012, 2019.

[110] E. C. Zeballos *et al.*, "A new type of resistive plate chamber: The multigap rpc," *Nuclear Instruments and Methods in Physics Research Section A: Accelerators, Spectrometers, Detectors and Associated Equipment*, vol. 374, no. 1, pp. 132–135, 1996.

[111] I. Crotty, E. C. Zeballos, J. L. Valverde, D Hatzifotiadou, M. Williams, and A Zichichi, "The wide gap resistive plate chamber," *Nuclear Instruments and Methods in Physics Research Section A: Accelerators, Spectrometers, Detectors and Associated Equipment*, vol. 360, no. 3, pp. 512–520, 1995.

[112] E. C. Zeballos *et al.*, "A comparison of the wide gap and narrow gap resistive plate chamber," *Nuclear Instruments and Methods in Physics Research Section A: Accelerators, Spectrometers, Detectors and Associated Equipment*, vol. 373, no. 1, pp. 35–42, 1996.

[113] Y. Wang and Y. Yu, "Multigap resistive plate chambers for time of flight applications," *Applied Sciences*, vol. 11, no. 1, p. 111, 2020.

[114] E. C. Zeballos *et al.*, "Resistive plate chambers with secondary electron emitters and microstrip readout," *Nuclear Instruments and Methods in Physics Research Section A: Accelerators, Spectrometers, Detectors and Associated Equipment*, vol. 392, no. 1-3, pp. 150–154, 1997.

[115] K. Lee *et al.*, "Tests of multigap rpcs for high-η triggers in cms," *Journal of Instrumentation*, vol. 7, no. 10, P10009, 2012.

[116] Y. Wang *et al.*, "Production and quality control of star-tof mrpc," *Nuclear Instruments and Methods in Physics Research Section A: Accelerators, Spectrometers, Detectors and Associated Equipment*, vol. 613, no. 2, pp. 200–206, 2010.

[117] N. Herrmann *et al.*, "Technical design report for the cbm time-of-flight system (tof)," *GSI, Darmstadt*, 2014.

[118] G. Battistoni *et al.*, "The fluka code: Description and benchmarking," in *AIP Conference proceedings*, American Institute of Physics, vol. 896, 2007, pp. 31–49.

[119] S. Agostinelli *et al.*, "Geant4—a simulation toolkit," *Nuclear instruments and methods in physics research section A: Accelerators, Spectrometers, Detectors and Associated Equipment*, vol. 506, no. 3, pp. 250–303, 2003.

[120] A. Gelmi, "The cms rpc system upgrade project for hl-lhc," *PhD Thesis*, 2020.

[121] A. Gelmi, E. Voevodina, C. Collaboration, *et al.*, "Background rate study for the cms improved-rpc at hl-lhc using geant4," *Nuclear Instruments and Methods in Physics Research Section A: Accelerators, Spectrometers, Detectors and Associated Equipment*, vol. 936, pp. 430–432, 2019.

[122] P. Kumari *et al.*, "Improved-rpc for the cms muon system upgrade for the hl-lhc," *Journal of Instrumentation*, vol. 15, no. 11, p. C11012, 2020.

[123] Z. Aftab *et al.*, "Geometrical layout and mechanical details of cms end cap rpcs," *CMS Internal Note*, 2002.

[124] S Park *et al.*, "Production of gas gaps for the forward rpcs of the cms experiment," *Nuclear Instruments and Methods in Physics Research Section A: Accelerators, Spectrometers, Detectors and Associated Equipment*, vol. 550, no. 3, pp. 551–558, 2005.

[125] K. Lee *et al.*, "Study of thin double-gap rpcs for the cms muon system," *Journal of the Korean Physical Society*, vol. 73, pp. 1080–1087, 2018.

[126] S. Meola *et al.*, "Towards a two-dimensional readout of the improved cms resistive plate chamber with a new front-end electronics," *Journal of Instrumentation*, vol. 16, no. 04, p. C04001, 2021.

[127] "Y connector data sheet," [Online]. Available: `https://docs.rs-online.com/caab/A700000006772830.pdf`.

[128] "L and t connectors data shee," [Online]. Available: `https://www.parker.com/content/dam/Parker-com/Literature/LPCE/product-experience/compression-fittings/Brass-Compression-Fittings-Datasheet.pdf`.

[129] "Irpc: Edms data location," [Online]. Available: https://edms.cern.ch/ui/\#!master/navigator/project?P:100464440:100702818:subDocs.

[130] K. Shchablo *et al.*, "Front-end electronics for cms irpc detectors," *Journal of Instrumentation*, vol. 16, no. 05, p. C05002, 2021.

[131] H Kou *et al.*, "Ramp;D; of back-end electronics for improved resistive plate chambers for the phase 2 upgrade of the CMS end-cap muon system," *Rad. Det. Tech. Meth.*, vol. 6, no. 3, pp. 306–316, 2022. DOI: 10.1007/s41605-022-00340-6. [Online]. Available: https://cds.cern.ch/record/2826896.

[132] "Oregon wmr200 weather station," [Online]. Available: https://www.oregonscientificstore.com/p-31-oregon-scientific-wmr200a-professional-weather-station-center.aspx.

[133] "Phillips xp1911/uv pmts," [Online]. Available: https://hallcweb.jlab.org/DocDB/0008/000809/001/PhotonisCatalog.pdf.

[134] "Bronkhorst flowdde software," [Online]. Available: https://www.bronkhorst.com/int/products/accessories-and-software/flowware/flowview/.

[135] "El026 / el030 : Humidity / temperature converter sensor," [Online]. Available: https://www.analyticalelectronics.in/testequipment/picotech/enviromon/el026_el030_converter_sensor.html.

[136] "Enviromon data logger," [Online]. Available: http://enviromon.eu/.

[137] "Leak test setup details," [Online]. Available: https://docs.google.com/document/d/1H-Wn7sFx77dGszF8IZWk06Fi8NlMykDbyUA4UAaijTQ/edit?usp=sharing.

[138] "Qc2: Leak test+spacer test manual," [Online]. Available: https://docs.google.com/presentation/d/1pHwZXUKIuLNLdL2KZGFQKgsMlqITli5p/edit?usp=sharing&ouid=116270212628209111840&rtpof=true&sd=true.

[139] "Cms rpc construction data base," [Online]. Available: https://apex-sso.cern.ch/pls/htmldb_cmsr/f?p=125:195:102753289746556:::::.

[140] E. Asilar, "The new improved rpcs of cms prevailing the challenges of high-lumi lhc," Tech. Rep., 2022.

[141] M Abbrescia *et al.*, "Cosmic ray tests of double-gap resistive plate chambers for the cms experiment," *Nuclear Instruments and Methods in Physics Research Section A: Accelerators, Spectrometers, Detectors and Associated Equipment*, vol. 550, no. 1-2, pp. 116–126, 2005.

[142] "Irpc: List of components for production," [Online]. Available: https://docs.google.com/spreadsheets/d/1eUVH_jwN7bQ9DreOPnccmKRgjsKh2B60gbq_svmgxSc/edit?usp=sharing.

[143] "Irpc: Assembly manual," [Online]. Available: https://livebueedu-my.sharepoint.com/:w:/g/personal/basma_mahdy_bue_edu_eg/EXx0HxlVFyRJiOjmU_zj5a8B6f4DSt0Rit9YIYxZgkIKgA?e=kIpRGG.

[144] "Fluorinated greenhouse gases 2019," [Online]. Available: https://www.eea.europa.eu/publications/fluorinated-greenhouse-gases-2019.

[145] C Ahdida *et al.*, "The ship experiment at the proposed cern sps beam dump facility," *The European Physical Journal C*, vol. 82, no. 5, pp. 1–23, 2022.

[146] M. Capeans, R. Guida, and B. Mandelli, "Strategies for reducing the environmental impact of gaseous detector operation at the cern lhc experiments," *Nuclear Instruments and Methods in Physics Research Section A: Accelerators, Spectrometers, Detectors and Associated Equipment*, vol. 845, pp. 253–256, 2017.

[147] M. Shopova *et al.*, "The cms rpc system readiness for lhc run-3 data taking," *Nuclear Instruments and Methods in Physics Research Section A: Accelerators, Spectrometers, Detectors and Associated Equipment*, vol. 1052, p. 168 272, 2023.

[148] B. Mandelli, M. Corbetta, R. Guida, and G. Rigoletti, "Strategies for reducing the use of greenhouse gases from particle detectors operation at the cern lhc experiments," in *Journal of Physics: Conference Series*, IOP Publishing, vol. 2374, 2022, p. 012 159.

[149] R Guida, B Mandelli, and G Rigoletti, "Performance studies of rpc detectors with new environmentally friendly gas mixtures in presence of lhc-like radiation background," *Nuclear Instruments and Methods in Physics Research Section A: Accelerators, Spectrometers, Detectors and Associated Equipment*, vol. 958, p. 162 073, 2020.

[150] M. Abbrescia *et al.*, "Preliminary results of resistive plate chambers operated with eco-friendly gas mixtures for application in the cms experiment," *Journal of Instrumentation*, vol. 11, no. 09, p. C09018, 2016.

[151] A Bianchi *et al.*, "Characterization of tetrafluoropropene-based gas mixtures for the resistive plate chambers of the alice muon spectrometer," *Journal of Instrumentation*, vol. 14, no. 11, P11014, 2019.

[152] B. Liberti *et al.*, "Further gas mixtures with low environment impact," *Journal of Instrumentation*, vol. 11, no. 09, p. C09012, 2016.

[153] R Albanese *et al.*, "Rpc-based muon identification system for the neutrino detector of the ship experiment," *Journal of Instrumentation*, vol. 18, no. 02, P02022, 2023.

[154] L. Quaglia, "Development of eco-friendly gas mixtures for Resistive Plate Chambers," Presented 26 Apr 2023, 2023. [Online]. Available: `https://cds.cern.ch/record/2861614`.

[155] M Abbrescia *et al.*, "High-rate tests on resistive plate chambers operated with eco-friendly gas mixtures," *arXiv preprint arXiv:2311.08259*, 2023.

[156] P Dupieux, B Joly, F Jouve, S Manen, and R Vandaele, "Upgrade of the alice muon trigger electronics," *Journal of Instrumentation*, vol. 9, no. 09, p. C09013, 2014.

[157] M Abbrescia *et al.*, "New developments on front-end electronics for the cms resistive plate chambers," *Nuclear Instruments and Methods in Physics Research Section A: Accelerators, Spectrometers, Detectors and Associated Equipment*, vol. 456, no. 1-2, pp. 143–149, 2000.

[158] M. Chakraborty and A. P. Kundan, "Grafana," in *Monitoring Cloud-Native Applications: Lead Agile Operations Confidently Using Open Source Software*, Springer, 2021, pp. 187–240.

[159] G. Rigoletti *et al.*, "Studies of rpc detector operation with eco-friendly gas mixtures under irradiation at the cern gamma irradiation facility," *POS PROCEEDINGS OF SCIENCE*, vol. 364, p. 164, 2020.

[160] S Park *et al.*, "Development of re1/1 rpcs for the cms muon trigger system," *Nuclear Instruments and Methods in Physics Research Section A: Accelerators, Spectrometers, Detectors and Associated Equipment*, vol. 602, no. 3, pp. 665–667, 2009.

[161] M. Gul *et al.*, "Detector control system and efficiency performance for cms rpc at gif++," *Journal of Instrumentation*, vol. 11, no. 10, p. C10013, 2016.

[162] G Aielli *et al.*, "Ageing test of atlas rpcs at cern's gamma irradiation facility," in *IEEE Symposium Conference Record Nuclear Science 2004.*, IEEE, vol. 1, 2004, pp. 226–230.

[163] "Mirion rds-31itx s/r dosimeter," [Online]. Available: `https://www.mirion.com/products/rds-31-modular-radiation-survey-meter`.

[164] J. Eysermans and M. I. Pedraza Morales, "Aging studies for the cms rpc system," Tech. Rep., 2017.

[165] S. Simsek, "The atlas rpc upgrade project for the high luminosity lhc program," ATL-COM-MUON-2022-008, Tech. Rep., 2022.

[166] C. Abellan Beteta, F. Domingo Bonal, M. Roselló Canal, L. Collaboration, *et al.*, "Framework tdr for the lhcb upgrade: Technical design report," 2012.

[167] A Ferretti, "The upgrade of the rpc-based alice muon trigger," *Journal of Instrumentation*, vol. 14, no. 06, p. C06011, 2019.

[168] E. George, "Cosmic rays measure overburden of tunnel," *Commonwealth Engineer*, vol. 455, 1955.

[169] L. W. Alvarez *et al.*, "Search for hidden chambers in the pyramids: The structure of the second pyramid of giza is determined by cosmic-ray absorption.," *Science*, vol. 167, no. 3919, pp. 832–839, 1970.

[170] International Atomic Energy Agency, "Muon imaging: Present status and emerging applications," IAEA, Vienna, IAEA TECDOC 2012, 2022. [Online]. Available: `https://www.iaea.org/publications/15182/muon-imaging`.

[171] L. Oláh, H. K. Tanaka, and D. Varga, Eds., *Muography: Exploring Earth's Subsurface with Elementary Particles*. John Wiley & Sons, 2022, ISBN: 9781119723028.

[172] M. D'Errico *et al.*, "The MURAVES experiment: study of the Vesuvius Great Cone with Muon Radiography," *Journal for Advanced Instrumentation in Science*, vol. 1, p. 273, 2022. eprint: `arXiv:2202.12000`.

[173] S Procureur, "Muon imaging: Principles, technologies and applications," *Nuclear Instruments and Methods in Physics Research Section A: Accelerators, Spectrometers, Detectors and Associated Equipment*, vol. 878, pp. 169–179, 2018.

[174] A. Lechmann *et al.*, "Muon tomography in geoscientific research – A guide to best practice," *Earth-Science Reviews*, vol. 222, p. 103 842, 2021. DOI: `10.1016/j.earscirev.2021.103842`.

[175] M. Weekes *et al.*, "Material identification in nuclear waste drums using muon scattering tomography and multivariate analysis," *Journal of Instrumentation*, vol. 16, no. 05, P05007, 2021.

[176] S. Barnes *et al.*, "Cosmic-ray tomography for border security," *Instruments*, vol. 7, no. 1, p. 13, 2023.

[177] C. L. Morris *et al.*, "Horizontal cosmic ray muon radiography for imaging nuclear threats," *Nucl. Instr. Meth B*, vol. 330, pp. 42–46, 2014.

[178] P. Martinez Ruiz del Arbol, P. Gomez Garcia, C. Diez Gonzalez, and A. Orio Alonso, "Non-destructive testing of industrial equipment using muon radiography," *Philosophical Transactions of the Royal Society A*, vol. 377, no. 2137, p. 20 180 054, 2019.

[179] V. F. Hess, "Concerning observations of penetrating radiation on seven free balloon flights," in *A Source Book in Astronomy and Astrophysics, 1900–1975*, Harvard University Press, 1979, pp. 13–20.

[180] J Clay, P. Van Alphen, *et al.*, "Results of the dutch cosmic ray expedition 1933: Ii. the magnetic latitude effect of cosmic rays a magnetic longitude effect," *Physica*, vol. 1, no. 7-12, pp. 829–838, 1934.

[181] B. Rossi, "Early days in cosmic rays," *Physics today*, vol. 34, no. 10, pp. 34–41, 1981.

[182] P. K. Grieder, *Cosmic rays at Earth*. Elsevier, 2001.

[183] T. K. Gaisser, R. Engel, and E. Resconi, *Cosmic rays and particle physics*. Cambridge University Press, 2016.

[184] S. Verpoest, "Studies of tev muons in cosmic-ray air showers detected with icetop and icecube," Ph.D. dissertation, Ghent University, 2022.

[185] L. Bonechi *et al.*, "The muraves project and other parallel activities on muon absorption radiography," in *EPJ Web of Conferences*, EDP Sciences, vol. 182, 2018, p. 02 015.

[186] L Bonechi, "Development of the adamo detector: Test with cosmic rays at different zenith angles," 2005.

[187] L. Bogdanova, M. Gavrilov, V. Kornoukhov, and A. Starostin, "Cosmic muon flux at shallow depths underground," *Physics of Atomic Nuclei*, vol. 69, pp. 1293–1298, 2006.

[188] L. Dorman, *Cosmic Rays in Magnetospheres of the Earth and other Planets*. Springer Science & Business Media, 2009, vol. 358.

[189] D. Heck, J. Knapp, J. Capdevielle, G Schatz, T Thouw, *et al.*, "Corsika: A monte carlo code to simulate extensive air showers," *Report fzka*, vol. 6019, no. 11, 1998.

[190] P. Antonioli *et al.*, "A three-dimensional code for muon propagation through the rock: MUSIC," *Astropart. Phys.*, vol. 7, no. 4, p. 357, 1997, ISSN: 0927-6505. DOI: https://doi.org/10.1016/S0927-6505(97)00035-2. [Online]. Available: http://www.sciencedirect.com/science/article/pii/S0927650597000352.

[191] M. Tueros and S. Sciutto, "Tierras: A package to simulate high energy cosmic ray showers underground, underwater and under-ice," *Computer Physics Communications*, vol. 181, no. 2, pp. 380–392, 2010.

[192] M. Guan, M.-C. Chu, J. Cao, K.-B. Luk, and C. Yang, "A parametrization of the cosmic-ray muon flux at sea-level," *arXiv preprint arXiv:1509.06176*, 2015.

[193] R. Kellogg, H Kasha, and R. Larsen, "Momentum spectra, charge ratio, and zenith-angle dependence of cosmic-ray muons," *Physical review D*, vol. 17, no. 1, p. 98, 1978.

[194] Y Muraki *et al.*, "Measurement of the cosmic-ray muon spectrum and charge ratio at large zenith angles in the momentum range 100 gev/c to 10 tev/c using a magnet spectrometer," *Physical Review D*, vol. 28, no. 1, p. 40, 1983.

[195] L. Cimmino, "Principles and perspectives of radiographic imaging with muons," *Journal of Imaging*, vol. 7, no. 12, p. 253, 2021.

[196] D. E. Groom, N. V. Mokhov, and S. I. Striganov, "Muon stopping power and range tables 10 mev–100 tev," *Atomic Data and Nuclear Data Tables*, vol. 78, no. 2, pp. 183–356, 2001.

[197] L. Bonechi *et al.*, "Atmospheric muons as an imaging tool," *Rev. Phys.*, vol. 5, p. 100 038, 2020. DOI: 10.1016/j.revip.2020.100038. arXiv: 1906.03934 [physics.ins-det].

[198] E. Rutherford, "Lxxix. the scattering of α and β particles by matter and the structure of the atom," *The London, Edinburgh, and Dublin Philosophical Magazine and Journal of Science*, vol. 21, no. 125, pp. 669–688, 1911.

[199] M. Tanabashi *et al.*, "Review of particle physics: Particle data groups," *Physical Review D*, vol. 98, no. 3, pp. 1–1898, 2018.

[200] G. R. Lynch and O. I. Dahl, "Approximations to multiple coulomb scattering," *Nuclear Instruments and Methods in Physics Research Section B: Beam Interactions with Materials and Atoms*, vol. 58, no. 1, pp. 6–10, 1991.

[201] Y.-S. Tsai, "Pair production and bremsstrahlung of charged leptons," *Reviews of Modern Physics*, vol. 46, no. 4, p. 815, 1974.

[202] Z Papandreoua, R Hakobyanb, and N Kolevb, "Bcal radiation length calculations," in *Technical Report (439)*, GlueX, 2005.

[203] G Saracino *et al.*, "Applications of muon absorption radiography to the fields of archaeology and civil engineering," *Philosophical Transactions of the Royal Society A*, vol. 377, no. 2137, p. 20 180 057, 2019.

[204] A. Tarantola and B. Valette, "Generalized nonlinear inverse problems solved using the least squares criterion," *Reviews of Geophysics*, vol. 20, no. 2, pp. 219–232, 1982.

[205] W. H. Press, *Numerical recipes 3rd edition: The art of scientific computing*. Cambridge university press, 2007.

[206] A. Tarantola, *Inverse problem theory and methods for model parameter estimation*. SIAM, 2005.

[207] H. K. Tanaka, "Muographic mapping of the subsurface density structures in miura, boso and izu peninsulas, japan," *Scientific reports*, vol. 5, no. 1, p. 8305, 2015.

[208] J. Marteau *et al.*, "Muon tomography applied to active volcanoes," *arXiv preprint arXiv:1510.05292*, 2015.

[209] N. Lesparre, D. Gibert, J. Marteau, J.-C. Komorowski, F. Nicollin, and O. Coutant, "Density muon radiography of la soufriere of guadeloupe volcano: Comparison with geological, electrical resistivity and gravity data," *Geophysical Journal International*, vol. 190, no. 2, pp. 1008–1019, 2012.

[210] D. Bryman *et al.*, "Muon geotomography—bringing new physics to orebody imaging," 2014.

[211] D. Schouten, "Muon geotomography: Selected case studies," *Philosophical Transactions of the Royal Society A*, vol. 377, no. 2137, p. 20 180 061, 2019.

[212] L. Bonechi, R. D'Alessandro, N. Mori, and L. Viliani, "A projective reconstruction method of underground or hidden structures using atmospheric muon absorption data," *Journal of Instrumentation*, vol. 10, no. 02, P02003, 2015.

[213] A. Barnoud *et al.*, "Bayesian joint muographic and gravimetric inversion applied to volcanoes," *Geophysical Journal International*, vol. 218, no. 3, pp. 2179–2194, 2019.

[214] F. Cella, M. Fedi, G. Florio, M. Grimaldi, and A. Rapolla, "Shallow structure of the somma–vesuvius volcano from 3d inversion of gravity data," *Journal of volcanology and geothermal research*, vol. 161, no. 4, pp. 303–317, 2007.

[215] G De Natale, C Troise, F Pingue, G Mastrolorenzo, and L Pappalardo, "The somma–vesuvius volcano (southern italy): Structure, dynamics and hazard evaluation," *Earth-Science Reviews*, vol. 74, no. 1-2, pp. 73–111, 2006.

[216] S Calvari *et al.*, "Major eruptive style changes induced by structural modifications of a shallow conduit system: The 2007–2012 stromboli case," *Bulletin of volcanology*, vol. 76, pp. 1–15, 2014.

[217] G. Saracino *et al.*, "The muraves muon telescope: Technology and expected performances," *Annals of Geophysics*, 2017.

[218] K. Jourde *et al.*, "Experimental detection of upward going cosmic particles and consequences for correction of density radiography of volcanoes," *Geophysical Research Letters*, vol. 40, no. 24, pp. 6334–6339, 2013.

[219] J. Peña-Rodríguez *et al.*, "Muography in colombia: Simulation framework, instrumentation and data analysis," *arXiv preprint arXiv:2201.11160*, 2022.

[220] H Gómez *et al.*, "Forward scattering effects on muon imaging," *Journal of Instrumentation*, vol. 12, no. 12, P12018, 2017.

[221] P. KF, *Cosmic Rays at Earth: Researcher's Reference Manual and Data Book*. Elsevier, 2001.

[222] T. Hebbeker and C. Timmermans, "A compilation of high energy atmospheric muon data at sea level," *Astroparticle Physics*, vol. 18, no. 1, pp. 107–127, 2002.

[223] L. Bonechi, M. Grandi, F. Taccetti, and E. Vannuccini, "Adamo, an altazimuthal detector for atmospheric cosmic–ray observation," in *Proceedings, 28th International Cosmic Ray Conference (ICRC 2003): Tsukuba, Japan*, vol. 2003, 2003, pp. 3485–3488.

[224] C. Hagmann, D. Lange, and D. Wright, "Cosmic-ray shower generator (CRY) for Monte Carlo transport codes," in *2007 IEEE Nuclear Science Symposium Conference Record*, IEEE, vol. 2, 2007, pp. 1143–1146.

[225] G. Baccani *et al.*, "The mima project. design, construction and performances of a compact hodoscope for muon radiography applications in the context of archaeology and geophysical prospections," *Journal of Instrumentation*, vol. 13, no. 11, P11001, 2018.

[226] A Anastasio *et al.*, "The mu-ray experiment. an application of sipm technology to the understanding of volcanic phenomena," *Nuclear Instruments and Methods in Physics Research Section A: Accelerators, Spectrometers, Detectors and Associated Equipment*, vol. 718, pp. 134–137, 2013.

[227] A. Bonneville *et al.*, "Borehole muography of subsurface reservoirs," *Philosophical Transactions of the Royal Society A*, vol. 377, no. 2137, p. 20 180 060, 2019.

[228] J. Gluyas *et al.*, "Passive, continuous monitoring of carbon dioxide geostorage using muon tomography," *Philosophical Transactions of the Royal Society A*, vol. 377, no. 2137, p. 20 180 059, 2019.

[229] R Acquafredda *et al.*, "The opera experiment in the cern to gran sasso neutrino beam," *Journal of Instrumentation*, vol. 4, no. 04, P04018, 2009.

[230] A. Ariga *et al.*, "A nuclear emulsion detector for the muon radiography of a glacier structure," *Instruments*, vol. 2, no. 2, p. 7, 2018.

[231] V. Tioukov *et al.*, "First muography of stromboli volcano," *Scientific reports*, vol. 9, no. 1, p. 6695, 2019.

[232] K. Morishima *et al.*, "Discovery of a big void in khufu's pyramid by observation of cosmic-ray muons," *Nature*, vol. 552, no. 7685, pp. 386–390, 2017.

[233] R. Nishiyama *et al.*, "First measurement of ice-bedrock interface of alpine glaciers by cosmic muon radiography," *Geophysical Research Letters*, vol. 44, no. 12, pp. 6244–6251, 2017.

[234] R. Nishiyama *et al.*, "Bedrock sculpting under an active alpine glacier revealed from cosmic-ray muon radiography," *Scientific reports*, vol. 9, no. 1, p. 6970, 2019.

[235] L. Oláh *et al.*, "Mwpc-based muographic observation system for remote monitoring of active volcanoes," *Nuclear Instruments and Methods in Physics Research Section A: Accelerators, Spectrometers, Detectors and Associated Equipment*, vol. 936, pp. 57–58, 2019.

[236] G. Hamar *et al.*, "Underground muography with portable gaseous detectors," in *Journal of Physics: Conference Series*, IOP Publishing, vol. 2374, 2022, p. 012 186.

[237] L. Oláh, G. Hamar, S. Miyamoto, H. K. Tanaka, and D. Varga, "The first prototype of an mwpc-based borehole-detector and its application for muography of an underground pillar,", vol. 71, pp. 161–168, 2018.

[238] A. Sharma, "Multiwire gaseous detectors: Basics and state-of-the-art," Tech. Rep., 2000.

[239] Y Giomataris, "Development and prospects of the new gaseous detector "micromegas"," *Nuclear Instruments and Methods in Physics Research Section A: Accelerators, Spectrometers, Detectors and Associated Equipment*, vol. 419, no. 2-3, pp. 239–250, 1998.

[240] H Gómez, "Muon tomography using micromegas detectors: From archaeology to nuclear safety applications," *Nuclear Instruments and Methods in Physics Research Section A: Accelerators, Spectrometers, Detectors and Associated Equipment*, vol. 936, pp. 14–17, 2019.

[241] V Glasser and R Lipton, "Data analysis and detector troubleshooting for the silicon muon scanner," Fermi National Accelerator Lab.(FNAL), Batavia, IL (United States), Tech. Rep., 2018.

[242] O. Catalano, M. Del Santo, T. Mineo, G. Cusumano, M. C. Maccarone, and G. Pareschi, "Volcanoes muon imaging using cherenkov telescopes," *Nuclear Instruments and Methods in Physics Research Section A: Accelerators, Spectrometers, Detectors and Associated Equipment*, vol. 807, pp. 5–12, 2016.

[243] M. Del Santo *et al.*, "Looking inside volcanoes with the imaging atmospheric cherenkov telescopes," *Nuclear Instruments and Methods in Physics Research Section A: Accelerators, Spectrometers, Detectors and Associated Equipment*, vol. 876, pp. 111–114, 2017.

[244] J. P. Rodríguez *et al.*, "Calibration and first measurements of mute: A hybrid muon telescope for geological structures," *PoS (ICRC2019)*, vol. 381, 2019.

[245] J. Dournaux *et al.*, "Operating performance of the gamma-ray cherenkov telescope: An end-to-end schwarzschild–couder telescope prototype for the cherenkov telescope array," *Nuclear Instruments and Methods in Physics Research Section A: Accelerators, Spectrometers, Detectors and Associated Equipment*, vol. 845, pp. 355–358, 2017.

[246] H. K. Tanaka, "Japanese volcanoes visualized with muography," *Philosophical Transactions of the Royal Society A*, vol. 377, no. 2137, p. 20 180 142, 2019.

[247] R. D'Alessandro *et al.*, "Volcanoes in italy and the role of muon radiography," *Philosophical Transactions of the Royal Society A*, vol. 377, no. 2137, p. 20 180 050, 2019.

[248] G. Saracino and C. Cârloganu, "Looking at volcanoes with cosmic-ray muons," *Physics Today*, vol. 65, no. 12, pp. 60–61, 2012.

[249] I. Guerrero *et al.*, "Design and construction of a muon detector prototype for study the galeras volcano internal structure," in *Journal of Physics: Conference Series*, IOP Publishing, vol. 1247, 2019, p. 012 020.

[250] J. P. Rodríguez, "Minimute: A muon telescope prototype for studying volcanic structures with cosmic ray flux.," *Scientia et technica*, vol. 23, no. 3, pp. 386–391, 2018.

[251] H. K. Tanaka *et al.*, "High resolution imaging in the inhomogeneous crust with cosmic-ray muon radiography: The density structure below the volcanic crater floor of mt. asama, japan," *Earth and Planetary Science Letters*, vol. 263, no. 1-2, pp. 104–113, 2007.

[252] H. K. Tanaka *et al.*, "Radiographic imaging below a volcanic crater floor with cosmic-ray muons," *American Journal of Science*, vol. 308, no. 7, pp. 843–850, 2008.

[253] H. K. Tanaka, T. Kusagaya, and H. Shinohara, "Radiographic visualization of magma dynamics in an erupting volcano," *Nature Communications*, vol. 5, no. 1, p. 3381, 2014.

[254] P. Noli *et al.*, "Muography of the puy de dôme," *Annals of Geophysics*, vol. 60, no. FERMILAB-PUB-16-725-PPD, 2017.

[255] K. Jourde, D. Gibert, J. Marteau, J. de Bremond d'Ars, and J.-C. Komorowski, "Muon dynamic radiography of density changes induced by hydrothermal activity at the la soufrière of guadeloupe volcano," *Scientific reports*, vol. 6, no. 1, p. 33 406, 2016.

[256] D. Carbone, D. Gibert, J. Marteau, M. Diament, L. Zuccarello, and E. Galichet, "An experiment of muon radiography at mt etna (italy)," *Geophysical Journal International*, vol. 196, no. 2, pp. 633–643, 2014.

[257] A Vesga-Ramírez *et al.*, "Simulated annealing for volcano muography," *Journal of South American Earth Sciences*, vol. 109, p. 103 248, 2021.

[258] K. Azuma, H. K. Tanaka, H. Suenaga, and K. Suzuki, "Muographic test measurements for monitoring groundwater," in *ISRM International Symposium-Asian Rock Mechanics Symposium*, ISRM, 2014, ISRM–ARMS8.

[259] F. Hivert, I. L. Roche, J.-b. Decitre, J. Brunner, J. Busto, and S. Gaffet, "Muography sensitivity to hydrogeological rock density perturbation: Roles of the absorption and scattering on the muon flux measurement reliability," *Near Surface Geophysics*, vol. 15, no. 2, pp. 121–129, 2017.

[260] V Pazzi, "Oral presentation at the egu general assembly 2019," 2019.

[261] M. Ihl, "Muon tomography of ice-filled cleft systems in steep bedrock permafrost: A proposal," *arXiv preprint arXiv:1008.1241*, 2010.

[262] J Klinger *et al.*, "Simulation of muon radiography for monitoring co2 stored in a geological reservoir," *International Journal of Greenhouse Gas Control*, vol. 42, pp. 644–654, 2015.

[263] L. Oláh, G. Barnaföldi, G Hamar, H. Melegh, G Surányi, and D Varga, "Ccc-based muon telescope for examination of natural caves," *Geoscientific Instrumentation, Methods and Data Systems*, vol. 1, no. 2, pp. 229–234, 2012.

[264] E Caffau, F Coren, and G Giannini, "Underground cosmic-ray measurement for morphological reconstruction of the "grotta gigante" natural cave," *Nuclear Instruments and Methods in Physics Research Section A: Accelerators, Spectrometers, Detectors and Associated Equipment*, vol. 385, no. 3, pp. 480–488, 1997.

[265] L Malmqvist, G Jönsson, K Kristiansson, and L Jacobsson, "Theoretical studies of in-situ rock density determinations using underground cosmic-ray muon intensity measurements with application in mining geophysics," *Geophysics*, vol. 44, no. 9, pp. 1549–1569, 1979.

[266] A Harel and D Yaish, "Lingacom muography," *Philosophical Transactions of the Royal Society A*, vol. 377, no. 2137, p. 20 180 133, 2019.

[267] H. Gomez *et al.*, "Studies on muon tomography for archaeological internal structures scanning," in *Journal of Physics: Conference Series*, IOP Publishing, vol. 718, 2016, p. 052 016.

[268] S Aguilar, R Alfaro, and E Belmont, "Using cosmic muons to search for cavities in the pyramid of the sun, teotihuacan: Preliminary results," 2013.

[269] R. Schwitters, "The university of texas maya muon project," 2007.

[270] G. Saracino *et al.*, "Imaging of underground cavities with cosmic-ray muons from observations at mt. echia (naples)," *Scientific reports*, vol. 7, no. 1, p. 1181, 2017.

[271] L. Cimmino *et al.*, "3d muography for the search of hidden cavities," *Scientific reports*, vol. 9, no. 1, p. 2974, 2019.

[272] K. Chaiwongkhot *et al.*, "Development of a portable muography detector for infrastructure degradation investigation," *IEEE Transactions on Nuclear Science*, vol. 65, no. 8, pp. 2316–2324, 2018.

[273] L. Thompson *et al.*, "The application of muon tomography to the imaging of railway tunnels," *arXiv preprint arXiv:1906.05814*, 2019.

[274] K. Nagamine *et al.*, "Probing the inner structure of blast furnaces by cosmic-ray muon radiography," *Proceedings of the Japan Academy, Series B*, vol. 81, no. 7, pp. 257–260, 2005.

[275] F Riggi *et al.*, "The muon portal project: Commissioning of the full detector and first results," *Nuclear Instruments and Methods in Physics Research Section A: Accelerators, Spectrometers, Detectors and Associated Equipment*, vol. 912, pp. 16–19, 2018.

[276] P Checchia *et al.*, "Infn muon tomography demonstrator: Past and recent results with an eye to near-future activities," *Philosophical Transactions of the Royal Society A*, vol. 377, no. 2137, p. 20 180 065, 2019.

[277] S Vanini *et al.*, "Muography of different structures using muon scattering and absorption algorithms," *Philosophical Transactions of the Royal Society A*, vol. 377, no. 2137, p. 20 180 051, 2019.

[278] D Poulson *et al.*, "Cosmic ray muon computed tomography of spent nuclear fuel in dry storage casks," *Nuclear Instruments and Methods in Physics Research Section A: Accelerators, Spectrometers, Detectors and Associated Equipment*, vol. 842, pp. 48–53, 2017.

[279] G Jonkmans, V. Anghel, C Jewett, and M Thompson, "Nuclear waste imaging and spent fuel verification by muon tomography," *Annals of Nuclear Energy*, vol. 53, pp. 267–273, 2013.

[280] O. Kamaev, E. T. Rand, B. M. van der Ende, M. Thompson, S. Livingstone, and V. V. Golovko, "Complementary non-destructive detection of nuclear materials with passive neutron and gamma-ray detectors, and a large-volume muon tomography system," *Nuclear Instruments and Methods in Physics Research Section A: Accelerators, Spectrometers, Detectors and Associated Equipment*, vol. 944, p. 162 503, 2019.

[281] D. Poulson, J. Bacon, M. Durham, E. Guardincerri, C. Morris, and H. R. Trellue, "Application of muon tomography to fuel cask monitoring," *Philosophical Transactions of the Royal Society A*, vol. 377, no. 2137, p. 20 180 052, 2019.

[282] A. Clarkson *et al.*, "Characterising encapsulated nuclear waste using cosmic-ray muon tomography (mt)," in *2015 4th international conference on Advancements in Nuclear Instrumentation Measurement Methods and their Applications (ANIMMA)*, IEEE, 2015, pp. 1–7.

[283] D. Mahon *et al.*, "First-of-a-kind muography for nuclear waste characterization," *Philosophical Transactions of the Royal Society A*, vol. 377, no. 2137, p. 20 180 048, 2019.

[284] K. Borozdin *et al.*, "Cosmic ray radiography of the damaged cores of the fukushima reactors," *Physical review letters*, vol. 109, no. 15, p. 152 501, 2012.

[285] S. Procureur *et al.*, "Precise characterization of a corridor-shaped structure in Khufu's Pyramid by observation of cosmic-ray muons," *Nature Communications*, vol. 14, no. 1, p. 1144, 2023.

[286] M. Moussawi *et al.*, "A portable muon telescope for exploration geophysics in confined environments," in *First International Meeting for Applied Geoscience & Energy*, Society of Exploration Geophysicists, 2021, pp. 3034–3038.

[287] M. Moussawi, A. Giammanco, V. Kumar, and M. Lagrange, "Muons for cultural heritage," arXiv:2309.08394 [physics.ins-det], 2023. arXiv: 2309.08394 [physics.ins-det].

[288] H. K. Tanaka, "Muometric positioning system (muPS) utilizing direction vectors of cosmic-ray muons for wireless indoor navigation at a centimeter-level accuracy," *Scientific Reports*, vol. 13, no. 1, p. 15 272, 2023.

[289] D. Varga and H. K. M. Tanaka, "Developments of a centimeter-level precise muometric wireless navigation system (MuWNS-V) and its first demonstration using directional information from tracking detectors," arXiv:2308.10108 [physics.ins-det], 2023. arXiv: 2308.10108 [physics.ins-det].

[290] A. Giammanco, E. Cortina Gil, S. Andringa, and M. Tytgat, "Resistive Plate Chambers in Muography," in *Muography: Exploring Earth's Subsurface with Elementary Particles*, ser. Geophysical Monograph Series (ISSN: 0065-8448), L. Olah, H. Tanaka, and D. Varga, Eds., AGU - Wiley, 2021, ch. 18. DOI: 10.1002/9781119722748.ch18.

[291] M Abbrescia *et al.*, "The resistive plate chambers for cms and their simulation," *Nuclear Instruments and Methods in Physics Research Section A: Accelerators, Spectrometers, Detectors and Associated Equipment*, vol. 471, no. 1-2, pp. 55–59, 2001.

[292] "Bohle glass cleaner," [Online]. Available: https://www.bohle.com/nl-nl/producten/glasverlijming/reinigen/181/bohle-professional-glasreiniger.

[293] D. Loterman, M. Tytgat, and A. Fagot, "Development of a glass resistive plate chamber for the phase-2 upgrade of the cms detector at the large hadron collider," 2014.

[294] "Asturomec-spraygun," [Online]. Available: https://www.walmec.it/en/products/asturomec-sprayguns/serie-om-im-sp.

[295] "Scp silver conductive paint-data sheet," [Online]. Available: https://www.farnell.com/datasheets/3202178.pdf.

[296] "Urethan-71 data sheet," [Online]. Available: https://www.farnell.com/datasheets/318257.pdf.

[297] T. Coutts, "Percolation conduction in mixed insulator-conductor systems," *Thin Solid Films*, vol. 38, no. 3, pp. 313–321, 1976.

[298] "Concentric ring probe," [Online]. Available: http://documents.vermason.co.uk/PDF/TB-7549.pdf.

[299] "Thickness measurement equipment: Pwb swiss tool master 2d," [Online]. Available: http://www.royaltool.co.uk/toolmaster_older.php.

[300] H. Seiler, "Secondary electron emission in the scanning electron microscope," *Journal of Applied Physics*, vol. 54, no. 11, R1–R18, 1983.

[301] "Caen qdc v792," [Online]. Available: https://www.caen.it/products/v792/.

[302] S. Wuyckens, A. Giammanco, P. Demin, and E. Cortina Gil, "A portable muon telescope based on small and gas-tight Resistive Plate Chambers," *Phil. Trans. R. Soc. A*, vol. 377, p. 0139, 2018. DOI: 10.1098/rsta.2018.0139. arXiv: 1806.06602 [physics.ins-det].

[303] C. Binetti, R. Liuzzi, F. Loddo, B. Marangelli, and A. Ranieri, "A new Front-End Board for RPC detector of CMS," *CMS Note-1999/047*, 1999.

[304] R. Gamage *et al.*, "Portable resistive plate chambers for muography in confined environments," in *E3S Web of Conferences*, EDP Sciences, vol. 357, 2022, p. 01 001.

[305] "Eltos pcb manufactures," [Online]. Available: https://eltos.com/en/.

[306] "Polybull 3d printing company," [Online]. Available: https://www.polybull.be/.

[307] M. Boone, "New imaging modalities in high resolution x-ray tomography," Ph.D. dissertation, Ghent University, 2013.

[308] "Center for x-ray tomography, ugent," [Online]. Available: https://www.ugent.be/we/ugct/en.

[309] R. Veenhof, "Garfield, a drift chamber simulation program," in *Conf. Proc. C*, World Scientific, vol. 9306149, 1993, pp. 66–71.

[310] "Liquid electrical tape," [Online]. Available: https://www.classicinternational.eu/antennes-montage/montagemateriaal/afdichting/liquid-electrical-tape/.

[311] "Geological map of major volcanoes in italy," [Online]. Available: https://geology.com/volcanoes/vesuvius/mount-vesuvius-map.gif.

[312] R. Scandone, L. Giacomelli, and P. Gasparini, "Mount vesuvius: 2000 years of volcanological observations," *Journal of volcanology and geothermal research*, vol. 58, no. 1-4, pp. 5–25, 1993.

[313] G. Imbò, *L'attività eruttiva vesuviana e relative osservazioni nel corso dell'intervallo intereruttivo 1906-1944 ed in particolare del parossismo del marzo 1944*. G. Genovese, 1951.

[314] "Vesuvius national park," [Online]. Available: https://www.vesuviusnationalpark.it/.

[315] "Ingv vesuvius observatory," [Online]. Available: https://www.ov.ingv.it/.

[316] "Sesmic event monitoring at ingv," [Online]. Available: https://terremoti.ov.ingv.it/gossip/vesuvio/index.html.

[317] "Mt. vesuvius eruption: Evacuation plan," [Online]. Available: http://www.protezionecivile.gov.it/jcms/it/view_pde.wp?contentId=PDE12771.

[318] B. De Vivo and G. Rolandi, "Vesuvius: Volcanic hazard and civil defense," *Rendiconti Lincei*, vol. 24, pp. 39–45, 2013.

[319] F. Ambrosino *et al.*, "The mu-ray project: Detector technology and first data from mt. vesuvius," *Journal of Instrumentation*, vol. 9, no. 02, p. C02029, 2014.

[320] M. D'Errico *et al.*, "The muraves experiment: Study of the vesuvius great cone with muon radiography," *arXiv preprint arXiv:2202.12000*, 2022.

[321] V. Niess, A. Barnoud, C. Cârloganu, and E. Le Ménédeu, "Backward monte-carlo applied to muon transport," *Computer Physics Communications*, vol. 229, pp. 54–67, 2018.

[322] R. J. Lisle, "Google earth: A new geological resource," *Geology today*, vol. 22, no. 1, pp. 29–32, 2006.

[323] M. D'Errico, "Muon radiography applications: The study of the mt. vesuvius great cone and the search and 3d modeling of underground cavities," *PhD Thesis*, 2018-2021.

[324] "Muraves power system supplier:," [Online]. Available: https://www.victronenergy.it/.

[325] "Asd-rgb1c-p sipms," [Online]. Available: http://www.advansid.com/.

[326] S. Callier, C. D. Taille, G. Martin-Chassard, and L. Raux, "Easiroc, an easy & versatile readout device for sipm," *Physics Procedia*, vol. 37, pp. 1569–1576, 2012.

[327] G. Vilardo, G. Ventura, E. Bellucci Sessa, and C. Terranova, "Morphometry of the campi flegrei caldera (southern italy)," *Journal of maps*, vol. 9, no. 4, pp. 635–640, 2013.

[328] N Lesparre, D Gibert, J Marteau, Y Déclais, D Carbone, and E. Galichet, "Geophysical muon imaging: Feasibility and limits," *Geophysical Journal International*, vol. 183, no. 3, pp. 1348–1361, 2010.

[329] V. Kudryavtsev, "Muon simulation codes MUSIC and MUSUN for underground physics," *Comput. Phys. Comm.*, vol. 180, no. 3, p. 339, 2009, ISSN: 0010-4655. DOI: https://doi.org/10.1016/j.cpc.2008.10.013. [Online]. Available: http://www.sciencedirect.com/science/article/pii/S0010465508003640.

[330] D. Pelowitz *et al.*, "MCNPX Users Manual Version 2.7.0," Los Alamos National Laboratory, Tech. Rep. LA-CP-11-00438, 2011.

[331] R. Brun, A. McPherson, P Zanarini, M Maire, and F Bruyant, "Geant 3: User's guide geant 3.10, geant 3.11," CERN, Tech. Rep., 1987.

[332] P. Schreiner, J Reichenbacher, and M. Goodman, "Interpretation of the underground muon charge ratio," *Astroparticle Physics*, vol. 32, no. 1, pp. 61–71, 2009.

[333] B. Rastin, "A study of the muon charge ratio at sea level within the momentum range 4 to 2000 gev/c," *Journal of Physics G: Nuclear Physics*, vol. 10, no. 11, p. 1629, 1984.

[334] M. Dobbs and J. B. Hansen, "The HepMC C++ Monte Carlo event record for High Energy Physics," *Comput. Phys. Commun.*, vol. 134, pp. 41–46, 2001. DOI: 10.1016/S0010-4655(00)00189-2.

[335] D. Pagano, G. Bonomi, A. Donzella, A. Zenoni, G. Zumerle, and N. Zurlo, "EcoMug: An Efficient COsmic MUon Generator for cosmic-ray muon applications," *Nucl. Inst. Meth. A*, vol. 1014, p. 165 732, 2021.

[336] V. Niess, A. Barnoud, C. Cârloganu, and O. Martineau-Huynh, "TURTLE: A C library for an optimistic stepping through a topography," *Comp. Phys. Comm.*, vol. 247, p. 106 952, 2020, ISSN: 0010-4655. DOI: https://doi.org/10.1016/j.cpc.2019.106952. arXiv: 1904.03435 [physics.comp-ph]. [Online]. Available: https://www.sciencedirect.com/science/article/pii/S0010465519303078.